ORNL
MASTER COPY

DOE-HTGR-100229
ORNL-6836

HTGR

FUEL CAPSULE HRB-21 POSTIRRADIATION EXAMINATION DATA REPORT

No longer applies

[redacted]

[redacted] Atomic Energy Act.

AUTHORS/CONTRACTORS

R. Acharya
C. A. Baldwin
G. L. Bell
L. C. Emerson
M. L. Grossbeck
F. C. Montgomery
R. N. Morris
B. F. Myers
N. H. Packan
J. T. Parks
O. M. Stansfield

OAK RIDGE NATIONAL LABORATORY
Oak Ridge, Tennessee
managed by
MARTIN MARIETTA ENERGY SYSTEMS, INC.
for the
U.S. DEPARTMENT OF ENERGY
April 1995

DOE-HTGR-100229
ORNL-6836

FUEL CAPSULE HRB-21 POSTIRRADIATION EXAMINATION DATA REPORT

C. A. Baldwin, G. L. Bell, L. C. Emerson, M. L. Grossbeck,
R. N. Morris, B. F. Myers, N. H. Packan, J. T. Parks,
O. M. Stansfield, R. Acharya, and F. C. Montgomery

Date Published: April 1995

NOTICE This document contains information of a preliminary nature. It is subject to revision or correction and therefore does not represent a final report.

Prepared for the
U.S. Department of Energy
Office of Advanced Reactor Programs
AF 20 50 10 0

Prepared by the
OAK RIDGE NATIONAL LABORATORY
Oak Ridge, Tennessee
managed by
MARTIN MARIETTA ENERGY SYSTEMS, INC.
for the
U.S. DEPARTMENT OF ENERGY
under contract DE-AC05-84OR21400

CONTENTS

LIST OF APPENDICES vii

LIST OF FIGURES ix

LIST OF TABLES xix

SUMMARY xxiii

1. INTRODUCTION 1-1
   1.1 REFERENCES 1-5

2. DESCRIPTION OF EXPERIMENT 2-1
   2.1 OBJECTIVES 2-1
   2.2 DESCRIPTION OF FUEL SPECIMENS 2-2
      2.2.1 Coated Particles 2-2
      2.2.2 Fuel Compacts 2-2
         2.2.2.1 Compact Designs 2-2
         2.2.2.2 Compact Fabrication 2-3
         2.2.2.3 Supplemental Particle and Compact Quality Control 2-7
      2.2.3 Description of Encapsulated Piggyback Specimens 2-8
         2.2.3.1 Standard Fuel Particles 2-8
         2.2.3.2 Defective Fuel Particle 2-10
         2.2.3.3 Sorptivity Specimens 2-10
         2.2.3.4 Coated B_4C Specimens 2-12
         2.2.3.5 Dosimetry and Flux Monitors 2-13
   2.3 CAPSULE DESIGN 2-13
      2.3.1 General Description 2-13
      2.3.2 Design 2-15
         2.3.2.1 Irradiation Temperature 2-15
            2.3.2.2 Fuel Burnup 2-16
            2.3.2.3 Fluence 2-16
      2.3.3 Design Thermal Analysis 2-16
      2.3.4 Design Fuel Loadings 2-17
   2.4 IRRADIATION FACILITY 2-17
      2.4.1 Brief Description of the High Flux Isotope Reactor 2-17
      2.4.2 Materials Irradiation Facility 2-19
      2.4.3 HRB-21 Monitoring of Operation 2-19
      2.4.4 Data Acquisition 2-20

2.5 REFERENCES 2-20

3. CAPSULE OPERATION AND EVALUATION 3-1
3.1 OPERATING HISTORY 3-1
3.1.1 Operating Temperatures 3-1
3.1.2 Piggyback Specimen Temperatures 3-8
3.1.3 Fuel Temperature Uncertainty 3-20
3.1.4 Lessons Learned 3-21
3.2 FISSION GAS RELEASE 3-23
3.2.1 Methods of Monitoring Fission Gas Release 3-23
3.2.1.1 Gas Release in High Flux Isotope Reactor Experiments 3-23
3.2.1.1.1 Grab Samples 3-24
3.2.1.1.2 Transient Fission-Gas Release 3-28
3.2.1.2 Gas Release in TRIGA Experiments 3-28
3.2.1.2.1 Calibration Method 3-28
3.2.1.2.2 Absolute Method 3-30
3.2.2 Results of Monitoring Fission-Gas Release 3-31
3.2.2.1 Gas Release in High Flux Isotope Reactor Experiments 3-31
3.2.2.1.1 Release Rate/Birth Rate Measurements 3-31
3.2.2.1.2 Transient Fission-Gas Release 3-43
3.2.2.2 TRIGA Release Rate/Birth Rate Measurements 3-46
3.3 HRB-21 NEUTRON DOSIMETRY 3-47
3.3.1 General 3-47
3.3.2 HRB-21 Dosimetry Description 3-49
3.3.3 Analysis Results and Conclusions 3-50
3.4 HRB-21 BURNUP DETERMINATION 3-54
3.4.1 Recommended Neutronic Values 3-58
3.5 REFERENCES 3-58

4. POSTIRRADIATION EXAMINATION RESULTS 4-1
4.1 CAPSULE DISASSEMBLY 4-1
4.1.1 Shipping 4-1
4.1.2 Visual Examination of Capsule 4-1
4.1.3 Gamma Scanning of Capsule 4-2
4.1.4 Cutting Through Containment Tubes 4-3
4.1.5 Removal of Graphite Bodies 4-5
4.1.6 Removal of Boron Carbide Specimens 4-6
4.1.7 Removal of Components from Graphite Bodies 4-6

4.2 COMPONENT EXAMINATION 4-12
4.2.1 Visual Examination of Graphite Bodies 4-12
4.2.2 Gamma Scanning of Graphite Bodies 4-12
4.2.3 Visual Examination of Fuel Compacts 4-12
4.3 DIMENSIONAL CHANGE ANALYSIS 4-19
4.3.1 Metrology of Fuel Compacts 4-19
4.3.2 Metrology of Graphite Bodies 4-19
4.3.3 Measurement of Pushout Forces for Graphite Body End Plugs 4-36
4.4 OPENING PIGGYBACK SPECIMEN CAPSULES 4-37
4.4.1 Opening Specimen Capsules 4-37
4.4.2 Visual Examination of Piggyback Samples 4-41
4.5 IRRADIATED-MICROSPHERE GAMMA ANALYZER RESULTS ... 4-46
4.5.1 Fuel Compact Deconsolidation 4-47
4.5.1.1 Visual Exam of Particles and Debris 4-49
4.5.1.2 Analysis of Compact Deconsolidation Electrolyte 4-59
4.5.2 Particles Deconsolidated from Fuel Compacts 4-59
4.5.2.1 HRB-21 Compacts 5C, 7A, and 8A 4-60
4.5.2.2 HRB-21 Compact 5B (Leach-Burn-Leach) 4-76
4.5.3 Piggyback Fuel Particles 4-79
4.6 CERAMOGRAPHIC EXAMINATION 4-85
4.6.1 Unirradiated Fuel 4-85
4.6.1.1 Compact Ceramography 4-85
4.6.2 Irradiated Fuel 4-87
4.6.2.1 Examination Procedure 4-87
4.6.2.2 Irradiation Effects in ThO_2 and Low-Enriched Uranium UCO Kernels 4-87
4.6.2.3 Irradiation Effects in TRISO Coatings 4-92
4.6.2.3.1 IPyC 4-98
4.6.2.3.2 SiC 4-100
4.6.2.3.3 PPyC/OPyC 4-117
4.6.2.3.4 Compact Matrix 4-119
4.6.3 Summary Discussion 4-124
4.7 SCANNING ELECTRON MICROSCOPY 4-125
4.7.1 Introduction 4-125
4.7.2 Scanning Electron Microscopy Method 4-126
4.7.3 Scanning Electron Microscopy Results 4-128
4.7.3.1 Particle 5C-Fertile 4-129
4.7.3.2 Particle 5C-P1 Fissile 4-129
4.7.3.3 Particle 5C-P2 Fissile 4-133

4.7.3.4 Particle 5C-P11 Fissile 4-135
4.7.3.5 Particle 5C-P15 Fissile 4-136
4.8 LEACH-BURN-LEACH MEASUREMENTS 4-137
4.9 COMPARISON OF POSTIRRADIATION EXAMINATION TECHNIQUES AND ESTIMATES OF UNCERTAINTY 4-149
4.10 REFERENCES 4-152

5. FUEL PERFORMANCE EVALUATION 5-1
5.1 COATED PARTICLE PERFORMANCE 5-1
5.2 FUEL COMPACT IRRADIATION PERFORMANCE 5-6
5.3 REFERENCES 5-8

6. CONCLUSIONS 6-1
6.1 LESSONS LEARNED 6-5
6.2 REFERENCES 6-7

LIST OF APPENDICES

		Page
A-1	R/B Values Measured During HRB-21 Irradiation	A1-1
A-2	Capsule Conditions at R/B Sampling Times	A2-1
A-3	Fission Gas Concentration in Sweep Gas	A3-1
B	Ionization Chamber Spike Data	B-1
C	TRIGA Steady-State R/B Results for HRB-21 Compacts	C-1
D-1	Compilation of Ceramographic Data on HRB-21 Compact Particles	D1-1
D-2	Particles with SiC Damage (not including circumferential cracks)	D2-1
D-3	Particles with IPyC Damage	D3-1
D-4	HRB-21 Particle Failure Summary	D4-1

LIST OF FIGURES

Figure		Page
2.1	Schematic horizontal cross section of capsule HRB-21 showing the arrangement of the fuel compacts, encapsulated piggyback specimens, flux monitors, and thermocouples	2-14
3.1*(a)*	Measured temperatures in the graphite fuel body in position 1 of capsule	3-4
3.1*(b)*	Measured temperatures in the graphite fuel body in position 2 of capsule	3-4
3.1*(c)*	Measured temperatures in the graphite fuel body in position 3 of capsule	3-5
3.1*(d)*	Measured temperatures in the graphite fuel body in position 4 of capsule	3-5
3.1*(e)*	Measured temperatures in the graphite fuel body in position 5 of capsule	3-6
3.1*(f)*	Measured temperatures of the graphite fuel body in position 6 of capsule	3-6
3.1*(g)*	Measured temperatures of the graphite fuel body in position 7 of capsule	3-7
3.1*(h)*	Measured temperatures of the graphite fuel body in position 8 of capsule	3-7
3.2*(a)*	Predicted volume-averaged and maximum fuel temperatures (by Mapping code) as a function of effective full-power days of reactor operation for position 1 (fuel body 9)	3-9
3.2*(b)*	Predicted volume-averaged and maximum fuel temperatures (by Mapping code) as a function of effective full-power days of reactor operation for position 2 (fuel body 2)	3-9
3.2*(c)*	Predicted volume-averaged and maximum fuel temperatures (by Mapping code) as a function of effective full-power days of reactor operation for position 3 (fuel body 3)	3-10
3.2*(d)*	Predicted volume-averaged and maximum fuel temperatures (by Mapping code) as a function of effective full-power days of reactor operation for position 4 (fuel body 4)	3-10

3.2*(e)* Predicted volume-averaged and maximum fuel temperatures (by Mapping code) as a function of effective full-power days of reactor operation for position 5 (fuel body 5) 3-11

3.2*(f)* Predicted volume-averaged and maximum fuel temperatures (by Mapping code) as a function of effective full-power days of reactor operation for position 6 (fuel body 6) 3-11

3.2*(g)* Predicted volume-averaged and maximum fuel temperatures (by Mapping code) as a function of effective full-power days of reactor operation for position 7 (fuel body 7). 3-12

3.2*(h)* Predicted volume-averaged and maximum fuel temperatures (by Mapping code) as a function of effective full-power days of reactor operation for position 8 (fuel body 8) 3-12

3.2*(i)* Capsule average fuel temperature and helium concentration in purge gas 3-13

3.3*(a)* Predicted volume-averaged fuel temperature as a function of fissile particle burnup for compacts in graphite fuel bodies 9 and 8 3-13

3.3*(b)* Predicted volume-averaged fuel temperature as a function of fissile particle burnup for compacts in graphite fuel bodies 2 and 7 3-14

3.3*(c)* Predicted volume-averaged fuel temperature as a function of fissile particle burnup for compacts in graphite fuel bodies 3 and 6 3-14

3.3*(d)* Predicted volume-averaged fuel temperature as a function of fissile particle burnup for compacts in graphite fuel bodies 4 and 5 3-15

3.4*(a)* Predicted power density of fuel bodies 9 and 8 (Zone 1) 3-15

3.4*(b)* Predicted power density of fuel bodies 2 and 7 (Zone 2) 3-16

3.4*(c)* Predicted power density of fuel bodies 3 and 6 (Zone 3) 3-16

3.4*(d)* Predicted power density of fuel bodies 4 and 5 (Zone 4) 3-17

3.5 Fast fluence as a function of effective full-power days 3-17

3.6*(a)* Comparison of compact powers predicted by CACA-2 and MAPPING codes for graphite bodies 9 and 8 3-18

3.6*(b)* Comparison of compact powers predicted by CACA-2 and MAPPING codes for graphite bodies 2 and 7 3-18

3.6(*c*) Comparison of compact powers predicted by CACA-2 and MAPPING codes for graphite bodies 3 and 6 3-19

3.6(*d*) Comparison of compact powers predicted by CACA-2 and MAPPING codes for graphite bodies 4 and 5. 3-19

3.7 Release rate/birth rate of selected fission gases as a function of effective full-power days during the HRB-21 irradiation 3-33

3.8 ^{85m}Kr Release rate/birth rate and High Flux Isotope Reactor region 4 average compact temperature as a function of effective full-power days 3-35

3.9 Release rate/birth rate and region 4 compact average temperature during the first cycle of irradiation 3-36

3.10 Measured release rate/birth rate in HRB-21 capsule during the first cycle compared to the release rate/birth rate predicted using the exposed kernel model 3-37

3.11 Release rate/birth rate and region 4 compact temperature during cycle 2 as a function of effective full-power days 3-38

3.12 Release rate/birth rate as a function of the fast fluence 3-40

3.13 Half-life dependence of release rate/birth rate in HRB-21 3-41

3.14 Transient fission gas spikes and ^{85m}Kr release rate/birth rate as a function of effective full-power days 3-44

3.15 Ionization chamber spikes and estimated average compact temperature in High Flux Isotope Reactor region 4 3-45

3.16 HRB-21 Flux monitor axial location in each graphite body 3-49

3.17 Neutron flux profile measured in capsule HRB-21 3-51

3.18 Activity of ^{55}Mn flux wire from HRB-21 3-51

3.19 Activity of ^{54}Fe and ^{46}Ti flux wires from HRB-21 3-52

3.20 Activity of ^{93}Nb and ^{58}Fe flux wires from HRB-21 3-52

3.21 Comparison of neutron spectrum predicted by Pacific Northwest Laboratory STAL'SL code and the 1985 High Flux Isotope Reactor measurements 3-53

3.22 Comparison of neutron spectrum in HRB-21 as predicted by DORT at Oak Ridge National Laboratory and by Greenwood at Pacific Northwest Laboratory 3-53

4.1 Position of HRB-21 capsule disassembly cuts 4-2

4.2 Gamma scan of fuel column "B" of capsule HRB-21 prior to opening. Scan shows compact positions 8, 7, 6, 5, 4, 3, 2, and 9 4-4

4.3 Capsule HRB-21 in milling machine, after completion of upper circumferential cut 4-5

4.4 Pushout fixture, including (detached) receiving tray in foreground and installed force gage 4-6

4.5 Top view of the upper insulator with the three boron carbide holders partially out 4-7

4.6 Boron carbide specimen holders from capsule HRB-21 4-7

4.7 Schematic view of the major graphite body components. See text for references to numbered items 4-8

4.8 Fuel compact 9A, side view 4-10

4.9 Fuel compact 9A after breaking 4-10

4.10 Graphite fuel body 9, side view 4-13

4.11 Graphite fuel body 9, top view 4-13

4.12 Graphite fuel body 3, side view 4-14

4.13 Graphite fuel body 4, side view 4-14

4.14 Graphite fuel body 4, top view 4-15

4.15 Graphite fuel body 4, bottom view 4-15

4.16 Graphite fuel body 6, top view 4-16

4.17 Graphite fuel body 9, top view 4-16

4.18 Graphite fuel body 6, bottom view 4-17

4.19 Graphite fuel body 7, top view 4-17

4.20 Gamma scans (before unloading) of graphite body 7, showing intact compact 7C and broken compact 7B 4-18

4.21 Fuel compact 9B as removed, lying in tray 4-20

4.22 Fuel compact 9C in graphite body 4-20

4.23 Fuel compact 9C, upper section 4-21

4.24 Fuel compact 7A 4-21

4.25 The two sections of fuel compact 7B 4-22

4.26 Fuel compact 2A 4-22

4.27 Fuel compact 2C 4-23

4.28 Fuel compact 4A 4-23

4.29 Fuel compact 4B 4-24

4.30 Fuel compact 5A 4-24

4.31 Fracture surface of fuel compact 9B (lower segment) 4-25

4.32 Fracture surface of compact 6C (upper segment) 4-25

4.33*(a)* Comparison of measured and calculated diameter changes of fuel compacts 4-35

4.33*(b)* Comparison of measured and calculated diameter changes in the graphite fuel bodies 4-35

4.33*(c)* Comparison of measured and calculated diameter changes in the graphite fuel body holes 4-36

4.34 Piggyback specimen holder used in HRB-21. All dimensions are in millimeters 4-39

4.35 Peeled-back niobium containment with adhering fragments of graphite particle holders for piggyback capsule 2A (above) and 3A (below) 4-40

4.36 Photographs of the standard piggyback fissile particles 4-42

4.37 Photographs of the standard piggyback fertile particles after irradiation 4-43

4.38 Photographs of debris from bufferless fissile particles after irradiation 4-45

4.39 Irradiated-Microsphere Gamma Analyzer automated particle handler 4-46

4.40 Fuel compact deconsolidation apparatus 4-48

4.41 Processing sequence for compact 5C 4-50

4.42 Processing sequence for compact 6B 4-51

4.43 Processing sequence for compact 7A 4-52

4.44 Processing sequence for compact 8A 4-53

4.45 Material from the electrolytic deconsolidation of HRB-21 compact 5C: *(a)* large graphite shim and undeconsolidated portions of the compact, *(b)* unbonded fuel particles, and *(c)* small graphite shim and coating fragment debris 4-54

4.46 Examples of particles with damaged SiC coatings from HRB-21 compact 5C: *(a)* sample of particles with the more common chipped or missing SiC coating and *(b)* two particles with small hole-type defects in the SiC coating 4-56

4.47 Examples of HRB-21 compact 5C: *(a)* particles and *(b)* SiC coating fragments after burning the undeconsolidated portions of the compact and graphite debris in air at 750°C for a total of 53.5 h 4-57

4.48 Material from the electrolytic deconsolidation of HRB-21 compact 8A: *(a)* large graphite shim and undeconsolidated portions of the compact, *(b)* unbonded fuel particles, and *(c)* small graphite shim and coating fragment debris 4-58

4.49 Sample of particles from HRB-21 compact 7/A after it was electrolytically deconsolidated and then burned in air at 750°C for a total of 48 h 4-60

4.50 Normalized ^{137}Cs: ^{144}Ce ratios for fissile particles from compact 5C 4-64

4.51 Normalized ^{137}Cs: ^{144}Ce ratios for fissile particles from compact 7A 4-65

4.52 Normalized ^{137}Cs: ^{144}Ce ratios for fissile particles from compact 8A 4-66

4.53 Normalized ^{137}Cs: ^{144}Ce ratios for fertile particles from compact 5C 4-67

4.54 Normalized ^{137}Cs: ^{144}Ce ratios for fertile particles from compact 7A 4-68

4.55 Normalized ^{137}Cs: ^{144}Ce ratios for fertile particles from compact 8A 4-69

4.56 Selected fertile particles from HRB-21 compact 5C: *(a)* four particles with low ^{137}Cs: ^{144}Ce ratios and *(b)* three particles with slightly high ^{137}Cs: ^{144}Ce ratios. Note the significant difference in diameters 4-71

4.57 Portions of the random sample of material from HRB-21 compact 5B: *(a)* typical sample of particles as received, *(b)* sample of coating fragment debris, and *(c)* intact UCO buffers 4-77

4.58 Normalized ^{137}Cs: ^{144}Ce ratios for fissile particles from compact 5B 4-80

4.59 Normalized ^{137}Cs: ^{144}Ce ratios for fertile particles from compact 5B 4-81

4.60 The PyC seal coating on the buffer layer was bonded to the inner surface of the IPyC, and it remained with the IPyC as the buffer underwent irradiation-induced shrinkage. Debonding of compact matrix from PPyC and PPyC/OPyC contributed to the observed weakness of the irradiated compacts 4-88

4.61 The UCO kernel swelling was restrained by the buffer until cracks developed in the buffer. The UCO kernel swelled into the radial cracks when they developed in the buffer 4-90

4.62 Some UCO kernels showed rejected carbon on one side of the kernel in addition to kernel swelling into the buffer region. The rejected carbon which exhibited optical anisotropy under polarized light, in photo *(b)*, was the result of the "amoeba effect" kernel migration. The thickness of the rejected carbon layer, on the lower right kernel surface, was used to determine the kernel migration rate and the kernel migration coefficient 4-91

4.63 The kernel migration coefficient obtained from observed migration in three HRB-21, compact 4A, UCO particles was two orders of magnitude greater than the design curve for UCO and about a factor of two greater than the design curve for pure UO_2 4-93

4.64 Failure of the SiC layer was usually associated with failure of the IPyC layer, but not all particles with failed IPyC had failed SiC: *(a)* UCO fissile and *(b)* ThO_2 fertile 4-99

4.65 When the IPyC was failed, it usually pulled away from the SiC, and a radial crack was frequently observed nearby in the SiC 4-101

4.66 The IPyC coating provided a barrier to fission products and attack of the SiC when it was not cracked even when there was kernel swelling into buffer cracks, as in *(a)*. When cracks developed in the IPyC, fission product attack of the SiC took place, primarily at the tip of the IPyC crack, as in *(b)* 4-103

4.67 An illustration of a typical radial SiC crack. Cracks in the IPyC did not propagate into the SiC but were frequently near SiC cracks. Also illustrated is that cracks in the PPyC did not always propagate into the seal coat and OPyC 4-104

4.68 Circumferential cracks in the SiC did not always terminate at the SiC surface or remain at a constant radius 4-105

4.69 Deconsolidated from compact 5C and characterized by Irradiated Microsphere Gamma Analyzer, particle P3, about 95% of Cs was released during irradiation. Some porosity and corrosion were evident at the tip of IPyC cracks. Kernel swelling took place into buffer cracks 4-108

4.70 Deconsolidated from compact 5C and characterized by Irradiated-Microsphere Gamma Analyzer, particle P3, about 95% of Cs was released from the particle during irradiation. Corrosion of SiC was evident at the tip of the IPyC crack 4-109

4.71 Deconsolidated from compact 5C and characterized by Irradiated-Microsphere Gamma Analyzer, particle P1, about 80% of Cs was released from the particle during irradiation. There was some porosity in SiC near the IPyC crack as shown in photo *(a)*. The polarized light photo in *(b)* does not show optical activity in the IPyC at the IPyC crack tip, so graphitization of PyC, often observed in PyC with high fission product content, had not taken place 4-110

4.72 Deconsolidated from compact 5C and characterized by Irradiated-Microsphere Gamma Analyzer, particle P13. No Cs loss during irradiation. Very slight SiC porosity; no cracks in IPyC 4-111

4.73 Deconsolidated from compact 5C and characterized by Irradiated-Microsphere Gamma Analyzer, particle P11. No Cs loss during irradiation. No SiC corrosion or porosity at tip of IPyC crack 4-112

4.74 A discontinuity observed in some SiC layers was the feature known as a "gold spot". No cracks or other deleterious effects were associated with gold spots which were introduced into the SiC during coating deposition 4-113

4.75 Relatively spherical particles developed cracks in the SiC 4-114

4.76 Particles with markedly non-spherical SiC coating layers survived without SiC cracking even when other coating layers were failed. The survival of non-spherical particles at high burnup indicates that there was significant performance margin in pressure vessel design 4-115

4.77 About 1% of HRB-21 fertile particles were dimpled at the SiC stage of coating. Examples were found where dimpled fertile particles survived irradiation and did not release cesium. This provides another indication of significant margin in the pressure-vessel design 4-116

4.78 Cracks in the PPyC layer originated at the outer surface and propagated inward. Cracks in the IPyC layer originated at the inner IPyC surface and propagated outward 4-118

4.79 Illustration of typical HRB-21 compact matrix showing H-451 graphite shim particles and coated fuel particles bonded by carbonized graphite flour/petroleum pitch matrix. Shrinkage of matrix during irradiation caused extensive cracking, but no deleterious coating/matrix interaction was evident 4-120

4.80 Cross section of compact 2A (top portion), 2.3×10^{25} n/m^2 fluence, 18% FIMA (fissile), 1.2% FIMA (fertile), 957°C compact average temperature 4-122

4.81 Cross section of compact 2A (mid-section), 2.3×10^{25} n/m^2 fluence, 18% FIMA (fissile), 1.2% FIMA (fertile), 957°C compact average temperature 4-123

4.82 Energy dispersive X-ray spectrum from the region of the kernel in particle 5C-P1. Major peaks are labeled with the element of origin 4-127

4.83 Fertile particle 5C. The above view shows the entire particle, and the bottom is a closeup of the damaged area 4-130

4.84 Cross section of non retentive particle 5C-P1 fissile. This particle was deconsolidated from compact 5C and processed through Irradiated-Microsphere Gamma Analyzer. Particle P1 released ~80% of Cs during irradiation. No SiC cracks visible. Large amount of kernel swelling (~3× unirradiated volume) 4-132

4.85 Palladium X-ray scan of the outer region of non rententive particle 5C-P1 fissile showing concentration of Pd in the SiC layer. The light specks at the buffer-IPyC interface could not be associated with the segregation of any element 4-134

4.86 Photomicrograph of a cross section of the non retentive fuel particle 5C-P2 fissile 4-135

4.87 Scanning electron microscopy (secondary electron image) of non retentive particle 5C-P2 fissile, at ~125× 4-136

4.88 Scanning electron microscopy (secondary electron image) picture of non retentive particle 5C-P2 fissile showing 7 o'clock crack (~300×) 4-137

4.89 Scanning electron microscopy (secondary electron image) picture of non retentive particle 5C-P2 showing 4 o'clock crack (~300×) 4-138

4.90 Higher magnification (850×) scanning electron microscopy (secondary electron image) picture of the 4 o'clock crack in 5C-P2 fissile 4-139

4.91 Scanning electron microscopy (secondary electron image) picture of a region of SiC containing several flaws. Particle 5C-P2 fissile, 800× 4-140

4.92 Photomicrograph of retentive particle 5C-P15 fissile (~125×) 4-141

4.93 Scanning electron microscopy (back-scattered electrons) image of SiC/IPyC interface showing segregation of heavy elements (1000×). Particle 5C-P15 4-142

4.94 Local Pd L_α X-ray map of area shown in Figure 4.93 of particle 5C-P15 fissile (1000×) 4-143

4.95 Hot-cell apparatus used for leach-burn-leach test 4-144

4.96 Equivalent number of failed particles extracted from compact 5B in leach-burn-leach test as a function of the total extraction time 4-147

4.97 Equivalent number of failed particles extracted by leach-burn-leach test in compact 7C as a function of the total leach time 4-148

LIST OF TABLES

Table		Page
S-1	Measured particle failure fractions in capsule HRB-21	xxvi
2.1	Properties of UCO kernel batch NU38-10003	2-4
2.2	Properties of ThO_2 kernel batch 8778-54	2-5
2.3	Selected HRB-21 fissile particle properties	2-5
2.4	Selected HRB-21 fertile particle properties	2-6
2.5	Capsule HRB-21 coated-particle batch mean attribute data	2-6
2.6	Measured (actual) HRB-21 fuel loadings per graphite body	2-7
2.7	HRB-21 encapsulated specimen test matrix	2-9
2.8	Location and identification of sorptivity experiment samples	2-11
2.9	Coated B_4C particle piggyback specimens	2-12
2.10	Coating properties of the B_4C particles	2-13
2.11	Calculated HRB-21 fuel loadings per graphite body	2-17
3.1	HRB-21 capsule time-integrated average fuel temperature (°C)	3-20
3.2	HRB-21 capsule time-integrated average piggyback particle temperatures (°C)	3-21
3.3	Uncertainty predictions for HRB-21 in removable beryllium position	3-21
3.4	Particle failures estimated by TRIGA	3-48
3.5	Flux wire materials used in HRB-21	3-50
3.6	Measured versus calculated burnup for the UCO particles	3-56
3.7	Positional average burnup versus calculated burnup for the UCO particles	3-57
3.8	Measured versus calculated burnup for the ThO_2 particles	3-57

4.1 HRB-21 compact removal 4-11

4.2 Dimensional (diameter) changes of compact 4-26

4.3 Dimensional (length) changes of fuel compacts 4-29

4.4 Dimensional (diameter) changes of graphite bodies 4-31

4.5 Dimensional (length) changes of graphite bodies 4-32

4.6 Diameter changes of graphite body fuel holes 4-32

4.7 Push-out forces for cemented-in plugs 4-37

4.8 HRB-21 encapsulated specimen test matrix 4-38

4.9 Number of intact bufferless piggyback particles in HRB-21 4-44

4.10 Nominal compact loadings and irradiation parameters for selected HRB-21 compacts 4-61

4.11 Fuel performance based on ^{137}Cs release for selected HRB-21 compacts 4-70

4.12 Activity distribution parameters for retentive UCO particles from experiment HRB-21, compact 5C 4-73

4.13 Activity distribution parameters for ThO_2 particles from experiment HRB-21, compact 5C 4-73

4.14 Activity distribution parameters for retentive UCO particles from experiment HRB-21, compact 7A 4-74

4.15 Activity distribution parameters for ThO_2 particles from experiment HRB-21, compact 7A 4-74

4.16 Activity distribution parameters for retentive UCO particles from experiment HRB-21, compact 8A 4-75

4.17 Activity distribution parameters for fertile particles from experiment HRB-21 compact 8A 4-75

4.18 Summary of UCO particle examinations for compact HRB-21 5B 4-79

4.19 Summary of ThO_2 particle examinations for compact HRB-21 5B 4-79

4.20 Activity parameters for retentive UCO particles from compact HRB-21 5B 4-82

4.21 Activity parameters for retentive ThO_2 particles from compact HRB-21 5B 4-82

4.22 Piggyback fuel particles examined by the Irradiated-Microsphere Gamma Analyzer system 4-83

4.23 Mean ^{137}Cs:^{144}Ce ratios for various samples of particles examined by the Irradiated-Microsphere Gamma Analyzer system 4-84

4.24 Mean activities for particles recovered from piggyback capsules and examined by the Irradiated-Microsphere Gamma Analyzer system 4-86

4.25 Summary of ceramographic coating failure data for compact 1C 4-94

4.26 Summary of ceramographic coating failure data for compact 2A 4-95

4.27 Summary of ceramographic coating failure data for compact 2B 4-96

4.28 Summary of ceramographic coating failure data for compact 4A 4-97

4.29 SiC failure in particles with IPyC failure 4-102

4.30 Release versus SiC condition 4-107

4.31 Element distribution in the particles 4-131

4.32 Leach-burn-leach processing time 4-145

4.33 The number of failed particles in HRB-21 compacts based on the method of analyzing the leach solutions 4-146

4.34 Measurements of particle failure fractions in HRB-21 compacts 4-150

5.1 Measured particle failure fractions in capsule HRB-21 5-4

FUEL CAPSULE HRB-21 POSTIRRADIATION EXAMINATION DATA REPORT*

C. A. Baldwin, G. L. Bell, L. C. Emerson, M. L. Grossbeck, R. N. Morris,
B. F. Myers, N. H. Packan, J. T. Parks, O. M. Stansfield,
R. Acharya†, and F. C. Montgomery†

SUMMARY

The HRB-21 irradiation capsule experiment was carried out to provide a demonstration of the performance capability of reference Nuclear Energy Modular High-Temperaure Gas-Cooled Reactor (NE-MHTGR) fuel which consisted of uranium oxycarbide (UCO) fissile and ThO_2 fertile TRISO particles bonded into compacts. The HRB-21 irradiation test was designed to provide a fuel performance demonstration at the upper boundaries of burnup, temperature, and fast neutron fluence. The fuel was exposed to accelerated irradiation conditions in the High Flux Isotope Reactor (HFIR) test facilities at Oak Ridge National Laboratory (ORNL). The capsule was irradiated at a volume-average temperature of 932°C for 105 effective full-power days from June 20, 1991, to November 21, 1991. During irradiation, the capsule was purged with a flow of helium and neon gas, and the fission gas content of the capsule exhaust gas was monitored to provide a measure of the retentive capability of fuel as irradiation proceeded.

The initial fission gas release (release rate/birth rate, "R/B") from the capsule was extremely low ($< 5 \times 10^{-8}$ R/B ^{85m}Kr), which was a reflection of the fact that the exposed heavy metal contamination of the fuel compacts was less than 10^{-5} fraction of the fuel content. However, the fuel began to release fission gas when the fast neutron fluence exceeded about 0.7×10^{25} n/m^2. The fission gas activity of the purge gas increased rapidly to release rates on the order of 10^{-4} R/B ^{85m}Kr. During this time, numerous activity "spikes" were seen by the instruments continuously monitoring the capsule exhaust. While it is not possible to infer a clear one-to-one correspondence between activity spikes and particle failure, it was obvious long before the capsule was removed from the reactor that the fuel was suffering early failure.

---

*Research sponsored by the Office of Advanced Reactor Programs, Division of HTGRs, U.S. Department of Energy, under contract DE-AC05-84OR21400 with Martin Marietta Energy Systems, Inc.

†On loan from General Atomics, San Diego, California.

The breeding of ^{233}Pa in fertile particles and the longer-than-anticipated delays between reactor cycles allowed significant amounts of the ^{233}Pa (27-d half-life) to decay to ^{233}U which increased the amount of fissile material in the compacts. This resulted in increased power production in the fuel. In addition, the changes in the heat-transfer characteristics of the fuel compacts because of radiation-induced pyrocarbon damage made heat rejection more difficult. The net result of these two effects made temperature control increasingly difficult. After five of the planned six cycles of HFIR irradiation, the peak fuel test temperature could not be controlled within the design limit (< 1250°C), and the irradiation phase of the test was terminated.

The HRB-21 capsule was transferred to the ORNL hot cells in February 1992 and detailed examination of fuel started in June 1992. The delay was caused by conflicts with other programs and Department of Energy (DOE)-mandated improvements to the facilities performing the postirradiation examination (PIE) work. The compacts were relatively weak but they were extracted from the graphite holders without significant damage or debonding of particles. The 12 compacts in the lower half of the capsule were shipped to General Atomics, San Diego, California, where fission gas release from individual compacts was determined by activation and heating in TRIGA. The TRIGA results paralleled the large in-pile releases.

Ceramography, scanning electron microscopy (SEM), gamma analysis of individual particle fission product inventory [Irradiated Microsphere Gamma Analyzer (IMGA)], and leach-burn-leach procedures were carried out at ORNL on selected fuel compacts to characterize fuel condition. Burnup determinations were also made using IMGA data. Initial examination showed a large amount of protective pyrocarbon coating (PPyC) and outer pyrocarbon coating (OPyC) failure, with failure greatest in the high-fluence compacts. The ceramographic examination showed that the failure of the PyC coating layers increased rapidly with increasing fast neutron exposure above an exposure of about 0.7×10^{25} n/m^2. There was nearly 100% failure of the PPyC and OPyC layers in the highest fluence compacts. Failure was correlated with fast neutron fluence and compact temperature, although there is greater uncertainty in the temperature correlation because the massive pyrocarbon failure probably altered the thermal conductance of the compacts an unknown amount. The IMGA and ceramographic results indicated that particles with the lowest neutron exposure had no observable irradiation-induced coating failure, but the highest

exposure compacts had approximately 6% cracked or porous SiC coatings. The TRIGA results were essentially confirmed by PIE; the compacts with the highest TRIGA releases also showed the greatest fuel failure. There was qualitative agreement between the different PIE methods, but their sensitivity differed. However, the percent-level failures of the highest fluence compacts are clearly and consistently visible. Table S-1 summarizes the particle failure (loss of retentive capability) results.

There was a high fraction (21%) of fertile particles at low exposure in compact 1C which exhibited a long circumferential crack in the SiC. The crack usually entered and exited at the same surface so that it did not represent a source of fission product release. Neither fissile nor fertile particles at higher exposure showed SiC circumferential cracks. The circumferential cracks in the SiC were most likely induced by inward forces on the inner pyrocarbon coating (IPyC) and SiC due to the removal of SiC during grinding and polishing. Therefore, these cracks in SiC were not included in the fraction failed during irradiation.

Some buffer coatings developed radial cracks as a result of irradiation-induced shrinkage. The cracks often expanded to 20- to 50-μm width under the influence of circumferential shrinkage after the initial crack development. Shrinkage of the buffer in the radial direction was observed in some cases. The buffer cracking and swelling of the kernel were observed primarily in the UCO fission particles. The fertile, ThO_2 kernels retained their spherical shape, and buffer damage was less than in fissile particles.

Minor fission product attack of the SiC was observed at the IPyC-SiC interface of several particles examined by ceramography. The attack of the SiC took place at the tip of cracks in the IPyC where transport of fission products to the SiC was enhanced. SEM did not detect high localized concentrations of fission products in the SiC, but low levels of palladium were detected extending 5 to 10 μm uniformly into the SiC from the inner surface. Fission product attack does not appear to have played an important role in the fuel failure, at least at the percent-level failure observed.

The IPyC coating was usually in contact with the SiC. A cracked SiC was often observed when the IPyC layer was cracked. In some cases where the IPyC was cracked radially, the IPyC debonded from the SiC and curled away from the SiC as a result of irradiation-induced shrinkage of the IPyC. Observations were made of SiC tearing and fragments of SiC being pulled away as the IPyC coating curled inward. No evidence showing propagation of cracks between SiC and IPyC coating layers was observed, but the frequent

Table S-1

MEASURED PARTICLE FAILURE FRACTIONS IN CAPSULE HRB-21

Compact	Fast fluence, 10^{25} n/m^2	Burnup % FIMA[a]		SiC failure fraction						TRIGA (exposed kernel)
				Fissile			Fertile			
		Fissile	Fertile	IMGA	LBL[b]	Met[c]	IMGA	LBL[d]	Met	
4C	3.5	22	2.2			0.05			0.05	
5B	3.5	22	2.2		0.078			0.017		0.06
5C	3.5	22	2.2	0.046			0.008			0.06
2A	2.3	18	1.2			0.00			0.00	
2B	2.3	18	1.2			0.00			0.03	
7C	2.3	18	1.2		0.015			0.019		0.01
1C	1.5	14	0.5			0.00				
8A	1.5	14	0.5	0.00			0.010		0.00	2×10^{-5}

[a]FIMA = Fissions per initial metal atom. Based on calculated burnup values; Irradiated Microsphere Gamma Analyzer (IMGA) determined burnup values are approximately 15% less. See Table 3.7 in body of text.

[b]LBL = Leach-burn-leach. Based on sum of particle failures measured by ^{238}U in leach solutions (1) before burn, and (2) first leach after burn.

[c]Met = Metallography.

[d]Based on sum of particle failures measured by ^{233}U in leach solutions (1) before burn, and (2) first leach after burn.

occurrence of both coatings failed in the same particle suggested the failure mechanisms may be related. A relatively high incidence of debonding between the IPyC and SiC was present in the high-fluence compacts, usually, but not always in conjunction with a radial crack in the IPyC. A relatively small number of radial cracks in the SiC were found, nearly always with a radial crack in the IPyC in the vicinity of (but usually not in line with) the SiC crack. Thus, the PIE provides some supporting evidence for a mechanical interaction between coating layers contributing to the SiC failure mechanism.

The overall view of the fuel exposed to high fast neutron fluence was that of massive pyrocarbon failure with SiC failure at the percent level. It also appears that temperature effects, in addition to fluence, may affect fuel failure rates. Some, or all, of the SiC failure may have been induced by coating layer interactions; current PIE techniques cannot provide the necessary three-dimensional picture of the fuel to fully examine this hypothesis.

The particles contained in the piggybacks fared somewhat better than the particles in the compacts. There was far less pyrocarbon damage in the standard particles, and for both the standard fissile and standard fertile particles, there was no detectable difference in the performance of the TRISO versus the TRISO-P-type coatings.

Supplemental quality control (QC) inspections/tests were performed on samples of archived as-manufactured HRB-21 fissile and fertile fuel particles and compacts to determine if the fuel failure in the HRB-21 capsule was the result of an undetected manufacturing defect.

The SiC defect fraction for the fertile particles as measured by mercury-intrusion testing was 8.9×10^{-5}. This is about 10 times higher than the defect fraction obtained from the burn-leach test but approximately 300 times lower than the fuel particle failure fraction estimated for the irradiated HRB-21 capsule. The SiC defect fraction for the compacted fissile particles as measured by Cs-release testing was 3.3×10^{-4}. This is about 60 times higher than the defect fraction obtained from the burn-leach test but a factor of 60 lower than the failure fraction in the irradiated capsule. Overall, there is no reason to believe that the fuel began the irradiation with massive SiC defects, based on the current QC methods.

The results of the PIE leave many loose ends as is always the case when one can only see one moment in a time history and less than three dimensions in geometry, but

subsequent analysis in conjunction with this work leads one to two schools of thought:

1. **No coating interaction interpretation:** The fuel failed because the pyrocarbon (PPyC/OPyC combination) had poor irradiation stability causing the coating to fail at low fluence, and percent-level (undetected) defects existed in the SiC. Only major improvements in both coatings will produce the fuel desired by the program.
2. **Coating interaction interpretation:** Cracks in the PPyC propagated into the OPyC which caused it to fail; shrinkage and cracking of the IPyC caused high local tensile stresses in the SiC due to the strong bonding between the SiC and the IPyC (and loss of the OPyC). These high tensile stresses then caused failure of the SiC. This condition may have been enhanced by some weak SiC.

The first item may be considered to be the "pre-HRB-21 view" and the second item the "post-HRB-21 view" of fuel performance modeling. The simple fuel performance models of the past have assumed that the SiC coating is the dominant layer, and its failure is due to (in the conditions of interest for HRB-21) simple pressure-vessel destruction. The second viewpoint has emerged as a more sophisticated view of the particle as a complex structure has come into focus. While this PIE cannot conclusively demonstrate that Item 2 is the direct cause of the fuel problems, the results of the PIE buttress the argument, and process improvements along with the analysis tools developed for that theory will certainly be a step in the right direction.

During the course of this PIE, the fuel manufacturer has pursued the second option and formulated the following fuel design recommendations:

1. Eliminate the PPyC layer and return to the five-layer TRISO fuel design. Improvement in the compacting process should eliminate the need for this protective layer.
2. Reduce the thickness of the IPyC layer. Analysis has shown that thinner IPyC imposes lower local stresses on the SiC.
3. Make more isotropic and denser inner and outer pyrocarbons. Reducing irradiation-induced dimensional change in the pyrocarbons lowers the stress levels in the coating layers and thus reduces the failure level.

In addition, the optimum coating conditions for the pyrocarbon and SiC layers and improved microstructure and SiC defect characterization methods will be examined in the light of this work and past irradiation capsules. Finally, the work on capsule HRB-21 has identified a set of "lessons learned" that would benefit future programs.

SECTION 1

INTRODUCTION

As the Nuclear Energy Modular High-Temperature Gas-Cooled Reactor (NE-MHTGR) reference design evolved during the 1980s, the decision was made as part of the optimization process to eliminate the reactor containment building. The development of the MHTGR concept without a reactor containment building required that the coated fuel particle have a higher level of fission product retention than had previously been demonstrated in the U.S. program under normal and accident conditions. Confidence that such a TRISO fuel could be manufactured was generated by the success of the German high-temperature reactor (HTR) program.

The requirements for the improved fuel were thought to reside in two major areas. The first area was the reduction of heavy metal (HM) contamination in the fuel coatings and compact; the second area was the reduction of fuel particle damage during the compact fabrication process. In addition, improvements were made in the fuel to increase fission product retentivity. The fuel design, specification, and manufacturing processes were changed with the intention of improving the particle shape, reducing defective coatings, and achieving increased thermal stability of the fuel.

In order to accomplish the requirements for improved fuel, two design changes were made to the fuel particle, which represented a relatively large increment in the evolution of the TRISO coating. Those changes were (1) an increase in thickness of the inner pyrocarbon (IPyC) coating from 35 to 50 μm and (2) the application of a low-density protective pyrocarbon (PPyC) coating onto the outer pyrocarbon coating (OPyC). Coating process equipment and operation changes were also made, and they included the use of a draft tube in the coater apparatus and the addition of hydrogen to the coating gas when depositing hydrocarbons. This fuel was produced by General Atomics (GA) in their San Diego facility.

The specification of increased IPyC thickness was accompanied by increases in allowable density and anisotropy of the PyC. These changes were made in response to evidence that the frequency of SiC defects in TRISO-coated particles detected by the burn-leach method could be reduced by these IPyC specification changes. The reduction in SiC defects was thought to be related to decreased IPyC permeability for the chlorine which was

produced during subsequent SiC coating deposition. It was postulated that a reaction between the chlorine and kernel would produce gaseous reaction products which were thought to disrupt the structure of the depositing SiC coating. Therefore, changes which could reduce the permeability of the IPyC were made. To achieve the reduced permeability, it was necessary to allow a higher IPyC anisotropy which was known to lead to greater dimensional changes of the layer under irradiation. The reduced stability of the IPyC was thought to be acceptable because the IPyC was expected to have no important effect on the overall integrity of the TRISO fuel particle after the coating process was complete. After the irradiation of the fuel, more detailed structural analysis revealed that the assumption of insignificant structure impact by the IPyC layer may have been optimistic.

The PPyC layer was added to the TRISO particle design when other methods for preventing particle damage during compact fabrication were unsuccessful. The PPyC provided a relatively soft, sacrificial outer coating which prevented damage to the retentive OPyC and SiC coatings during compact fabrication. The low-density PPyC was expected to shrink and fail under irradiation conditions, but again it was assumed that its presence would not alter the overall structural behavior of the TRISO particle under irradiation conditions. It was thought that the OPyC would dominate the behavior of the outer carbon layers under irradiation, and the interaction between outer carbon layers would be unimportant.

With the thickened IPyC and the addition of the PPyC coating layer, the goal of $< 5 \times 10^{-5}$ fraction SiC defects and $< 1.0 \times 10^{-5}$ fraction of HM contamination in fuel compacts was achieved. The HRB-21 fuel had the lowest SiC defect fraction and HM contamination of high-temperature gas-cooled reactor (HTGR) coated-particle fuel manufactured in the United States until that time. The unknown price of the improved preirradiation performance was increased structural/dimensional instability under irradiation which ultimately led to poor fuel performance.

The HRB-21 capsule was an irradiation test designed to provide the first demonstration that the fuel product improvements discussed above would result in the required level of fission product retention under normal service conditions. This experiment is also part of a cooperative effort between the U.S. Department of Energy (DOE) and the Japan Atomic Energy Research Institute (JAERI). The participants are Oak Ridge National Laboratory (ORNL), GA, and the JAERI Tokai Research Establishment. Capsule HRB-21 contained the U.S. MHTGR fuel specimens, and a companion capsule, HRB-22, contains

the JAERI fuel. The JAERI fuel is of a somewhat different design than the U.S. fuel, both in particle design and compact fabrication. At the time of the postirradiation examination (PIE) of HRB-21, the irradiation of the HRB-22 capsule had not yet been carried out, but plans for irradiation were in place. The irradiation of the HRB-22 capsule was completed in the summer of 1994, and its performance was far superior to that of HRB-21, with only 4 particle failures out of a total of 32,400 particles.

The HRB-21 capsule internal test assembly consisted of eight graphite fuel holders, each containing three prototypical fuel compacts, plus special packages of neutron fluence monitors and unbonded fuel and control material particles. The fuel and capsule were fabricated in 1987 (ref. 1-1) with the expectation that the effect of the fuel design changes would be demonstrated in 1988 during irradiation in the High Flux Isotope Reactor (HFIR) at ORNL. An unexpected shutdown of HFIR for safety-related reviews resulted in more than a 3-year delay before restart of HFIR and irradiation of the HRB-21 capsule.

The irradiation of HRB-21 took place from June 20 to November 21, 1991. The test was originally scheduled to be irradiated for six reactor cycles in the modified removable beryllium (RB*) position of the HFIR. However, because of difficulty in maintaining test temperature control, the test was terminated after five reactor cycles, obtaining a peak fluence of 3.5×10^{25} n/m^2 and a peak fissile fuel burnup of 22% FIMA (fissions per initial metal atom). The fertile particles achieved a peak burnup of 2.2%. The test average temperature was about 932°C, but the maximum temperature was about 1300°C by the end of the fifth cycle of irradiation. The operational phase of the HRB-21 test has been reported previously.[1-2]

The initial fission-gas release from the capsule was extremely low [$< 5 \times 10^{-8}$ release rate/birth rate (R/B) for Kr^{85m}], which was a reflection of the low, exposed HM contamination of the fuel compacts. This initial, excellent performance was followed by rapidly increasing R/B levels when the fast neutron fluence exceeded about 0.7×10^{-25} n/m^2; ultimately, release rates of the order of 10^{-4} R/B for Kr^{85m} were reached.

Temperature control of the capsule was lost because of the additional heat produced by fissions in the bred U^{233}. The breeding of U^{233} had been accounted for in the initial heat-transfer calculations, but the reactor operation had been assumed to be almost continuous with only brief shutdowns for refueling. Actual reactor operation included longer refueling times which allowed more U^{233} to accumulate in the fuel from the decay of Pa^{233} (half-life of

27 d) than planned. Also, the thermal conductivity of the compacts may have changed to a greater degree than expected during the irradiation [changes in compact thermal conductivity would not have affected thermocouple (TC) readings]. The net result was a greater fission rate than expected in the later cycles and the final loss of temperature control.

After irradiation was completed, PIE of the fuel was carried out in the Building 3525 hot cells at ORNL. A considerable delay (5 months) was incurred between the end of irradiation and the beginning of the PIE work. This delay occurred because of conflicts with other programs and DOE-mandated improvements to the building where PIE work is done. The irradiated fuel compacts were relatively weak, but they were extracted from the graphite holders without significant damage or debonding of the particles.

The overall picture of the PIE was that considerable fuel failure took place. In the highest fluence compacts, there was almost 100% failure of the PPyC and the OPyC, in addition to an SiC failure rate of approximately 6%. The failure of the PPyC and OPyC layers was a function of fast neutron fluence and, to at least some extent, temperature. The effect of temperature is difficult to determine because of the uncertainties in the fuel thermal conductivity due to the massive pyrocarbon failure. The IPyC coating was usually observed to be in contact with the SiC layer. A cracked SiC layer was often associated with a cracked IPyC layer. No evidence showing crack propagation between the SiC and IPyC layer was noted, but the frequent occurrence of both coating failures in the same particle suggested a relationship between the two failure mechanisms.

Supplemental quality control (QC) inspections/tests were performed on samples of archived as-manufactured HRB-21 fissile and fertile fuel particles and compacts to improve the characterization of the as-manufactured fuel in support of the evaluation of the causes of the fuel failure in the HRB-21 capsule.[1-3]

Approximately 2.2% of the fertile particles and 0.04% of the fissile particles examined were found to have one or more "gold spots" (the optical manifestation of SiC soot inclusions). The SiC defect fraction for the fertile particles as measured by mercury-intrusion testing is 8.9×10^{-5}. This is about 10 times higher than the defect fraction obtained from the burn-leach test but approximately 300 times lower than the fuel particle failure fraction estimated for the irradiated HRB-21 capsule. The SiC defect fraction for the compacted fissile particles as measured by Cs-release testing is 3.3×10^{-4}. This is about

60 times higher than the defect fraction obtained from the burn-leach test but a factor of 60 lower than the failure fraction in the irradiated capsule.

Overall, there is no reason to believe that the fuel began the irradiation with massive SiC defects, based on the current QC methods.

1.1 REFERENCES

1-1. Capsule HRB-21 Pre-Irradiation Report, DOE-HTGR-88357, Rev. C, Martin Marietta Energy Systems, Inc., Oak Ridge Natl. Lab., April 1991.

1-2. G. L. Bell et al., HRB-21 Irradiation Phase Test Report, DOE-HTGR-90322, Rev. 0, Martin Marietta Energy Systems, Inc., Oak Ridge Natl. Lab., January 1994.

1-3. Testing of Archived HRB-21 Capsule Fuel, DOE-HTGR-88554, Rev. N/C, Martin Marietta Energy Systems, Inc., Oak Ridge Natl. Lab., November 1993.

SECTION 2

DESCRIPTION OF EXPERIMENT

2.1 OBJECTIVES

The objectives of capsule HRB-21 (ref. 2-1) are listed below in order of priority to the MHTGR Program:

- Provide the first in-reactor test of U.S. fuel meeting MHTGR fuel quality specifications, and provide a portion of the data necessary to validate the U.S. reference fuel performance models under normal operating conditions
- Provide a portion of the samples needed for a series of conduction cooldown simulation tests designed to provide data in support of update, as necessary, and provide data in support of the validation of the U.S. reference fuel performance model under Licensing Basis Events (LBE) conditions
- Provide in-reactor coating failure data for confirmation or revision of the defective particle performance models
- Provide irradiated, unbonded fuel particles of MHTGR reference quality for (1) direct comparison to irradiated defective particles performance and (2) selected postirradiation investigations of their structure and performance
- Provide data on partition coefficients and sorptivity isotherms of Cs, Sr, I, and Ag on MHTGR core materials
- Provide data on the irradiation performance of potential control material consisting of both pyrolytic carbon (PyC)-coated and PyC/SiC-coated particles containing boron carbide (B_4C)

Because of the poor in-pile fuel performance and abbreviated PIE, the first five of these objectives were, for all practical purposes, not met. Information on the last item may be obtained in the future, but no schedule has been set. It is not likely that the program will use this fuel design again, so the information gained from this test is of little use for fuel performance validation. The most likely outcome of this test is to influence fuel design and manufacturing. This test will add to the pyrocarbon database and may provide data on coated B_4C performance.

2.2 DESCRIPTION OF FUEL SPECIMENS

2.2.1 Coated Particles

Low-defect fuels are required for the MHTGR to meet the low fission product release limits for this reactor design. Exposed HM contamination levels in fuel compacts (uranium and thorium exposed to coolant) must be $\leq 5 \times 10^{-5}$ fraction, and the defective SiC coating fraction (fraction of uranium or thorium particles with defective SiC layer but intact OPyC and IPyC) must be $\leq 5 \times 10^{-5}$ fraction in the heat-treated fuel compacts. The specifications for the TRISO-coated uranium oxycarbide (UCO) [19.7% enriched] and ThO_2 fuel particle batches were defined in a specific document for the HRB-21 test.[2-2] A more detailed discussion of all properties is provided in refs. 2-3 through 2-5.

2.2.2 Fuel Compacts

MHTGR fuel is formed by binding the fuel particles together with a suitable matrix material and molding this combination into a rod shape which is called a "compact." The compacts are then placed into graphite fuel blocks, or in the case of the HRB-21 experiment, into graphite fuel bodies. It is important to keep clear the distinction between the fuel particles, the fuel compacts, and the graphite fuel bodies.

2.2.2.1 Compact Designs

Twenty-four fuel compacts were irradiated in capsule HRB-21 in eight H-451 graphite fuel bodies containing three compacts each. Four fissile/fertile particle loadings were specified by ORNL personnel.[2-5] These loadings and the four graphite fuel body/containment gaps were designed to flatten the temperature profile along the length of the capsule while it is irradiated in the HFIR RB* Facility. The graphite bodies with the largest body/containment gap and the compacts containing the higher uranium loadings were placed on the ends of the capsule to compensate for the lower thermal neutron flux at the capsule ends. The graphite bodies with the smaller gaps and lower uranium loadings were placed in the axial center of the capsule where the thermal neutron flux was greatest. This resulted in compacts with fissile particle loadings ranging from 7.7 to 16 vol %, fertile particle loadings of 35.1 to 37.6 vol %, and shim particle loadings of 7.4 to 12.2 vol %. The shim particles used were from Fort St. Vrain Segment 10 production and were made of unimpregnated H-451 graphite. No unfueled TRISO particles were used in the compacts.

Details on the various attributes for the fissile and fertile kernel batches used in fabrication of the compacts for HRB-21 are shown in Tables 2.1 and 2.2. Selected particle properties are shown in Tables 2.3 through 2.5. Refer to refs. 2-2 through 2-5 for more detail.

2.2.2.2 Compact Fabrication

The compacts were fabricated according to the specified weights and types of fuel and other materials as well as all pertinent process conditions. The design loading weights of the driver fissile, fertile, and shim particles were measured on an analytical balance, and the particles were placed in separate, labeled vials. The three particle charges from the vials for each compact were blended with pulses of N_2 in a single-hole blender to achieve a uniform mixture. The mixed particles were then loaded into each of the cavities of the developmental, four-hole injection molding press. In order to minimize particle breakage, a gap of approximately 1 mm was left at the top of the particle bed, and no particle bed packing force was applied to the particles by the cavity pistons prior to injection of the hot matrix. During matrix injection, a 1-mm-thick zone of pure matrix, called an end cap, was formed at the injection end of the compact as a result of the gap left during particle loading.

The four compacts were cooled after injection and then ejected from the mold. The green compacts were carbonized in alumina powder in nitrogen. After cooldown, the alumina was removed from the crucibles and brushed from the carbonized compacts. Final firing in an argon atmosphere was accomplished with the compacts freestanding in the crucibles without alumina packing. One-hundred-and sixty compacts of each blend made were fired in order to provide enough samples for QC evaluation, capsule and backup compacts, and historical samples.

The compacts were characterized to evaluate their conformance to the design specifications. The various tests and measurements were done to verify the even distribution of fuel, the total HM loading, the amount of HM outside particle coatings, and the properties and preirradiation condition of the compacts themselves. Properties measured on the actual capsule compacts were weight, dimensions, surface condition, overall fuel homogeneity, and fission gas release by TRIGA activation. All other properties and measurements were made on companion compacts. Since some of these tests are necessarily destructive ones, properties thus determined are assumed to be representative of all compacts in the fabrication lot since they were all fabricated at essentially the same time under the same conditions. The fuel loadings for the compacts are given in Table 2.6.

Table 2.1.

PROPERTIES OF UCO KERNEL BATCH NU38-10003

Property	Specification	Measured value
Density, mg/m^3	≥ 10.5	10.65
Mean diameter, μm	340 ≤ d ≤ 360	351, SD[a] = 9.70
Diameter greater than 400 μm	≤ 1.0%	< 0.1%
Weight % U	≥ 87.0	88.56
Carbon/uranium (atomic ratio)	≤ 0.4	0.2
Oxygen/uranium (atomic ratio)	≥ 1.6	1.65
Impurities, ppm[b]		
Fe	≤ 100	≤ 50[c]
Cr	≤ 100	≤ 10[c]
Ni	≤ 100	≤ 10[c]
Carbon, wt %	[d]	1.05
Oxygen, wt %	[d]	9.85
Uranium composition, wt %		
^{235}U	19.7 to 19.9	19.660
^{234}U	[d]	0.151
^{236}U	[d]	0.117
^{238}U	[d]	80.072

[a]SD = Standard deviation.
[b]ppm = Parts per million.
[c]Minimum detection value.
[d]Not specified.

Table 2.2

PROPERTIES OF ThO_2 KERNEL BATCH 8778-54

Property	Specification	Measured value
Density, mg/m^3	≥ 9.5	9.94
Mean diameter, µm	490 ≤ d ≤ 510	512 SD[a] = 8.6
Impurity, ppm[b]		
Fe	≤ 100	≤ 50[c]
Cr	≤ 100	≤ 5[c]
Ni	≤ 100	≤ 1[c]
Total impurities, ppm[b]	≤ 5000	≤ 287
Crush strength, kg	[d]	11.1 SD[a] = 3.2

[a]SD = Standard deviation.
[b]ppm = Parts per million.
[c]Minimum detection value.
[d]Not specified.

Table 2.3.

SELECTED HRB-21 FISSILE PARTICLE PROPERTIES

Layer	Thickness (µm)	Density (g/cm^3)	BAF_0	Mean defect fraction
Buffer	105.0	0.97		2.0×10^{-5a}
Seal	< 5.0			
IPyC	52.8	1.90	1.074	1.0×10^{-5a}
SiC	32.6	3.22		1.5×10^{-6b}
OPyC	46.8	1.84[c]	1.038	$\leq 6.9 \times 10^{-6a}$
O-Seal	< 5.0			
PPyC	46.4	0.998[d]		3.3×10^{-7e}

[a]X-Radiography on 100,000 particles.
[b]Determined by burn-leach prior to loading into compacts.
[c]Bulk density.
[d]Calculated density.
[e]Heavy metal contamination by TRIGA/HCL leach.

Table 2.4

SELECTED HRB-21 FERTILE PARTICLE PROPERTIES

Layer	Thickness (μm)	Density (g/cm^3)	BAF_0	Mean defect fraction
Buffer	67.1	1.02		$\leq 6.9 \times 10^{-6}$[a]
Seal	< 5.0			
IPyC	56.8	1.91	1.106	1.0×10^{-5}[a]
SiC	36.0	3.19		8.6×10^{-6}[b]
OPyC	41.1	1.84[c]	1.042	$\leq 6.9 \times 10^{-6}$[a]
O-Seal	< 5.0			
P-PyC	45.4	0.88[d]		7.0×10^{-8}[e]

[a]X-Radiography on 100,000 particles.
[b]Determined by burn-leach prior to loading into compacts.
[c]Bulk density.
[d]Calculated density.
[e]Heavy metal contamination by TRIGA/HCL leach.

Table 2.5.

CAPSULE HRB-21 COATED-PARTICLE BATCH MEAN ATTRIBUTE DATA

Parameter	Fissile	Fertile
Batch number	8876-70-0	8876-58-0
Kernel composition	UCO	ThO_2
Particle diameter, μm	904	988
Particle density, mg/m^3	2.14	3.02
Particle volume, cm^3	3.87×10^{-4}	5.05×10^{-4}
Number of particles per g	1207	656
g of U per particle	2.12×10^{-4}	
g of ^{235}U per particle	4.18×10^{-5}	
g of Th per particle		6.32×10^{-4}
U wt % per particle	25.55	
Th wt % per particle		41.44

Table 2.6.

MEASURED (ACTUAL) HRB-21 FUEL LOADINGS PER GRAPHITE BODY (3 COMPACTS PER GRAPHITE BODY)

Graphite body No.	Blend No.	Total ^{235}U load (g)	Total ^{238}U load (g)	Total $^{235+238}U$ load (g)	Total ^{232}Th load (g)	No. of fissile particles[a]	No. of fertile particles[a]
9,8[b]	1	0.304	1.244	1.548	7.065	7,490	12,590
2,7	2	0.237	0.969	1.206	7.620	5,840	13,580
3,6	3	0.176	0.718	0.894	7.620	4,340	13,580
4,5	4	0.146	0.598	0.744	7.500	3,600	13,370
Total for 8 graphite bodies (24 compacts)						42,540	106,240

[a]Based on 4.06×10^{-5} g ^{235}U per particle and 5.61×10^{-4} g Th per particle.
[b]Body No. 9 replaced body No. 1 which was not used.

2.2.2.3 Supplemental Particle and Compact Quality Control

Supplemental QC inspections/tests were performed on samples of archived as-manufactured HRB-21 fissile and fertile fuel particles and compacts to improve the characterization of the as-manufactured fuel in support of the evaluation of the causes of the fuel failure in the HRB-21 capsule (see ref. 1-3, Sect. 1.1).

Approximately 2.2% of the fertile particles and 0.04% of the fissile particles examined were found to have one or more "gold spots" (the optical manifestation of SiC soot inclusions). The SiC defect fraction for the fertile particles as measured by mercury-intrusion testing is 8.9×10^{-5}. This is about 10 times higher than the defect fraction obtained from the burn-leach test but approximately 300 times lower than the fuel particle failure fraction estimated for the irradiated HRB-21 capsule. The SiC defect fraction for the compacted fissile particles as measured by Cs-release testing is 3.3×10^{-4}. This is about 60 times higher than the defect fraction obtained from the burn-leach test but a factor of 60 lower than the failure fraction in the irradiated capsule. These tests suggest that the burn-leach test may not find all defects in the SiC, but there is no reason to believe that the fuel began the irradiation with massive SiC defects, based on the current QC methods. In

addition, the microstructural examination of the particles revealed no structural defects other than the gold spots and little evidence of metallic impurities within the coating layers.

The HRB-21 fuel was also compared to the German MHTGR Program proof-test particles. Both particle populations are characterized by columnar grains, but the average grain length is smaller in the German particles (2 to 5 μm) than in the HRB-21 particles (8 to 12 μm). The German SiC coatings also have more porosity than the SiC coatings in either the HRB-21 fertile or fissile particles. One coating difference was that the SiC coating penetrates in the IPyC layer in the German particles but not in the HRB-21 particles. The SiC defect fraction measured by mercury-intrusion testing is substantially higher for the German particles than for the HRB-21 fertile or fissile particles. However, the SiC defect fraction measured by Cs-release testing is lower for the German particles than for the compacted or loose HRB-21 fissile particles.

While the testing performed on samples of archived, as-manufactured HRB-21 fissile and fertile fuel particles and compacts provided additional information on the consistency of QC methods and fuel microstructure, no indication of massively defective fuel was found.

2.2.3 Description of Encapsulated Piggyback Specimens

Each of the HRB-21 capsule graphite bodies included three 2.38-mm (0.094-in.) -diam holes for encapsulated specimens ("piggybacks"). The piggyback samples were sealed within niobium tubes up to 52 mm (2.00 in.) long by 2.21 mm (0.087 in.) diam and placed in specimen holes in the graphite fuel bodies. The general loading arrangement for these specimens is shown in Table 2.7. Samples of unbonded fissile and fertile particles from the same particle batches that were used in the fuel compacts were included to compare with the bufferless defective particle performance. Piggyback sorptivity experiments were designed to determine the partition coefficients of several fission products on core materials. Coated B_4C samples were included as a first irradiation performance test of coated B_4C control materials. Dosimetry and flux monitors were included in each graphite fuel body as piggyback experiments but were located in three separate flux monitor holes in each body. The various sample types are described in more detail below. For greater detail, see ref. 2-3.

2.2.3.1 Standard Fuel Particles

Samples of unbonded standard fissile and fertile TRISO fuel particles from the same batches used in the compacts were placed in hole A within graphite bodies 2 and 7 (see

Table 2.7.

HRB-21 ENCAPSULATED SPECIMEN TEST MATRIX

Graphite body No.	Piggyback sample hole		
	A	B	C
9	S	S	D (U) TRISO
2	Standard (U) TRISO-P	D (U) TRISO	D (U) TRISO
3	Standard (U) TRISO	D (U) TRISO	D (U) TRISO
4	S	S	D (U) TRISO
5	S	S	D (Th) TRISO
6	Standard (Th) TRISO	D (Th) TRISO	D (Th) TRISO
7	Standard (Th) TRISO-P	D (Th) TRISO	D (Th) TRISO
8	S	S	D (Th) TRISO

NOTES:

S = Sorptivity specimens.
D (U) = Fissile, defective (missing buffer) particles (batch 8876-96).
D (Th) = Fertile, defective (missing buffer) particles (batch 8876-100).
Standard (U) = Fissile, nondefective particles (batch 8876-70).
Standard (Th) = Fertile, nondefective particles (batch 8878-58).
TRISO refers to coating without protective coat (batches 8876-70 and 8876-58).
TRISO-P refers to coating with protective coat (batches 8876-70-0 and 8876-58-0).

Table 2.7) and TRISO particles without the protective coat (PPyC) in bodies 3 and 6. These latter particles (GA coating batches 8876-70 and 8876-58) were identical to the substrate of the reference TRISO batches of fissile and fertile particles since the protective coat (PPyC) was added to only a portion of these coating batches to produce the reference fuel. The purpose of these samples was to compare the irradiation performance of the TRISO particles with and without the PPyC coating. The unbonded standard particles were also included for selected postirradiation analyses and investigations regarding materials performance and fission product transport.

2.2.3.2 Defective Fuel Particle

Particles with missing buffer layers are predicted to fail and be the most significant contributors to fission product release during LBEs involving conduction cooldown or water ingress in the MHTGR. Data are needed for potential revision of the bufferless particle failure model to reduce the uncertainty associated with the present correlation.

TRISO-coated UCO and ThO_2 particles with missing buffer coatings were prepared in a standard batch load by adding 10% of the kernels to the batches after the buffer and seal coating layers had been deposited on 90% of the kernels. The IPyC, SiC, and OPyC coating layers were deposited on the full coated-particle batches after the addition of the bare kernels at the end of the seal coating stage. Separation of the fraction of the batch with the missing buffer coatings was conducted by screening the materials through the appropriate screen sizes to isolate these missing buffer-coated particles from the remainder of the batches.

2.2.3.3 Sorptivity Specimens

An array of in-reactor sorptivity experiments was included to allow determination of the partition coefficients of several selected fission products on core materials as a function of temperature, fast neutron fluence, fission product concentration, material, and extent of material oxidation. The results of previous irradiation tests are reported in ref. 2-6. The method consists of encapsulating several solid materials in a small, niobium tube, along with a known quantity of a fission product. Consequently, the contained system consists of a gaseous phase and several solid phases. A redistribution of fission products occurs with increasing irradiation damage and approaches a thermodynamic equilibrium. The gas phase concentration is sufficiently small, so that upon cooling from the relatively high temperature of the experiment, the gaseous fission products condensing on the solid phase do not appreciably alter the distribution established at the higher temperatures.

A summary description of the experiments is given in Table 2.8. There were 44 samples for the HRB-21 sorptivity experiments. Twenty-eight of these were put into the reactor, and 16 were to be heated in laboratory experiments at ORNL. In Table 2.8, the graphite body position, fast neutron fluence, and hole location of each experiment are given. The experiments are further identified by the materials and by the fission product elements involved. The materials are represented by the letters "G" for graphite, "M" for matrix, "P"

Table 2.8.

LOCATION AND IDENTIFICATION OF SORPTIVITY EXPERIMENT SAMPLES

Graphite body position	Calculated fluence at EOL (10^{25}n/m^2)	Hole A		Hole B	
		Material	Simulated fission product X(i)	Material	Simulated fission product X(i)
1	2.2	h_GMPS GM GM	Cs+Ag(1) Ag(1) I(1)	h_{Go}MPS GM GM	Cs+Ag(1) Ag(2) I(2)
4	4.9	h_GMPS GM GM	Cs+Ag(1) Ag(1) I(1)	h_{Go}MPS GM GM	Cs+Ag(1) Ag(2) I(2)
5	4.9	GoM GM GM GM	Ag(1) Cs+I(1) Sr(1) Sr(2)	GoM GoM GoM GoM	I(1) Cs+I(1) Sr(1) Sr(2)
8	2.2	GoM GoM GM GM	Ag(1) Ag(2) Cs+I(1) Sr	GoM GoM GoM GoM	I(1) I(2) Cs+I(1) Sr
NA	0.0	h_GMPS GM GM	Cs+Ag(1) Ag(1) I(1)	h_{Go}MPS GM GM	Cs+Ag(1) I(2) I(2)
NA	0.0	GoM GoM GM GM GM	Ag(1) Ag(2) Cs+I(1) Sr(1) Sr(2)	GoM GoM GoM GoM GoM	I(1) I(2) Cs+I(1) Sr(1) Sr(2)

NOTE:

G = graphite cylinder, M = matrix cylinder, P = standard inert particle, S = OPyC denuded inert particle, h_G = graphite hollow cylinder, Go = oxidized graphite (1 wt % burnoff), X(i) = fission product X at concentration Level i, EOL = end of life, and NA = not applicable.

for inert particle, "S" for OPyC denuded particle, and "Go" for oxidized graphite. Fission product elements listed have associated numbers (in parentheses) to indicate the concentrations, either at a value of one or two. See ref. 2-3 for details. The sorptivity specimens were fabricated at ORNL using materials supplied by GA.

2.2.3.4 Coated B_4C Specimens

The coated B_4C particles consisted of two types. One batch of particles was PyC coated, and the other had a PyC/SiC coating. The particles were placed within 5.1-mm (0.200-in.) outside diameter (OD) POCO graphite crucibles with a length of 28 mm (1.10 in.). Each graphite crucible was loaded with approximately 500 particles of each B_4C particle type as shown in Table 2.9. Six of the B_4C crucibles were located in the upper insulator of the HRB-21 capsule. This insulator was located just above graphite body position 1 and is in a position approximately 260 mm above the HFIR horizontal midplane.

Table 2.9.

COATED B_4C PARTICLE PIGGYBACK SPECIMENS

B_4C particle identification	Crucible identification[a]	Net weight of B_4C particles (g)	Estimated No. of B_4C particles[b]
8876-110	1	0.0201	510
8876-110	2	0.0196	497
8876-110	3	0.0202	512
8876-112	4	0.0282	489
8876-112	5	0.0284	493
8876-112	6	0.0290	503

[a]Numbers are scribed on the crucible body.

[b]Based on measured particle weights of 3.994×10^{-5} and 5.761×10^{-5} g per particle for batches 8876-110 and 8876-112, respectively. (Approximate kernel weight per particle = 5.8×10^{-5} g.)

Boron carbide (B_4C) is expected to be used as the neutron poison in the control assemblies of the MHTGR. Exposure to moisture in the reactor could result in the loss of boron from the burnable poison compacts or the reserve shutdown pellets in the MHTGR and could present serious fission control problems for the reactor system. Test samples with protective coatings were included in the HRB-21 capsule to demonstrate that this coating would remain intact during irradiation. PyC and SiC coatings were deposited on crushed

B_4C granules in the 240-mm coater. The coating properties for the two B_4C-coated particle batches produced for use in the capsule are presented in Table 2.10.

Microscopic examination of the coated B_4C particles indicated that the PyC and SiC coating microstructures were of high quality and similar in appearance to those coatings deposited on nuclear fuel particles.

Table 2.10.

COATING PROPERTIES OF THE B_4C PARTICLES

Run No.	Thickness (μm)	Density (mg/m^3)
8876-110		
Buffer	18.0	Not measured
Seal	Not measured	Not measured
IPyC	22.7	1.87
8876-112		
Buffer	20.2	Not measured
Seal	Not measured	Not measured
SiC	22.1	Not measured

2.2.3.5 Dosimetry and Flux Monitors

Appropriate dosimetry obtained from Argonne National Laboratory was placed in each graphite body of HRB-21. It is of the same type of dosimetry used in the ORNL Magnetic Fusion Energy Program's irradiation capsules. The dosimeter material was such that the total fluence, thermal fluence, and fast neutron fluence could be determined by postirradiation analysis of the dosimetry.

2.3 CAPSULE DESIGN

2.3.1 General Description

The HRB-21 irradiation capsule was the first of a new, larger diameter capsule design to be irradiated in one of three new positions in the RB reflector in the HFIR. These reflector positions permitted purged graphite fuel bodies to contain three full-diameter fuel

compact stacks (rather than one, as in HRB-1 through -18) in graphite bodies that were 38.1 mm (1.5 in.) in diameter rather than 23.9 mm (0.94 in.) as in previous HFIR capsules. The eight graphite fuel bodies each contained three piggyback holes in which coated fuel particles or sorptivity experiments in sealed niobium containers were irradiated. Each fuel body was also designed to contain TCs and dosimetry samples. The test operating procedures are given in ref. 2-7.

The HRB-21 irradiation capsule consisted of a double-contained, single-purged cell with fuel compacts contained in H-451 graphite bodies (see Figure 2.1). The fuel compacts,

ORNL-DWG 88-11041

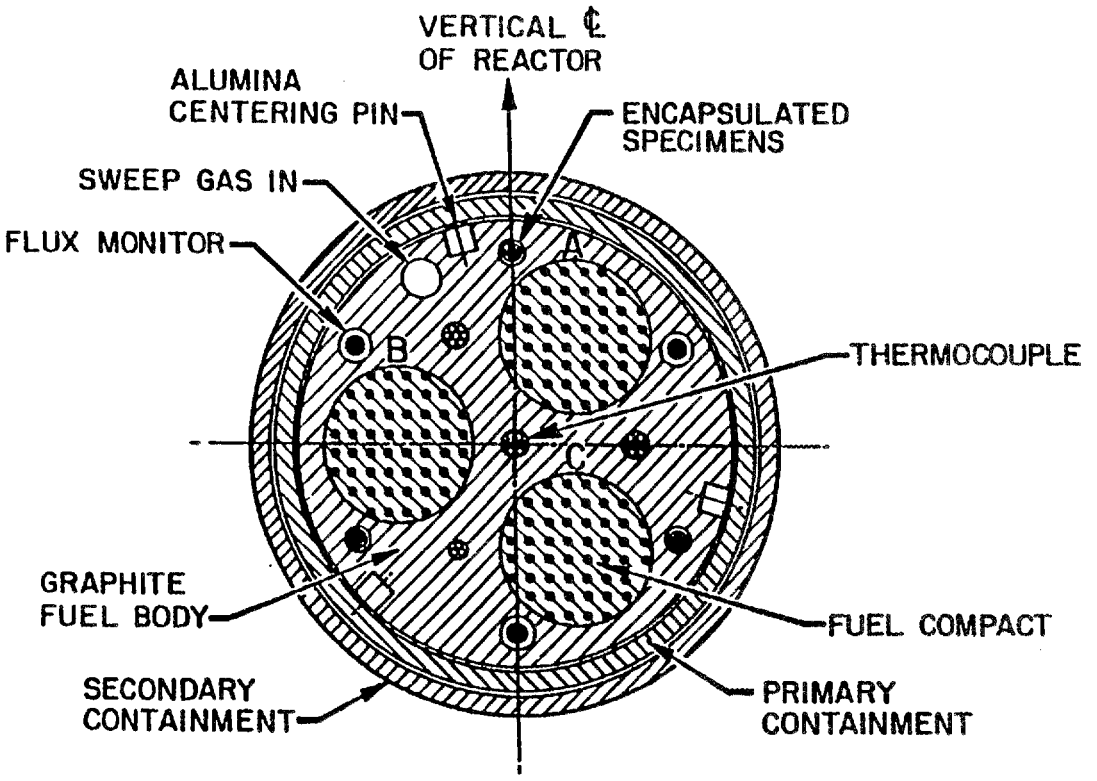

Figure 2.1.

SCHEMATIC HORIZONTAL CROSS SECTION OF CAPSULE HRB-21 SHOWING THE ARRANGEMENT OF THE FUEL COMPACTS, ENCAPSULATED PIGGYBACK SPECIMENS, FLUX MONITORS, AND THERMOCOUPLES.

three per graphite body, were composed of the TRISO-coated UCO and ThO_2 particles with protective coatings embedded in graphite matrix material. The eight graphite bodies were contained within two Inconel 718 containment tubes designed to independently withstand 6.9 MPa (1000 psi) internal or external pressure. During HFIR operation, pure helium at 5.5 MPa (800 psi) was contained between the primary and secondary Inconel containments. A gas mixture of helium (He) and neon (Ne) flowed between the primary Inconel containment and the graphite body surface. By varying this gas mixture within the primary containment, the radial conductance of heat to the surrounding HFIR cooling water system was controlled, and the operating temperature of the fuel compacts was regulated. The entire capsule was fitted within an outer aluminum liner designed to protect the HFIR beryllium reflector.

The use of the stronger Inconel 718, in place of the stainless steel 304 primary containment used in earlier HRB capsules, allowed thinner containment walls and larger graphite fuel bodies so that irradiation of a larger number of particles was possible. This was especially important because large sample sizes were needed to validate the very low failure fraction expectations for the MHTGR candidate fuel of HRB-21.

2.3.2 Design

2.3.2.1 Irradiation Temperature

Capsule HRB-21 was designed to have a target fuel compact centerline mean temperature of 975°C. The design of the capsule took place when the expected operational power of HFIR was 100 MW. Before the capsule was irradiated, the operational power of HFIR had been downgraded to 85 MW. The reduced power level resulted in no operational problems or difficulties in meeting the target temperatures. The graphite body radial gaps and fuel compact loadings were specified to maintain the 975°C target temperature as uniformly as possible over the length of the capsule. Fuel compact temperatures were inferred from knowledge of the power, graphite TC temperature data, and the preirradiation design thermal analysis. In-reactor temperature control was maintained by adjusting the Ne and He concentrations in the sweep gas. After irradiation and completion of the fuel/graphite metrology, a detailed thermal analysis was performed to obtain in-reactor fuel compact temperatures.

No TCs were placed within the fuel compacts. The fuel operating temperature uncertainty during irradiation was estimated to be as much as ±125°C. The average value for the graphite operating temperature was expected to be approximately 650°C. Details of the capsule history are described in Sect. 3.

2.3.2.2 Fuel Burnup

The HRB-21 fissile and fertile particle fuel burnup estimates were made at ORNL using the CACA-II fuel depletion code[2-8] for a six-cycle irradiation in the HFIR RB* Facility. The maximum, expected end-of-life (EOL) burnup near the HFIR midplane (positions 4 and 5) was predicted to be 24.4% FIMA for the fissile fuel and 2.7% for the fertile fuel. The minimum expected EOL burnup at graphite body positions 1 and 8 was 15.5% FIMA for fissile particles and 0.7% FIMA for fertile particles. Calculations of burnup based on dosimetry data and unbonded particle analysis were performed during HRB-21 PIEs and are reported in Sect. 3.4.

2.3.2.3 Fluence

The expected HRB-21 fast fluence exposure values were calculated utilizing dosimetry data acquired previously.[2-9] Due to the modifications to the RB reflector (designated the RB* positions) the fluence predictions are not known precisely and may be in error by approximately 10%. Dosimetry located within the HRB-21 graphite bodies provided measured flux and energy spectrum values.

2.3.3 Design Thermal Analysis

The HRB-21 design thermal analysis was performed at ORNL with the HEATING7 (ref. 2-10) code utilizing a three-dimensional (3-D) model in cylindrical coordinates. The model consisted of a graphite holder with insulated boundary conditions on the top, bottom, and planes of symmetry. The model is rather involved, and the reader is referred to the references at the end of this chapter for the history of the design and the details.

All of the TCs in HRB-21 were placed within the graphite bodies. A total of 24 junctions were used to monitor the graphite temperatures in four separate thermocouple array assemblies.

2.3.4 Design Fuel Loadings

The calculated design HRB-21 fuel loadings per graphite fuel body are shown in Table 2.11. Note that graphite body 1 was replaced with graphite body 9 prior to irradiation. Unfortunately, the program did not rename this graphite body but did rename the compacts it contains. This can lead to some confusion. The compacts in graphite body 9 are 1A, 1B, and 1C. For all purposes except QC paperwork, one may regard the graphite fuel body numbers 1 and 9 as the same.

Table 2.11

CALCULATED HRB-21 FUEL LOADINGS PER GRAPHITE BODY (3 COMPACTS PER GRAPHITE BODY)

Capsule position No.	Graphite body No.	Total ^{235}U load (g)	Total ^{238}U load (g)	Total $^{235+238}U$ load (g)	Total ^{232}Th load (g)
1,8	9,8	0.288	1.173	1.460	7.500
2,7	2,7	0.139	0.975	1.214	7.500
3,6	3,6	0.176	0.716	0.891	7.500
4,5	4,5	0.146	0.594	0.740	7.500

Note that graphite body 1 was replaced by graphite body 9 prior to irradiation. The compacts were not renumbered, so graphite body 9 contains compacts 1A, 1B, and 1C. The nuclear and thermal environment remained unchanged.

2.4 IRRADIATION FACILITY

2.4.1 Brief Description of High Flux Isotope Reactor

HFIR is a beryllium-reflected, light-water-cooled and moderated flux-trap-type reactor which uses highly enriched ^{235}U (HEU) as the fuel. HFIR is a versatile isotope production and test reactor with the capability and facilities for performing a wide variety of irradiation experiments. HFIR is a pressurized light-water-cooled and moderated thermal nuclear reactor designed to operate at 100-MW(t) steady-state power. Current operation is limited to 85 MW(t) to extend the reactor vessel service life.

HFIR was designed and built in the early 1960s. Initial criticality and commencement of low-power physics testing began in early 1965. Full power was first achieved on September 9, 1966. HFIR is unique in the sense that it provides the highest neutron fluxes available in any of the world's reactors, and neutron currents from the four horizonal beam tubes are among the highest available. A brief summary of the primary characteristics is as follows:

CHARACTERISTICS OF THE HFIR

Design power.....100 MW(t)

Current operation.....85 MW(t)

NOTE: Current operation limited to 85 MW to extend reactor vessel life.

Coolant/moderator.....Pressurized light water

Reflector.....Beryllium

Typical neutron fluxes (unperturbed):

Reactor area	Thermal neutron flux [n/cm^2∘ s]	Fast flux (> .183 MeV) [n/cm^2∘ s]
Target region	~2 × 10^{15}	~1 × 10^{15} [a]
Experiments	0.2 to 1 × 10^{15}	0.01 to 0.8 × 10^{15} [a]
RB*	1 to 2 × 10^{15}	2 to 4 × 10^{14} [a]

[a]To convert to equivalent graphite damage flux for HTGR, multiply by 0.93 (refs. 2-11 and 2-12).

A fuel cycle for HFIR normally consists of full-power operation for a period of from 21 to 23 d (depending on the experiment and radioisotope load in the reactor) followed by an end-of-cycle (EOC) shutdown for refueling and changeout of targets and tests. This corresponds to ~1800 to 2000 MWd per cycle at 85-MW thermal power.

HFIR cycles 298 through 302 irradiated the HRB-21 test in position RB-38. The reactor data were monitored and informally reviewed by the principal investigator as they were collected as part of the data validation process. The data exhibited no unusual or inexplicable characteristics.

2.4.2 Materials Irradiation Facility

Instrument and control functions for each experiment are provided by the Material Irradiation Facility (MIF). Each MIF consists of an integrated set of instruments, recorders, and controllers, plus associated piping, wiring, and power supplies, and an automated data acquisition system (DAS).

The system is designed to be connected directly with an in-pile experiment assembly to provide test monitoring, gas flow and temperature control, and data collection. The test can be located in any HFIR irradiation position. The MIF also serves as the data interface between the test specimens, the reactor control room, and the test sponsor. Instruments which are key to proper test control provide a local MIF panel alarm and a remote common alarm in the reactor control room. The reactor control system is designed to permit selected direct inputs from the MIF to the reactor control system and to provide automatic power reduction, if required.

Currently, there are five operational MIFs in the HFIR Facility Experiment Control Room (ECR). Capsule HRB-21 utilized MIF 2. Most of the experiments which utilize the MIFs have similar control and monitoring needs. The equipment common to the operation of five similar facilities, i.e., electrical power source, gas bottle stations, molecular sieve and titanium sponge gas-cleanup systems, sweep gas sampling system, etc., is installed in the HFIR ECR.

2.4.3 HRB-21 Monitoring of Operation

Operating temperatures in HRB-21 were measured by 24 TCs incorporated into 4 discrete thermocouple central array tubes (TCATs). The locations of the TCATs and the individual TC junctions are discussed in Sect. 3.5.

The gas pressure between the primary and secondary containment vessels (nominally 800 psig) was monitored continuously by three strain-gage-type pressure transducers. The outputs of these transducers were connected to an automated power reduction system such that a loss of pressure, through a leak in either the primary or secondary containments, would reduce the reactor power to 10% of full power.

The He and Ne sweep gas (secondary gas system) flows were measured by three mass flowmeters, two on the inlet side measuring the individual gas flows and one on the outlet side measuring the combined flows. The pressure of the sweep gas system was also

monitored through the use of two pressure transducers, one on the inlet and one on the outlet lines.

In addition to flow and pressure, the sweep gas outlet lines were monitored for radioactivity through the use of two ionization chambers. About 15 ft of the 0.125-in. offgas outlet-line tubing was coiled around the monitors. This system was sensitive enough to discern single particle failures through the burst of activity released by such failures. The output of the monitors was continuously recorded on strip-chart recorders, and the analysis of these data is discussed in Sect. 4.4 of this report.

2.4.4 Data Acquisition

TC outputs, primary and secondary gas pressures, and sweep gas flow rates were recorded every 6 s on a hard disk using Kayeview software on a personal computer connected to a Kaye Digi-4 combination strip-chart recorder and DAS. During steady-state operation, these data were printed at 5-min intervals. All of the hard-disk data were transferred to 5.25-in. Bernoulli disks for storage. The data were managed and evaluated in accordance with the "Fuel Material Testing Group Data Management Guideline" as outlined in the operating guideline, Fuel Materials Testing Group Mission Statement and Responsibility Matrix (document MET-NFM-GP-001).

2.5 REFERENCES

2-1. HRB-21 Test Specification, DOE-HTGR-88331, Rev. N/C, General Atomics, San Diego, Calif., September 1989.

2-2. T. F. Hefferman, Fuel Product Specification for Irradiation Capsule HRB- 21, DOE-HTGR-88539, General Atomics, San Diego, Calif., April 1991.

2-3. T. F. Heffernan, Capsule HRB-21 Preirradiation Report, DOE-HTGR-88357, Rev. C, General Atomics, San Diego, Calif., April 1991.

2-4. Fuel Product Specification for MHTGR, DOE-HTGR-86081, Rev. F, General Atomics, San Diego, Calif., June 1989.

2-5. D. T. Goodin, M. J. Kania, and B. W. Patton, Experimental Plan for Irradiation Experiment HRB-21, DOE-HTGR-87091, General Atomics, San Diego, Calif., April 1989.

2-6. B. F. Myers, Fission Product Transport in Reactor Experiments, HTGR-085-115, 908309, Rev. 0, Martin Marietta Energy Systems, Inc., Oak Ridge Natl. Lab., September 1985.

2-7. N. H. Packan et al., Operating Plan for Capsule HRB-21 Irradiation, DOE-HTGR-88370, Martin Marietta Energy Systems, Inc., Oak Ridge Natl. Lab., December 1989.

2-8. E. J. Allen, CACA II: Revised Version of CACA-I Heavy Isotopes and Fission Product Concentration Calculational Code for Experimental Irradiation Capsules, ORNL/TM 5266, Union Carbide Corp. Nuclear Div., Oak Ridge Natl. Lab., February 1976.

2-9. Gas-Cooled Reactor Programs, High-Temperature Gas-Cooled Reactor Technology Development Program, Annual Progress Report for Period Ending December 31, 1981, ORNL-5871, Union Carbide Corp. Nuclear Div., Oak Ridge Natl. Lab., June 1982.

2-10. D. C. Elrod et. al., Heating 6: Multidimensional Heat Conduction Analysis with the Finite-Difference Formulation, ORNL Radiation Shielding Information Center Documentation for RSIC Code Package PSR-199, Feb. 1, 1985.

2-11. H. T. Kerr et al., Lattice Displacement Calculations and Compilations for Different Irradiation Facilities, ORNL/TM-5269, Union Carbide Corp. Nuclear Div., Oak Ridge Natl. Lab., 1976.

2-12. B. F. Myers, Compilation of Data on Reactor Experiment for Use in Fission Product Transport Calculations, HBK-IB-05184, Kernforschungsanlage, Jülich Gmbh, Germany, 1984.

SECTION 3
CAPSULE OPERATION AND EVALUATION

A detailed description of the operation of the capsule, the thermal analysis methodology used, and the results can be found in the HRB-21 Irradiation Phase Report.[3-1] After the irradiation phase report was published, important features, such as a detailed representation of the change in the graphite dimensions as a function of fast neutron fluence, were incorporated into the computer model, and the thermal analysis was repeated. These improvements did not change the average fuel operating temperatures significantly. The following sections are devoted to a brief discussion of the methodology, followed by a discussion of the final thermal analysis results and recommendations for improving the capsule design from a thermal performance viewpoint.

3.1 OPERATING HISTORY

The HRB-21 was irradiated in HFIR for a total of five reactor cycles. The irradiation was performed in the RB Facility. The capsule was in the reactor during cycles 299 through 303, accumulating a total of 105 effective reactor full-power [85 MW(t)] days of operation.

The test was originally scheduled to be irradiated for six reactor cycles in the modified RB* position of the HFIR. However, because of difficulty in maintaining test temperature control, the test was terminated after five reactor cycles, obtaining a peak fluence of ~ 3.5×10^{25} n/m^2 and a peak fuel fissile burnup of ~ 22% FIMA. Both cycles 4 and 5 were run at 100% helium sweep gas.

3.1.1 Operating Temperatures

The HRB-21 capsule did not have TCs in direct contact with the fuel compacts because of the high temperature of operation. The irradiation capsule consisted of eight graphite fuel bodies, each containing three fuel compacts. TCs were installed in the graphite fuel body at positions corresponding to the axial midplane of the fuel compact. The temperature of the fuel compacts was calculated based on the measurements of the graphite fuel body temperatures, the thermal properties of the graphite, and the thermal properties of the fuel compacts.

The calculated fuel temperatures are a function of several variables, including the measured graphite body temperature, the thermal conductivities of the graphite body and the fuel compact, the gas gap between the fuel compact and the graphite body, the gas gap between the graphite fuel body and the Inconel pressure vessel, and the gas composition in the gaps. Irradiation, i.e., fast neutron damage, causes shrinkage of both the graphite body and the fuel compact. The fast neutron damage is a function of time and flux. The calculations to obtain an estimate of the fuel compact average temperature take into account the time variations of these variables. The fundamental materials property data were obtained from the fuel and graphite design data manuals.[3-2,3-3] The method used in the analysis to predict the operating temperature history of the fuel compacts is as follows.

The thermal analysis was performed using a 3-D, thermal-analysis code HEATING 7.0 (ref. 3-4). This computer code can be used to compute the temperature profiles in the fuel and the graphite body for a given time during the irradiation, given the current values of the parameters. It is not capable of following time-dependent variables, such as thermal conductivity, fuel-compact gaps, etc., throughout the irradiation phase. It was used to compute the temperature field in the fuel compacts and the graphite fuel body for a given set of parameters.

This set of parameters is:

Pv = the power generation rate in the compact,

K_g = the thermal conductivity of graphite,

K_f = the thermal conductivity of the fuel,

f_g = radial gas gap between the fuel and the graphite,

g_inc = radial gap between the primary containment and the graphite fuel body, and

%He = percentage of helium in the sweep gas (in the gas gaps).

During the irradiation, all of these parameters change as a function of time because of fuel burnup, irradiation-induced thermal-conductivity change, and irradiation-induced dimensional change of the graphite fuel body and the fuel compacts. The irradiation-induced dimensional change is caused by fast neutron damage. The thermal conductivities of the fuel compacts and the graphite fuel bodies are also functions of the fast fluence and temperature. Fortunately, these changes occur on a time scale that is slow compared to the thermal equilibrium time of the capsule. This fact allows one to take a thermostatic approach to long-term temperature computation. A new, simplified computer code named

HRBAVEx.f, where x denotes a pair of compacts in a given axial location in the irradiation capsule, was developed and used to account for the long time dependence of the variables. The collection of eight programs, HRBAVE1.f through HRBAVE8.f, is referred to as MAPPING because these programs map the average TC temperature to the volume-average fuel temperature. The MAPPING code was extensively used to compute the time history of the fuel compact temperatures predicted in this report.

The fast neutron flux used in the calculation of material properties is given by the expression:

$$Flux(z) = \alpha \sum_{i=1}^{5} a_i z^i , \qquad (3\text{-}1)$$

where z is the distance in inches from the top of the 50.8-cm-long core; α = 0.85*0.93 for RB position; and $a_0 = 1.551390 \times 10^{18}$, $a_1 = 0.357201 \times 10^{18}$, $a_2 = 3.22098 \times 10^{16}$, $a_3 = -4.89680 \times 10^{15}$, $a_4 = 1.06604 \times 10^{14}$, and $a_5 = 6.60525 \times 10^{11}$.

The coefficients, a_i, were developed to describe the fast flux for the old HFIR operating power of 100 MW. The 0.85 factor is an approximation to adjust for the current operating level of 85 MW (ref. 3-5), and the 0.93 factor is an adjustment to model the HTGR flux.

To follow the slowly changing physical environment during irradiation, a set of HEATING 7.0 runs was made wherein one of the above parameters was varied over its expected range while holding all other parameters constant. The fuel compact average temperature predictions from these runs were then used to define a set of scaling equations for each of the parameters. These scaling equations were incorporated into the HRBAVEx.f code such that, by providing the graphite temperatures as a function of time and the known reactor operating conditions as input, an estimate of the average temperature of the fuel compacts could be computed.

The measured TC temperatures (graphite body) as a function of time are shown in Figures 3.1*(a)-(h)* for the HRB-21 capsule. The plot includes temperature measured by the centerline TC and an average of the two outboard TCs. There was a significant difference between temperatures measured by the two outboard TCs. The probable causes for such

ORNL-DWG 95-5771

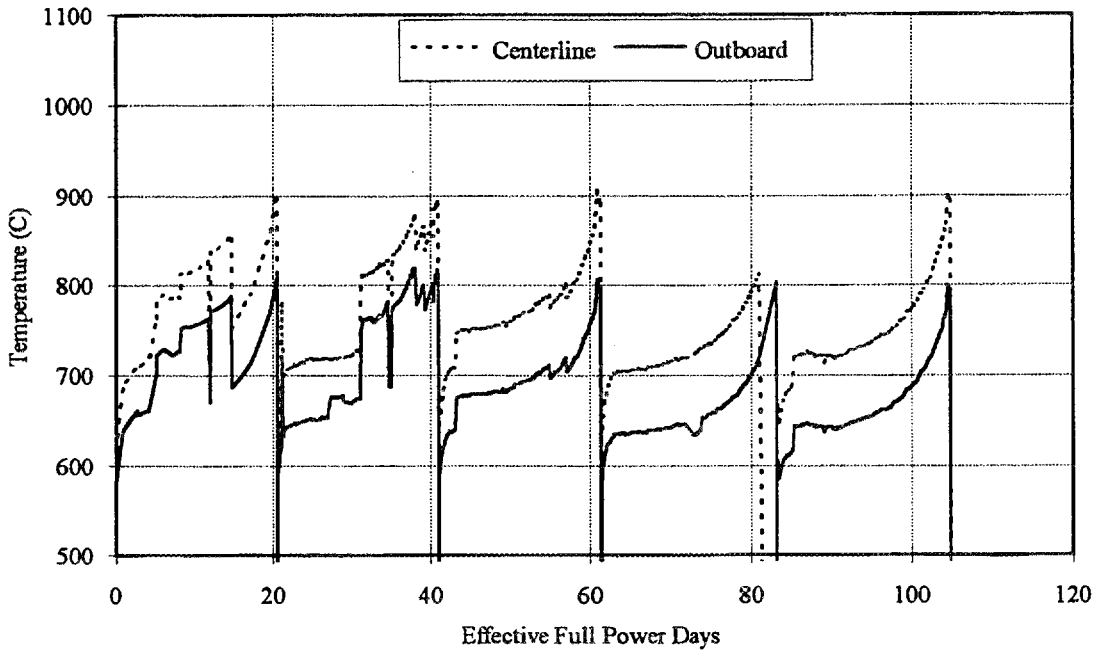

Figure 3.1*(a)*.

MEASURED TEMPERATURES IN THE GRAPHITE FUEL BODY IN POSITION 1 OF CAPSULE.

ORNL-DWG 95-5772

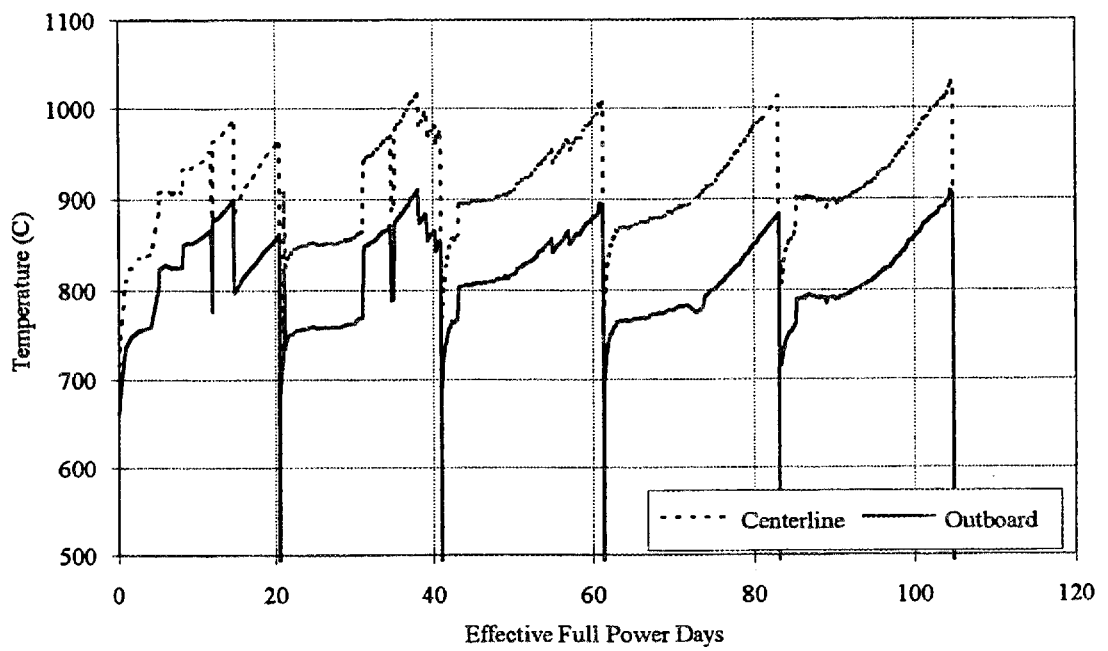

Figure 3.1*(b)*.

MEASURED TEMPERATURES IN THE GRAPHITE FUEL BODY IN POSITION 2 OF CAPSULE.

ORNL-DWG 95-5773

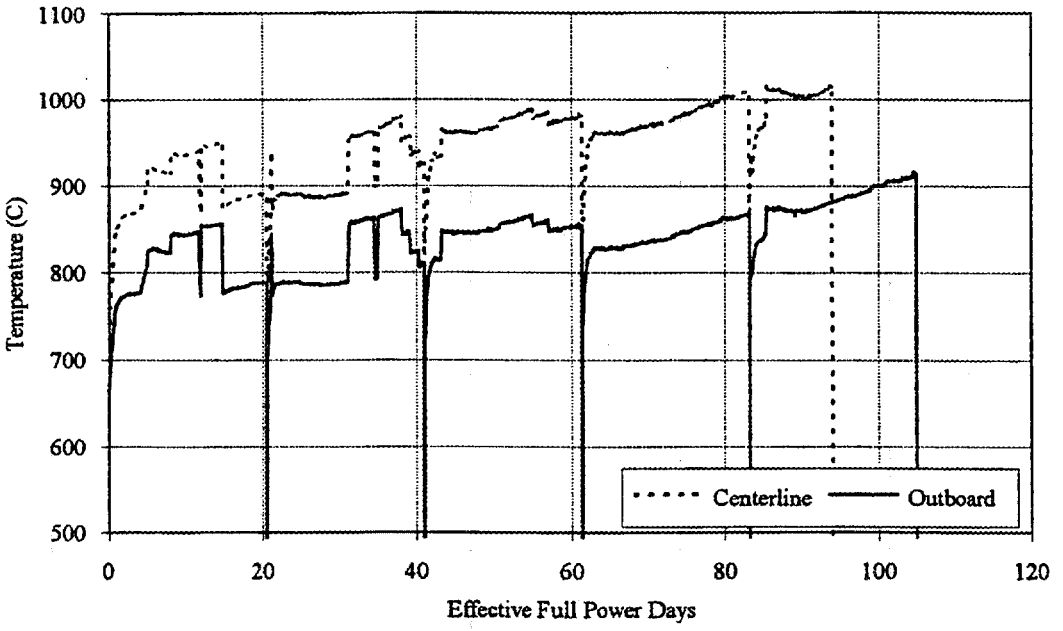

Figure 3.1*(c)*.

MEASURED TEMPERATURES IN THE GRAPHITE FUEL BODY IN POSITION 3 OF CAPSULE.

ORNL-DWG 95-5774

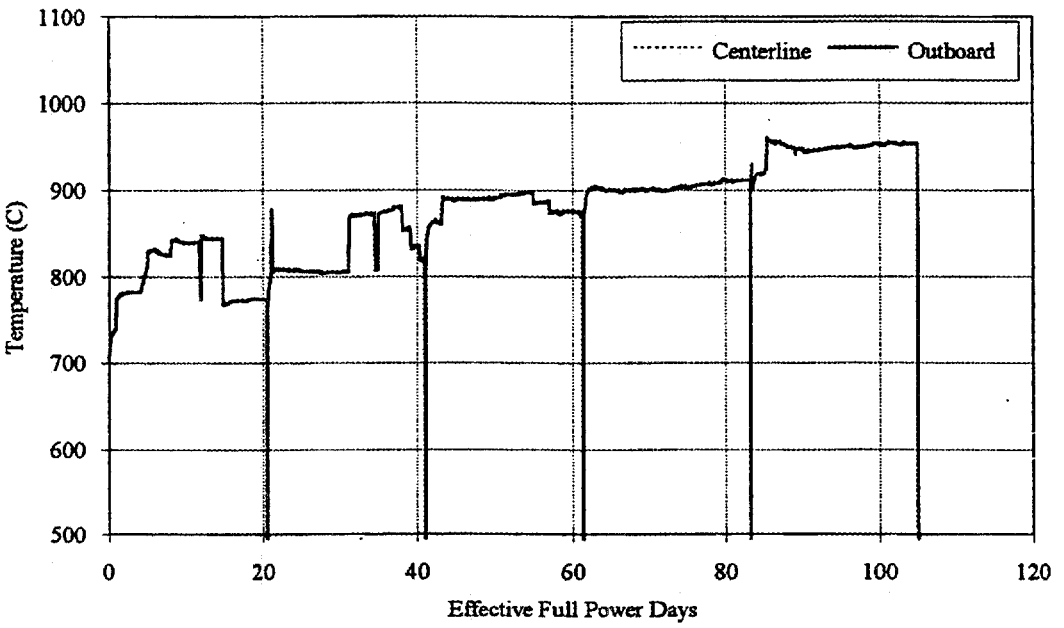

Figure 3.1*(d)*.

MEASURED TEMPERATURES IN THE GRAPHITE FUEL BODY IN POSITION 4 OF CAPSULE. (NOTE: NO CENTERLINE THERMOCOUPLE IN THIS POSITION).

ORNL-DWG 95-5775

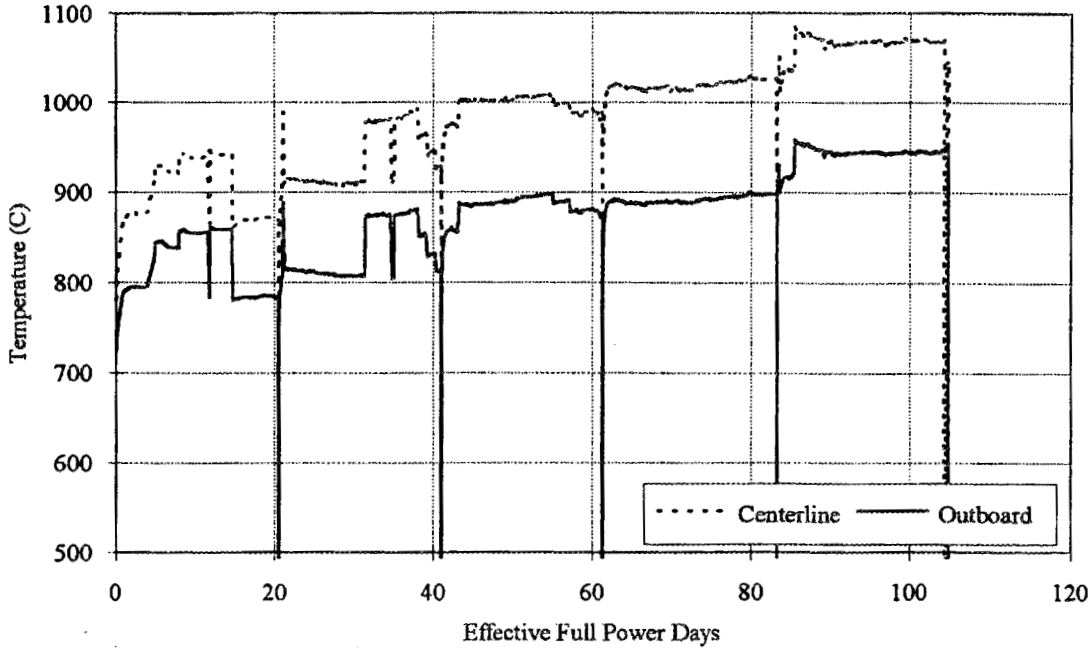

Figure 3.1*(e)*.

MEASURED TEMPERATURES IN THE GRAPHITE FUEL BODY IN POSITION 5 OF CAPSULE.

ORNL-DWG 95-5776

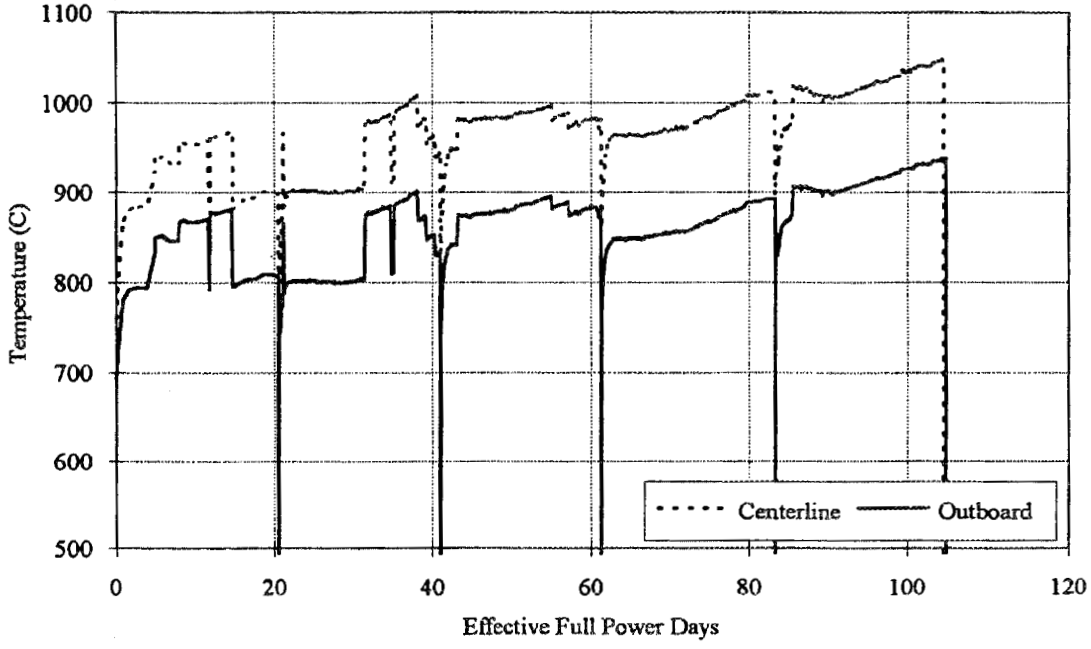

Figure 3.1*(f)*.

MEASURED TEMPERATURES OF THE GRAPHITE FUEL BODY IN POSITION 6 OF CAPSULE.

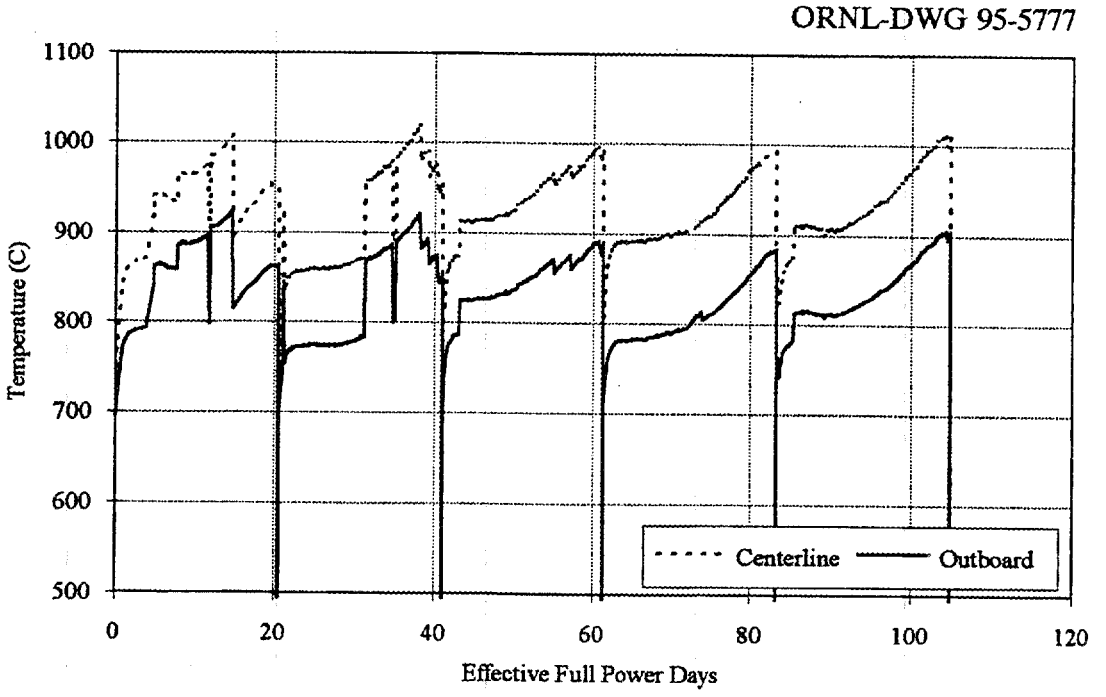

Figure 3.1*(g)*.

MEASURED TEMPERATURES OF THE GRAPHITE FUEL BODY IN POSITION 7 OF CAPSULE.

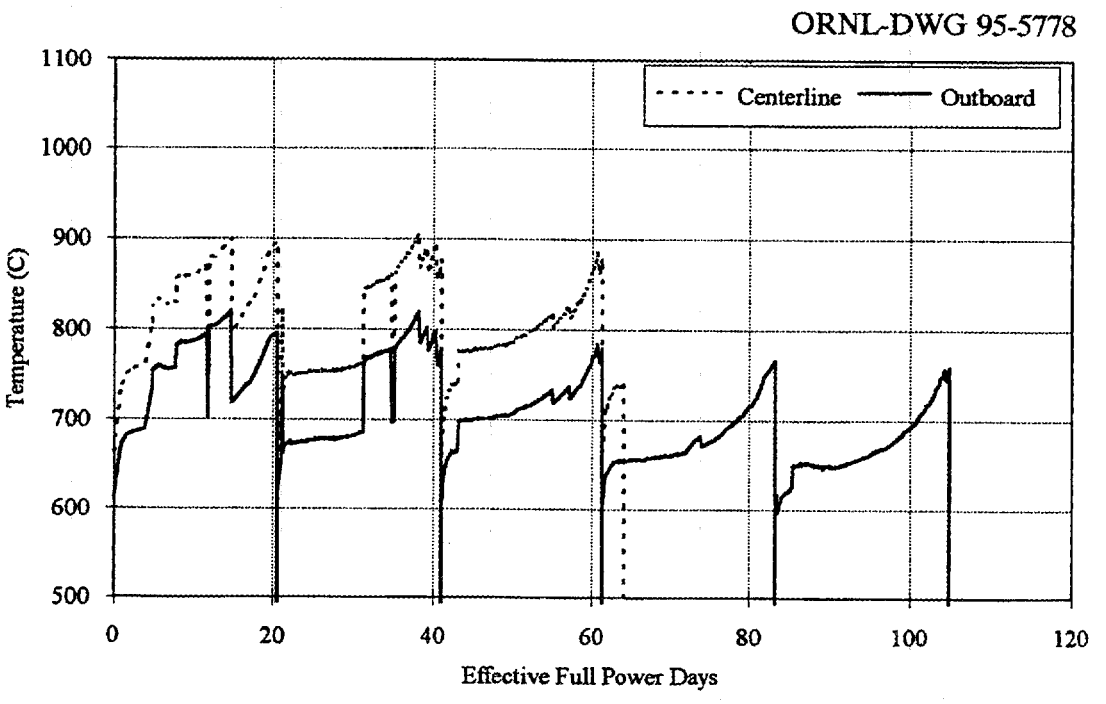

Figure 3.1*(h)*.

MEASURED TEMPERATURES OF THE GRAPHITE FUEL BODY IN POSITION 8 OF CAPSULE.

behavior are discussed in a later section. There was no centerline TC in the No. 4 graphite body position.

The fuel compact operating temperatures (volume average and local maximum) computed by the MAPPING code are shown in Figures 3.2*(a)-(h)* and 3.3*(a)-(d)*. The plots show the temperatures as a function of (1) effective full-power days (EFPDs) of operation of the HFIR (see Figure 3.2), (2) helium concentration [see Figure 3.2*(i)*], and (3) burnup (see Figure 3.3). The fuel particle burnup (FIMA) was calculated using the CACA-2 computer program.[3-6] Figures 3.4*(a)-(d)* show fuel (fissile particle) power density as a function of EFPDs of operation of the HFIR. The fast fluence was calculated using Eq. (3-1) and is shown as a function of EFPDs in Figure 3.5.

Fuel compact power density as a function of time may be calculated using CACA-2 or the MAPPING code. CACA-2 calculates fission power as a function of time. By adding the gamma heating contribution to the fission power calculated by CACA-2, the total power of the compacts can be computed. The MAPPING code also calculates the total compact power from measured temperatures, known initial geometry of the capsule, and inferred geometry changes during irradiation. The MAPPING power predictions include both fission power and gamma heating in the compacts. The predictions from these two codes are compared in Figures 3.6*(a)-(d)*. This comparison shows that the MAPPING code predictions are reasonably close to the CACA-2 predictions. Since the MAPPING code power predictions are the only ones used to predict the fuel operating temperatures, this favorable comparison increases the confidence in the thermal analysis predictions. See Table 2.11 for the mapping between capsule positions and graphite bodies. Remember that graphite body 1 was replaced by graphite body 9 prior to irradiation.

Plots of measured temperatures and predicted compact volume averages provide a visual understanding of the thermal performance. For an understanding of the fuel performance in terms of fission gas release, etc., a better way to display temperature data may be in the form of tables. Table 3.1 presents the time-integrated fuel temperature for each HFIR cycle. This table provides best estimates of volume average temperature for each compact and for each reactor cycle.

3.1.2 Piggyback Specimen Temperatures

Independent analysis of the piggyback fuel particles in the HRB-21 capsule was not performed, but a detailed analysis of the piggyback fuel particles from the New Production

ORNL-DWG 95-5779

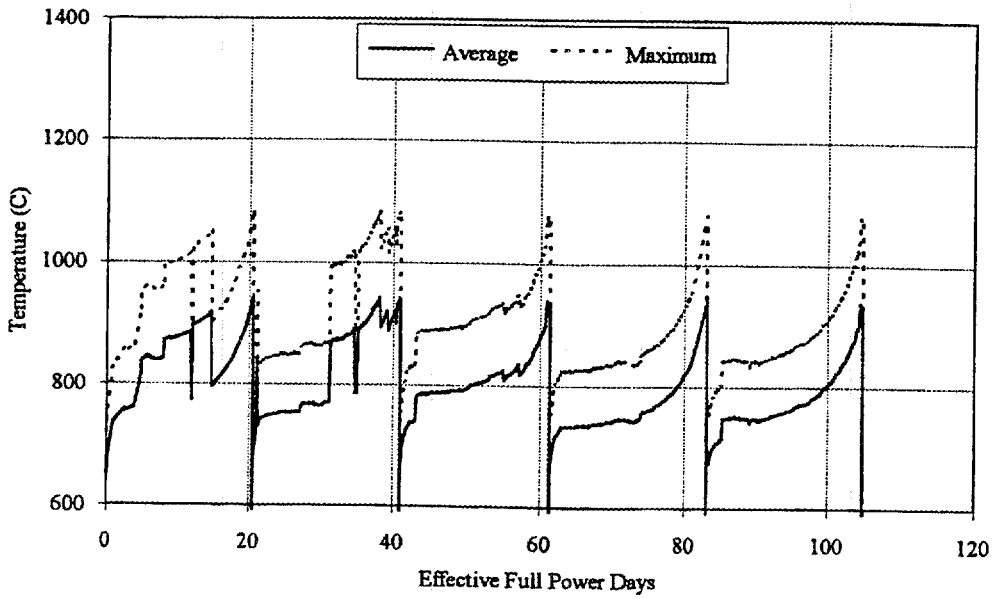

Figure 3.2*(a)*.

PREDICTED VOLUME-AVERAGED AND MAXIMUM FUEL TEMPERATURES (BY MAPPING CODE) AS A FUNCTION OF EFFECTIVE FULL-POWER DAYS OF REACTOR OPERATION FOR POSITION 1 (FUEL BODY 9).

ORNL-DWG 95-5780

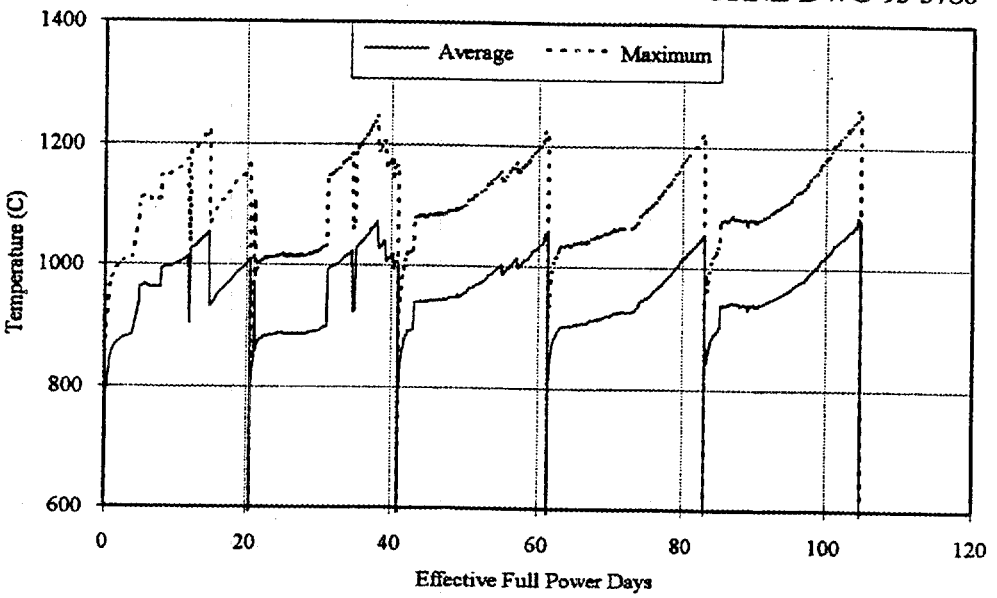

Figure 3.2*(b)*.

PREDICTED VOLUME-AVERAGED AND MAXIMUM FUEL TEMPERATURES (BY MAPPING CODE) AS A FUNCTION OF EFFECTIVE FULL-POWER DAYS OF REACTOR OPERATION FOR POSITION 2 (FUEL BODY 2).

ORNL-DWG 95-5781

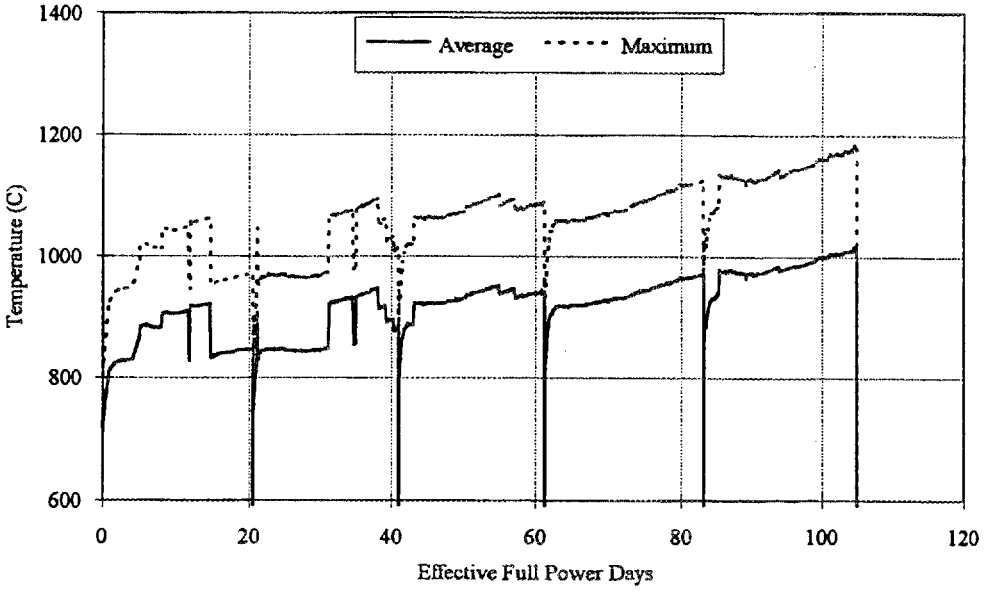

Figure 3.2*(c)*.

PREDICTED VOLUME-AVERAGED AND MAXIMUM FUEL TEMPERATURES [BY MAPPING CODE] AS A FUNCTION OF EFFECTIVE FULL-POWER DAYS OF REACTOR OPERATION FOR POSITION 3 (FUEL BODY 3).

ORNL-DWG 95-5782

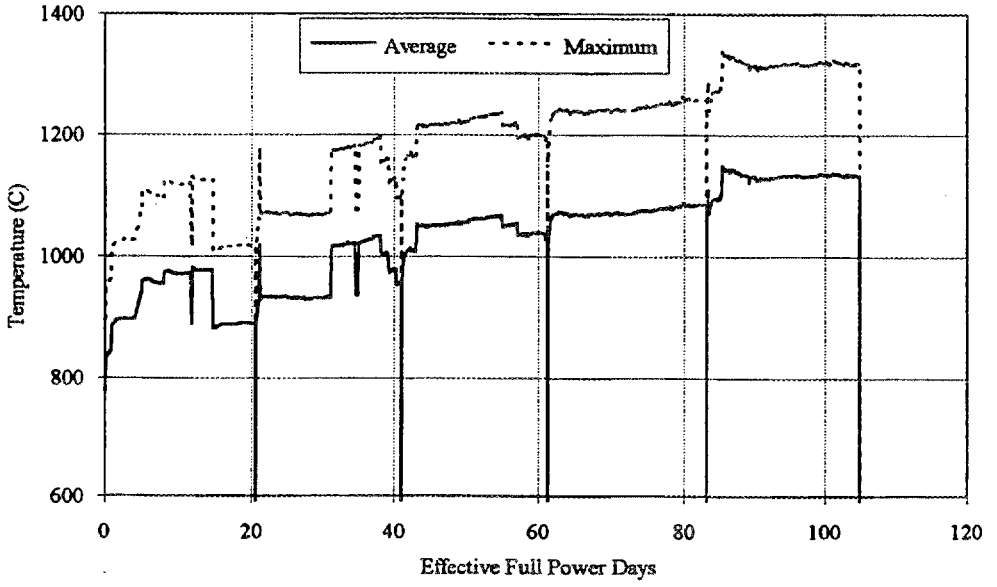

Figure 3.2*(d)*.

PREDICTED VOLUME-AVERAGED AND MAXIMUM FUEL TEMPERATURES (BY MAPPING CODE) AS A FUNCTION OF EFFECTIVE FULL-POWER DAYS OF REACTOR OPERATION FOR POSITION 4 (FUEL BODY 4).

ORNL-DWG 95-5783

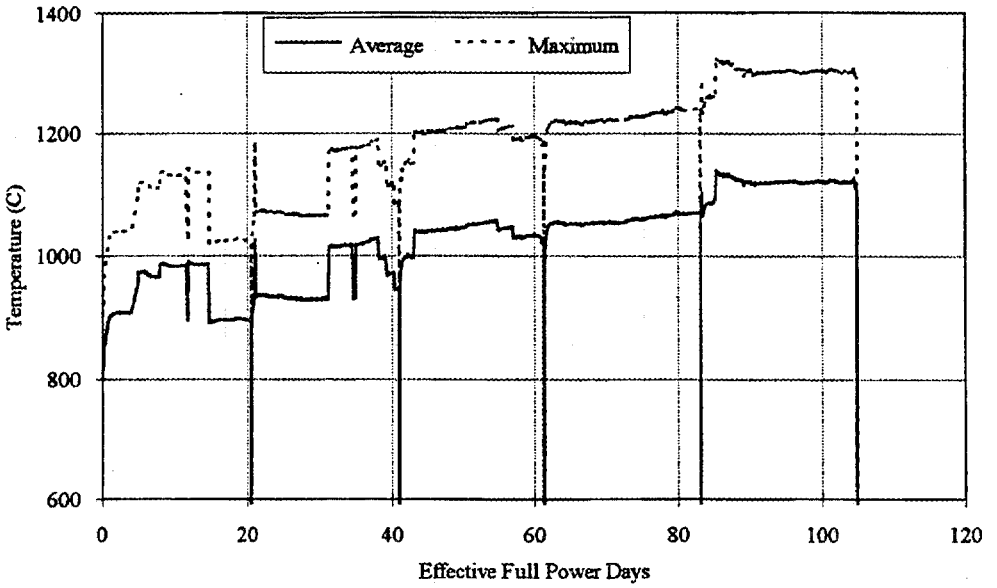

Figure 3.2*(e)*.

PREDICTED VOLUME-AVERAGED AND MAXIMUM FUEL TEMPERATURES [BY MAPPING CODE] AS A FUNCTION OF EFFECTIVE FULL-POWER DAYS OF REACTOR OPERATION FOR POSITION 5 (FUEL BODY 5).

ORNL-DWG 95-5784

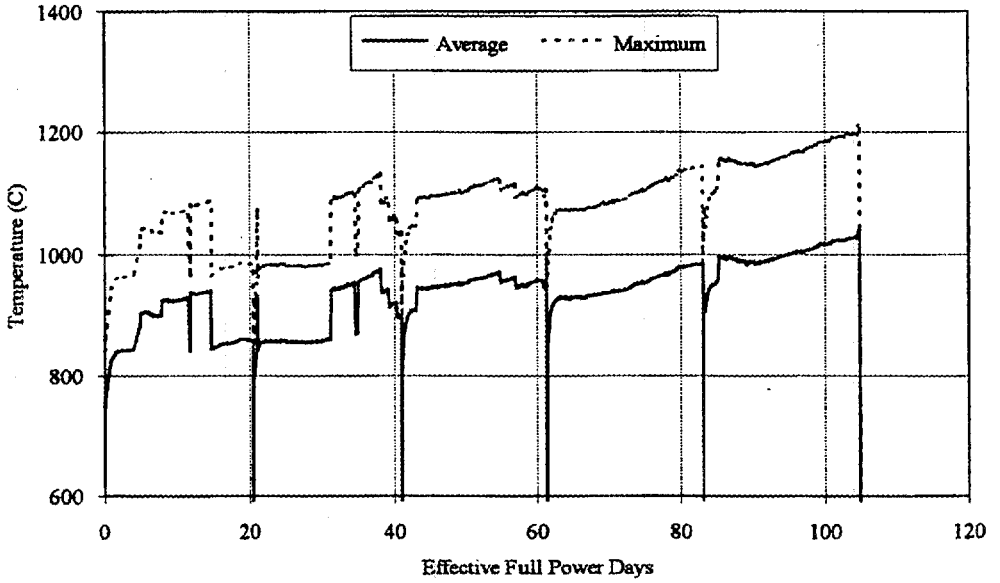

Figure 3.2*(f)*.

PREDICTED VOLUME-AVERAGED AND MAXIMUM FUEL TEMPERATURES [BY MAPPING CODE] AS A FUNCTION OF EFFECTIVE FULL-POWER DAYS OF REACTOR OPERATION FOR POSITION 6 (FUEL BODY 6).

ORNL-DWG 95-5785

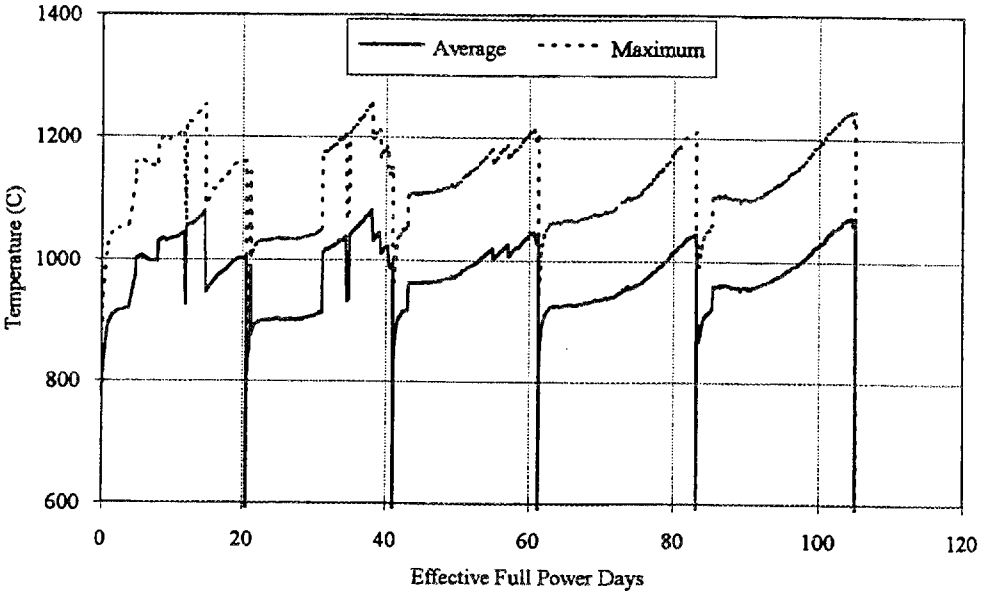

Figure 3.2*(g)*.

PREDICTED VOLUME-AVERAGED AND MAXIMUM FUEL TEMPERATURES [BY MAPPING CODE] AS A FUNCTION OF EFFECTIVE FULL-POWER DAYS OF REACTOR OPERATION FOR POSITION 7 (FUEL BODY 7).

ORNL-DWG 95-5786

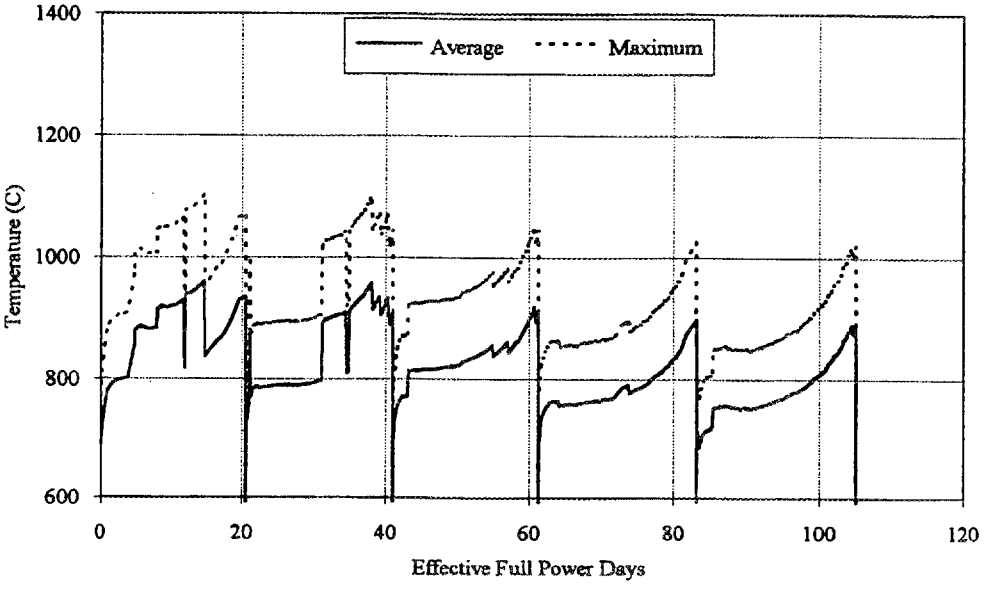

Figure 3.2*(h)*.

PREDICTED VOLUME-AVERAGED AND MAXIMUM FUEL TEMPERATURES [BY MAPPING CODE] AS A FUNCTION OF EFFECTIVE FULL-POWER DAYS OF REACTOR OPERATION FOR POSITION 8 (FUEL BODY 8).

ORNL-DWG 95-5787

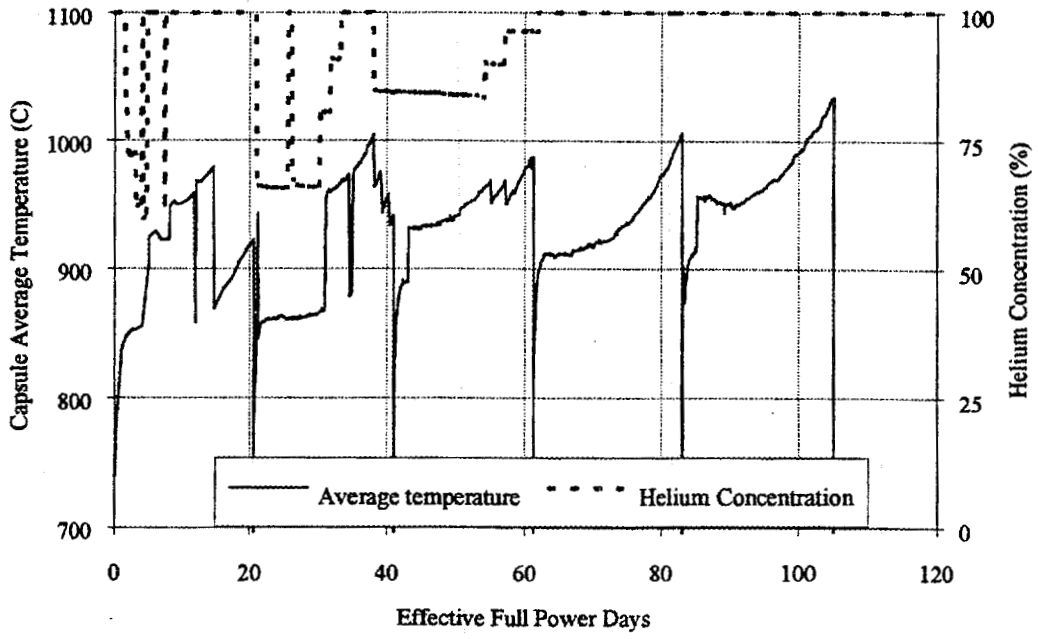

Figure 3.2*(i)*.

CAPSULE AVERAGE FUEL TEMPERATURE AND HELIUM CONCENTRATION IN PURGE GAS.

ORNL-DWG 95-5788

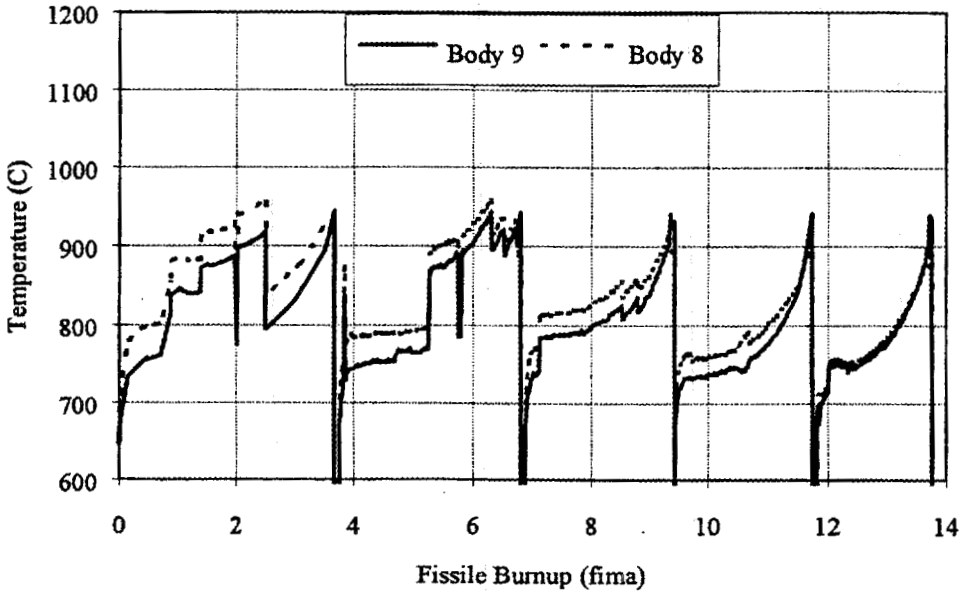

Figure 3.3*(a)*.

PREDICTED VOLUME-AVERAGED FUEL TEMPERATURE AS A FUNCTION OF FISSILE PARTICLE BURNUP FOR COMPACTS IN GRAPHITE FUEL BODIES 9 AND 8.

ORNL-DWG 95-5789

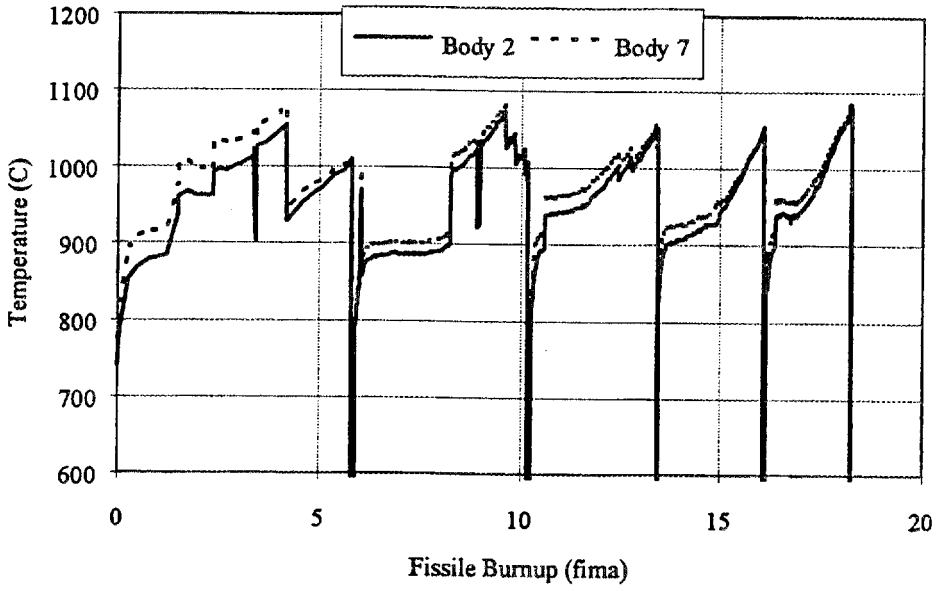

Figure 3.3*(b)*.

PREDICTED VOLUME-AVERAGED FUEL TEMPERATURE
AS A FUNCTION OF FISSILE PARTICLE BURNUP
FOR COMPACTS IN GRAPHITE FUEL
BODIES 2 AND 7.

ORNL-DWG 95-5790

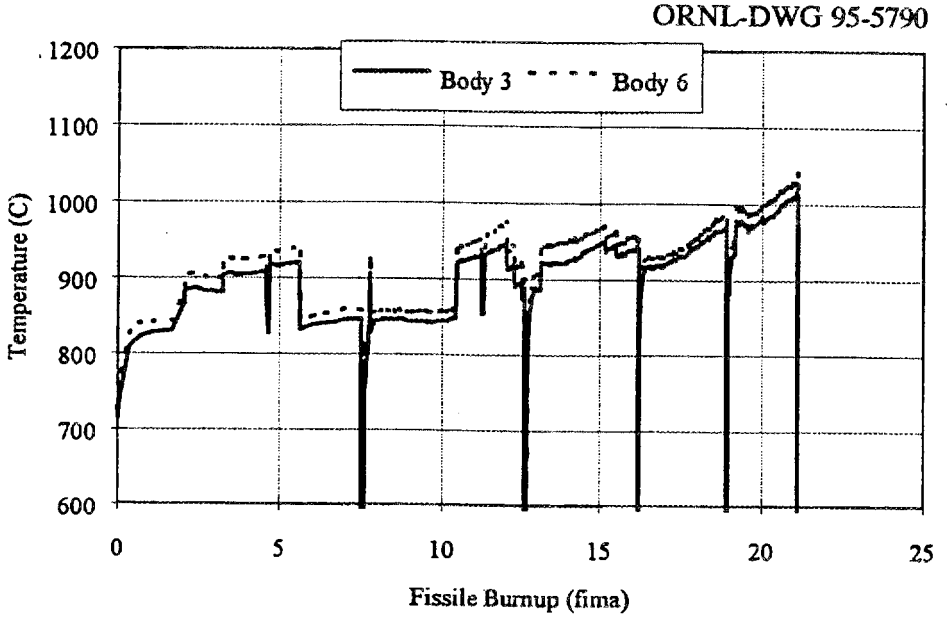

Figure 3.3*(c)*.

PREDICTED VOLUME-AVERAGED FUEL TEMPERATURE
AS A FUNCTION OF FISSILE PARTICLE BURNUP
FOR COMPACTS IN GRAPHITE FUEL
BODIES 3 AND 6.

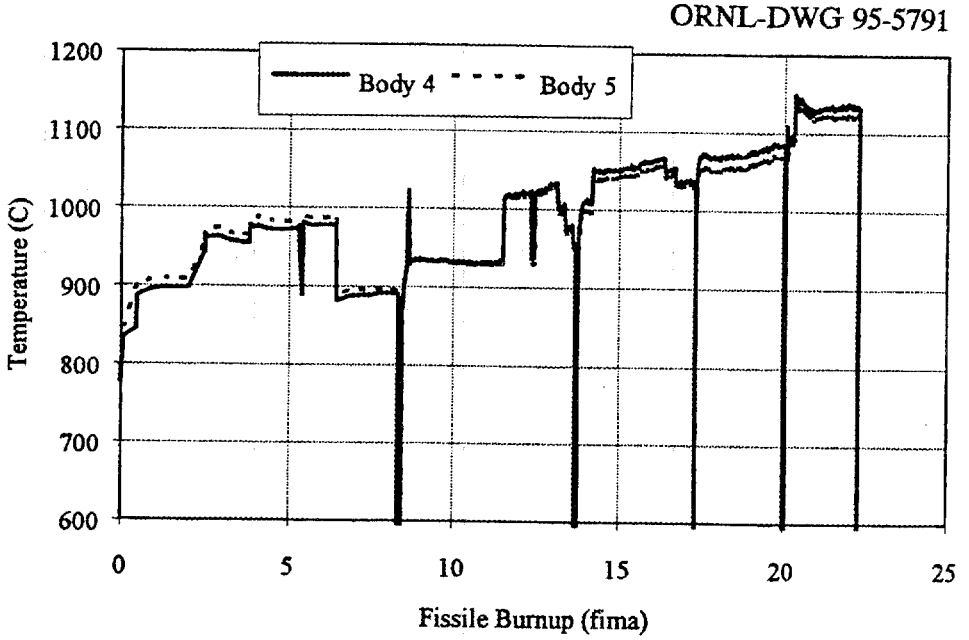

Figure 3.3*(d)*.

PREDICTED VOLUME-AVERAGED FUEL TEMPERATURE AS A FUNCTION OF FISSILE PARTICLE BURNUP FOR COMPACTS IN GRAPHITE FUEL BODIES 4 AND 5.

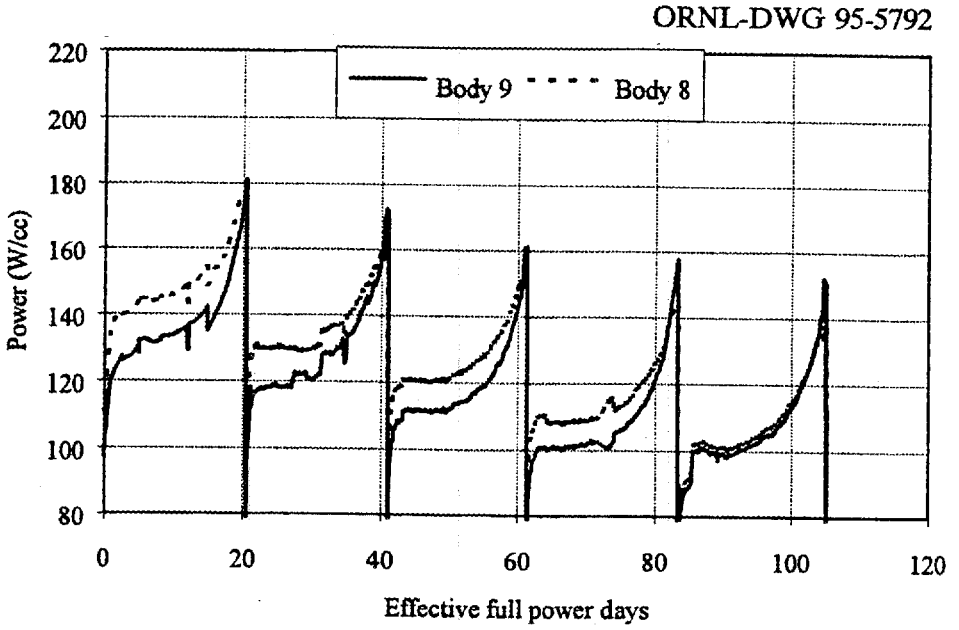

Figure 3.4*(a)*.

PREDICTED POWER DENSITY OF FUEL BODIES 9 AND 8 (ZONE 1).

ORNL-DWG 95-5793

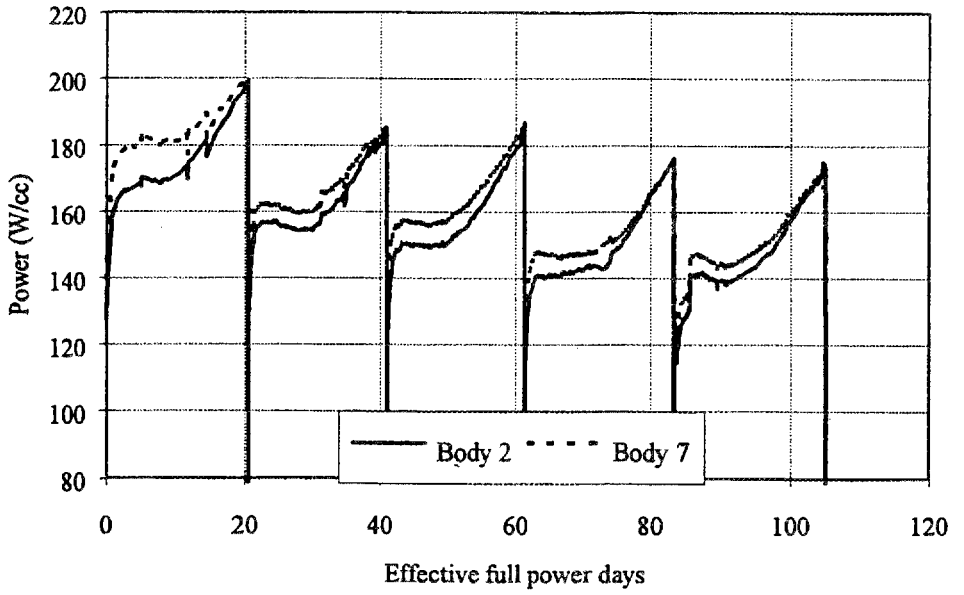

Figure 3.4*(b)*.

PREDICTED POWER DENSITY OF FUEL BODIES 2 AND 7 (ZONE 2).

ORNL-DWG 95-5794

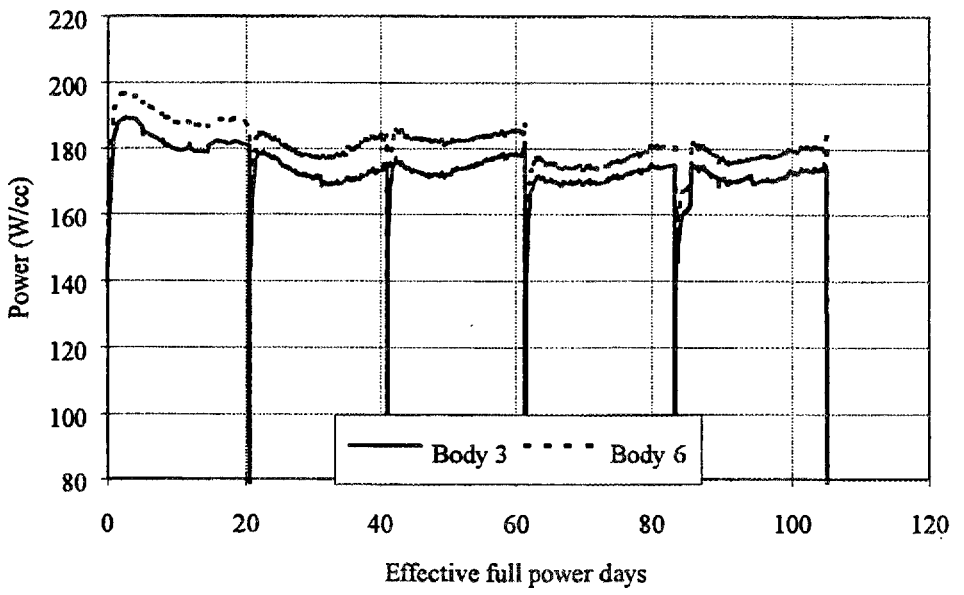

Figure 3.4*(c)*.

PREDICTED POWER DENSITY OF FUEL BODIES 3 AND 6 (ZONE 3).

ORNL-DWG 95-5795

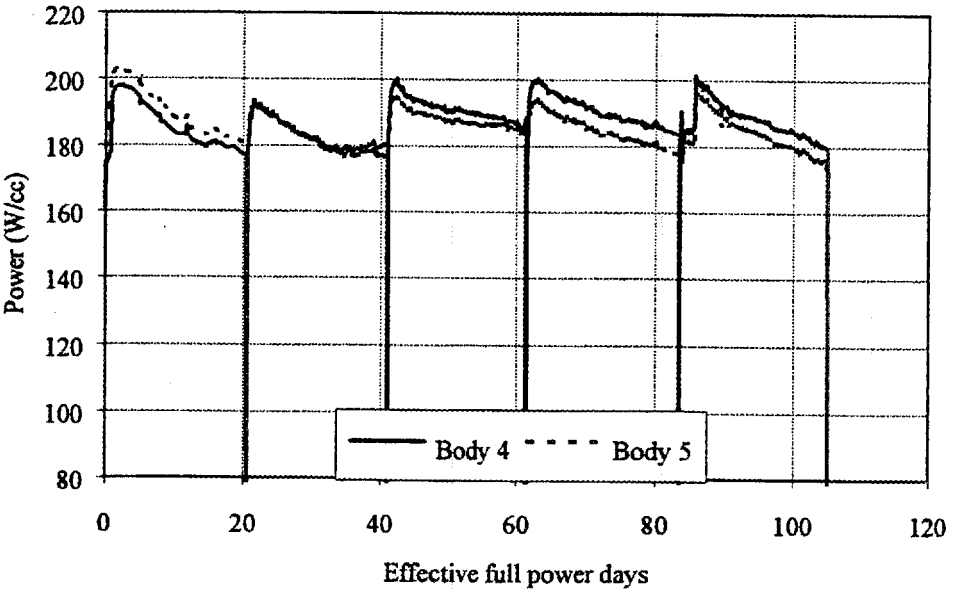

Figure 3.4*(d)*.

PREDICTED POWER DENSITY OF FUEL BODIES 4 AND 5 (ZONE 4).

ORNL-DWG 95-5796

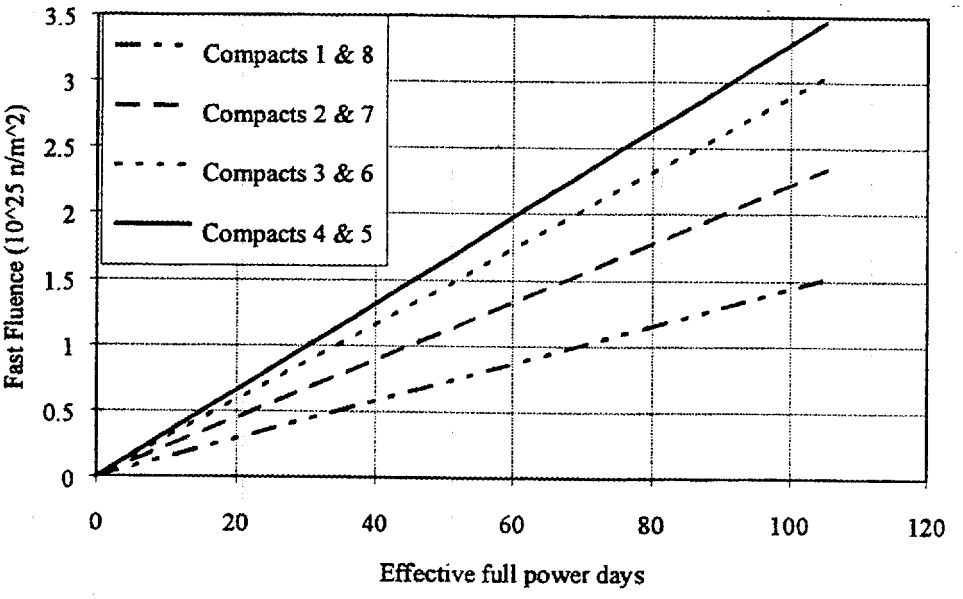

Figure 3.5.

FAST FLUENCE AS A FUNCTION OF EFFECTIVE FULL-POWER DAYS.

ORNL-DWG 95-5797

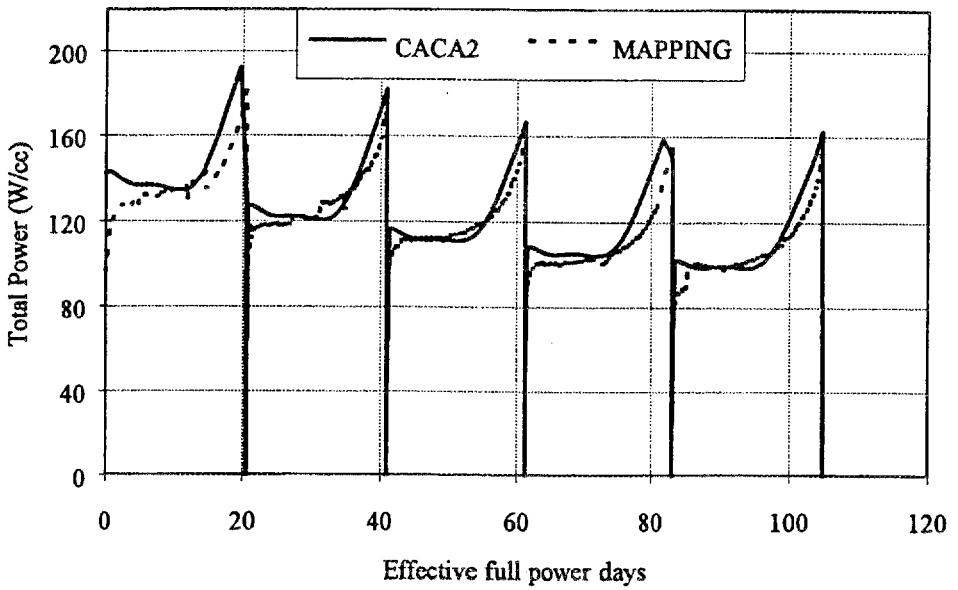

Figure 3.6*(a)*.

COMPARISON OF COMPACT POWERS PREDICTED BY CACA-2 AND MAPPING CODES FOR GRAPHITE BODIES 9 AND 8.

ORNL-DWG 95-5798

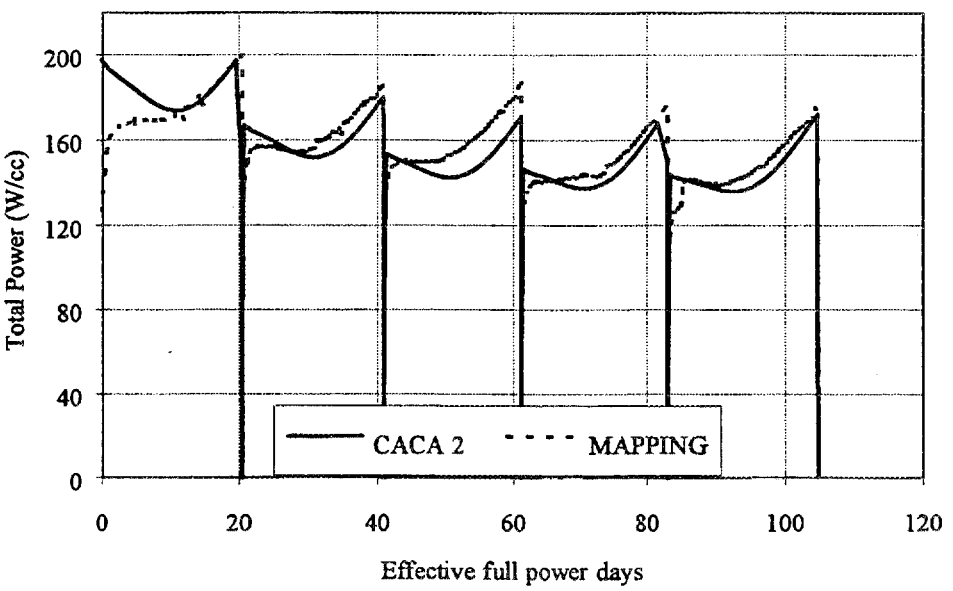

Figure 3.6*(b)*.

COMPARISON OF COMPACT POWERS PREDICTED BY CACA-2 AND MAPPING CODES FOR GRAPHITE BODIES 2 AND 7.

ORNL-DWG 95-5799

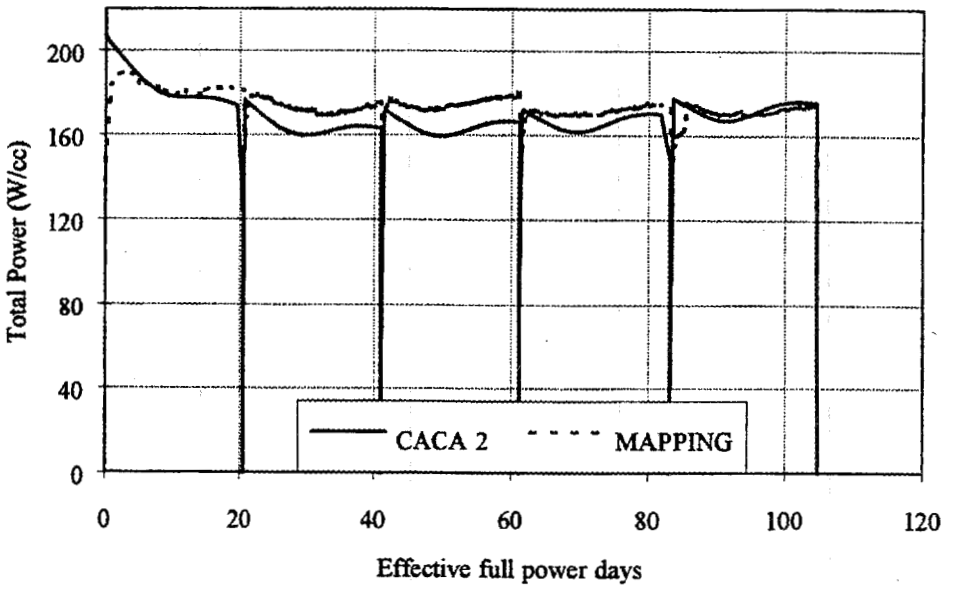

Figure 3.6*(c)*.

COMPARISON OF COMPACT POWERS PREDICTED BY CACA-2 AND MAPPING CODES FOR GRAPHITE BODIES 3 AND 6.

ORNL-DWG 95-5800

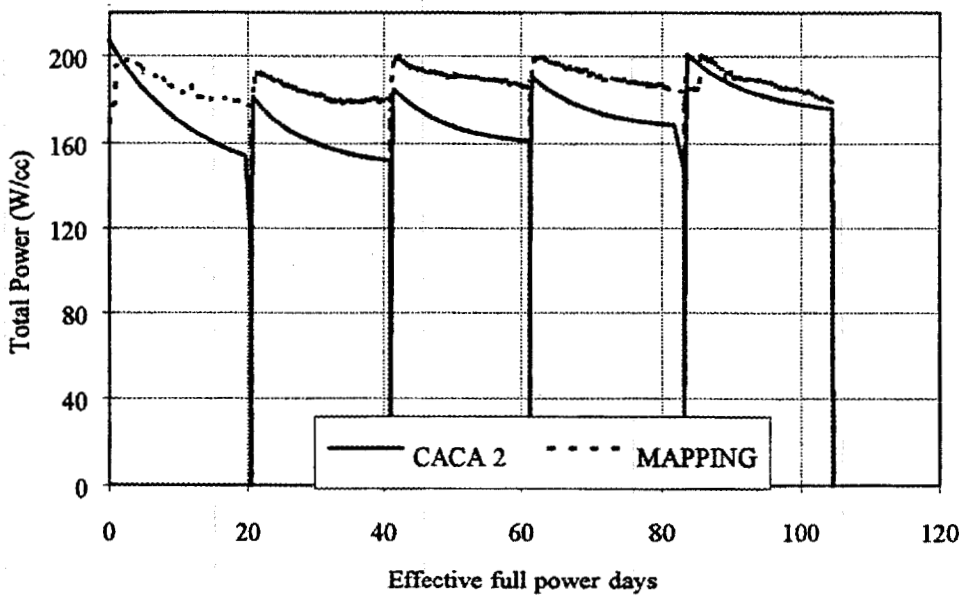

Figure 3.6*(d)*.

COMPARISON OF COMPACT POWERS PREDICTED BY CACA-2 AND MAPPING CODES FOR GRAPHITE BODIES 4 AND 5.

Table 3.1.

HRB-21 CAPSULE TIME-INTEGRATED AVERAGE FUEL TEMPERATURES (°C)

Cycles	Capsule position 1	Capsule position 2	Capsule position 3	Capsule position 4	Capsule position 5	Capsule position 6	Capsule position 7	Capsule position 8	Cycle average
299	830	954	862	925	935	879	983	871	905
300	821	949	879	968	965	897	962	847	911
301	805	966	927	1046	1037	948	984	831	943
302	764	945	935	1074	1058	948	958	786	934
303	774	972	980	1129	1119	998	985	779	967
Compact average	799	957	916	1028	1023	934	974	823	932

Reactor (NPR-1) capsule using HEATING 7.0 code has been performed, and the results were reported in ref. 3-7. Results of the NPR capsule piggyback particle analysis are applicable to the HRB-21 capsule.

The piggyback capsule runs essentially at the temperature of the graphite fuel body in which it is contained. The surface of the fuel particle inside the piggyback capsule is estimated to run approximately 40°C higher than the graphite fuel body. Based on this conclusion from the NPR-1 capsule analysis, the HRB-21 piggyback particle surface temperature estimate was performed and is shown in Table 3.2 below. Note that these temperature estimates are for the axial center of each graphite fuel body at or near the outboard TC positions. The HRB-21 design with eight individual graphite bodies resulted in significant axial temperature gradients at the end of each compact and fuel body. Since the piggyback particles are located at or near the axial center, the temperatures listed in Table 3.2 are reasonable.

3.1.3 Fuel Temperature Uncertainty

Because of the lack of time and inadvertent loss of computer resources, a separate fuel temperature uncertainty analysis was not performed for the HRB-21 capsule irradiation, but the uncertainty analysis performed for the NPR-1 capsule is essentially applicable to capsule HRB-21. Reference 3-7 discusses the methodology and results obtained for the NPR-1 capsule.

Table 3.2.

HRB-21 CAPSULE TIME-INTEGRATED AVERAGE PIGGYBACK PARTICLE TEMPERATURES (°C)[a]

Cycles	Capsule position 1	Capsule position 2	Capsule position 3	Capsule position 4	Capsule position 5	Capsule position 6	Capsule position 7	Capsule position 8	Cycle average
299	767	867	849	844	859	870	893	795	843
300	755	850	856	872	874	874	864	767	839
301	734	866	886	923	923	914	882	753	860
302	667	799	847	908	897	867	813	686	811
303	706	858	921	987	982	949	875	710	874
Piggyback average	726	848	872	907	907	895	865	742	845

[a]Reported temperatures include 40°C added to themocouple temperature to estimate piggyback particle surface temperature.

The predictions of the cumulative uncertainty of the average fuel temperature during the irradiation of NPR-1 capsule in the RB position using the Monte-Carlo technique is given in Table 3.3. The same uncertainty is assumed to exist for the HRB-21 irradiation based on the similarities in power densities, capsule dimensions, and irradiation locations.

Table 3.3.

UNCERTAINTY PREDICTIONS FOR HRB-21 IN REMOVABLE BERYLLIUM POSITION

Capsule	Zone 1	Zone 2	Zone 3	Zone 4
NPR-1 T average σ (°C)	38	45	40	38

3.1.4 Lessons Learned

The following salient points quantify the lessons learned from the thermal performance analysis of the HRB-21 irradiation capsule.

1. Individual graphite fuel bodies add to the temperature uncertainty. Graphite has a high thermal conductivity, and this design results in establishing large axial

temperature gradients at the ends of each fuel compact. Heat is transported both axially from the ends of the compact and radially across the ends of the graphite fuel body. The NPR type of design with compacts stacked on top of each other is far superior.

2. Centrally locating eight individual graphite bodies inside the pressure vessel is a formidable task, since the holes for the TCATs do not match properly between the different graphite bodies. As a matter of fact, the normal assembly procedure had to be modified for this capsule. The alumina spacers on each graphite fuel body are of little use since the thermal expansion of the Inconel pressure vessel exceeds that of the graphite body under irradiation conditions.
3. The uranium loading of the compacts was too high, resulting in an extremely small initial gap between the graphite fuel body and the pressure vessel. In an effort to maximize the statistical value of the experiment, the uranium loading was initially high (number of fuel particles was increased). This resulted in poor temperature control during the latter half of the irradiation. Small gaps for temperature control are technically feasible, but the change in the gap due to thermal expansion and irradiation-induced shrinkage is almost as large as the initial gap. When the change in the gap is comparable to the gap itself, uncertainties in the material properties can strongly influence temperature control because the net gap (and its temperature drop) now has a larger relative uncertainty. A recommended minimum initial as-built radial gap of 0.010 in. would be expected to change to about 0.012 in. at the end of irradiation. This will result in a smaller effect on the operating temperature.
4. The mechanical design of the capsule was not ideally suited to centrally locate the graphite fuel bodies. Using a single or at most two graphite bodies can assist in the centering of the fuel bodies, which in turn reduces the nonuniformity of the radial or axial temperature distribution.
5. Since the thermal conductivity and the irradiation-induced dimensional change of the fuel compacts are functions of particle loading and shim volume fraction, it is advisable to use identical compacts at all locations in the capsule. This reduces the uncertainties.

Clearly, any experiment is a balance between operational ease and data uncertainty. In future experiments, it is recommended that these operation issues receive greater attention in favor of reduced data uncertainty.

3.2 FISSION GAS RELEASE

To obtain a measure of the irradiation performance of the fuel compacts in experiment HRB-21, three methods of monitoring fission gas release were employed. The results were used to estimate the fraction of coated fuel particles embedded in compacts which failed to retain fission gases under the irradiation conditions. The coatings of the releasing particles had to have a connected pore system through which the fission gases released from the kernels could escape from the particles. Contributing to this pore system presumably were cracks developing under the effects of irradiation, gas pressure buildup, chemical interactions, the permeabilities of the coatings as manufactured, and through changes during service. The measurement of fission-gas release provides an indicator of fuel particle performance by detecting when the last fission-gas barrier fails, but no information is provided to determine the sequence of events leading to failure of the particle to retain fission gases. Even with this limitation, the measurement of fission gas release provides the most sensitive method for detecting when particles lose the ability to retain gases.

3.2.1 Methods of Monitoring Fission Gas Release

The three methods of monitoring fission-gas release involved: (1) the measurement of fission-gas content in a series of samples of the capsule sweep gas during irradiation in HFIR, (2) monitoring of the ionization chamber signal resulting from radiodecay of fission products in the HFIR effluent sweep gas, and (3) determination of the ratio of released fission gas to that from a sample of uranium stearate in TRIGA experiments on compacts before or after irradiation in HFIR.

3.2.1.1 Gas Release in High Flux Isotope Reactor Experiments

Throughout the irradiation of capsule HRB-21, the sweep gas was constantly monitored for signs of particle damage, and periodic samples were taken to establish an R/B history.

3.2.1.1.1 Grab Samples

In the first method,[3-8,3-9] a small volume of the effluent sweep gas was taken periodically and the number density of atoms of each isotope determined. The release rate, R, was calculated as:

$$R_i = N_i f_r , \tag{3-2}$$

where

R_i = release rate (atom/s) for isotope i,

N_i = number density of atoms (atom/cm^3) for isotope i,

f_r = flow rate (cm^3/s).

Equation (3-2) applies to the rate at which fission gas is released into, and collected by, the sweep gas. The release rate from the individual sources in the compact could be higher, especially for the short-lived species. The number density of atoms was determined by measuring the fission gas inventory collected in the serum bottle using a gamma spectrometer fitted with a high-efficiency germanium detector. The efficiency of the gamma spectrometer at various photon energies was measured using a simulated gas source containing known amounts of radioactive isotopes placed inside a serum bottle.

The flow rate through the capsule was determined by a mass flowmeter in the exit tubing of the capsule and by flowmeters measuring the inlet flows of helium and neon. The exit flowmeter reading was used for the calculations and generally was within ±10% of the combined inlet flows.

In order to account for decay during the transit of the gas from the outlet of the capsule to the gas sampling station, gamma counting data were back-corrected to an effective sampling time. This time was calculated using the measured flow rate and assuming slug flow in the tubing:

$$SampleTime_{eff} = clocktime - \frac{V_{tube}}{60\ f_r} , \tag{3-3}$$

where

sample $time_{eff}$ = the time the sample exited the capsule (h),

Clock time = actual time the sample was obtained (h),

V = volume of tubing between the capsule and the sampling station (cm^3),

f_r = flow rate (cm^3/min).

In many cases, the time between obtaining the grab sample and the gamma analysis was sufficiently long that ^{89}Kr (with a 3.18-min half-life) had decayed so that its concentration was below the detectable limit of the spectrometer. In these instances, the initial ^{89}Kr in the grab sample was estimated from the concentration of its daughter, ^{89}Rb, using the growth and decay equation:

$$N_{kr} = \frac{N_{rb}\,(\lambda_{rb} - \lambda_{kr})}{\lambda_{kr}\,(e^{-\lambda_{kr} t} - e^{-\lambda_{rb} t})}\,, \tag{3-4}$$

where

N_{kr} = the number density of ^{89}Kr (atoms/cm^3) at the capsule sample time,

N_{rb} = the number density of ^{89}Rb (atoms/cm^3) at the start of gamma counting,

λ_i = the decay constant for nuclide i (1/s),

t = delay time between sampling and gamma counting (s).

The release rate, R, was normalized to the birth rate, B, to obtain the release rate-to-birth rate ratio, R_i/B_i. The birth rate, B_i, of fission gas nuclides which are produced by decay of precursor nuclides with much shorter half-lives than the fission gas (^{85m}Kr, ^{87}Kr, ^{88}Kr, ^{89}Kr, and ^{138}Xe) was determined from:

$$B_i = \Phi \sum_j \sigma_j N_j Y_i\,, \tag{3-5}$$

where

B_i = birth rate of isotope i (atom/s),

ϕ = neutron flux (n/m^2-s),

σ_j = fission cross section for neutron capture of U or Pu isotopes (m^2),

N_j = number of atoms of ^{235}U, ^{239}Pu, and ^{241}Pu (dimensionless),

Y_i = cumulative fission yield of isotope i.

The birth rate for fission gases that have a precursor nuclide with a similar or longer half-life than the gas depends on the decay rate of the precursor. Thus, for ^{133}Xe, ^{135m}Xe, and ^{135}Xe, the birth rate was calculated via :

$$B_i = N_{i-1}\lambda_{i-1}f_i + \Phi\sum \sigma_j N_j DY_i \,, \tag{3-6}$$

where

N_{i-1} = number of atoms of the precursor nuclide in the capsule,

λ_{i-1} = decay constant of the precursor nuclide (1/s),

f_i = branching ratio (fraction of precursor disintegrations that yield the fission gas),

DY_i = direct fission yield of the fission gas *i*.

The remaining symbols have been defined in the preceding equations.

The number of atoms of the precursor nuclide in Eq. (3-6) and the fission-generated birth rates were computed using the CACA-2 code. This code uses the capsule fissile and fertile particle loadings, the HFIR cross sections, and the actual irradiation history to compute the time-dependent, fission product production rate.

The R/B values thus determined, $(R_i/B_i)_{capsule,t}$, represent the average R/B ratio at time, t, in an irradiation capsule throughout which the temperature, burnup, fission rate density, and fast fluence varied. Normally, R/B represents the steady state, fractional fission-gas release and therefore would apply to constant values of R/B. To encompass the variation in the deduced R/B, the assumption is normally made that the release is always close to the steady state and that recovery of R/B from a perturbation in the steady state, or a change in gas release, is sufficiently rapid.

To determine the fraction of particles with a connected pore system, i.e., the fraction of particles "failed," using the measured values of $(R_i/B_i)_{capsule,t}$, the following relation is required:

$$\left(\frac{R_i}{B_i}\right)_{capsule,t} = \frac{\sum_{volumes,k=1}^{n} f_{f,k} \left(\frac{R}{B}\right)_{particle,k} B_k}{\sum_{k=1}^{n} B_k}, \tag{3-7}$$

where

$f_{f,k}$ = the fraction of particles "failed,"

$(R/B)_{particle,k}$ = the R/B for an individual failed particle.

This equation is an approximation which neglects the fission gas released from HM contamination in the fuel compact. The large increase in R/B when particles began to fail shows that the release from failed particles was more important than the release from contamination.

In lieu of measurements of $(R_i/B_i)_{particle,k}$, it is necessary to calculate this quantity at selected times in determining the fractional particle failure. To do so requires a model for release from failed particles and a correlation between the occurrence, or at least the beginning, of failure and the reactor parameters.

A complication in the above approach to determining the fraction of particles "failed" is the release of stored fission gas from bubbles. This type of release may occur when particle coatings fail and from failed particles following increases in temperature or addition of oxidants to the system. The release is greater than normal and is transient. As a consequence, the release declines with time after the onset, and the number of contributing failed particles is difficult to assess.

In the process of the coatings of a particle becoming permeable to gases, developing complete radial cracks, or fragmenting, a connected pore system can be established provided all coatings undergo one or more of these changes; then fission gas released from the kernel can escape from the particle. The gas release is clearly not an indicator of the sequence in which the coatings undergo these changes.

3.2.1.1.2 Transient Fission-Gas Release

Transient fission-gas release is monitored by the response of an ionization chamber to the pulses of radioactivity in the effluent gas flowing through a tube helically wound around the wall of an ionization chamber. The ionization chamber signals are difficult to interpret for normally configured fuel particles when the gas composition and temperature in the capsule change during the irradiation. When temperatures above those reached with He as the sweep gas are desired, neon is added to the sweep gas to reduce the thermal conductivity. The consequences of this addition are: (1) the ionization chamber signal is increased as a result of the decay following the excitation of neon to ^{23}Ne (the latter decays by emitting a photon at 440 keV and an electron at 4.38 MeV), and (2) the increased temperature following neon addition may induce the release of stored fission gas. The possibility arises that particles having exposed kernels could emit fission gas transiently in response to the increase in temperature. Thus, two or more transients could represent pulsed fission-gas release from a single particle.

3.2.1.2 Gas Release in TRIGA Experiments

3.2.1.2.1 Calibration Method

Twelve fuel compacts were irradiated in the TRIGA Mark I reactor at a temperature of 1100°C, and the released fission gases were collected in a cooled charcoal trap and gamma counted.[3-10] Four of the compacts were also tested at 900°C. To provide a calibration factor representing a known fractional release of fission gases generated, this procedure was repeated but at room temperature with uranyl stearate (shown to be almost 100% releasing). The irradiations were conducted for 30 min, and gas was collected for an additional 15 min.

The measurement of the fission gas released from the compact is reported in the gamma spectrum analyses as "activity" of the compact according to the relation:

$$A' = \frac{C}{(t_c\ b\ \alpha)}\ , \qquad (3\text{-}8)$$

where

C = counts (dimensionless),

t_c = live counting time (s),

b = branching ratio (fraction of the gammas that result in the measured gamma peak),

α = a constant = 3.7E+04 d/(s·μC_i),

d = disintegration (dimensionless),

A' = "activity" (μC_i).

The term to account for radiodecay during collecting fission gas in the trap is not explicitly included since the same factor occurs in the calibration factor which is a divisor to A'. A companion measurement under the same conditions but without a compact was made to evaluate the background contribution to A'; this contribution was then subtracted from A':

$$\Delta A' = A_{sample} - A_{background} , \tag{3-9}$$

where $\Delta A'$ is the true sample "activity" for compact or stearate.

If the detector efficiency is known, then $\Delta A'$ can be converted to a "pure" number of μC_i, thus:

$$A = \frac{\Delta A'}{\epsilon} , \tag{3-10}$$

where

A = activity (μC_i),

ϵ = detector efficiency representing the ratio of the number of counts to the number of disintegrations (dimensionless).

The R/B from measurements with the compact and the uranyl stearate can be determined using a version of $\Delta A'$ in which the common factors b and α are omitted and by

correcting for the differences in the quantities of fissionable isotopes in the compact and uranyl stearate, provided the counting geometry is the same for compact and stearate. Thus:

$$\frac{R}{B} = \frac{\Delta A'_{compact}}{\Delta A'_{stearate}} \times \frac{U^{235}_{stearate}}{U^{235}_{eq,compact}} . \tag{3-11}$$

The compacts contain not only ^{235}U but also ^{239}Pu and ^{241}Pu; the equivalent ^{235}U content of the compacts is obtained as:

$$U^{235}_{eq,compact} = \sum_i m_i \left(\frac{\sigma_i}{\sigma}\right) \left(\frac{Y_i}{Y}\right) , \tag{3-12}$$

where

m_i = mass of fissionable isotope i,

σ_i = cross section for fissionable isotope i,

σ = cross section for ^{235}U,

Y_i = fission yield for fissionable isotope i,

Y = fission yield for ^{235}U.

The R/B derived with the calibration method requires a correction for steady state. There are three considerations: (1) a model of fission-gas release must be adopted from which the ratio of R/B, at times large compared with λt, to the R/B at 30 min can be determined; and (2) for the TRIGA data, the release at the end of 30 min of irradiation must be derived from the measured release after 30 min of irradiation and 15 min of postirradiation collection.

3.2.1.2.2 Absolute Method

The TRIGA data can also be used to calculate the R/B without relying on relative measurements. Thus, the release rate, R, can be calculated as follows:

$$R_i = \frac{C_i}{t_c \cdot e \cdot b \cdot \lambda \cdot t \cdot f_i} , \tag{3-13}$$

where

R_i = release rate of isotope i (atom/s),

C_i = counts for isotope i (dimensionless),

t_c = counting time (s),

e = detector efficiency representing the ratio of the number of counts to the number of disintegrations (dimensionless),

b = branching ratio (dimensionless),

λ = radiodecay constant (1/s),

t = collection time (s),

$f_i = \{(1-e^{-\lambda t})/\lambda t\}$ = fractional reduction in counts from radiodecay during collection of isotope i.

The birth rate is given by Eqs. (3-5) and (3-6) above.

If the absolute method is applied to the results of the standard TRIGA method (i.e., fission gas collection during 30 min of irradiation and 15 min of postirradiation conditions), then steady state considerations (1) and (2) presented above apply.

3.2.2 Results of Monitoring Fission-Gas Release

3.2.2.1 Gas Release in High Flux Isotope Reactor Experiments

3.2.2.1.1 Release Rate/Birth Rate Measurements

Measurements of the fission-gas release rates were carried out using the grab sample technique for sampling the sweep gas after exiting from the fuel capsule. The gas samples were collected in serum bottles at the HFIR. They were then transported to the Irradiated Fuels Examination Laboratory (IFEL) where they were analyzed for fission gas inventory. Because of the distance between IFEL and HFIR, the delay before analysis was at least 15 min, and the short half-life fission gases could not be measured. The reactor startup sequence was modified for this test to minimize the probability of particle failures due to rapid increases in power generated per particle. Hold times of 10 to 15 min were instituted at reactor power levels of 10, 30, 50, 70, and 90% of full power (85 MW). The sweep gas was sampled for R/B measurements at each of the hold points, and two samples were taken when full power was achieved. Following each startup, two samples per day were taken for

the first 5 d of operation. Then, for the remainder of each cycle, two samples per day were taken generally 3 d per week.

The gas sampling system in the MIF at the HFIR includes a holdup tank which reduces the activity of the gas flowing into the off-gas system. This plumbing was modified for this test to include a line (which contains a volume of about 17 cm^3) bypassing the tank so that short-lived fission gas could be measured either after passing through the tank or without decay in the tank. Except when obtaining a fission gas sample, this bypass line was closed by a valve. During sampling, both the bypass line and the inlet valve to the tank were open. With this valve alignment, gas could have been withdrawn from the tank into the evacuated grab sample bottle. In order to equilibrate the gas in the bypass line with the capsule sweep gas, the grab sample was evacuated and then backfilled with the sweep gas passing through the bypass line. The bottle was then re-evacuated, and a second sample of sweep gas was obtained. This procedure resulted in two additional experimental problems. First, with large sample bottles, the initial backfilling resulted in a rapid flow increase in the capsule. Second, with small bottles, the volume of the bottle was not adequate to completely exchange the gas in the bypass line. Thus, it was impossible to apply an accurate correction to account for decay in the lines from the capsule to the sampling station. Hence, the most accurate release data are for the isotopes with the half-lives greater than 1 h (^{85m}Kr, ^{88}Kr, ^{87}Kr, ^{133}Xe, and ^{135}Xe).

The initial results, as reported in the irradiation phase report,[3-11] have been updated to reflect small changes in the capsule sweep-gas flow rates and refinements in the CACA-2 code calculation of the fission gas birth rate. In addition, the release of ^{89}Kr has been calculated based on the amount of ^{89}Rb using Eq. (3-4). The calculated R/B values, some estimated fuel conditions at the time the samples were obtained, and the measured specific activity in the sweep gas are reported in Appendix A. The R/B for selected isotopes (^{133}Xe,^{138}Xe, ^{85m}Kr, and ^{87}Kr) is plotted as a function of the EFPDs in Figure 3.7. Initial R/B ratios were very low ($\sim 10^{-8}$) supporting the low HM contamination reported for the fuel as well as the low measured preirradiation fission gas release[3-12] values and predictions[3-13] for the test. For example, the R/B for one isotope of interest, ^{85m}Kr, was:

- 10^{-8} to 10^{-7} preirradiation measurement
- 10^{-7} or 10^{-6} pretest predictions based on the GA defective SiC model and HM contamination model, respectively
- 10^{-8} increasing to 10^{-4} during the test

ORNL-DWG 95-5801

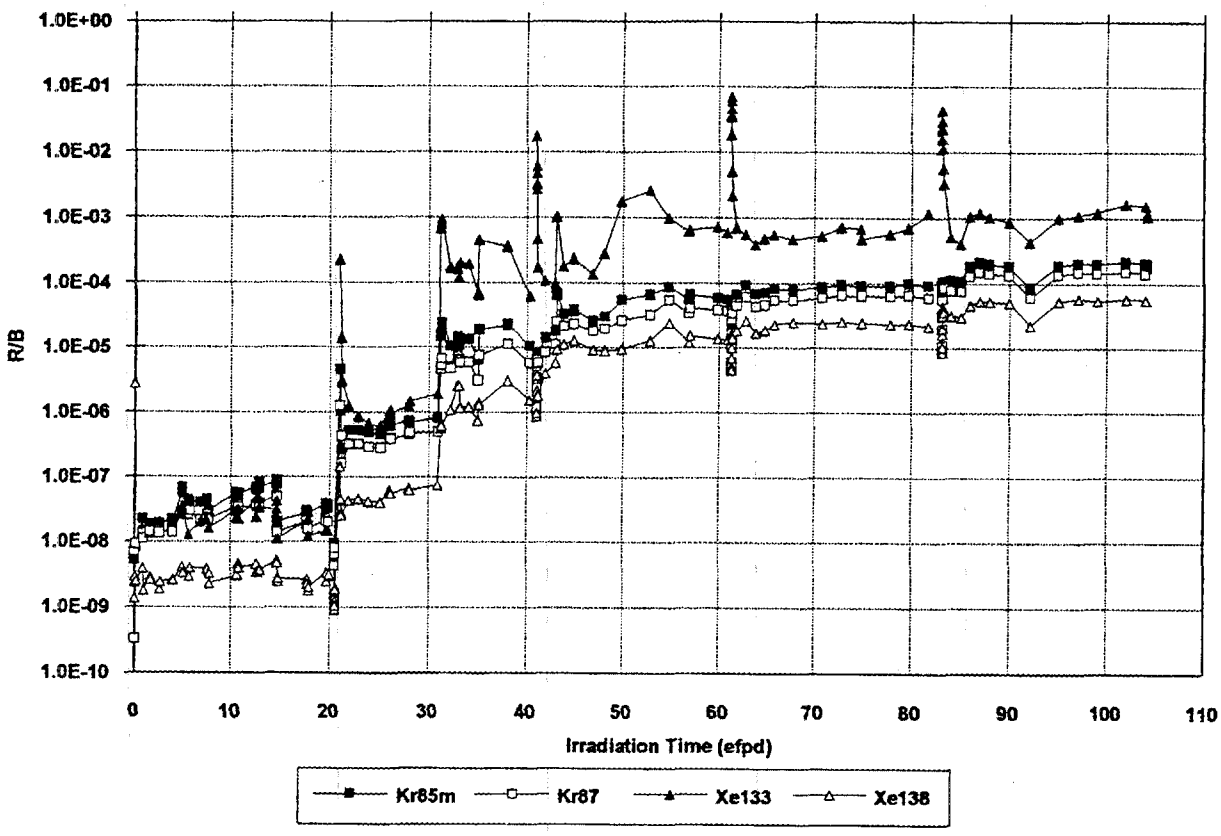

Figure 3.7.

RELEASE RATE/BIRTH RATE OF SELECTED FISSION GASES AS A FUNCTION OF EFFECTIVE FULL-POWER DAYS DURING THE HRB-21 IRRADIATION.

As shown in Figure 3.7, the R/B remained low during the first cycle but increased rapidly in the second cycle and continued to increase for the remainder of the irradiation. As discussed in Sect. 3.2.1, R/B is generally reported after reaching a steady-state value. The approach to steady state is seen in the data shown in Figure 3.7 after the restarts at 20, 40, 60, and 80 EFPDs. The approach to steady state results from a release mechanism in which a diffusional process is the controlling step. Provided that the release rate from the source is small when compared to the radiodecay constant, the concentration of fission gas in the source reaches a steady-state value when the production rate is balanced by the decay rate. The approach to steady state is given by:

$$N_i = \frac{B_i}{\lambda_i}\left(1-e^{-\lambda_i t}\right) , \qquad (3\text{-}14)$$

where the terms have been defined in the previous equations. During HFIR shutdowns for refueling, which usually takes 6 to 10 d, ^{133}Xe accumulates in the HRB-21 fuel compact because of ^{133}I decay. The accumulated ^{133}Xe is released upon HFIR startup because of the associated increase in temperature. This is seen clearly in Figure 3.7 after each HFIR restart. The rapid decline in the ^{133}Xe R/B immediately after startup is caused when the stored ^{133}Xe is released and is removed from the capsule by the sweep gas.

The R/B of ^{135m}Xe is about a factor of 1.5 greater than the R/B for the ^{138}Xe. Since both of these isotopes have similar half-lives (15.3 and 14.2 min, respectively), the difference in R/B is not a half-life effect. Most likely, the difference is due to the mobility of the iodine precursor. ^{135m}Xe is formed in greater than 99% yield by decay of ^{135m}I, whereas only 26% of the ^{138}Xe is formed by decay of ^{138}I (ref. 3-14). Furthermore, ^{135m}I has a 6.5-h half-life and ^{138}I has only a 6.5-s half-life. The longer half-life of ^{135m}I results in transport of ^{135m}I to locations in which the daughter ^{135m}Xe has an accessible path to the void space in the capsule. The temperature in the capsule has an effect on this ratio. ^{135m}Xe was not detected during the first two irradiation cycles of the NPR-2 capsule, even though ^{138}Xe was found in almost every grab sample. In the NPR-1 test and in this HRB-21 test, both isotopes were found in almost every sample, which may be due to the higher temperatures in these tests.

The ^{85m}Kr R/B is plotted in Figure 3.8 as a function of the EFPDs with an overplot of the estimated volume-averaged fuel temperature for the compacts in HFIR region 4. Region 4 temperatures were plotted because the compacts in this region experienced the most fast neutron fluence. The large temperature decreases are caused by reactor shutdowns, during which the temperature of the compacts decreases to less than 100°C. The smaller temperature changes are caused when neon is added or removed from the capsule sweep gas. An analysis of the effects that temperature had on the R/B measured in HRB-21 is complicated by the fact that both the axial and the radial temperature profiles varied widely during the test.

^{85m}Kr and ^{133}Xe release during the first cycle is shown along with the estimated region 4 temperature in Figure 3.9. In order to increase the temperature in the capsule, neon is added to the capsule sweep gas. During the first irradiation cycle, when neon was added, the R/Bs of ^{85m}Kr and ^{133}Xe increased, and when it was removed at the end of the cycle, the R/Bs decreased to values which were about the same as the values at the start of

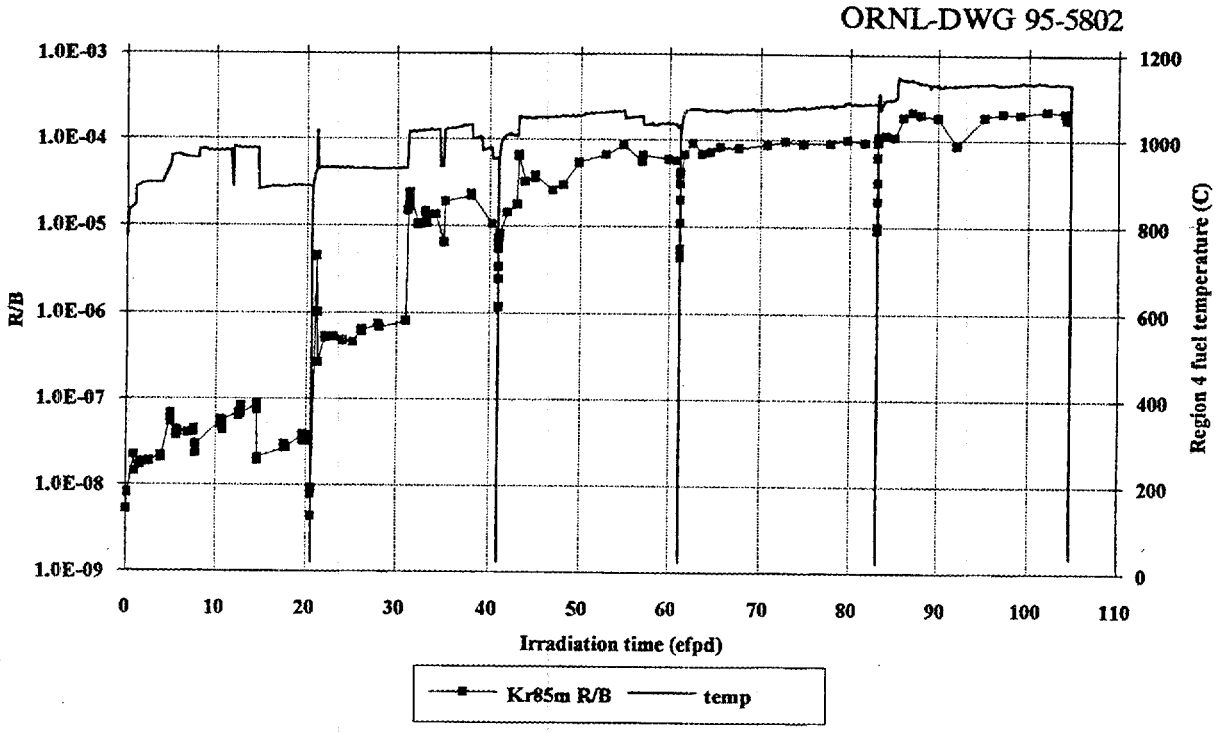

Figure 3.8.

^{85m}Kr RELEASE RATE/BIRTH RATE AND HIGH FLUX ISOTOPE REACTOR REGION 4 AVERAGE COMPACT TEMPERATURE AS A FUNCTION OF EFFECTIVE FULL-POWER DAYS.

irradiation. Furthermore, the changes in the release of ^{133}Xe corresponded with changes in the release of ^{85m}Kr. For this cycle, the release of Kr fission gas is estimated well using the GA model for release from fuel particles with exposed kernels. In this model,[3-3] the fractional steady-state release of fission gas from fuel particles with exposed, unhydrolyzed kernels is given by Eq. (3-15).

$$\left(\frac{R}{B}\right)_{kjiTFS} = \frac{\left(\frac{H}{B}\right)_{kji} \cdot f_T + f_s}{1 + f_s} \cdot E_{f,r} \,, \tag{3-15}$$

The terms of Eq. (3-15) are defined as follows:

$$\left(\frac{R}{B}\right)_{kji} = 3 \cdot \left(\frac{\xi_{kj}}{\lambda_i}\right)^{\frac{1}{2}} \,, \tag{3-16}$$

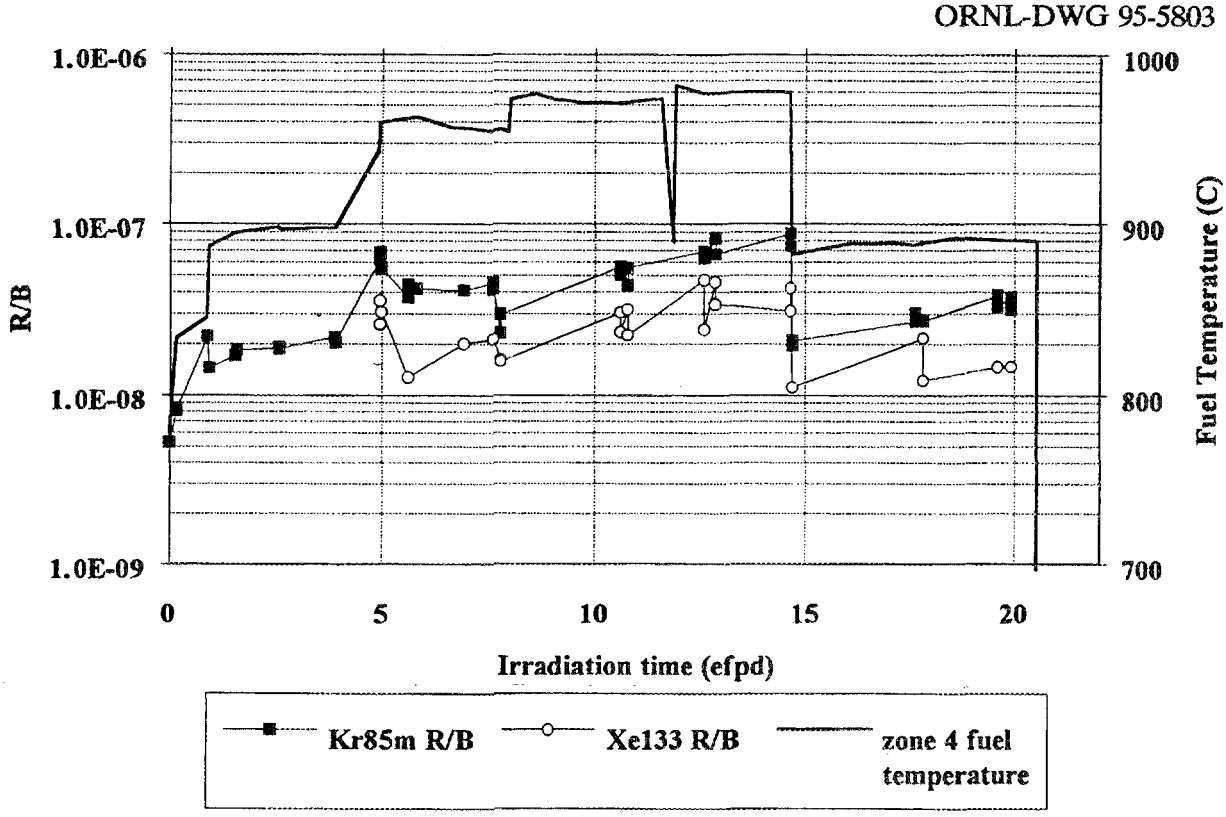

Figure 3.9.

RELEASE RATE/BIRTH RATE AND REGION 4 COMPACT AVERAGE TEMPERATURE DURING THE FIRST CYCLE OF IRRADIATION.

$$f_s = e^{s \cdot (T - T_s)} , \tag{3-17}$$

and

$$f_T = \frac{(R/B)_m}{(R/B)_o} + [1 - \frac{(R/B)_m}{(R/B)_o}] \cdot e^{\frac{Q}{RT_o}} \cdot e^{-\frac{Q}{RT}} , \tag{3-18}$$

where

$E_{f,r}$ = exposed kernel fraction in each HFIR region,

Q = activation energy for fission gas release (J/mol),

R = gas constant (8.314 J/mol-K),

$(R/B)_o$ = release fraction at 1373 K,

$(R/B)_m$ = curve-fitting parameter,

a, T_s = constants.

In order to rigorously apply these equations to a capsule irradiation, the axial and radial temperature distributions and the fission gas production rate distributions are needed. To simplify this calculation, we have weighted the estimated fuel temperature in each HFIR region based on the fission rate in that zone. The predicted ^{85m}Kr values agree well with the measured R/B values (see Figure 3.10) by using the measured compact U contamination as the exposed kernel fraction. The ^{133}Xe is overestimated by about a factor of five. A similar calculation using the GA model for release from U contamination predicts that the R/B during cycle 1 should be about 10^{-6}.

ORNL-DWG 95-5804

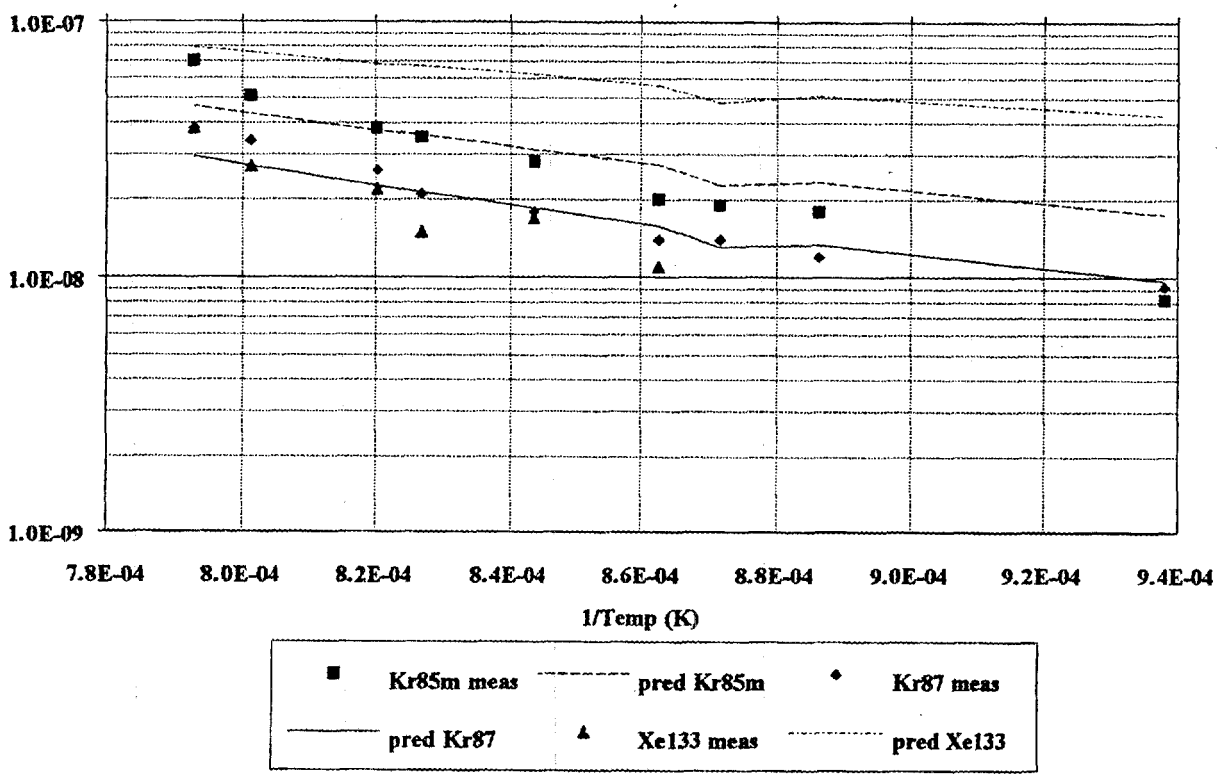

Figure 3.10.

MEASURED RELEASE RATE/BIRTH RATE IN HRB-21 CAPSULE DURING THE FIRST CYCLE COMPARED TO THE RELEASE RATE/BIRTH RATE PREDICTED USING THE EXPOSED KERNEL MODEL.

The models predict that the R/B of ^{133}Xe should be about twice as large as the R/B of ^{85m}Kr. The higher release of ^{133}Xe was seen in the earlier HRB capsules and is a consequence of the longer half-life of ^{133}Xe. As shown in Figure 3.9, the R/B of ^{133}Xe is lower than that of ^{85m}Kr during the first irradiation cycle. This behavior was also observed during the NPR-1 and -2 irradiations.[3-7] HRB-21 and NPR-1/2 were the first irradiations in which the fuel compacts were manufactured with an extremely low HM contamination fraction. This is evident from the initial R/B values which were around 10^{-8} for the latter capsules and 10^{-6} for the earlier HRB tests.

In the second irradiation cycle, the characteristics of the fission-gas release were different than during the first cycle. At the start of the second cycle (see Figure 3.11), when

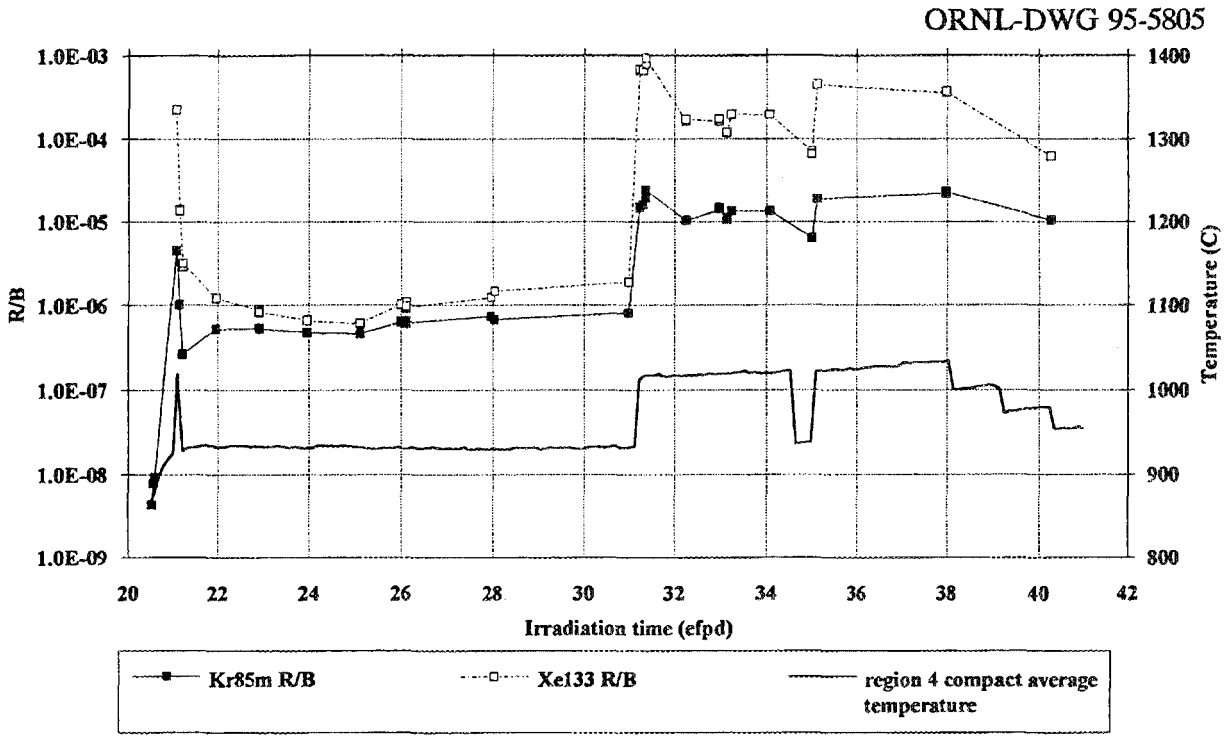

Figure 3.11.

RELEASE RATE/BIRTH RATE AND REGION 4 COMPACT TEMPERATURE DURING CYCLE 2 AS A FUNCTION OF EFFECTIVE FULL-POWER DAYS.

the capsule was being swept with He, the R/B values were somewhat lower than the values obtained at the end of the first cycle. This was caused by a difference in the axial power profile in the capsule at the end of one cycle and the beginning of the subsequent cycle. Due to the control rod positions, more power is generated in the center compacts at the beginning of an HFIR cycle than is produced in the end compacts. This causes an axial temperature gradient which peaks in the compacts near the axial centerplane of the core. As the irradiation cycle progresses, the relative power in the end compacts increases resulting in an increase in temperature.

When Ne was added after 21 EFPDs in cycle 2, the R/B increased, as it did in cycle 1, but by about a factor of 100. Unlike cycle 1, the removal of Ne from the He sweep gas did not result in the R/B decreasing to the level before the Ne addition. Instead, the R/B for ^{85m}Kr remained a factor of 50 greater than when 100% He was previously used as the sweep gas. Similar behavior was observed for the release of ^{133}Xe. The addition of Ne after 31 EFPDs of irradiation also caused a similar release pattern. This suggests that when the fuel temperatures were increased by the addition of Ne, the coatings on some of the particles failed.

The R/B is plotted as a function of the HTGR fast fluence (E > 29 fJ, >0.18 MeV) in Figure 3.12. The particles began to fail after 0.7×10^{25} n/m^2 based on the exposure of the compacts in capsule position 4 (graphite bodies 4 and 5). There was about a 30% fast fluence change radially across the HRB-21 capsule and an axial gradient of about a factor of two. If we assume that the initial failure occurred in the capsule position 4 compact nearest to the HFIR core (because of the higher fluence), then the fluence at the time failure initiated could have been as high at 0.8×10^{25} n/m^2. Figure 3.11 indicates that the temperature in the fuel may have played a role in causing failure of the particles. Alternately, it may have been the insult that finally broke already fatally damaged particles. Since the temperatures and fluences at this point in the irradiation were within the range of known HTGR fuel capabilities, one would not expect a sudden increase in fuel failure with this magnitude of temperature increase. After the initial failure was detected by the ionization chamber response, the temperature in the capsule was reduced by removing the neon from the sweep gas. The R/B decreased because of the lower temperature and, for the next 10 d, remained fairly constant showing that the particle failure rate decreased even though the fluence increased from 0.7 to almost 1. When neon was again added to the

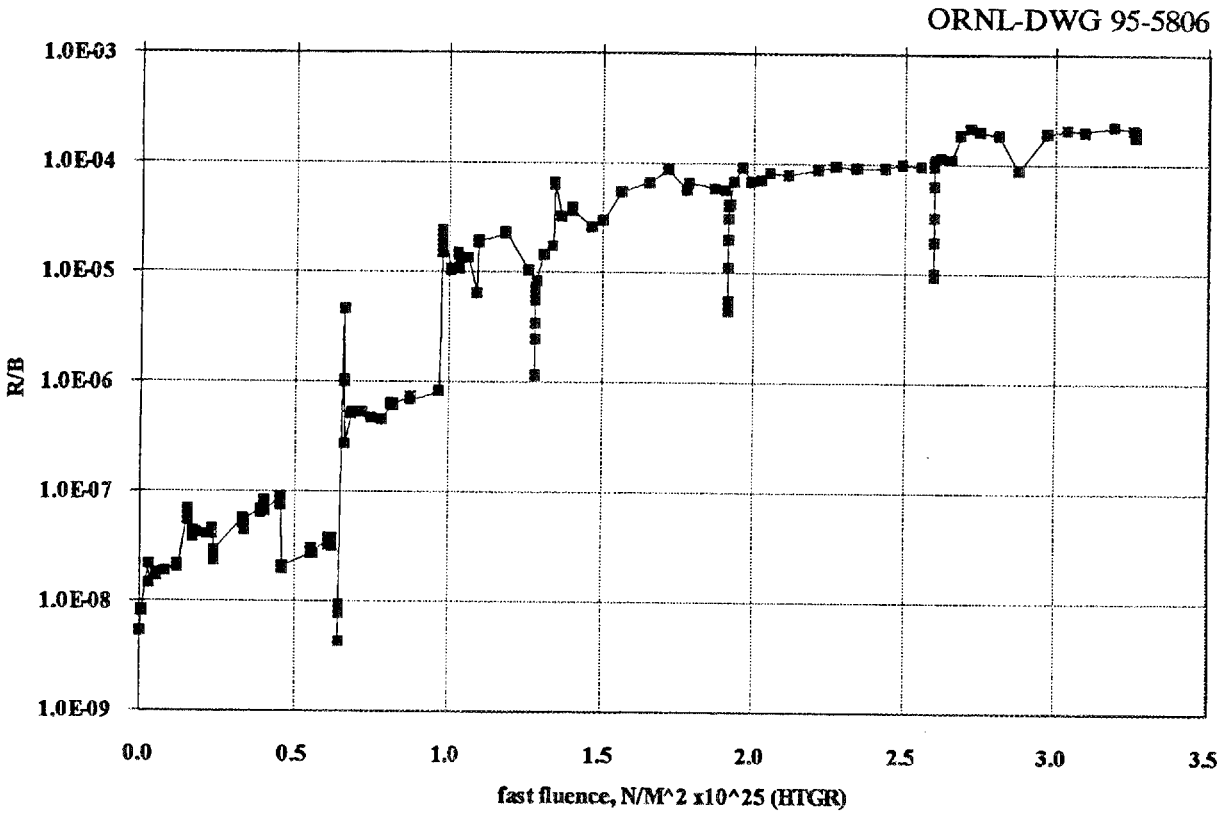

Figure 3.12.

RELEASE RATE/BIRTH RATE AS A FUNCTION OF THE FAST FLUENCE.

sweep gas and the fuel temperature increased, the R/B increased rapidly by about a factor of ten and remained close to that level even when the capsule was cooled by about 70°C when the neon flow was shut off at 35 EFPDs.

Insight into the release mechanism of fission gases may often be obtained by the dependence of R/B on the decay constant. If

$$\frac{R}{B} \propto \left(\frac{1}{\lambda}\right)^{n}, \qquad (3\text{-}19)$$

then

$$\ln\left(\frac{R}{B}\right) \propto n \ln\left(\frac{1}{\lambda}\right), \qquad (3\text{-}19)$$

and n can be obtained from the value of $-\partial \ln(R/B)/\partial \ln \lambda$. Shown in Figure 3.13 are the n-values calculated using the R/B for ^{85m}Kr, ^{87}Kr, and ^{88}Kr. Also plotted on the figure are the ^{85m}Kr R/B values. The normal range of the n-value when the capsule was under steady-state conditions for the Kr isotopes was 0.28 to 0.5. The values below 0.2 were usually caused when the data were obtained before the capsule had reached steady state after a reactor startup. Particle failure increased the n-value to as high as one. This was caused by an increase in the release rate of the long-lived isotopes and is an indication that fission gas which had been stored was being released.

ORNL-DWG 95-5807

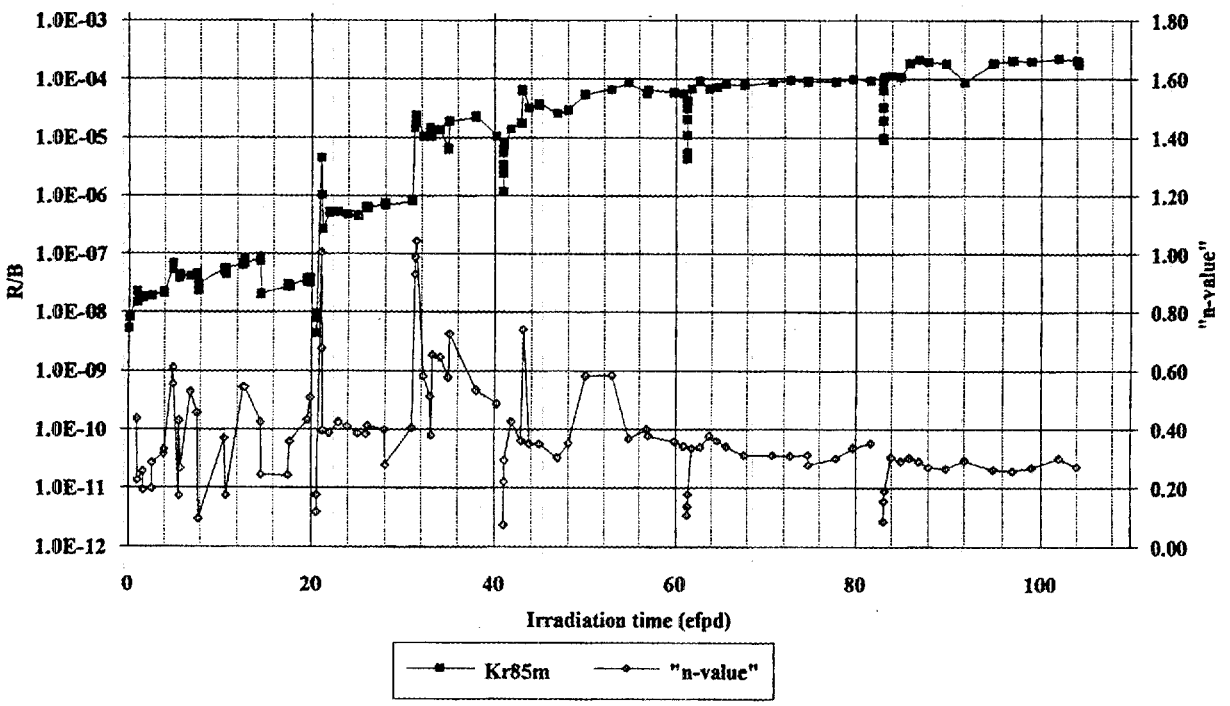

Figure 3.13.
HALF-LIFE DEPENDENCE OF RELEASE RATE/BIRTH RATE IN HRB-21.

To determine the fraction of particles with a connected pore system, the release from a single particle under identical irradiation conditions must be known. The latter quantity has not been measured; measurement would have required a capsule design in which the fission-gas release from small isolated groups of laser-failed particles homogeneously distributed could have been measured independently of the gas release from fuel compacts.

A crude estimate of the number of failed particles may be obtained from reported data on the release from failed particles irradiated in TRIGA tests.

The release from laser-failed UCO particles has been measured in TRIGA experiments after irradiation in HFIR capsules.[3-15] Particles with an initial enrichment of about 20% ^{235}U irradiated to 18.5% FIMA have an ^{85m}Kr R/B at 850°C of 0.3% as measured in the GA TRIGA reactor. However, the burnup influences the R/B, and particles irradiated to 24% FIMA have a TRIGA R/B of approximately 0.8%.

Twice, during cycle 2, the R/B was measured before and after a single particle failure. One failure (spike 43 in Appendix B) occurred after 21.446 EFPDs and was sandwiched between R/B samples 42 and 43. The other failure, spike 44, occurred at 25.809 EFPDs between R/B samples 46 and 47. Both of these failures happened when the sweep gas was 100% He, and the temperature in the capsule was not changing. Examination of the data in Appendix B shows that the two ion chamber spikes which resulted from these failures were similar in magnitude. Furthermore, there was no ion chamber activity during the 4.5 d between the spikes. It is possible that each ion chamber spike was the result of multiple failures. However, the low probability that several failures occurred simultaneously, when no failures were observed for several days between the spikes, suggests that these ion chamber peaks represented a single failure. The increase in ^{85m}Kr R/B due to the particle failure was 2.6×10^{-7} and 1.7×10^{-7}, respectively. These data allow one to get an estimate of the release of a failed particle. Since the birth rate is the same just before and just after the failure, the increase in the R/B is due only to the increase in the release rate for a given population (fissile or fertile):

$$\Delta\left[\frac{R}{B}\right] = \frac{\Delta R}{B} = \frac{R_p}{n_p B_p}, \tag{3-20}$$

where $\mathbf{R_p}$ is the release from the failed particle, $\mathbf{B_p}$ is the birth rate for a particle (failed or not, ignoring fission gradients), and $\mathbf{n_p}$ is the total number of particles. This equation can be

rearranged to give an estimate for the failed particle release rate:

$$\frac{R_p}{B_p} = n_p \Delta\left[\frac{R}{B}\right]. \tag{3-21}$$

If we assume that these early failures occurred in fissile particles, then using $n_p = 4.25 \times 10^4$ and the average of the R/B increases, 2.15×10^{-7}, one estimates that the $[R/B]_{failed}$ is approximately 0.009 for the early failures in HRB-21. This value is close to the value obtained in the early TRIGA tests.

3.2.2.1.2 Transient Fission-Gas Release

Transient fission-gas release is monitored by the response of a radiation detector to pulses of radioactivity in the capsule effluent gas. The radiation level of the sweep-gas exiting the capsule was continuously monitored by two independent ionization chambers (IC) connected to strip-chart recorders. The chart records for the ICs were examined, and a compilation of the pulse heights, time of occurrence, and the full width of the spikes at half-maximum is given in Appendix B. Transient spikes are characterized by a very rapid increase in radiation level of only 1 to 2 min duration at half-height, followed by slower return to a level somewhat higher than before the spike (see the irradiation phase test report[3-11] for examples of transient pluses).

Small, transient fission-gas release spikes were first detected in the initial irradiation cycle. Except for one spike, the magnitude of these spikes was less than 1.5×10^{-12} A. The one larger spike was caused by an increase in the neon concentration. Almost all of these small spikes are attributed to fission gas sampling. They occur when the flow rate from the capsule increases as the evacuated grab sample bottle is backfilled with the sweep gas. The first spikes that appear to be caused by particle failure occurred at the start of cycle 2 just after 20 EFPDs. Figure 3.14 shows the heights of the transient fission gas spikes detected by the sweep gas monitor. Overlayed on the figure is the R/B for ^{85m}Kr. Rapid increases in R/B coincided with a high activity of transient gas release. The onset of the transient spikes corresponded to a burnup in the capsule position 4 (graphite bodies 4 and 5) compacts of about 8.6% FIMA and a fluence of 0.7×10^{25} N/m^2.

ORNL-DWG 95-5808

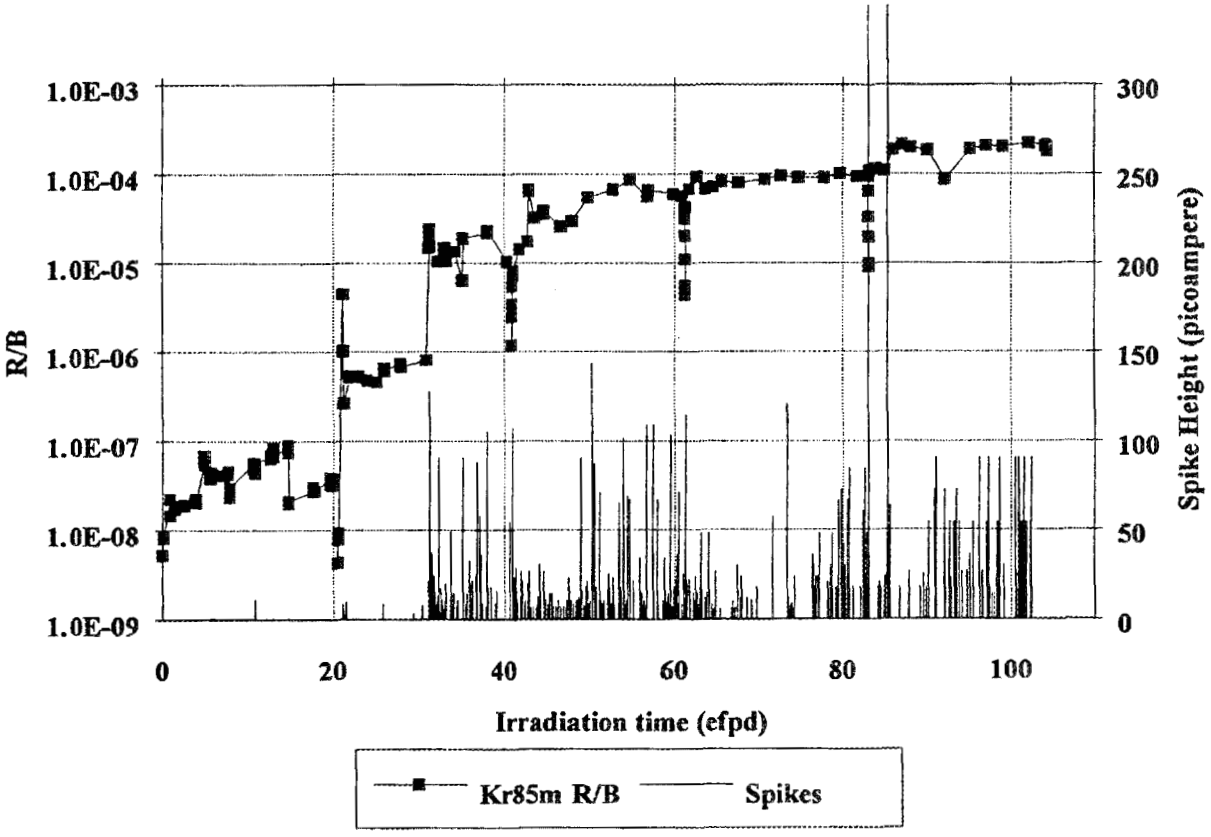

Figure 3.14

TRANSIENT FISSION GAS SPIKES AND ^{85m}KR RELEASE RATE/BIRTH RATE AS A FUNCTION OF EFFECTIVE FULL-POWER DAYS.

Details of transient gas release are seen in Figure 3.15, which shows the cumulative number of spikes that occurred during the second irradiation cycle and the estimated average compact temperature in the HFIR region 4 compacts at the time of the spike. At the beginning of the cycle, neon was added and the temperature increased to greater than 1000°C. A series of spikes were observed as the neon concentration was being increased. Because of the spike activity, the neon was then removed from the sweep gas, the temperatures decreased, and the spike activity ceased. For the next 10 d, only 3 failures were recorded even though the fluence increased by 0.3×10^{25} N/cm^2. When the temperature was again increased, the transient spike activity resumed. Furthermore, the transient spike activity ceased for 2 d when the neon was inadvertently shut off by a reactor safety system. Thus, temperature (or the presence of neon) was one of the important factors causing particle failure.

ORNL-DWG 95-5809

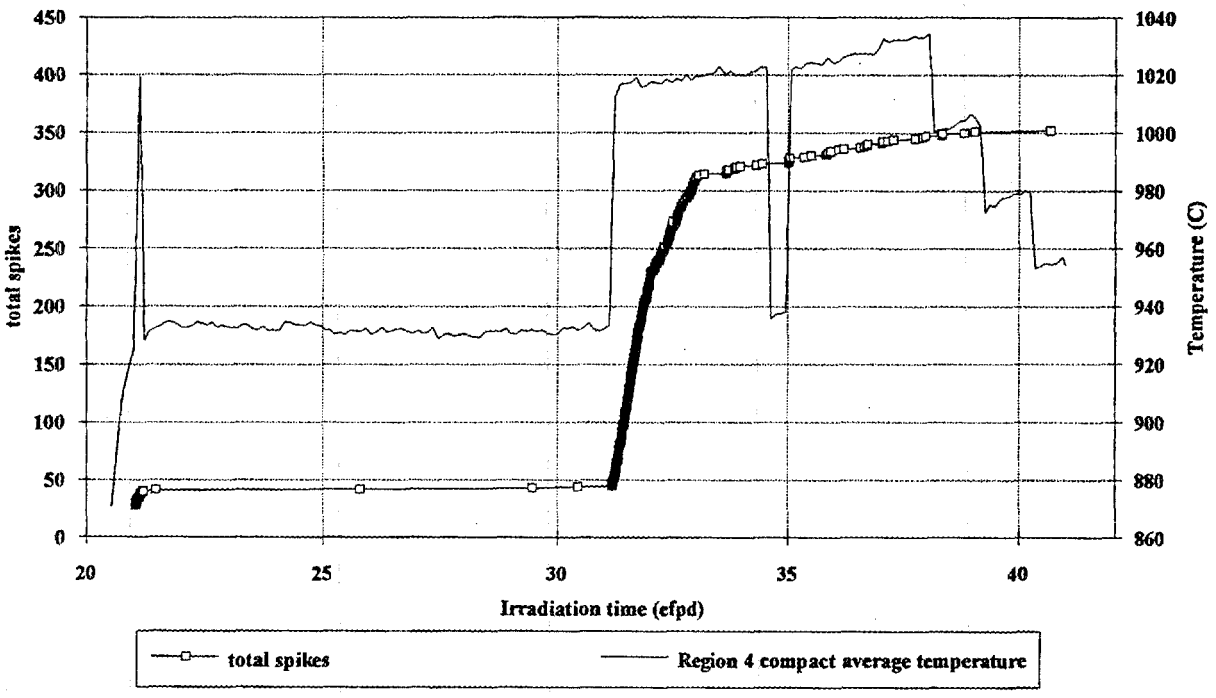

Figure 3.15.

IONIZATION CHAMBER SPIKES AND ESTIMATED AVERAGE COMPACT TEMPERATURE IN HIGH FLUX ISOTOPE REACTOR REGION 4.

There were about 730 spikes which were attributed to gas released from particles during the irradiation. However, one must be cautious when assessing the total number of particle failures based on the number of these transient gas release spikes. Transient fission-gas release occurs (1) when the kernels of intact particles are exposed, (2) when exposed kernels are subjected to rapid increases in temperature, and (3) when oxidants or other chemical species that readily diffuse in the fuel kernels are added to the particle system. Thus, it is possible that one particle failure could result in several spikes during the irradiation. The magnitude of the transient release caused by each of these mechanisms has not been quantified for the range of irradiation conditions in HRB-21. The largest spikes may be caused by rupture of the SiC in particles with the PyC layers already failed or may be the result of gas released as several particles fail almost simultaneously. Small spikes may be due to (1) failure of coatings other than the SiC and (2) fission gas bubbles being vented to open porosity in particles with failed coatings due to changes in fuel temperatures. Furthermore, the size of the spike caused when an SiC coating fails on a specific particle will

probably be a function of that particular particle's fission rate, the gas inventory which is stored in its open porosity, and its temperature. These attributes would depend on the type of particle (fissile or fertile), the location in the compact, and the location of the compact in the capsule.

In addition, during the last week of operation, the full-scale sensitivity of the IC was changed to 3000 pA. Since peaks smaller than about 1 mm were not counted, some spikes with magnitudes of up to 20 pA would not be included in the total.

Transient fission-gas release was also observed 7 to 8 min after the reactor was shut down. In this case, the pulse height was larger than the spikes obtained at full power, and the full width at half maximum (FWHM) was at least 3 min. Fission-gas release at shutdown of UO_2 fuel elements which had operated at 1400°C is known to occur. This gas is believed to have been stored in the center of the element after migrating up the thermal gradient.[3-16] Because the hot center portion is plastic and uncracked, the gas collected in this region is sealed off from the pore volume that intersects the free surface. When the reactor is shut down, the rapid cooling results in cracks which open to the free volume. Metallographic PIE of fuel particles shows that the fuel kernel has many void spaces; for example, see Figure 4.72 in Sect. 4.6.2.3.2. These spaces probably were formed by the accumulation of fission gas. Thus, it seems plausible that the transient gas release observed at reactor shutdown is caused by release from fission gas bubbles in failed particles in a manner similar to that explained above.

3.2.2.2 TRIGA Release Rate/Birth Rate Measurements

After the irradiation, fuel compacts were removed from the capsule and transported to GA for measurements of the R/B of individual compacts. The R/B of compacts irradiated in each HFIR region was measured in a TRIGA King Furnace[3-17] at 900 and 1100°C using the procedure described in Sect. 3.2.1.2. The results for several fission gases are reproduced in Appendix C (ref. 3-10).

The TRIGA-measured R/B values were found to depend on the location at which the compacts were irradiated in HFIR. The compacts irradiated in the end locations of the HFIR core had an average ^{85m}Kr R/B at 1100°C of 1.4×10^{-6}. The R/B of compacts irradiated in the center of the HFIR core was 4.1×10^{-4}. The composite R/B for the capsule can be estimated after weighting the TRIGA data for the fraction of fission gas produced in each HFIR region at the end of the HFIR irradiation. CACA2 predicts that these fractional

birth rates for ^{85m}Kr are 0.22, 0.25, 0.26, and 0.27 for HFIR regions 1, 2, 3, and 4. Using the average steady-state TRIGA ^{85m}Kr R/B values at 1100°C given in Appendix C, one calculates that the capsule R/B would be 2.0×10^{-4}. The measured capsule R/B averaged over the last 7 d of irradiation was $2.1 \pm 0.1 \times 10^{-4}$.

Richards[3-18] at GA has analyzed the TRIGA data and computed the fraction of exposed kernels using:

$$\left(\frac{R}{B}\right)_{compact} = F_{EK,fs} \times \left(\frac{R}{B}\right)_{EK,fs} \times \beta_{fs} + F_{EK,fr} \times \left(\frac{R}{B}\right)_{EK,fr} \times (1-\beta_{fs}) , \qquad (3\text{-}22)$$

where

$F_{EK,fs}$ = fissile fuel exposed kernel fraction,

$F_{EK,fr}$ = fertile fuel exposed kernel fraction,

β_{fs} = fractional birth rate in fissile fuel,

$(R/B)_{EK,fs}$ = R/B for a fissile exposed kernel = 0.0094,

$(R/B)_{EK,fr}$ = R/B for a fertile exposed kernel = 0.0567.

Since the metallographic examinations showed that the amount of fissile particle failure was about the same as fertile failure, $F_{EK,fs} = F_{EK,fr}$. The R/B value for exposed fissile kernels was not measured but was estimated based on the U.S. fission-gas release models. The R/B value for the exposed fertile kernel was based on the average of three laser-failed THO_2 particles with burnups ranging from 1.2 to 6% FIMA. The TRIGA R/B values are the result of a 30-min irradiation and are not corrected to steady-state conditions as are the data given in Appendix C. The results of Richards' calculations are shown in Table 3.4.

This gives a total of about 2100 failed particles for one-half of the capsule compacts. Thus, the total number of failed particles is about 4200 based on the TRIGA data.

3.3 HRB-21 NEUTRON DOSIMETRY

3.3.1 General

The key parameters of interest in the experiment are all directly related to the nuclear reaction rates in the specimens and holders. Design analyses performed in support of the test are made based on assumed nuclear reaction rates, previous empirical data,

Table 3.4.

PARTICLE FAILURES ESTIMATED BY TRIGA

Compact	Number of particles		TRIGA ^{85m}Kr R/B 1100°C	F_{EK}	Number of failed particles
	Fissile	Fertile			
5A	1200	4457	4.9×10^{-4}	0.083	470
5B	1200	4457	3.3×10^{-4}	0.056	320
5C	1200	4457	3.7×10^{-4}	0.063	350
6A	1447	4527	3.2×10^{-4}	0.054	320
6B	1447	4527	2.1×10^{-4}	0.035	210
6C	1447	4527	2.0×10^{-4}	0.034	200
7A	1947	4527	7.0×10^{-5}	0.011	71
7B	1947	4527	7.5×10^{-5}	0.012	78
7C	1947	4527	9.3×10^{-5}	0.015	97
8A	2497	4197	1.8×10^{-7}	2.6×10^{-5}	0
8B	2497	4197	2.8×10^{-6}	4.0×10^{-4}	3
8C	2497	4197	1.0×10^{-6}	1.4×10^{-4}	1

and/or detailed nuclear (neutronics) calculations. However, to verify assumptions about nuclear reaction rates for a particular test, neutron dosimetry should be an integral part of the test design, placed as close to the test articles as practical. This is especially important in providing the final estimates of fast neutron fluence on graphite specimens. Other test objectives, such as fuel burnup and integrated fission density, can be directly inferred in several ways, but there is no other direct measurement of accumulated neutron fluence above specific neutron energies than in analyzing selected flux wires.

Each nuclear reaction is strongly dependent on the neutron energy spectrum; therefore, dosimetry materials are selected on the basis of known reaction energy thresholds, as well as other factors such as the decay rate and burnup rate of the primary daughter products of the nuclear reaction of interest, i.e., the one related to the particular energy threshold. Other factors taken into account are the estimated neutron and gamma fluxes;

irradiation environment (temperature, chemistry, etc.); irradiation time; and potential postirradiation handling and analysis problems.

3.3.2 HRB-21 Dosimetry Description

The neutron dosimetry packages (flux monitors) for the HRB-21 test were strategically located in the graphite body, adjacent to the fuel compacts. Each of the eight graphite bodies contained three separate monitor packages (A, B, and C) located 120° apart azimuthally, near the outside edge of the graphite, as shown in Figure 3.16. The dosimetry materials selected for the HRB-21 test are shown in Table 3.5 along with some of the important nuclear reactions. The actual analysis included other nuclear reactions as well. The monitor packages were positioned approximately in the midplane of each graphite body.

ORNL-DWG 95-5810

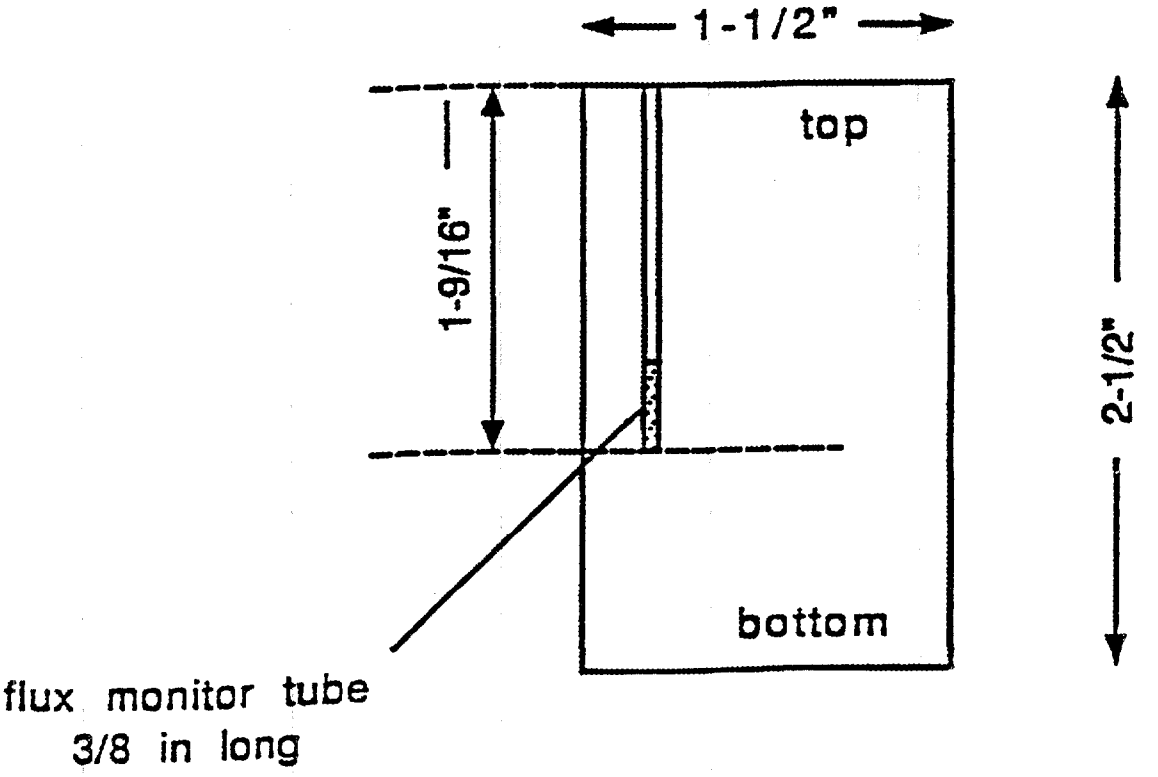

Figure 3.16.
HRB-21 FLUX MONITOR AXIAL LOCATION IN EACH GRAPHITE BODY.

Table 3.5

FLUX WIRE MATERIALS USED IN HRB-21

Flux monitor	Reaction	Useful threshold energy
0.5 Co/V	$Co(n,\gamma)Co^{60}$	Thermal
Nb	$Nb(n,n')Nb^{93m}$	0.5 MeV
Ni	$Ni(n,p)Co^{60}$	2.1 MeV
Fe	$Fe(n,p)Mn^{54}$	2.2 MeV
Ti	$Ti(n,p)Sc^{46}$	4.4 MeV
80.2 Mn/Cu	$Cu(n,\alpha)Co^{60}$	5.0 MeV

3.3.3 Analysis Results and Conclusions

Two entire sets of monitors, A and B, were sent to Pacific Northwest Labs (PNL) for counting and analysis. Set C was kept at ORNL in case problems developed in either the shipping or handling at PNL. The results of the PNL analysis of Sets A and B are reported in ref. 3-19. The primary PNL results of interest are shown in Figures 3.17 through 3.20. Considerable difficultly occurred with the analysis because of severe degradation of the Mn/Cu wires due to the high operating temperature. The degradation resulted in the transfer of material from the Mn/Cu wires to other wires in the dosimetry capsule. Chemical etching of the wires was necessary to remove this transferred material. In addition, three nuclear reactions could not be used because of burnup effects that could not be unfolded. They were the $^{58}Ni(n,p)^{58}Co$ reaction because of the high thermal burnup effect due to ^{58}Co, the $^{60}Ni(n,p)^{60}Co$ reaction because the previous reaction generates ^{59}Co from ^{58}Co which then generates ^{60}Co, and the $^{63}Cu(n,\alpha)^{60}Co$ reaction because of cobalt impurities in the Mn/Cu alloy. Overall, a parabolic curve fit the axial profile of the flux within an error of about 10%, although the scatter in a couple of the isotopes was considerably greater. The overall counting error of the isotopes was about 2%, but the problem with the Mn/Cu material probably increased this uncertainty several times.

Detailed comparison of the PNL results with ORNL assumptions indicates reasonable agreement on the neutron energy spectrum, as indicated in Figure 3.21 using 1985 DORT calculations and in Figure 3.22 using 1993 DORT calculations.[3-20] The overall

ORNL-DWG 95-5811

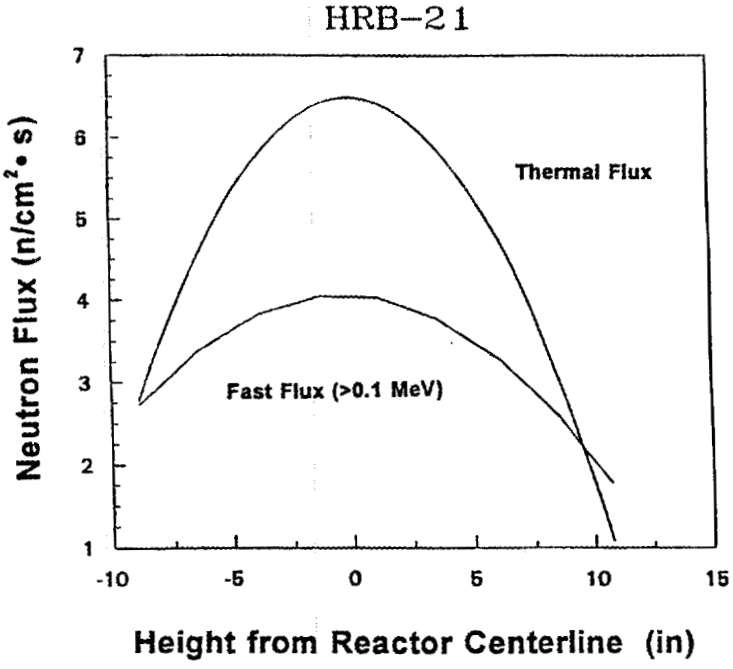

Figure 3.17.

NEUTRON FLUX PROFILE MEASURED IN CAPSULE HRB-21.

ORNL-DWG 95-5812

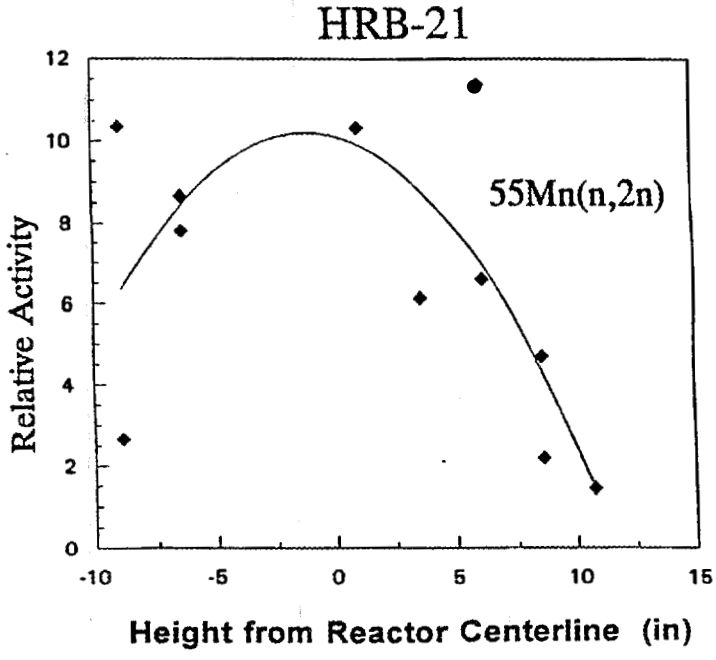

Figure 3.18.

ACTIVITY OF ^{55}Mn FLUX WIRE FROM HRB-21.

ORNL-DWG 95-5813

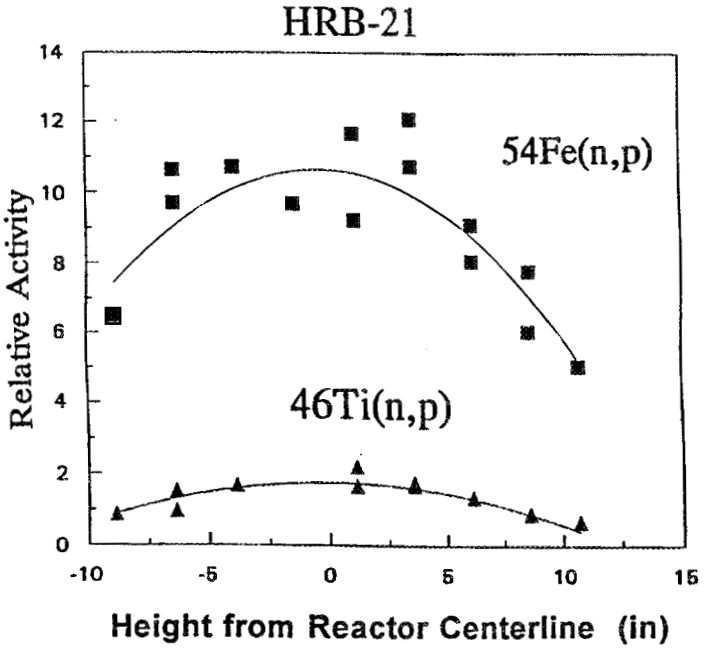

Figure 3.19.

ACTIVITY OF ^{54}FE AND ^{46}TI FLUX WIRES FROM HRB-21.

ORNL-DWG 95-5814

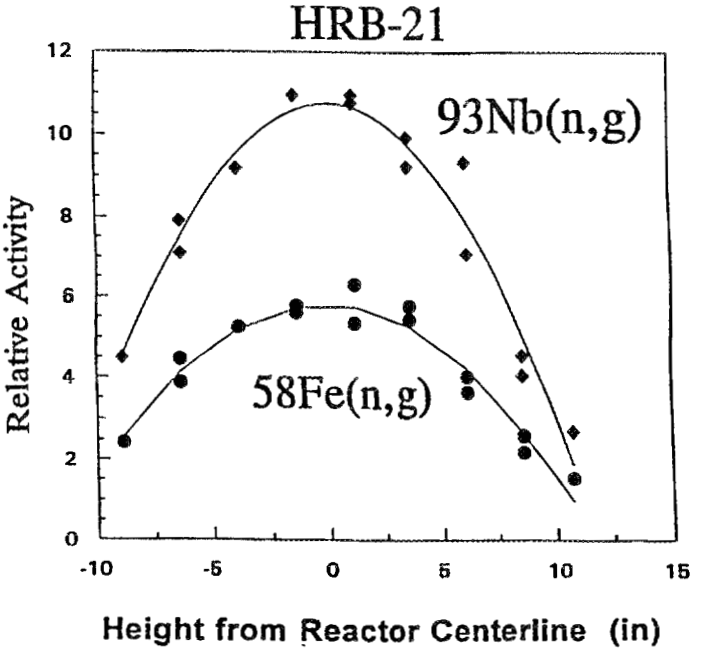

Figure 3.20.

ACTIVITY OF ^{93}Nb AND ^{58}Fe FLUX WIRE FROM HRB-21.

ORNL-DWG 95-5815

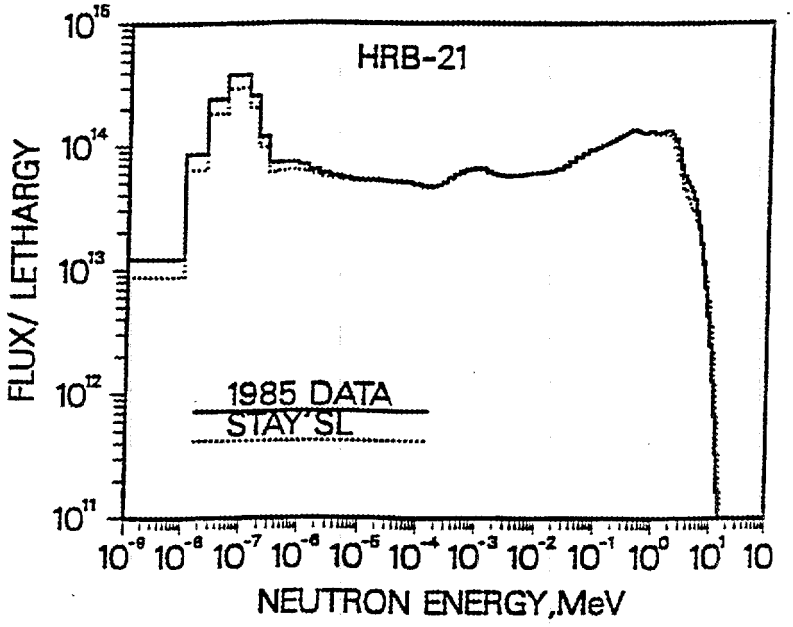

Figure 3.21.

COMPARISON OF NEUTRON SPECTRUM PREDICTED BY PACIFIC NORTHWEST LABORATORY STAL'SL CODE AND THE 1985 HIGH FLUX ISOTOPE REACTOR MEASUREMENTS.

ORNL-DWG 95-5816

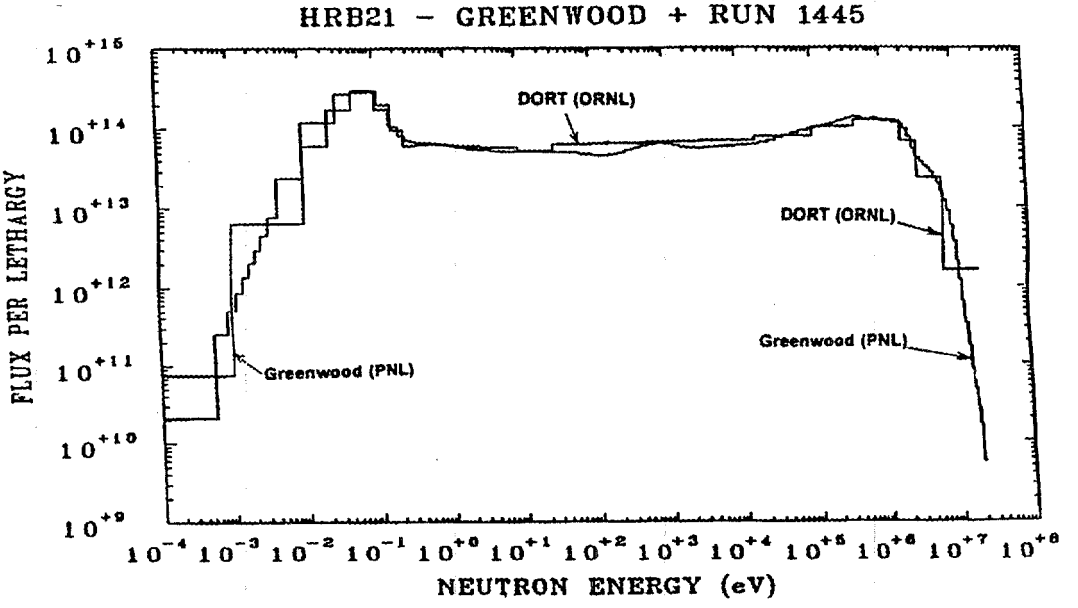

Figure 3.22.

COMPARISON OF NEUTRON SPECTRUM IN HRB-21 AS PREDICTED BY DORT AT OAK RIDGE NATIONAL LABORATORY AND BY GREENWOOD AT PACIFIC NORTHWEST LABORATORY.

agreement is within 12%, the thermal flux within 13%, and the fast flux within 23%. Because of the problems associated with the dosimetry, this result and its uncertainties are the effective end limit of the analysis. Overall, the dosimetry produced no surprises about the neutron flux and confirmed earlier estimates.

An attempt was made to infer thermal information from the degradation of the Mn/Cu wires, but no useful information was obtained. The mass transfer could have occurred over a rather broad temperature range by vapor phase and diffusive mechanisms at the capsule operating temperature. Modelling of this effect would have been time consuming, and the lack of good data on the quantity and history of the mass transfer made this task of marginal value.

3.4 HRB-21 BURNUP DETERMINATION

The burnup determination is extremely important for the following reasons:

1. The burnup measurement provides an estimate of the fission product inventory at the end of the test, which can be decay-corrected to the date of burnup measurement to compare the measured inventory with the predicted inventory to identify any missing isotopes, such as ^{137}Cs, indicating particle failure.
2. The burnup measurement is a direct indicator of the total ^{235}U depletion (fission plus capture), which implies an average fission rate. The average fission rate can then be compared to the total heat rate assumed in the thermal analysis (fission plus gamma), in order to reduce the overall uncertainties in the fuel compact temperature calculations.
3. The endpoint burnup measurement reduces the uncertainties in the estimated stresses due to the assumed fission gas pressure buildup.

Determination of the burnup of MHTGR fissile and fertile particles by radiochemical methods is an expensive and laborious process that creates a significant amount of hazardous waste if more than a few particles are to be analyzed. One way of avoiding the radiochemical method is by estimating the inventory of several gamma-emitting fission products in the particle based on gamma spectroscopy. Once the inventory of several key isotopes is known, the burnup can be determined by making use of the radionuclide's decay constant and fission yield. Since the measurement of the particle's inventory is already part of the PIE program, this method makes economical use of the collected data.

Determination of a particle's inventory of several gamma-emitting fission products has been accomplished by using the Irradiated-Microscope Gamma Analyzer (IMGA) device. Typically, a particle's inventory of ^{95}Zr, ^{103}Ru, ^{106}Ru, ^{137}Cs, ^{141}Ce, and ^{144}Ce was determined in several minutes using this device. The averaging of a large number of particle measurements provided a good mean value for the burnup calculation. One advantage of this method is that the geometry is well known, and system calibration is easy. Also, no mechanical grinding or chemical dissolution of the particle is required, eliminating additional sources of uncertainty. The method works with both fertile and fissile particles.

A single-group neutronics model was used to determine a set of equations that relates the end-of-irradiation radionuclide inventory to the number of fissions that have taken place during the course of the irradiation.[3-21] The fission rate is then modelled by a set of test functions with adjustable parameters. A least-squares minimization technique is then used to find the best values for the parameters in the fission rate that leads to the least error between the IMGA-measured particle inventory and the inventory calculated by the single-group model using the estimated fission rate. Typically, the errors between the model-calculated and the IMGA-measured values for the radionuclides are less than a few percent. A major strength of this technique is that it makes use of all the collected data—both the radionuclide inventory and its standard deviation. This fact reduces the error introduced by the measurement of any one radionuclide and can also point out possible losses of radionuclides. The burnup is estimated by integrating the fission rate for the fissile isotope of interest. Finally, the standard deviation of the burnup is estimated. The technique can also determine the burnup as a function of time during the irradiation, subject to the limitations of the model.

The estimated burnups for the UCO particles as determined by CACA2 calculations for the actual reactor operation and the results of the HRB-21 burnup estimate based on IMGA measurements are shown in Table 3.6. Note that the piggybacks have considerable variation in their burnup. The positional averages of the measurements and the calculations are shown in Table 3.7 using both piggyback and compact data. Note than the greatest error is in the middle region and that the calculations overestimated the burnup by roughly 20%. Only small sample sizes were available for piggyback analysis, so considerable variation in burnup could be possible for the piggybacks. The overall burnup agreement between IMGA and calculations for all measurements is within 18%. The agreement based on compacts

Table 3.6.

MEASURED VERSUS CALCULATED BURNUP FOR THE UCO PARTICLES

Body location	Item	IMGA[a] burnup % FIMA[b]	Calculated burnup % FIMA[b]	Percent difference (IMGA-Cal)/IMGA[a]
1	Piggyback 1c	11.5	13.8	-20.00
2	Piggyback 2a	13.7	18.3	-33.58
	Piggyback 2b	15.5	18.3	-18.06
	Piggyback 2c	14.5	18.3	-26.21
3	Piggyback 3a	17.8	21.1	-18.54
	Piggyback 3b	18.2	21.1	-15.93
	Piggyback 3c	17.4	21.1	-21.26
4	Piggyback 4c	18.8	22.3	-18.62
5	Compact 5b	19.2	22.3	-16.15
	Compact 5c	19.5	22.3	-14.36
7	Compact 7a	15.7	18.3	-16.56
8	Compact 8a	12.3	13.8	-12.20

[a]IMGA = Irradiated-Microsphere Gamma Analyzer.
[b]FIMA = Fissions per initial metal atom.

only is better at 15% (bottom half of Table 3.6). The compact data consisted of considerably more particles than the piggyback data. The CACA2 overestimation of the burnup may be due to a slightly lower actual thermal flux (see Sect. 3.3) and the use of cross sections that are slightly too large for the actual neutron spectrum seen by the capsule. Also, the model used in determining the burnup assumes a time-invariant neutron spectrum.

The estimated burnups for the ThO_2 particles as determined by CACA2 calculations for the actual reactor operation and IMGA measurements are shown in Table 3.8. There were not enough data to do a positional average. The overall agreement is within 12%. Note that the IMGA measurements are generally slightly low. Also, note that the new calculated burnups are slightly greater than the original calculations; the new calculations take into account the fact that the total time in the reactor (additional downtime) was longer than expected, thus more ^{233}Pa decayed to ^{233}U.

Table 3.7.

POSITIONAL AVERAGE BURNUP VERSUS CALCULATED BURNUP FOR THE UCO PARTICLES

Body location	IMGA[a] burnup % FIMA[b]	Calculated burnup % FIMA[b]	Percent difference (IMGA-Cal)/IMGA[a]
1,8	11.9	13.8	-15.97
2,7	14.9	18.3	-22.82
3,6[c]	17.8	21.1	-18.54
4,5	19.2	22.3	-16.15
Average difference			-18.37

[a]IMGA = Irradiated-Microsphere Gamma Analyzer.
[b]FIMA = Fissions per initial metal atom.
[c]Calculated using only data from body 3.

Table 3.8.

MEASURED VERSUS CALCULATED BURNUP FOR THE ThO_2 PARTICLES

Body location	Item	IMGA[a] burnup % FIMA[b]	Calculated burnup % FIMA[b]	Percent difference (IMGA-Cal)/IMGA[a]
5	Compact 5b	2.00	2.24	-12.00
	Compact 5c	2.00	2.24	-12.00
6	Piggyback 6a	1.77	1.86	-5.08
7	Piggyback 7a	1.09	1.18	-8.26
	Compact 7a	1.10	1.18	-7.27
8	Compact 8a	0.54	0.52	3.70

[a]IMGA = Irradiated-Microsphere Gamma Analyzer.
[b]FIMA = Fissions per initial metal atom.

3.4.1 Recommended Neutronic Values

Overall, the agreement is reasonably good between the various methods. The best burnup data (largest sample), the compact examination, agree with the calculations within 15%; the neutronics data from Sect. 3.3 agree with overall neutron spectrum calculations within 12% and within 23% for the fast flux. Given the difficulties that were encountered during PIE, these results are very favorable. For the purposes of this report, the calculated burnup with an uncertainty of ±15% may be used as the burnup value, and the calculated fluence with an uncertainty of ±23% may be used as the fluence value.

3.5 REFERENCES

3-1. G. L. Bell et al., HRB-21 Irradiation Phase Test Report, DOE-HTGR-90322, Rev. 0 (ORNL/TM-12238, Rev. 0), Martin Marietta Energy Systems, Inc., Oak Ridge Natl. Lab., January 1993.

3-2. Graphite Design Handbook, DOE-HTGR-8811, Rev. 0, General Atomics, San Diego, Calif., September 1988.

3-3. Fuel Design Data Manual, Issue F, GA-901866, General Atomics, San Diego, Calif., August 26, 1987.

3-4. K. W. Childs, HEATING 7.0 User's Manual, K/CSD/INF/90-32, Martin Marietta Energy Systems, Inc., Oak Ridge Gaseous Diffusion Plant, July 1990.

3-5. Gas-Cooled Reactors, High-Temperature Gas-Cooled Reactor Technology Development Program, Annual Progress Report for Period Ending December 31, 1981, ORNL-5871, Union Carbide Corp. Nuclear Div., Oak Ridge Natl. Lab., 1982.

3-6. E. J. Allen, CACA-2: Revised Version of CACA-A Heavy Isotope and Fission Product Concentration Calculational Code for Experimental Irradiation Capsules, ORNL/TM-5266, Union Carbide Corp., Nuclear Div., Oak Ridge Natl. Lab., February 1976.

3-7. The New Production Reactor Fuel Post Irradiation Examination Data Report for Capsules NPR-1, NPR-2 and NPR-1A, ORNL/TM-2849, Martin Marietta Energy Systems, Inc., Oak Ridge Natl. Lab., September 1993.

3-8. E. D. Clemmer, "Sweep Gas Sampling," Engineering Technology Division Procedure ETD-IE-SOP-005, Oak Ridge Natl. Lab., December 1988.

3-9. L. C. Emerson, "HFIR Sweep Gas Counting and Analysis," Metals and Ceramics Division Procedure, MET-FMT-OG-002, Oak Ridge Natl. Lab., July 1993.

3-10. J. J. Saurwein and J. Greenwood, "Fission Gas Release Testing of Fuel Compacts from Irradiation Capsule HRB-21," General Atomics Letter Report GA/ORNL-020-92, October 1, 1992.

3-11. G. L. Bell et al., HRB-21 Irradiation Phase Test Report, ORNL/TM-12238, Rev. 0, Martin Marietta Energy Systems, Inc., Oak Ridge Natl. Lab., January 1993.

3-12. Capsule HRB-21 Pre-Irradiation Report, DOE-HTGR-88357, Rev. C, General Atomics, San Diego, Calif., April 1991.

3-13. "Pre-test Prediction for HRB-21 Capsule," GA/ORNL-014-91, unpublished data of F. E. Hooks and M. B. Richards, General Atomics, San Diego, Calif., transmitted in letter from G. C. Bramblett to M. J. Kania, Oak Ridge Natl. Lab., July 10, 1991.

3-14. M. E. Meek and B. F. Rider, Compilation of Fission Product Yields, NEDO-12154-1, General Electric Vallecitos Nuclear Center, January 26, 1974.

3-15. F. C. Montgomery and R. J. Presourt, Test Status Report R/B Failed UCO Fuel, GA-906427, Issue/1, General Atomics, San Diego, Calif., March 1982.

3-16. M.J.F. Notley and J. R. MacEwan, Nucl. Appl. 2, 447 (1966).

3-17. E. E. Anderson et al., "An In-core Furnace for the High-Temperature Irradiation Testing of Reactor Fuels," Nucl. Technol., 11, 259-65 (1971).

3-18. "HRB-21 Compact Failure Fractions," CEGA-M-93-0996, private communication from M. Richards, Combustion Engineering General Atomics, San Diego, Calif., July 15, 1993.

3-19. L. R. Greenwood, "Neutron Measurements for the HRB-21 Experiment," PNL-19450, Letter Report to J. Parks, June 1, 1993.

3-20. The DORT results were provided by Ward Engle of the Engineering Physics and Mathematics Division, Oak Ridge Natl. Lab., via personal communication. The MHTGR spectrum was taken from a facsimile transmission from R. Turner (General Atomics) to J. T. Parks, July 1991. The notes reference the computer code MICROX, run dates 7-6-92 and 7-15-92. The note further directs questions to Bob Rucker. This figure was generated to allow a rough comparison of the spectrum in the HFIR as compared with a typical spectrum in a 450-MW(t) MHTGR and is

not intended to be a data reference. Total flux (10^{14} neutrons/cm^{2}s): MHTGR = 1.98, DORT = 23.7.

3-21. R. N. Morris, MHTGR Fissile and Fertile Particle Burnup Determination by Gamma Spectroscopy, ORNL/TM-12310, Martin Marietta Energy Systems, Inc., Oak Ridge Natl. Lab., February 1994.

SECTION 4

POSTIRRADIATION EXAMINATION RESULTS

4.1 CAPSULE DISASSEMBLY

Disassembly and associated tasks on capsule HRB-21 were carried out in accordance with procedure MET-FME-ESP-11, Rev. 0, "HRB-21 Capsule Disassembly, Visual Examination, and Component Metrology."[4-1]

4.1.1 Shipping

The HRB-21 experiment was the first fuel experiment to be irradiated with a rigid tubular extension to the pressure-vessel head. This 12-ft-long rigid assembly required that both the transfer cask and the procedures for loading in the HFIR pool[4-2] and unloading into the hot cells[4-3] be modified. In the HFIR pool, the experiment leads were cut above the junction box and crimped.[4-4] The crimped leads were kept above water level to ensure that the experiment remained dry. In the charging area of the hot cells, the junction box was removed by cutting through the containment sleeve, including the TC leads and gas tubes, with a hacksaw. The cask was then placed against the cell loading port, the lower part of the assembly was pushed into the cell, and the bottom 36 in. of the assembly containing the capsule portion were cut off with a hydraulic shear. The remaining containment sleeve was cut into several pieces so that it could be pushed into the cell as well.

4.1.2 Visual Examination of Capsule

The capsule was examined visually through the cell window and with the Kollmorgen periscope.[4-1] The capsule appeared to be in good condition with no obvious deformation or damage. There was a white film, or scale, on the bottom 24 in. of the capsule. Following the visual examination, the capsule was placed in a rotating chuck in the milling machine, and a circumferential cut ("trim cut") was made with an end mill at 24 in. from the bottom to remove the extraneous containment sleeve (see Figure 4.1). The first attempts at cutting with a high-speed steel cutter were unsuccessful because of end mill slippage in the collet and very fast tool wear. A solid Carballoy end mill was then used which cut through the sleeve with little difficulty. The gas tube and TC leads were cut with a hacksaw.

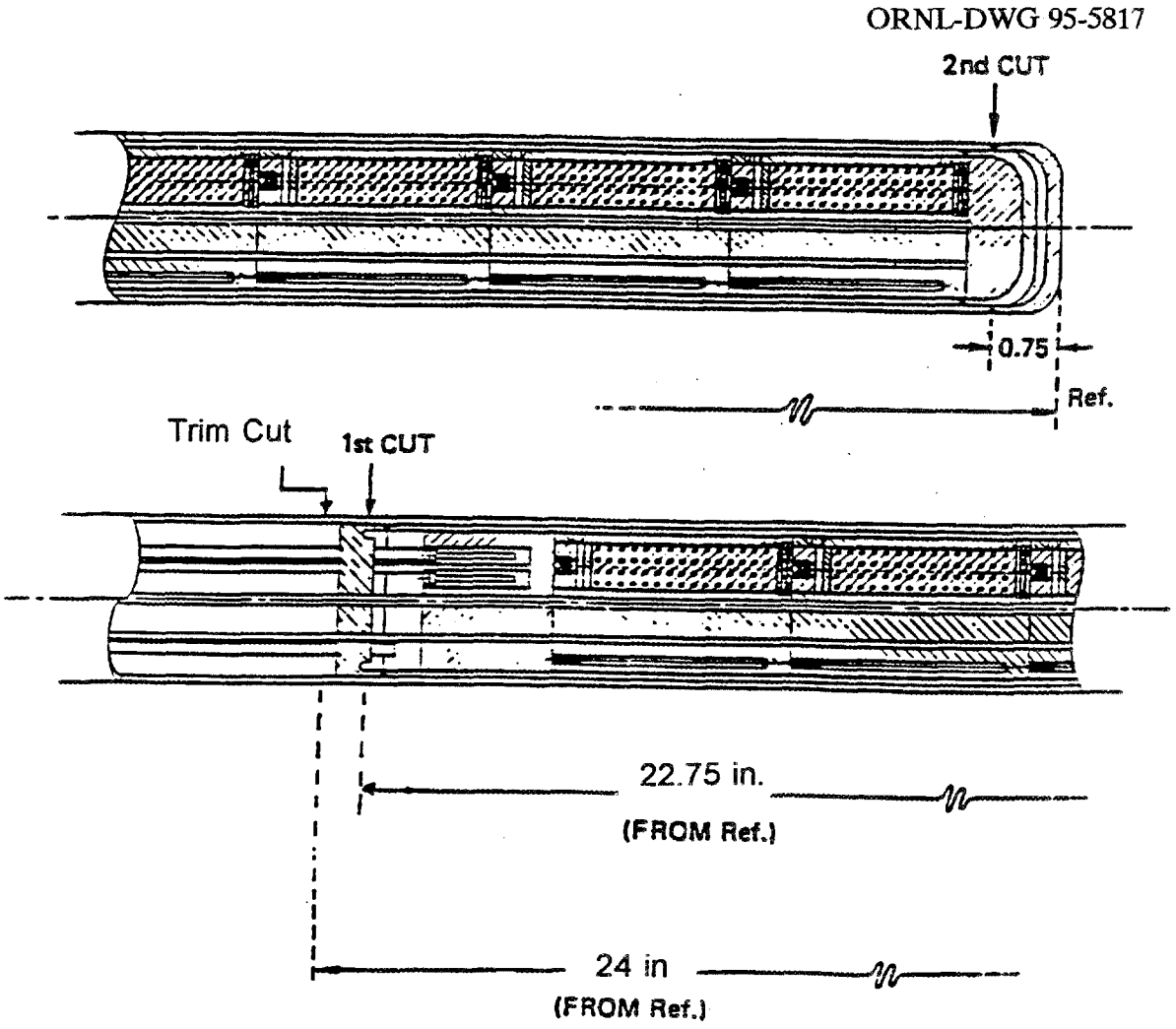

Figure 4.1.
POSITION OF HRB-21 CAPSULE DISASSEMBLY CUTS.

4.1.3 Gamma Scanning of Capsule

The intact capsule was placed in a 2-in.-diam by 24.5-in.-long aluminum tube for gamma scanning to ensure that all components were in place. An O-ring centered the capsule at the bottom of the tube while three clips, labelled A, B, and C, were used to shim the top of the tube and mark the location of the fuel columns. Gamma scanning was accomplished according to the generic gamma scanning procedure;[4-5] the output is an analog trace on a chart recorder of integrated gamma intensity. The region of interest (ROI) was set at 550 to 800 keV (in order to exclude most gammas from the Inconel cladding

activation), and longitudinal scans were made with a 0.062-in.-diam collimator. Scans were made at both 0 and 90° and also at 60, 180, and 300° to align with fuel columns A, B, and C, respectively. These scans showed that the graphite fuel bodies were in the expected position except that the separation between the fuel compacts of bodies 9 [which replaced No. 1 during assembly] and 2 was about 0.2 in. more than expected (see Sect. 4.1.5 below). One scan also gave indication of a fracture in fuel compact 7B (later confirmed in the unloading). The chart record for fuel column "B" shown in Figure 4.2 gives subtle evidence for both of the above observations. The small asymmetry about the centerline is not representative of any reactor flux asymmetry; small, unavoidable misalignments between the compact column and the scanning apparatus can introduce such minor discrepancies. The scans corresponding to the other fuel compacts did not reveal any evidence of compact irregularities.

4.1.4 Cutting Through Containment Tubes

The capsule was placed in the rotating chuck on the milling machine for cutting through the containment tubes. A slot was milled through both containments at the 0° location as a reference for orientation of the containment tubes. The first circumferential cut ("1st cut" in Figure 4.1) was made 0.5 in. down from the top face of the upper containment head using a 0.375-in. carbide end mill bit. The secondary (outer) containment was cut without incident and the upper section removed. As the cut through the primary containment neared completion, the tool grabbed and cocked the upper section of the primary containment. A gap of about 0.125 in. opened at the 180° position. A 0.125-in. end mill was installed and used to remove the burr at the 0° location on the primary containment. Figure 4.3 depicts the capsule in the milling machine after these operations.

At this point, the assembly was moved to the pushout fixture, and the upper pressure head with the TCATs was removed easily by pulling on the pressure head. The TCATs appeared to be in good condition. The upper insulator was visible, at this time, flush with the trim cut and caught by a burr. The B_4C holders were protruding slightly from the upper insulator so an attempt was made to extract them with tweezers. Numbers 1, 4, and 6 came out easily. The others were pushed back down into the upper insulator for later removal. The inside diameter (ID) of the primary tube cut was partially deburred. The capsule was turned around in the rotary chuck for the ("2nd cut") circumferential cut at the bottom. This cut was made with a 0.25-in. carbide end mill. The first pass completely removed the

ORNL-DWG 95-5818

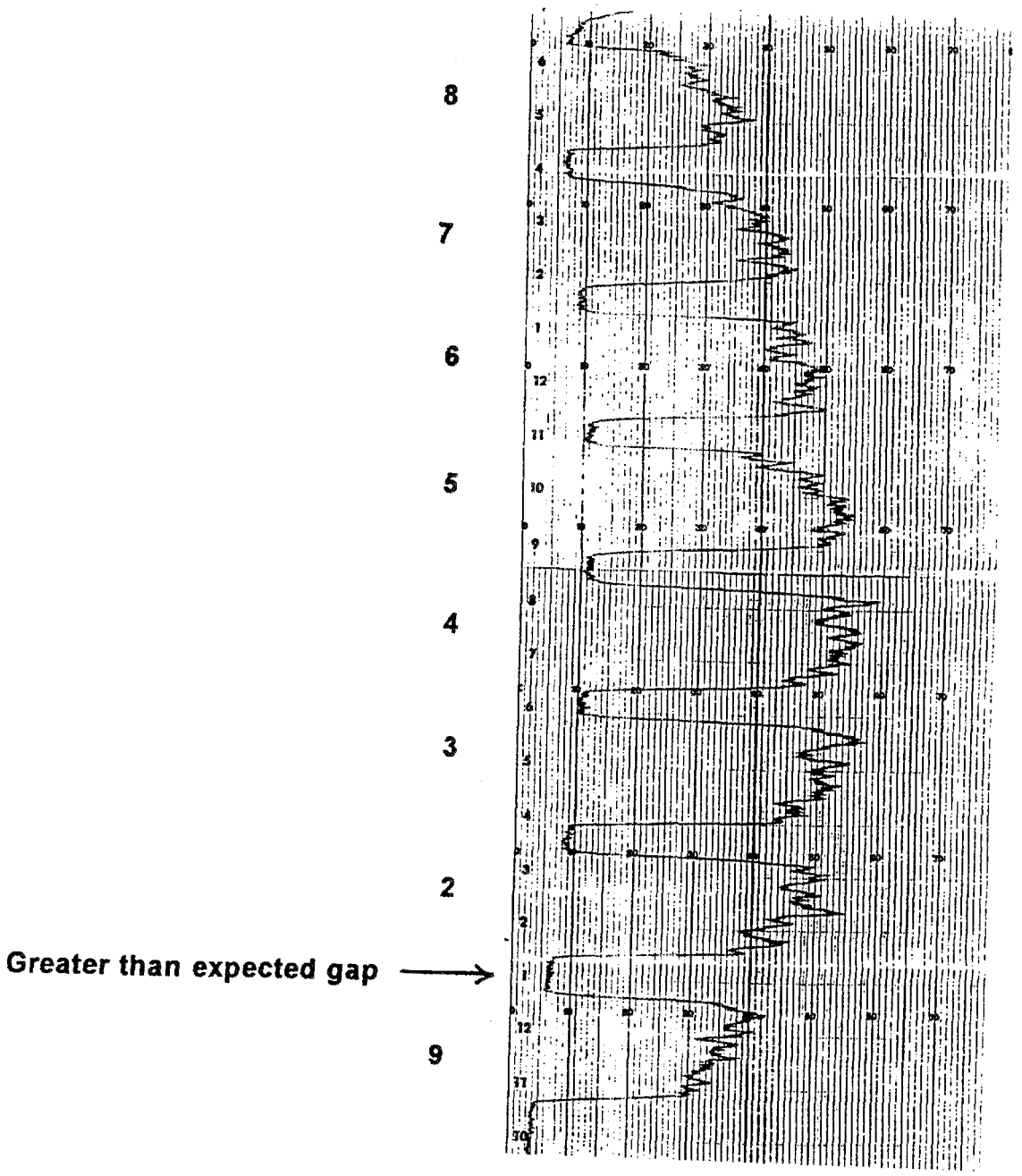

Figure 4.2.

GAMMA SCAN OF FUEL COLUMN "B" OF CAPSULE HRB-21 PRIOR TO OPENING. SCAN SHOWS COMPACT POSITIONS 8, 7, 6, 5, 4, 3, 2, AND 9 (REPLACED 1).

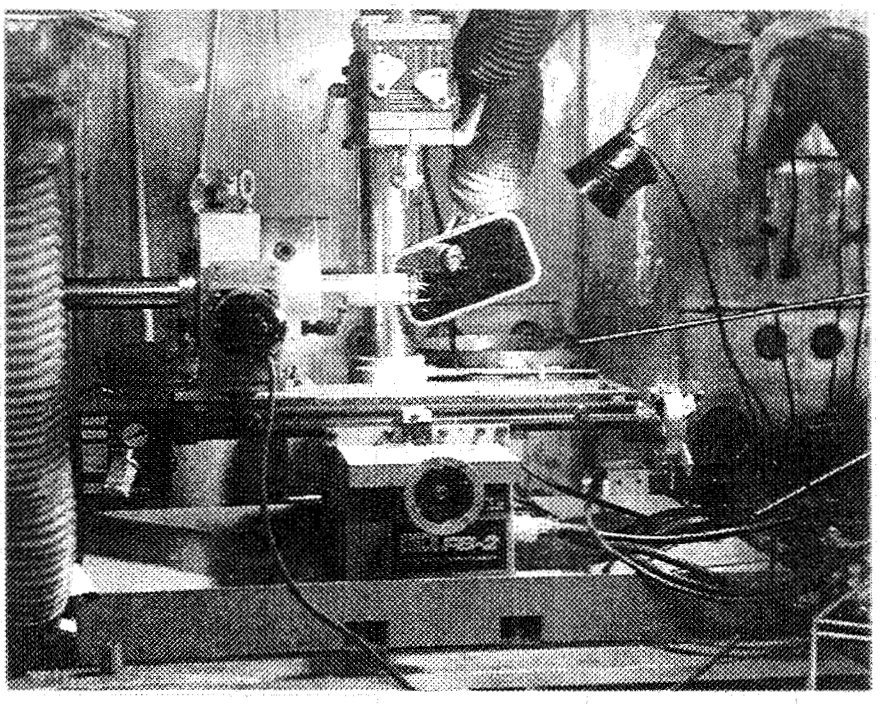

Figure 4.3.

CAPSULE HRB-21 IN MILLING MACHINE, AFTER COMPLETION OF UPPER CIRCUMFERENTIAL CUT.

lower end of the secondary tube. The second pass completely removed the lower end of the primary tube. The cut looked very smooth. The lower insulator also appeared to be in good condition. The upper end of the primary tube was then deburred with the mill turned to horizontal position.

4.1.5 Removal of Graphite Bodies

The capsule was transferred to the pushout fixture (shown in Figure 4.4) for removal of the insulators and graphite bodies. The upper insulator came out easily. The bodies could not be pushed out by push rod and manipulator alone. They had to be pushed fully out with the screw mechanism; however, very little force, < 1 lbf, was required. The screw turned just as easily as it did under no load. The fixture worked well with all eight fuel bodies (numbered 9, 2, 3, 4, 5, 6, 7, and 8, respectively) emerging without incident onto the receiving tray. Upon emergence, body 9 was found to be oriented inverted (with its compact

R80186

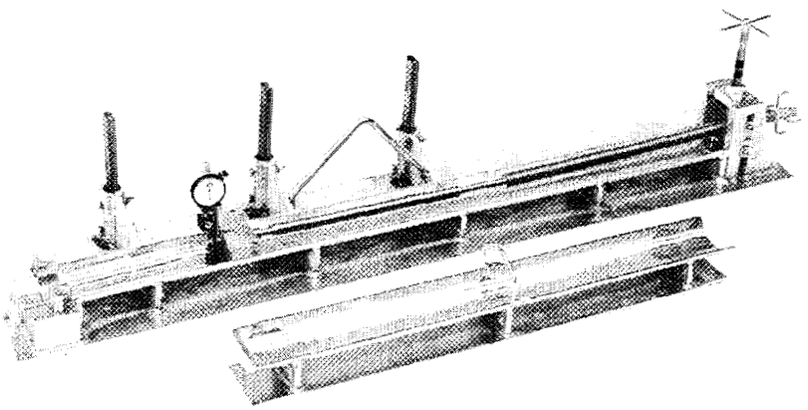

Figure 4.4.
PUSHOUT FIXTURE, INCLUDING (DETACHED) RECEIVING TRAY IN FOREGROUND AND INSTALLED FORCE GAGE.

access plugs facing upward in the capsule) relative to all the other graphite bodies. This explained the excess compact axial spacing (between locations 9 and 2) detected in the gamma scans.

4.1.6 Removal of Boron Carbide Specimens

The upper insulator prior to removal of the final three B_4C holders is shown in Figure 4.5 (Photo R80192). The six holders (graphite tubes containing coated B_4C particles) are shown in Figure 4.6 (Photo R80248). All appeared to be in good condition except that some graphite stuck to them. The B_4C holders and the two fluence monitor packages located in the upper insulator were stored in marked, small screw-top aluminum containers. The insulator was broken in the process of removing the final three holders and the two fluence monitor packages.

4.1.7 Removal of Components from Graphite Bodies

Following visual examination and gamma scanning of the graphite bodies (see below), removal of the fuel compacts was initiated. A fixture was made to align a screwdriver blade above any screw slot so that the blade could be turned with the in-cell manipulator with no downward or misalignment force on the graphite cap. This system worked well, and most of the screws were removed easily. The small screws (Item 4 in Figure 4.7) in the pushout

R80192

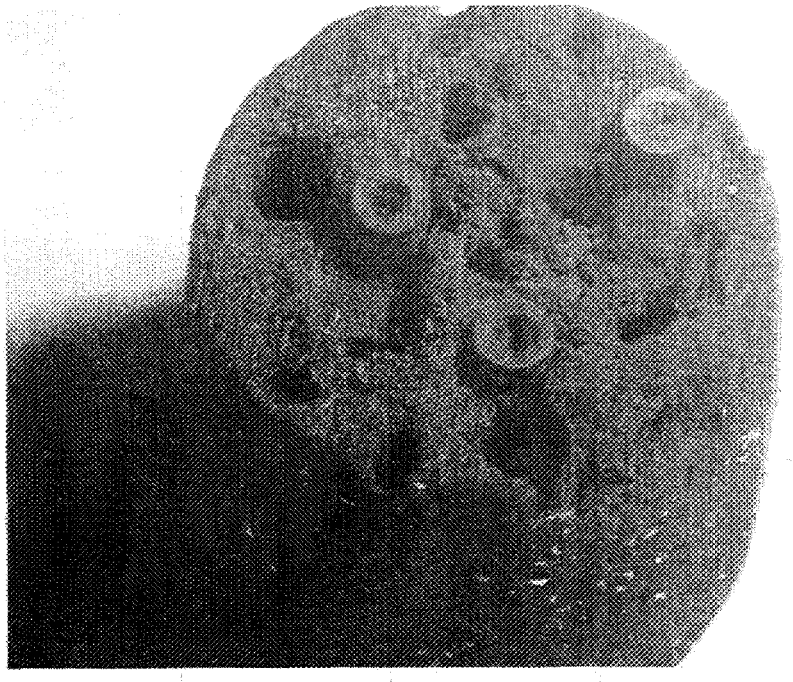

Figure 4.5.

TOP VIEW OF THE UPPER INSULATOR WITH THE THREE BORON CARBIDE HOLDERS PARTIALLY OUT.

R80248

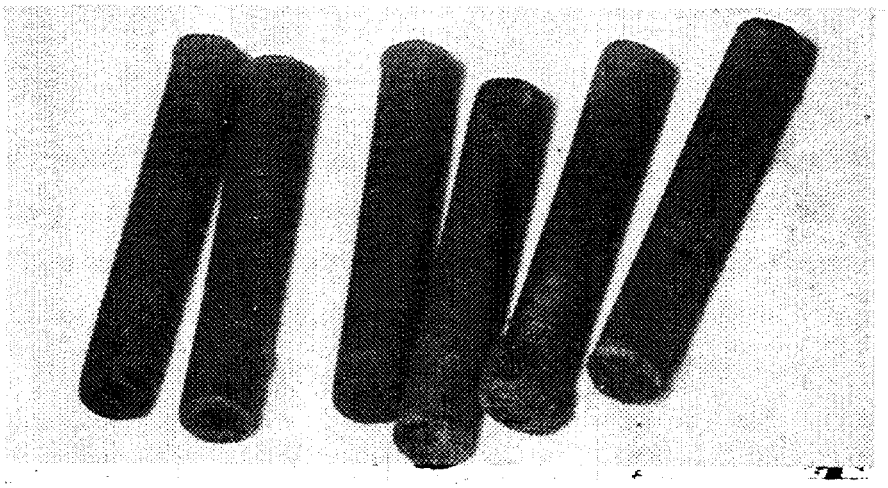

Figure 4.6.

BORON CARBIDE SPECIMEN HOLDERS FROM CAPSULE HRB-21.

ORNL-DWG 95-5819

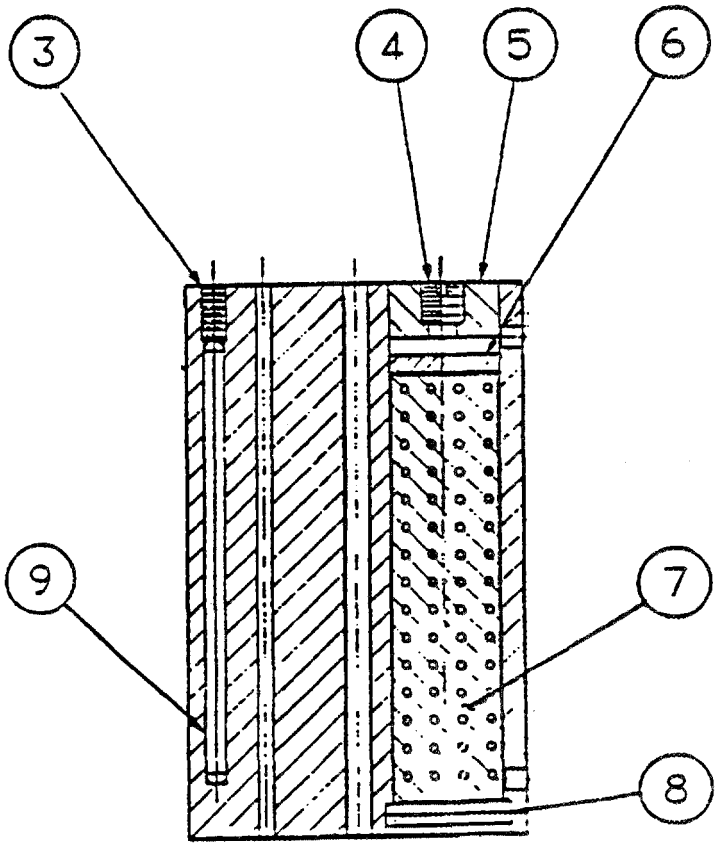

Figure 4.7.

SCHEMATIC VIEW OF THE MAJOR GRAPHITE BODY COMPONENTS. SEE TEXT FOR REFERENCES TO NUMBERED ITEMS.

holes in the center of the glued-in plugs (Item 5) in the top of the holder were removed first. Then the body was inverted, and the large screw-in plugs (Item 8) were removed. No problems were encountered in any of these screws for the eight bodies with the exception of the small screw for the push-rod hole in compact 5B which broke and was drilled out.

Compacts were removed in accordance with Sect. 16.5 of procedure MET-FME-ESP-11, Rev. 0, which specifies no more than 25 lbf pushout force to be employed. To control this process, a Dillon universal force gauge (0- to 100-lb capacity, calibrated by the manufacturer to a tolerance of ±1%) was acquired and installed in the load-applying section of the screw-driven pushout fixture.

In general, the first attempt to remove a compact was to allow it to slide out by gravity or to push it out with only very light "hand force" using the pushout rod through the

top end pushout hole, against the pushout disk inside. Initial pushing was in the horizontal position and subsequently, if necessary, in the vertical position (holding the compact down with the push rod and pulling up with the body). If the compact did not move, the effort was switched to other fuel compacts, saving the ones which needed the force of a screw-driven jig for later. The compacts needing the screw-driven jig required no more than 4 lbf to drive them out.

The first fuel compact to be removed was 9A. This compact pushed out easily with only light hand pressure on the pushout rod (less than 1 lbf). After the compact was about three-fourths out, the push rod required repositioning and the thin pushout disk (Item 6 in Figure 4.7) evidently cocked and jammed within the bore of the graphite body. The compact was gently grasped and removed with rubber-tipped tweezers. The photograph of 9A in the receiver tray (see Figure 4.8) shows the compact to be intact and in good condition. However, upon attempting to rotate the compact in the tray with the tweezers, it broke, as shown in Figure 4.9, indicating the very delicate condition of the as-irradiated compacts.

The condition of the compacts as they were removed and some comments are in Table 4.1. Of the 24 compacts, 16 appeared to be in good condition with no obvious cracks visible with casual inspection, 5 compacts had obvious cracks, and 3 were broken into two pieces with some debris. All fuel compacts were stored in marked, medium-size screw-top aluminum containers.

The piggyback specimens (Item 9 in Figure 4.7) were removed by first removing the screw plug retaining them in the blind hole and attempting to pour them out. If this did not work, a 0.125-in. hole was drilled from the bottom to just touch the tip of the v-bottom of the piggyback hole. A 0.125-in. plug cutter was then used to ream open the piggyback cavity without hitting the specimens. A 0.062-in. metal rod was then used to push the specimens out. All the small screws were removed with no trouble. Nineteen of the 24 specimen holes did not have to be drilled out. The piggyback specimens either came out easily or came out with slight tapping of the body. Five of the holes had to be drilled from the back and the specimens pushed out. Only the bottom two specimens in graphite body 5, hole B, required significant force to be removed (they required 30 lbf). Specimen 5B1 was dented slightly on the bottom by the pushing. A large mushroom-shaped weld on one end of 5B2 was apparently the cause of the sticking. None of the other piggyback specimens appeared to be

R80252

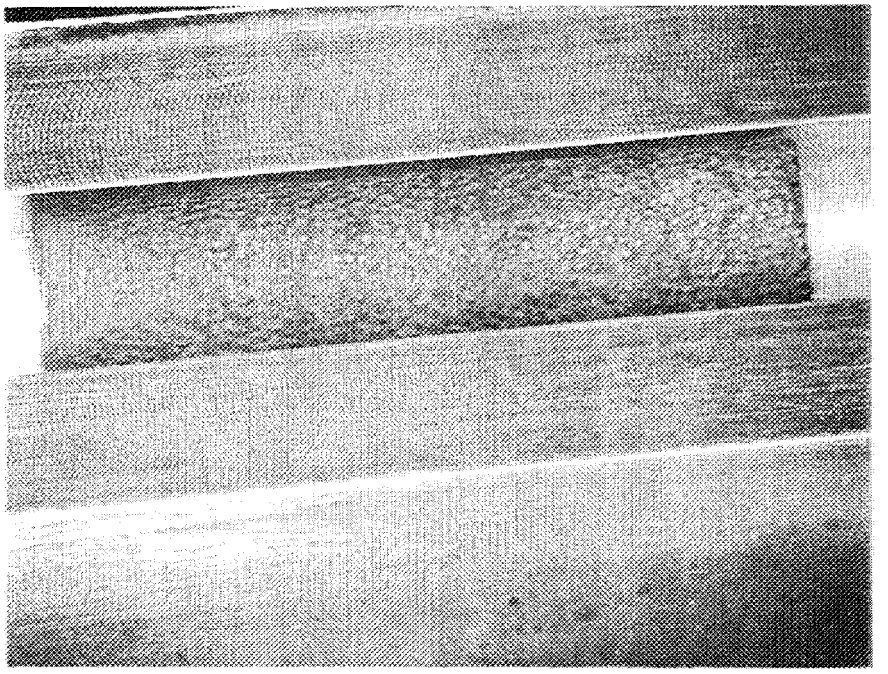

Figure 4.8.

FUEL COMPACT 9A, SIDE VIEW.

R80253

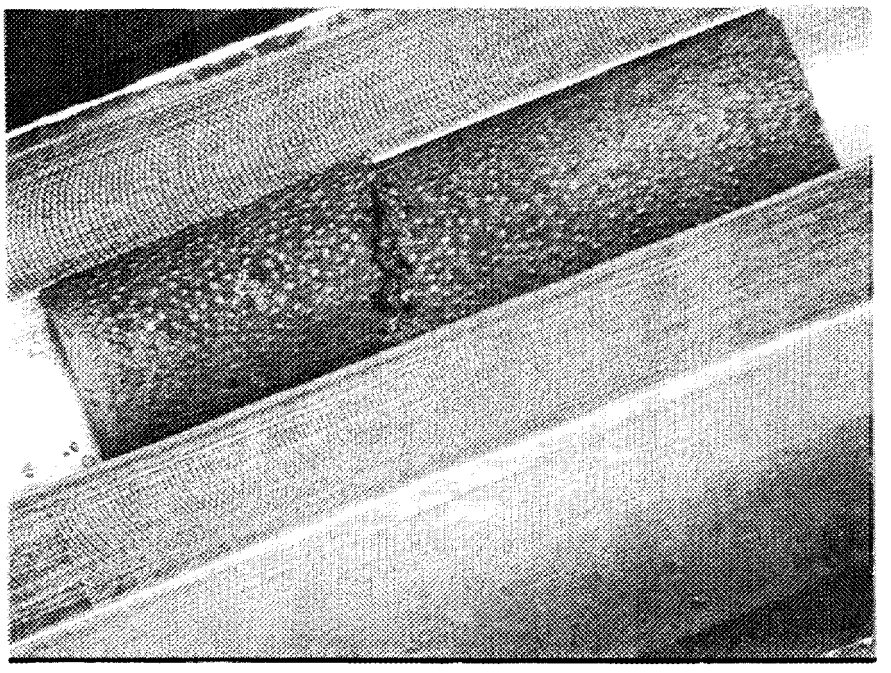

Figure 4.9.

FUEL COMPACT 9A AFTER BREAKING.

TABLE 4.1.

HRB-21 COMPACT REMOVAL[a]

Body No.	Compact A	Compact B	Compact C
9	hand pushout, intact, broke during handling	hand pushout, broken	hand pushout, broken, bottom end came out easily, top harder to push
2	hand pour out, intact, crack near bottom end	hand pushout, intact	hand pushout, intact, crack near bottom end
3	hand pushout, intact	hand pushout, intact	hand pushout, intact, crack near bottom end
4	screw pushout, 3.5 lbf, intact	screw pushout, 4 lbf, intact, 3 loose particles	screw pushout, 2 lbf, intact
5	screw pushout, 2 lbf, intact, crack near top end, broke later	broke top screw, drilled out, screw pushout, 1 lbf, intact, broke later	screw pushout, 2 lbf, intact, crack near top end
6	hand pushout, intact	hand pushout, intact	hand pushout, intact, broke during photography
7	hand pushout, intact, broke later	hand pushout, broken, 2 pieces + debris	hand pushout, intact, broke later
8	hand pour out, intact with edge nick, loose particle	hand pour out, intact, nick at top edge	hand pour out, intact, nick at top edge

[a]All compacts except those in body 9 were loaded with the end cap "down" relative to the High Flux Isotope Reactor (HFIR) core. In body 9, the compact end caps were observed to be "up" relative to the HFIR core.

harmed by the removal process. All piggyback specimens were stored in marked, small screw-top aluminum containers.

The fluence monitor capsules were removed by first removing the small retaining screw from the blind hole and attempting to pour or tap the capsules out. All the screws were removed with no trouble; however, only 4 of the 24 fluence monitor capsules were removed by pouring or tapping. The remaining 20 had to be drilled from the bottom side and the capsules pushed out. None of the capsules was apparently harmed in the removal process.

4.2 COMPONENT EXAMINATION

4.2.1 Visual Examination of Graphite Bodies

The graphite fuel bodies appeared to be in very good condition—essentially the same as when they were loaded into the experiment. Some scratches were evident and also some small cracks and grain separations. Typical photographs of the fuel bodies are in Figures 4.10 through 4.19. The faint lines across the glued-in plugs in Figure 4.16 are from the slot in the adjacent screw plug above that body in the experiment.

4.2.2 Gamma Scanning of Graphite Bodies

An aluminum holder was fabricated for gamma scanning the graphite fuel bodies. The holder could be rotated so that individual fuel compacts were placed in front of the collimator. The 0.062-in.-diam collimator was used, and longitudinal scans were made in a manner to view each fuel compact individually. Two separate scans were made for each compact with the ROI set for 720.5 to 761 keV (to detect ^{95}Zr) and 308.1 to 315.1 KeV (to detect ^{233}Pa). These data are used later in the analysis of the experiment to correlate burnup, fission power, etc., for the various fuel compact positions. These scans corroborated the observation from the overall capsule scans that fuel compact 7B was cracked (see Figure 4.20). In addition, the scans of fuel compacts 9B and 9C indicated cracks in these compacts.

4.2.3 Visual Examination of Fuel Compacts

The general condition of the fuel compacts as they were removed from the fuel bodies was given in Table 4.1. Three of the compacts were broken in two or more pieces with some debris of loose particles and graphite. Five of the compacts had obvious cracks.

R80196

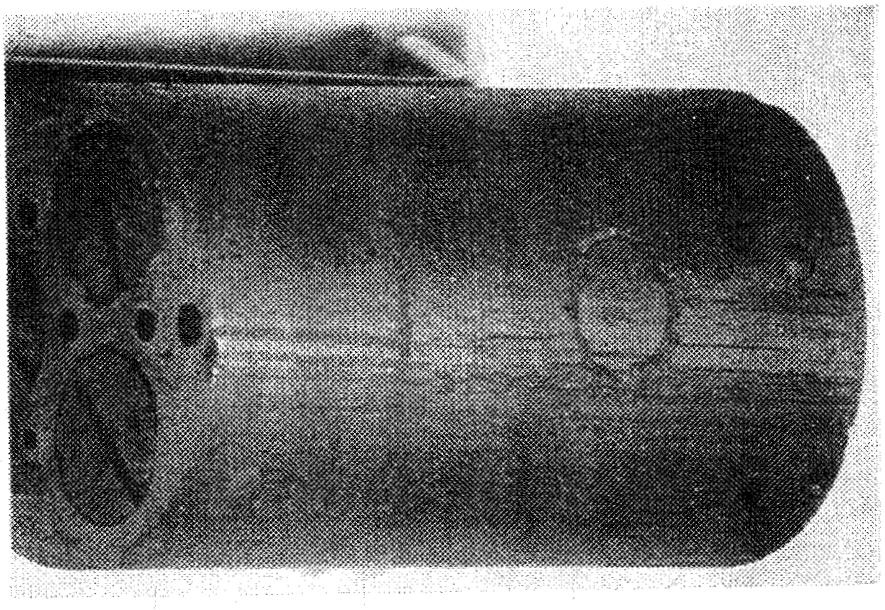

Figure 4.10.

GRAPHITE FUEL BODY 9, SIDE VIEW.

R80198

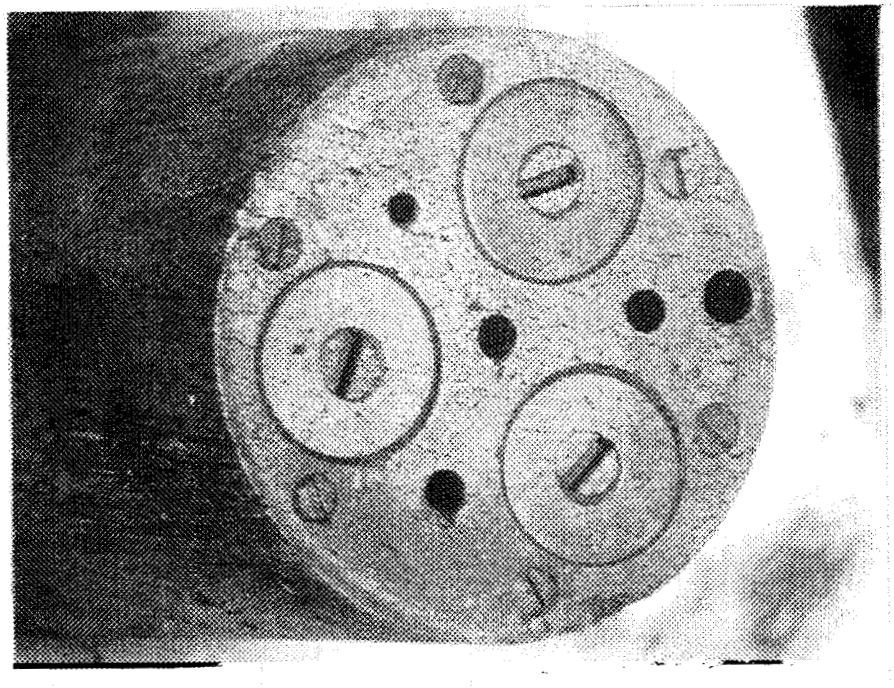

Note: Body 9 was installed inverted, so orientation "top" is opposite that of the other bodies in the capsule.

Figure 4.11.

GRAPHITE FUEL BODY 9, "TOP VIEW." THIS FUEL BODY HAD BEEN INSTALLED INVERTED.

R80204

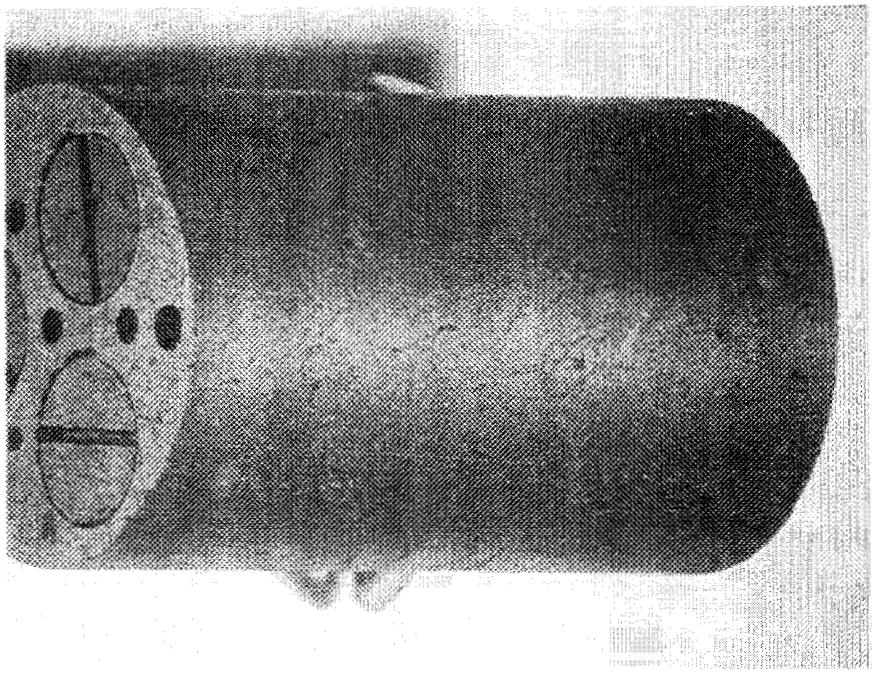

Figure 4.12.
GRAPHITE FUEL BODY 3, SIDE VIEW.

R80209

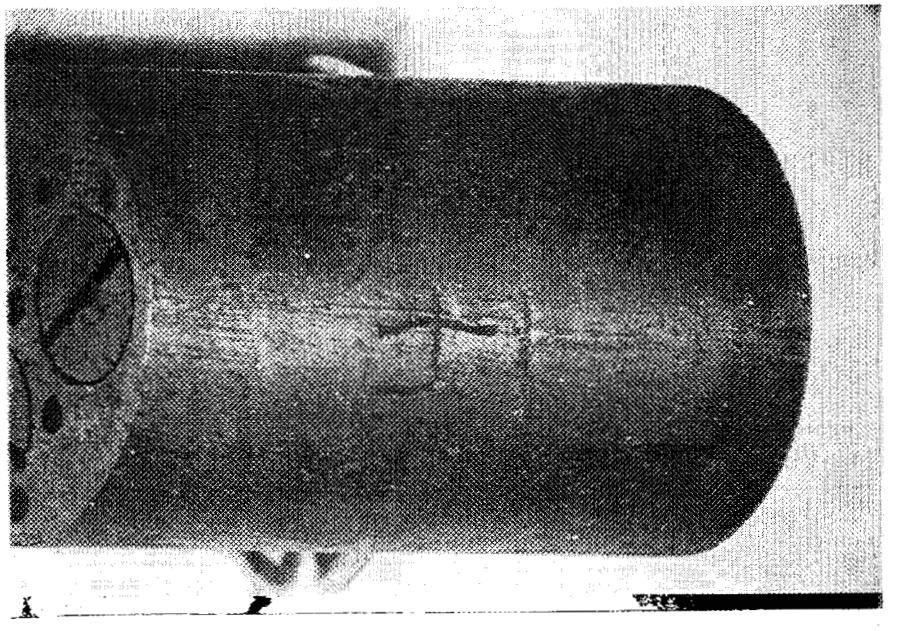

Figure 4.13.
GRAPHITE FUEL BODY 4, SIDE VIEW.

R80210

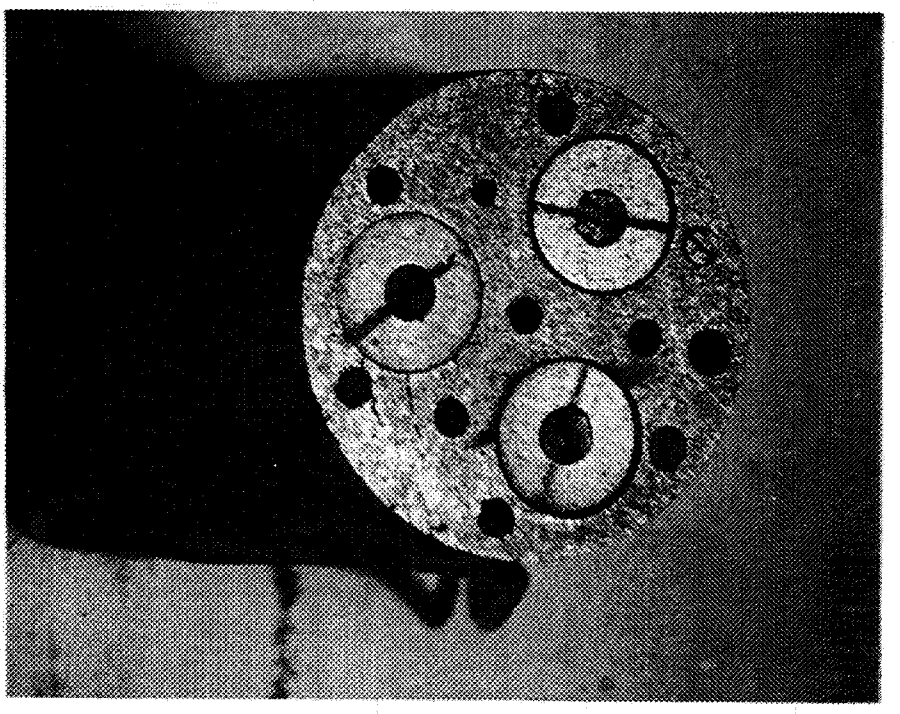

Figure 4.14.

GRAPHITE FUEL BODY 4, TOP VIEW.

R80211

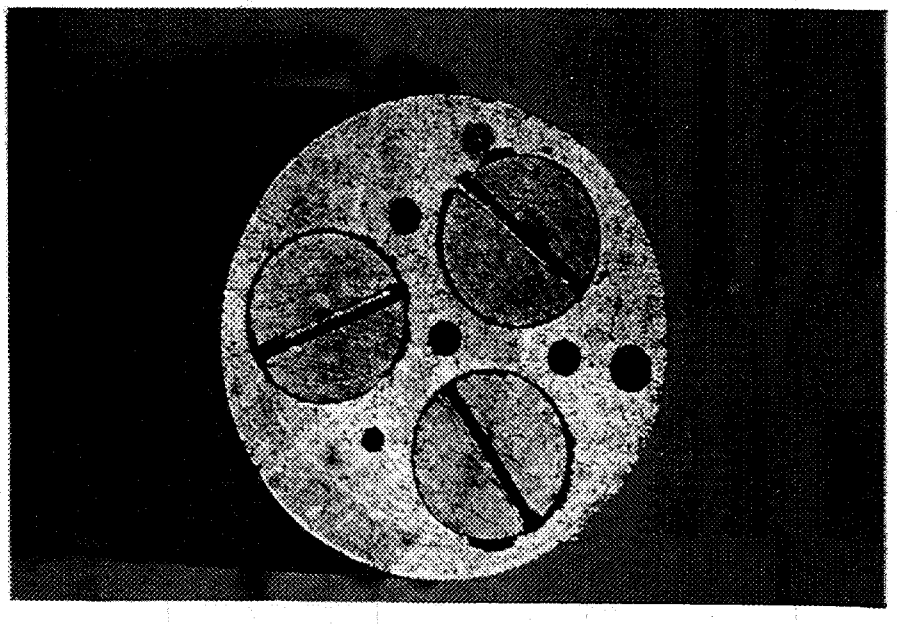

Figure 4.15.

GRAPHITE FUEL BODY 4, BOTTOM VIEW.

R80218

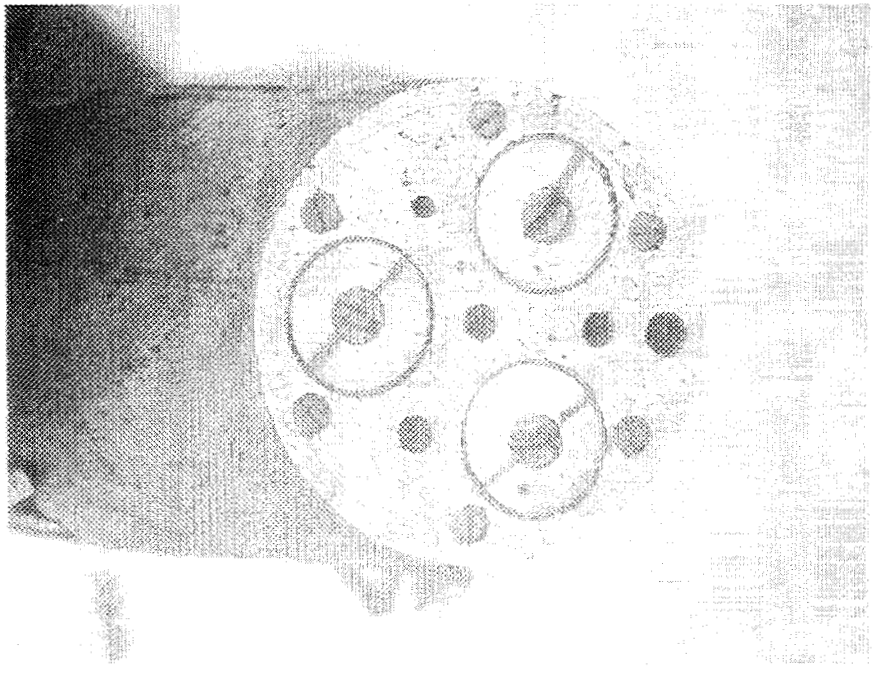

Figure 4.16.

GRAPHITE FUEL BODY 6, TOP VIEW.

R80229

Figure 4.17.

GRAPHITE FUEL BODY 9, TOP VIEW.

R80238

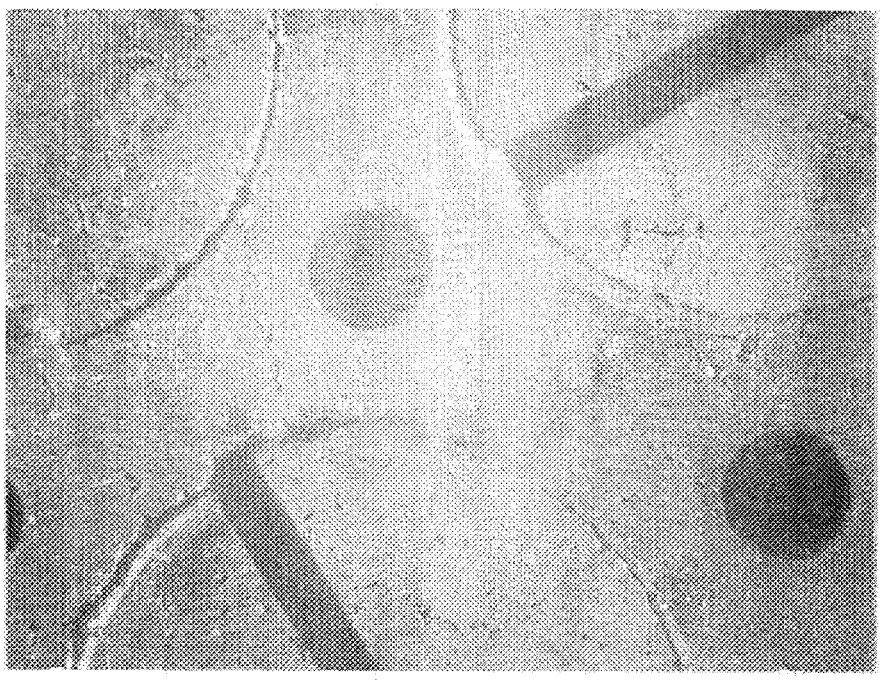

Figure 4.18.
GRAPHITE FUEL BODY 6, BOTTOM VIEW.

R80241

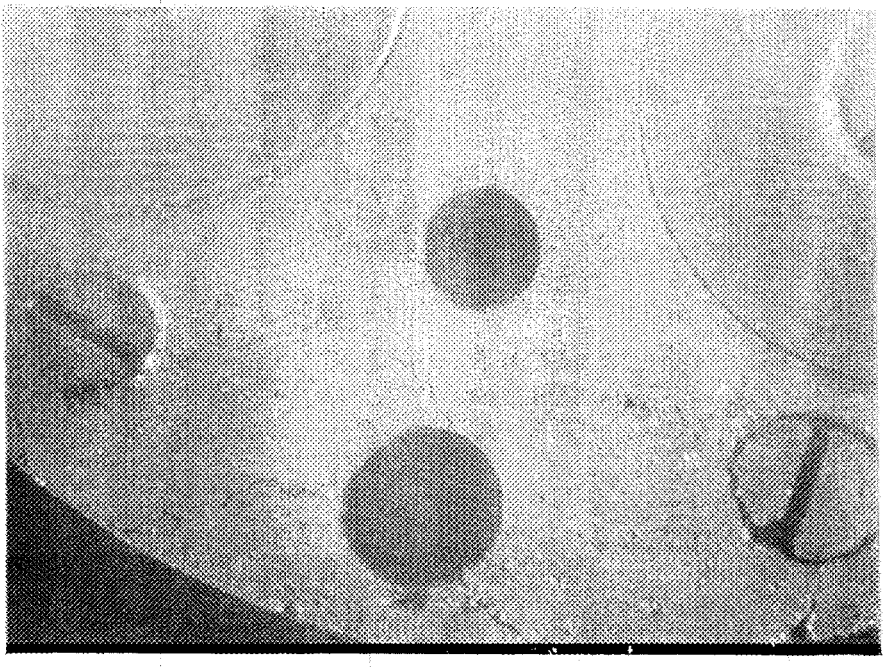

Figure 4.19.
GRAPHITE FUEL BODY 7, TOP VIEW.

ORNL-DWG 95-5820

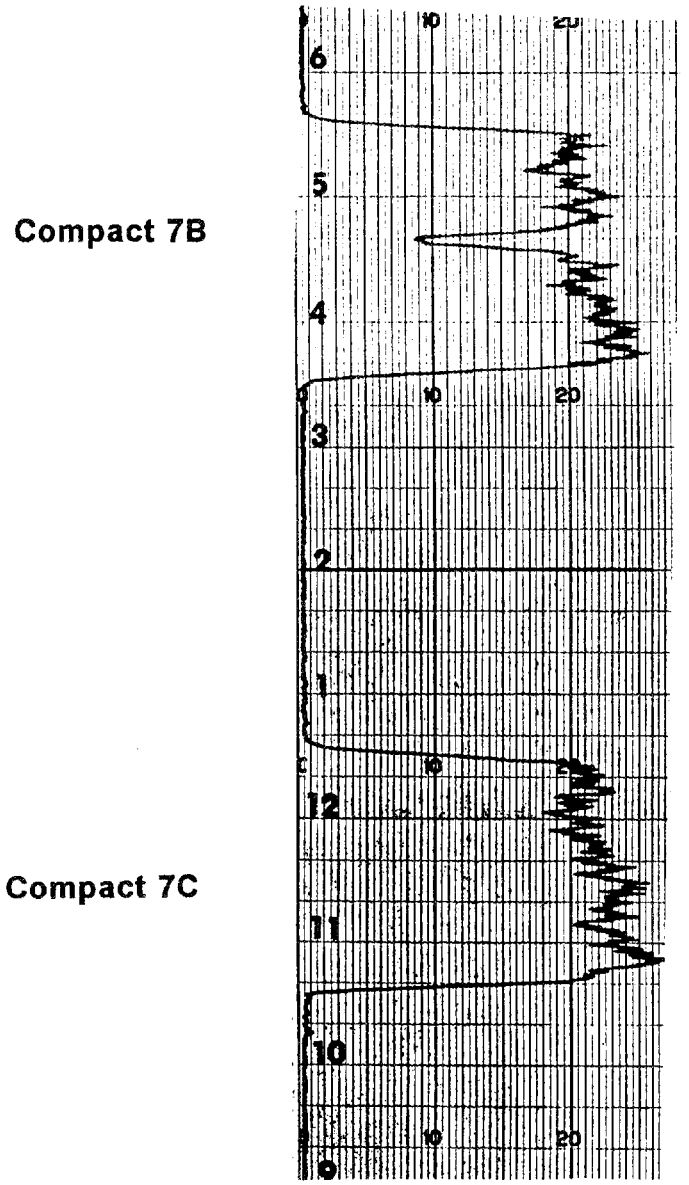

Figure 4.20.

GAMMA SCANS (BEFORE UNLOADING) OF GRAPHITE BODY 7, SHOWING INTACT COMPACT 7C AND BROKEN COMPACT 7B.

The remaining 16 compacts are noted as intact and appeared to be in good condition. The compacts were obviously very delicate since six or more broke in handling. The graphite matrix at the exterior of all compacts showed many small cracks. No obviously broken kernels were observed in the external examination. Some particles appeared to have breaks in the outer low-density PPyC coating and/or the OPyC coating. Figures 4.21 through 4.30 illustrate typical compact appearance. Enlarged macrophotographs of the fracture surfaces of compact 9B (already broken before unloading) and 6C (broken during subsequent handling) are given in Figures 4.31 and 4.32, respectively.

4.3 DIMENSIONAL CHANGE ANALYSIS

4.3.1 Metrology of Fuel Compacts

The compacts were measured for diameter and length according to procedure MET-FME-SOP-09, Rev. 1, "Determination of Diameters and Lengths of Cylindrical Objects Using Comparator Stand, Dial Gage and V-Block."[4-6] Diameters were measured at the top, middle, and bottom (end cap end) at two orientations. The end cap was actually the "top" for the compacts in fuel body 9 because it had been installed upside down during assembly. For consistency, the end cap was used as the "bottom" in all cases. The lengths were measured at three orientations (rotated 120° between them). Reference was made to certified standard cylinders before and after taking measurements of each compact. Due to the cracks and friable nature of the compacts, some locations could not be accurately measured. Obviously, the broken compacts could not be measured for length. The results of the dimensional measurements are in Tables 4.2 and 4.3, including calculated changes from the preirradiation measurements.[4-7] The compacts in the higher fluence, higher burnup central portion of the test exhibited small (~0 to 0.5%) diametral and length increases while the compacts near the ends of the capsule generally showed shrinkage (1 to 2%).

The fuel compact irradiation-induced dimensional change in design of the capsule was calculated to be a net shrinkage. The expansion observed at peak exposure was probably the result of the pyrocarbon damage and spalling.

4.3.2 Metrology of Graphite Bodies

The dimensions of the graphite fuel bodies are needed for calculating the gas gaps for the postirradiation thermal analysis. The diameters and lengths were measured for this purpose using the same procedure as described for compacts above. Fuel compact bore hole

R80254

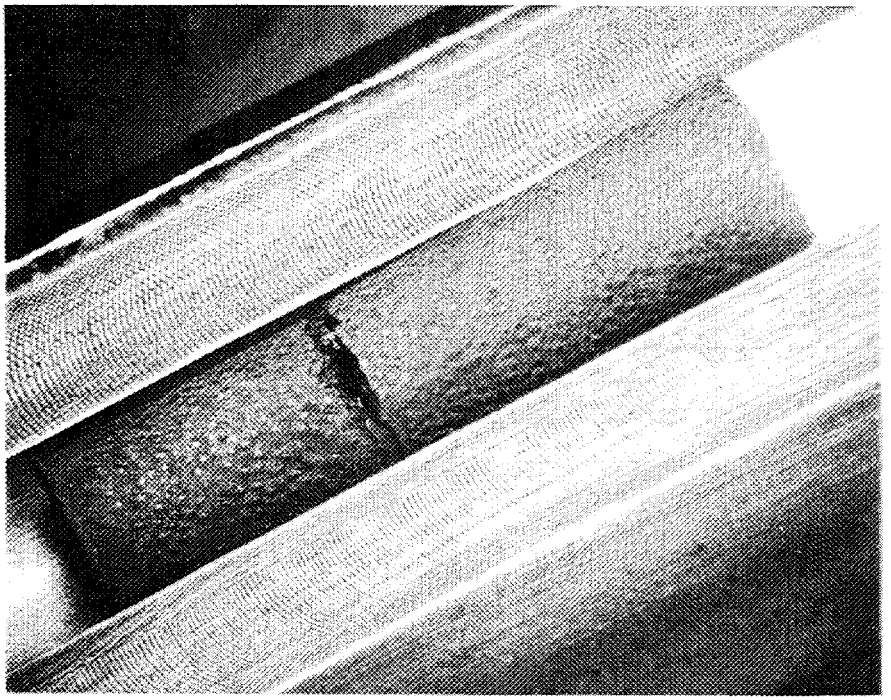

Figure 4.21.

FUEL COMPACT 9B AS REMOVED, LYING IN TRAY.

R80258

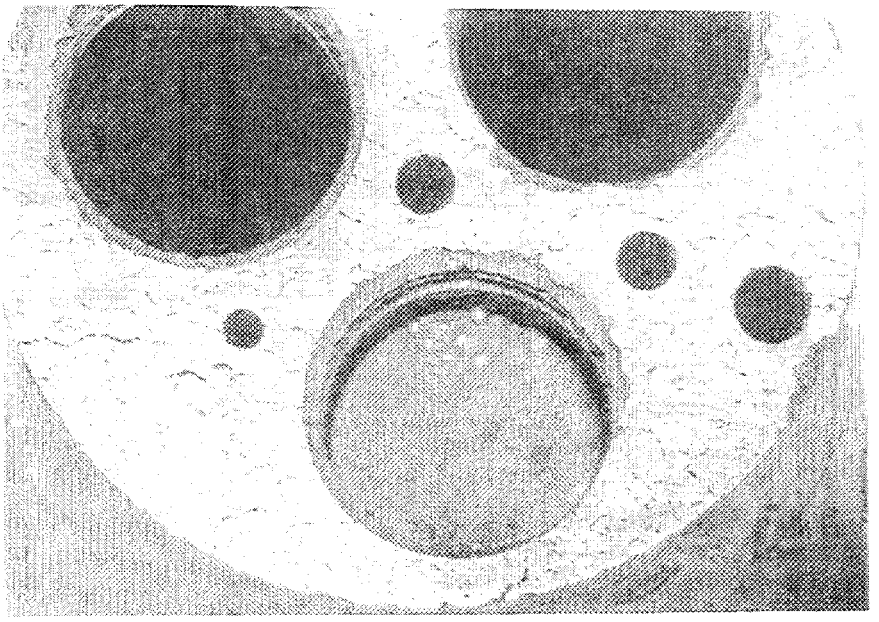

Figure 4.22.

FUEL COMPACT 9C IN GRAPHITE BODY.

R80257

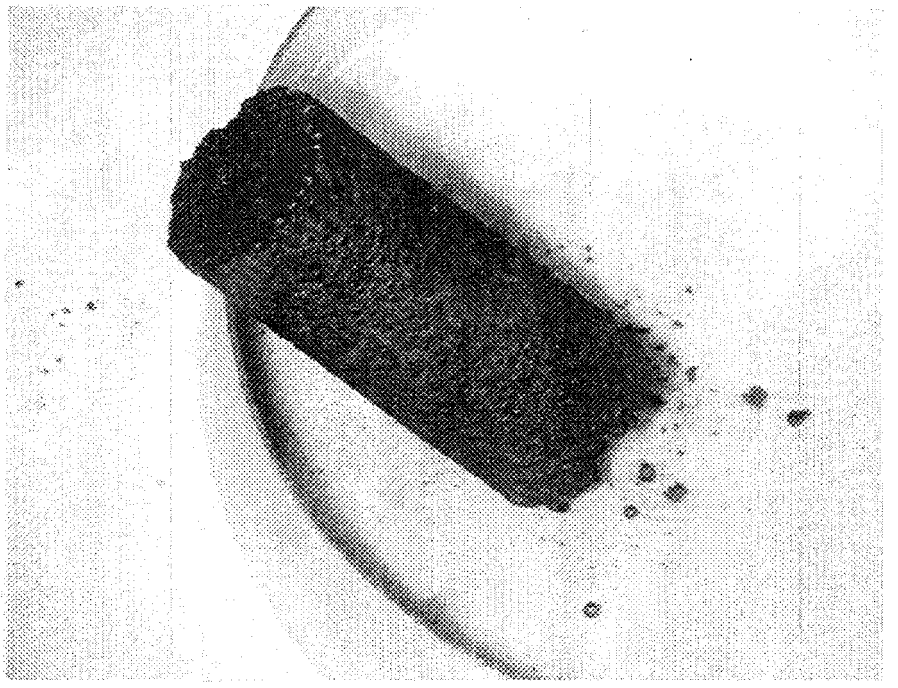

Figure 4.23.
FUEL COMPACT 9C UPPER SECTION.

R80271

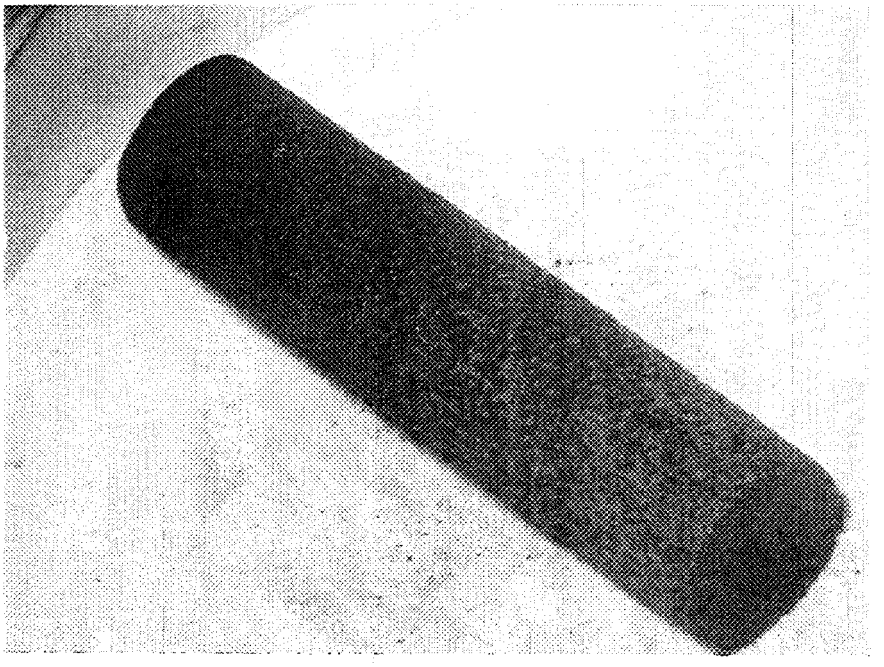

Figure 4.24.
FUEL COMPACT 7A.

R80273

Figure 4.25.
THE TWO SECTIONS OF FUEL COMPACT 7B.

R80285

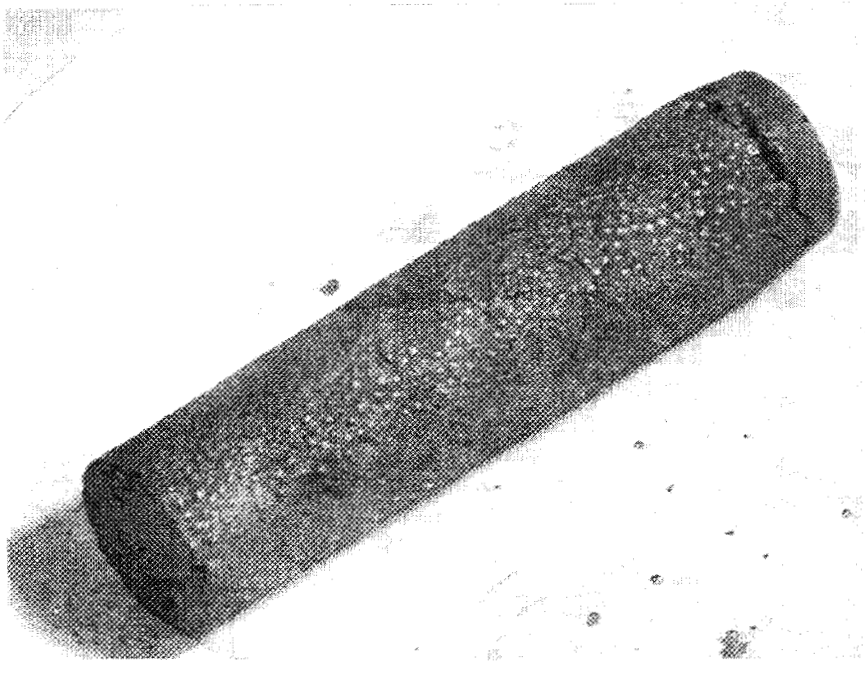

Figure 4.26.
FUEL COMPACT 2A.

R80290

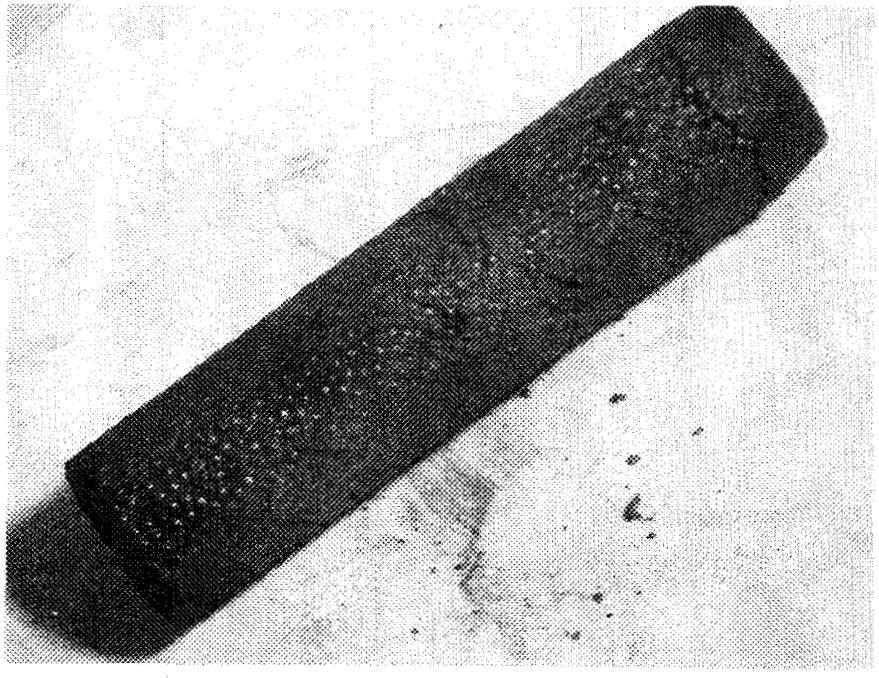

Figure 4.27.
FUEL COMPACT 2C.

R80299

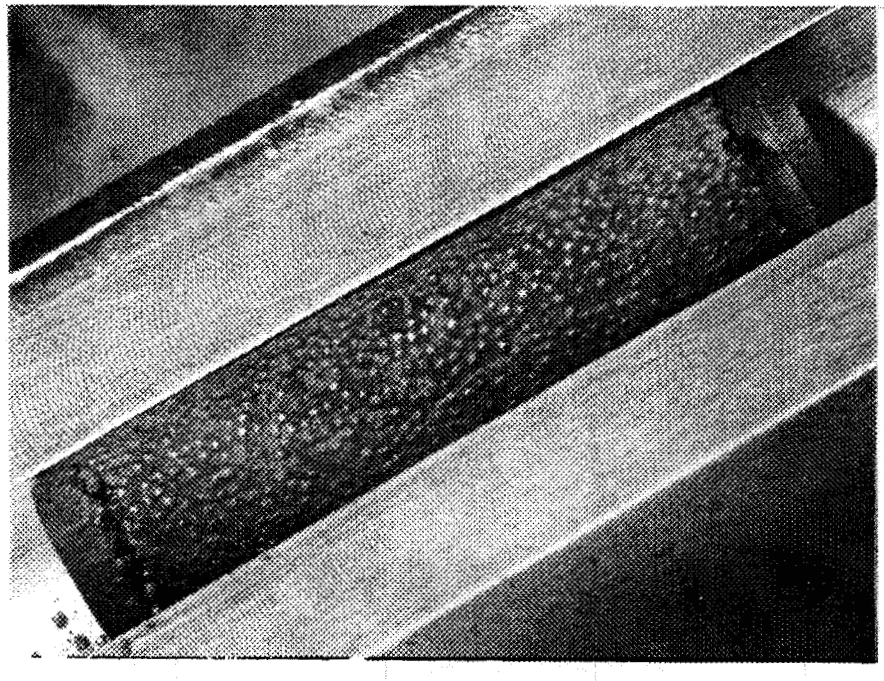

Figure 4.28.
FUEL COMPACT 4A.

R80301

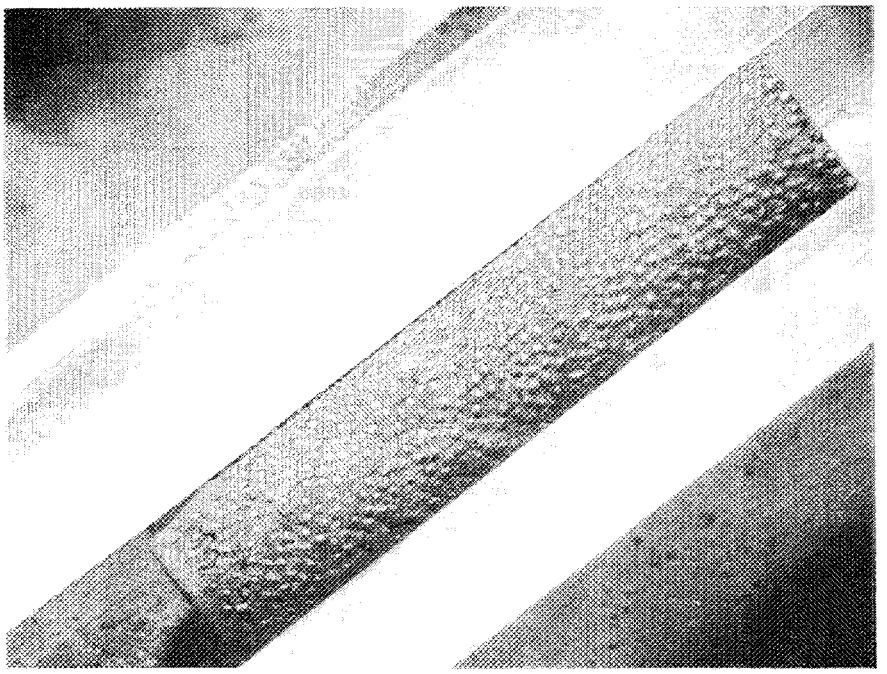

Figure 4.29.
FUEL COMPACT 4B.

R80304

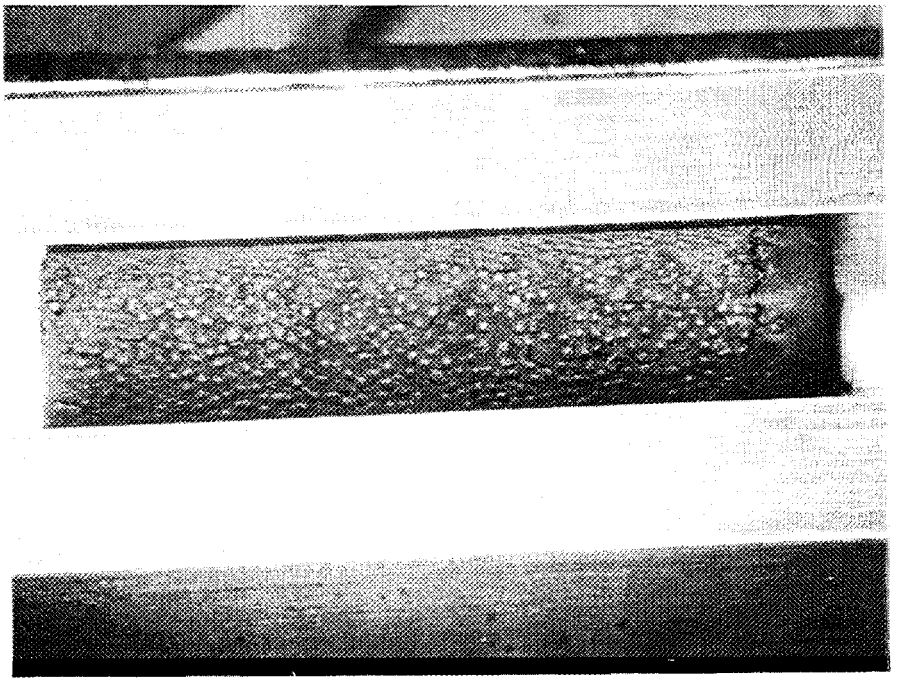

Figure 4.30.
FUEL COMPACT 5A.

R80322

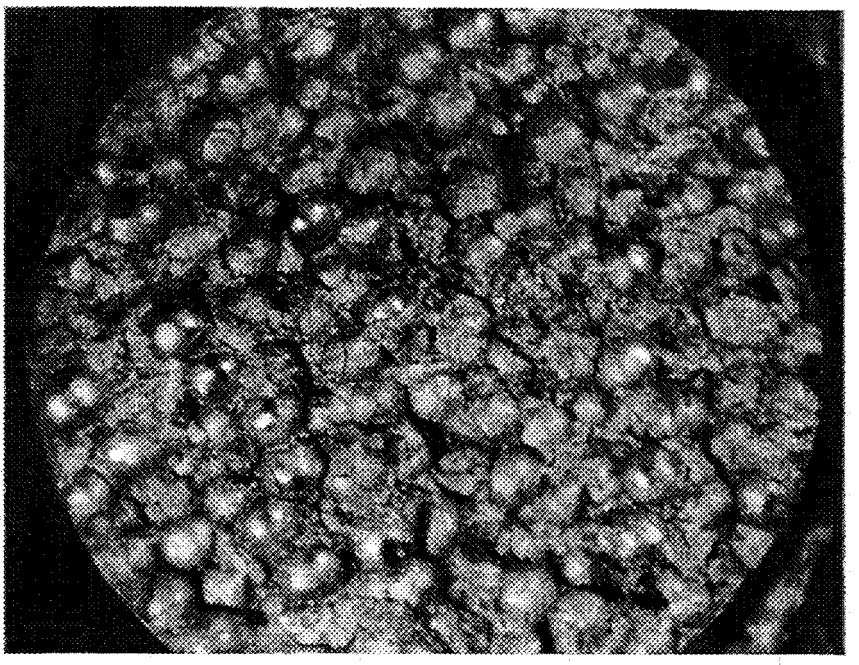

Figure 4.31.

FRACTURE SURFACE OF FUEL COMPACT 9B
(LOWER SEGMENT).

R80433

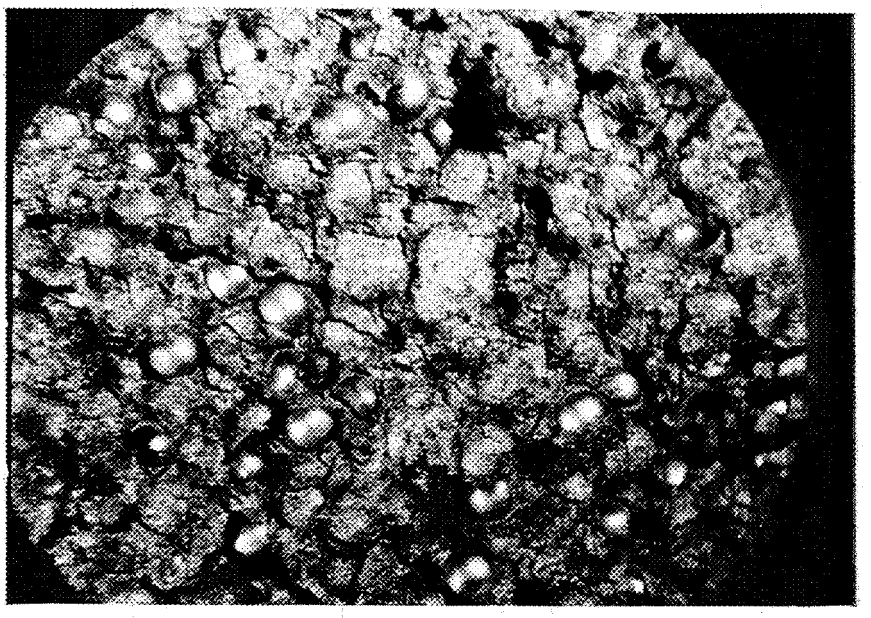

Figure 4.32.

FRACTURE SURFACE OF COMPACT 6C
(UPPER SEGMENT).

Table 4.2.

DIMENSIONAL (DIAMETER) CHANGES OF COMPACT

Compact No.	Location on fuel	Measured				Calculated		
		Pre-irrad D_p	Post-irrad D_m	$(D_p-D_m)/D_p$ (%)	Average (%)[b]	Pre-irrad D_{pc}	Post-irrad D_c	$(D_{pc}-D_c)/D_{pc}$ (%)
	top	0.4902	0.4842	1.22	1.58	0.48819	0.48520	0.61
9-A	middle	0.4898	0.4803	1.94				
[a]	bottom	0.4831	0.4744	1.80				
	top	0.4906	0.4849	1.16	1.50	0.48819	0.48520	0.61
9-B	middle	0.4902	0.4812	1.84				
	bottom	0.4835	0.4805	0.62				
	top	0.4906	0.4875	0.63	1.27	0.48819	0.48520	0.61
9-C	middle	0.4902	0.4808	1.92				
	bottom	0.4823	0.4736	1.80				
	top	0.4913	0.4848	1.32	0.72	0.48896	0.48530	0.75
2-A	middle	0.4909	0.4903	0.12				
	bottom	0.4870	0.4873	-0.06				
	top	0.4898	0.4867	0.63	0.45	0.48896	0.48530	0.75
2-B	middle	0.4909	0.4896	0.26				
	bottom	0.4862	0.4887	-0.51				
	top	0.4902	0.4870	0.65	0.37	0.48896	0.48530	0.75
2-C	middle	0.4902	0.4898	0.08				
	bottom	0.4862	0.4842	0.41				
	top	0.4913	0.4899	0.28	0.05	0.48896	0.48530	0.75
3-A	middle	0.4906	0.4915	-0.18				
	bottom	0.4874	0.4877	-0.06				
	top	0.4906	0.4906	0.00	-0.08	0.48896	0.48530	0.75
3-B	middle	0.4898	0.4906	-0.16				
	bottom	0.4878	0.4818	1.23				
	top	0.4906	0.4891	0.31	-0.05	0.48896	0.48530	0.75
3-C	middle	0.4894	0.4914	-0.41				
	bottom	0.4854	0.4858	-0.08				
	top	0.4906	0.4923	-0.35	-0.25	0.48937	0.48626	0.64
4-A	middle	0.4909	0.4917	-0.16				
	bottom	0.4846	0.4903	-1.18				

Table 4.2.

(CONTINUED)

Compact No.	Location on fuel	Measured				Calculated		
		Pre-irrad D_p	Post-irrad D_m	$(D_p-D_m)/D_p$ (%)	Average (%)[b]	Pre-irrad D_{pc}	Post-irrad D_c	$(D_{pc}-D_c)/D_{pc}$ (%)
	top	0.4925	0.4918	0.14	-0.03	0.48937	0.48626	0.64
4-B	middle	0.4906	0.4916	-0.20				
	bottom	0.4850	0.4882	-0.66				
	top	0.4913	0.4912	0.02	-0.24	0.48937	0.48626	0.64
4-C	middle	0.4906	0.4931	-0.51				
	bottom	0.4850	0.4919	-1.42				
	top	0.4921	0.4896	0.51	-0.71	0.48937	0.48608	0.67
5-A	middle	0.4906	0.4927	-0.43				
	bottom	0.4854	0.4902	-0.99				
	top	0.4917	0.4922	-0.10	-0.53	0.48937	0.48608	0.67
5-B	middle	0.4894	0.4909	-0.31				
	bottom	0.4862	0.4899	-0.76				
	top	0.4917	0.4892	0.51	-0.56	0.48937	0.48608	0.67
5-C	middle	0.4921	0.4923	-0.04				
	bottom	0.4858	0.4910	-1.07				
	top	0.4898	0.4903	-0.10	0.46	0.48896	0.48568	0.67
6-A	middle	0.4906	0.4912	-0.12				
	bottom	0.4862	0.4811	1.05				
	top	0.4906	0.4887	0.39	-0.40	0.48896	0.48568	0.67
6-B	middle	0.4894	0.4916	-0.45				
	bottom	0.4870	0.4887	-0.35				
	top	0.4906	0.4853	1.08	-0.42	0.48896	0.48568	0.67
6-C	middle	0.4902	0.4890	0.24				
	bottom	0.4862	0.4915	-1.09				
	top	0.4906	0.4754	3.10	-0.30	0.48896	0.48528	0.75
7-A	middle	0.4886	0.4900	-0.29				
	bottom	0.4870	0.4885	-0.31				

Table 4.2.

(CONTINUED)

Compact No.	Location on fuel	Measured				Calculated		
		Pre-irrad D_p	Post-irrad D_m	$(D_p-D_m)/D_p$ (%)	Average (%)[b]	Pre-irrad D_{pc}	Post-irrad D_c	$(D_{pc}-D_c)/D_{pc}$ (%)
	top	0.4909	0.4905	0.08	1.04	0.48896	0.48528	0.75
7-B	middle	0.4894	0.4887	0.14				
	bottom	0.4862	0.4768	1.93				
	top	0.4906	0.4904	0.04	0.27	0.48896	0.48528	0.75
7-C	middle	0.4894	0.4892	0.04				
	bottom	0.4874	0.4850	0.49				
	top	0.4902	0.4831	1.45	1.33	0.48819	0.48530	0.59
8-A	middle	0.4898	0.4840	1.18				
	bottom	0.4850	0.4778	1.48				
	top	0.4902	0.4835	1.37	1.06	0.48819	0.48530	0.59
8-B	middle	0.4902	0.4838	1.31				
	bottom	0.4854	0.4814	0.82				
	top	0.4902	0.4816	1.75	0.80	0.48819	0.48530	0.59
8-C	middle	0.4898	0.4833	1.33				
	bottom	0.4848	0.4835	0.27				

[a]Body 9 replaced body 1.

[b]The averages are based on only two measurements, i.e., the measurements at the end cap position were ignored in the average computation for obvious reasons. A positive value for the percentage of dimensional change indicates shrinkage.

Table 4.3.

DIMENSIONAL (LENGTH) CHANGES OF FUEL COMPACTS

[Positive values indicate shrinkage]

Compact No.		Measured			Calculated			
		Pre-irrad L_p	Post-irrad L_m	$(L_p-L_m)/L_p$ (%)	Average (%)	Pre-irrad L_{pc}	Post-irrad L_c	$(L_{pc}-L_p)/L_{pc}$ (%)
9-A	[a]	1.9348	broken					
9-B		1.9342	broken					
9-C		1.9409	broken					
2-A		1.9402	1.9301	0.52		1.9402	1.92568	0.75
2-B		1.9409	1.9306	0.53	0.58	1.9409	1.92637	0.75
2-C		1.9394	1.9263	0.68		1.9394	1.92488	0.75
3-A		1.9402	1.9452	-0.26		1.9402	1.92568	0.75
3-B		1.9406	1.9450	-0.23	-0.14	1.9406	1.92607	0.75
3-C		1.9409	1.9394	0.08		1.9409	1.92637	0.75
4-A		1.9417	1.9548	-0.67		1.9417	1.92936	0.64
4-B		1.9417	1.9471	-0.28	-0.38	1.9417	1.92936	0.64
4-C		1.9417	1.9452	-0.18		1.9417	1.92936	0.64
5-A		1.9421	broken					
5-B		1.9421	broken					
5-C		1.9417	1.9525	-0.56	-0.56	1.9417	1.92865	0.67
6-A		1.9429	1.9428	0.01	-0.11	1.9429	1.92987	0.67
6-B		1.9417	1.9460	-0.22		1.9417	1.92867	0.67
6-C		1.9402	broken					
7-A		1.9421	broken					
7-B		1.9421	broken					
7-C		1.9394	broken					
8-A		1.9378	1.9131	1.27		1.9378	1.92633	0.59
8-B		1.9378	1.9117	1.35	1.25	1.9378	1.92633	0.59
8-C		1.9354	1.9133	1.14		1.9354	1.92395	0.59

[a]Body 9 replaced body 1.

IDs were measured using a Dorsey BG-2 precision gage in accordance with Sect. 5.2 (for ID measurements) of procedure MET-FME-SOP-04, Rev. 1 (ref. 4-8). Multiple readings were made of the ID of each fuel compact hole (A, B, and C) of each graphite body at three axial locations: the mid-length and at a distance 0.125 in. in from each end (to avoid the end cap threaded region). Comparison was made with a class "X" precision ring gage, 0.4800-in. ID, before and after each series of hole measurements.

The graphite body external dimensions are in Tables 4.4 and 4.5. It can be seen from the data that the bodies have contracted in diameter and length by amounts ranging from about 0.06% (those on the ends of the capsule) to 0.3% (those in the middle). The graphite fuel hole body diameters, given in Table 4.6, are all less (0.55 to 0.85%) than initially, with the greatest shrinkage in the center of the test.

The tables also include the calculated dimensional changes. These calculations were made by the MAPPING code discussed in Sect. 3. A comparison of the calculated change and the measured change is shown in Figures 4.33*(a)-(c)*.

The design data on the dimensional change of the compacts show that during the irradiation only shrinkage is expected. Figure 4.33*(a)* shows significant expansion of the compact in position 5 of the capsule and minor expansion in positions 4 and 6. The physical appearance of these compacts after irradiation indicates that the expansion probably resulted from debonding of the shim and fuel particles.

The graphite fuel bodies were predicted to shrink during the irradiation as shown in Figures 4.33*(b)* and *(c)*. The measured shrinkage of the outside surface of the graphite fuel body is consistently less than the predicted shrinkage. The fuel bodies subjected to higher fast fluence displayed greater shrinkage as compared to the fuel bodies with lower fast fluence. Temperature does not appear to have as much impact on the shrinkage as predicted by the correlations in the graphite design data manual.

The measured shrinkage of the fuel holes in the graphite bodies was consistently higher than the expected shrinkage. This behavior was opposite to that observed for the outside dimension of the graphite fuel body. The shrinkage of these holes was around 0.6% and was independent of the location in the capsule (fast fluence). It may be surmised that the process of inserting and removing the compacts from the holes may have degraded the geometry of the holes to display this behavior.

Table 4.4.

DIMENSIONAL (DIAMETER) CHANGES OF GRAPHITE BODIES

[Positive values indicate shrinkage]

Body No.	Location on body	Measured: Pre-irrad D_p (in.)	Measured: Post-irrad D (in.)	Measured: $(D_p-D)/D$ (%)	Measured: Average (%)	Calculated: Pre-irrad D_c (in.)	Calculated: Post-irrad D_{pc} (in.)	Calculated: $(D_c-D_{pc})/D_c$ (%)
	top	1.4977	1.4972	0.033	0.060	1.4976	1.4964	0.082
9	middle	1.4977	1.4966	0.073				
	bottom	1.4977	1.4966	0.073				
	top	1.4995	1.4980	0.100	0.116	1.4997	1.4944	0.353
2	middle	1.4995	1.4978	0.113				
	bottom	1.4995	1.4975	0.133				
	top	1.5039	1.4998	0.273	0.268	1.5037	1.4950	0.581
3	middle	1.5039	1.4998	0.273				
	bottom	1.5039	1.5000	0.259				
	top	1.5040	1.4996	0.293	0.297	1.5047	1.4941	0.705
4	middle	1.5040	1.4995	0.299				
	bottom	1.5040	1.4995	0.299				
	top	1.5043	1.4995	0.319	0.299	1.5047	1.4939	0.715
5	middle	1.5043	1.4995	0.319				
	bottom	1.5043	1.5004	0.259				
	top	1.5035	1.4997	0.253	0.242	1.5037	1.4947	0.597
6	middle	1.5035	1.4995	0.266				
	bottom	1.5035	1.5004	0.206				
	top	1.4990	1.4978	0.080	0.071	1.4997	1.4942	0.369
7	middle	1.4990	1.4977	0.087				
	bottom	1.4990	1.4983	0.047				
	top	1.4975	1.4966	0.060	0.109	1.4976	1.4962	0.092
8	middle	1.4975	1.4967	0.053				
	bottom	1.4975	1.4943	0.214				

Table 4.5.

DIMENSIONAL (LENGTH) CHANGES OF GRAPHITE BODIES

[Positive values indicate shrinkage]

		Measured				Calculated		
Body No.		Pre-irrad Lp (in.)	Post-irrad L (in.)	$(L_p-L)/L_p$ (%)[a]		Pre-irrad L_c (in.)	Post-irrad L_{pc} (in.)	$(L_c-L_{pc})/L_p$ (%)
9		2.5000	2.4984	0.064		2.5000	2.4980	0.082
2		2.5000	2.4954	0.184		2.5000	2.4912	0.353
3		2.5000	2.4925	0.300		2.5000	2.4855	0.581
4		2.5000	2.4910	0.360		2.5000	2.4824	0.705
5		2.5000	2.4909	0.364		2.5000	2.4821	0.715
6		2.5000	2.4928	0.288		2.5000	2.4851	0.597
7		2.5000	2.4952	0.192		2.5000	2.4908	0.369
8		2.5000	2.4985	0.060		2.5000	2.4977	0.092

[a]Postirradiation length changes were derived from calculated diameter changes.

Table 4.6.

DIAMETER CHANGES OF GRAPHITE BODY FUEL HOLES

	Measured				Calculated			
Compact No.	Location in hole	Pre-irrad D_p	Post-irrad D	$(D_p-D)/D_p$ (%)	Average (%)	Pre-irrad D_{pc}	Post-irrad D_c	$(D_{pc}-D_c)/D_{pc}$ (%)
	top	0.4968	0.4940	0.564	0.604	0.49675	0.4965	0.05
9-A	middle	0.4968	0.4935	0.664				
	bottom	0.4968	0.4939	0.584				
	top	0.4968	0.4940	0.564	0.604	0.49675	0.4965	0.05
9-B	middle	0.4968	0.4936	0.644				
	bottom	0.4968	0.4938	0.604				
	top	0.4968	0.4940	0.564	0.604	0.49675	0.4965	0.05
9-C	middle	0.4968	0.4937	0.624				
	bottom	0.4968	0.4937	0.624				
	top	0.4968	0.4938	0.604	0.651	0.49675	0.4950	0.35
2-A	middle	0.4968	0.4934	0.684				
	bottom	0.4968	0.4935	0.664				
	top	0.4968	0.4935	0.664	0.664	0.49675	0.4950	0.35
2-B	middle	0.4968	0.4935	0.664				
	bottom	0.4968	0.4935	0.664				

Table 4.6.

(CONTINUED)

Compact No.	Measured				Calculated			
	Location in hole	Pre-irrad D_p	Post-irrad D	$(D_p-D)/D_p$ (%)	Average (%)	Pre-irrad D_{pc}	Post-irrad D_c	$(D_{pc}-D_c)/D_{pc}$ (%)
	top	0.4968	0.4938	0.604	0.671	0.49675	0.4950	0.35
2-C	middle	0.4968	0.4934	0.684				
	bottom	0.4968	0.4932	0.725				
	top	0.4968	0.4929	0.785	0.805	0.49675	0.4939	0.57
3-A	middle	0.4968	0.4928	0.805				
	bottom	0.4968	0.4927	0.825				
	top	0.4968	0.4932	0.725	0.725	0.49675	0.4939	0.57
3-B	middle	0.4968	0.4932	0.725				
	bottom	0.4968	0.4932	0.725				
	top	0.4968	0.4928	0.805	0.778	0.49675	0.4939	0.57
3-C	middle	0.4968	0.4929	0.785				
	bottom	0.4968	0.4931	0.745				
	top	0.4968	0.4924	0.886	0.879	0.49675	0.4932	0.71
4-A	middle	0.4968	0.4925	0.866				
	bottom	0.4968	0.4924	0.886				
	top	0.4968	0.4929	0.785	0.792	0.49675	0.4932	0.71
4-B	middle	0.4968	0.4928	0.805				
	bottom	0.4968	0.4929	0.785				
	top	0.4968	0.4929	0.785	0.792	0.49675	0.4932	0.71
4-C	middle	0.4968	0.4929	0.785				
	bottom	0.4968	0.4928	0.805				
	top	0.4968	0.4925	0.866	0.637	0.49675	0.4932	0.71
5-A	middle	0.4968	0.4928	0.805				
	bottom	0.4968	0.4956	0.242				
	top	0.4968	0.4935	0.664	0.644	0.49675	0.4932	0.71
5-B	middle	0.4968	0.4930	0.765				
	bottom	0.4968	0.4943	0.503				
	top	0.4968	0.4930	0.765	0.658	0.49675	0.4932	0.71
5-C	middle	0.4968	0.4928	0.805				
	bottom	0.4968	0.4948	0.403				
	top	0.4968	0.4930	0.765	0.745	0.49675	0.4938	0.59
6-A	middle	0.4968	0.4930	0.765				
	bottom	0.4968	0.4933	0.705				

Table 4.6.

(CONTINUED)

Compact No.	Measured				Calculated			
	Location in hole	Pre-irrad D_p	Post-irrad D	$(D_p-D)/D_p$ (%)	Average (%)	Pre-irrad D_{pc}	Post-irrad D_c	$(D_{pc}-D_c)/D_{pc}$ (%)
	top	0.4968	0.4933	0.705	0.731	0.49675	0.4938	0.59
6-B	middle	0.4968	0.4930	0.765				
	bottom	0.4968	0.4932	0.725				
	top	0.4968	0.4928	0.805	0.751	0.49675	0.4938	0.59
6-C	middle	0.4968	0.4930	0.765				
	bottom	0.4968	0.4934	0.684				
	top	0.4968	0.4935	0.664	0.644	0.49675	0.4949	0.37
7-A	middle	0.4968	0.4937	0.624				
	bottom	0.4968	0.4936	0.644				
	top	0.4968	0.4937	0.624	0.611	0.49675	0.4949	0.37
7-B	middle	0.4968	0.4938	0.604				
	bottom	0.4968	0.4938	0.604				
	top	0.4968	0.4936	0.644	0.611	0.49675	0.4949	0.37
7-C	middle	0.4968	0.4937	0.624				
	bottom	0.4968	0.4940	0.564				
	top	0.4968	0.4929	0.785	0.684	0.49675	0.4963	0.09
8-A	middle	0.4968	0.4935	0.664				
	bottom	0.4968	0.4938	0.604				
	top	0.4968	0.4929	0.785	0.664	0.49675	0.4963	0.09
8-B	middle	0.4968	0.4935	0.664				
	bottom	0.4968	0.4941	0.543				
	top	0.4968	0.4930	0.765	0.658	0.49675	0.4963	0.09
8-C	middle	0.4968	0.4938	0.604				
	bottom	0.4968	0.4938	0.604				

ORNL-DWG 95-5821

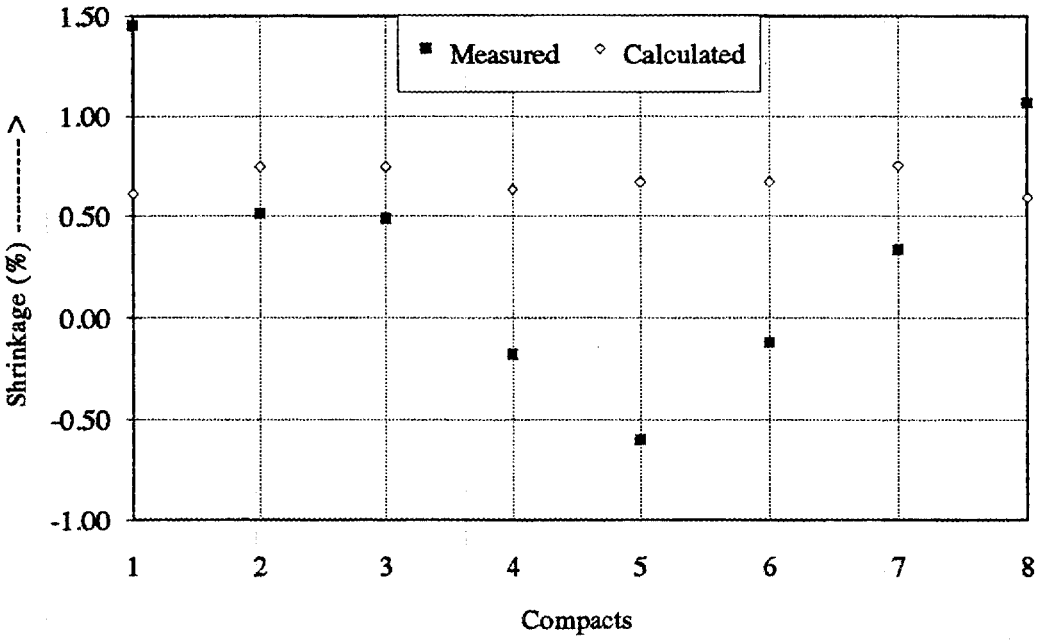

Figure 4.33*(a)*.

COMPARISION OF MEASURED AND CALCULATED DIAMETER CHANGES OF FUEL COMPACTS.

ORNL-DWG 95-5822

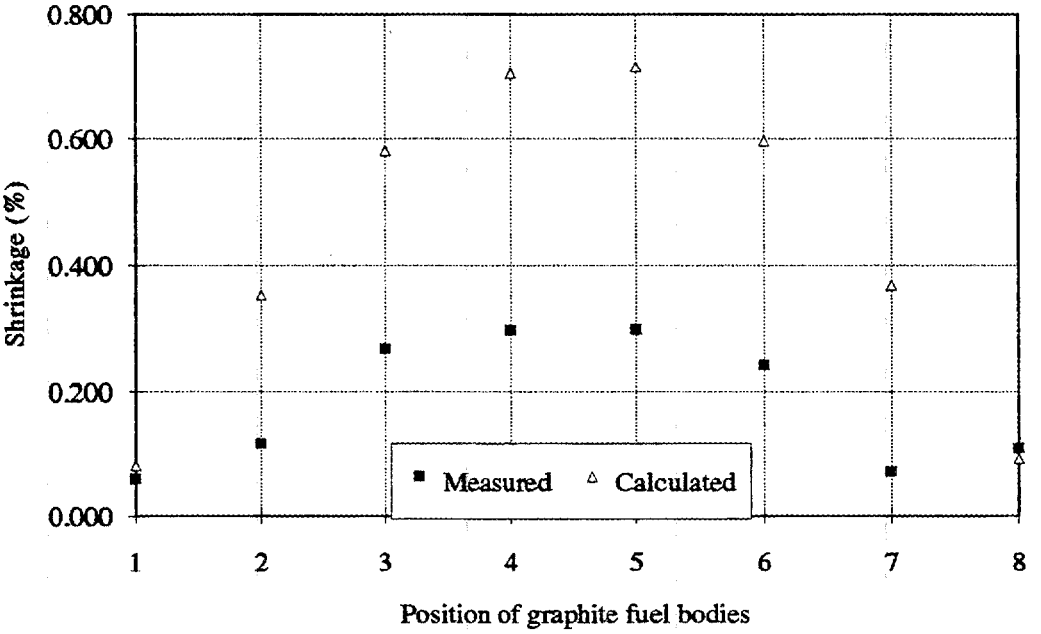

Figure 4.33*(b)*.

COMPARISON OF MEASURED AND CALCULATED DIAMETER CHANGES IN THE GRAPHITE FUEL BODIES

ORNL-DWG 95-5823

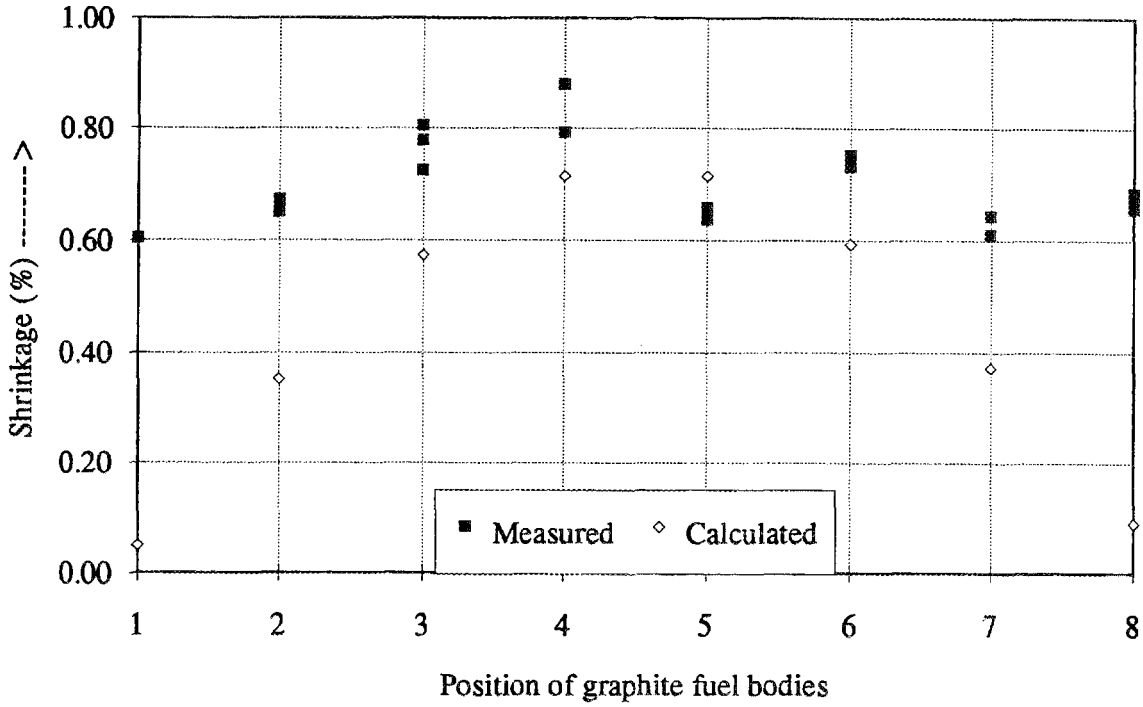

Figure 4.33*(c)*.

COMPARISION OF MEASURED AND CALCULATED DIAMETER CHANGES IN THE GRAPHITE FUEL BODY HOLES.

4.3.3 Measurement of Pushout Forces for Graphite Body End Plugs

A unique task included in the disassembly of capsule HRB-21 was the measurement of the bonding strength of the upper fuel closure plugs (part 5 in Figure 4.7) which were cemented into the graphite bodies at the time of fabrication. Knowledge of the bond strength was needed to assist in the design of equipment to handle irradiated full-size fuel elements where retention of the plug was required. The removal force was expected to be within a range of 22 to 445 N (5 to 100 lbf). The same pushout fixture with installed Dillon force gage already used for fuel compact removal (see Sect. 4.1.7) was used to carry out the closure plug removal. The push rod bearing on the closure plugs was about 0.41 in. diam. The closure plugs were examined after removal: those for holes 3A and 3B had a notable amount of "loose" (black) powder around the top periphery, while plug 7A retained a small chip from the top surface of GB-7. The measured pushout forces are given in Table 4.7.

All graphite body parts (screw plugs, push disks, cemented top plugs, etc.) were stored in marked, small aluminum containers, one for each fuel hole; the emptied graphite bodies themselves are in marked, large aluminum containers.

Table 4.7.

PUSH-OUT FORCES FOR CEMENTED-IN PLUGS

Body No.	Pushout force (lbf)		
	Hole A	Hole B	Hole C
9	21	13	14
2	23.5	39	22
3	47.5	56.5	30.5
4	34	38	35
5	42	29[a]	28
6	26.5	34	33
7	18	45	21
8	48	26	16

[a]Reading may be flawed since the plug was seen to slip down slightly while drilling out the center screw to permit compact removal.

4.4 PIGGYBACK SPECIMEN CAPSULES

4.4.1. Opening Specimen Capsules

Sixteen piggyback capsules were opened in the HRB-21 PIE (see Table 4.8). The first four capsules opened were the piggyback capsules located in piggyback hole "A," the two in graphite bodies 2 and 3 containing standard fissile (UCO) particles and the two in graphite bodies 6 and 7 containing fertile (ThO_2) particles. The final twelve were the bufferless fissile and fertile particles in piggyback holes "B" and "C." As shown in Figure 4.34, each capsule was a sealed 50.8-mm-long Nb tube containing two POCO graphite holders with individual holes for 16 particles per holder. Each holder was covered with a thin, narrow full-length strip of Grafoil aligned with the flat tops of the holders to prevent the particles from contacting the outer Nb tube.

Opening of an Nb capsule commenced with the cutoff of each end using a slow-speed Isomet saw fitted with a 0.375-mm-thick diamond abrasive blade. The ends were deburred using a small drill bit, and the capsule body was inserted into a special pushout

Table 4.8.

HRB-21 ENCAPSULATED SPECIMEN TEST MATRIX

Graphite holder No.	Fuel compact hole		
	A	B	C
9	S[a]		Def(U)[b]
2	Std(U)[c]	Def(Th)[d]	Def(U)
3	Std(U)	Def(Th)	Def(U)
4	S		Def(U)
5	S		Def(Th)
6	Std(Th)[e]	Def(Th)	Def(Th)
7	Std(Th)	Def(Th)	Def(Th)
8	S	S	Def(Th)

[a]S = Sorptivity specimen.
[b]Def(U) = Bufferless fissile particle (UCO).
[c]Std(U) = Standard fissile particle (UCO).
[d]Def(Th) = Bufferless fertile particle (ThO_2).
[e]Std(Th) = Standard fertile particle (ThO_2).

holder designed to retain the outer tubing segment but allow the graphite boat to emerge into a separate collector well. Surprisingly, for the first four piggyback capsules containing the standard particles, application of up to the 6-lb preassigned maximum force (measured with the large pushout facility Dillon force gage; see Figure 4.4) failed to move any of the capsule contents.

In order to retrieve the graphite containers from these capsules, it was necessary to machine full-length slits just through the 0.25-mm wall. Custom holders were made that clamped the capsule between jaws having shallow v-grooves with only the tubing thickness protruding above the jaws. The holder was then mounted and carefully aligned on a milling machine to allow making the full-length slots. Making a single slot proved insufficient to permit pushout of any piggyback contents. It was necessary to make two opposing slots, and adequate clamping of the capsule for the second slot was difficult. For the case of piggyback

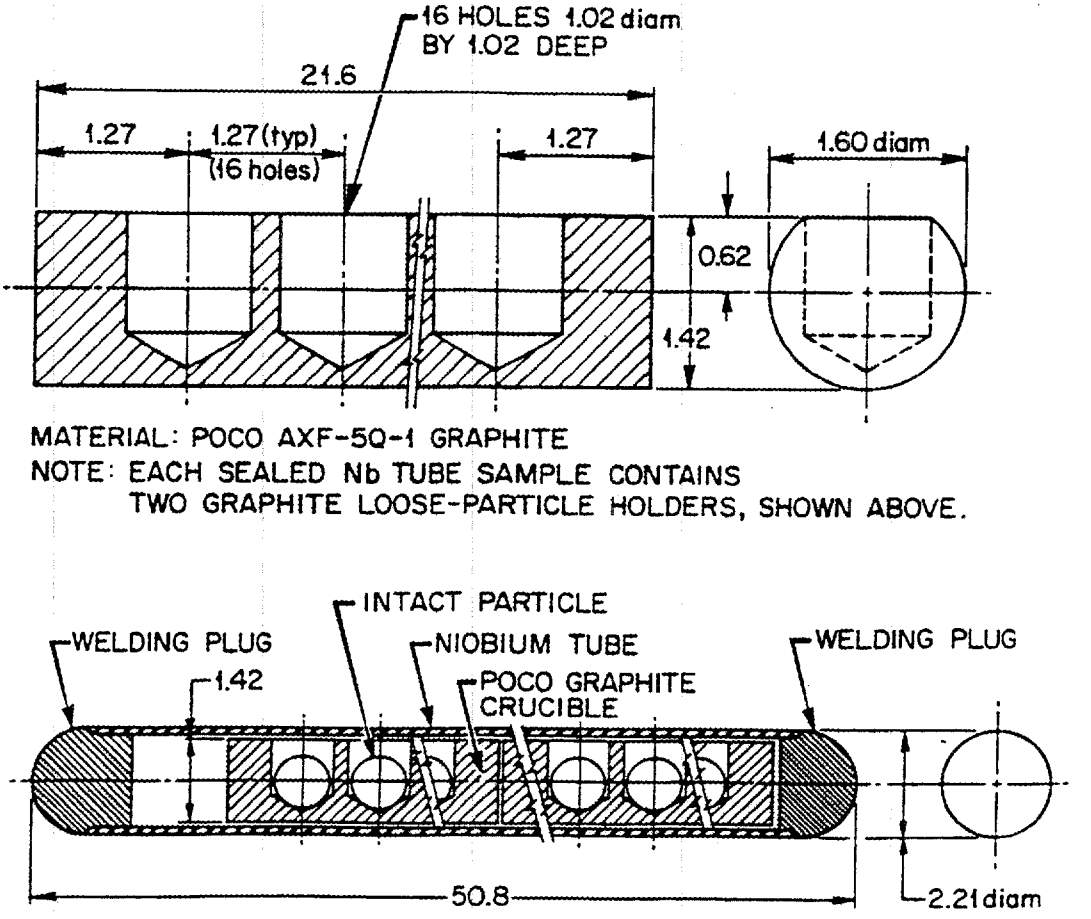

Figure 4.34.

PIGGYBACK SPECIMEN HOLDER USED IN HRB-21. ALL DIMENSIONS ARE IN MILLIMETERS.

capsule 6A, a protruding section of tubing or Grafoil apparently was caught by the cutter and pulled out one of the graphite containers resulting in loss of some particles.

Final disassembly after slitting was still not straightforward. The containment tube segments had to be peeled off the graphite holders (see Figure 4.35), because bonding (perhaps niobium-carbide formation) had evidently occurred during the irradiation/thermal exposure. The first peel-open was carried out in a white photographic tray for visibility and containment, but the freed fuel particles acquired static charges and attached to the tray wall, or in some cases, became imbedded into the soft plastic tray. Subsequent openings were conducted in a stainless steel tray.

YP15210

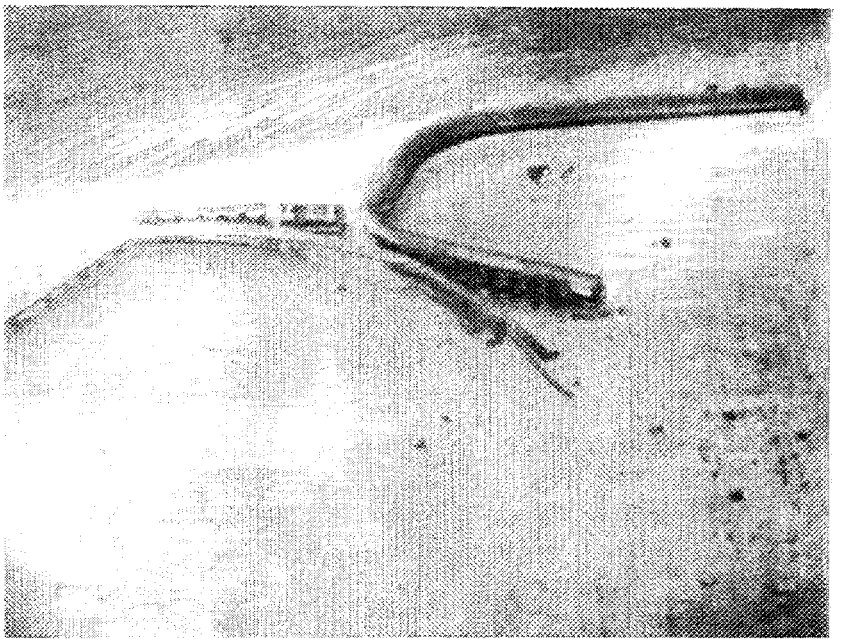

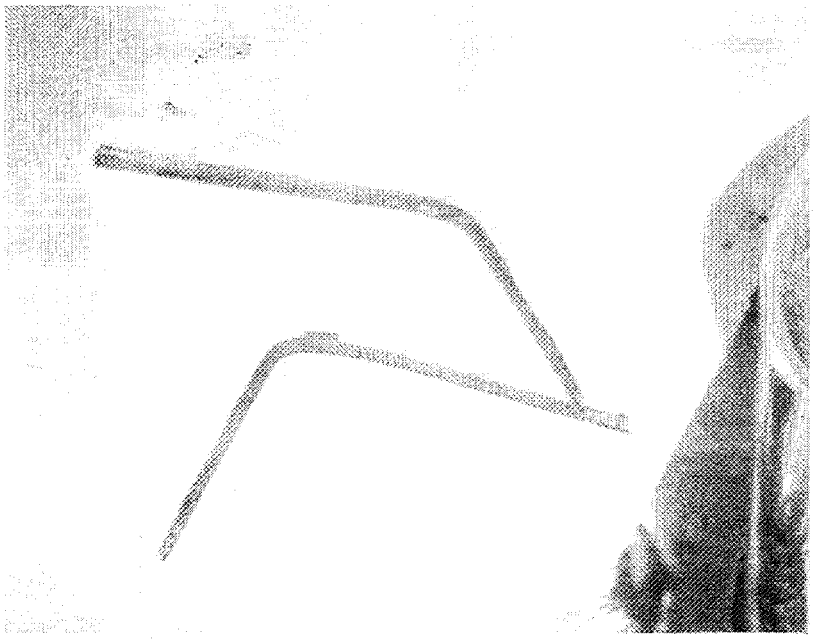

Figure 4.35.

PEELED-BACK NIOBIUM CONTAINMENT WITH ADHERING FRAGMENTS OF GRAPHITE PARTICLE HOLDERS FOR PIGGYBACK CAPSULE 2A (ABOVE) AND 3A (BELOW).

The graphite containers in the last twelve capsules containing the bufferless particles were easy to retrieve using the special pushout holder. These 12 capsules were opened following a special procedure[4-9] in which the end cuts were made further from the end than in the initial 4 capsules opened. In these cases, the initial cut-off resulted in cutting through the end of the graphite crucibles. Because the location of the crucibles inside the Nb tube was not fixed or known, occasionally, the initial cut was sufficiently far from the end that it passed through the first particle hole, and the end particle was lost.

4.4.2 Visual Examination of Piggyback Samples

A photo-visual examination of the particles from HRB-21 piggyback containers was performed prior to IMGA examination of the particles. Photographs of the unbonded standard fissile particles are shown in Figure 4.36, and standard fertile particles are shown in Figure 4.37. During the visual examination, it was found that one particle in the PB-2A batch was stuck in the graphite holder. Close examination revealed that the particle was being held in place by the crushed side of the graphite holder. A particle in the PB-3A batch was found to be a ThO_2 particle indicating some cross-contamination from either the PB-6A or -7A batch. Finally, one particle in the PB-7A batch was found to have a section of its outer PPyC coating missing. All other standard fissile particles appeared to be intact and showed no signs of cracking in the OPyC layer as was observed in particles deconsolidated from compacts.

The visual examination of the bufferless particles revealed that many of the fissile particles had broken during the irradiation. Table 4.9 shows the number of intact bufferless particles retrieved and the calculated failure fraction. All of the bufferless fertile particles remained intact during the irradiation. About half of the bufferless fissile particles in the piggyback samples in graphite bodies 2, 3, and 4 failed during the irradiation. In graphite body 1, which had the lowest fast fluence, all of the fissile particles remained intact. The pre-irradiation predictions[4-10] indicated that the failure fraction for the bufferless fissile particles in bodies 1, 2, 3, and 4 would be about 5, 50, 100, and 100%, respectively. The predicted fertile failure was less than 2% for all locations.

As an example of the debris from the broken bufferless particles, representative photographs of PB-3C and PB-4C are shown in Figure 4.38. Several intact particles, many particle fragments, and a few rectangular pieces of the Grafoil crucible covering can be seen. Usually, the size of the particle fragments was about one-eighth to one-quarter of the

R80368-1

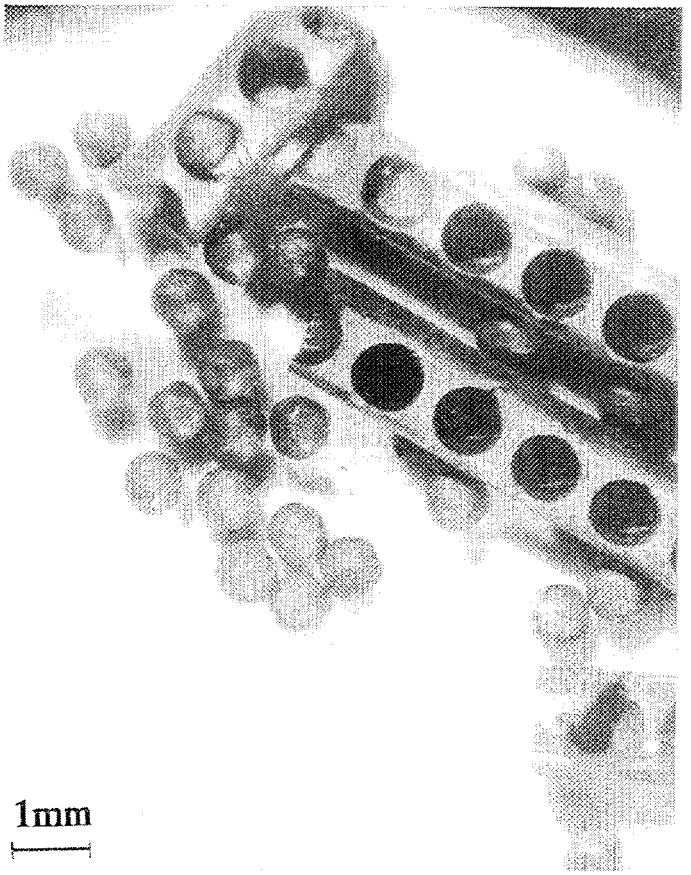

R80376-1

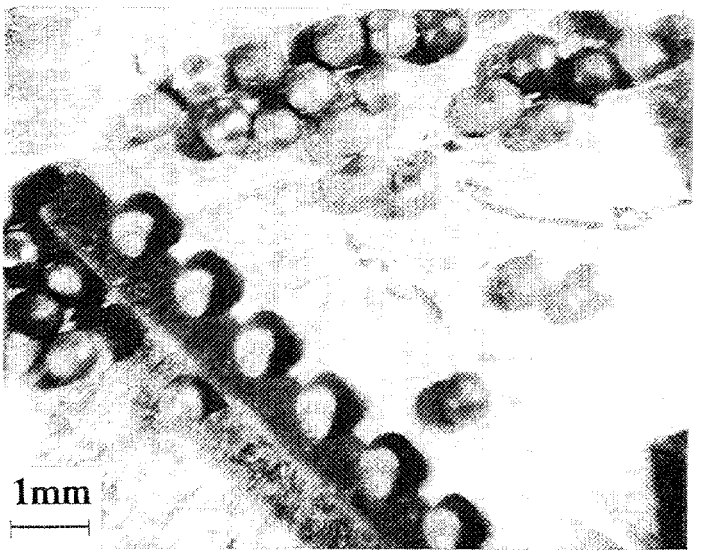

Figure 4.36.

PHOTOGRAPHS OF THE STANDARD PIGGYBACK FISSILE PARTICLES.

R80580

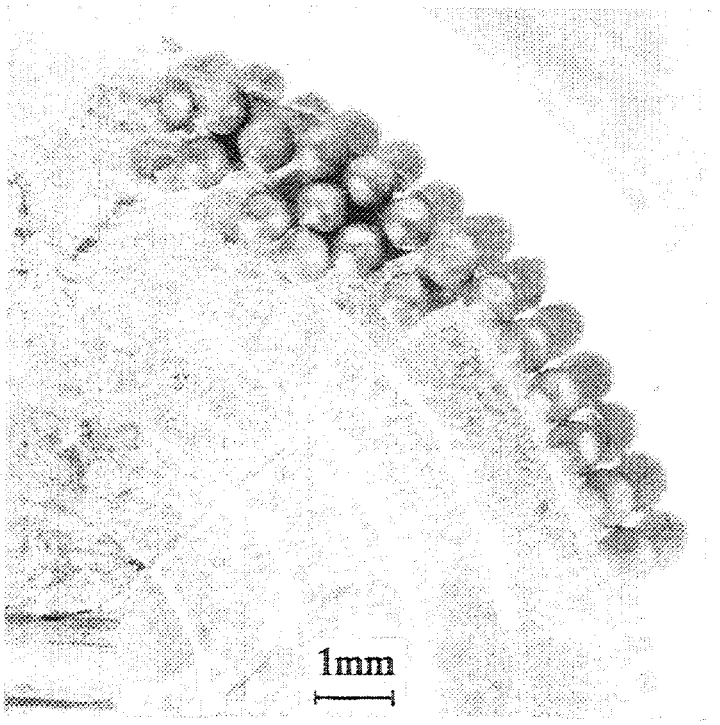

R80371-1

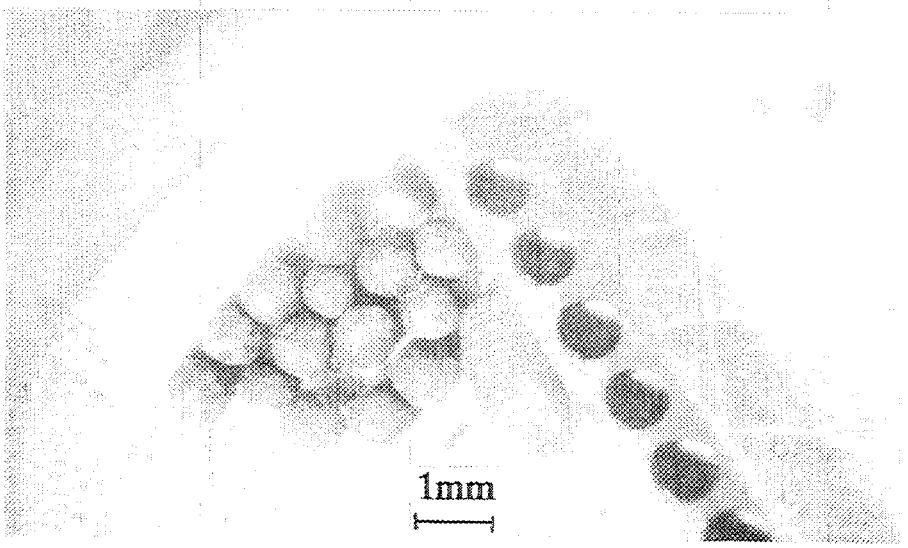

Figure 4.37.

PHOTOGRAPHS OF THE STANDARD PIGGYBACK FERTILE PARTICLES AFTER IRRADIATION.

Table 4.9.

NUMBER OF INTACT BUFFERLESS PIGGYBACK PARTICLES IN HRB-21

Graphite holder No.	Time-averaged temp., °C	Fluence × 10^{25} n/m^2	Piggyback graphite body			
			B		C	
			Number intact	Percent failed	Number intact	Percent failed
9	726	1.5			32	0
2	848	2.3	24	25.0	15[a]	51.6
3	872	3.0	17[a]	45.2	14	56.3
4	907	3.5			17	46.9
5	907	3.5			32	0
6	895	3.0	32	0	32	0
7	865	2.3	32	0	31[a]	0
8	742	1.5			32	0

[a]Indicates particles lost during disassembly of the piggyback containers; there were 32 particles in each container.

particle. The inner edge of the IPyC was covered with a shiny coating which probably was a remnant of the kernel, since the IPyC was deposited directly onto the kernel in these particles. No spherical, intact kernels were observed.

Although none of the bufferless fertile particles appeared broken, the contents of PB-6C included three small spheres which were about 0.2 mm in diameter. No analysis of these spheres was conducted.

The surface of the holes in the graphite crucibles which had held the bufferless particles was also visually examined. All of the holes which had contained the fertile particles were smooth and clean from deposits. The holes which had contained fissile particles that had fragmented during the irradiation had deposits adhering to the hole walls; holes which had contained fissile particles that remained intact were clean. Fragments of the coatings were seen stuck to these deposits. The deposits had a metallic luster, ranged in size, and were deposited sporadically over most of the inner surface. No analysis of the deposits was attempted.

YPC-140

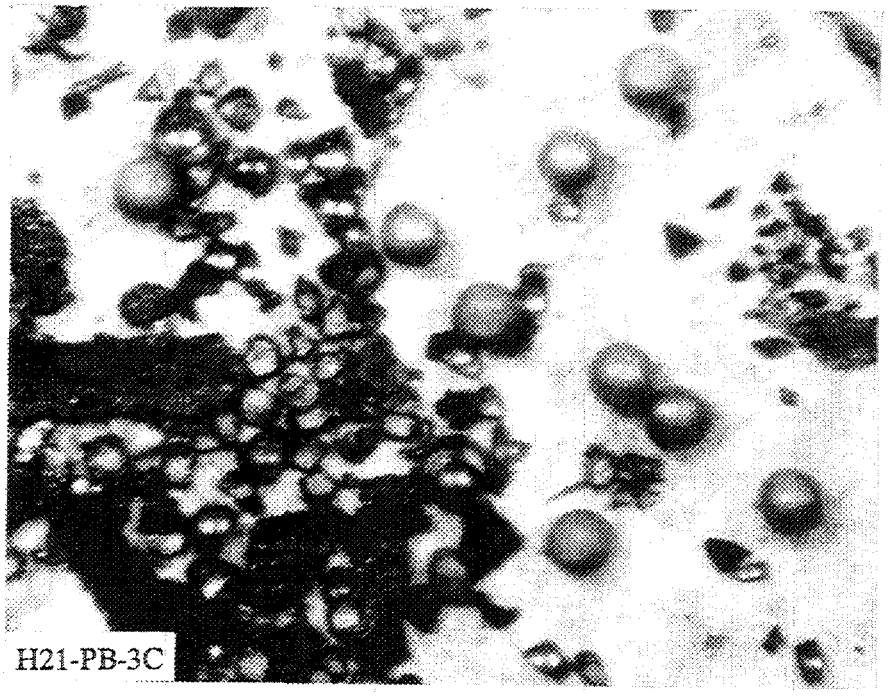

YPC-141

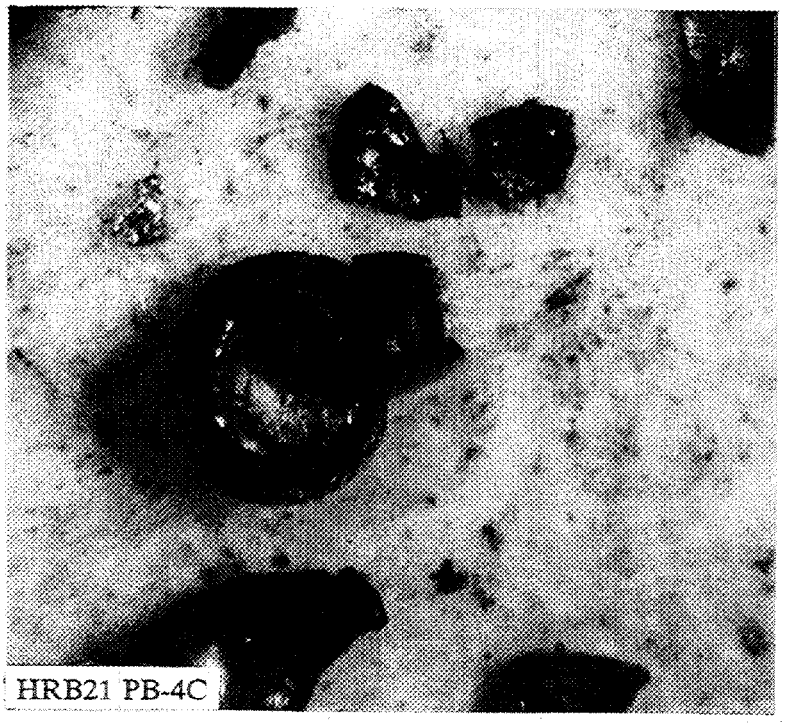

Figure 4.38.

PHOTOGRAPHS OF DEBRIS FROM BUFFERLESS FISSILE PARTICLES AFTER IRRADIATION.

4.5 IRRADIATED-MICROSPHERE GAMMA ANALYZER RESULTS

The IMGA system is a unique research tool located in the IFEL at ORNL.[4-11,4-12] The primary function of the IMGA system is to accurately measure radioisotopic inventories of individual coated fuel particles used in MHTGR applications. This is accomplished by detecting the gamma radiation given off by the fuel particles as various fission products decay. The system consists of three major components: (1) a high-resolution gamma-ray spectrometer, (2) a computer-based multichannel analyzer, and (3) an automated particle-handling system. These three components have been integrated into a sophisticated system capable of automatic operation.

The automated particle handler shown in Figure 4.39 is the unique component in the IMGA system. It is composed of a singularizer, a sample changer, and a sample collector

YP9976

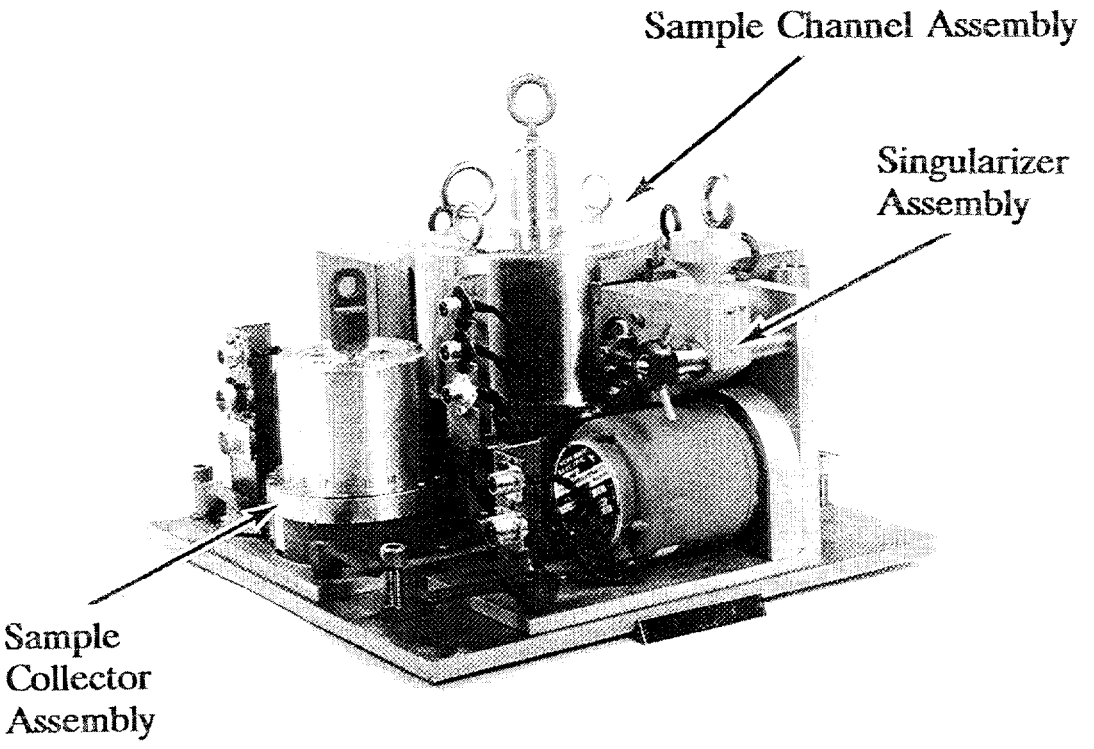

Figure 4.39.

IRRADIATED-MICROSPHERE GAMMA ANALYZER AUTOMATED PARTICLE HANDLER.

which are all synchronized and controlled by the computer. The singularizer isolates an individual microsphere from a given sample and transfers it to the sample changer. The sample changer moves the microsphere from the loading position below the singularizer to the counting position in front of the spectrometer. After the microsphere is counted, the sample changer moves the particle to the unloading position above the sample collector which contains 20 bin locations. Bin-selection criteria are based on the measured photopeak intensities, so it is possible to physically separate particles as a function of their ability to retain key radioisotopes. As part of the examination process, the measured photopeak intensities for each particle are recorded in a disk file for later off-line detailed evaluation.

Fuel particles irradiated in the HRB-21 experiment capsule and subsequently examined by the IMGA system fall into two main categories, those deconsolidated from fuel compacts and a small number of special unbonded particles contained in piggyback containers. The following sections present the results of the IMGA examination and analysis of these particles and discuss the performance of the fuel based on the measurements.

4.5.1 Fuel Compact Deconsolidation

To obtain unbonded particles for IMGA examination, it was necessary to decompose the irradiated compacts into their constituent fuel particles and graphite shim material. One method of performing this task was to electrolytically deconsolidate the compacts in a nitric acid solution. This process was carried out for HRB-21 compacts 5C, 6B, 7A, and 8A following standard operating procedure MET-FME-SOP-18, Rev. 0. Briefly, a compact is loaded into the deconsolidation apparatus as shown in Figure 4.40. Next, a current is applied across the compact with the compact acting as the anode and the wire-mesh basket acting as the cathode. Anodic oxidation of the compact occurs causing the carbonaceous matrix material holding the compact together to disintegrate into a fine powder releasing the particles and graphite shim material. As the particles fall away from the compact, the circuit is broken thus halting further oxidation of the OPyC layer of the particle. The particles and matrix debris are collected in a wire-mesh basket below the deconsolidation tube and are later retrieved and washed. The mixture is then dried and poured through a series of sieves to grade the material by size. The material from the intermediate sieve is processed one step further to separate the round, unbonded particles from the randomly shaped pieces of

ORNL-DWG 95-5824

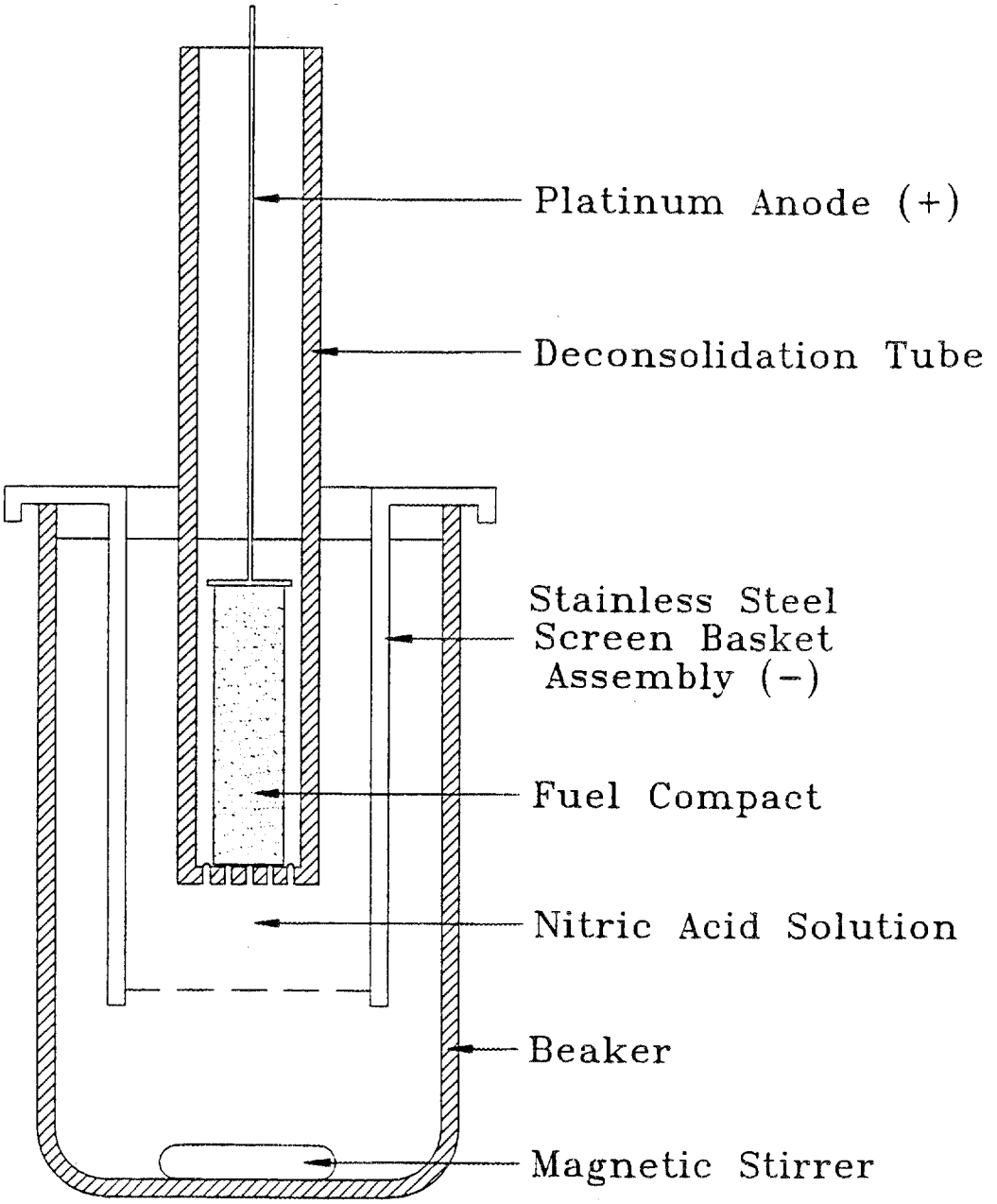

Figure 4.40.
FUEL COMPACT DECONSOLIDATION APPARATUS.

graphite shim material. Shape separation is accomplished with a vibrating table assembly that produces particle and non-particle fractions.

The procedure used to deconsolidate the HRB-21 compacts called for the entire compact to be submerged in the electrolyte when the current was first applied. This caused the compacts to break up too quickly resulting in a mixture of unbonded fuel particles, graphite debris, and sections of intact compact material. After recovering as many clean particles as possible from the initial deconsolidations, the undeconsolidated portions of compacts 5C and 8A were returned to the deconsolidation apparatus. A second attempt was made to deconsolidate the material from each compact; however, in both cases, the repeat attempt proved to be largely ineffective. Work to retrieve additional particles from compact 8A halted at this stage. For compact 5C, a burn step was incorporated to remove all exposed graphite from the remaining material and thus free the remaining particles. The material was burned in air at 750°C for a total of 53.5 h according to Step 6 of procedure MET-FME-SOP-27, Rev. 0. Due, in part, to the experience obtained with compact 5C, a decision was made to burn all the material from compacts 6B and 7A prior to examination. Compact 6B was burned in air at 750°C for a total of 58.7 h, and compact 7A was burned in air at 750°C for a total of 48 h. Processing flow charts for each of the deconsolidated compacts are shown in Figures 4.41 through 4.44.

It is recommended that, in future compact deconsolidations, the compact be immersed slowly in the electrolyte so that deconsolidation occurs in a limited region where the compact contacts the surface of the electrolyte. This should mitigate the problem of premature breakup of the compact before the matrix graphite has sufficient time to disintegrate. After normal processing to recover all clean intact particles, any remaining material should be burned to recover SiC coating fragments and any particles not completely free of matrix graphite. The unbonded particles and SiC coating fragments should then be randomly split as desired to obtain samples for IMGA examination. Ideally, IMGA examination of particles should not begin until all particles from a given compact are available for sampling. In addition, the electrolyte from the deconsolidation step should be analyzed to determine the absolute inventories of both HMs and gamma-emitting isotopes.

4.5.1.1 Visual Exam of Particles and Debris

Figure 4.45 illustrates samples of the material obtained from the electrolytic deconsolidation of compact 5C. In the figure, photograph *(a)* shows large graphite shim

ORNL-DWG 95-5825

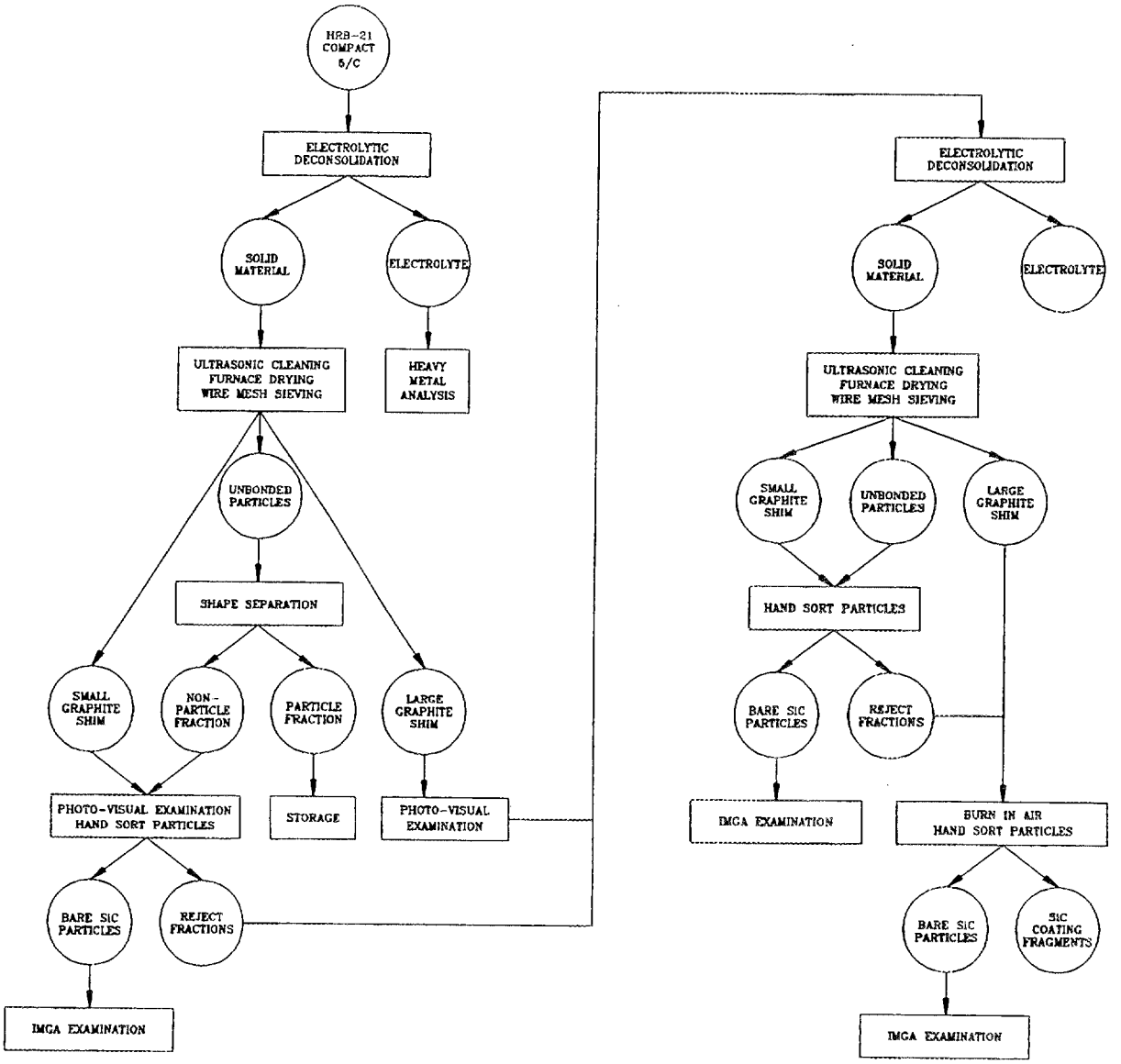

Figure 4.41.

PROCESSING SEQUENCE FOR COMPACT 5C.

ORNL-DWG 95-5826

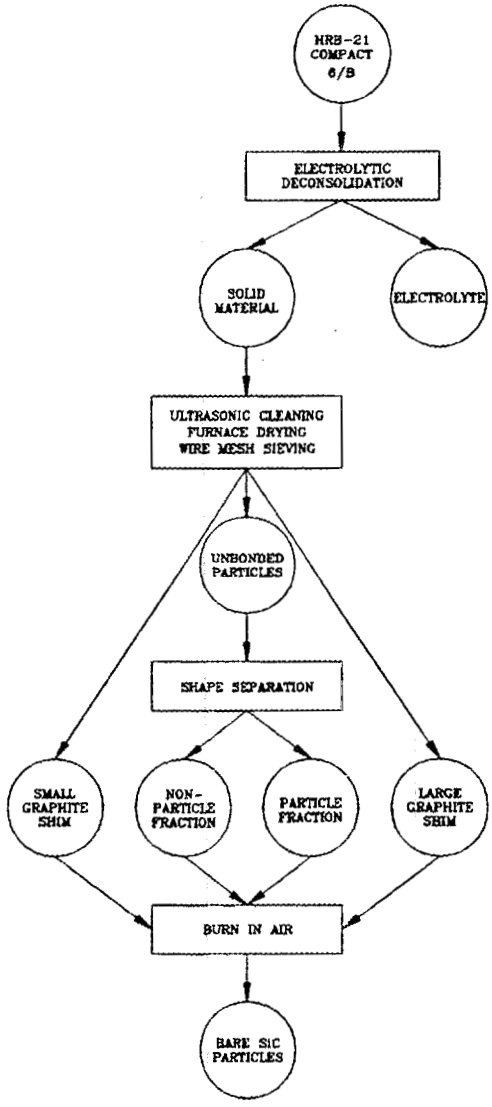

Figure 4.42.

PROCESSING SEQUENCE FOR COMPACT 6B.

ORNL-DWG 95-5827

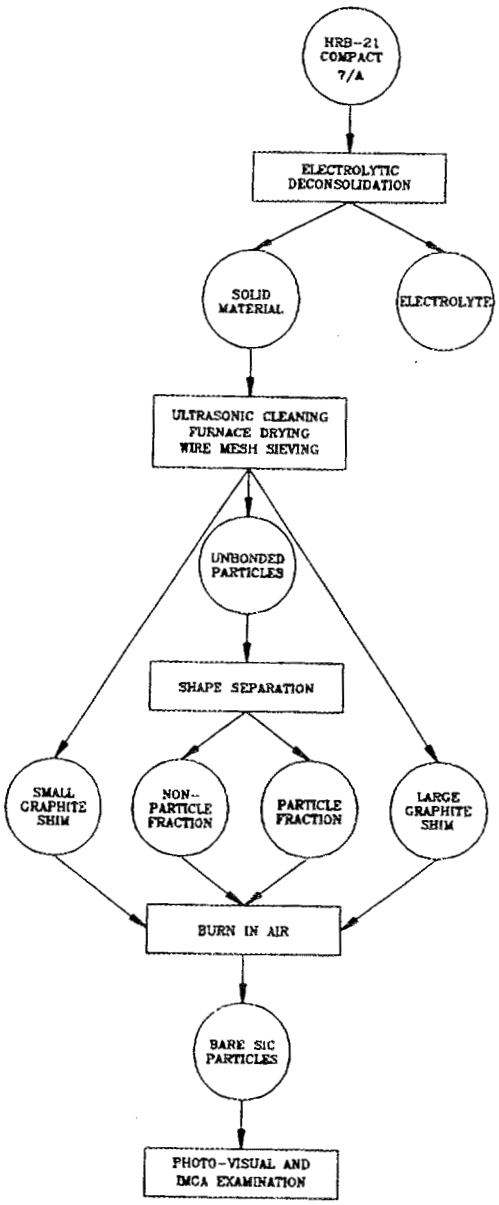

Figure 4.43.

PROCESSING SEQUENCE FOR COMPACT 7A.

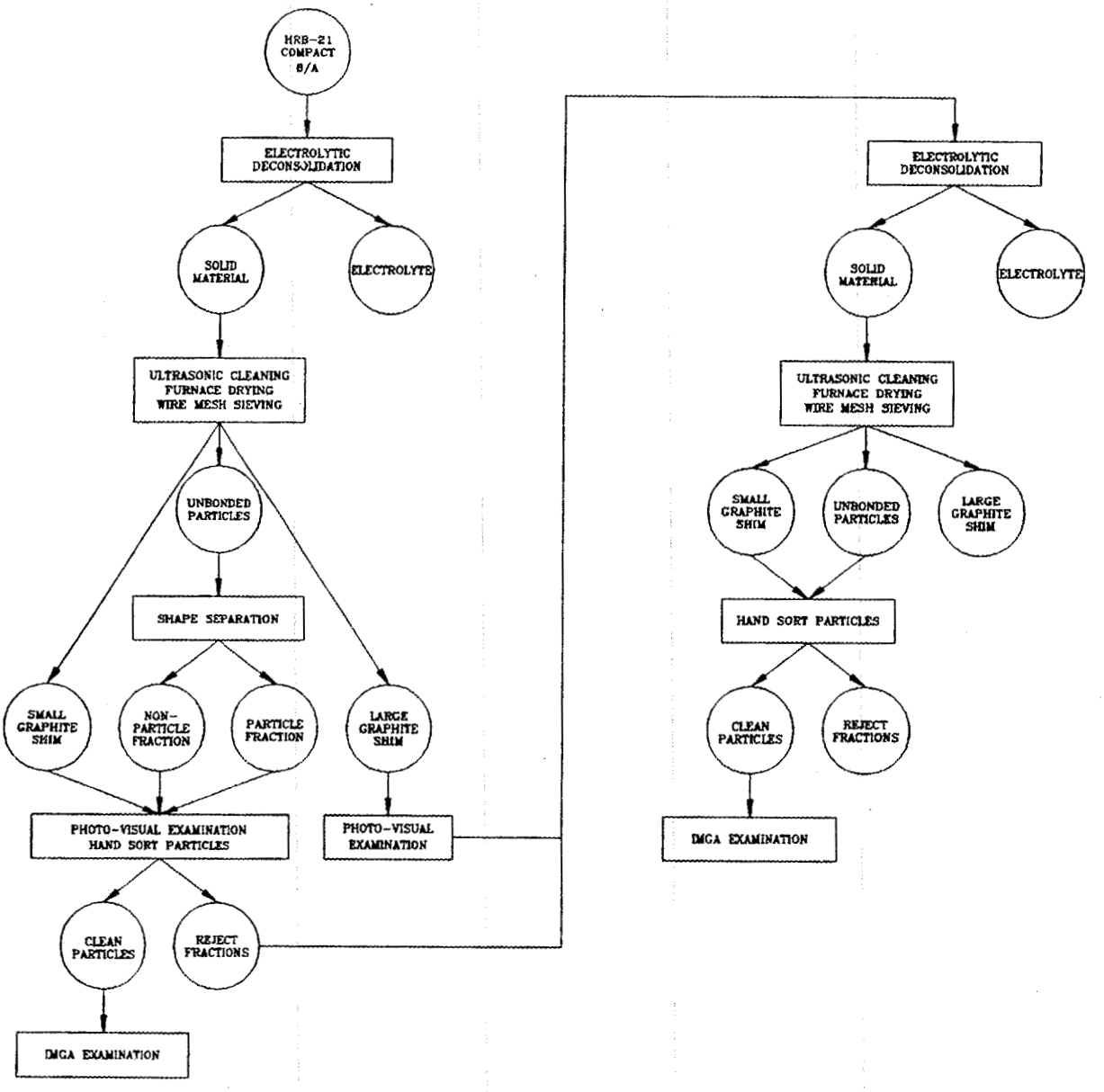

Figure 4.44.
PROCESSING SEQUENCE FOR COMPACT 8A.

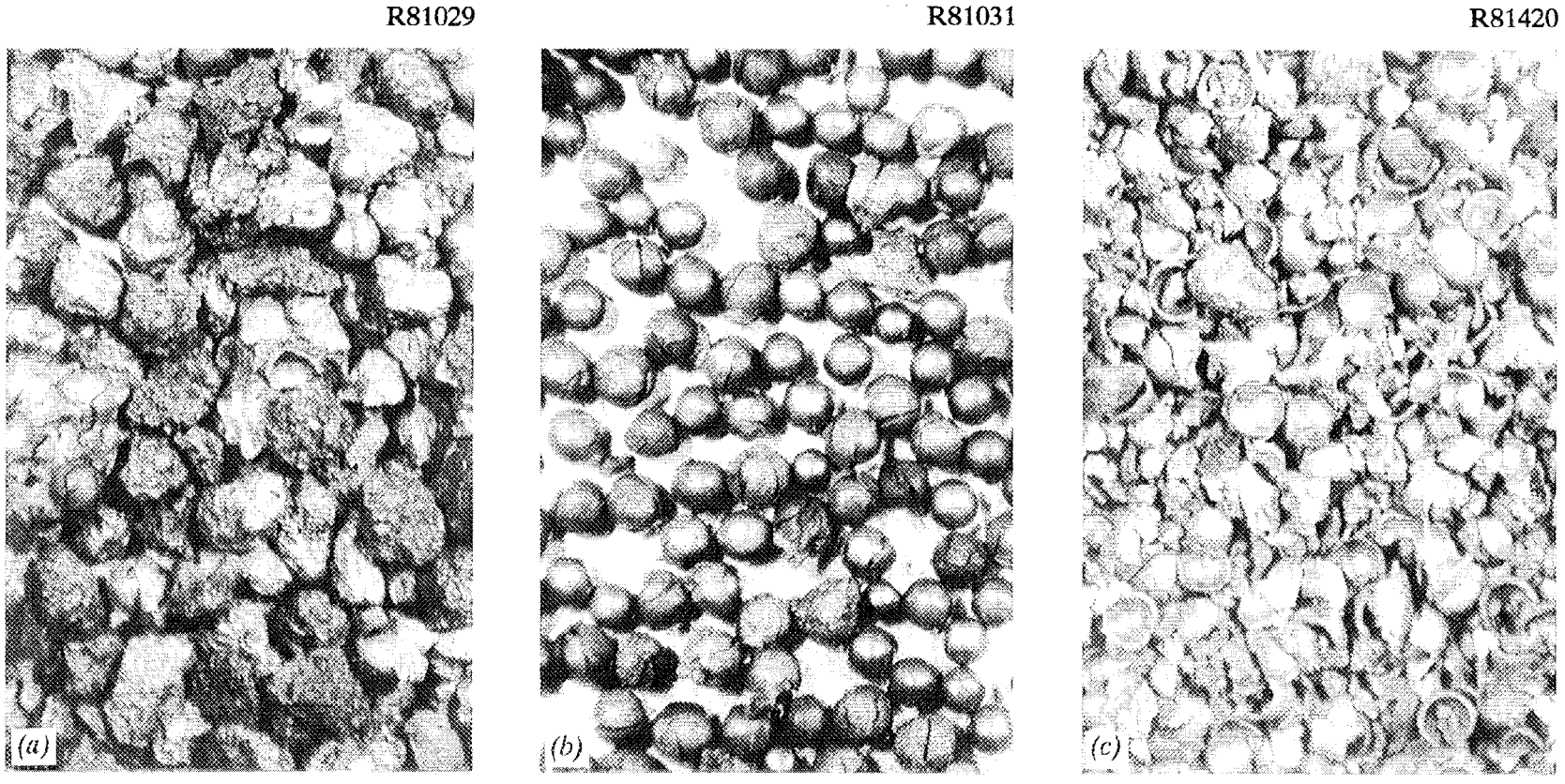

Figure 4.45.

MATERIAL FROM THE ELECTROLYTIC DECONSOLIDATION OF HRB-21 COMPACT 5C: *(a)* LARGE GRAPHITE SHIM AND UNDECONSOLIDATED PORTIONS OF THE COMPACT, *(b)* UNBONDED FUEL PARTICLES, AND *(c)* SMALL GRAPHITE SHIM AND COATING FRAGMENT DEBRIS.

material and undeconsolidated portions of the compact, photograph *(b)* shows a sample of unbonded fuel particles, and photograph *(c)* shows small graphite shim material and coating fragment debris. From the visual exam, it was apparent that virtually all of the particles in the 5C compact had failed OPyC coatings. Many of the particles were completely lacking the OPyC coating, and in those that had retained the coating, the coating was cracked down to the SiC layer. In addition to the OPyC coating damage, approximately 5% of the particles were found to have cracked or chipped SiC coatings that separated easily from the underlying IPyC coating. In extreme cases, the SiC coating was completely missing, and what remained was a relatively intact IPyC coating. A few particles were also found that appeared to have holes which penetrated both the SiC and IPyC coatings. Examples of particles with missing or damaged SiC coatings are shown in Figure 4.46. In the figure, photograph *(a)* shows a sample of particles with the more common chipped or missing SiC coating damage. The majority of these particles were found to be fertile particles with no detectable loss of their fission product inventories. Photograph *(b)* in Figure 4.46 shows two particles with the hole-type defect; these two particles were found to be fissile particles with most of their kernels leached. After sorting through the material from the compact to separate particles suitable for IMGA examination, the remaining material was burned to remove all exposed graphite. Figure 4.47 shows the resulting particles and SiC coating fragments recovered after the burn. Much of the SiC coating fragment debris undoubtedly came from particles like those shown in Figure 4.46*(a)*. After the burn step was completed, an estimate was made of the number of particles accounted for from the compact. It was found that only two-thirds of the particles from the compact were present. A review of the deconsolidation records was made, and it was determined that a container of particles from the shape separation step had been inadvertently placed in storage and not sent to the IMGA cubicle for examination. These particles were retrieved from storage and visually examined. They accounted for the missing one-third of the particles and resemble those in Figure 4.45*(b)*.

Figure 4.48 illustrates samples of the material obtained from the electrolytic deconsolidation of compact 8A. In the figure, photograph *(a)* shows large graphite shim material and undeconsolidated portions of the compact, photograph *(b)* shows a sample of unbonded fuel particles, and photograph *(c)* shows small graphite shim material and coating fragment debris. The large graphite shim material and undeconsolidated portions of

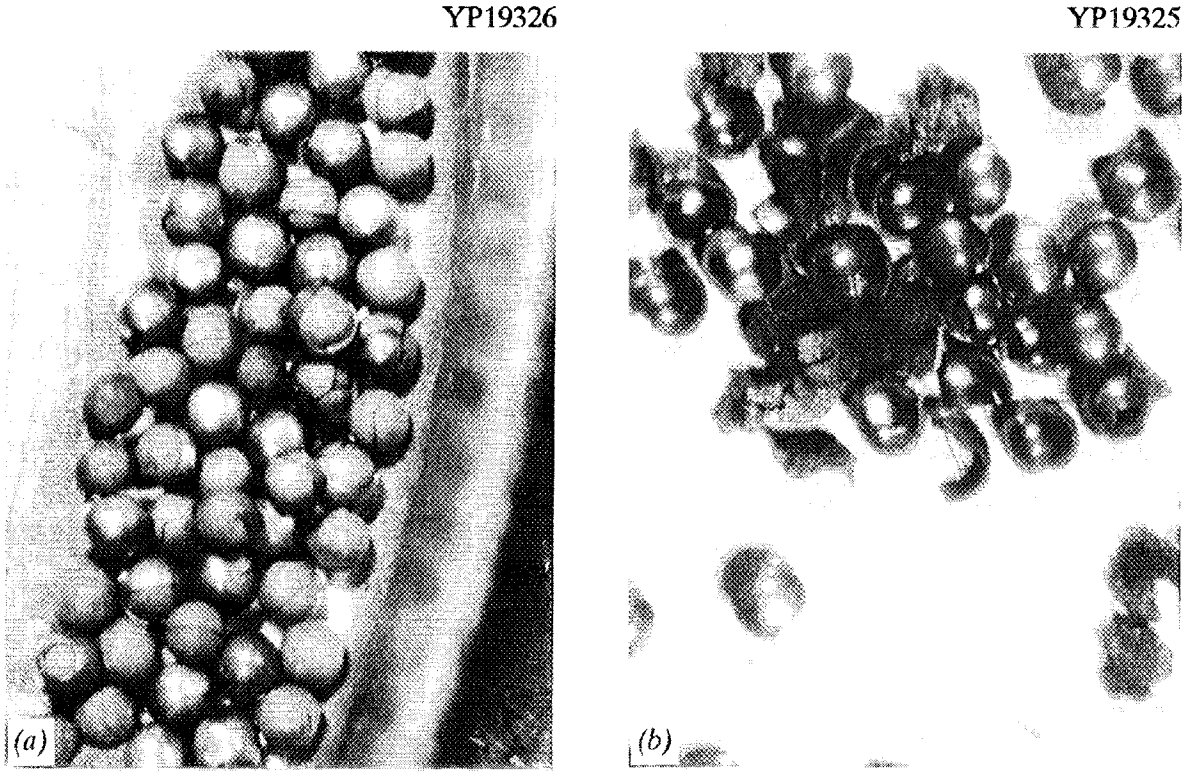

Figure 4.46.

EXAMPLES OF PARTICLES WITH DAMAGED SiC COATINGS FROM HRB-21 COMPACT 5C: *(a)* SAMPLE OF PARTICLES WITH THE MORE COMMON CHIPPED OR MISSING SiC COATING AND *(b)* TWO PARTICLES WITH SMALL HOLE-TYPE DEFECTS IN THE SiC COATING.

R81767

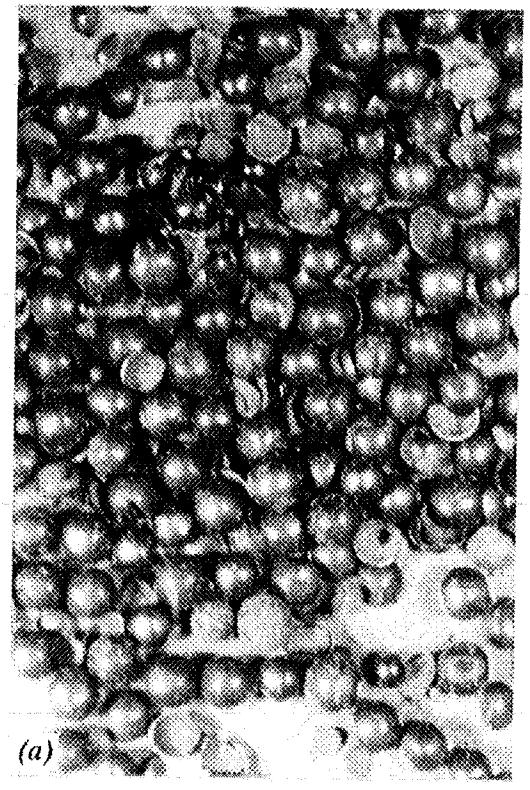

R81839

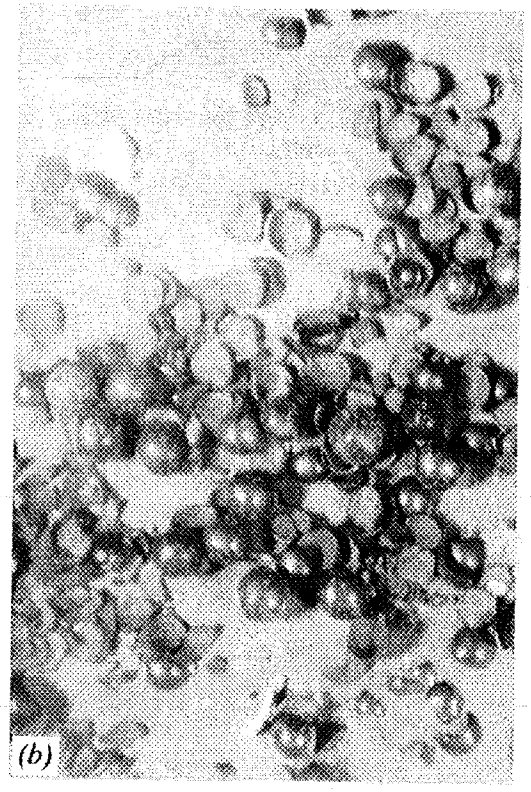

Figure 4.47.

EXAMPLES OF HRB-21 COMPACT 5C: *(a)* PARTICLES AND *(b)* SiC COATING FRAGMENTS AFTER BURNING THE UNDECONSOLIDATED PORTIONS OF THE COMPACT AND GRAPHITE DEBRIS IN AIR AT 750°C FOR A TOTAL OF 53.5 h.

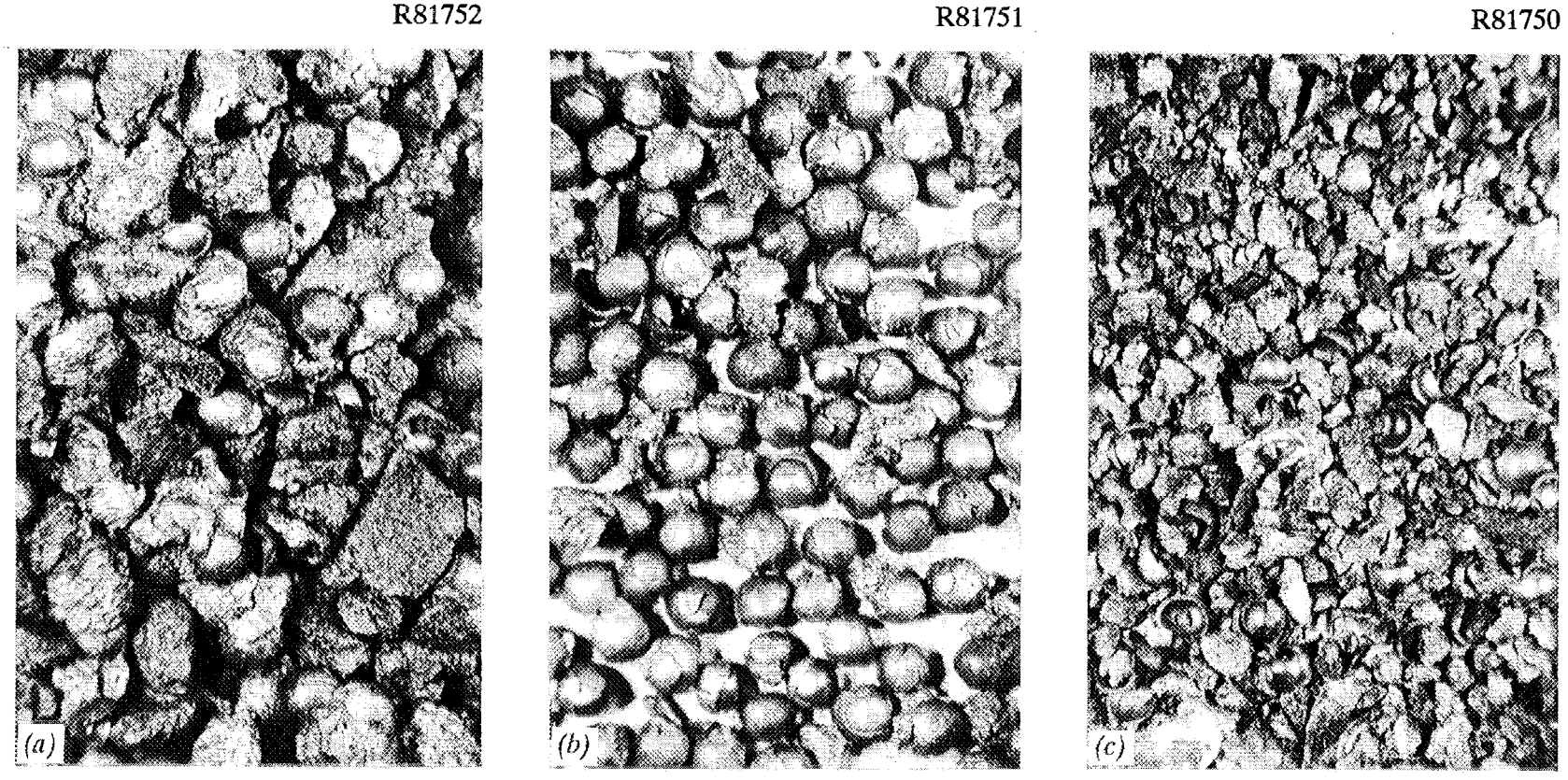

Figure 4.48.

MATERIAL FROM THE ELECTROLYTIC DECONSOLIDATION OF HRB-21 COMPACT 8A: *(a)* LARGE GRAPHITE SHIM AND UNDECONSOLIDATED PORTIONS OF THE COMPACT, *(b)* UNBONDED FUEL PARTICLES, AND *(c)* SMALL GRAPHITE SHIM AND COATING FRAGMENT DEBRIS.

compact 8A look the same as similar material from compact 5C. Unbonded fuel particles from compact 8A exhibit cracking in the OPyC coating layer, and many particles have sections of the OPyC coating missing. A few particles have lost all of their OPyC coating layer, although not nearly as many as in compact 5C. No particles were found with visible defects in the SiC coating layer, and no SiC coating fragments were detected in the debris. The small graphite shim material from compact 8A had a lower percentage of OPyC coating fragment debris than the corresponding material from compact 5C, which was consistent with the observation that there were fewer bare SiC particles in compact 8A.

Because of time limitations, work on compact 6B was canceled, and the material was never visually examined. A limited amount of work was done on compact 7A, which was prepared in a manner similar to compact 6B. Figure 4.49 is a photograph of the material from compact 7A as received after burning to remove all exposed graphitic material. No particles were observed with defects in the SiC coating layer, and no SiC coating fragments were found.

4.5.1.2 Analysis of Compact Deconsolidation Electrolyte

Following deconsolidation of HRB-21 compacts 5C and 7A and subsequent to the removal of loose particles and debris, the remaining solution was analyzed to determine radioisotopic content, with special emphasis on HMs. The primary purpose of the analysis was to determine the percentage of equivalent exposed kernels which were leached out as part of the deconsolidation process. This information, if meaningful, would be factored into the final estimate of particle failure fraction.

The results of these analyses were inconclusive, as far as the percentage of leached kernels was concerned, due to the relatively large uncertainties. The large uncertainties were mainly the results of the large dilution of the original sample necessary to meet radiological control requirements. Once this fact became apparent, the use of this analysis method was discontinued and the use of a high-level method explored.

4.5.2 Particles Deconsolidated from Fuel Compacts

Four HRB-21 compacts were deconsolidated and some portion of their fuel particles examined by the IMGA system. The compacts were composed of two types of particles, a fissile 19.7% enriched UCO TRISO-P coated particle and a fertile ThO_2 TRISO-P coated particle. Nominal compact loadings and estimated irradiation parameters for the four

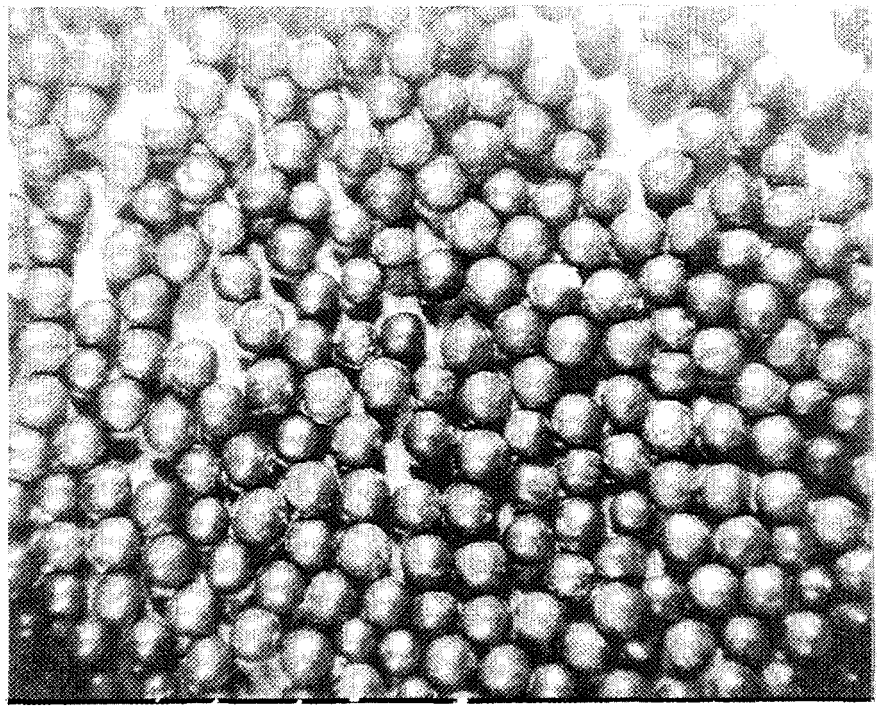

Figure 4.49.

SAMPLE OF PARTICLES FROM HRB-21 COMPACT 7A AFTER IT WAS ELECTROLYTICALLY DECONSOLIDATED AND THEN BURNED IN AIR AT 750°C FOR A TOTAL OF 48 h.

compacts are given in Table 4.10. Temperature, fluence, and compact loading parameters were taken from preirradiation and postirradiation reports, and the particle burnups were estimated from IMGA activity measurements using a least-squares minimization technique developed at ORNL.[4-13] Three of the compacts were deconsolidated specifically for analysis by the IMGA system as described in Sect. 4.5.1, and the fourth was deconsolidated as the result of the leach-burn-leach (LBL) analysis described in Sect. 4.8. Due to significant differences in the deconsolidation methods, the results for the three electrolytically deconsolidated compacts (5C, 7A, and 8A) will be discussed separately from the LBL compact (5B) in Sects. 4.5.2.1 and 4.5.2.2, respectively.

4.5.2.1 HRB-21 Compacts 5C, 7A, and 8A

Particles from compact 8A were examined first by the IMGA system. During initial trial runs, it became obvious that the fissile and fertile particles from this compact would

Table 4.10.

NOMINAL COMPACT LOADINGS AND IRRADIATION PARAMETERS FOR SELECTED HRB-21 COMPACTS

Compact	Operating temp., °C	Fast[a] fluence, n/m^2	Number of UCO particles	UCO[b] burnup, % FIMA	Number of ThO_2 particles	ThO_2[b] burnup, % FIMA
5/B	1023	3.5×10^{25}	1200	19.2	4460	2.00
5/C	1023	3.5×10^{25}	1200	19.5	4460	2.00
7/A	974	2.3×10^{25}	1950	15.7	4530	1.10
8/A	823	1.5×10^{25}	2500	12.3	4200	0.54

[a] ($E \geq 0.18$ MeV).
[b] Determined from Irradiated-Microsphere Gamma Analyzer measurements.

have to be counted separately. This was necessary because the gross activity of the fissile particles was approximately five times higher than that of the fertile particles. This difference in gross activity levels was exploited in the initial examination run to discriminate against the fertile particles. They were simply treated as inert particles and set aside, thus accelerating the pace at which the fissile particle data could be obtained. Fertile particles were counted later in a separate examination run where the source-to-spectrometer geometry was optimized for the significantly lower count rate. A total of 1759 fissile particles and 925 fertile particles were eventually examined from the 8A compact. This represents 70% of the fissile and 22% of the fertile particles nominally in the compact. Additional fertile particles from compact 8A were available for IMGA examination but were bypassed to allow for higher priority work.

Particles from compact 5C were examined next. It was possible to count the fissile and fertile particles from compact 5C in the same run and to separate them based on their characteristic thorium and uranium X rays. A great deal of difficulty was encountered with these particles because fragments from the fractured OPyC coatings quickly obstructed the

singularizer and particle trap mechanisms. In order to obtain any data, it was necessary to hand select only particles free of the OPyC coating for examination. Eventually, as described in Sect. 4.5.1, the particles with fractured OPyC coatings were burned to remove the coating and then examined. In all, a total of 483 fissile and 2167 fertile particles from compact 5C were examined. This represents 40% of the fissile and 49% of the fertile particles nominally in the compact. Particles from the initial electrolytic deconsolidation of the compact that were inadvertently placed in storage were not examined by IMGA.

Particles from compact 7A were the last from this series to be examined by the IMGA system. Like the particles from compact 5C, the fissile and fertile particles from this compact were counted in the same run and separated based on their characteristic uranium and thorium X rays. Since there were no OPyC coatings on these particles, it was not necessary to do any hand sorting prior to examination. A total of 500 fissile and 1076 fertile particles were examined, representing 26% of the fissile and 24% of the fertile particles in the compact.

At the time the fuel particles from the experiment were counted, the predominate gamma rays in the spectra were produced by the decay of ^{95}Zr, ^{106}Ru, ^{134}Cs, ^{137}Cs, and ^{144}Ce. The isotopes ^{137}Cs and ^{144}Ce are of particular interest in evaluating individual particle performance because, at the temperatures encountered during irradiation, cesium is known to be mobile and can readily escape defective coatings if present in sufficient concentrations. Cerium, on the other hand, forms chemically stable compounds in oxide and oxycarbide fuel which tend to remain in the kernel even at high temperatures. The ratio of ^{137}Cs to ^{144}Ce, therefore, can provide a measure of the retention of the metallic fission product cesium within a particle and forms the basis of the methodology used to evaluate IMGA measurements. If it is assumed that individual particles are responsible for fission product release, it should be possible to distinguish releasing particles from a distribution of nonreleasing particles. To that end, a simple histogram method is employed to analyze the individual particle data. First, the activity ratio ^{137}Cs:^{144}Ce is computed for each particle in a given sample and the resulting activity ratio distribution scrutinized to determine the retentive and nonretentive particles. Nonretentive particles are generally easy to identify because they have low ratios and are separated from a normal-like distribution of retentive particles. Next, the nonretentive particle records are removed from the data set and the activity ratio distribution reanalyzed to determine the mean and standard deviation for the

retentive particles alone. The overall ^{137}Cs:^{144}Ce activity ratio distribution is subsequently recomputed and normalized to the mean value of the retentive particles to provide a consistent basis for comparison. A final histogram representation of the particle data is obtained by defining intervals 1% wide and counting the number of normalized ratios which fall within each interval. The resulting ^{137}Cs:^{144}Ce ratio histograms for the fissile and fertile particles from compacts 5C, 7A, and 8A are shown in Figures 4.50 through 4.55. In the figures, the particle data (vertical bars) have been superimposed over a theoretical normal distribution (gray) that is calculated using the standard deviation of the retentive particles and the total number of particles in each sample.

The following observations were made with respect to the ^{137}Cs:^{144}Ce activity ratio distributions for the fissile particles from compacts 5C, 7A, and 8A. First, there were 23 particles from compact 5C which exhibited a significant release of ^{137}Cs. Of these 23 particles, 9 had a piece of the SiC coating missing or a crack in the SiC coating. In addition to the damaged SiC coating, the nine particles had some portion of their kernels leached by the electrolyte used to deconsolidate the compact. In the histogram representation (see Figure 4.50), the nine damaged particles were normalized by using the mean ^{144}Ce inventory determined from the retentive particles. Because of the missing kernel material, the actual ^{137}Cs loss during irradiation for these nine particles is probably exaggerated in the histogram. The remaining 14 releasing particles from compact 5C had no visible defects in their SiC coatings, and their absolute ^{144}Ce inventories indicated they had intact kernels. Only one fissile particle from compact 7A was found to have a low ^{137}Cs inventory as shown in Figure 4.51. The particle had no visible defects in the SiC coating, and the absolute ^{144}Ce inventory of the particle indicates the kernel is intact. For compact 8A, no fissile particles with low ^{137}Cs inventories were detected. Table 4.11 summarizes these findings and shows the percentage of fissile particles releasing ^{137}Cs for each of the three compacts.

For the fertile particles from compacts 5C, 7A, and 8A, the ^{137}Cs:^{144}Ce activity ratio distribution results were inconclusive. In compact 5C, for example, the visual examination revealed that approximately 5% of the fertile particles had broken SiC coatings, but the IMGA analysis was unable to differentiate these particles from those with intact SiC coatings. This is consistent with an evaluation by Gillespie[4-14] which suggests that the expected maximum release of ^{137}Cs from fertile particles in the HRB-21 experiment may be

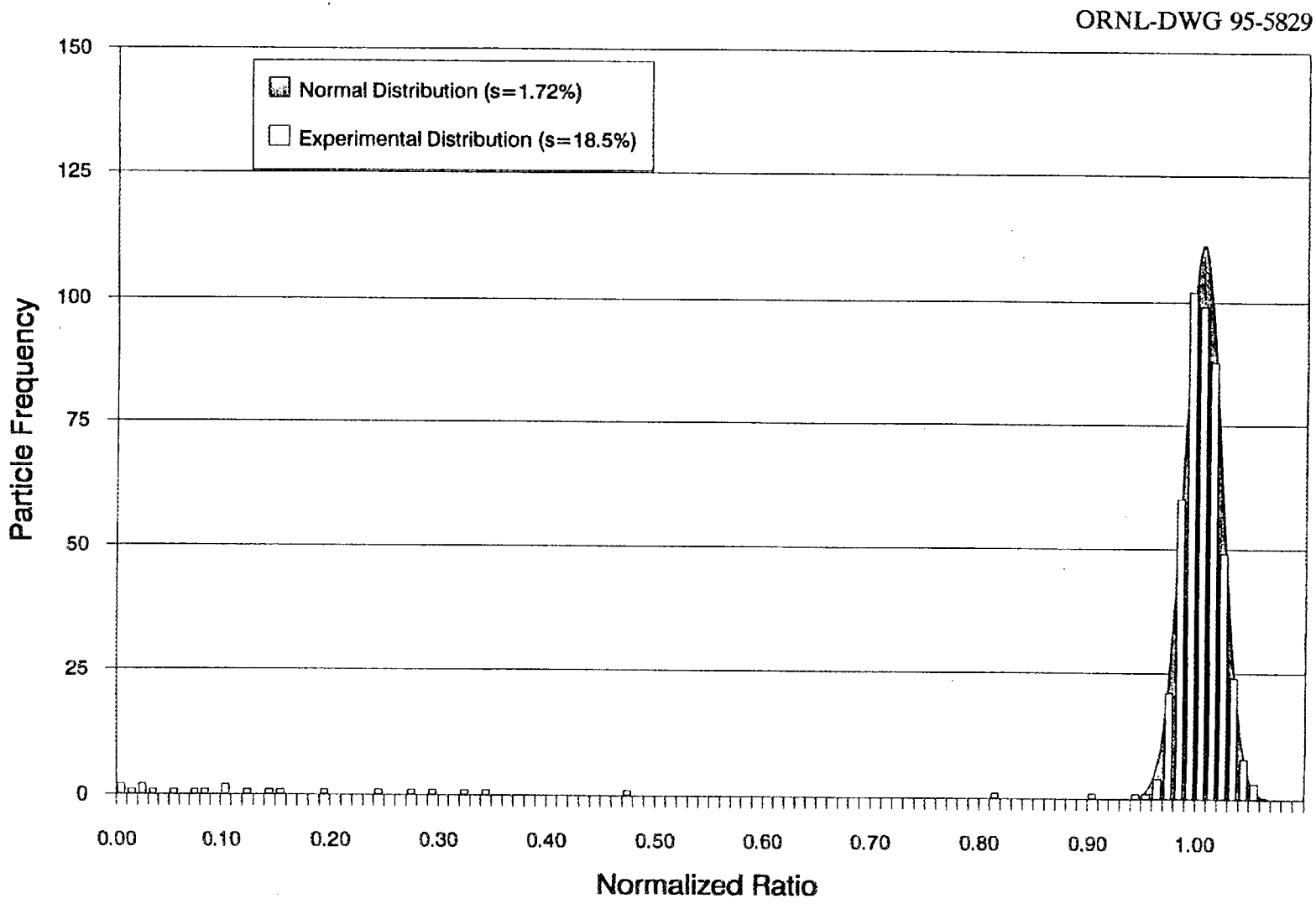

Figure 4.50.

NORMALIZED ^{137}Cs: ^{144}Ce RATIOS FOR FISSILE PARTICLES FROM COMPACT 5C.

ORNL-DWG 95-5830

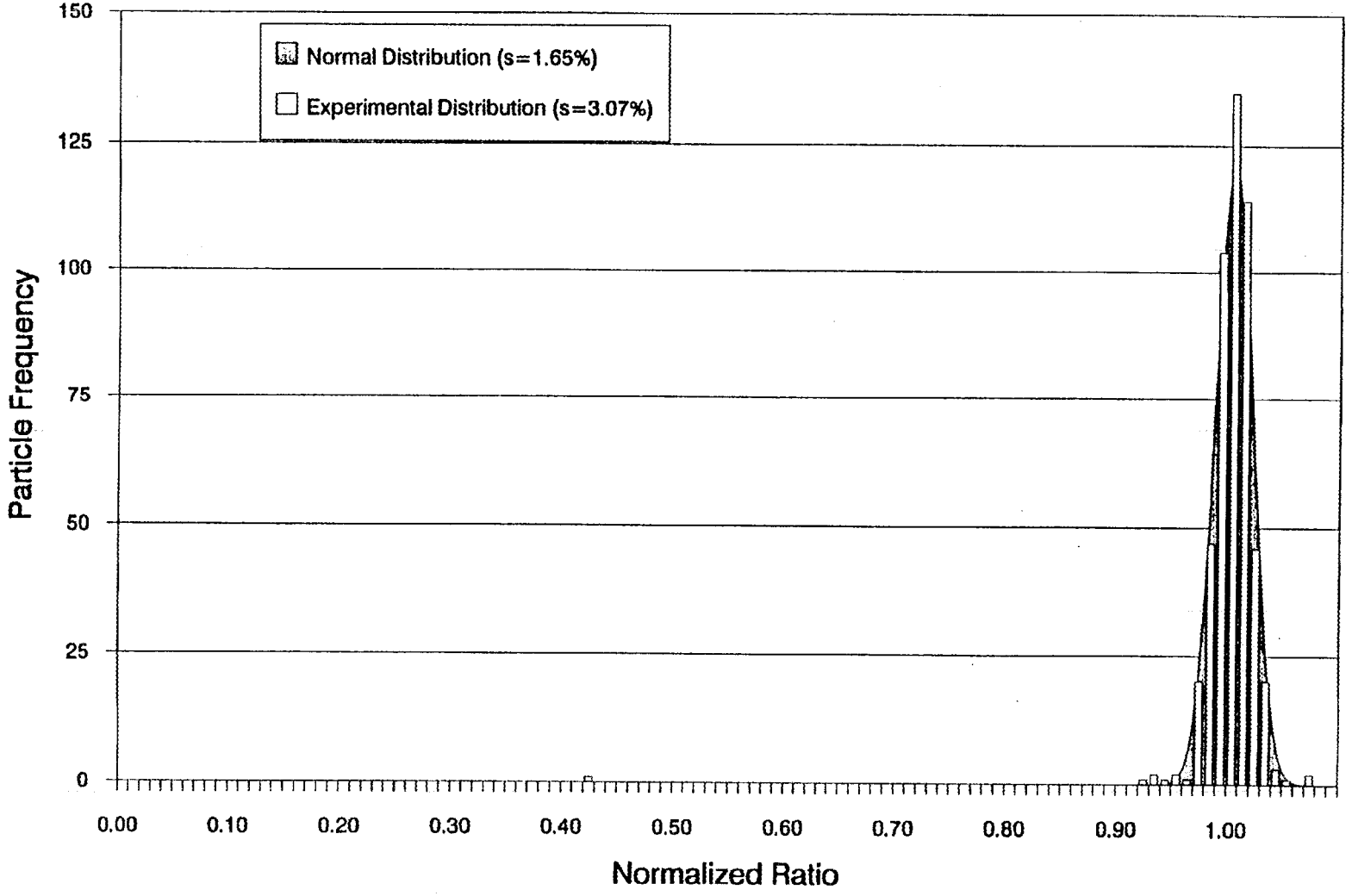

Figure 4.51.

NORMALIZED ^{137}Cs: ^{144}Ce RATIOS FOR FISSILE PARTICLES FROM COMPACT 7A.

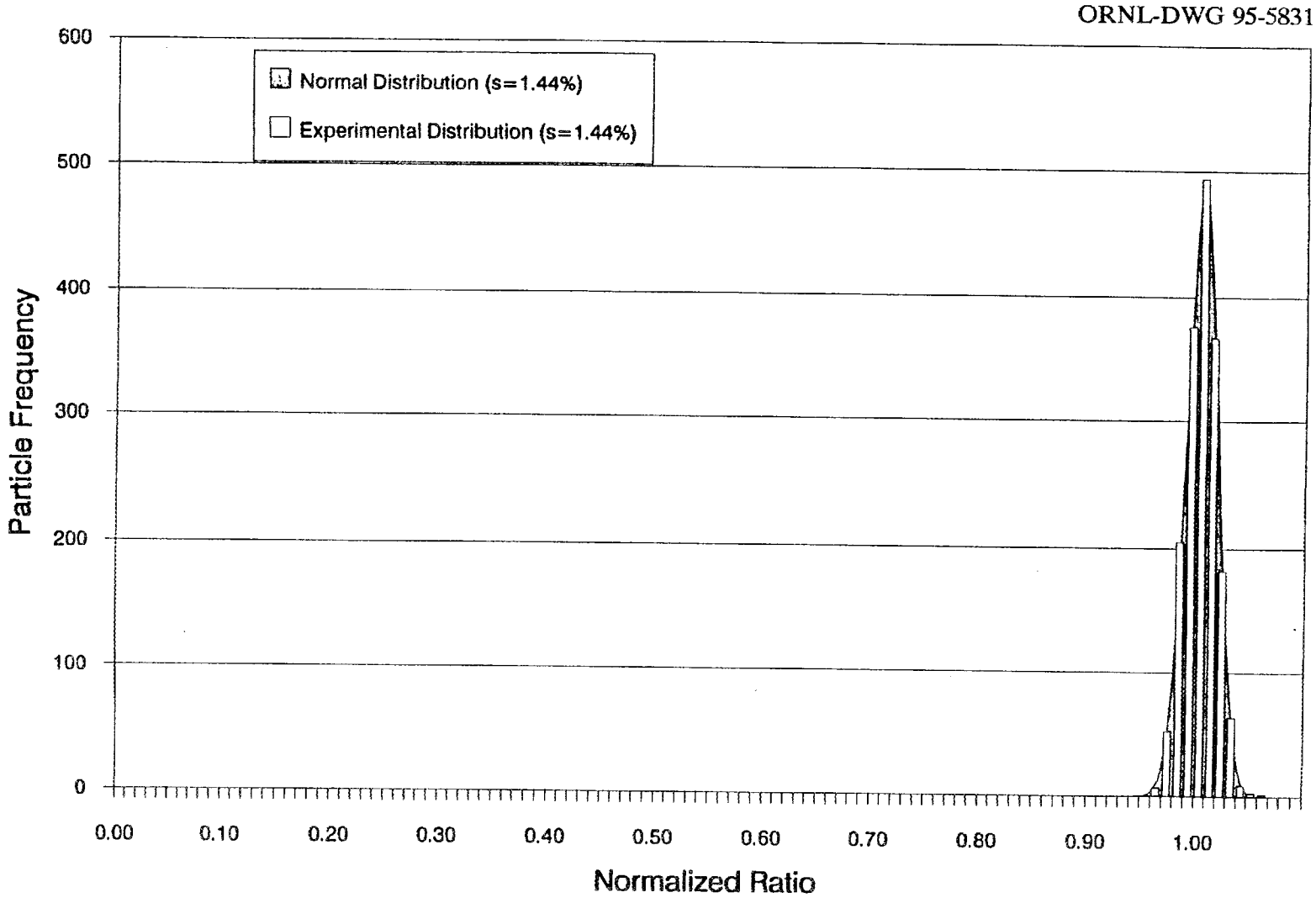

Figure 4.52.

NORMALIZED ^{137}Cs: ^{144}Ce RATIOS FOR FISSILE PARTICLES FROM COMPACT 8A.

ORNL-DWG 95-5832

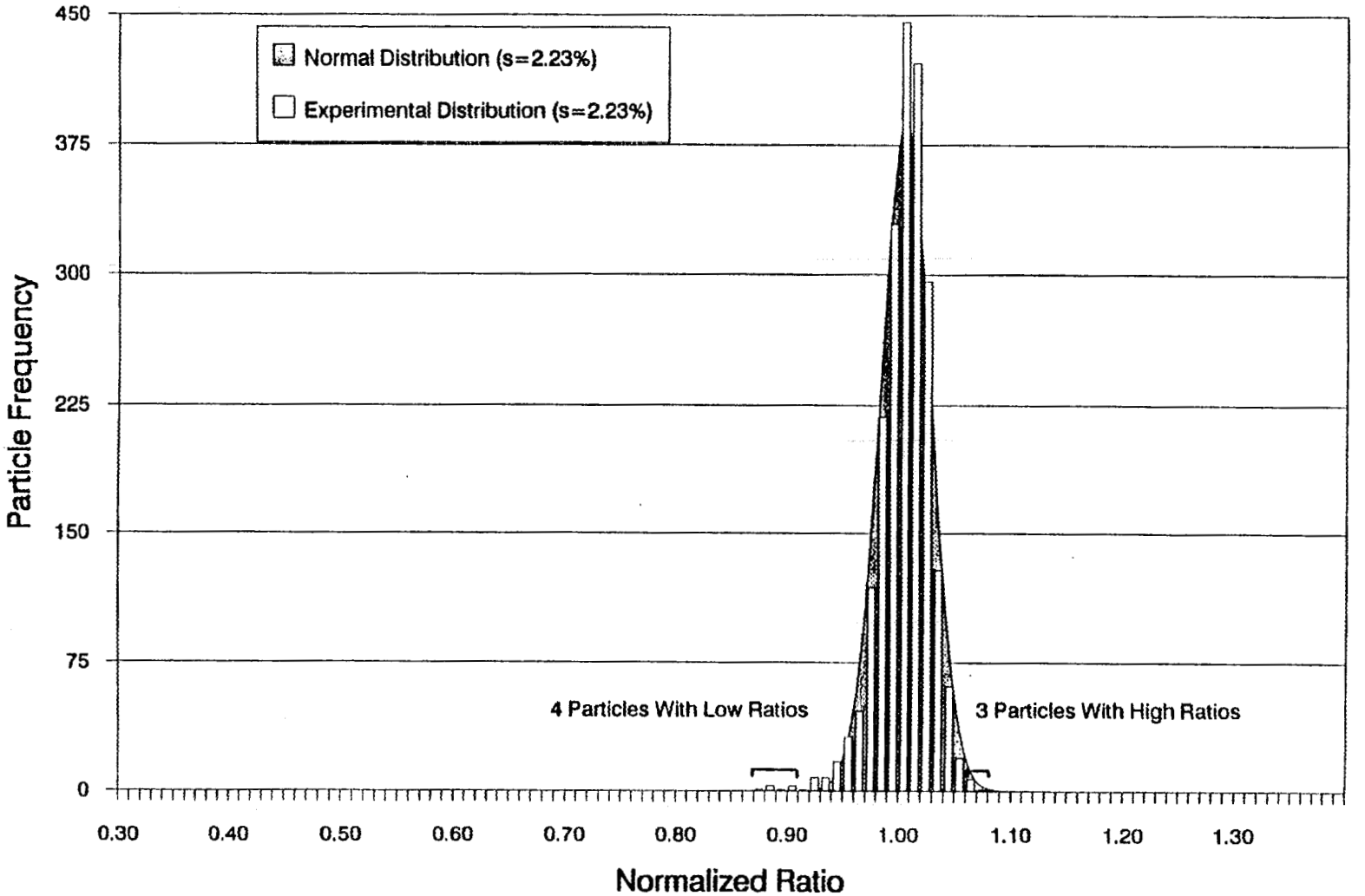

Figure 4.53.

NORMALIZED ^{137}Cs: ^{144}Ce RATIOS FOR FERTILE PARTICLES FROM COMPACT 5C.

ORNL-DWG 95-5833

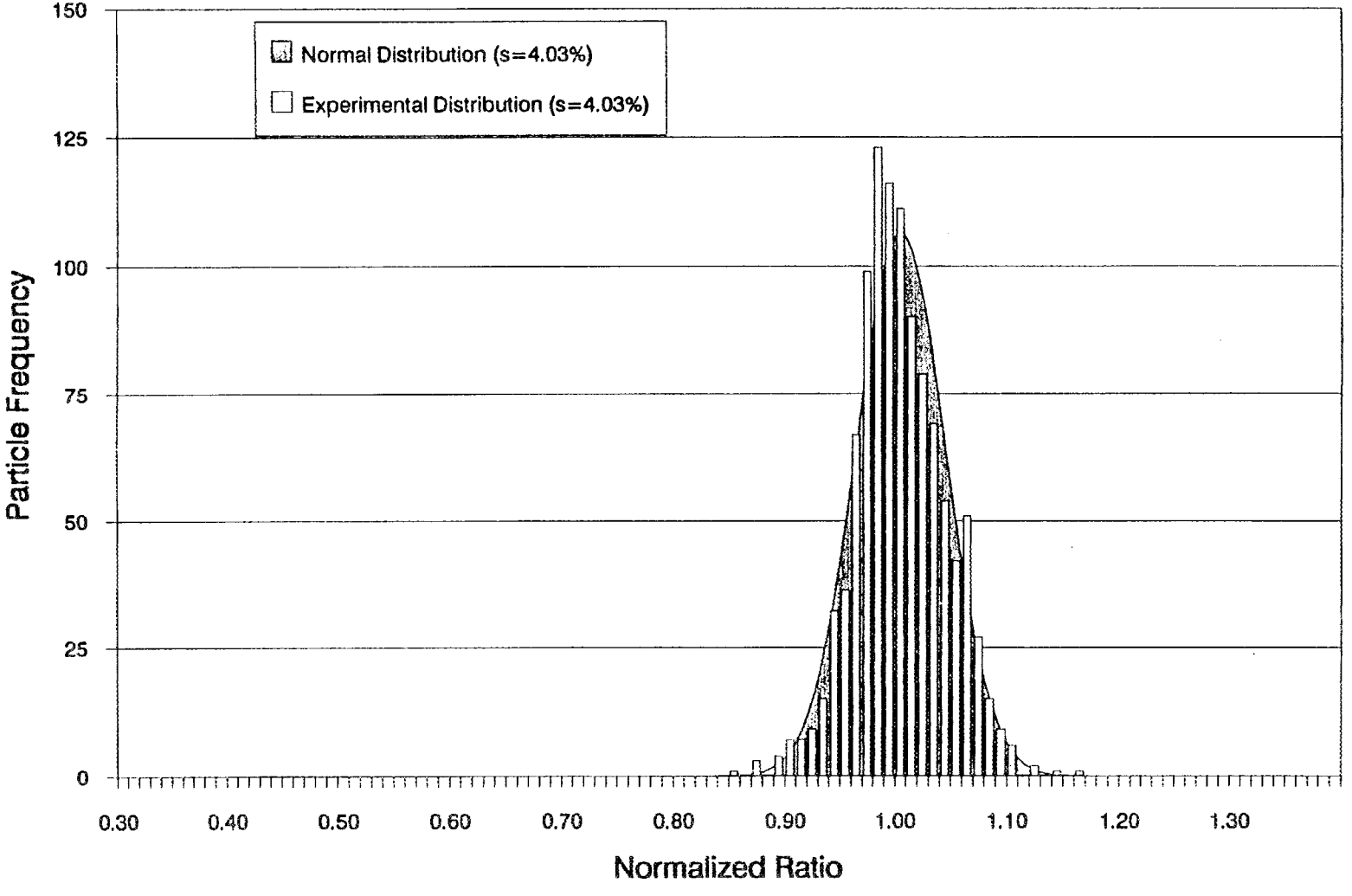

Figure 4.54.

NORMALIZED ^{137}Cs: ^{144}Ce RATIOS FOR FERTILE PARTICLES FROM COMPACT 7A.

ORNL-DWG 95-5834

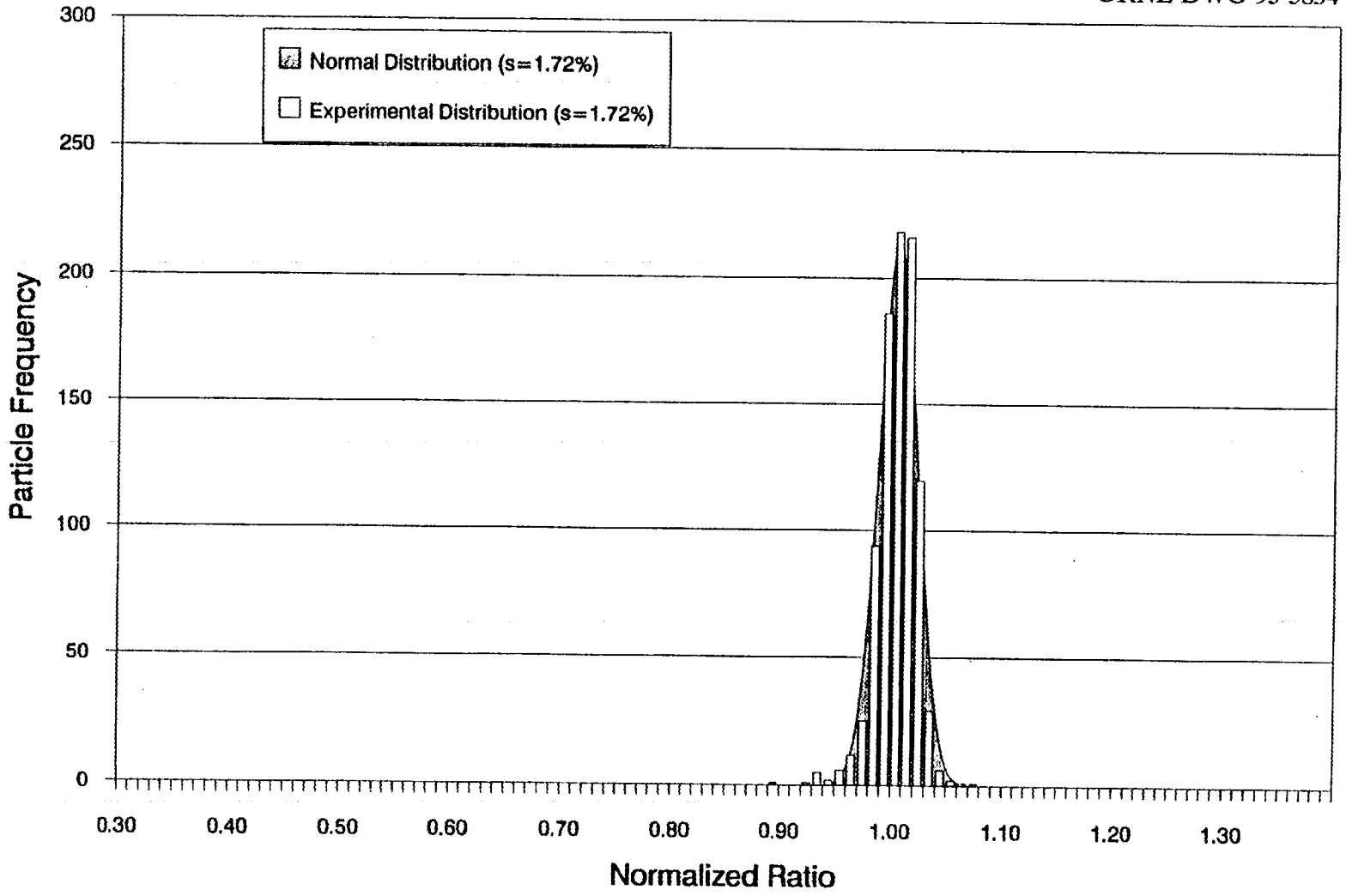

Figure 4.55.

NORMALIZED ^{137}Cs: ^{144}Ce RATIOS FOR FERTILE PARTICLES FROM COMPACT 8A.

Table 4.11.

FUEL PERFORMANCE BASED ON ^{137}Cs RELEASE FOR SELECTED HRB-21 COMPACTS

Compact	Particle type	Particles releasing ^{137}Cs	Total particles examined	Percent releasing ^{137}Cs
5C	UCO	23	483	4.8
	ThO_2	0	2167	0.0
7A	UCO	1	500	0.2
	ThO_2	0	1076	0.0
8A	UCO	0	1759	0.0
	ThO_2	0	925	0.0

too low to be detectable by the IMGA method. There were, however, an unexpected number of fertile particles with slightly low ratios in both the high- (5C) and low-fluence (8A) compacts. This anomaly was investigated further during the final examination run of compact 5C particles by taking special care in programming the binning function. As a result, four fertile particles with slightly low ^{137}Cs:^{144}Ce ratios and three fertile particles with slightly high ^{137}Cs:^{144}Ce ratios were isolated from the regions shown in Figure 4.53. Photographs of these particles taken with a series of stainless steel calibration spheres are shown in Figure 4.56. Using the calibration spheres as a reference, it was determined that the four particles with low ratios ranged from 675 to 715 μm in diameter with an average diameter of 695 μm. The three particles with slightly high ratios ranged from 760 to 860 μm in diameter with an average diameter of 810 μm. For comparison, the Capsule HRB-21 Preirradiation Report [ref. 4-7, Sect. 4.10] gives the nominal diameter of a fertile particle's SiC layer as 810 μm, which is in agreement with the larger diameter particles. The difference in diameter for the two sets of particles is important if the difference is primarily due to the ThO_2 kernel. Analysis of IMGA measurements involves making corrections for self-absorption of gamma rays within a particle. Most self-absorption takes place in the high-density kernel and is energy dependent. If the kernels in the small-diameter particles

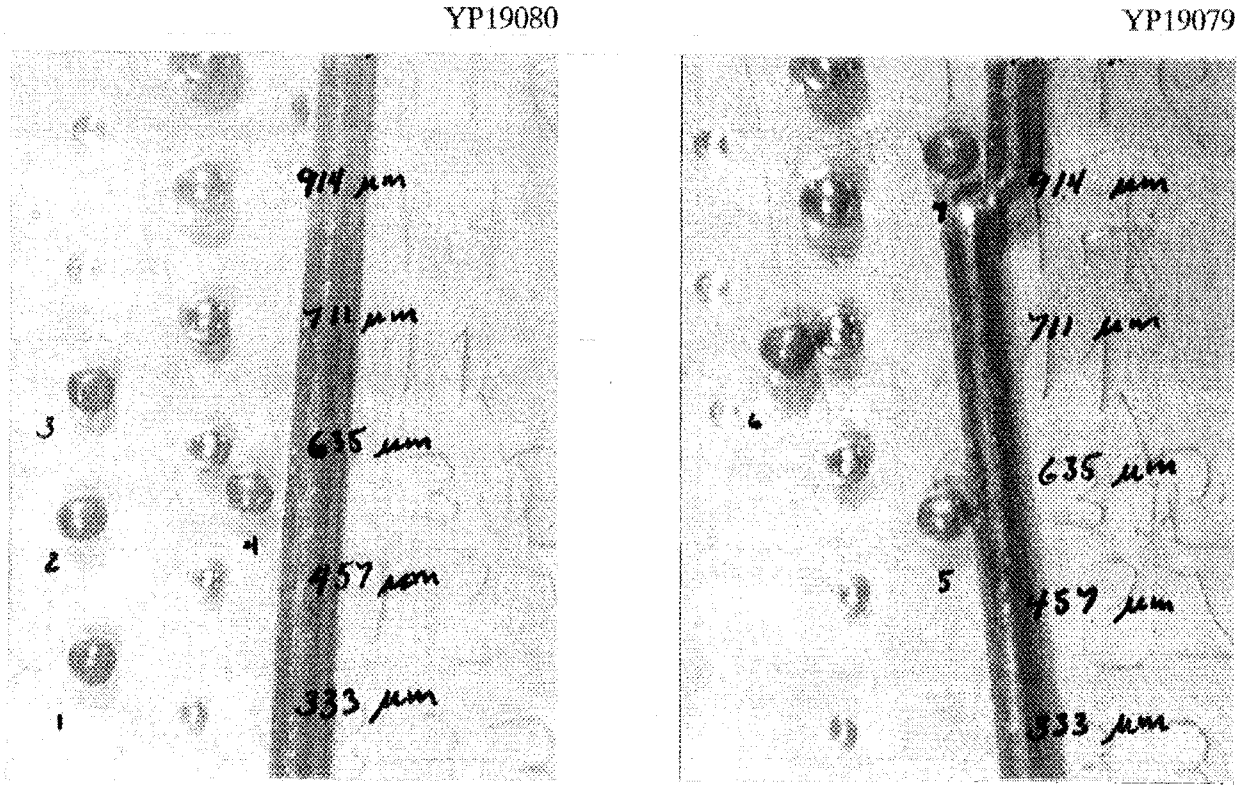

Figure 4.56.

SELECTED FERTILE PARTICLES FROM HRB-21 COMPACT 5C: *(a)* FOUR PARTICLES WITH LOW ^{137}Cs:^{144}Ce RATIOS AND *(b)* THREE PARTICLES WITH SLIGHTLY HIGH ^{137}Cs:^{144}Ce RATIOS. NOTE THE SIGNIFICANT DIFFERENCE IN DIAMETERS.

are approximately 100 μm less than the nominal diameter of 500 μm, then the self-shielding correction for ^{144}Ce (133 keV) would be overestimated by 6%. The change in the self-shielding correction for ^{137}Cs (661 keV) would be negligible. The inflated ^{144}Ce inventory for the small-diameter particles would make the ^{137}Cs:^{144}Ce ratio for the particles appear low by the same amount. The ^{137}Cs:^{144}Ce ratio distribution for fertile particles from compact 5C was prepared using self-shielding parameters calculated for a nominal diameter particle. It appears that if the small-diameter particles were adjusted for the change in self-shielding, they would fall within the expected variation for this distribution and not be considered low in cesium. If these small-diameter particles are randomly distributed, it would explain why fertile particles from both high- and low-fluence regions in the experiment capsule exhibit the same ^{137}Cs:^{144}Ce ratio behavior. For the fertile particles from compact 7A, the ^{137}Cs:^{144}Ce ratio distribution is somewhat broader than the distributions for compacts 5C or 8A. This is probably due to the less-than-ideal counting geometry, which was dictated by the fissile particles in the compact. Had there been sufficient time, it would have been better to separate the fissile and fertile particles and count the fertile particles in a second run as was done for compact 8A.

In addition to the analysis of the ^{137}Cs:^{144}Ce ratio distributions, the fissile and fertile particle fractions for each compact were characterized in terms of absolute fission product inventories. To obtain the best estimate of the average particle inventory, nonretentive particle records were removed from the data sets before analysis. The maximums, minimums, means, and standard deviations were then calculated for each set of particles.

The results are summarized in Tables 4.12 through 4.17 for each compact. The mean particle activities and standard deviations for the various isotopes were used in calculating the burnup estimates for each compact that are reported in Tables 3.6 and 3.8.

In summary, there are a number of uncertainties associated with the IMGA evaluation of compacts 5C, 7A, and 8A. Absolute counting uncertainties for the key isotopes ^{137}Cs and ^{144}Ce were less than ±5%. Uncertainties associated with correcting the counting results for self-shielding may be as high as ±6% for ^{144}Ce in the fertile particles because of variations in kernel size. Self-shielding uncertainties for the other isotopes of interest appear to be negligible because of the higher energy gamma rays used in their analysis. By far, the most important uncertainty with regard to overall fuel performance involves how well the particles examined from a given compact represent the total compact. Initially, it was planned that all

Table 4.12.

ACTIVITY DISTRIBUTION PARAMETERS FOR RETENTIVE UCO PARTICLES FROM EXPERIMENT HRB-21 COMPACT 5C[a,b]

Isotope	Maximum particle activity (Bq)	Minimum particle activity (Bq)	Mean particle activity (Bq)	Std. dev. mean (%)
^{95}Zr	3.74E+08	2.65E+08	3.13E+08	5.06
^{106}Ru	3.65E+07	2.83E+07	3.21E+07	3.98
^{134}Cs	1.07E+07	8.40E+06	9.50E+06	4.04
^{137}Cs	5.54E+06	4.30E+06	4.96E+06	3.85
^{144}Ce	1.35E+08	1.05E+08	1.19E+08	4.04

[a]Activities corrected to November 21, 1991.

[b]Based on measurements of 460 particles by Irradiated-Microsphere Gamma Analyzer.

Table 4.13.

ACTIVITY DISTRIBUTION PARAMETERS FOR ThO_2 PARTICLES FROM EXPERIMENT HRB-21 COMPACT 5C[a,b]

Isotope	Maximum particle activity (Bq)	Minimum particle activity (Bq)	Mean particle activity (Bq)	Std. dev. mean (%)
^{95}Zr	2.35E+08	7.62E+07	1.55E+08	8.53
^{106}Ru	3.01E+06	8.09E+05	1.79E+06	11.29
^{134}Cs	2.14E+06	6.91E+05	1.40E+06	8.41
^{137}Cs	2.29E+06	7.68E+05	1.54E+06	7.99
^{144}Ce	5.20E+07	1.93E+07	3.68E+07	7.11

[a] Activities corrected to November 21, 1991.

[b] Based on measurements of 2167 particles by Irradiated-Microsphere Gamma Analyzer.

Table 4.14.

ACTIVITY DISTRIBUTION PARAMETERS FOR RETENTIVE UCO PARTICLES FROM EXPERIMENT HRB-21 COMPACT 7A[a,b]

Isotope	Maximum particle activity (Bq)	Minimum particle activity (Bq)	Mean particle activity (Bq)	Std. dev. mean (%)
^{95}Zr	4.30E+08	2.13E+08	2.85E+08	8.78
^{106}Ru	2.75E+07	1.26E+07	1.99E+07	10.47
^{134}Cs	7.79E+06	3.57E+06	5.42E+06	12.38
^{137}Cs	5.37E+06	2.90E+06	3.93E+06	6.75
^{144}Ce	1.34E+08	7.15E+07	1.01E+08	6.43

[a]Activities corrected to November 21, 1991.

[b]Based on measurements of 499 particles by Irradiated-Microsphere Gamma Analyzer.

Table 4.15.

ACTIVITY DISTRIBUTION PARAMETERS FOR ThO_2 PARTICLES FROM EXPERIMENT HRB-21 COMPACT 7A[a,b]

Isotope	Maximum particle activity (Bq)	Minimum particle activity (Bq)	Mean particle activity (Bq)	Std. dev. mean (%)
^{95}Zr	1.45E+08	1.96E+07	8.51E+07	20.20
^{106}Ru	1.64E+06	2.23E+05	9.66E+05	21.75
^{134}Cs	1.11E+06	1.76E+05	5.41E+05	22.88
^{137}Cs	1.29E+06	3.36E+05	8.35E+05	15.54
^{144}Ce	3.18E+07	9.44E+06	2.05E+07	15.44

[a] Activities corrected to November 21, 1991.

[b] Based on measurements of 1076 particles by Irradiated-Microsphere Gamma Analyzer.

Table 4.16.

ACTIVITY DISTRIBUTION PARAMETERS FOR UCO PARTICLES FROM EXPERIMENT HRB-21 COMPACT 8A[a,b]

Isotope	Maximum particle activity (Bq)	Minimum particle activity (Bq)	Mean particle activity (Bq)	Std. dev. mean (%)
^{95}Zr	3.05E+08	1.81E+08	2.26E+08	6.82
^{106}Ru	1.63E+07	8.17E+06	1.15E+07	13.69
^{134}Cs	4.02E+06	1.71E+06	2.69E+06	17.71
^{137}Cs	3.95E+06	2.32E+06	2.99E+06	7.93
^{144}Ce	1.08E+08	6.55E+07	8.28E+07	7.50

[a]Activities corrected to November 21, 1991.

[b]Based on measurements of 1759 particles by Irradiated-Microsphere Gamma Analyzer.

Table 4.17.

ACTIVITY DISTRIBUTION PARAMETERS FOR FERTILE PARTICLES FROM EXPERIMENT HRB-21 COMPACT 8A[a,b]

Isotope	Maximum particle activity (Bq)	Minimum particle activity (Bq)	Mean particle activity (Bq)	Std. dev. mean (%)
^{95}Zr	6.42E+07	1.91E+07	4.18E+07	19.46
^{106}Ru	8.26E+05	2.20E+05	4.84E+05	20.05
^{134}Cs	3.13E+05	6.10E+04	1.67E+05	30.49
^{137}Cs	6.26E+05	1.78E+05	4.01E+05	19.67
^{144}Ce	1.53E+07	4.53E+06	1.01E+07	19.31

[a]Activities corrected to November 21, 1991.

[b]Based on measurements of 925 particles by Irradiated-Microsphere Gamma Analyzer.

particles from a given compact would be examined. As work on the various compacts progressed, it became obvious that the total recovery of all particles in a compact and their eventual examination would not be possible. This sampling uncertainty was most significant in compact 5C where many of the particles disintegrated during the deconsolidation process and were not available for examination. A final uncertainty is associated with the ability of the IMGA method to detect very low releases of cesium, especially in fertile particles. It was shown that, in compact 5C, fertile particles with damaged or missing SiC coatings could not be differentiated from intact particles indicating a high degree of cesium retention in the kernel. Because of the sampling uncertainties and the limitations of the method, the failure fractions based on cesium release for these compacts are likely to be lower-bound estimates. The actual failure fractions could be higher because the most seriously damaged particles were those least likely to survive an IMGA examination.

4.5.2.2 HRB-21 Compact 5B (Leach-Burn-Leach)

Unbonded particles from compact 5B were obtained as a by-product of an LBL analysis discussed in detail in Sect. 4.8. A random sample was taken from the initial population of 1200 UCO particles and 4460 ThO_2 particles by dividing the particles four times using a random splitter. The resulting analysis sample of roughly 350 particles was then visually examined and photographed prior to the IMGA examination. The visual examination revealed SiC and presumably IPyC coating fragments in a range of sizes. Nine intact buffer coatings were also found and later identified as UCO buffers due to their ^{106}Ru inventories. These observations indicate that some particles fragmented after the burn step during the second leach. Although some of the SiC/IPyC coating fragments must have come from particles represented by the intact UCO buffers, some of the larger SiC shell fragments appear to have come from ThO_2 particles. Figure 4.57 shows photographs of *(a)* a typical sample of intact particles, *(b)* coating fragment debris, and *(c)* the intact UCO buffers.

All intact particles and the nine intact UCO buffer coatings in the random sample were examined by the IMGA system using the semi-manual mode of operation. In this mode, particles are separated one at a time from the sample using a micromanipulator. The individual particles are then transferred by hand to a bypass opening that feeds directly to the sample changer module. This was done to prevent any possibility of damage to a particle prior to it being counted. All other operations, such as data acquisition, classification, and binning, were handled in the usual automatic mode. Of the 345 particles

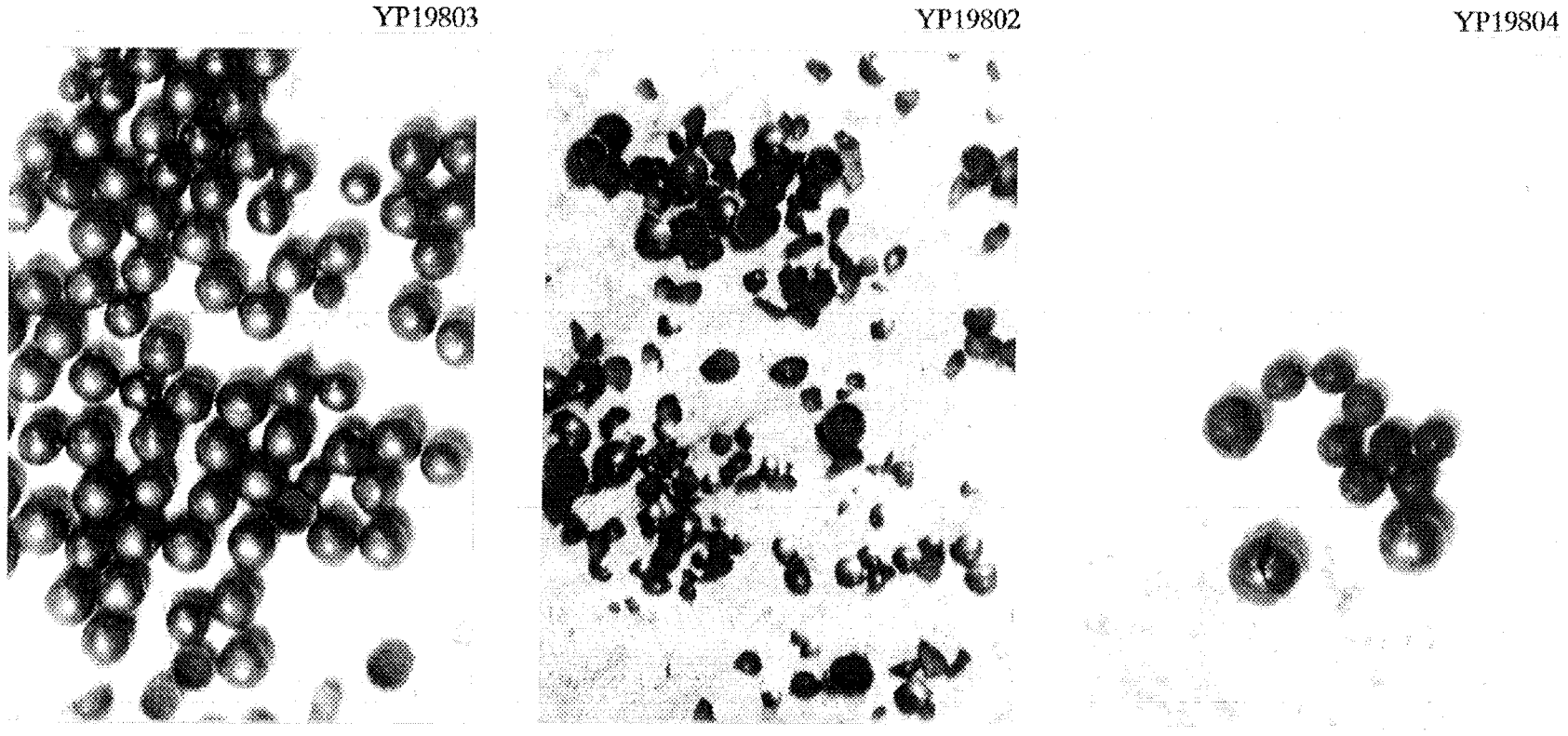

Figure 4.57.

PORTIONS OF THE RANDOM SAMPLE OF MATERIAL FROM HRB-21 COMPACT 5B: *(a)* TYPICAL SAMPLE OF PARTICLES AS RECEIVED, *(b)* SAMPLE OF COATING FRAGMENT DEBRIS, AND *(c)* INTACT UCO BUFFERS.

examined by IMGA, 52 were determined to be UCO particles and 293 were determined to be ThO_2 particles. Because of the quantity and condition of the coating fragment debris associated with the random sample, only a subjective estimate can be made with regard to the number and type of particles represented. It was assumed that the intact UCO buffers adequately represent the UCO particles in the coating fragment debris. For the ThO_2 particles, the larger SiC coating shards were counted, and an estimate was made of the likely number of particles they represent. The relative performance of each batch of particles is summarized in Tables 4.18 and 4.19 for the fissile and fertile particles, respectively.

In Tables 4.18 and 4.19, the particles from compact 5B have been broken down into categories of those with partially or completely leached kernels, those with intact kernels but low ^{137}Cs inventories, and those which have retained their fission product inventories. Particles with leached kernels were identified by both visual examination and IMGA measurements of absolute particle inventories. Particles with intact kernels and low ^{137}Cs inventories were identified by analysis of the ^{137}Cs:^{144}Ce ratios of the particles in a manner similar to the previous evaluations of the 5C, 7A, and 8A compacts. Figures 4.58 and 4.59 show histogram representations of normalized ^{137}Cs:^{144}Ce ratios for the fissile and fertile particles, respectively. In the figures, particles with leached kernels have been normalized by substituting the appropriate mean ^{144}Ce inventory, and failed particles detected in the visual exam have been included by simulating their records with zero ^{137}Cs:^{144}Ce ratios.

The fissile and fertile particle fractions were also characterized in terms of absolute fission product inventories. As before, to obtain the best estimate of the average particle inventory, nonretentive particle records were removed from the data sets prior to analysis. The maximums, minimums, means, and standard deviations were then calculated for each set of particles. The results are summarized in Tables 4.20 and 4.21 for the fissile and fertile particles, respectively. The mean particle activities and standard deviations for the various isotopes were used in calculating the burnup estimates that are reported in Tables 3.6 and 3.8.

There is evidence (see Sect. 4.8) that many of the particles in this compact may have been damaged by an aggressive LBL procedure. For that reason, failure fractions inferred from the IMGA measurements should be considered suspect and not representative for other compacts. Nevertheless, the methodology used in the IMGA analysis of this compact should be the model for all future compacts. Specifically, results of both the visual

Table 4.18.

SUMMARY OF UCO PARTICLE EXAMINATIONS FOR COMPACT HRB-21 5B

Method of analysis	Retentive UCO particles	^{137}Cs low kernel intact	Kernel leached	Total particles
IMGA[a]	30	8	14	52
Visual Exam		0	0	
Totals	30	8	14	52

[a]IMGA = Irradiated-Microsphere Gamma Analyzer.

Table 4.19.

SUMMARY OF ThO_2 PARTICLE EXAMINATIONS FOR COMPACT HRB-21 5B

Method of analysis	Retentive ThO_2 particles	^{137}Cs low kernel intact	Kernel leached	Total particles
IMGA[a]	284	6	3	293
Visual Exam			10 ± 5	10
Totals	284	6	13 ± 5	303

[a]IMGA = Irradiated-Microsphere Gamma Analyzer.

examination and the IMGA examination should be incorporated into the final evaluation of the failure fraction. The method of random sampling makes this approach feasible when structural failures result in considerable amounts of coating fragment debris.

4.5.3 Piggyback Fuel Particles

The piggyback capsules irradiated in the HRB-21 experiment are described in Sect. 2.2.3. Some of the piggyback capsules contained unbonded fuel particles, and following irradiation, they were opened to recover the particles for PIE. Details of piggyback capsule disassembly and photo-visual examination of the particles and graphite holders are discussed

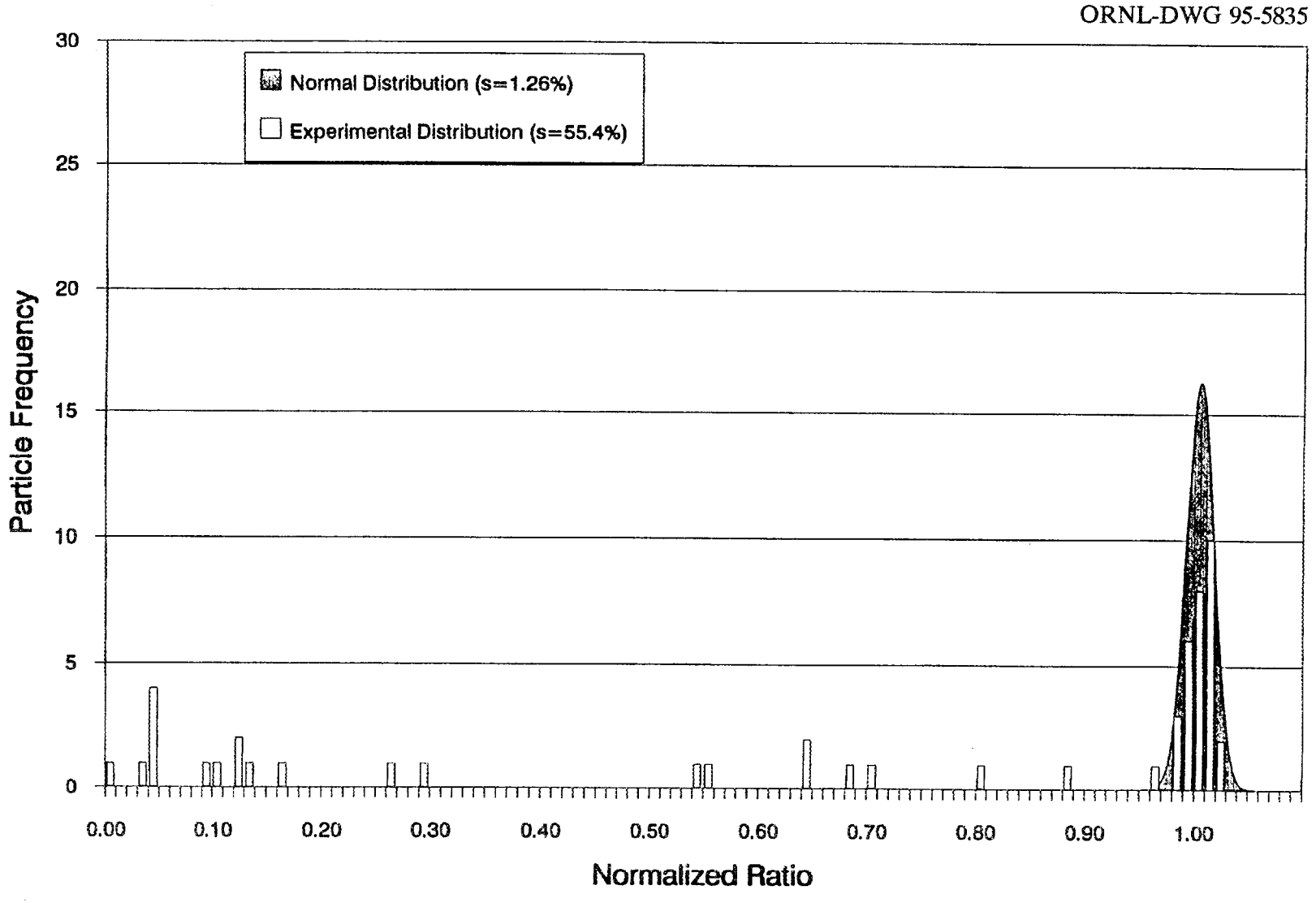

Figure 4.58.

NORMALIZED ^{137}Cs: ^{144}Ce RATIOS FOR FISSILE PARTICLES FROM COMPACT 5B.

ORNL-DWG 95-5836

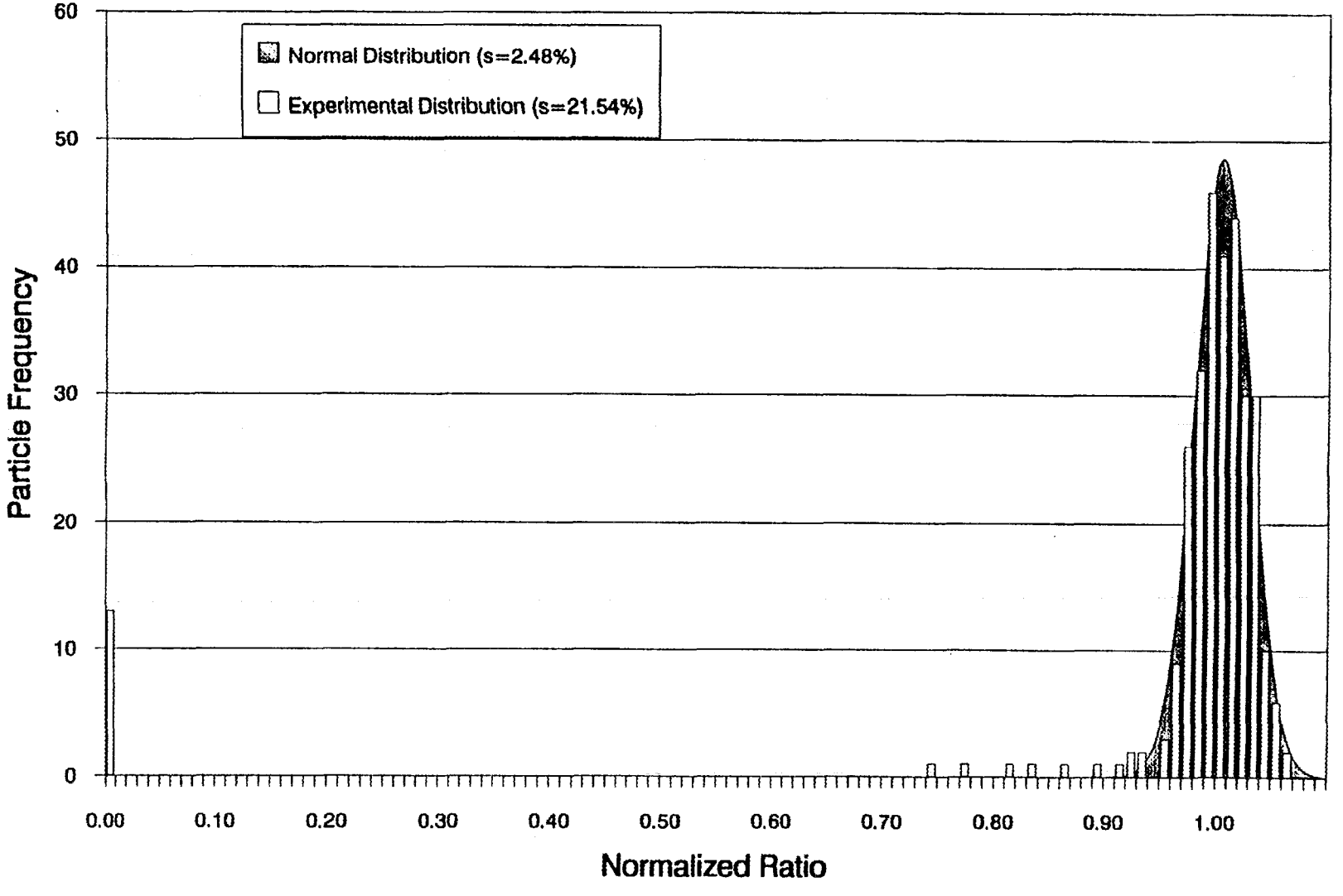

Figure 4.59

Normalized ^{137}Cs: ^{144}Ce RATIOS FOR FERTILE PARTICLES FROM COMPACT 5B.

Table 4.20.

ACTIVITY PARAMETERS FOR RETENTIVE UCO PARTICLES FROM COMPACT HRB-21 5B[a,b]

Isotope	Maximum particle activity (Bq)	Minimum particle activity (Bq)	Mean particle activity (Bq)	Std. dev. mean (%)
^{95}Zr	4.70E+08	2.59E+08	3.52E+08	12.24
^{106}Ru	3.53E+07	2.81E+07	3.19E+07	5.03
^{134}Cs	1.03E+07	8.41E+06	9.29E+06	4.71
^{137}Cs	5.39E+06	4.50E+06	4.90E+06	4.60
^{144}Ce	1.32E+08	1.10E+08	1.20E+08	4.22

[a]Activities corrected to November 21, 1991.

[b]Based on measurements of 30 particles by Irradiated-Microsphere Gamma Analyzer.

Table 4.21.

ACTIVITY PARAMETERS FOR RETENTIVE ThO_2 PARTICLES FROM COMPACT HRB-21 5B[a,b]

Isotope	Maximum particle activity (Bq)	Minimum particle activity (Bq)	Mean particle activity (Bq)	Std. dev. mean (%)
^{95}Zr	2.25E+08	7.20E+07	1.59E+08	16.01
^{106}Ru	2.52E+06	1.09E+06	1.84E+06	9.76
^{134}Cs	1.83E+06	8.19E+05	1.37E+06	7.42
^{137}Cs	2.07E+06	9.28E+05	1.54E+06	6.70
^{144}Ce	4.90E+07	2.32E+07	3.74E+07	6.24

[a]Activities corrected to November 21, 1991.

[b]Based on measurements of 284 particles by Irradiated-Microsphere Gamma Analyzer.

in Sect. 4.4. Upon completion of the photo-visual examination, the particles listed in Table 4.22 were examined by the IMGA system in order to determine their absolute fission product inventories. Ratios of ^{137}Cs to ^{144}Ce were then computed for each particle in an effort to determine the ability of each particle to retain the metallic fission product cesium. Because of the limited number of particles in each sample, the usual histogram method of evaluating cesium release was foregone, and instead the means and standard deviations for each sample of particles were computed and compared with the retentive particle data from the compact examinations. Table 4.23 gathers the ^{137}Cs:^{144}Ce ratio distribution means and standard deviations from the piggyback samples and the compacts in a single location for ease in comparison. All of the mean values and associated standard deviations for the piggyback samples appeared to be consistent with the corresponding compact data. The implication was that none of the piggyback particles examined by IMGA exhibited a significant release of cesium.

Table 4.22.

PIGGYBACK FUEL PARTICLES EXAMINED BY THE IRRADIATED-MICROSPHERE GAMMA ANALYZER SYSTEM

Capsule No.	Particle type	Total particles recovered
PB-2A	UCO TRISO-P	28
PB-3A	UCO TRISO	28
PB-6A	ThO_2 TRISO	19
PB-7A	ThO_2 TRISO-P	17
PB-1C	UCO bufferless	32
PB-2B	UCO bufferless	24
PB-2C	UCO bufferless	15
PB-3B	UCO bufferless	17
PB-3C	UCO bufferless	14
PB-4C	UCO bufferless	17

Table 4.23.

MEAN ^{137}Cs:^{144}Ce RATIOS FOR VARIOUS SAMPLES OF PARTICLES EXAMINED BY THE IRRADIATED-MICROSPHERE GAMMA ANALYZER SYSTEM

Fuel body	Piggyback capsule			Fuel compact (retentive fissile)			Fuel compact (retentive fertile)		
	A	B	C	A	B	C	A	B	C
1			Bufferless 3.57E-02 ±1.6%						
2	TRISO-P 3.90E-02 ±2.1%	Bufferless 3.98E-02 ±1.9%	Bufferless 3.98E-02 ±1.2%						
3	TRISO 4.12E-02 ±1.2%	Bufferless 4.25E-02 ±2.8%	Bufferless 4.14E-02 ±1.9%						
4			Bufferless 4.28E-02 ±1.9%						
5					TRISO-P 4.08E-02 ±1.3%	TRISO-P 4.16E-02 ±1.7%		TRISO-P 4.11E-02 ±2.5%	TRISO-P 4.18E-02 ±2.2%
6	TRISO 4.18E-02 ±1.8%								
7	TRISO-P 4.09E-02 ±2.6%			TRISO-P 3.89E-02 ±1.7%			TRISO-P 4.08E-02 ±4.0%		
8				TRISO-P 3.62E-02 ±1.4%			TRISO-P 3.96E-02 ±1.7%		

In addition to the evaluation of the ^{137}Cs:^{144}Ce activity ratios, mean inventories of several key isotopes were calculated for each sample of piggyback particles. The resulting mean values and associated standard deviations are reported in Table 4.24. The mean activities and standard deviations for the various isotopes were used in calculating the burnup estimates that are reported in Tables 3.6 and 3.8.

Although the sample sizes for the piggyback capsules were quite small, some interesting observations can be made about the IMGA examination results. For both the standard fissile and standard fertile particles, there was no detectable difference in the performance of the TRISO versus the TRISO-P-type coatings. Whether this has any significance with regard to the performance of the TRISO-P-type coatings used in the compacted particles is unknown. For the bufferless UCO particles that survived the irradiation intact, there was no indication of fission product release. Thus, it seems possible that the bufferless particles were able to retain their fission product inventories up to the point of structural failure.

4.6 CERAMOGRAPHIC EXAMINATION

Ceramography, in which polished surfaces of fuel materials are prepared and examined at high magnification, provides valuable data regarding material microstructure and mechanical condition of the fuel. The work described here was carried out on fuel specimens with different levels of irradiation exposure in a systematic attempt to gain a better understanding of fuel material and design features which may have contributed to the less-than-expected retention of fission products.

4.6.1 Unirradiated Fuel

4.6.1.1 Compact Ceramography

Unirradiated fuel was examined by ceramography prior to the irradiation of capsule HRB-21. The preirradiation examination showed that the kernel and coating microstructure appearance was consistent with expectations for the process conditions and resulting fuel properties. The results of that work are shown in ref. 4-7, Sect. 4.10.

After the irradiation of HRB-21 showed a higher-than-expected fraction of failed coatings, additional ceramographic examination of unirradiated fuel was carried out in an attempt to characterize coating features which had previously escaped detection but may have contributed to the higher-than-expected failure of coatings. During this latter

Table 4.24.

MEAN ACTIVITIES FOR PARTICLES RECOVERED FROM PIGGYBACK CAPSULES AND EXAMINED BY THE IRRADIATED-MICROSPHERE GAMMA ANALYZER SYSTEM[a]

Capsule No.	^{95}Zr Mean	Std dev (%)	^{106}Ru Mean	Std dev (%)	^{134}Cs Mean	Std dev (%)	^{137}Cs Mean	Std dev (%)	^{144}Ce Mean	Std dev (%)
PB-2A	2.50E+08	3.91	1.72E+07	10.19	4.66E+06	12.83	3.42E+06	6.20	8.76E+07	4.90
PB-3A	2.92E+08	4.68	2.67E+07	5.72	7.94E+06	6.49	4.52E+06	4.73	1.10E+08	4.42
PB-6A	1.35E+08	6.31	1.53E+06	7.72	1.12E+06	7.89	1.36E+06	6.93	3.25E+07	5.80
PB-7A	8.36E+07	17.52	9.43E+05	18.49	5.22E+05	21.71	8.27E+05	17.18	2.02E+07	15.68
PB-1C	2.59E+08	16.86	1.13E+07	14.37	2.55E+06	19.55	2.85E+06	9.47	7.97E+07	8.68
PB-2B	3.00E+08	20.30	1.95E+07	10.73	5.41E+06	12.86	3.97E+06	8.59	9.97E+07	7.51
PB-2C	2.93E+08	13.55	1.84E+07	10.20	5.09E+06	12.37	3.73E+06	7.09	9.35E+07	6.44
PB-3B	3.35E+08	20.49	2.71E+07	7.45	8.27E+06	8.37	4.74E+06	6.61	1.12E+08	5.69
PB-3C	3.18E+08	18.54	2.61E+07	7.52	7.89E+06	7.98	4.47E+06	5.90	1.08E+08	5.30
PB-4C	3.75E+08	12.34	3.12E+07	5.55	9.51E+06	5.68	4.93E+06	5.62	1.15E+08	5.61

[a]Mean activities (Bq/particle) have been corrected to November 21, 1991.

examination, a reduction in porosity of the PPyC coatings was observed in the unirradiated fuel compacts. The reduction in PPyC porosity was attributed to intrusion of pitch from the matrix during the high-pressure matrix injection phase of compact fabrication.

4.6.2 Irradiated Fuel

4.6.2.1 Examination Procedure

Compacts were selected from capsule HRB-21, as shown in the HRB-21 test specification, which were exposed under the full range of fuel temperature, fast neutron fluence, and burnup. Two compacts, 4A and 1C, were selected for examination to provide information on the condition of fuel after maximum and minimum fast neutron exposure and HM burnup, respectively. A third compact, 2B, was selected to characterize fuel condition after intermediate fast neutron exposure and HM burnup.

The compacts were very fragile so the first step in ceramographic preparation was to impregnate the compact with an epoxy resin. This was accomplished by enclosure of the compact in a metal tube which was then filled with resin. After the resin cured, transverse cuts were made through the compact with a low-speed, diamond-impregnated circular saw. The cuts through the compact were made about 15 mm from each end, and the two end pieces were mounted in resin for grinding and polishing. The specimens were mounted so that grinding was in the axial direction in the compact, and circular cross sections were obtained. In the following sections, the observations made are organized in terms of fuel components, starting with the kernel and proceeding outward. In most cases, there is interaction of components so more than one must be discussed at one time, but an attempt has been made in each section to focus on the primary fuel material affected.

4.6.2.2 Irradiation Effects in ThO_2 and Low-Enriched Uranium (LEU) UCO Kernels

The ThO_2 kernels viewed in cross section usually appeared featureless. At the highest exposure, small gas voids became more numerous, but the kernel retained its spherical shape. An example of the appearance of typical kernel cross sections at low and high exposure in HRB-21 is shown in Figure 4.60.

The UCO kernels in each compact examined contained gas voids which varied from small to large as the burnup and fluence increased. The kernels were contained by the buffer coating, some of which remained intact at the low exposure. However, if the buffer cracked, the UCO kernel swelled into the crack. These observations show that the buffer

R80570

Capsule HRB-21
Fuel Compact 4A, Fertile ThO_2
2.2% FIMA Burnup, 3.5×10^{25} n/m^2

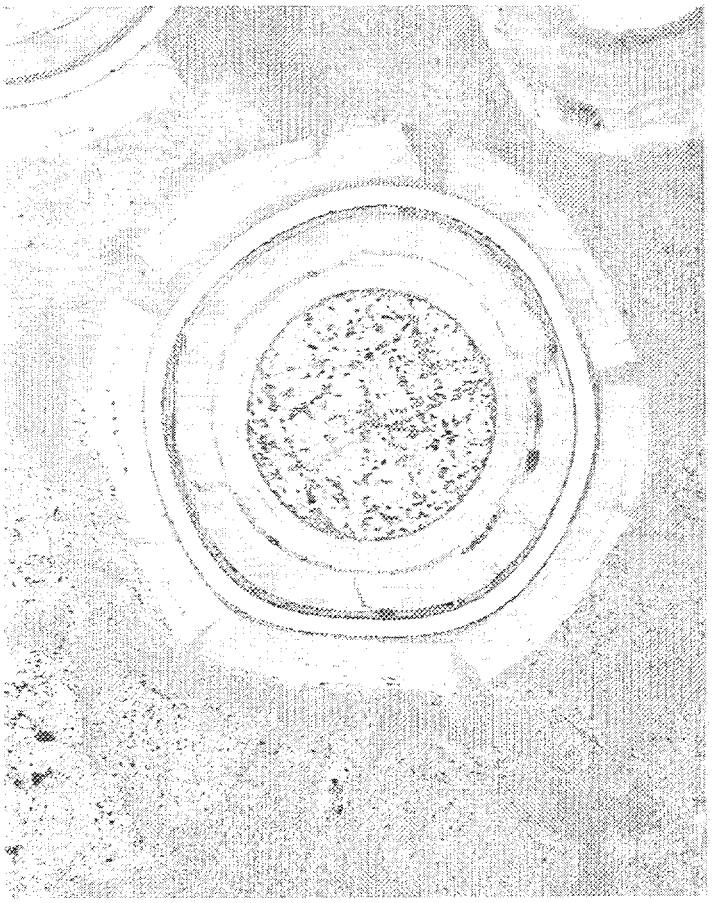

Figure 4.60.

THE PyC SEAL COATING ON THE BUFFER LAYER WAS BONDED TO THE INNER SURFACE OF THE IPyC, AND IT REMAINED WITH THE IPyC AS THE BUFFER UNDERWENT IRRADIATION-INDUCED SHRINKAGE. DEBONDING OF COMPACT MATRIX FROM PPyC AND PPyC/OPyC CONTRIBUTED TO THE OBSERVED WEAKNESS OF THE IRRADIATED COMPACTS.

coating retained some mechanical strength which was able to restrain the kernel swelling effect as long as the buffer was not failed. Compact 2B at intermediate exposure showed examples of both types of kernel behavior as shown in Figure 4.61.

Although accurate kernel dimensions could not be determined from ceramography of the kernel microsphere and the initial dimensions of the specific kernel under examination were not known, it is reasonable to assume that UCO and ThO_2 kernel swelling took place as a result of fission and the development of gas bubbles within the kernel. The amount of kernel swelling is estimated to be on the order of 35 and 5 vol % for UCO and ThO_2, respectively.[4-15] This is a crude estimate based on visual observation of the highest burnup kernels. The LEU UCO kernel material normally contained a continuous matrix of grey material with a dispersion of voids. The kernels of all the fuel observed had an HM burnup of up to 22.5% FIMA.

In three particles in compact 4A, which had the highest exposure, there was what appeared to be a carbon deposit at the kernel-buffer interface. The deposit showed optical activity in polarized light, which is typical for the carbon rejected on the cool side of UO_2 and UC_2 kernels heated in a thermal gradient. The rejection of the carbon on the cool side is associated with migration of the kernel up the temperature gradient in what has been called the "amoeba effect."[4-16] These observations in HRB-21 represent the first evidence of the amoeba effect in UCO particles.

The KMC was calculated for the three kernels with observed migration using the thickness of the rejected carbon as a measure of kernel migration. One of the particles with a measurable thickness of rejected carbon used in KMC calculation is shown in Figure 4.62.

The KMC was calculated using the following expression:

$$KMC = \frac{T^2 \frac{dx}{dt}}{\frac{dT}{dr}}, \qquad (4\text{-}1)$$

where

KMC = kernel migration coefficient (m^2K/s),

T = kernel temperature (K),

x = kernel migration distance (m),

dT/dr = temperature gradient across the particle (K/m),

Capsule HRB-21
Fuel Compact 2B, Fissile UCO
Burnup=18% FIMA Fast Fluence=2.3×10^{25} n/m^2

R80550

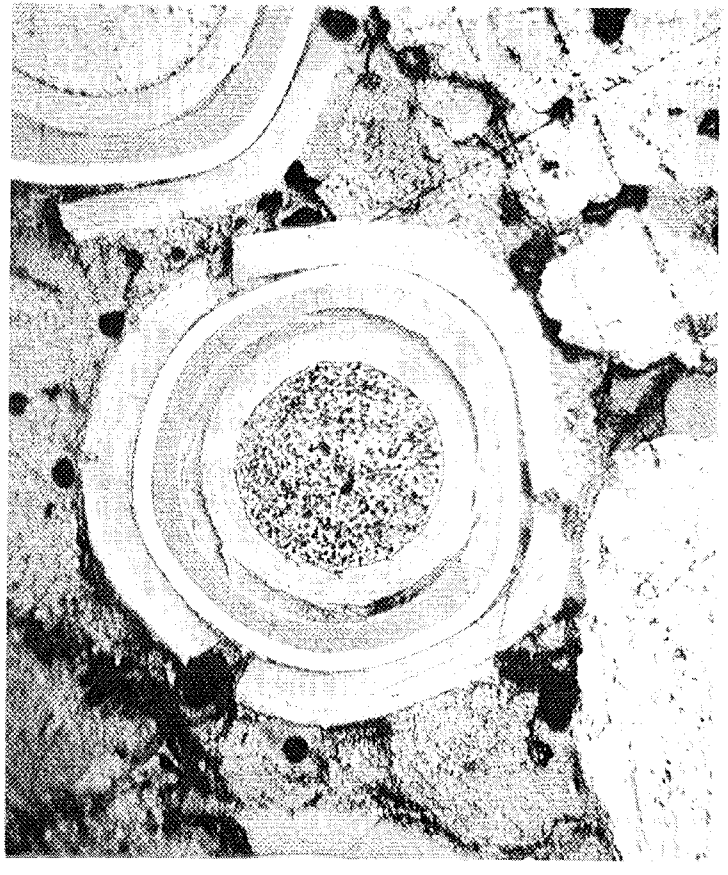

R80544

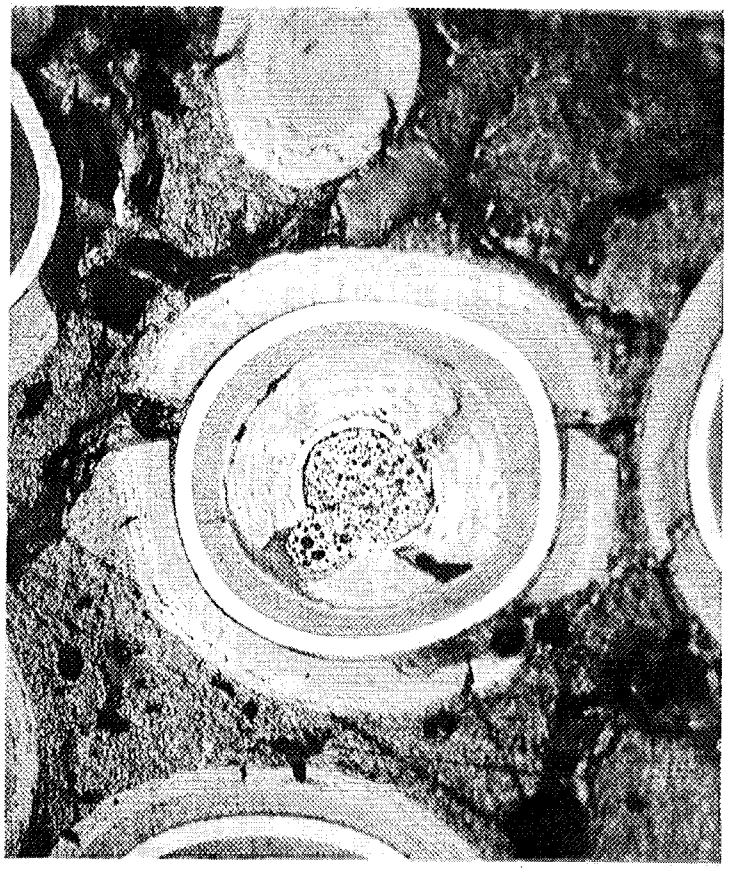

Figure 4.61.

THE UCO KERNEL SWELLING WAS RESTRAINED BY THE BUFFER UNTIL CRACKS DEVELOPED IN THE BUFFER. THE UCO KERNEL SWELLED INTO THE RADIAL CRACKS WHEN THEY DEVELOPED IN THE BUFFER.

Capsule HRB-21
Fuel Compact 4A, Fissile UCO
Burnup=22% FIMA Fast Fluence=3.5×10^{25} n/m^2

YP16318

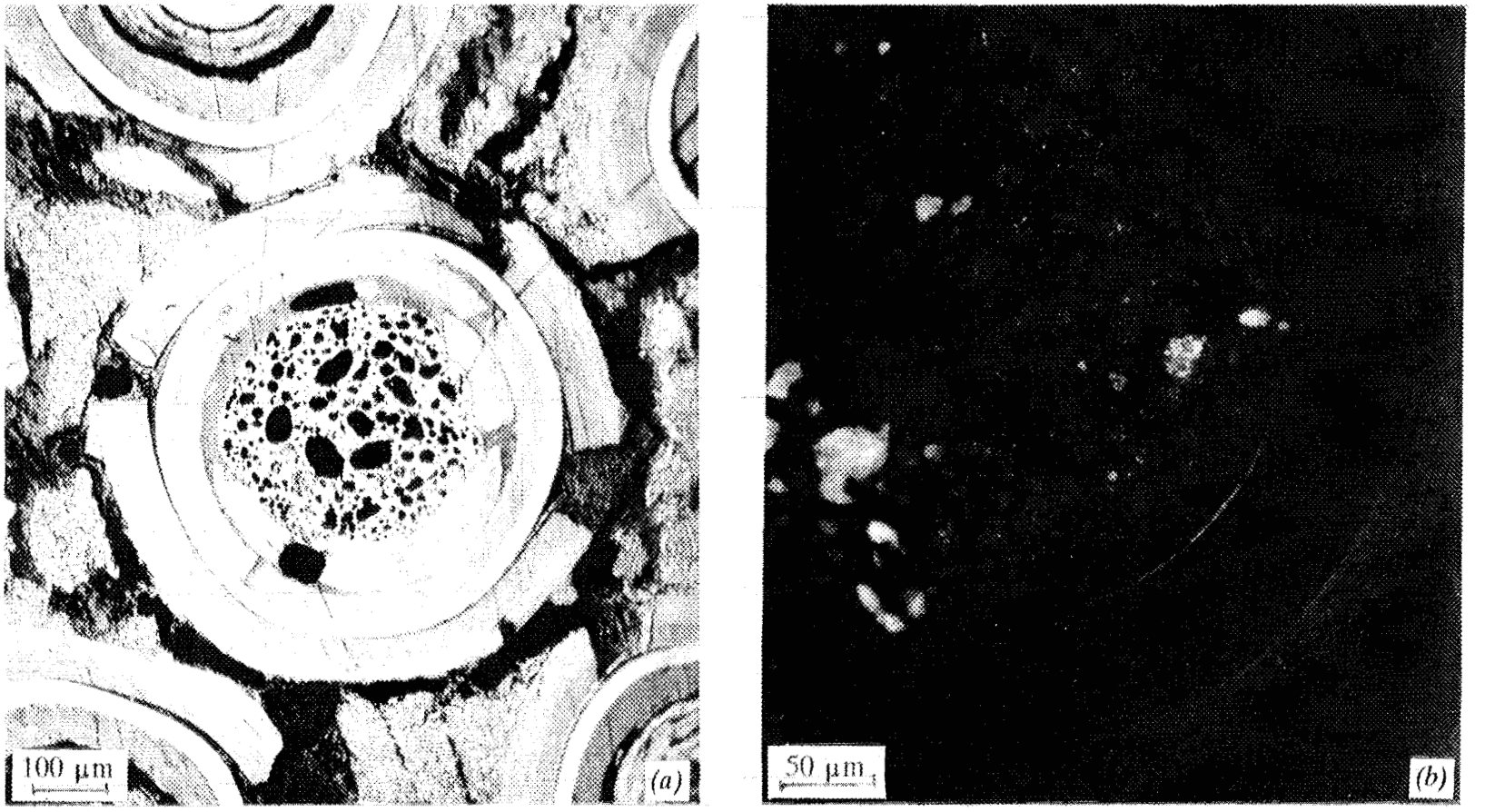

Figure 4.62.

SOME UCO KERNELS SHOWED REJECTED CARBON ON ONE SIDE OF THE KERNEL IN ADDITION TO KERNEL SWELLING INTO THE BUFFER REGION. THE REJECTED CARBON WHICH EXHIBITED OPTICAL ANISOTROPY UNDER POLARIZED LIGHT, IN PHOTO *(b)*, WAS THE RESULT OF THE "AMOEBA EFFECT" KERNEL MIGRATION. THE THICKNESS OF THE REJECTED CARBON LAYER, ON THE LOWER RIGHT KERNEL SURFACE WAS USED TO DETERMINE THE KERNEL MIGRATION RATE AND THE KERNEL MIGRATION COEFFICIENT.

t = exposure time (s),

dx/dt = calculated average kernel migration rate.

From Table 3.1, the compact average temperature for compact 4 was 1028°C which leads to a particle temperature of 1301 K, a gradient of 1.6×10^4 K/m, and a t of 9×10^6s (105 d). The KMC for the three particles was about 10^{-10} m^2K/s, which was two orders of magnitude larger than the design value for UCO at the planned irradiation temperature (950°C) and larger than the design value for pure UO_2 kernels. The relationship is shown in Figure 4.63. While the data are limited and only approximate, the difference is great enough to warrant investigation.

The development of fission gas and solid fission products produced a force for swelling of the UCO kernels. At the highest exposure, where radial cracks developed in most of the buffer coatings, the kernel swelled into cracks in the buffer. An illustration of this effect is shown in Figures 4.61 and 4.62.

4.6.2.3 Irradiation Effects in TRISO Coatings

After a surface of the compact was adequately polished, it was examined in detail and the condition of coatings with regard to cracks or other unusual features recorded. During the grinding and polishing process, about 75% of the kernels and many buffer layers fell from the center of the particles and were lost. This may have been due to insufficient potting material, or the coatings may have been more friable that the current polishing techniques can handle. In order to keep the database as uniform as possible, the decision was made to collect data for structural coatings only from those particles which had kernels. However, this may bias the data somewhat; the particles with very severe damage could have been ignored. Observations were not recorded for the buffer layer which was usually cracked in the high-exposure compacts and usually not cracked in the low-exposure compact. In order to obtain an adequate number of observations of particles with kernels, it was necessary to prepare two or three polished surfaces for each ceramographic mount. Each surface was more than 1 mm further into the mount, so under normal circumstances, the same particles were not examined twice. Using this approach, a total of 263 UCO particles and 579 ThO_2 particles with kernels were examined in the four compacts. The total number of particles, with and without kernels, which were in the ceramographic mount was not recorded. The observations for each compact are summarized in Tables 4.25 through 4.28.

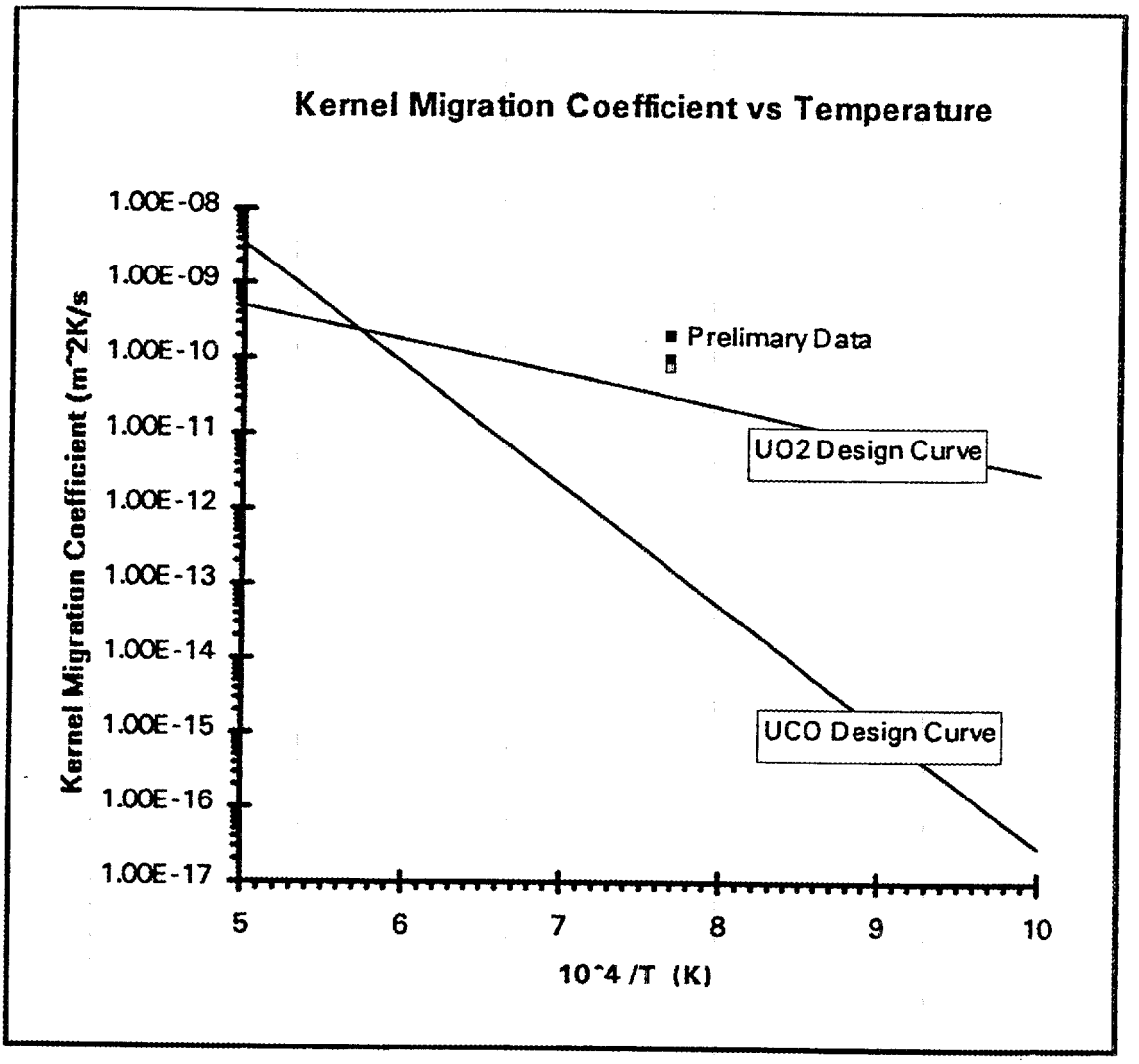

Figure 4.63.

THE KERNEL MIGRATION COEFFICIENT OBTAINED FROM OBSERVED MIGRATION IN THREE HRB-21 COMPACT 4A UCO PARTICLES WAS TWO ORDERS OF MAGNITUDE GREATER THAN THE DESIGN CURVE FOR UCO AND ABOUT A FACTOR OF TWO GREATER THAN THE DESIGN CURVE FOR PURE UO_2.

Table 4.25.

SUMMARY OF CERAMOGRAPHIC COATING FAILURE DATA FOR COMPACT 1C

Neutron fluence: 1.5×10^{25} n/m^2, E > 0.18 MeV

Burnup: 14% FIMA (fissions per initial metal atom) fissile, 0.5% FIMA fertile

Particle type: Uranium oxycarbide (UCO) fissile, ThO_2 fertile

Comments: Only particles with kernels retained in the polished cross section were characterized.

Circumferential cracks were considered to be artifacts.

Particles with circumferential SiC cracks did not have a failed IPyC coating.

See Appendix D for particle details.

Particle type	Number examined	Failures (number/percent of total)			
		IPyC	SiC	OPyC	PPyC
Fissile	99	0 / 0.0%	0 / 0.0%	32 / 32%	78 / 79%
Fertile	197	1 / 0.5%	2 / 1.0%	39 / 20%	147 / 75%
Total	296	1 / 0.3%	2 / 0.7%	71 / 24%	225 / 76%

Table 4.26.

SUMMARY OF CERAMOGRAPHIC COATING FAILURE DATA FOR COMPACT 2A

Neutron fluence: 2.3×10^{25} n/m^2, E > 0.18 MeV

Burnup: 18% FIMA (fissions per initial metal atom) fissile, 1.2% FIMA fertile

Particle Type: Uranium oxycarbide (UCO) fissile, ThO_2 fertile

Comments: Only particles with kernels retained in the polished cross section were characterized.

Circumferential cracks were considered to be artifacts.

Particles with circumferential SiC cracks did not have a failed IPyC coating.

See Appendix D for particle details.

Particle type	Number examined	Failures (number/percent of total)			
		IPyC	SiC	OPyC	PPyC
Fissile	67	6 / 9%	0 / 0%	51 / 76%	62 / 93%
Fertile	141	16 / 11%	0 / 0%	112 / 79%	137 / 97%
Total	208	22 / 11%	0 / 0%	163 / 78%	199 / 96%

Table 4.27.

SUMMARY OF CERAMOGRAPHIC COATING FAILURE DATA FOR COMPACT 2B

Neutron fluence: 2.3×10^{25} n/m^2, E > 0.18 MeV

Burnup: 18% FIMA (fissions per initial metal atom) fissile, 1.2% FIMA fertile

Particle type: Uranium oxycarbide (UCO) fissile, ThO_2 fertile

Comments: Only particles with kernels retained in the polished cross section were characterized.

Circumferential cracks were considered to be artifacts.

Particles with circumferential SiC cracks did not have a failed IPyC coating.

See Appendix D for particle details.

Particle type	Number examined	Failures (number/percent of total)			
		IPyC	SiC	OPyC	PPyC
Fissile	66	1 / 1.5%	0 / 0%	26 / 39%	40 / 61%
Fertile	134	5 / 3.7%	4 / 3%	38 / 28%	97 / 72%
Total	200	6 / 3.0%	4 / 2%	64 / 32%	137 / 69%

Table 4.28.

SUMMARY OF CERAMOGRAPHIC COATING FAILURE DATA FOR COMPACT 4A

Neutron fluence: 3.5×10^{25} n/m^2, E > 0.18 MeV

Burnup: 22% FIMA (fissions per initial metal atom) fissile, 2.2% FIMA fertile

Particle Type: Uranium oxycarbide (UCO) fissile, ThO_2 fertile

Comments: Only particles with kernels retained in the polished cross section were characterized.

Circumferential cracks were considered to be artifacts.

Particles with circumferential SiC cracks did not have a failed IPyC coating.

See Appendix D for particle details.

Particle type	Number examined	Failures (number/percent of total)			
		IPyC	SiC	OPyC	PPyC
Fissile	31	9 / 29%	2 / 6%	31 / 100%	31 / 100%
Fertile	107	46 / 43%	5 / 5%	105 / 98%	107 /100%
Total	138	55 / 40%	7 / 5%	136 / 99%	138 /100%

Appendix D provides information on the examined particles. The ceramographic observations are discussed for each coating layer, starting with the IPyC, in the following sections.

4.6.2.3.1 IPyC

Typically, when the buffer shrunk away from the IPyC, the highly anisotropic PyC seal coating deposited on the buffer during manufacture remained bonded to the IPyC. The seal coating was deposited to provide a smooth surface on the buffer layer so that the IPyC could be easily separated from the buffer for characterization during manufacturing QC measurements. The fact that during irradiation the seal coating was torn from the buffer layer, rather than parting as expected at the seal-IPyC interface, indicates that the bond at the IPyC interface was relatively strong. The observation also indicates that the IPyC had higher strength than the buffer layer, an expected result. The PyC seal coat can be seen adhering to the IPyC in the high-magnification photos of Figures 4.60 and 4.61.

The frequency of particles with cracked IPyC increased with fast neutron exposure. Cracks which developed in the IPyC did not propagate into the SiC layer (as viewed in the metallographic mounts). However, there was a tendency for cracked SiC and cracked IPyC to appear in the same particle. In the highest-fluence compact examined, 4A, all cracked SiC was accompanied by cracked IPyC. The metallographic mounts only provide a limited view of the particle coatings, so it is very likely that all cracks were not found; the method is biased toward large cracks that span a major portion of the coating diameter. SiC cracks are the most difficult to find because SiC is stable under irradiation, and the cracks do not open up like cracks in the shrinking pyrocarbon. No mechanistic connection was observed between the IPyC crack and development of a crack in SiC or to indicate that a crack in the SiC caused the IPyC to fail. Examples of typical IPyC and SiC cracks appearing in the same particle are shown in Figure 4.64.

In some cases, when the IPyC was cracked, it appeared that irradiation-induced shrinkage caused the IPyC to pull away from the SiC and curl toward the particle center. This action left a gap between the IPyC and the SiC at the location of the IPyC crack. This phenomenon may have resulted in a complex interaction between IPyC and SiC in the vicinity of the IPyC crack or gap. If the interaction resulted in local tensile stresses in the SiC, it may have contributed to the observation of cracked SiC near cracks or gaps in the IPyC. The development of a gap between cracked IPyC and the SiC coating, as well as the

Capsule HRB-21
Fuel Compact 4A
Fertile ThO2 Burnup 2.2% FIMA, Fissile UCO Burnup 22% FIMA
Fast Neutron Fluence 3.5×10^{25} n/m^2

R80565

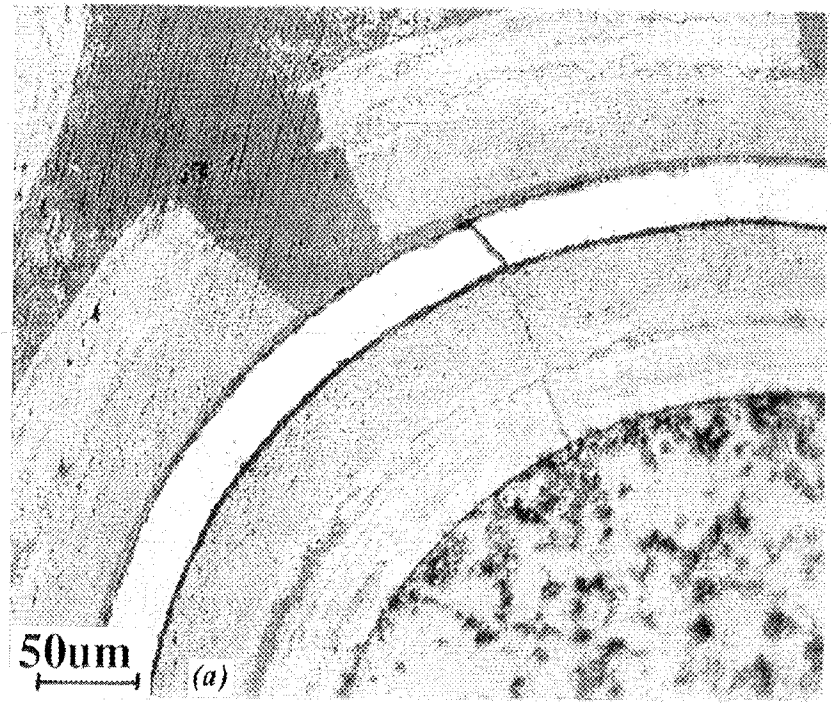

R80661

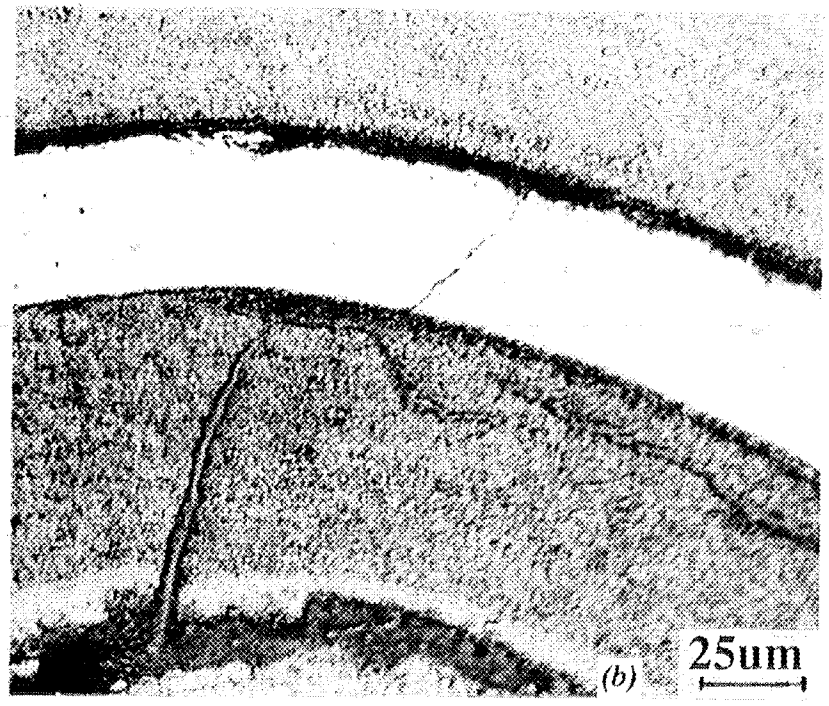

Figure 4.64.

FAILURE OF THE SiC LAYER WAS USUALLY ASSOCIATED WITH FAILURE OF THE IPyC LAYER, BUT NOT ALL PARTICLES WITH FAILED IPyC HAD FAILED SiC: *(a)* UCO FISSILE AND *(b)* ThO_2 FERTILE.

nearby crack in the SiC, is illustrated in Figure 4.65. The mounts do not allow stress distributions to be determined, and modelling must be relied upon to infer the structural state of the coatings.

With this concept in mind, it is useful to examine the data to see if IPyC and SiC failure can be connected in some way. These results are shown in Table 4.29. SiC with circumferential cracks has been eliminated (see the section below). These data have a large uncertainty associated with them because of the difficulty of finding cracks; nonetheless, a trend is apparent. The highest exposure compact has the greatest SiC failures associated with IPyC failure. These results provide circumstantial evidence for the stress-driven failures. It should be noted that six cases of SiC failure without IPyC failure were also found; they were found in compacts 1C and 2B. Since particle coatings cannot be thoroughly checked for cracks and damage is possible during mount preparation, hard evidence to prove or disprove the stress theory is difficult to come by.

The IPyC effectively protected the SiC from the swelling kernel. In a small number of particles, the buffer layer was broken, and the UCO kernel swelled into the void left by the shrinking buffer. In some cases, the kernel swelled up against the IPyC layer. Under the irradiation conditions of these tests, the IPyC was not attacked by the kernel, and no evidence of significant SiC attack by fission products from the kernel was observed. An example of kernel material in contact with IPyC and no SiC attack evident is shown in Figure 4.66.

4.6.2.3.2 SiC

The SiC coating is the primary barrier to fission product release in the TRISO-coated particle. The ceramographic sections of compacts were examined at high magnification to characterize cracks or other flaws which might give rise to fission product release. Two types of fractures were observed in the SiC. The crack signifying coating damage was a relatively straight radial crack across the thickness of the SiC layer. An example of the radial crack in SiC is shown in Figure 4.67. The second type of SiC crack was circumferential and did not propagate through the coating. There were several forms of the circumferential cracks. Some circumferential cracks were only 10 to 30 μm in length and proceeded at a shallow angle from the SiC outer or inner surface and into the SiC. Examples of circumferential cracks are shown in Figure 4.68.

Capsule HRB-21
Fuel Compact 4A, Fertile ThO_2
Burnup=2.2% FIMA Fast Fluence=3.5×10^{25} n/m^2

R80572

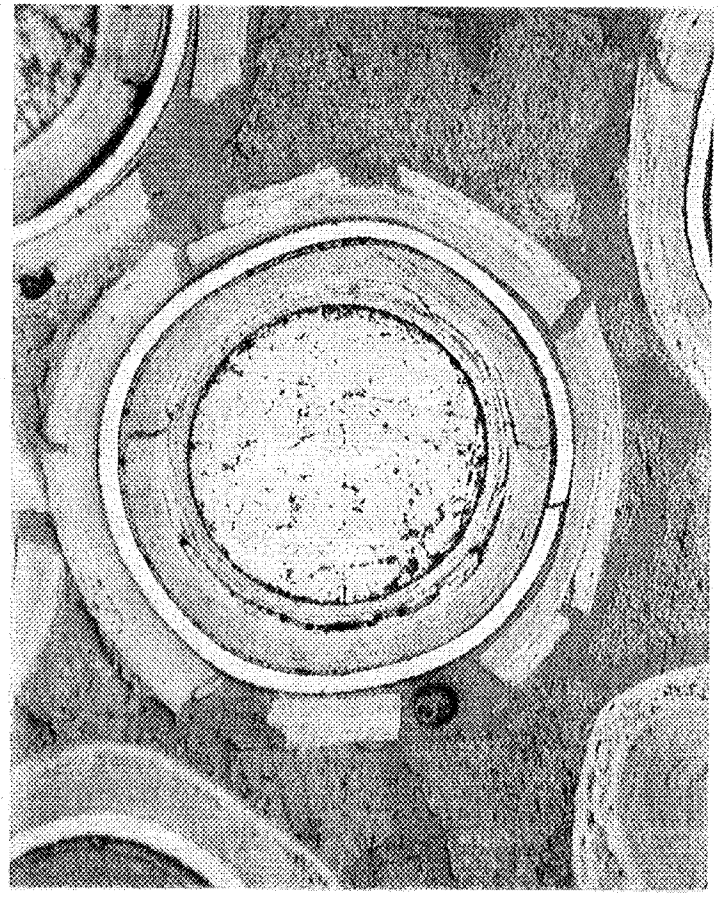

R80574

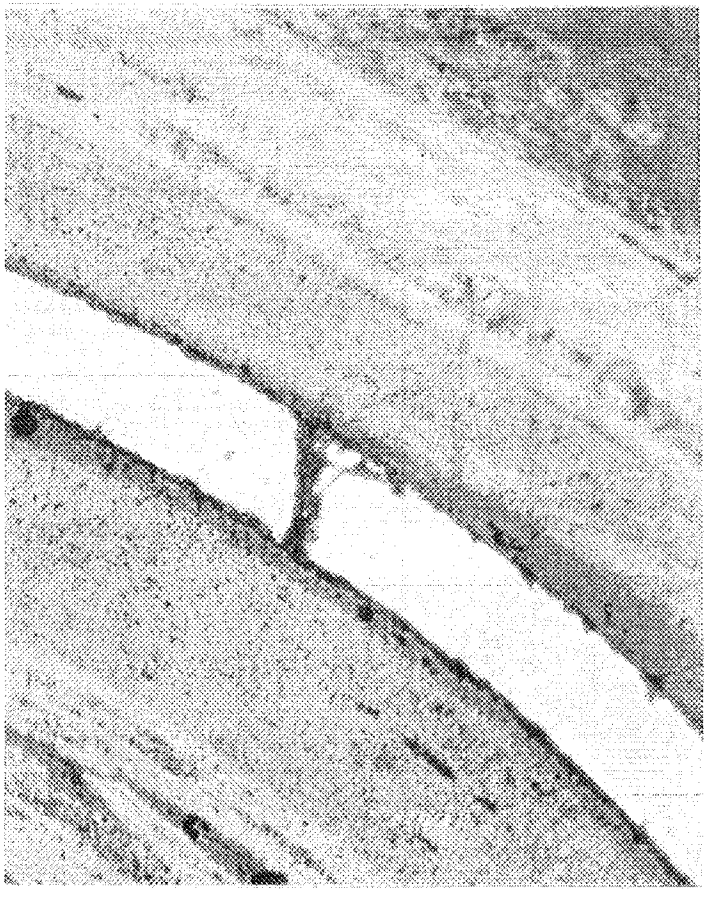

Figure 4.65.

WHEN THE IPyC WAS FAILED, IT USUALLY PULLED AWAY FROM THE SiC, AND A RADIAL CRACK WAS FREQUENTLY OBSERVED NEARBY IN THE SiC.

Table 4.29.

SiC FAILURE IN PARTICLES WITH IPyC FAILURE

Compact	Particle type	Number of IPyC failures observed	Number of associated SiC failures observed	Percent SiC failure with IPyC failure
1C	fertile and fissile	1	0	0
2A	fertile and fissile	22	0	0
2B	fertile and fissile	6	0	0
4A	fertile and fissile	55	7	13
4A	fissile	6	2	33
4A	fertile	49	5	10

Circumferential cracks which extended for 100 μm or more were observed in the fertile particles of compact 1C, which had a relatively low fast neutron exposure of 1.5×10^{25} n/m^2. Over 20% of the fertile particles showed circumferential cracks, but less than 1% of the fissile particles exhibited such cracks. The fact that the circumferential cracks did not appear in particles with higher exposure but similar thermal conditions indicated that the cracks must have developed not during irradiation but as a result of subsequent treatment. Perhaps the residual SiC coating stress in particles at low exposure was greater than in high-exposure particles where PyC creep or other effects may have alleviated the stress. The removal of a portion of the SiC shell in the grinding and polishing process may have removed supporting material so that the SiC coating cracks in the circumferential direction. Compacts 2A and 2B have quite different values for pyrocarbon and SiC damage, and this may reflect mount preparation damage and the fact that the fuel was in a highly stressed state after irradiation.

HRB-21 Fissile Particle
Compact 4A 22% FIMA 3.5×10^{25} Fluence

R80737 R80898

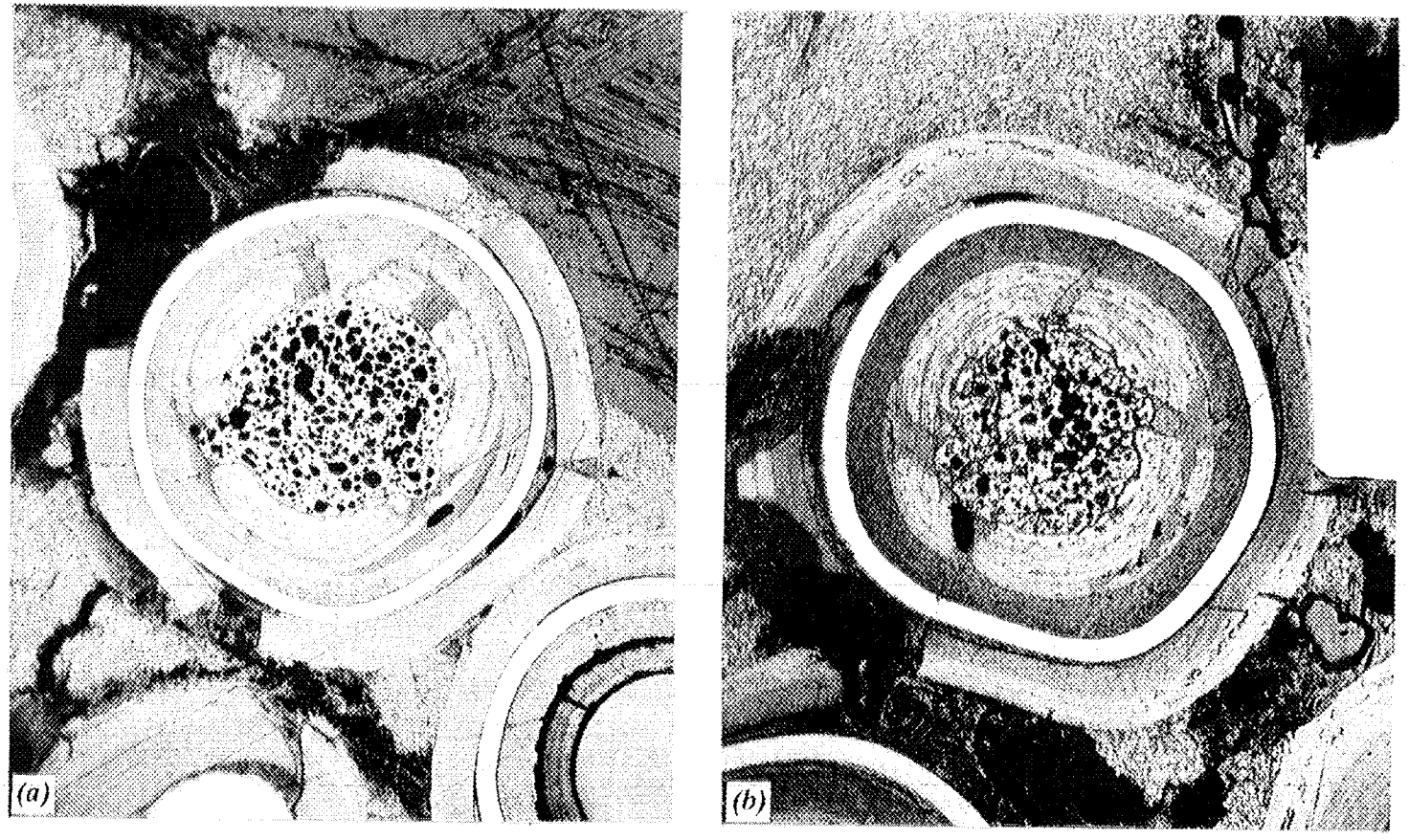

Figure 4.66.

THE IPyC COATING PROVIDED A BARRIER TO FISSION PRODUCTS AND ATTACK OF THE SiC WHEN IT WAS NOT CRACKED EVEN WHEN THERE WAS KERNEL SWELLING INTO BUFFER CRACKS, AS IN *(a)*. WHEN CRACKS DEVELOPED IN THE IPyC, FISSION PRODUCT ATTACK OF THE SiC TOOK PLACE, PRIMARILY AT THE TIP OF THE IPyC CRACK, AS IN *(b)*.

Capsule HRB-21
Compact 4A, Fertile ThO_2
2.2% FIMA 3.5 × 10^{25} n/m^2 Fluence Temp 1028° C

R80573

Figure 4.67.

AN ILLUSTRATION OF A TYPICAL RADIAL SiC CRACK. CRACKS IN THE IPyC DID NOT PROPAGATE INTO THE SiC BUT WERE FREQUENTLY NEAR SiC CRACKS. ALSO ILLUSTRATED IS THAT CRACKS IN THE PPyC DID NOT ALWAYS PROPA-GATE INTO THE SEAL COAT AND OPyC.

Capsule HRB-21
Fuel Compact 1C, Fertile ThO_2
Burnup=0.5% Fast Neutron Fluence 1.5×10^{25} n/m^2

R80727 R80728

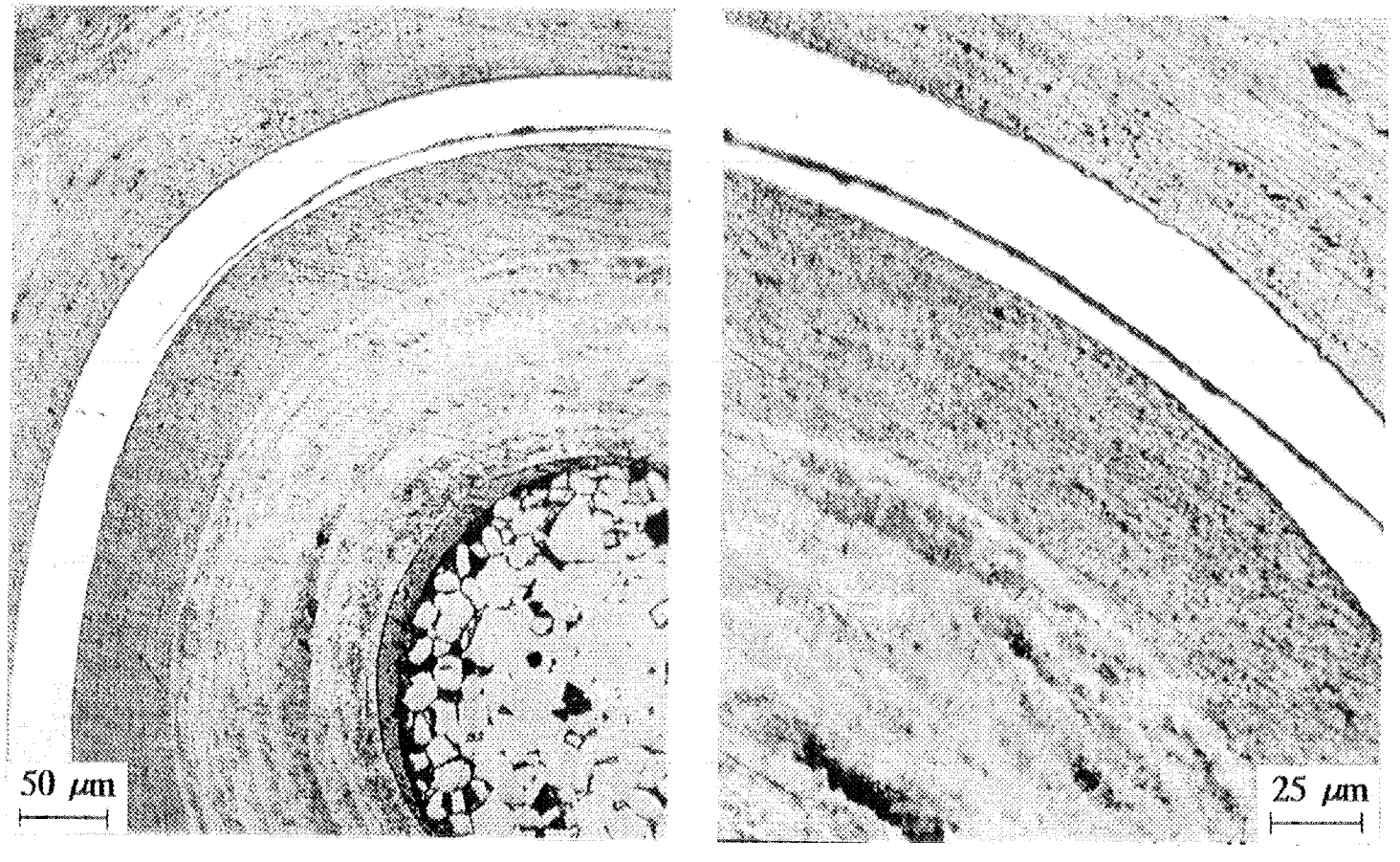

Figure 4.68.

CIRCUMFERENTIAL CRACKS IN THE SiC DID NOT ALWAYS TERMINATE AT THE SiC SURFACE OR REMAIN AT A CONSTANT RADIUS.

Ceramographic mounts were prepared with particles identified by IMGA as having released and having retained cesium during irradiation. Two each retentive and nonretentive particles were prepared and examined. The purpose of the work was to correlate the condition of the SiC coating with retention capability. The particles which had released cesium during irradiation were shown to have porosity in the SiC, while the particles that had been retentive showed no porosity or cracks. The results of the ceramographic examination of particles characterized by IMGA are shown in Table 4.30. The SiC porosity observed in nonretentive particles is shown in Figures 4.69 through 4.71. The condition of the SiC in retentive particles is shown in Figures 4.72 and 4.73.

Lenticular flaws oriented parallel to the deposition plane were detected in the SiC of several particles. These flaws had the appearance of a feature known as "gold spots." The gold spot term was derived from the fact that when the OPyC is burned from the particle, the flaw appears gold in color when observed through the thin outer layer of SiC. Analysis of the contents of the flaw has shown it to be Si and C. The flaw is formed during SiC coating in a spouting fluidized bed when the particle is momentarily ejected and touches the coater wall above the bed. Some Si and carbon soot are picked up on the surface of the particle, which then falls back into the bed, and the SiC coating process is completed. About 2% of fertile and 0.04% of fissile particles in HRB-21 had gold spots.[4-17] Although the gold spot represents a discontinuity in the SiC, it was never associated with cracks in the SiC coating. An example of a gold spot in SiC is shown in Figure 4.74.

Consideration of the coated particle as a pressure vessel would favor perfect spheres for the maximum pressure containment capability. However, many particles deviate from perfect sphericity. The SiC coating elastic modulus is much higher than the PyC coatings so that, eventually, most of the load for gas pressure containment is borne by the SiC, and overpressure conditions cause failure of the SiC. In the case where greater-than-expected SiC failure takes place, as in capsule HRB-21, the particles which deviate most from spherical geometry would appear to be probable sources of failure. However, examination of particles over the range of shapes showed no correlation of SiC failure and the degree of sphericity. An example of a relatively spherical SiC coating which cracked is shown in Figure 4.75 while the nonspherical particle shown in Figure 4.76 did not crack. Additional observations were made on the ability of nonspherical particles to survive irradiation without failure of the SiC. An unirradiated archive compact of HRB-21 was burned in air to expose

Table 4.30.

RELEASE VERSUS SiC CONDITION

Particles characterized as retentive of releasing for cesium by Irradiated-Microsphere Gamma Analyzer provided some ceramographic evidence that releasing particles had cracked or porous SiC, but slight porosity may not always be an indication of an SiC coating which releases cesium.

Particle mount	IMGA identified releasing cesium	SiC cracked or porous
HRB-21 5C (P1)	yes	yes
HRB-21 5C (P3)	yes	yes
HRB-21 5C (P11)	no	no
HRB-21 5C (P13)	no	slight porosity

the SiC coating. Examination of the burned particles revealed that about 1% of the fertile particles had a concave indentation in the SiC coating which had apparently been created during the coating process. Such a deviation from sphericity would be expected to reduce the ability to survive internal gas pressure during irradiation.

In order to determine if any of the indented particles survived irradiation, the particles from compact 5C, which had been characterized by IMGA, were examined under a microscope to determine if any dimpled particles remained. The particles from 5C were chosen for examination since most of the PPyC and OPyC coatings had cracked and spalled off leaving the SiC coating exposed in the same manner as burned particles. Several dimpled particles were observed in the cesium-retentive population of ThO_2 particles. This observation showed that the margin for pressure vessel performance must be very large in the TRISO coating design for such particles to survive. These results are consistent with those made from ceramographic sections discussed above. This observation is not foolproof, however, because low-burnup ThO_2 kernels can retain cesium, and thus fertile particles can give a false indication of integrity. Examples of unirradiated and irradiated dimpled particles are shown in Figures 4.76 and 4.77.

Capsule HRB-21 Compact 5C, Fissile UCO
22% FIMA 3.5 × 10^{25} n/m^2 Fluence Temp 1023°C

R81009

R81011

Figure 4.69.

DECONSOLIDATED FROM COMPACT 5C AND CHARACTERIZED BY IRRADIATED-MICROSPHERE GAMMA ANALYZER, PARTICLE P3, ABOUT 95% OF Cs WAS RELEASED DURING IRRADIATION. SOME SiC POROSITY AND CORROSION WERE EVIDENT AT THE TIP OF IPyC CRACKS. KERNEL SWELLING TOOK PLACE INTO BUFFER CRACKS.

Capsule HRB-21
Compact 5C, Fissile UCO
Burnup 22%, Fast-Neutron Fluence 3.5×10^{25} n/m^2

R81015 R81016

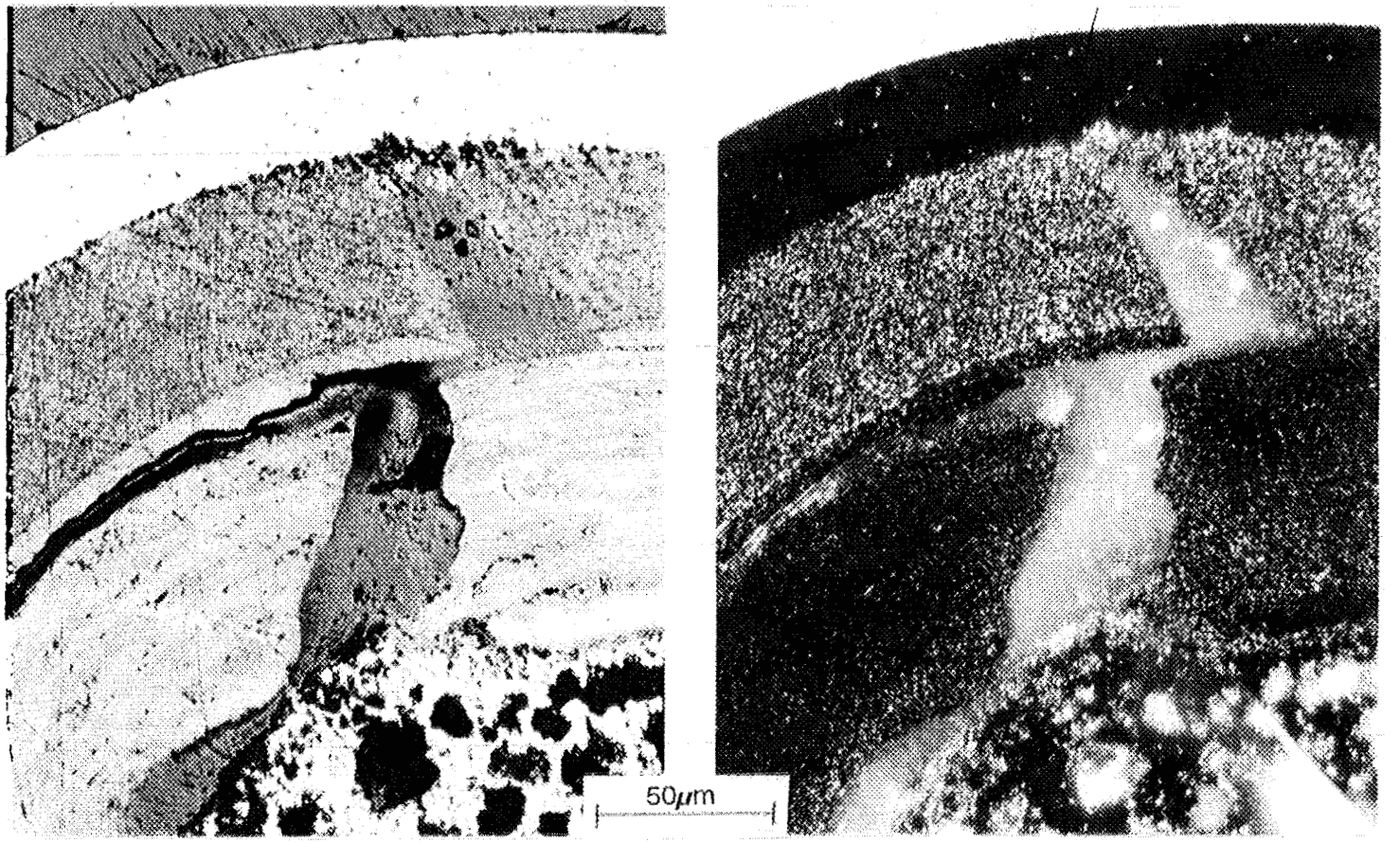

Figure 4.70.

DECONSOLIDATED FROM COMPACT 5C AND CHARACTERIZED BY IRRADIATED-MICROSPHERE GAMMA ANALYZER, PARTICLE P3, ABOUT 95% OF Cs WAS RELEASED FROM THE PARTICLE DURING IRRADIATION. CORROSION OF SiC WAS EVIDENT AT THE TIP OF IPyC CRACK.

Capsule HRB-21 Compact 5C, Fissile UCO
22% FIMA 3.5×10^{25} n/m^2 Fluence Temp 1023°C

R81003 R81002

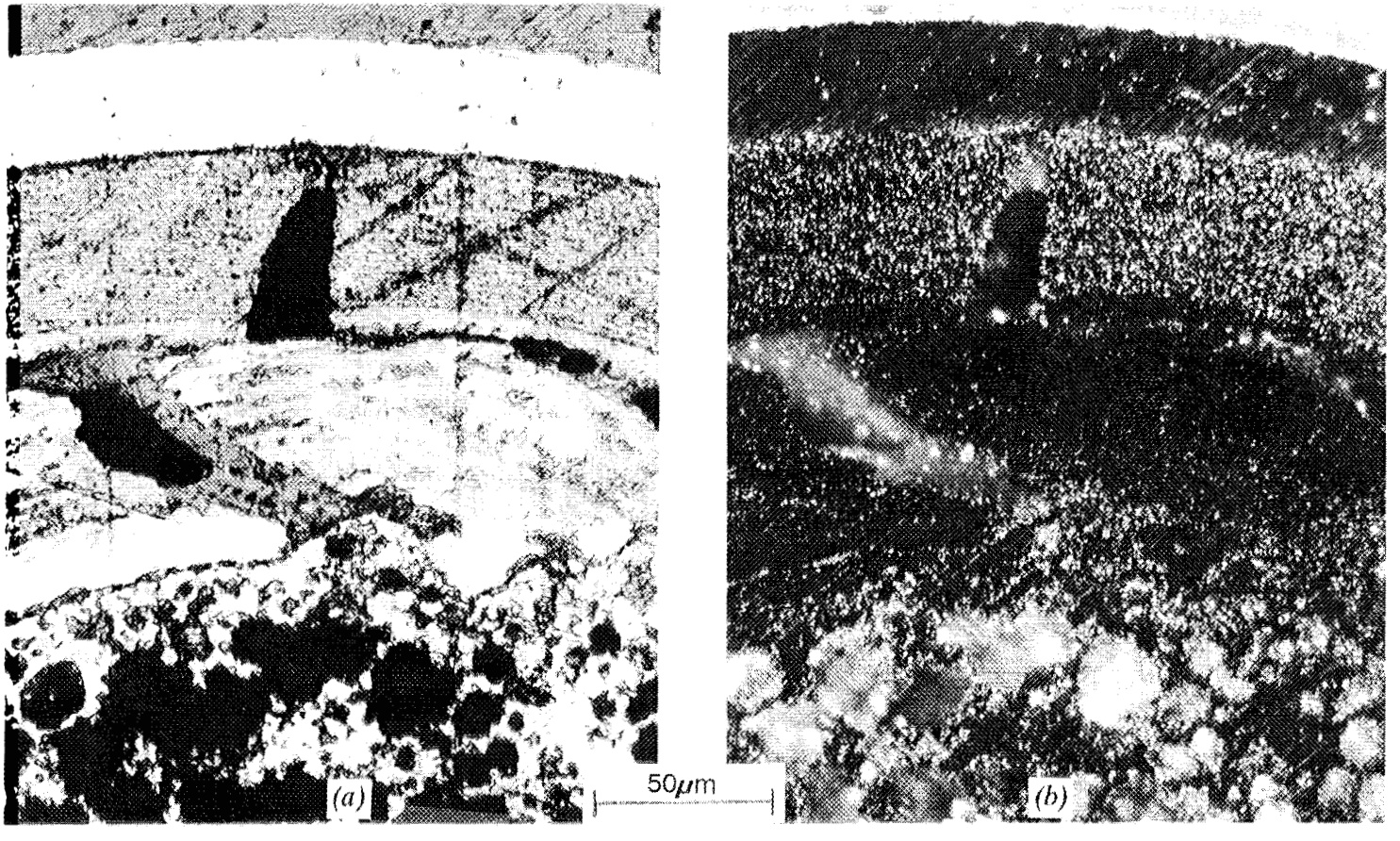

Figure 4.71.

DECONSOLIDATED FROM COMPACT 5C AND CHARACTERIZED BY IRRADIATED-MICROSPHERE GAMMA ANALYZER, PARTICLE P1, ABOUT 80% OF Cs WAS RELEASED FROM THE PARTICLE DURING IRRADIATION. THERE WAS SOME POROSITY IN SiC NEAR THE IPyC CRACK AS SHOWN IN PHOTO *(a)*. THE POLARIZED LIGHT PHOTO IN *(b)* DOES NOT SHOW OPTICAL ACTIVITY IN IPyC AT IPyC CRACK TIP, SO GRAPHITIZATION OF PyC, OFTEN OBSERVED IN PyC WITH HIGH FISSION PRODUCT CONTENT, HAD NOT TAKEN PLACE.

Capsule HRB-21 Compact 5C, Fissile UCO
22% FIMA 3.5 × 10^{25} n/m^2 Fluence Temp 1023°C

R81025

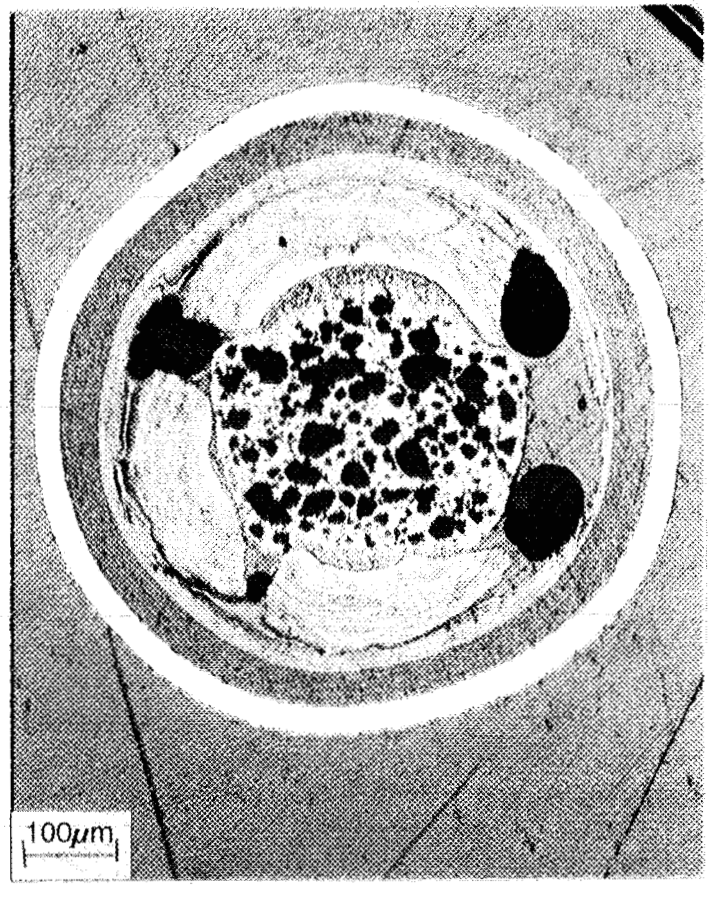

R81028

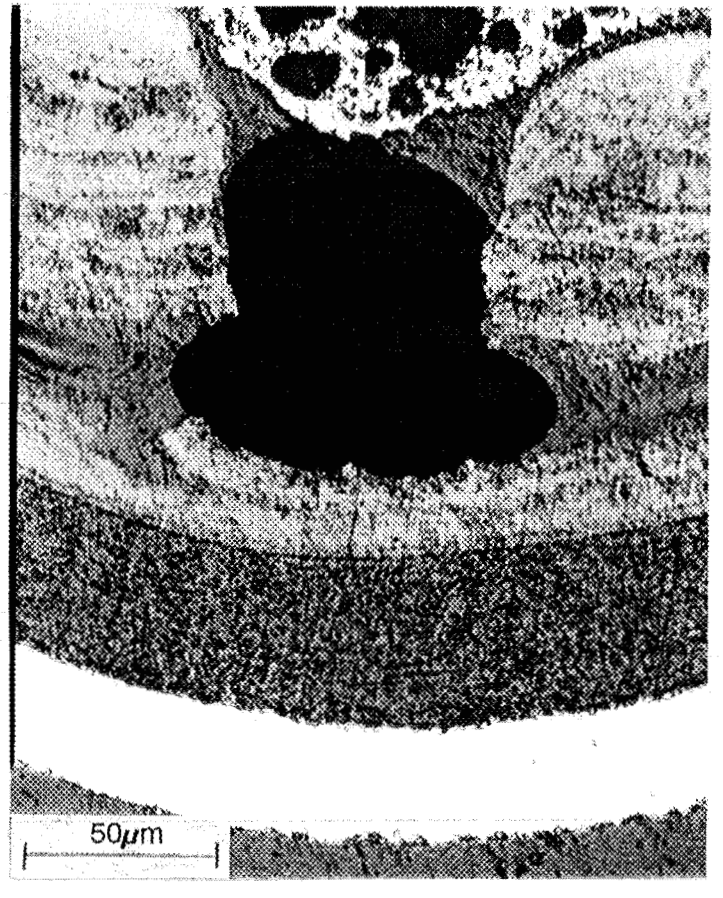

Figure 4.72.

DECONSOLIDATED FROM COMPACT 5C AND CHARACTERIZED BY IRRADIATED-MICROSPHERE GAMMA ANALYZER, PARTICLE P13. NO Cs LOSS DURING IRRADIATION. VERY SLIGHT SiC POROSITY; NO CRACKS IN IPyC.

Capsule HRB-21 Compact 5C Fissile UCO
22% FIMA 3.5 × 10^{25} n/m^2 Fluence Temp 1023°C

R81019

R81021

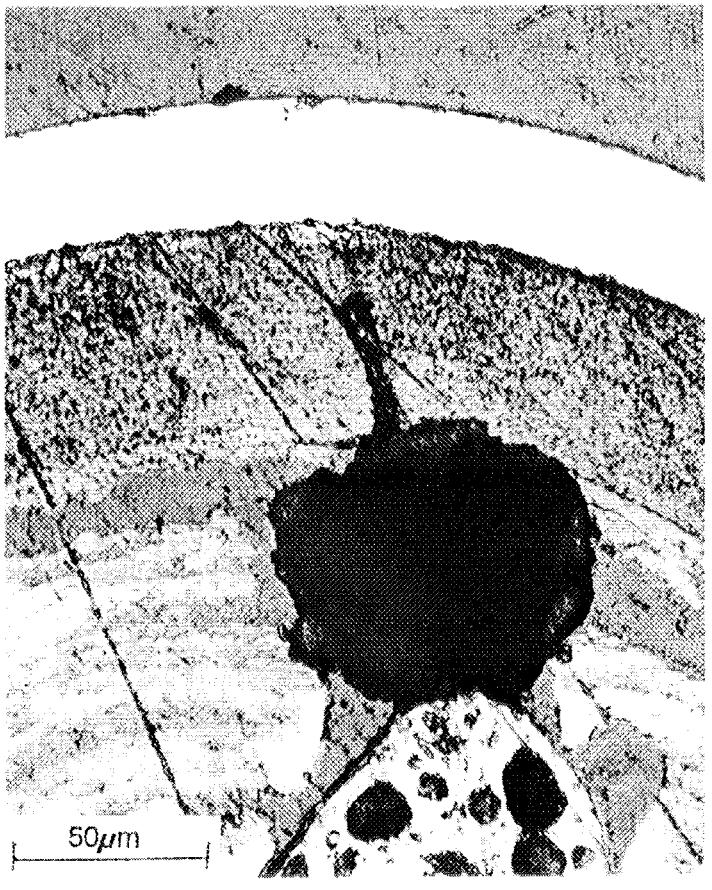

Figure 4.73.

DECONSOLIDATED FROM COMPACT 5C AND CHARACTERIZED BY IRRADIATED-MICROSPHERE GAMMA ANALYZER, PARTICLE P11. NO Cs LOSS DURING IRRADIATION. NO SiC CORROSION OR POROSITY AT TIP OF IPyC CRACK.

Capsule HRB-21
Fuel Compact 4A, Fertile ThO_2
Burnup=22% FIMA Fast Fluence=3.5×10^{25} n/m^2

R80732

Figure 4.74.

A DISCONTINUITY OBSERVED IN SOME SiC LAYERS WAS THE FEATURE KNOWN AS A "GOLD SPOT." NO CRACKS OR OTHER DELETERIOUS EFFECTS WERE ASSOCIATED WITH GOLD SPOTS WHICH WERE INTRODUCED INTO THE SiC DURING COATING DEPOSITION.

Capsule HRB-21
Fuel Compact 4A, Fertile ThO_2
Burnup 22% FIMA and Fluence 3.5×10^{25} n/m^2

R80564

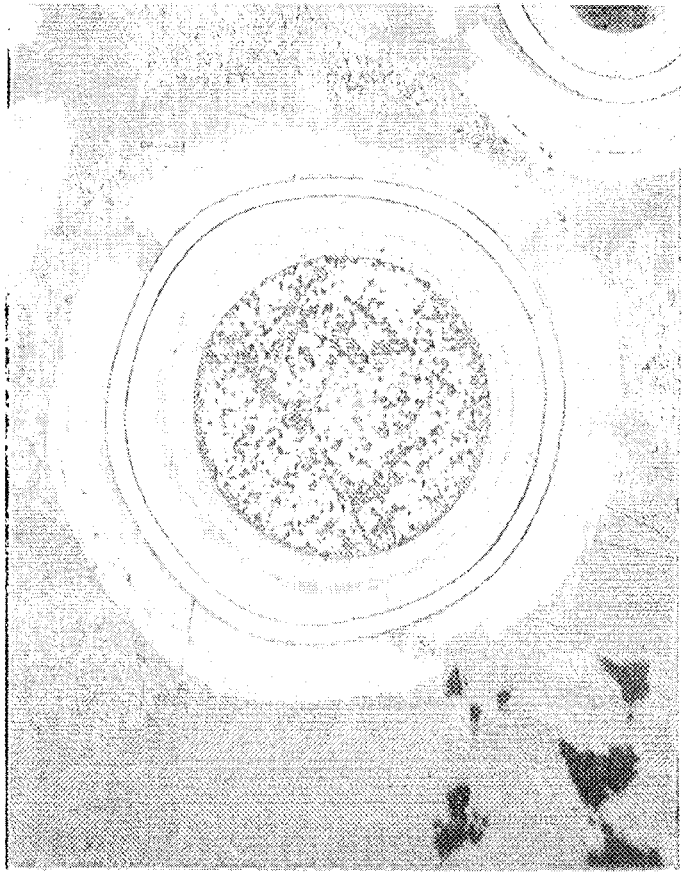

R80565

Figure 4.75.
RELATIVELY SPHERICAL PARTICLES DEVELOPED CRACKS IN THE SiC.

Capsule HRB-21
Fuel Compact 2B, Fissile UCO
Burnup = 18% FIMA Fast Fluence = 2.3×10^{25} n/m^2

R80550 R80551

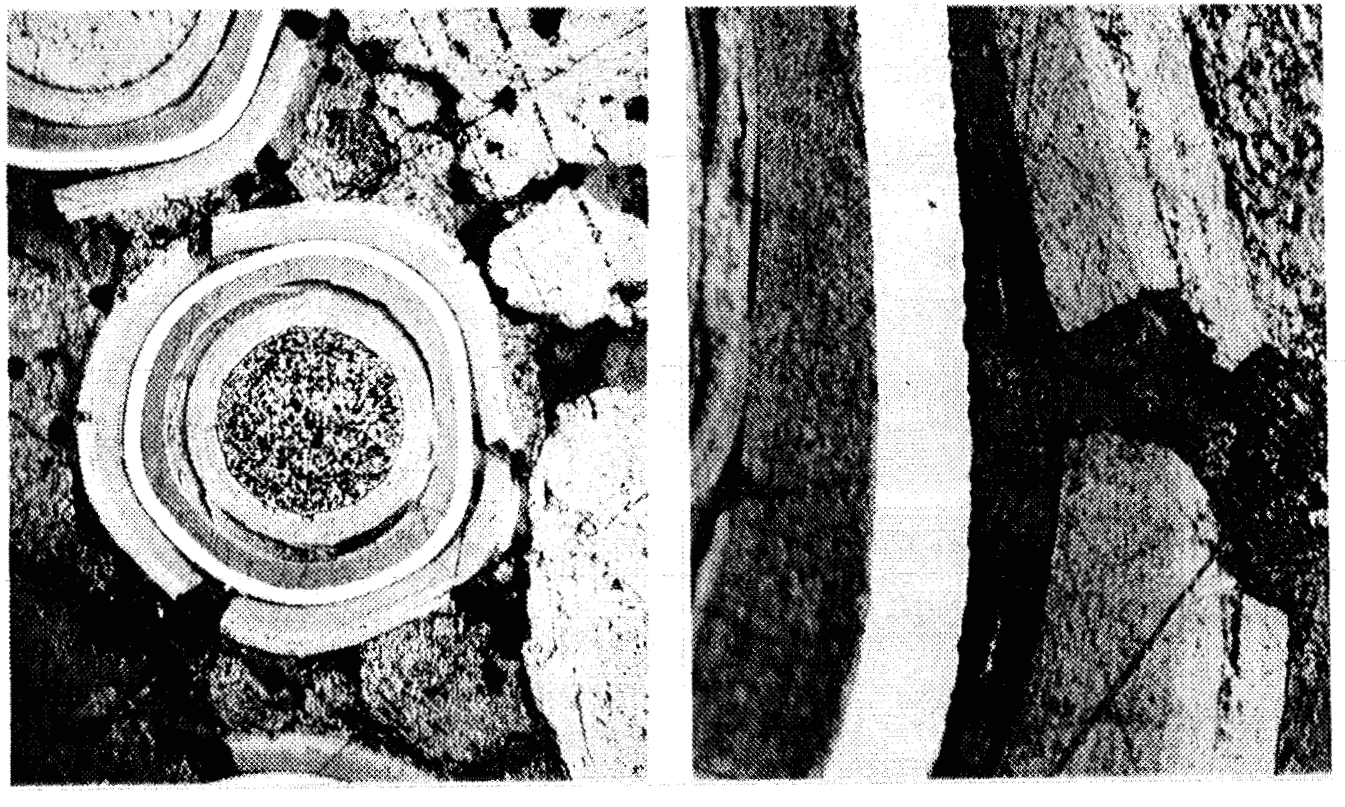

Figure 4.76.

PARTICLES WITH MARKEDLY NON-SPHERICAL SiC COATING LAYERS SURVIVED WITHOUT SiC CRACKING EVEN WHEN OTHER COATING LAYERS WERE FAILED. THE SURVIVAL OF NON-SPHERICAL PARTICLES AT HIGH BURNUP INDICATES THAT THERE WAS SIGNIFICANT PERFORMANCE MARGIN IN PRESSURE VESSEL DESIGN.

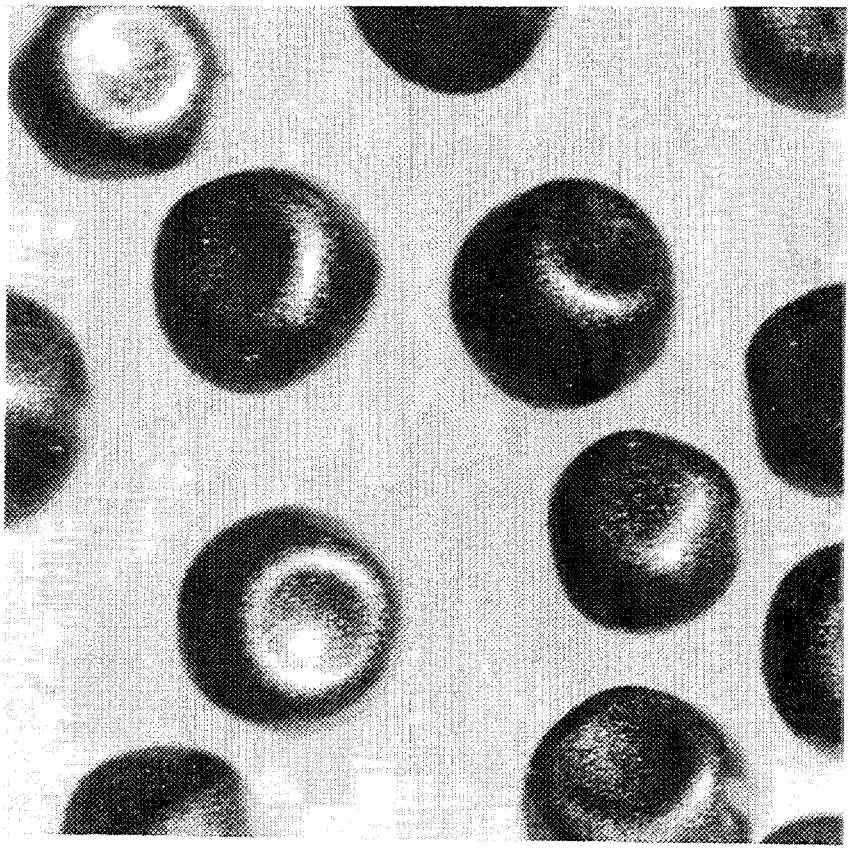

HRB-21 Unirradiated ThO_2 burned back to SiC selected non-spherical particles

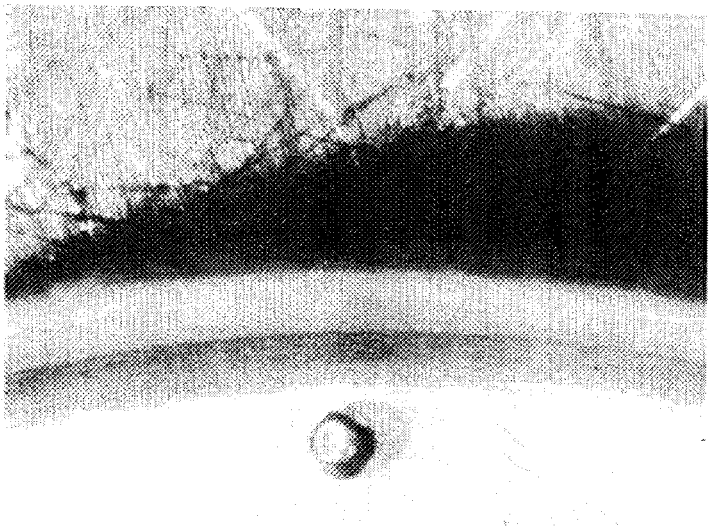

HRB-21 Irradiated ThO_2 Compact 5C, Temp 1023°C 3.5×10^{25} n/m^2, 2.2% FIMA SiC coating exposed by failed PPyC and OPyC. Through IMGA, no Cs release.

Figure 4.77.

ABOUT 1% OF HRB-21 FERTILE PARTICLES WERE DIMPLED AT THE SiC STAGE OF COATING. EXAMPLES WERE FOUND WHERE DIMPLED FERTILE PARTICLES SURVIVED IRRADIATION AND DID NOT RELEASE CESIUM. THIS PROVIDES ANOTHER INDICATION OF SIGNIFICANT MARGIN IN THE PRESSURE-VESSEL DESIGN.

The SiC coatings were carefully examined to determine if any reactions had taken place. No second phases, indicative of fission metal attack, were observed. However, porosity throughout the SiC and a rough, inner SiC surface was created from some form of corrosion of the SiC at the tip of cracks in the IPyC coating. The appearance of the SiC in the corrosion zone resembled the corrosion observed in unirradiated TRISO particles without IPyC where CO/CO_2 or Cl_2 attack of the SiC may have taken place.[4-18] Attack by Cl_2 would be expected only if Cl_2 infiltrated the IPyC and was retained in the buffer during the SiC deposition from methyltrichlorosilane. Since the IPyC was thicker than in prior designs and tests during manufacture showed the IPyC to be impermeable, it is unlikely the attack was by Cl_2.

Attack of SiC by CO/CO_2 oxidation effects is a possibility if the kernel was deficient in UC_2 at the time of manufacture. The variation of composition of individual kernels is not measured in acceptance tests; only the mean composition is measured. It is possible that nearly pure UO_2 kernels could be mixed with kernels containing excess UC_2, and the mean UO_2/UC_2 composition specified for the kernel batches would be met.

The UCO kernel had effectively retained the rare earth fission products, and even the release of Pd was low enough that no SiC attack was observed. However, examination by scanning electron microscopy (SEM), discussed in Sect. 4.7, revealed that Pd and Ag had penetrated the SiC at very low concentrations.

4.6.2.3.3 PPyC/OPyC

Failure of the PPyC coating resulted from tensile stress which developed as a result of irradiation-induced shrinkage of the low-density PPyC material around the unyielding substrate of OPyC and SiC. It should be noted that approximately 50% of the PPyC had small cracks prior to irradiation. One scenario for the failure of the PyC layers is that cracks initiated in the PPyC, which failed and continued to shrink in a circumferential direction, transmitted local stresses to the OPyC. In this way, the PPyC contributed to an already high tensile stress component developing in the OPyC as a result of irradiation-induced shrinkage in that coating. Through the combination of PPyC shrinkage and shrinkage in the OPyC, the tensile stress in the OPyC became large enough to result in radial cracking of the OPyC coating. The cracks normally propagated from the PPyC through the seal coating and OPyC, as shown in Figure 4.78. However, it is not possible to disprove the possibility that the OPyC failure was independent of the PPyC in at least some of the cases.

Capsule HRB-21
Fuel Compact 2B, Fissile UCO and Fertile ThO_2
Burnup: UCO = 18% FIMA, ThO_2 = 1.2% FIMA; Fluence = 2.3×10^{25} n/m^2

YP17386

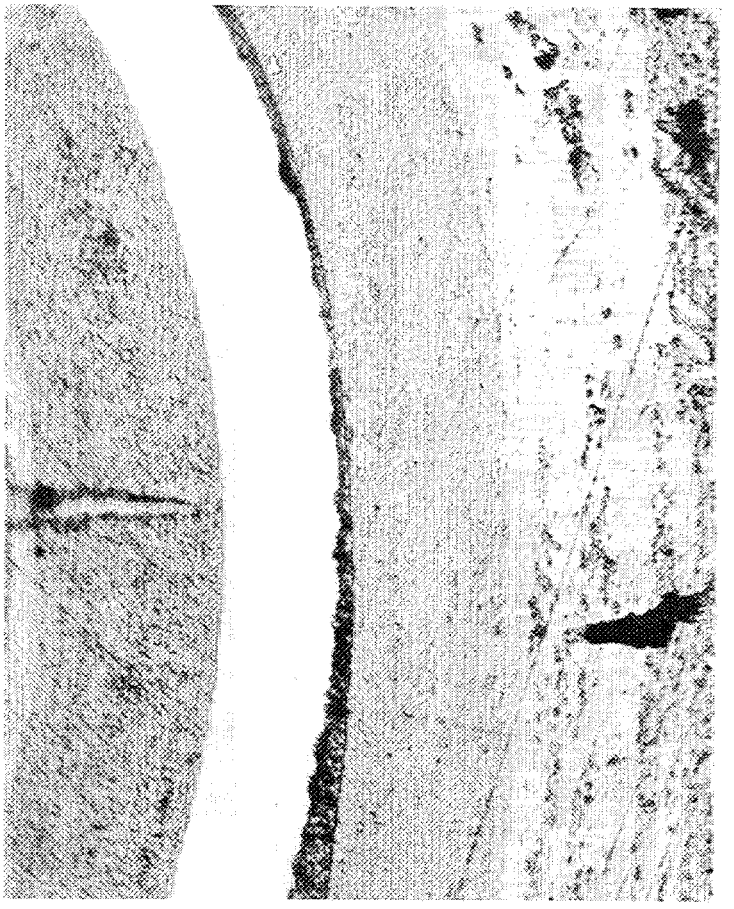

Figure 4.78.

CRACKS IN THE PPyC LAYER ORIGINATED AT THE OUTER SURFACE AND PROPAGATED INWARD. CRACKS IN THE IPyC LAYER ORIGINATED AT THE INNER IPyC SURFACE AND PROPAGATED OUTWARD.

The failure of the PPyC and OPyC was highly dependent on the fast neutron fluence. As the fluence increased above 1.5×10^{25} n/m^2 (E > 0.18 MeV), the frequency of failure increased rapidly. The failure of the retentive OPyC coating as fluence increased correlates, to some degree, with the rapid increase in fission-gas release observed in capsule HRB-21 at about the same fluence. This observation is consistent with failure of OPyC exposing previously failed or defective SiC. There was no evidence that cracks which developed in the PPyC and OPyC propagated directly into the SiC. Because of the high failure fraction of OPyC, it was not unusual for a crack in the OPyC to be near a crack in the SiC. However, the OPyC has a much lower elastic modulus than SiC and was not strongly bonded to the SiC as indicated by the fact that the OPyC spalled off the SiC when the OPyC was severely cracked. Therefore, propagation of cracks from the OPyC into the SiC is unlikely.

4.6.2.3.4 Compact Matrix

The compacts were very fragile, and particles were easily debonded from the surface by contact with containers and handling equipment. Ceramographic sections of the compacts showed that the compact matrix was very porous and laced with cracks. Bonding was maintained between the matrix and particles, but the high porosity and cracks which ran through the matrix resulted in a friable compact body.

The matrix was bonded to the particles, many of which had broken outer coatings. However, there was no obvious detrimental interaction between the matrix and particles. Detrimental interaction has been observed in prior irradiation tests where the shrinking matrix pulls the OPyC coatings away from the SiC substrate. Such dislocation was not observed in this fuel. An example of the matrix microstructure is illustrated in Figure 4.79.

The high particle packing fraction and high fraction of cracked outer PPyC coatings resulted in a very friable compact at the end of the irradiation exposure. The extensive cracking of the matrix resulted in the expansion of the compact observed when the dimensions were taken after irradiation. Shrinkage was predicted by the design calculations because the design curves were based on fuel with the five-layer TRISO particle which had less than 3% OPyC failure. In HRB-21, there was 100% failure of the PPyC at peak exposure which resulted in greater matrix debonding than accounted for by the design calculations.

The shrinkage of the PPyC coatings did result in shrinkage of compacts at the lower exposures, but compacts at the highest exposure exhibited expansion because of extensive

R80667

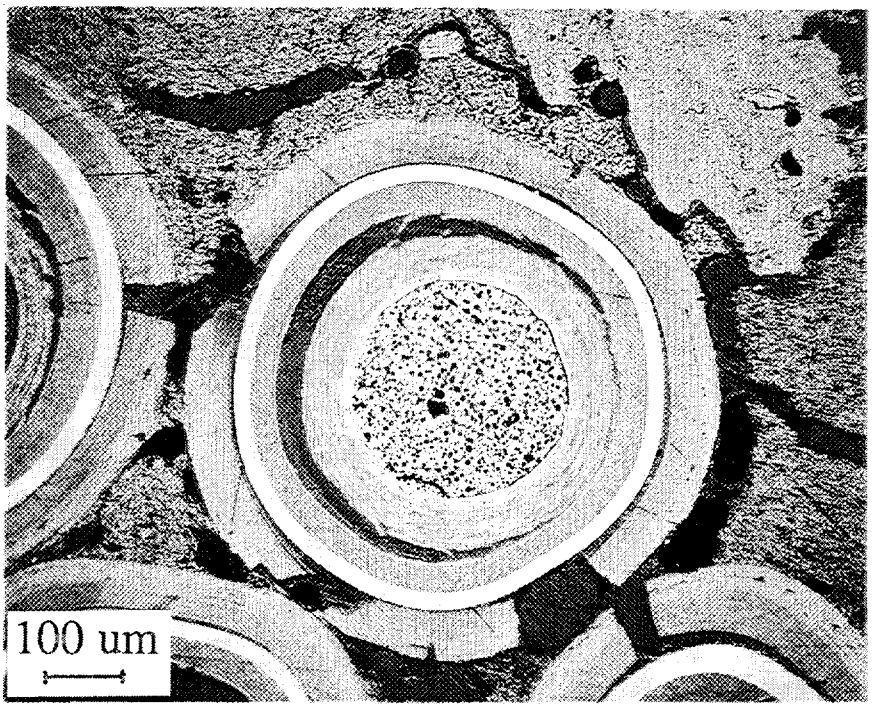

Figure 4.79.

ILLUSTRATION OF TYPICAL HRB-21 COMPACT MATRIX SHOWING H-451 GRAPHITE SHIM PARTICLES AND COATED FUEL PARTICLES BONDED BY CARBONIZED GRAPHITE FLOUR/PETROLEUM PITCH MATRIX. SHRINKAGE OF MATRIX DURING IRRADIATION CAUSED EXTENSIVE CRACKING, BUT NO DELETERIOUS COATING/ MATRIX INTERACTION WAS EVIDENT.

debonding and development of cracks in the compact matrix. The compact dimensional changes as a result of the irradiation exposure were discussed in Sect. 3.

To gain a better idea of the performance of the compact as a whole, an integral picture was pieced together from individual pictures for compact 2A. This composite picture is shown in Figures 4.80 (top of compact) and 4.81 (midsection). Note that the particle damage is greater along the axis of the compact. By contrast, the damage at the OD of the compact is much less. Since the temperature of an intact compact runs roughly 100°C hotter at the axis than at the edges, a temperature effect on coating damage may be inferred from the figures. Since this composite was only done on compact 2A, it is not clear how important the temperature effect is. Two issues are immediately apparent. This first is the magnitude of the temperature gradient and its cause. If the massive pyrocarbon failure resulted in a compact with significantly lower thermal conductivity, then the axis of the compact may have run much hotter than expected. A thermal runaway condition could have been established—some pyrocarbon damage occurs which lowers the thermal conductivity of the compact, which increases the compact temperature gradient, which results in more failures, etc. This scenario could explain the rapid increase in failures as the irradiation proceeded. The major difficultly with this scenario is that under the HRB-21 operating conditions, little pyrocabon damage should have taken place, especially at the point in the irradiation where the failures became apparent. Also, at higher temperatures, radiative heat transfer starts to dominate the heat-loss mechanisms which would have limited the temperature gradients that could have been supported by cracks and porous regions. Thus, it seems unlikely that temperatures far in excess of known HTGR fuel capability were encountered when fuel failure began.

The second issue is whether the temperature factor is a cause or an effect and leads to another scenario. Radiation damage is a function of temperature, but pyrocarbons that operate over a wide temperature and fluence range have been demonstrated. Any increase in the temperature gradient may simply have been the final insult to an already compromised and dimensionally unstable fuel. Again, massive pyrocarbon failure and cracking of the matrix material could easily lead to lower thermal conductivity and (somewhat) higher internal compact temperatures. The higher temperatures would tax the particles to a greater extent and accelerate their demise because of the effects of radiation damage of which temperature is a factor, but any increased temperature gradients are a symptom of

YP19216

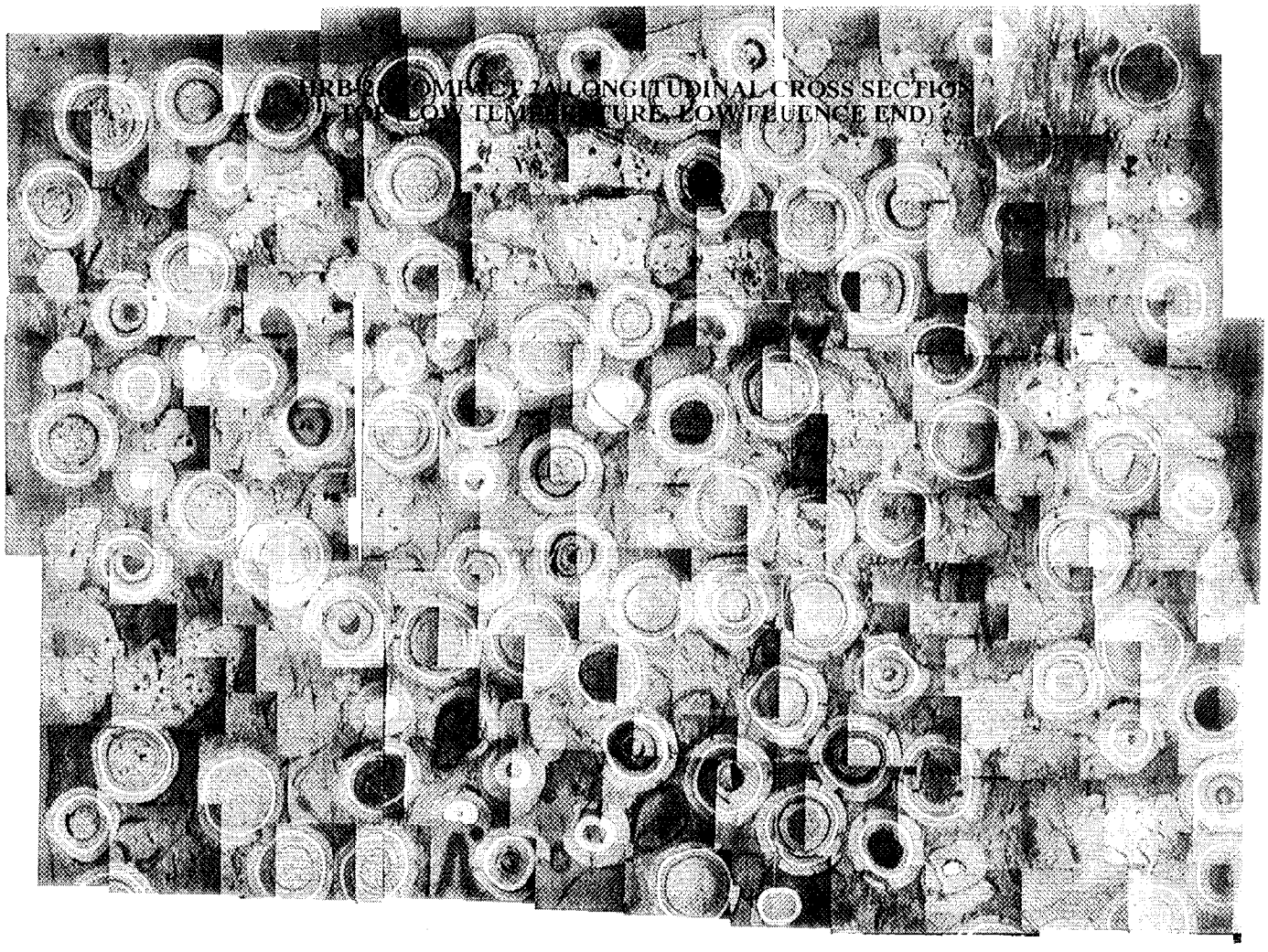

Figure 4.80.

CROSS SECTION OF COMPACT 2A (TOP PORTION), 2.3×10^{25} n/m^2 FLUENCE, 18% FIMA (FISSILE), 1.2% FIMA (FERTILE), AND 957°C COMPACT AVERAGE TEMPERATURE.

YP19217

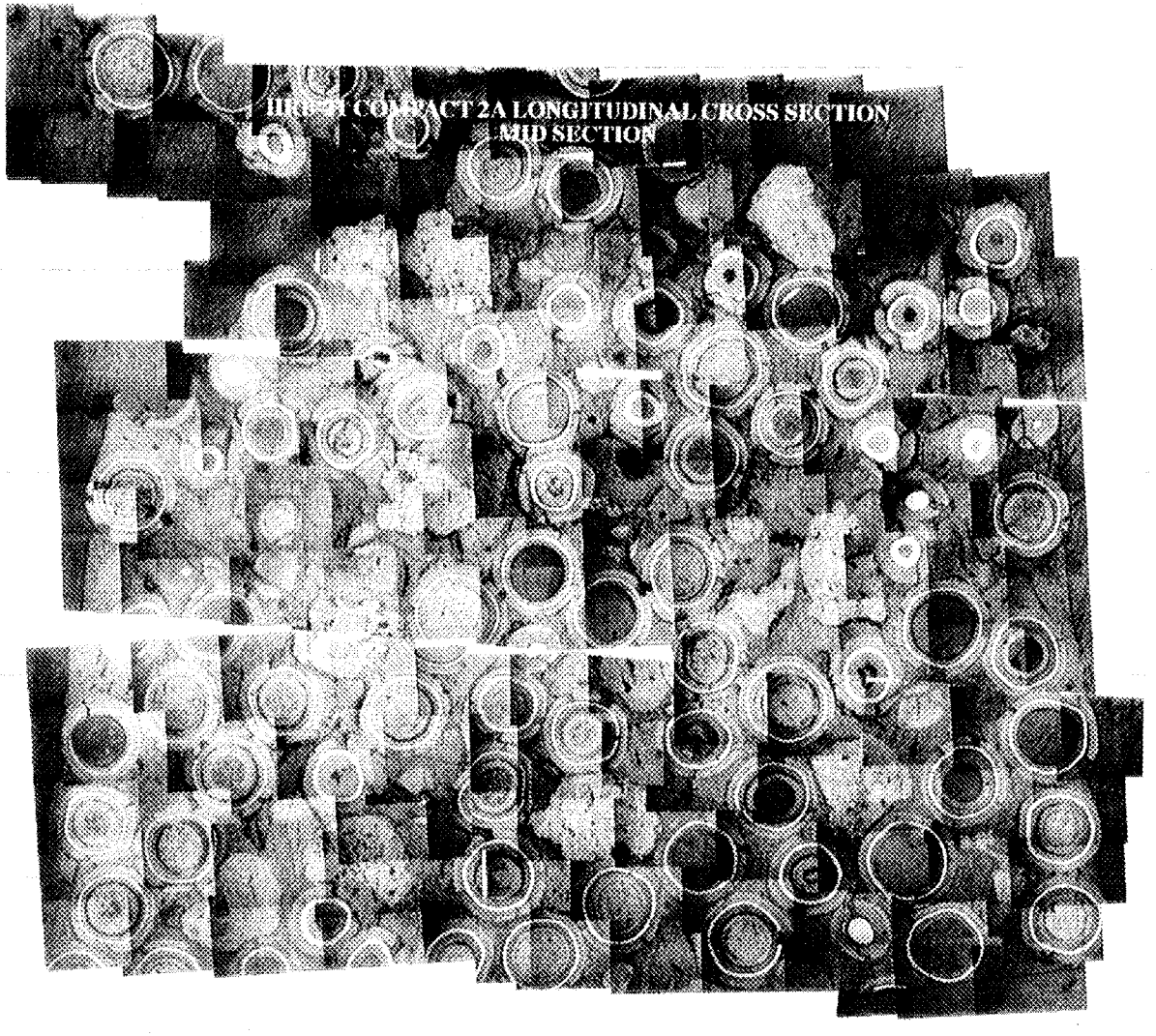

Figure 4.81.

CROSS SECTION OF COMPACT 2A (MID-SECTION), 2.3×10^{25} n/m^2 FLUENCE, 18% FIMA (FISSILE), 1.2% FIMA (FERTILE), AND 957°C COMPACT AVERAGE TEMPERATURE.

pyrocarbon problems rather than a direct cause. Failure would have eventually occurred anyway after the radiation damage reached a critical (low) level. The system would still have positive feedback, but the feedback is driven by a pyrocarbon flaw rather than a design limit. Since pyrocarbon failure was seen throughout the PIE, the evidence points to the irradiation instability of the particle coatings as the major cause. Temperature appears to have played a secondary, accelerating role.

4.6.3 Summary Discussion

The failure of the PPyC/OPyC coatings was a strong function of fast neutron exposure. At a temperature of about 900°C, the onset of major OPyC failure was at a fluence of between 0.7×10^{25} n/m^2 (R/B results) and 1.5×10^{25} n/m^2 (PIE results), and nearly 100% OPyC failure was observed at 2.3×10^{25} n/m^2. Fuel samples with the lowest fast neutron exposure had significantly less OPyC failure than the fuel with maximum exposure. The SiC coating failure fraction showed a strong correlation with fast neutron exposure as well. In addition, all SiC failures in the highest-fluence compact were accompanied by IPyC failure. Finally, a composite view of a medium-exposure compact indicates some temperature dependence.

Burnup of HM increased in the fuel along with fast neutron exposure, so increased coating failure had an apparent dependence on burnup. However, the similarity in coating performance between fertile and fissile particles with more than an order-of-magnitude difference in burnup indicates that burnup was not a significant variable influencing coating failure. There was also no strong evidence that kernel or fission product attack contributed to mechanical failure of the SiC coating.

Particle shape and the existence of the lenticular SiC flaw known as a "gold spot" did not appear to contribute to the observed failure of SiC or OPyC. Nonspherical and poorly shaped particles performed as well as spherical ones. Cracks in the SiC were never seen to connect with, or be associated with, the gold spot discontinuity in the SiC. The source of stress causing SiC failure acted independently of these shape and flaw features. Apparently, the margin for failure due to pressure-vessel effects is very large in MHTGR particle design. However, features which degrade pressure-vessel performance should be removed because they can be expected to become limiting when the nonpressure-vessel source of failure in these particles is identified and eliminated.

The fact that the cracks in the SiC were associated with a crack in the IPyC suggests that the mechanism of failure involves both coatings. Since the IPyC crack was not observed to be aligned with the SiC crack and the IPyC was typically debonded from the SiC in the vicinity of the crack, the conclusion was drawn that cracks in one coating did not propagate into the other. However, stress calculations[4-19,4-20] indicate that the debonding and cracking of the IPyC can lead to high local tensile stresses which can then crack the SiC, so direct crack propagation is not necessary for the IPyC to fail the SiC. While this conclusion of IPyC damage leading to SiC damage seems likely, the data are not conclusive since only a two-dimensional (2-D) view of the particle was observed. The data obtained here do not provide the required evidence to finally resolve this issue but do buttress the argument. The interested reader may wish to examine Appendix D.

4.7 SCANNING ELECTRON MICROSCOPY

4.7.1 Introduction

Five particles from HRB-21 compact 5C were examined. The particles were labeled 5C fertile, 5C-P1, 5C-P2, 5C-P11, and 5C-P15. These particular particles were studied by SEM techniques to determine differences in the coating layers (remaining) and in the kernel between the fertile and fissile particles and between the retentive (5C-P11 and 5C-P15) and nonretentive (5C-P1 and 5C-P2) particles, and the fission product distributions in the coatings and kernels of the different particles.

Prior to polishing, compact 5C was electrolytically deconsolidated. The separated fuel particles were examined by gamma spectral analysis in the IMGA in order to determine fission product retention. The ratio of Cs to Ce is indicative of the particle's ability to retain fission products. The test showed that particles 5C-P11 and 5C-P15 were fission product retentive, whereas particles 5C-P1 and 5C-P2 were nonretentive. See Sect. 4.5 for further discussion of the IMGA procedure and results.

The fertile particle, containing a ThO_2 kernel, was sufficiently low in activity that it could be removed from the hot cell with no further preparation. In order to reduce the radiation level for most of the fissile particles to permit examination in an unshielded SEM, the particles were remotely ground and polished to a level below the kernel. This was not necessary for particle 5C-P2, which was polished approximately to the mid-kernel level. For other particles, difficulties in monitoring remote polishing resulted in different layers

remaining. In the case of 5C-P1 and 5C-P15, a small portion of the kernel remained surrounded by the buffer layer, IPyC, and SiC layers. In the case of 5C-P11, only the IPyC and SiC remained.

4.7.2 Scanning Electron Microscopy Method

The SEM uses a very sharply focused electron beam (EB) that is scanned over the specimen, which can be a fuel particle itself, or a fuel particle that has been metallographically mounted and polished. In either case, the specimen is made conducting by depositing a thin layer of carbon, or another conducting material, on the specimen to provide electrical continuity between the specimen and ground through the specimen stage.

A cathode ray tube (CRT) is scanned in synchronism with the scanning EB. The ratio of the distance covered on the CRT to that covered on the specimen is the magnification. The signal supplied to the CRT is determined by the analysis desired. An EB causes several effects upon interacting with a specimen surface. One effect is the release of electrons (secondary electrons) from the specimen. These electrons are of low energy, and their emission rate is very sensitive to the distance from the surface at which they originate and thus to the surface topography. Secondary electrons are the most common signal [secondary electron imaging (SEI)] used for SEM.

Some of the electrons that strike the specimen are back-scattered. The back-scattered electrons (BSE), which are scattered proportionally to the electron density in the specimen surface (i.e., proportionally to the atomic number of the elements doing the scattering), can also be used as the signal for SEM imaging. Either SEI or BSE is capable of producing high-magnification images with high resolution and great depth of field.

Excitation of the specimen atoms by the EB also results in characteristic X-ray radiation. Since the energy of the emitted X rays is characteristic of the atom that emits the photon, the X-ray signal can be used for elemental analysis. A signal produced by a specific energy X-ray photon can be used to produce a map (an X-ray map) of a particular element. This is the mode that primarily was used in the analysis of the fuel particles.

Two analytical methods were used to examine the particles. The first was energy-dispersive spectroscopy (EDS) that employs a scintillation detector which produces an electrical pulse proportional to the energy of the X-ray photon that strikes the detector. This method was used to make a general determination of the elements present. A typical spectrum, from particle 5C-P1, is shown in Figure 4.82. The method of wavelength

ORNL-DWG 93-13493

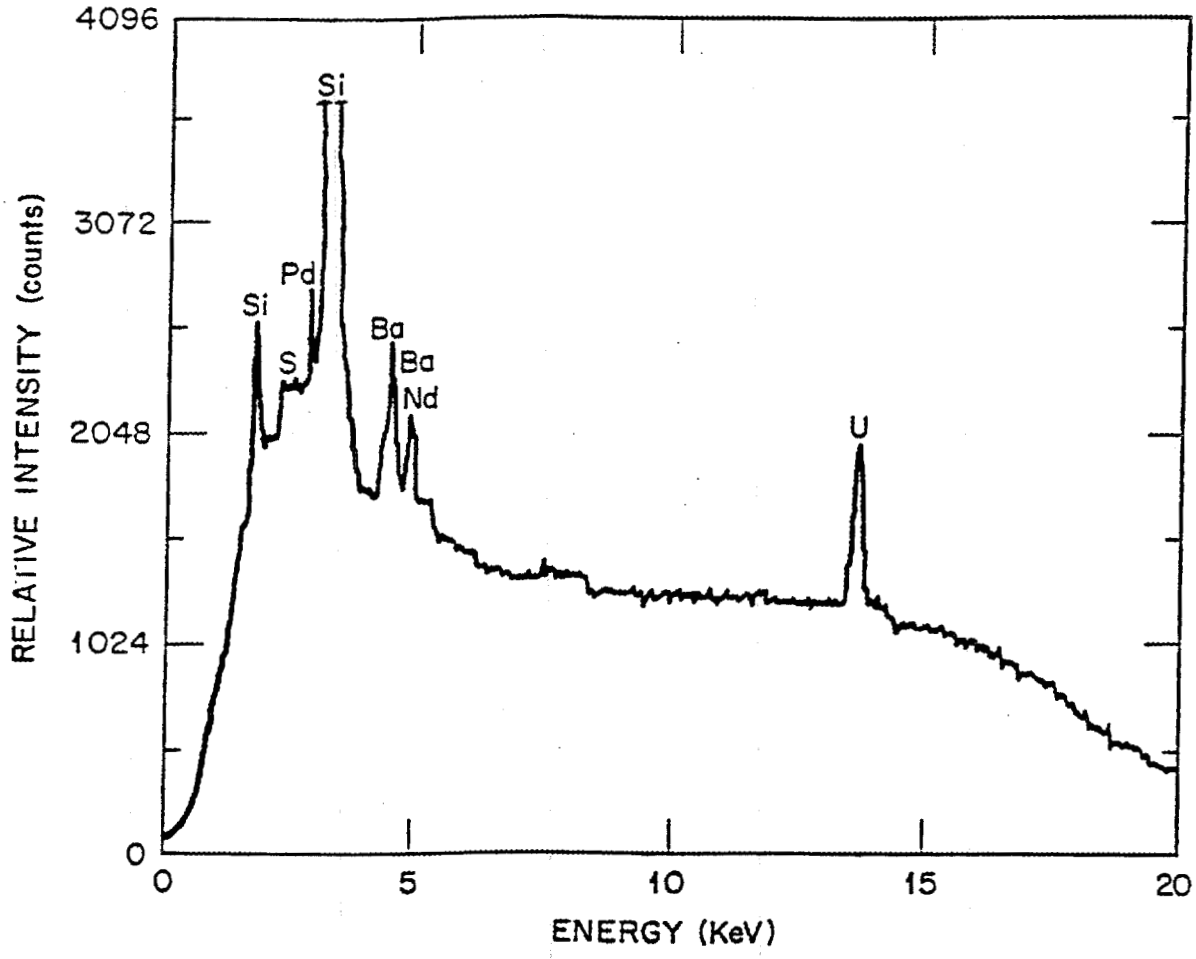

Figure 4.82.

ENERGY DISPERSIVE X-RAY SPECTRUM FROM THE REGION OF THE KERNEL IN PARTICLE 5C-P1. MAJOR PEAKS ARE LABELED WITH THE ELEMENT OF ORIGIN.

dispersive spectroscopy (WDS) was used to determine the distribution of elements within the fuel particle. This method uses a focusing single crystal with the spacing between diffracting planes chosen so that only X rays of specific wavelength are diffracted and reach the detector. This method is not susceptible to saturation by background from radioactive samples (as is the EDS method) and generally gives a higher signal-to-noise ratio than does EDS.

Since, in both cases, the EB is scanned over the surface of the specimen, either method of analysis can produce an X-ray image or map.

4.7.3 Scanning Electron Microscopy Results

Primary emphasis was placed on the integrity of the SiC coating layer. Particular emphasis was placed upon examination of cracks in the SiC and of any surface features present. Attempts were made to determine the distribution of fission products, especially with respect to cracks or porosity in the SiC coatings, and to the morphology of cracks in the SiC.

Most of the SEM photographs that follow were taken in a mode to optimize the X-ray signal (with a broad, high-intensity EB) resulting in lower resolution than can normally be obtained with an SEM. An EDS spectrum can show any element present at a particular position on the specimen in a short time. This method was, therefore, the first that was used for examination of a particle. Common fission products typically appear in the EDS spectrum as well as a large Si peak (from the SiC coating). In some cases, Cl, a remnant of the chemical vapor deposition process used to produce the SiC coating, was detected in the SiC. The elements Fe, Cr, Ni, and Cu sometimes appeared, probably the result of stainless steel and copper or brass either in the process line for manufacture of the particles or from the SEM itself. Careful attention was paid to elements such as Ag, Ba, Ce, Cs, I, La, Pd, Sr, and U. In many cases, only weak signals were obtained, which were homogeneous in origin from the specimen and difficult to distinguish from noise. In Figure 4.82, the EDS from a section of the non-retentive fissile particle 5C-P1 is shown. This spectra was taken from an area including part of the SiC coating and part of the adjacent IPyC layer. As expected, a strong Si peak is observed with fairly strong U and Ba peaks, weaker Nd and Pd peaks, and very weak S peaks.

The elements Ba, Ce, Cs, and Pd often produced strong signals from which elemental distributions could be determined, qualitatively, from X-ray maps for the particular element

of interest. Only a few such X-ray maps will be included in this report because they show almost no contrast after reproduction, although contrast can be observed in the original negatives or positives.

It must be remembered that, with the exception of the fertile particle, only a single plane through the particle was examined. A particle could have a large breach in the SiC that would not appear in the polished plane of the specimen. The cracks observed in the polished plane could have occurred during irradiation but could also have occurred during the metallographic mounting, grinding, and polishing operations. Since it is possible that such cracks could have started, during irradiation, from existing microcracks or regions of fission product interaction, they were examined in detail.

4.7.3.1 Particle 5C-Fertile

The fertile particle was removed from the hot cell, following IMGA analysis, without metallographic mounting or polishing. Only the SiC and inner layers remained on the particle. Due to extensive cracking during irradiation, the PPyC and OPyC coatings came off during deconsolidation. For this particle, part of the SiC and IPyC coatings also chipped off, making the buffer layer visible, as shown in Figure 4.83. The fracture surfaces were examined for fission fragments and impurity elements. As indicated in Table 4.31, only Fe and Cr were found on the SiC fracture surface (inside and on the outer surface of the coating) in a nonuniform distribution when Fe and Cr K-spectra X-ray maps were made by WDS.

4.7.3.2 Particle 5C-P1 Fissile

Figure 4.84 is a low-magnification photomicrograph of the polished surface of the particle showing the kernel (at the center of the particle) and the surrounding layers out to and including the SiC. Large cracks in the IPyC and the delamination of the IPyC, both visible in this figure, were examined carefully for segregation of fission products and impurities. No segregation at the crack tips or fracture surfaces was found.

Fission products, however, were found outside the kernel, as shown by the EDS spectra discussed in Sect. 4.7.3 and by wavelength dispersive studies. From Ba X-ray maps, Ba was found in the buffer and IPyC but did not appear to penetrate the SiC. Segregation at the IPyC-SiC interface also was found. By contrast, Pd penetrated the SiC layer about 25% and appeared to concentrate in the SiC in preference to the IPyC. This phenomenon

YP17095

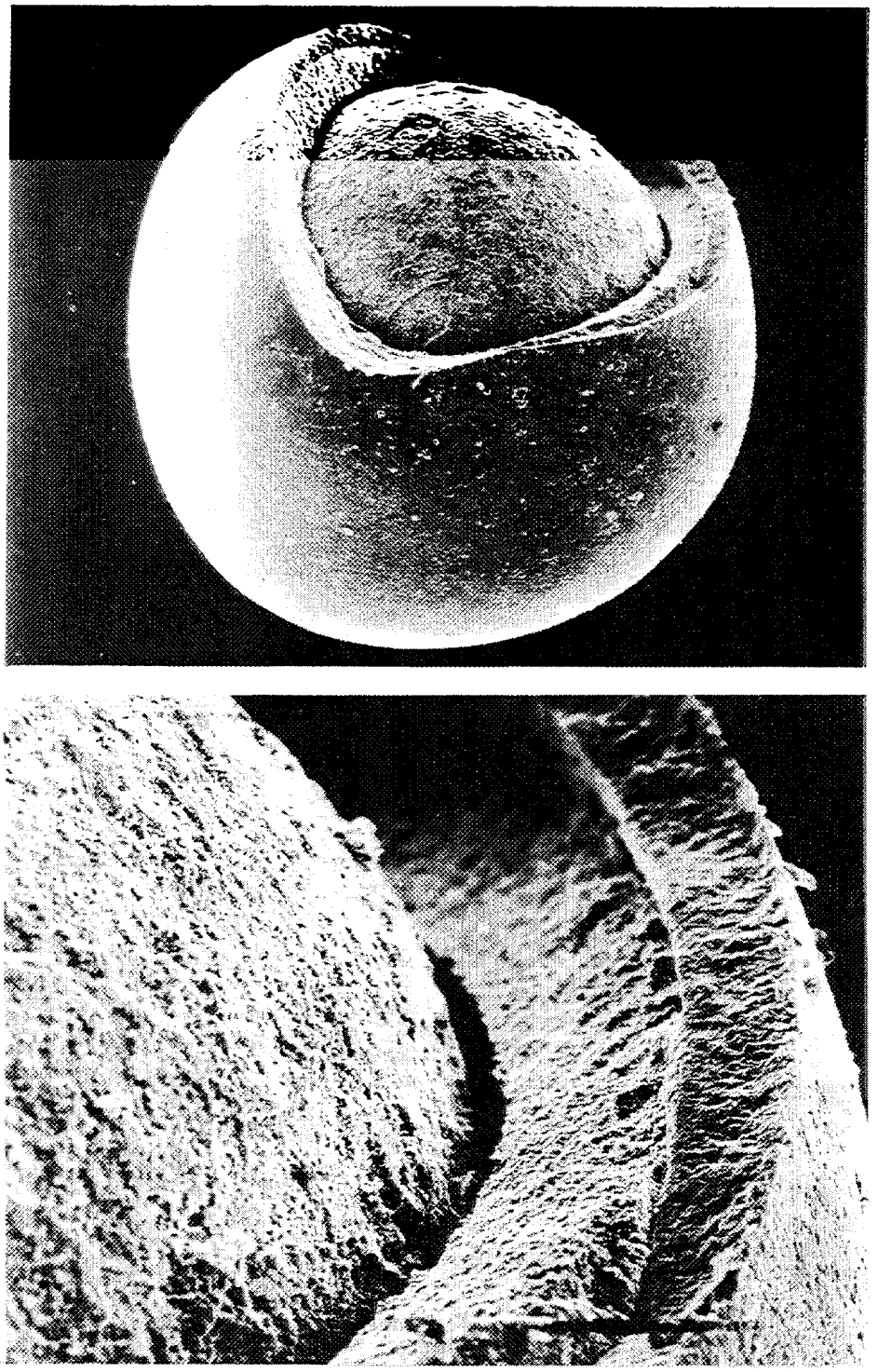

Figure 4.83.

FERTILE PARTICLE 5C. THE ABOVE VIEW SHOWS THE ENTIRE PARTICLE, AND THE BOTTOM IS A CLOSEUP OF THE DAMAGED AREA.

Table 4.31.

ELEMENT DISTRIBUTION IN THE PARTICLES

Element	5C - fertile SiC - IPyC - buffer - kernel	5C - P1 fissile non-retentive SiC - IPyC - buffer - kernel	5C - P11 fissile retentive SiC - IPyC
Ba		In IPyC and buffer does not penetrate SiC	
Pd		Penetrates ~ one-fourth into SiC concentrated in SiC	Weak signal in SiC and IPyC
Cs		Uniform in buffer and IPyC	Uniformly weak in SiC and IPyC
Ce		Penetrates ~ one-half through SiC concentrated in SiC	
Ag			Nonuniform in SiC
La		In IPyC - weak signal	
Fe	Nonuniform on SiC fracture surface		
Cr	Nonuniform on SiC fracture surface		
Th	Uniform in buffer		

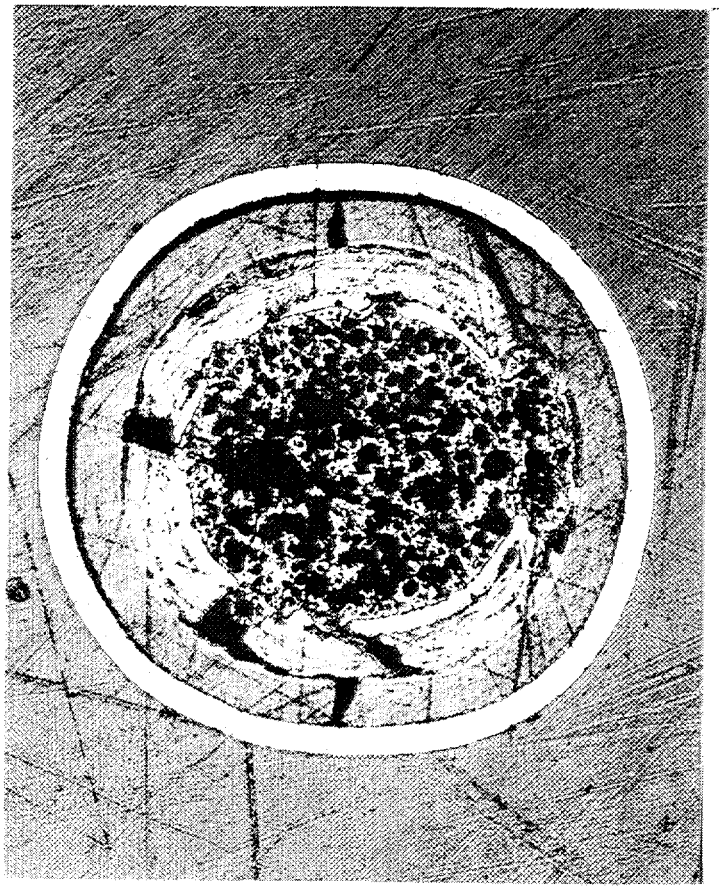

Figure 4.84.

CROSS SECTION OF NONRETENTIVE PARTICLE 5C-P1 FISSILE. THIS PARTICLE WAS DECONSOLIDATED FROM COMPACT 5C AND PROCESSED THROUGH IRRADIATED-MICROSPHERE GAMMA ANALYZER. PARTICLE P1 RELEASED ~80% OF Cs DURING IRRADIATION. NO SiC CRACKS VISIBLE. LARGE AMOUNT OF KERNEL SWELLING (~ 3X UNIRRADIATED VOLUME).

is shown in Figure 4.85. Cesium was detected in the buffer and IPyC but was uniformly distributed. Cerium behaved in a manner similar to Pd in that it penetrated the SiC, about halfway through. It also appeared to concentrate, to a small degree, in the SiC compared with the IPyC. Both Pd and Ce have been shown to react with SiC to form stable silicides.[4-21,4-22] The formation of silicides could be responsible for the concentration in the SiC. La was also detected in the IPyC, but no segregation was observed, and the signal was not strong enough to permit determination of the distribution.

Since particle 5C-P1 was a nonretentive fuel particle (for Cs), one would expect to see failures in the SiC coating. As Figure 4.84 shows, there were large cracks in the buffer layer and in the IPyC coating, but no through-coating cracks in the SiC were observed in this cross section. However, some porosity is observed, and that at 12 and 2 o'clock may have been due to cracks that penetrated the coating at a higher or lower level.

4.7.3.3 Particle 5C-P2 Fissile

This particle also was found, from IMGA studies, to be a particle that had not retained Cs. Therefore, one would expect to find through-wall cracks in the SiC coating. Such cracks, as well as several cracks in the IPyC and in the buffer, were observed in optical metallographic studies of this particle (see Figure 4.86); therefore, this particle was studied in more detail by SEM studies. Figure 4.87 is a secondary electron SEM picture of the same cross section and shows that the several through-wall cracks in the SiC are not exactly in the radial direction. The pairs of cracks at about 4 and 7 o'clock in Figure 4.87 were studied at higher magnifications, as shown in Figures 4.88 to 4.90. (The material outside the SiC coating and between the IPyC and SiC coatings in these pictures is plastic mounting material.)

Figure 4.90 shows one of the cracks in Figure 4.89 at 850× magnification. Several flaws in the SiC are seen in this picture, leading one to believe that the crack might run through some flaws and might start at such a flaw. However, there was no direct proof of this expectation. Also, the crack in Figure 4.90 appeared to start at the outer surface, but another possibility was that it ran above or below the plane of this cross section at the inner surface. In Figure 4.91, additional flaws in the SiC coating are shown, one of which appears to be the start of a crack.

Attempts were made to find fission products and any other foreign elements in the cracks in the SIC, but only spectra from Si were observed. Therefore, it is not probable that

0067

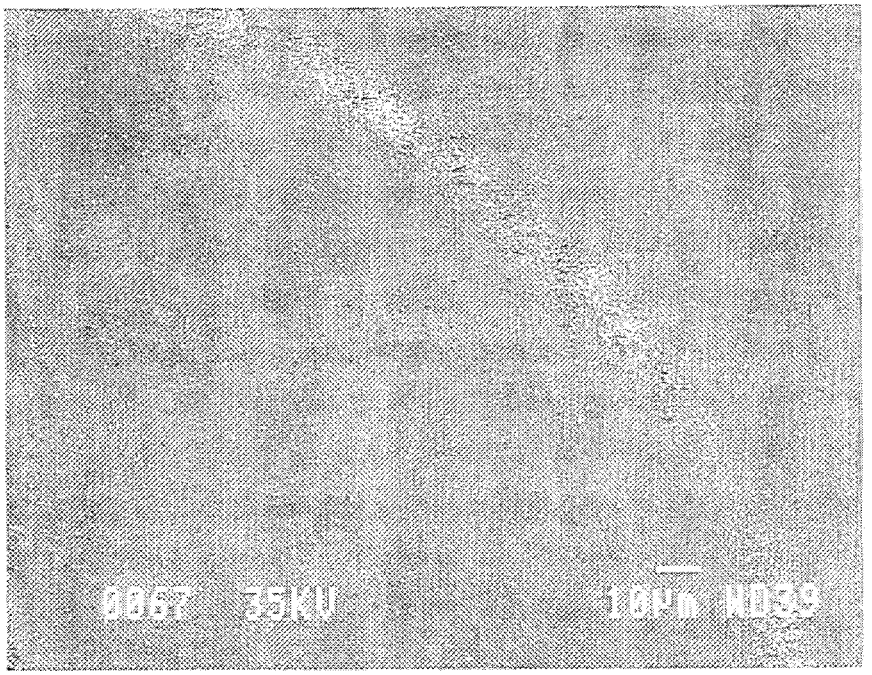

0065

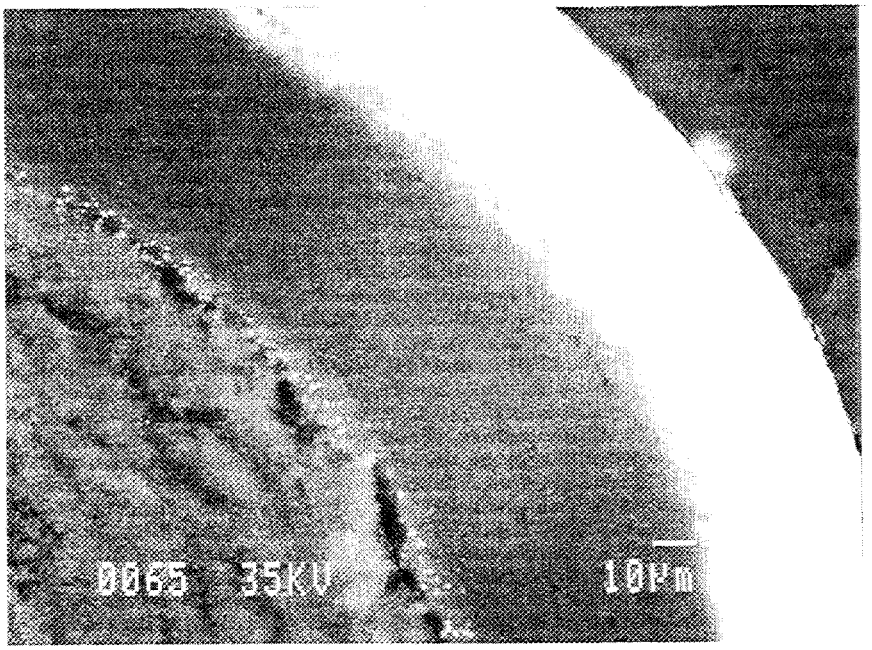

Figure 4.85.

PALLADIUM X-RAY SCAN OF THE OUTER REGION OF NONRETENTIVE PARTICLE 5C-P1 FISSILE SHOWING CONCENTRATION OF PD IN THE SIC LAYER. THE LIGHT SPECKS AT THE BUFFER-IPYC INTERFACE COULD NOT BE ASSOCIATED WITH THE SEGREGATION OF ANY ELEMENT.

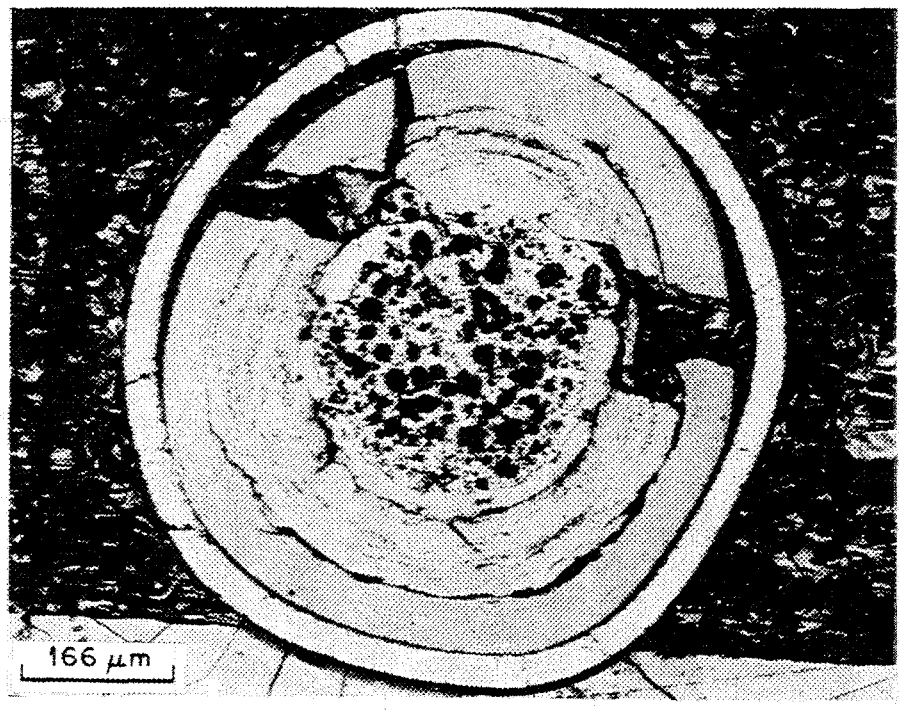

Figure 4.86.

PHOTOMICROGRAPH OF A CROSS SECTION OF THE NONRETENTIVE FUEL PARTICLE 5C-P2 FISSILE.

the through-wall cracks in the SiC were due to corrosion (from fission products); the cracks appear to be brittle in nature (as would be expected for SiC) and mechanical in origin.

X-ray maps for several elements in the kernel region were made for this particle with the following results: U, Ce, La, Nb, and Zn remained concentrated in the kernel, although some Ce, La, and Nb migrated into the buffer. Much more Cs migrated into (and, probably, through) the buffer.

4.7.3.4 Particle 5C-P11 Fissile

This particle was identified as a retentive particle by IMGA analysis. The particle was ground below the kernel and, in the process, the buffer was lost. Only the SiC and the IPyC remained in the specimen after mounting and coating with carbon. Apparent grain boundaries were observed in the SiC; a significant effort was made to search for elemental segregation along the grain boundaries, but none was detected.

YP21343

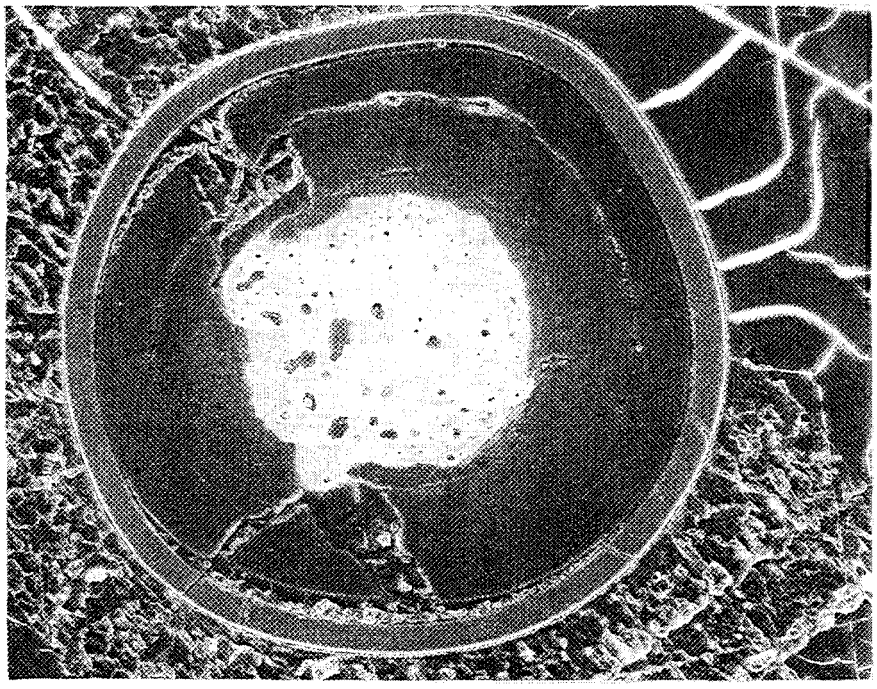

Figure 4.87.

SCANNING ELECTRON MICROSCOPY (SECONDARY ELECTRON IMAGE) OF NONRETENTIVE PARTICLE 5C-P2 FISSILE, AT ~ 125X.

The SEM analysis detected a very large difference in fission product concentrations between the two particles. As described in Sect. 4.7.3.2, 5C-P1 showed distinct concentrations of fission products, especially Ba, Pd, and Ce (see Table 4.31). In contrast, all signals were very weak in particle 5C-P11. No X-ray map of Ba could be obtained from 5C-P11, and only a weak signal of Pd could be obtained. Cs also was very weak and, like Pd, was uniformly distributed. Ce could not be positively identified in the specimen. Ag, however, was found nonuniformly distributed in the SiC; it was more highly concentrated in the IPyC and in the inner third of the SiC layer.

4.7.3.5 Particle 5C-P15 Fissile

This particle also was identified as a retentive particle by IMGA analysis. A photomicrograph of this particle at 125× magnification is shown in Figure 4.92. Although many scratches are seen in this picture, no cracks in the SiC or IPyC coatings are observed.

YP21344

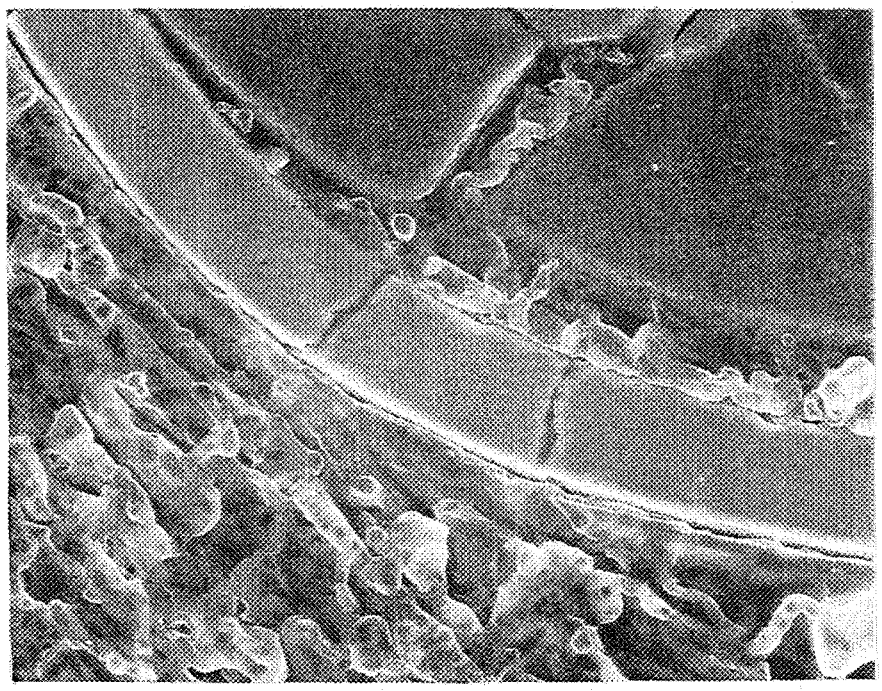

Figure 4.88.

SCANNING ELECTRON MICROSCOPY (SECONDARY ELECTRON IMAGE) PICTURE OF NONRETENTIVE PARTICLE 5C-P2 FISSILE SHOWING 7 0'CLOCK CRACK (~ 300X).

There are large cracks in the buffer, and only a small amount of kernel material is seen (this particle was polished to well below the midplane of the particle).

Some nonhomogeneous heavy-element segregation at the IPyC/SiC interface was observed for this particle. Figure 4.93 is a BSE image, at 1000× magnification, indicating such heavy-element segregation. Figure 4.94 is a Pd Lα X-ray image of this same area which shows Pd segregation. To a lesser extent, Ce and U also were concentrated in this region, extending into the IPyC, with lesser penetration of the SiC.

4.8 LEACH-BURN-LEACH MEASUREMENTS

The determination of the fraction of failed coatings in the HRB-21 compacts is very important in assessing the irradiation performance of the particle fuel. The LBL method is used routinely as a quality assurance test to determine the failed SiC layer fraction in unirradiated fuel particles. This method consists of leaching the fuel compact with an acidic

YP21345

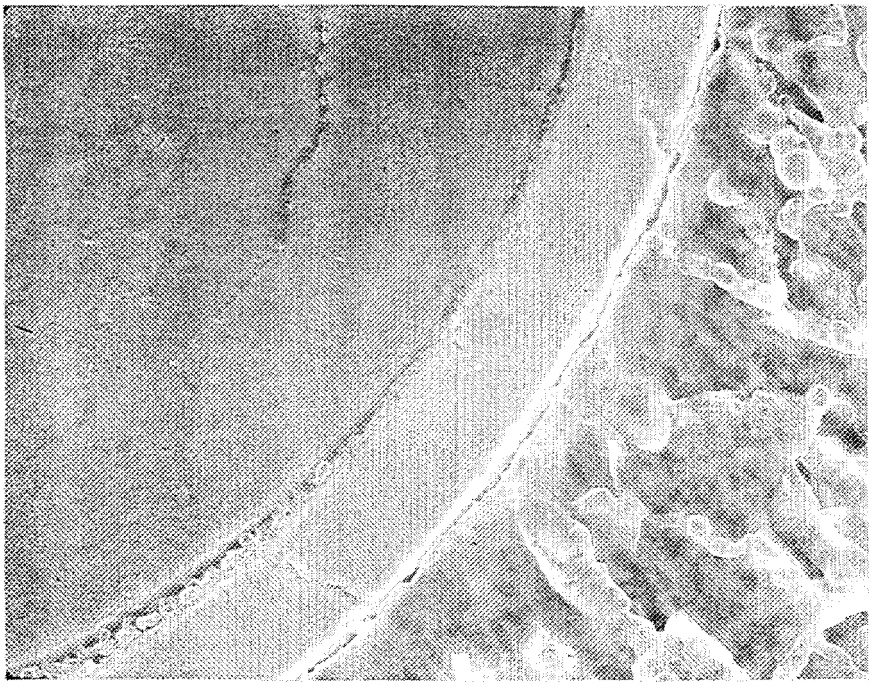

Figure 4.89.

SCANNING ELECTRON MICROSCOPY (SECONDARY ELECTRON IMAGE) PICTURE OF NONRETENTIVE PARTICLE 5C-P2 FISSILE SHOWING 4 0'CLOCK CRACK (~ 300X).

solution, oxidizing the compact, and leaching again. During the first leach step, the exposed fuel kernels and any HM contamination of the compact matrix material are extracted. The carbonaceous components of the compact matrix, as well as the OPyC on the particles, and the inner carbonaceous layers in particles having defective SiC are removed by oxidation in the "burn" step. The second leach removes the kernels in the particles which had defective SiC layers but had the IPyC intact.

The LBL test was completed on two compacts from HRB-21 (5B and 7C) following the procedures specifically developed to allow the test to be conducted in the ORNL hot cell at the IFEL.[4-23,4-24] Before the "burn" step, the compacts were leached twice for 12 to 18 h with 100 mL of a boiling solution containing 14 M HNO_3 and 0.03 M HF acids (see Figure 4.95). The burn step was then conducted inside the temperature-controlled cavity of a muffle furnace (NEY6-160A). This furnace was equipped with an exhaust fan which pulled air through the furnace at a rate sufficient to exchange the cavity atmosphere 2 to

YP21346

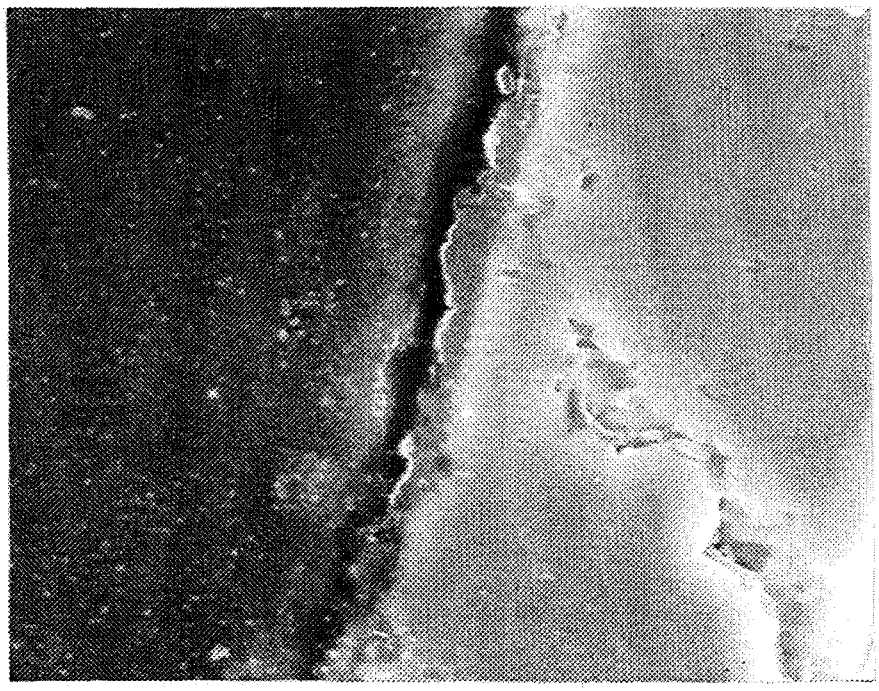

Figure 4.90.

HIGHER MAGNIFICATION (850X) SCANNING ELECTRON MICROSCOPY (SECONDARY ELECTRON IMAGE) PICTURE OF THE 4 O'CLOCK CRACK IN 5C-P2 FISSILE.

4 times a minute. The furnace control TC was used to measure the cavity temperature. The nominal temperature was 750°C. The temperature gradient in the furnace was not measured, but the rated control is ±10°C.

After the "burn" step, the particles from compacts were leached with 25 mL of the boiling acid solution. Because of restrictions in the hot cell, the solutions were only boiled for up to 8 h each day. Thus, the compacts were exposed to the leach solution at ambient temperature for considerably longer than when being heated. Table 4.32 gives the total times used for each processing step.

The concentrations of the extracted elements were measured on diluted alliquots of each leach solution. Because of the presence of significant fission product activity, the concentration measurements were conducted at the ORNL Transuranic (TRU) Laboratory. The amount of uranium and thorium in the aliquots was first measured using α-spectroscopy. The uranium and thorium were then separated from the fission products by ion-exchange chromatography, and their concentrations were measured using an inductively coupled

YP21347

Figure 4.91.

SCANNING ELECTRON MICROSCOPY (SECONDARY ELECTRON IMAGE) PICTURE OF A REGION OF SiC CONTAINING SEVERAL FLAWS. PARTICLE 5C-P2 FISSILE, 800X.

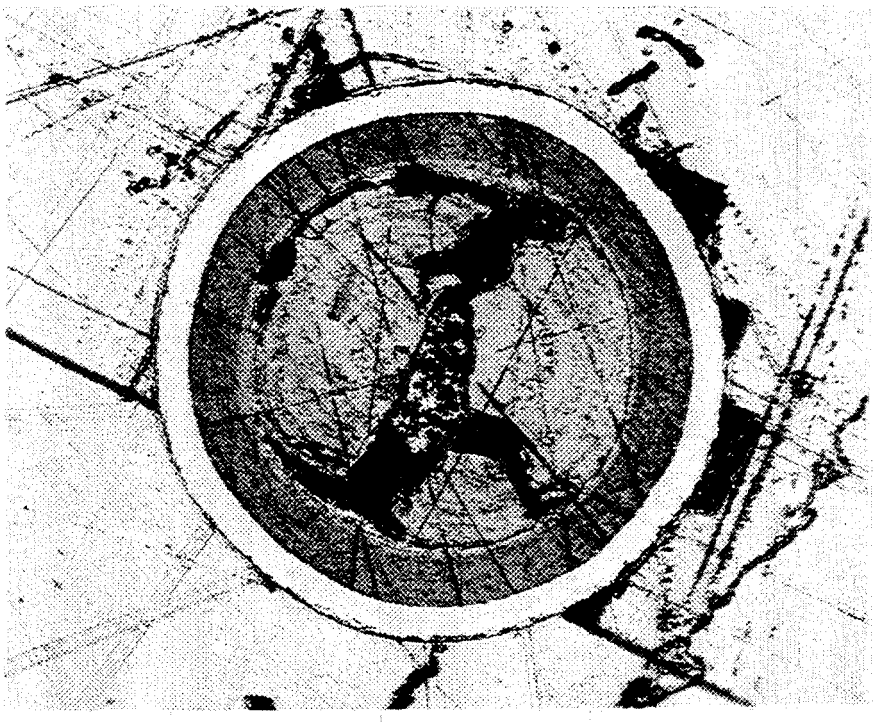

Figure 4.92.
PHOTOMICROGRAPH OF RETENTIVE PARTICLE
5C-P15 FISSILE (~125X).

plasma mass spectrometer (ICPMS). The ICPMS can detect quantities as low as 1×10^{-12} g. Fission product concentrations were measured by γ-ray spectroscopy.

The number of equivalent failed fissile particles that was extracted was calculated from the amount of ^{235}U, ^{238}U, and Pu in each leach solution based on the particle inventory calculated by the ORNL CACA2 computer code. Similarly, the number of equivalent failed fertile particles extracted was calculated from the ^{232}Th and the ^{233}U. The number of failed particles based on this analysis is given in Table 4.33.

The amounts of fissile and fertile kernel material in the leach solutions were dependent on the leach time. The equivalent number of failed particles is shown as a function of the total leaching time for the 5B compact in Figure 4.96 and for the 7C compact in Figure 4.97. The preburn results indicate that after irradiation significantly more of the 5B particles had completely failed coatings than did the 7C particles. Furthermore, there were more fissile particles with failed coatings than fertile particles with failed coatings, even though the ratio of fertile:fissile particles was 3.7 in 5B and 2.3 in 7C. The "preburn"

YP21348

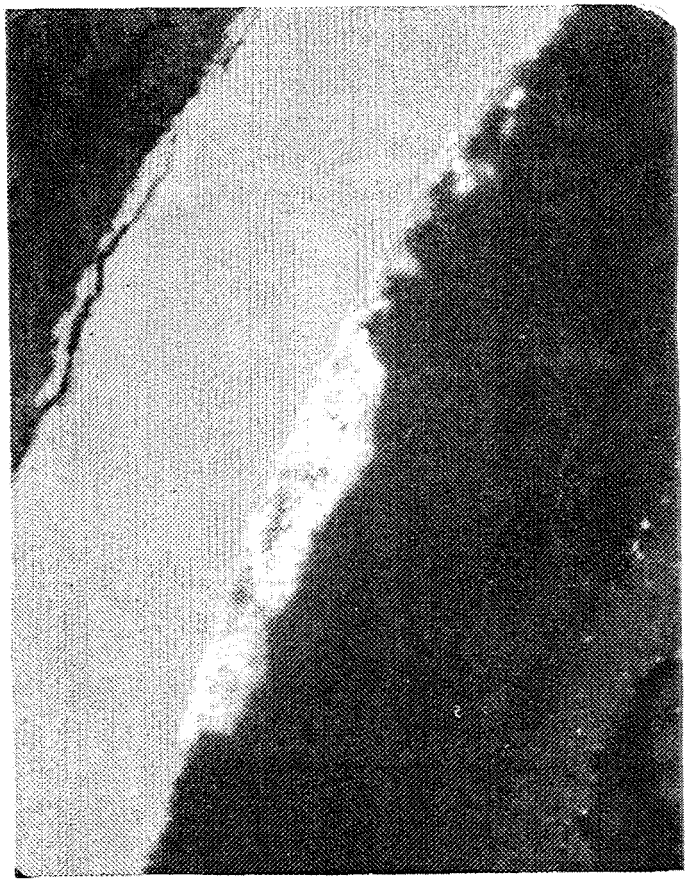

Figure 4.93.

SCANNING ELECTRON MICROSCOPY (BACK-SCATTERED ELECTRONS) IMAGE OF SiC/IPyC INTERFACE SHOWING SEGREGATION OF HEAVY ELEMENTS (1000X). PARTICLE 5C-P15.

YP21349

Figure 4.94.

LOCAL Pd L_α X-RAY MAP OF AREA SHOWN IN FIGURE 4.93 OF PARTICLE 5C-P15 FISSILE (1000X).

ORNL-DWG 95-5838

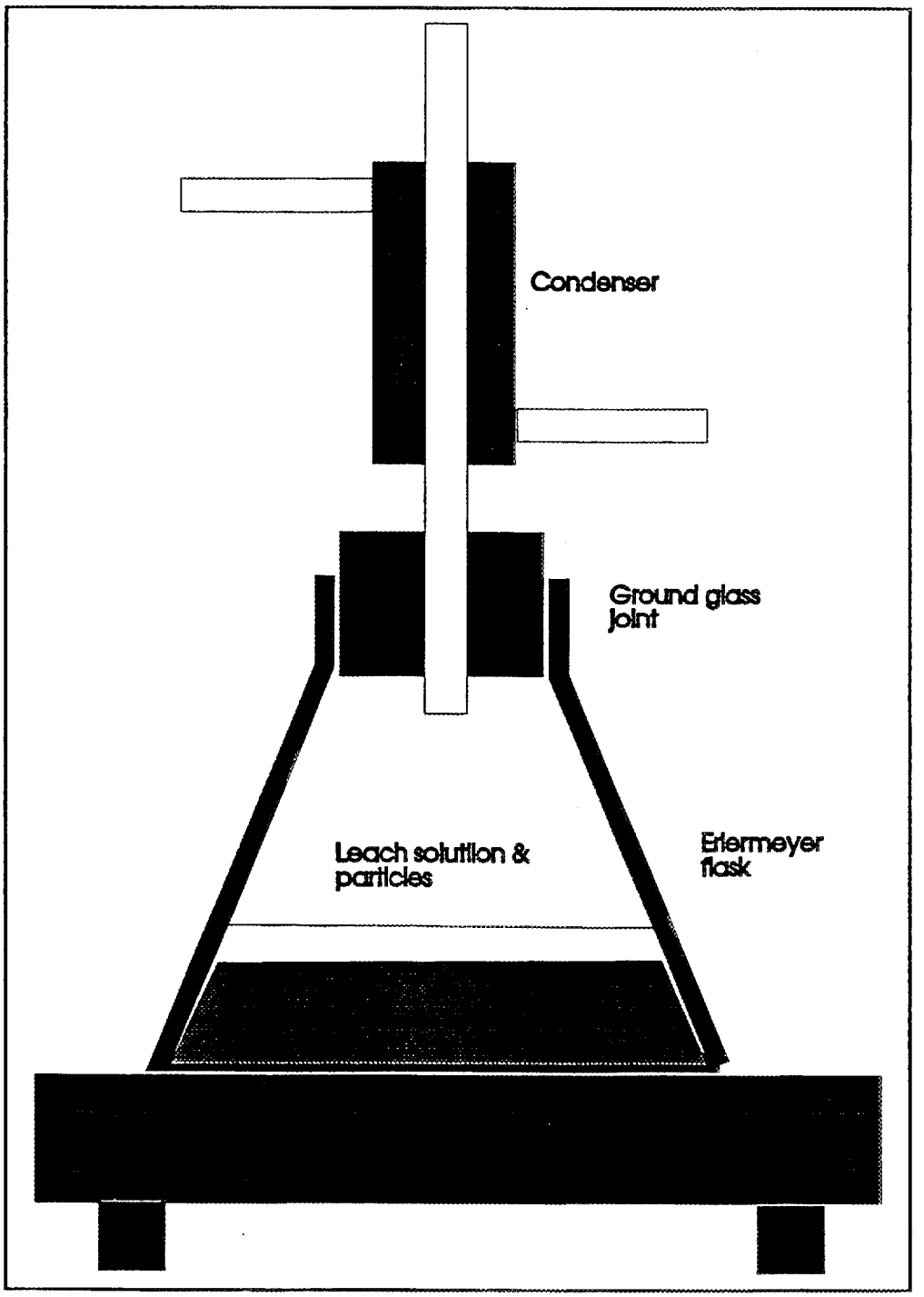

Figure 4.95.

HOT-CELL APPARATUS USED FOR LEACH-BURN-LEACH TEST

Table 4.32.

LEACH-BURN-LEACH PROCESSING TIME

Step	Total hot leach time (h)		Total cold leach (h)		Burn time (h)	
	5B	7C	5B	7C	5B	7C
leach	18.5	17.0	91	89.5		
leach	12.0	12.0	43.7	41.9		
burn					72	72
leach	12.1	12.0	39.7	115.0		
leach	12.4	12.0	18.8	41.5		
leach	12.0	12.0	13.0	95.6		
leach	12.0	12.0	25.3	91.2		
leach	11.8	12.0	91.9	95.0		
leach	12.0	12.0	89.9	25.8		
totals	102.9	101.0	537.4	595.4	72	72

ICPMS data show that the irradiation caused the SiC and all other coatings to fail and expose the kernel in 0.7% of the 5B fertile particles, which is higher than the 0% Cs release measured by IMGA for the 5C fertile particles. The "preburn" ^{238}U ICPMS data indicate the irradiation caused the SiC and all other coatings to fail and expose the kernel in 7.2% of the 5B fissile particles and 0.1% in 7C. IMGA analysis of 483 fissile particles from 5C showed 4.8% of the particles were low in cesium (see Table 4.11).

The "burn" step removes carbonaceous material from the compact matrix and, if the SiC layer has a crack larger than about 100 nm (ref. 4-25), removes the IPyC and buffer layers. The burn step exposed more fertile kernels than fissile kernels in both compacts. A larger number of 7C fertile particle kernels were exposed by the burn step than 5B fertile particle kernels. This suggests that the SiC in a fraction of the 7C fertile particles had failed, but the IPyC was intact after irradiation.

The multiple leach steps damaged the fissile particle SiC layer. Both Figures 4.96 and 4.97 show that the amount of fissile kernel material which was extracted in each leach solution increased after prolonged exposure to the solution. This was not the case for the

Table 4.33.

THE NUMBER OF FAILED PARTICLES IN HRB-21 COMPACTS BASED ON THE METHOD OF ANALYZING THE LEACH SOLUTIONS

Sample	Total leach time (h)	Incremental fissile particles failed Determined by:				Incremental fertile particles failed Determined by:		
		ICPMS[a]		α-Particle		ICPMS[a]		α-Particle
		^{235}U	^{238}U	^{239}Pu	^{238}Pu	^{232}Th	^{233}U	$^{233}U/^{229}Th$
5B/26-1/2	18.5	145.8	81.0	60.1	76.1	9.2	25.2	21.6
5B/26-2/1	30.5	9.4	5.1	7.8	10.7	4.0	4.5	3.7
Burn								
5B/27-1/1	42.6	22.2	7.4	5.5	11.9	41.7	39.0	62.1
5B/27-2/1	55.0	0.6	0.2	0.5	0.7	1.4	1.7	2.3
5B/27-3/1	67.0	2.2	1.1	5.5	8.6		0.6	4.9
5B/27-4/3	79.0	83.3	54.0	93.4	117.6		2.3	3.6
5B/27-5/3	90.8	312.5	182.3	140.2	179.9		8.1	0.0
5B/27-6/3	102.8	83.3	50.6	43.4	54.0		6.7	6.4
TOTAL		659.4	381.8	356.4	459.5		88.1	104.5
Failure fraction		0.55	0.32	0.30	0.38		0.022	0.026
7C/26-1/1	17.0	15.3	11.4	10.5	17.3	1.1	2.6	0.0
7C/26-2/1	29.0	1.2	1.1	2.3	2.5	0.8	1.8	1.7
BURN STEP								
7C/27-1/1	41.0	25.3	16.2	3.2	5.7	16.1	72.0	15.1
7C/27-2/1	53.0	0.0	0.1	0.0	0.0	0.3	0.7	0.0
7C/27-3/1	65.0	1.3	1.0	0.0	0.0		0.4	0.0
7C/27-6/1	77.0	0.1	0.1	0.0	0.0		0.4	0.0
7C/27-5/1	89.0	0.2	0.2	0.0	0.0		0.2	0.0
7C/27-4/1	101.0	10.1	6.5	7.7	11.7		1.4	1.2
TOTAL		53.4	36.7	23.6	37.2		79.4	18.1
Failure fraction		0.027	0.019	0.012	0.019		0.02	0.0045

[a]ICPMS=Inductively coupled plasma mass spectrometer.

ORNL-DWG 95-5839

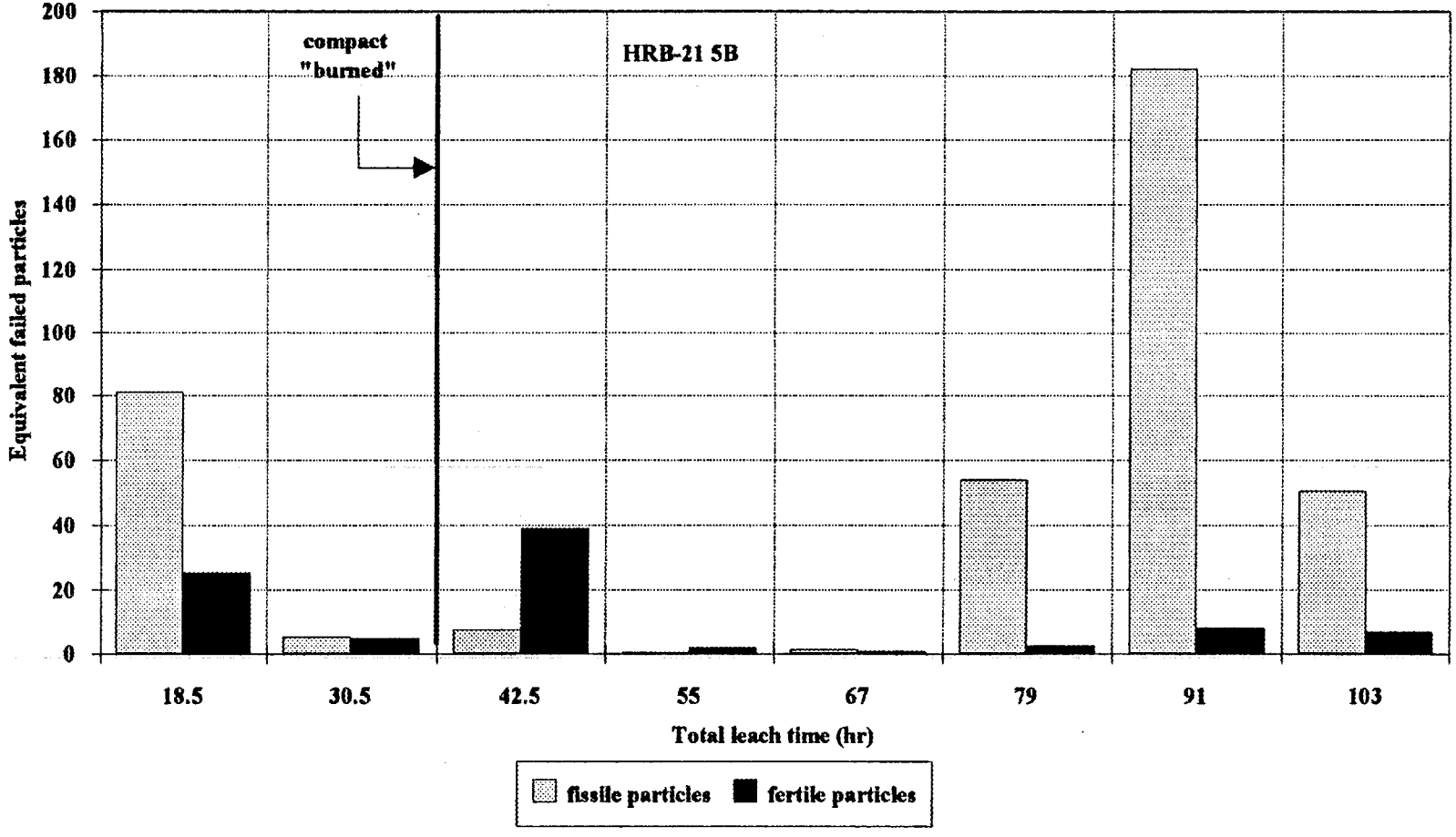

Figure 4.96.

EQUIVALENT NUMBER OF FAILED PARTICLES EXTRACTED FROM COMPACT 5B IN LEACH-BURN-LEACH TEST AS A FUNCTION OF THE TOTAL EXTRACTION TIME.

ORNL-DWG 95-5840

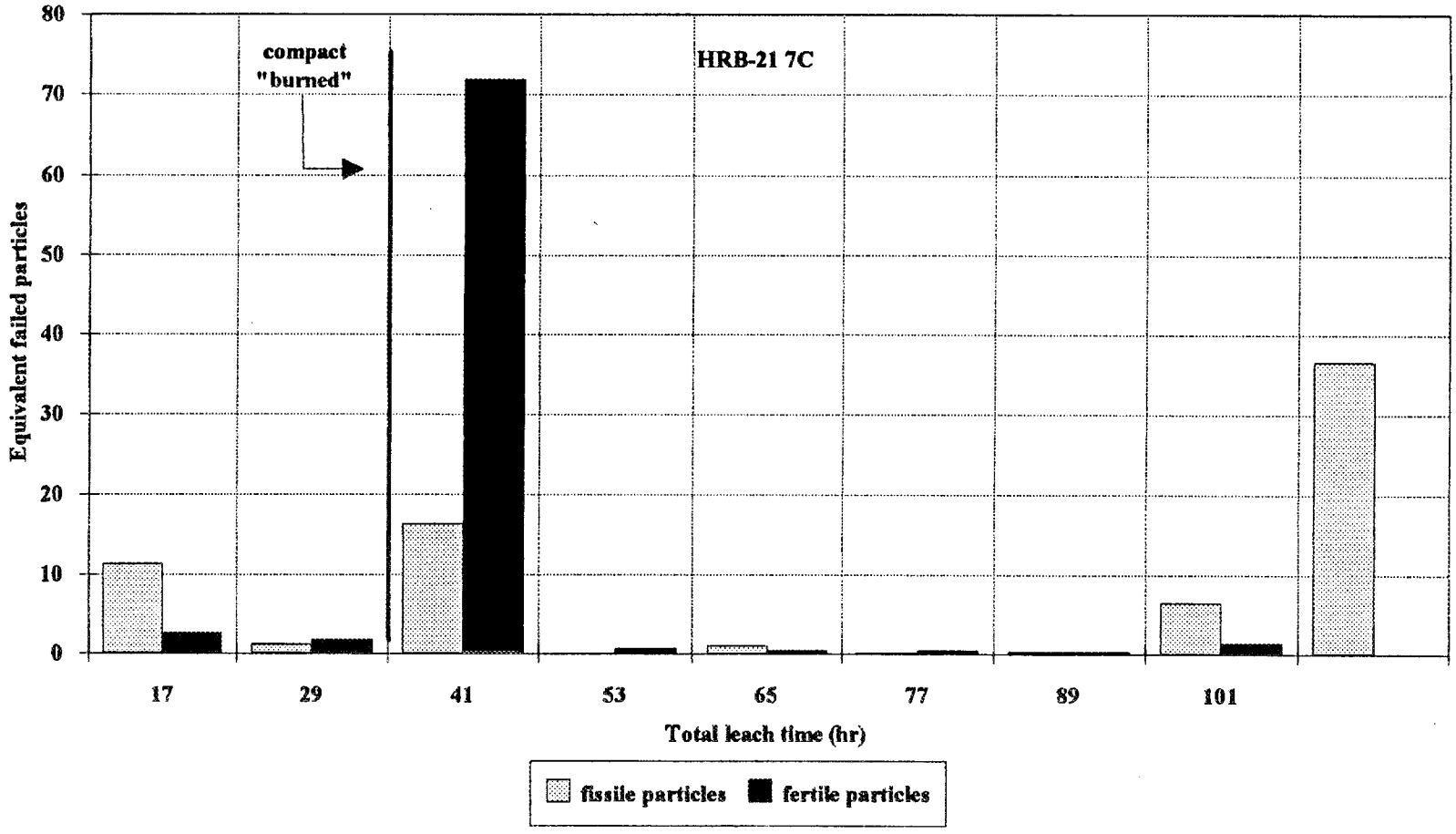

Figure 4.97.

EQUIVALENT NUMBER OF FAILED PARTICLES EXTRACTED BY LEACH-BURN-LEACH TEST IN COMPACT 7C AS A FUNCTION OF THE TOTAL LEACH TIME.

fertile particles. The prolonged exposure caused greater damage to the 5B fissile particles than to the 7C fissile particles. The reason for this is unknown and unexpected. Compact 5B saw a higher fluence than did 7C, but the SiC is not expected to significantly degrade because of fluence (at these levels).

4.9 COMPARISON OF POSTIRRADIATION EXAMINATION TECHNIQUES AND ESTIMATES OF UNCERTAINTY

Several PIE methods have been used to measure the coating failures in particles from HRB-21 compacts. Hobbins[4-26] has reviewed the PIE data and has reported the failure fractions as determined by each method in Table 4.34. For fissile particles at the higher burnup and fluence, there is good agreement among IMGA, LBL, and metallography as long as the leaching times are not excessive. The large fraction of exposed kernels is confirmed by the TRIGA results. Agreement is not as good for fertile particles; some of this discrepancy may be due to the fact that the ThO_2 kernels retain cesium much better than the fissile kernels at the HRB-21 irradiation conditions. As the burnup and fluence drop, the agreement is not as good. This may be an indication of the sensitivity of the techniques, the suboptimal state of the techniques, or failures in data interpretation.

At the present time, the absolute accuracy of the above techniques is unknown. Several conclusions may be drawn: (1) metallography gives reasonable values if the number of particles examined is in the range of 100 or more and the failure fractions are at the percent level; (2) IMGA gives reasonable values for the UCO particles with a sensitivity that depends on the kernel release properties; (3) IMGA may not work well with ThO_2 kernels because of cesium holdup; (4) LBL, if not carried to extremes, appears to work for UCO but may be low for ThO_2; and (5) TRIGA provides information on compact-to-compact variation.

Presently, there is no sound basis for the quantification of the uncertainty of the methods; however, one can define some rough guidelines from PIE experience. Metallography has a likely absolute uncertainty of the order of 10^{-2} of the total number of particles examined. This limit is from the inability to completely examine a particle and the possibility of particle damage occurring during ceramographic preparation. Thus, metallography is probably only useful for estimating failure fractions in low-quality fuel which has greater than 1% fuel failure. IMGA has a likely absolute uncertainty of the order of 10^{-4} of the total number of particles when used with particles that have minimum cesium

Table 4.34.

MEASUREMENTS OF PARTICLE FAILURE FRACTIONS IN HRB-21 COMPACTS.

Compact	Fast fluence, 10^{25}n/m^2	Burnup, % FIMA[a]		SiC failure fraction						Exposed kernel failure fraction				
				Fissile			Fertile			Fissile		Fertile		
		Fissile	Fertile	IMGA[b]	LBL[c]	Met[d]	IMGA[b]	LBL[c]	Met[d]	IMGA[b]	LBL[f]	IMGA[b]	LBL[g]	TRIGA
4C	3.5	22	2.2			0.05			0.05					
5B	3.5	22	2.2		0.078			0.017			0.072		0.007	0.06
5C	3.5	22	2.2	0.046			0.008			0.04		0.00		0.06
2A	2.3	18	1.2			0.00			0.00					
2B	2.3	18	1.2			0.00			0.03					
7C	2.3	18	1.2		0.015			0.019			0.006		0.001	0.01
1C	1.5	14	0.5			0.00								
8A	1.5	14	0.5	0.00			0.01		0.00					2E-5

[a]FIMA = Fissions per initial metal atom.

[b]IMGA = Irradiated-Microsphere Gamma Analyzer.

[c]LBL = Leach-burn-leach. LBL—Based on sum of particle failures measured by ^{238}U in leach solutions before burn and first leach after burn.

[d]Met = Metallography.

[e]Based on sum of particle failures measured by ^{233}U in leach solutions before burn and first leach after burn.

[f]Based on sum of particle failures measured by ^{238}U in leach solutions before burn.

[g]Based on sum of particle failures measured by ^{233}U in leach solutions before burn.

holdup. This limit is determined by the maximum number of particles that can be examined in a reasonable amount of time (roughly 10^4) and by the observation that a particle cesium loss of at least a few percent is necessary to confirm a failure. Thus, IMGA is useful for estimating failure fractions down to the 0.01% level if large numbers of particles can be processed through the equipment without problems. For smaller numbers of particles, the uncertainty would be roughly equal to the inverse of the number of particles examined.

The TRIGA testing was used to provide information on the fission-gas release so it cannot find a particle with intact pyrocarbons and damaged SiC. One would guess that the method would have an absolute uncertainty of the order of 10^{-4} to 10^{-5} of the total number of particles (for gas release), but this number is strongly influenced by the number of fissions that can be induced in the particles during testing and the release properties of the fuel. TRIGA is probably useful in conjunction with cesium release testing (see below). Finally, LBL probably has a best uncertainty near 10^{-5} to 10^{-6} of the total number of particles. Limitations of the technique come from damage to particles during compact deconsolidation (if done), damage to particles during the LBL process, and the analysis of the leach solution under hot-cell conditions. There is also some question as to whether LBL can find all the defects that lead to substandard performance.

LBL is probably the best candidate at present (that does not involve heating the particles) for examining high-quality fuel because it can handle the large number of particles required for analysis. IMGA can be used to locate the failed particles for further examination if the failure rate is not too small. Overall, the uncertainty bands for the PIE techniques are very broad, ill defined, and will require considerable examination and experimentation to obtain nuclear quality assurance (NQA-1) results. Cesium release testing by heating compacts or particles in a furnace and collecting the released cesium would help sort out the sensitivities of the methods because heating would best simulate the conditions under which release would take place in the reactor environment.

For the work done in this report, the reported values have considerable uncertainty because many particles were lost during PIE, and the examined sample is not truly representative of the compact particle population. Since the most friable particles were usually the ones lost, the failure estimate may be biased low. Nonetheless, the relative agreement among the different methods indicates that the reported values have an uncertainty within ±50%, at least for the high-exposure case.

The most serious problem with the PIE techniques is that there are no "good" and "bad" fuel samples that are well understood and which can be used for calibration and the development of procedures. Thus, none of the PIE techniques have the firm grounding that the program desires. This was not a problem for the HRB-21 capsule because the massive number of failures easily showed up with the use of any of the techniques, but when the program produces the desired fuel, none of the techniques may be able to provide quantitative measurements.

4.10 REFERENCES

4-1. "HRB-21 Capsule Disassembly, Visual Examination, and Component Metrology," Metals and Ceramics Division Procedure MET-FME-ESP-11, Rev. 0, Martin Marietta Energy Systems, Inc., Oak Ridge Natl. Lab.

4-2. "Modified ORNL Loop Transport Cask HFIR Underwater Loading Procedure," Research Reactors Division Procedure RRD-TP-23, Rev. 0, Martin Marietta Energy Systems, Inc., Oak Ridge Natl. Lab.

4-3. "Unloading Modified Loop Transport Cask 8S16-80," Metals and Ceramics Division Procedure MET-IFEL-OP-6, Rev. 0, Martin Marietta Energy Systems, Inc., Oak Ridge Natl. Lab.

4-4. "Disconnection of MHTGR Capsules from MIF Instrumentation," Engineering Technology Division Procedure ETD-IE-23, Rev. 0, Martin Marietta Energy Systems, Inc., Oak Ridge Natl. Lab.

4-5. "Gamma Scanning," Metals and Ceramics Division Procedure MET-FME-SOP-17, Rev. 0, Martin Marietta Energy Systems, Inc., Oak Ridge Natl. Lab.

4-6. "Determination of Diameters and Lengths of Cylindrical Objects Using Comparator Stand, Dial Gage, and V-Block," Metals and Ceramics Division Procedure MET-FME-SOP-9, Rev. 1, Martin Marietta Energy Systems, Inc., Oak Ridge Natl. Lab.

4-7. T. F. Hefferman, Capsule HRB-21 Pre-Irradiation Report, DOE-HTGR-88357, Rev. C, General Atomics, San Diego, Calif., April 1991.

4-8. "Dimensional and Weight Measurements on Fuel Compacts and Graphite Fuel-Holding Components," Metals and Ceramics Division Procedure MET-FME-SOP-04, Rev. 1, Martin Marietta Energy Systems, Inc., Oak Ridge Natl. Lab.

4-9. F. C. Montgomery, "HRB-21 Piggyback Capsule Disassembly," ORNL Fuel Materials Evaluation Group Special Procedure MET-FME-ESP-13A, Rev. 0, Martin Marietta Energy Systems, Inc., Oak Ridge Natl. Lab., December 6, 1993.

4-10. D. T. Goodin, M. J. Kania, and B. W. Patton, Experimental Plan for Irradiation Experiment HRB-21, DOE-HTGR-87091 (ORNL/TM-10987), Martin Marietta Energy Systems, Inc., Oak Ridge Natl. Lab., April 1989.

4-11. M. J. Kania and K. H. Valentine, The Irradiated-Microsphere Gamma Analyzer (IMGA) - An Integrated System for HTGR Coated Particle Fuel Performance Assessment, ORNL-5606, Martin Marietta Energy Systems, Inc., Oak Ridge Natl. Lab.

4-12. K. H. Valentine and M. J. Kania, IMGA Operating Manual, ORNL/TM-6576, Martin Marietta Energy Systems, Inc., Oak Ridge Natl. Lab.

4-13. R. N. Morris, MHTGR Fissile and Fertile Particle Burnup Determination by Gamma Spectroscopy, ORNL-TM-12310, Martin Marietta Energy Systems, Inc., Oak Ridge Natl. Lab., February 1994.

4-14. A. G. Gillespie, Internal Correspondence 846-AG-001-93, General Atomics, San Diego, Calif., March 1993.

4-15. B. F. Myers, Fission Product Transport in Reactor Experiments, HTGR-085-115, 908309, Rev. 0, Martin Marietta Energy Systems, Inc., Oak Ridge Natl. Lab., September 1985.

4-16. O. M. Stansfield, C. B. Scott, and J. Chin, "Kernel Migration in Coated Carbide Fuel Particles," Nucl. Technol. 25, 517-30 (March 1975).

4-17. Testing of Archived HRB-21 Capsule Fuel, DOE-HTGR-88554, Rev. N/C, November 1993.

4-18. O. M. Stansfield, SiC Corrosion in TRISO I Coated $(Th,U)O_2$ Particles, Gulf-GA-B12238, September 1972.

4-19. Fuel Particle Stress Analysis, CEGA-002883, Rev. 1, Combustion Engineering General Atomics, San Diego, Calif., October 1993.

4-20. N-MHTGR Fuel Particle Design Sensitivity Calculations, CEGA-002878, Rev. 0, Combustion Engineering General Atomics, San Diego, Calif., July 1993.

4-21. H. Grubmeier, A. Naoumidis, and B. A. Thiele, "Silicon Carbide Corrosion in High-Temperature Gas-Cooled Reactor Fuel Particles," Nucl. Technol. 35, 438-42 (September 1977).

4-22. H. Suzuki, T. Iseki, and T. Imanaka, "Reactions between SiC and Pd or CeO_2 at High Temperatures," J. Nucl. Sci. Technol. **14**, 438-42 (June 1977).

4-23. R. C. Martin, "Acid Leach of Fuel Compacts Prior to Burn," ORNL Procedure MET-FME-SOP-26, Rev. 0, Martin Marietta Energy Systems, Inc., Oak Ridge Natl. Lab., March 9, 1993.

4-24. R. C. Martin, "Burn/Leach of Fuel Compacts," ORNL Procedure MET-FME-SOP-27, Rev. 0, Martin Marietta Energy Systems, Inc., Oak Ridge Natl. Lab., April 26, 1993.

4-25. B. F. Myers, An Assessment of the Methods for Determining Defect of Failure Fractions in HTGR Coated Particle Fuels and Their Relationship to Particle Microstructure, ORNL/TM-10805 (DOE-HTGR-88260), Martin Marietta Energy Systems, Inc., Oak Ridge Natl. Lab., April 1989.

4-26. R. R. Hobbins, "Measurement of Coating Failures in Recent MHTGR Irradiations," Letter to HRB-21 Coordination Group, April 6, 1994.

SECTION 5

FUEL PERFORMANCE EVALUATION

5.1 COATED PARTICLE PERFORMANCE

The fuel design used in HRB-21 and NPR-1/1A/2 was different from other fuel tests in the United States because of two design changes. The first design change introduced the PPyC coating which was successful in achieving the desired low level of HM contamination and low fission-gas release from fuel compacts. Its merit was to reduce fuel damage during the compacting process. The achieved fission-gas release rate of $<5 \times 10^{-8}$ R/B ^{85m}Kr was lower than prior U.S. capsules and similar to German irradiation tests. The second design change was an increase in IPyC thickness from 35 to 50 μm in an attempt to reduce detection of defective SiC fraction produced during coating. This was also successful in reducing the fraction of defective SiC coatings detected. Detected defects were less than 3×10^{-5} for both HM contamination and SiC defects.

Unfortunately, the unknown price of this excellent preirradiation performance was early fuel failure. The performance of HRB-21 and those capsules with HEU fuel irradiated in the same time frame (NPR-1/1A/2) was similar and distinguished from previous experience by a rapid increase in fuel coating failure and fission-gas release at a fast neutron exposure beginning at 0.7×10^{25} n/m^2. This is far below the expected fast neutron fluence for such high levels of fuel failure. The release rate for HRB-21 increased during the remainder of irradiation until it reached about 2×10^{-4} R/B ^{85m}Kr at the peak fast neutron exposure of 3.5×10^{25} n/m^2.

A review of the previous HTGR Program test capsules was conducted to determine if such behavior was ever seen in the past. Coating failure in other capsules may have also occurred at low fast neutron fluence, but it may have been obscured by a high level of initially exposed fuel kernels. Such poor irradiation behavior had been observed in a prior experiment, SSL-1, where nearly 100% failure of OPyC early in irradiation was coupled with a high level of as-manufactured defective SiC coatings (6 to 10%) (refs. 5-1 through 5-3). In the case of capsule HRB-21, the PIE showed that failure of the PPyC and OPyC began at low fast neutron fluence and approached 100% at peak exposure, much like the SSL-1 experience. However, fuel characterization work at GA has shown that the as-manufactured SiC coating defects were no more than 3.3×10^{-4} fraction[5-4] even for compacted fuel. While

such an SiC defect fraction is higher than expected, it is not sufficient to explain the observed fission gas release in HRB-21. Failure of SiC coatings during irradiation, in addition to the initial as-manufactured SiC defect fraction, must have taken place to produce the high level of fission gas release observed.

The failure of the PPyC/OPyC coatings in compacts was a strong function of fast neutron exposure. In fuel compacts with the lowest fast neutron exposure, there was significantly less OPyC failure than in fuel with maximum exposure. In compacts, the onset of PPyC/OPyC failure was at a fast neutron exposure of about 0.7×10^{25} n/m^2. However, the unbonded piggyback particles with exposures from 2.3×10^{25} n/m^2 to 3.0×10^{25} n/m^2 did not exhibit cracks in the PPyC coating. Two possible explanations are likely. The first is that the cracking was dependent on temperature. The piggybacks operated at lower temperatures than the compacts. The second is that the particles in the compacts were apparently acted upon by the carbonaceous matrix in a way that promoted cracking of the PPyC, although no penetration of the PPyC or indication of mechanical interaction was apparent in the ceramographic cross sections of the irradiated fuel. The fuel manufacturer (GA) has reported that a large percentage, roughly 50%, of the PPyC was found to have minor cracks after the final fuel compact heat treatment, prior to any irradiation. However, none of the OPyC was observed to be damaged. Since the PPyC was a sacrificial layer with the singular purpose of preventing particle crushing during compacting, the damage to the PPyC was not considered relevant to fuel performance.

The PPyC coating of HRB-21 particles did not have an OPyC seal coat; the fuel for HRB-21 had already been fabricated when a fuel design decision was made to add the outer seal coat to the PPyC. A seal coat was found to be necessary for free flow in the loading hoppers of the production fuel compact press, and fuel manufactured after the HRB-21 fuel contained an OPyC seal coat. It was speculated that the PPyC of HRB-21 fuel might suffer a matrix coating interaction and a consequently higher failure rate (of the PPyC) than would occur with the presence of a seal coat. However, failure of the PPyC was not considered a significant risk to fuel performance because the PyC seal coat which existed between the PPyC and OPyC was expected to arrest cracks which might develop in the PPyC. In addition, the Fuel Design Data Manual[5-5] showed that failure of both the PPyC and OPyC would have no significant impact on SiC failure fraction. Therefore, the decision was made to use the HRB-21 fuel as originally fabricated.

The irradiation test results reported here clearly show that the PyC seal coat between the PPyC and OPyC did not stop irradiation-induced cracks in the PPyC from propagating into the OPyC (or vice versa). Nearly 100% failure was experienced by both coatings at high, fast neutron fluence exposure. However, results from an irradiation experiment with fuel containing an OPyC seal coat on the PPyC showed that the PPyC/OPyC performance was not improved relative to that reported for HRB-21 (ref. 5-6). Therefore, the fact that HRB-21 fuel had no outer seal coat had no significant impact on the observed fuel performance.

The SiC coating failure fraction showed no strong correlation with burnup. The range of burnup was large, ranging from 0.5% FIMA for fertile particles to 22.5% FIMA for fissile particles, but the occurrence of SiC failure determined by ceramography was similar at 1 to 8% for the two particle types at the highest fluence. There appears to have been some dependence of SiC failure on fast neutron exposure. Examples were found where the fast neutron fluence increased by a factor of 2.3 from the minimum to maximum exposure fuel samples while the SiC failure fraction, determined by ceramography, increased by a factor of 5 (compact 1C, 0.7%; compact 4A, 5%).

LBL results generally confirm the above results. There was qualitative agreement between the different PIE methods, but their sensitivity differed. However, the percent-level failures of the highest fluence compacts are clearly and consistently visible. Table 5.1 summarizes the particle failure (loss of retentive capability) results.

Ceramographic examination of the fuel revealed several examples of minor fission product attack of SiC, but cracking of the SiC or penetration of the SiC layer by the corrosion zone was not observed. Penetration of the SiC layer by palladium fission product was observed in SEM. Microprobe examination of cross sections of particles which were known to have released cesium, as determined by IMGA, showed that the penetration of palladium was uniform for 5 to 10 μm into the SiC from the inner surface; however, no concentration of palladium in nodules or at grain boundaries of the SiC was observed. The lack of significant corrosion of SiC by fission products was consistent with lack of correlation between SiC failure and HM burnup. Thus, SiC corrosion is not a likely candidate for the percenty level of failures.

Particle shape and the existence of lenticular flaws in the SiC known as "gold spots" did not contribute to the observed failure of SiC or OPyC. Poorly shaped particles

Table 5.1.

MEASURED PARTICLE FAILURE FRACTIONS IN CAPSULE HRB-21

Compact	Fast fluence, 10^{25} n/m^2	Burnup, % FIMA[a]		SiC failure fraction						TRIGA (exposed kernel)
				Fissile			Fertile			
		Fissile	Fertile	IMGA[b]	LBL[c]	Met[d]	IMGA[b]	LBL[e]	Met[d]	
4C	3.5	22	2.2			0.05			0.05	
5B	3.5	22	2.2		0.078			0.017		0.06
5C	3.5	22	2.2	0.046			0.008			0.06
2A	2.3	18	1.2			0.00			0.00	
2B	2.3	18	1.2			0.00			0.03	
7C	2.3	18	1.2		0.015			0.019		0.01
1C	1.5	14	0.5			0.00				
8A	1.5	14	0.5	0.00			0.010		0.00	2×10^{-5}

[a]FIMA = Fissions per initial metal atom. Based on calculated values. IMGA-measured values are approximately 15% lower. See Table 3.7.

[b]IMGA = Irradiated-microsphere gamma analyzer.

[c]LBL = Leach-burn-leach. Based on sum of particle failures measured by ^{238}U in leach solutions (1) before burn and (2) first leach after burn.

[d]Met = Metallography.

[e]Based on sum of particle failures measured by ^{233}U in leach solutions (1) before burn and (2) first leach after burn.

performed as well as nearly spherical particles. Cracks in the SiC were never seen to connect with or be associated with the gold spot discontinuity in the SiC. The source of stress causing SiC failure acted independently of these shape and flaw features. Apparently, the margin for failure due to pressure-vessel effects is very large in MHTGR particle design. However, features which degrade pressure-vessel performance should be removed to the degree possible, because they could be performance limiting when the non-pressure-vessel source of failure in these particles is identified and eliminated.

In general, the IPyC coating appeared to be firmly bonded to the SiC. However, in the vicinity of SiC cracks, IPyC debonding was often observed. The cracked IPyC tended to curl inward toward the buffer and away from the SiC. The fact that a crack in the SiC was usually associated with a crack in the IPyC suggests that the mechanism of failure involves both coatings. Since the IPyC crack was not observed to be aligned with the SiC crack and the IPyC was typically debonded from the SiC in the vicinity of the crack, the conclusion was drawn that cracks in one coating did not directly propagate into the other. While this layer interaction conclusion seems plausible, the data are not conclusive since only a 2-D view of the particle cross section was observed. However, stress calculations indicate that the debonding and cracking of the IPyC can lead to high local stresses in the nearby SiC, so direct crack propagation is not necessary for a failure mechanism. Thus, the present PIE evidence does buttress the IPyC/SiC interaction argument.

The buffer coating often cracked radially and underwent circumferential shrinkage which resulted in wide radial cracks. This behavior was a marked difference from buffer behavior in HEU UCO particles in the NPR-1, -2, and -1A irradiation experiments.[5-6] In the HEU UCO TRISO NPR test fuel particles, radial shrinkage resulted in tearing away from the IPyC coating and about 50% reduction in buffer thickness, but radial cracking of the buffer was rare.

The ThO_2 kernels, which had relatively low burnup of HM, retained their spherical shape. Extremely small gas bubbles developed in the ThO_2 with highest burnup ($\sim$2.2% FIMA), but no evidence of significant kernel swelling was observed.

Extrusion of the LEU UCO kernel was observed in particles where the buffer cracked. The kernel swelled into radial cracks in the buffer but, in no case, did the kernel penetrate the IPyC coating which remained attached to the SiC. As long as the IPyC remained unfailed, no fission product attack of the SiC was observed even when the

extruded kernel came into near contact with the IPyC. In the cases where the IPyC had a radial crack, minor SiC attack by fission products was sometimes observed. These observations demonstrate that the IPyC provides a retentive component in the transport of fission products from the particle.

In addition to kernel extrusion, several of the fissile particle kernels in the compact with the highest exposure exhibited kernel migration with the rejection on carbon on one side of the kernel. From the appearance of the kernels in the ceramographic examination, it was concluded that kernel migration up the radial temperature gradient (the amoeba effect) in the compact had taken place. The rate of migration estimated from the thickness of the carbon layer deposited on the cool side of the kernel was consistent with that expected for UO_2 kernels under the HRB-21 test conditions. It is possible that the UCO kernels of those particles exhibiting kernel migration were low in UC_2 content and equivalent to a pure UO_2 kernel, but since no kernel-by-kernel values of the C/O ratios are available, this area of investigation cannot be followed. Measurements of individual HEU UCO kernels have revealed the possibility of low UC_2 content, and a similar condition may have existed in the manufacture of LEU UCO kernels.[5-7] Control of the UC_2 content from kernel to kernel, rather than mean kernel batch composition as was used for HRB-21 fuel, may be necessary to avoid the kernel migration phenomenon.

5.2 FUEL COMPACT IRRADIATION PERFORMANCE

During irradiation, both the compact matrix and PPyC, which were initially about 50% dense, underwent irradiation-induced shrinkage. The extensive crack pattern in the matrix material, as revealed by ceramography during PIE, resulted from the shrinkage of the matrix at a rate greater than the particles which were in a nearly close-packed array. In prior fuel irradiation experiments with TRISO fuel produced with an OPyC but no PPyC, the shrinkage of the matrix resulted in crack development in the matrix. However, the strength of the compact was not affected as significantly as with the HRB-21 fuel compacts. The loss of strength in the irradiated HRB-21 compact may have been due to the massive pyrocarbon failure.

There was no obvious deleterious coating matrix interaction identified in ceramography, but the fact that unbonded piggyback particles did not show cracked PPyC while the PPyC in compacts was cracked at the same fast neutron exposure indicates that the matrix may have contributed in some manner to PPyC failure. This type of failure is

supported by the fact that the manufacturer has noted that roughly 50% of the PPyC cracked to some (minor) extent during compact final heat treatment. Temperature may have played an important part, however, because the particles in compacts operated at a higher temperature than unbonded piggyback particles, and the higher temperature may have contributed to more rapid PPyC dimensional change and failure under irradiation.

The HRB-21 fuel compacts did not show the degree of dimensional shrinkage expected at maximum fast neutron exposure. The expected shrinkage was based on prior experience with TRISO fuel produced without a PPyC. Compact dimensional shrinkage did take place in the HRB-21 compacts at low fast neutron exposure before development of matrix and coating cracks became significant. In fact, at the end of irradiation, the compacts at the ends of the capsule with the lowest fast neutron exposure exhibited greater shrinkage than predicted, but in compacts with the highest fast neutron exposure, the development of cracks in the matrix and PPyC/OPyC resulted in a net compact expansion of about 0.2% where 1.2% shrinkage was predicted. The massive pyrocarbon failure was the cause of the discrepancy. The OPyC coating was not bonded to the SiC, and it separated cleanly from the SiC when the OPyC was broken in several places.

Failure of the PPyC may have contributed to the failure of the OPyC and loss of the compressive stress component it supplied to the SiC pressure vessel. The SiC failure resulting from the loss of the OPyC compressive component was expected to be much smaller than the 1 to 8% failure observed in both fertile and fissile particles. Therefore, some additional contributor to SiC failure must have been active or the pressure-vessel model is not correctly predicting pressure effects. The irradiation-induced dimensional change of a relatively thick IPyC interacting with the SiC coating, as discussed above, was likely the primary contributor to failure of the SiC in the absence of any major flaw in the SiC coatings (none found). The PPyC/OPyC coating failure appears to have been enhanced by some aspect of the compacting process, matrix interaction, time at temperature, or all of these items, but its major role in the failure mechanism may have been simply to increase the likelihood of failure of the SiC layer by the IPyC/SiC interaction which generated large local tensile stresses (according to stress models).

5.3 REFERENCES

5-1. O. M. Stansfield et al., SSL-1 Spitfire Loop Experiment Post Irradiation Examination and Analysis, Dossier No. 6, GA-A14628, General Atomics, San Diego, Calif., July 1978.

5-2. GA-907394 (DOE-HTGR-88359), General Atomics, San Diego, Calif., January 1991.

5-3. W. J. Kovacs, "Characterization of Defective SiC Coatings in TRISO HTGR Fuel Particles," *J. Am. Ceram. Soc.* **66**(3), March 1982.

5-4. Testing of Archived HRB-21 Capsule Fuel, DOE-HTGR-88554, Rev. N/C, November 1993.

5-5. Fuel Design Data Manual, GA-901866, Rev. F, General Atomics, San Diego, Calif., April 1992.

5-6. C. A. Baldwin et al., The New Production Reactor Fuel Post Irradiation Examination Data Report for Capsules NPR 1, NPR 2, and NPR 1A, ORNL/M-2849, Martin Marietta Energy Systems, Inc., Oak Ridge Natl. Lab., September 1993.

5-7. C. R. Clark, UCO Stoichiometry Final Report, BWED-93-031, Rev 01, Babcock & Wilcox, Alliance, Ohio, June 22, 1993.

SECTION 6

CONCLUSIONS

The objectives of capsule HRB-21 (ref. 6-1) and the project success in achieving them are listed below in order of priority to the MHTGR Program:

1. **Goal:** Provide the first in-reactor test of U.S. fuel meeting MHTGR fuel quality specifications, and provide a portion of the data necessary to validate the U.S. reference fuel performance models under normal operating conditions.
   Achievement: This goal was not achieved. The fuel failed to perform as required and, in addition, major deficiencies in the structural design of the fuel and SiC defect detection methods were probably uncovered. Additional test capsules will be required to sort out the possible new fuel failure mechanisms and their solutions.
2. **Goal:** Provide a portion of the samples needed for a series of conduction cooldown simulation tests designed to provide data in support of update, as necessary, and provide data in support of the validation of the U.S. reference fuel performance model under LBE conditions.
   Achievement: This goal was abandoned after the poor fuel performance was apparent.
3. **Goal:** Provide in-reactor coating failure data for confirmation or revision of the defective particle performance models.
   Achievement: This goal was met to a limited degree. The PIE information will be useful to fuel designers for product improvement. It is likely that a major review of fuel performance models will be necessary because they are too simplistic in nature, and a fuel redesign is necessary. A major deficiency is that coating interactions are not modeled.
4. **Goal:** Provide irradiated, unbonded fuel particles of MHTGR reference-quality for (a) direct comparison to irradiated defective particles performance and (b) selected postirradiation investigations of their structure and performance.
   Achievement: Technically, this goal was met, but its major effect will be on fuel redesign rather than a licensing database.

5. **Goal:** Provide data on partition coefficients and sorptivity isotherms of Cs, Sr, I, and Ag on MHTGR core materials.

   Achievement: This goal was abandoned due to the need for resources to determine the reasons for the poor fuel performance. This work may be resumed in the future if funds become available.

6. **Goal:** Provide data on the irradiation performance of both PyC-coated and PyC/SiC-coated particles containing boron carbide (B_4C).

   Achievement: This goal was abandoned due to the need for resources to determine the reasons for the poor fuel performance. However, another program may perform a portion of this task. The schedule is unknown at present.

Performance at or above the required level of fission product retention was expected because of the PPyC design modification which protected the particle from damage during compact fabrication. In an attempt to reduce the fraction of particles coated with defective SiC, the IPyC design had also been changed to provide for a 50-μm-thick layer in place of the prior 35 μm thickness. There were also process improvements yielding more spherical particles through tabling and elutriation and more uniform coatings through use of a draft tube coater design. Confidence was high because of the success of the German program and the excellent preirradiation performance of the fuel and fuel compacts.

During irradiation of the capsules, the fuel was exposed at the design volume average temperature of 932°C with peak local temperatures approaching 1300°C. At the start of irradiation, the fission-gas release rate was less than 5×10^{-8} R/B ^{85m}Kr which was consistent with the low level of HM contamination achieved during fuel production. However, at a relatively low fast neutron exposure of about 0.7×10^{25} n/m^2, the fission-gas release rate began to rise rapidly as a result of coating failure. The fission-gas release rate increased with continued exposure until the end of irradiation where the fission-gas release rate was about 2×10^{-4} R/B ^{85m}Kr at a capsule maximum exposure of 3.5×10^{25} n/m^2 (capsule average exposure of 2.6×10^{25} n/m^2). Under these conditions, the coating failure and fission-gas release were higher than expected by at least two orders of magnitude.

Ceramography was one of the primary tools used to characterize the condition of the fuel particle coatings during PIE. From the appearance of coatings in ceramographic observations, it was concluded that failure of the PPyC and OPyC was a function of the fast neutron fluence; the highest fluence compacts had nearly 100% failure of the PPyC and

OPyC. This damage shows some temperature dependence as the neighboring piggybacks, which received a similar fluence at a lower average temperature, had far less pyrocarbon damage. Also, a cross-sectional view of compact 2A showed greater coating damage in the higher temperature regions of the compact. Although matrix intrusion into the PPyC was not observed in this PIE work, interaction of the matrix and PPyC to enhance PPyC failure in compacts cannot be ruled out because some intrusion was observed in metallography of unirradiated compacts.[6-2]

Irradiation-induced failure of the PPyC may have led to the failure of OPyC coatings. The OPyC coating was not strongly bonded to the SiC so that the failed OPyC readily separated from the SiC. The high failure fraction of OPyC at high exposure allowed fission gases to easily escape into the capsule purge gas stream when the SiC layer failed. The massive PPyC/OPyC failure made SiC failures readily apparent by increased purge gas activity. However, the failure of the OPyC coating probably did not initiate failure of the SiC coating; while the loss of the OPyC removed a compensating compressive stress component from the SiC, another mechanism appears to have driven the tensile failure of the SiC. As a result of the observations conducted during PIE, it was concluded that the coating failure and the fission-product release which took place during irradiation were probably not caused by fission-product attack of the SiC coating but were more likely the result of deleterious mechanical interaction of the SiC and IPyC coating layers of the TRISO particle. The PIE results did not indicate which coating failed first and contributed to failure in the other coating. This conclusion is based on the observation that cracked SiC was usually accompanied by cracked IPyC which was bonded to the SiC except in the vicinity of the IPyC crack. While the pyrocarbons were definitely flawed in some way, the failure of the SiC appears to be linked to some kind of coating interaction.

During PIE of HRB-21, the coating failure fraction was determined by several means. One of the first methods employed was the measurement of fission gases by use of TRIGA. With this method, it is not possible to separately determine fissile and fertile failure fraction. However, an average failure fraction can be estimated by assuming similar contributions from the fertile and fissile particles. The capsule average coating failure fraction determined by TRIGA fission-gas release was 3% capsule average and 6 to 8% in the compacts with peak exposure (assuming 1.6% R/B ^{85m}Kr per failed particle).

Failure fraction determined by ceramography has uncertainty resulting from the potential for damage during preparation, the limited number of particles that can be examined, and the limited volume of coating that can be examined for cracks or porosity. The fraction of cracked SiC coatings provides the best measure of fission product retention capability. The cracked SiC coating fraction observed in ceramography of compacts 1C, 2A, 2B, and 4A ranged from none to 6% and was about the same for fissile and fertile particles (21% circumferentially cracked SiC at low fluence in fertile fuel of compact 1C was considered a mount preparation artifact). Fissile particle coating failure fraction can also be determined by IMGA examination and identification of particles deficient in cesium. Two compacts, 8A and 5C, were characterized in this manner, and the results showed fissile particle failure fractions of 0% for 8A and 4.6% for 5C, consistent with the ceramography results. Finally, LBL examination of compacts 5B and 7C provided failure fraction measurements that were generally comparable with the other methods, fissile particle failure fractions of 1.5% for compact 7C and 7.8% for compact 5, and fertile particle failure fractions of 1.9% for compact 7C and 1.7% for compact 5C. The overall trend was greater SiC failure fraction in the higher fluence compacts.

On the basis of the three different techniques used for SiC failure fractions measurements, it was concluded that the coating failure fraction was <1% for both fertile and fissile particles at the ends of the capsule where exposure was minimal, and it increased with exposure to a PIE technique average of about 6% for fissile particles and about 2.5% for fertile particles at the center of the capsule where exposure was maximum.

In order to gain a complete understanding of fission product release from coated-particle fuel, it may be necessary to consider release pathways more subtle than mechanical cracks. For example, connected porosity in the SiC, which may develop during irradiation, is difficult to detect but may be significant with regard to fission product release. Evidence for such SiC porosity and absence of mechanical cracks was obtained from the ceramography of particles identified by IMGA as deficient in cesium. Whether or not the particles released fission gases was not determined. More complete characterization of SiC microstructure and correlation with fission product release would contribute significantly to understanding of fuel performance and point the way to improved materials and QC methods for detection of failed SiC.

6.1 LESSONS LEARNED

During the course of the HRB-21 capsule task, several problems and program bottlenecks were encountered. To aid future PIE programs, the following list of lessons has been compiled and is recommended for review:

1. Delays for procedure development and approval, personnel training, and equipment problems were encountered on several occasions. A well-planned and funded effort to define the required data for each procedure to be used and to develop and qualify equipment, procedures, and personnel, along with readiness reviews in advance of the start of the PIE, is necessary to provide high-quality results on schedule.
2. Delays in publication of key documents (test specifications, test plan) and limited resources for scheduling support reduced the effectiveness of these work management tools and led to occasional breakdowns in communications. Maintenance of working versions of these documents is necessary to manage the work effectively and to support a common understanding of status and scope among and within the organizations involved. A process and the necessary resources to maintain official working versions during the conduct of the work need to be established.
3. In some cases, interpretation of the PIE results was limited by differences in preirradiation and PIE methods. Where applicable, the preirradiation characterization and PIE should use the same procedures and, to the extent practical, be performed at the same location using the same equipment and personnel. This requirement should be called out in the PIE test specification and test plan and will require detailed development of applicable sections of the PIE plan and procedures sufficiently in advance to guide the preirradiation characterization.
4. Variations in methods for recording PIE data sometimes caused difficulty in the documentation and distribution of PIE results in a timely and effective manner. Definition of the format and content of data to be recorded and the structure for storage and retrieval in advance of the PIE is desirable. Networked database software could be developed to standardize storage and retrieval of preirradiation

and postirradiation data and to reduce the effort required for interim and final reporting of results.

5. Personnel with PIE experience should be included on the irradiation capsule design team.
6. Special fixtures, jigs, etc., used in the disassembly must be documented.
7. The piggyback holes in the graphite fuel bodies were blind holes. For ease of disassembly, through holes would be better.
8. The screw slots for the fuel compact plugs in the original design were not optimal. They should be smaller.
9. Procedures for loading the compacts into the graphite fuel bodies and the fuel bodies into the capsule should be adjusted to reduce the likelihood of misorientation in the capsule.
10. The thermal design of capsules should include a larger allowance for the peak fuel temperature margin under pure helium conditions at the planned end-of-irradiation conditions or the most demanding part of the irradiation cycle.
11. Simplification of the capsule geometry could increase confidence in the thermal analysis. In particular, a single column of stacked compacts in a single fuel body would be helpful.
12. The initial TRIGA R/B measurement should be performed at a temperature no greater than the end-of-irradiation value, with subsequent testing at a standard temperature if the end-of-irradiation temperature is less than the standard value. A longer test would also reduce uncertainties.
13. Equipment and procedure development work on unirradiated compacts does not necessarily apply to irradiated compacts when substantial failures in outer coatings are encountered. If in-pile R/B data indicate higher-than-expected release, contingency planning for adjustments to the deconsolidation and IMGA procedures to accommodate coating failures should be initiated.
14. The burn-back procedure should be examined to determine if it can be run at a lower temperature to reduce the likelihood of particle damage. Also, the LBL method needs to be characterized better.
15. The particle handling techniques should be adjusted so that a true random sample can be taken whenever possible.

16. Alternate methods for handling particles with the IMGA system need to the examined. Damaged particles result in the most handling problems. Also, results with low-burnup ThO_2 particles may not be reliable because of high cesium retention.
17. Significant information was not retained which could have improved the statistics and interpretation of the metallographic results. Improved guidance regarding information to be collected during metallographic examination would increase the value of the results.
18. The use of video taping and computer storage of metallographic images should be further developed and refined for future PIE work.
19. Metallographic results, in general, were considered to be significantly dependent on the individual performing the work. Further development of procedures and training should be considered with the objective of achieving a more standardized result.
20. The SEM system should be investigated to see if methods can be established to handle higher activity specimens.
21. More allowance for thermal margin and improved definition of data required should be considered in future specifications for capsule flux monitors.

6.2 REFERENCES

6-1. HRB-21 Test Specification, DOE-HTGR-88331, Rev. N/C, General Atomics, San Diego, Calif., September 1989.

6-2. MHTGR TRISO-P Fuel Failure Evaluation Report, DOE-HTGR-90390, Rev. 0, General Atomics, San Diego, Calif., October 1993.

APPENDIX A-1

R/B VALUES MEASURED DURING HRB-21 IRRADIATION

Appendix A-1

R/B VALUES MEASURED DURING HRB-21 IRRADIATED

Sample	^{85m}Kr	^{88}Kr	^{87}Kr	^{89}Kr	^{135}Xe	^{133}Xe	^{135m}Xe	^{138}Xe	^{137}Xe
cycle1									
HRB21_1	nd	nd	nd	nd	nd	nd	nd	2.18e-09	nd
HRB21_2	nd	nd	nd	nd	nd	nd	nd	1.37e-09	nd
HRB21_3	nd	nd	nd	nd	nd	nd	nd	2.39e-09	nd
HRB21_3B	nd	9.49e-09	nd	nd	nd	nd	nd	nd	nd
HRB21_4	nd	6.07e-05	nd	nd	nd	nd	nd	2.73e-06	nd
HRB21_5	5.24e-09	5.25e-09	7.03e-09	nd	nd	nd	nd	2.93e-09	nd
HRB21_6	nd	nd	3.27e-10	nd	nd	nd	nd	0.00	nd
HRB21_7	8.08e-09	1.04e-08	9.22e-09	nd	2.30e-09	nd	nd	2.51e-09	nd
HRB21_7B	nd	1.27e-04	nd	nd	3.29e-09	nd	nd	nd	nd
HRB21_7C	8.28e-09	nd	nd	nd	2.26e-09	nd	nd	nd	nd
HRB21_8	2.21e-08	2.10e-08	1.31e-08	nd	nd	nd	2.81e-09	3.96e-09	nd
HRB21_9	1.44e-08	1.43e-08	1.10e-08	nd	3.83e-09	nd	2.57e-09	1.77e-09	nd
HRB21_10	1.71e-08	2.09e-08	1.30e-08	3.46e-09	4.01e-09	nd	4.65e-09	2.85e-09	nd
HRB21_11	1.84e-08	1.48e-08	1.41e-08	3.82e-09	3.23e-09	nd	2.41e-09	2.63e-09	nd
HRB21_12	1.90e-08	1.66e-08	1.47e-08	7.84e-09	3.53e-09	nd	1.19e-09	1.90e-09	nd
HRB21_13	1.87e-08	1.96e-08	1.35e-08	3.09e-09	3.44e-09	nd	1.99e-09	2.43e-09	nd

*Not analyzed.
**Sample taken through the holdup tank.

Appendix A-1

(CONTINUED)

Sample	^{85m}Kr	^{88}Kr	^{87}Kr	^{89}Kr	^{135}Xe	^{133}Xe	^{135m}Xe	^{138}Xe	^{137}Xe
HRB21_14	2.20e-08	1.82e-08	1.46e-08	2.62e-09	5.75e-09	nd	1.79e-09	2.60e-09	nd
HRB21_15	2.04e-08	2.12e-08	1.39e-08	2.45e-09	2.84e-09	nd	2.91e-09	2.58e-09	nd
HRB21_16	6.23e-08	4.79e-08	2.89e-08	2.57e-09	3.94e-09	nd	nd	4.17e-09	nd
HRB21_16B	6.84e-08	3.89e-08	nd	nd	3.13e-09	3.57e-08	nd	nd	nd
HRB21_16C	nd	nd	nd	nd	nd	2.61e-08	nd	nd	nd
HRB21_17	5.48e-08	4.50e-08	2.74e-08	5.87e-09	2.83e-09	nd	3.92e-09	3.39e-09	nd
HRB21_17B	nd	nd	nd	nd	nd	3.07e-08	nd	nd	nd
HRB21_18	3.74e-08	3.99e-08	3.09e-08	7.57e-09	2.75e-09	nd	3.77e-09	2.99e-09	nd
HRB21_18B	4.42e-08	3.77e-08	2.58e-08	nd	5.08e-09	nd	nd	nd	nd
HRB21_18C	nd	nd	nd	nd	nd	1.28e-08	nd	nd	nd
HRB21_19	4.19e-08	3.73e-08	3.00e-08	4.09e-09	3.85e-09	nd	5.30e-09	3.97e-09	nd
HRB21_19B	nd	nd	nd	nd	nd	nd	nd	nd	nd
HRB21_20**	4.09e-08	3.47e-08	2.13e-08	nd	4.27e-09	nd	nd	nd	nd
HRB21_20B	nd	nd	nd	nd	nd	2.01e-08	nd	nd	nd
HRB21_21	4.51e-08	3.97e-08	2.57e-08	4.21e-09	nd	nd	nd	3.94e-09	nd
HRB21_21B	4.16e-08	3.59e-08	2.36e-08	3.68e-09	3.52e-09	nd	5.90e-09	3.83e-09	nd
HRB21_21C	nd	nd	nd	nd	nd	2.13e-08	nd	nd	nd

*Not analyzed.
**Sample taken through the holdup tank.

Appendix A-1

(CONTINUED)

Sample	^{85m}Kr	^{85}Kr	^{87}Kr	^{88}Kr	^{135}Xe	^{133}Xe	^{135m}Xe	^{138}Xe	^{137}Xe
HRB21_22	2.31e-08	3.83e-08	2.25e-08	3.96e-09	nd	nd	3.38e-09	3.32e-09	nd
HRB21_22B	2.96e-08	2.66e-08	2.15e-08	2.19e-09	4.69e-09	nd	2.01e-09	2.32e-09	nd
HRB21_22C	nd	nd	nd	nd	nd	1.62e-08	nd	nd	nd
HRB21_22D	nd	nd	nd	nd	nd	1.58e-08	nd	nd	nd
HRB21_23	5.62e-08	4.56e-08	3.50e-08	2.55e-09	nd	nd	2.94e-09	3.05e-09	nd
HRB21_23B	5.03e-08	4.31e-08	2.96e-08	4.81e-09	4.43e-09	3.05e-08	5.59e-09	3.18e-09	nd
HRB21_23C	nd	nd	nd	nd	nd	2.35e-08	nd	nd	nd
HRB21_24	4.36e-08	5.19e-08	3.66e-08	nd	nd	nd	4.37e-09	4.62e-09	nd
HRB21_24B	5.54e-08	4.78e-08	3.40e-08	2.81e-09	4.25e-09	3.16e-08	4.49e-09	4.02e-09	nd
HRB21_24C	nd	nd	nd	nd	0.00	2.25e-08	nd	nd	nd
HRB21_25	6.88e-08	5.88e-08	3.52e-08	5.05e-09	9.75e-09	nd	nd	4.56e-09	nd
HRB21_25B	6.31e-08	5.78e-08	3.79e-08	5.73e-09	5.28e-09	4.70e-08	5.56e-09	3.44e-09	nd
HRB21_25C	nd	nd	nd	nd	nd	2.42e-08	0.00	nd	nd
HRB21_26	8.23e-08	5.55e-08	4.04e-08	6.01e-09	nd	nd	5.47e-09	3.91e-09	nd
HRB21_26B	6.63e-08	5.69e-08	3.84e-08	3.75e-09	5.49e-09	4.57e-08	3.37e-09	3.67e-09	nd
HRB21_26C	nd	nd	nd	nd	nd	3.39e-08	nd	nd	nd
HRB21_27	8.81e-08	6.92e-08	5.11e-08	4.35e-09	1.07e-08	nd	4.19e-09	5.22e-09	nd

*Not analyzed.
**Sample taken through the holdup tank.

Appendix A-1

(CONTINUED)

Sample	^{85m}Kr	^{88}Kr	^{87}Kr	^{85}Kr	^{135}Xe	^{133}Xe	^{138m}Xe	^{138}Xe	^{137}Xe
HRB21_27B	7.41e-08	7.05e-08	4.88e-08	6.38e-09	6.86e-09	3.10e-08	4.68e-09	4.79e-09	nd
HRB21_27C	nd	nd	nd	nd	nd	4.21e-08	nd	nd	nd
HRB21_28	1.96e-08	1.87e-08	1.46e-08	3.83e-09	6.93e-09	nd	3.36e-09	2.48e-09	nd
HRB21_28B	2.08e-08	1.26e-08	1.39e-08	3.61e-09	5.62e-09	nd	5.51e-09	2.78e-09	nd
HRB21_28C	nd	nd	nd	nd	nd	1.11e-08	nd	nd	nd
HRB21_29	2.71e-08	3.03e-08	2.07e-08	1.65e-09	5.15e-09	nd	2.20e-09	2.69e-09	1.54e-09
HRB21_29B	3.01e-08	2.65e-08	1.80e-08	1.07e-09	4.13e-09	nd	3.18e-09	2.29e-09	nd
HRB21_29C	nd	nd	nd	nd	0.00	nd	nd	nd	nd
HRB21_30	2.76e-08	2.52e-08	1.78e-08	1.90e-09	4.82e-09	nd	3.41e-09	1.79e-09	nd
HRB21_30B	2.72e-08	2.20e-08	1.54e-08	2.74e-09	3.01e-09	2.16e-08	2.53e-09	2.02e-09	nd
HRB21_30D	nd	nd	nd	nd	nd	1.22e-08	nd	nd	nd
HRB21_31	3.83e-08	3.03e-08	2.20e-08	5.39e-09	4.69e-09	nd	3.38e-09	3.41e-09	nd
HRB21_31B	3.27e-08	2.90e-08	2.07e-08	3.61e-09	4.20e-09	nd	4.21e-09	2.47e-09	nd
HRB21_31C	nd	nd	nd	nd	4.37e-09	1.47e-08	nd	nd	nd
HRB21_32	3.73e-08	3.56e-08	2.02e-08	3.69e-09	3.16e-09	nd	3.82e-09	2.98e-09	1.16e-09
HRB21_32B	3.17e-08	2.84e-08	2.00e-08	4.28e-09	4.09e-09	nd	3.20e-09	3.15e-09	nd
HRB21_32C	nd	nd	nd	nd	1.58e-09	1.47e-08	nd	nd	nd

*Not analyzed.
**Sample taken through the holdup tank.

Appendix A-1

(CONTINUED)

Sample	^{85m}Kr	^{85}Kr	^{87}Kr	^{88}Kr	^{135}Xe	^{133}Xe	^{135m}Xe	^{136}Xe	^{137}Xe
cycle 2									
HRB21_33	nd	nd	nd	nd	nd	nd	nd	1.46e-09	nd
HRB21_34	nd	nd	1.27e-09	nd	nd	nd	nd	9.37e-10	nd
HRB21-35	nd	1.67e-09	1.58e-09	nd	nd	nd	nd	1.24e-09	nd
HRB21_36	nd	3.20e-09	1.52e-09	7.66e-10	nd	nd	1.24e-09	1.06e-09	nd
HRB21_37	4.33e-09	3.80e-09	4.28e-09	7.09e-10	nd	nd	3.00e-09	1.77e-09	nd
HRB21_38	7.82e-09	8.49e-09	6.45e-09	1.84e-09	nd	nd	nd	1.97e-09	nd
HRB21_39	9.27e-09	8.76e-09	7.98e-09	1.51e-09	4.93e-09	nd	2.82e-09	1.89e-09	nd
HRB21_40	4.46e-06	3.17e-06	1.28e-06	5.14e-08	7.83e-07	2.20e-04	5.21e-07	1.46e-07	nd
HRB21_40B	4.47e-06	3.15e-06	1.26e-06	4.47e-08	8.11e-07	2.18e-04	5.01e-07	1.44e-07	nd
HRB21_40D	nd	nd	nd	nd	1.03e-06	2.25e-04	nd	nd	nd
HRB21_40E	nd	nd	nd	nd	nd	2.25e-04	nd	nd	nd
HRB21_41	1.00e-06	8.06e-07	4.34e-07	6.35e-08	1.47e-06	1.40e-05	9.12e-07	4.39e-08	2.38e-08
HRB21_41B	1.03e-06	7.92e-07	4.24e-07	5.19e-08	1.54e-06	1.35e-05	8.92e-07	4.51e-08	nd
HRB21_42	2.66e-07	2.32e-07	1.63e-07	2.45e-08	1.72e-06	2.87e-06	1.03e-06	2.73e-08	nd
HRB21_42B	2.66e-07	2.32e-07	1.60e-07	2.69e-08	1.79e-06	3.12e-06	1.01e-06	2.54e-08	nd

*Not analyzed.
**Sample taken through the holdup tank.

Appendix A-1

(CONTINUED)

Sample	^{85m}Kr	^{88}Kr	^{87}Kr	^{89}Kr	^{135}Xe	^{133}Xe	^{135m}Xe	^{138}Xe	^{137}Xe
HRB21_43	5.29e-07	4.78e-07	3.28e-07	4.14e-08	2.85e-07	1.19e-06	1.89e-07	4.31e-08	1.61e-08
HRB21_43B	5.15e-07	4.66e-07	3.16e-07	4.31e-08	3.06e-07	1.21e-06	1.91e-07	4.28e-08	1.84e-08
HRB21_44	5.30e-07	4.88e-07	3.16e-07	3.94e-08	1.47e-07	8.71e-07	9.89e-08	4.59e-08	1.35e-08
HRB21_44B	5.24e-07	4.68e-07	3.21e-07	4.97e-08	1.50e-07	8.16e-07	9.81e-08	4.54e-08	nd
HRB21_45	4.79e-07	4.14e-07	2.87e-07	3.88e-08	1.18e-07	6.60e-07	7.20e-08	4.20e-08	1.55e-08
HRB21_45B	4.74e-07	4.21e-07	2.84e-07	4.26e-08	1.17e-07	6.43e-07	7.87e-08	4.20e-08	2.52e-08
HRB21_46	4.57e-07	3.93e-07	2.82e-07	4.38e-08	1.15e-07	5.90e-07	7.90e-08	4.07e-08	1.45e-08
HRB21_46B	4.58e-07	4.10e-07	2.74e-07	3.40e-08	1.10e-07	6.05e-07	7.20e-08	3.98e-08	nd
HRB21_47	6.32e-07	6.06e-07	3.98e-07	6.67e-08	1.45e-07	9.94e-07	1.05e-07	6.24e-08	2.20e-08
HRB21_47B	6.45e-07	5.70e-07	3.91e-07	6.11e-08	1.56e-07	9.97e-07	1.03e-07	5.97e-08	nd
HRB21_48	6.43e-07	5.83e-07	3.87e-07	5.84e-08	1.45e-07	1.06e-06	9.91e-08	5.75e-08	2.18e-08
HRB21_48A	6.02e-07	5.83e-07	3.92e-07	5.16e-08	1.52e-07	8.85e-07	1.03e-07	5.72e-08	3.08e-08
HRB21_48B	6.21e-07	5.53e-07	3.80e-07	5.51e-08	1.55e-07	9.37e-07	1.03e-07	5.52e-08	nd
HRB21_49	7.35e-07	6.53e-07	4.49e-07	6.52e-08	1.90e-07	1.20e-06	1.24e-07	6.63e-08	2.73e-08
HRB21_50	6.77e-07	5.91e-07	4.76e-07	5.14e-08	1.72e-07	1.42e-06	1.13e-07	6.18e-08	2.58e-08
HRB21_51	8.08e-07	7.16e-07	4.90e-07	9.00e-08	2.13e-07	1.83e-06	1.44e-07	7.50e-08	2.19e-08
HRB21_52	1.47e-05	9.91e-06	4.57e-06	3.62e-07	1.56e-06	6.43e-04	1.27e-06	5.68e-07	1.45e-07

*Not analyzed.
**Sample taken through the holdup tank.

Appendix A-1

(CONTINUED)

Sample	^{85m}Kr	^{85}Kr	^{87}Kr	^{88}Kr	^{135}Xe	^{133}Xe	^{135m}Xe	^{138}Xe	^{137}Xe
HRB21_52B	1.51e-05	1.01e-05	4.52e-06	3.35e-07	1.70e-06	6.67e-04	1.20e-06	5.55e-07	nd
HRB21_53	1.61e-05	1.05e-05	4.64e-06	3.20e-07	7.98e-06	6.42e-04	5.38e-06	5.66e-07	1.12e-07
HRB21_54	1.91e-05	1.23e-05	5.17e-06	3.75e-07	1.07e-05	7.67e-04	7.21e-06	6.57e-07	1.37e-07
HRB21_54G	2.16e-05	1.32e-05	5.40e-06	3.60e-07	1.25e-05	7.85e-04	7.09e-06	6.10e-07	nd
HRB21_54I	2.40e-05	1.35e-05	6.68e-06	nd	1.41e-05	8.95e-04	nd	nd	nd
HRB21_55	1.04e-05	7.73e-06	4.99e-06	6.26e-07	1.82e-05	1.62e-04	1.30e-05	1.08e-06	3.77e-07
HRB21_55B	1.03e-05	7.93e-06	4.72e-06	7.29e-07	1.99e-05	1.68e-04	1.28e-05	1.08e-06	2.78e-07
HRB21_56	1.41e-05	1.18e-05	7.44e-06	1.30e-06	1.54e-05	1.58e-04	1.16e-05	2.49e-06	1.01e-06
HRB21_56B	1.47e-05	1.13e-05	6.99e-06	8.08e-07	1.69e-05	1.69e-04	1.12e-05	2.47e-06	1.01e-06
HRB21_57	1.05e-05	9.15e-06	6.54e-06	1.24e-06	1.42e-05	1.16e-04	1.09e-05	2.54e-06	1.04e-06
HRB21_57B	1.11e-05	9.33e-06	6.34e-06	8.18e-07	1.59e-05	1.16e-04	1.06e-05	2.57e-06	9.45e-07
HRB21_58*	not analyzed because bottle contaminated								
HRB21_59**	1.33e-05	1.05e-05	5.87e-06	nd	1.62e-05	1.91e-04	4.84e-06	1.17e-06	nd
HRB21_59B	1.34e-05	1.03e-05	5.76e-06	nd	1.65e-05	1.91e-04	4.77e-06	1.15e-06	nd
HRB21_60**	1.34e-05	1.05e-05	5.99e-06	nd	1.45e-05	1.90e-04	4.55e-06	1.22e-06	nd
HRB21_60B	1.34e-05	1.05e-05	5.90e-06	nd	1.49e-05	1.90e-04	4.51e-06	1.19e-06	nd
HRB21_61**	6.36e-06	5.40e-06	3.12e-06	nd	8.99e-06	6.87e-05	2.58e-06	7.53e-07	nd

*Not analyzed.
**Sample taken through the holdup tank.

Appendix A-1

(CONTINUED)

Sample	^{85m}Kr	^{88}Kr	^{87}Kr	^{89}Kr	^{135}Xe	^{133}Xe	^{135m}Xe	^{138}Xe	^{137}Xe
HRB21_61B	6.30e-06	5.21e-06	3.08e-06	nd	9.03e-06	6.36e-05	2.58e-06	7.35e-07	nd
HRB21_62**	1.87e-05	1.42e-05	7.58e-06	nd	9.19e-06	4.38e-04	3.24e-06	1.42e-06	nd
HRB21_62B**	1.89e-05	1.47e-05	7.51e-06	nd	9.48e-06	4.39e-04	3.02e-06	1.30e-06	nd
HRB21_63**	2.20e-05	1.90e-05	1.14e-05	nd	2.01e-05	3.46e-04	6.36e-06	3.04e-06	nd
HRB21_63B	2.32e-05	1.91e-05	1.13e-05	nd	2.10e-05	3.61e-04	nd	nd	nd
HRB21_64**	1.04e-05	9.45e-06	5.75e-06	nd	7.88e-06	5.99e-05	2.56e-06	1.52e-06	nd
cycle 3									
HRB21_65	1.17e-06	1.11e-06	1.04e-06	2.10e-07	1.02e-06	2.70e-03	5.19e-07	8.56e-07	3.02e-07
HRB21_66	1.15e-06	1.22e-06	1.18e-06	2.38e-07	8.91e-07	4.68e-03	4.90e-07	9.53e-07	3.51e-07
HRB21-67	2.44e-06	2.49e-06	2.38e-06	3.41e-07	1.58e-06	6.02e-03	9.01e-07	1.63e-06	5.70e-07
HRB21_68	3.40e-06	3.46e-06	3.24e-06	5.43e-07	1.86e-06	3.15e-03	1.22e-06	2.13e-06	7.15e-07
HRB21_69	5.39e-06	5.55e-06	5.01e-06	9.37e-07	2.73e-06	3.26e-03	1.91e-06	3.27e-06	1.03e-06
HRB21_70	6.70e-06	7.48e-06	6.25e-06	1.47e-06	3.90e-06	1.71e-02	2.34e-06	3.70e-06	nd
HRB21_71**	7.13e-06	7.76e-06	5.57e-06	nd	4.31e-06	4.64e-04	1.41e-06	1.86e-06	nd
HRB21_72**	8.10e-06	8.56e-06	5.77e-06	nd	4.63e-06	1.70e-04	1.39e-06	1.76e-06	nd
HRB21_73	1.41e-05	1.25e-05	8.33e-06	2.04e-06	1.08e-05	1.06e-04	7.17e-06	3.92e-06	2.02e-06

*Not analyzed.
**Sample taken through the holdup tank.

Appendix A-1

(CONTINUED)

Sample	^{85m}Kr	^{88}Kr	^{87}Kr	^{89}Kr	^{135}Xe	^{133}Xe	^{135m}Xe	^{138}Xe	^{137}Xe
HRB21_74	1.74e-05	1.59e-05	1.12e-05	3.04e-06	1.61e-05	9.38e-05	1.19e-05	5.80e-06	2.59e-06
HRB21_75	6.33e-05	4.53e-05	2.49e-05	4.13e-06	2.50e-05	9.89e-04	1.84e-05	9.36e-06	3.71e-06
HRB21_75A	6.61e-05	4.33e-05	nd	nd	2.80e-05	1.03e-03	nd	nd	nd
HRB21_76	3.21e-05	2.89e-05	2.09e-05	4.72e-06	3.36e-05	1.74e-04	2.42e-05	1.11e-05	4.89e-06
HRB21_77	3.56e-05	3.25e-05	2.33e-05	5.68e-06	3.53e-05	2.22e-04	2.56e-05	1.27e-05	5.73e-06
HRB21_77A	3.83e-05	3.44e-05	2.28e-05	nd	3.96e-05	2.36e-04	nd	nd	nd
HRB21_78	2.58e-05	2.46e-05	1.79e-05	5.34e-06	1.89e-05	1.30e-04	1.43e-05	9.16e-06	4.45e-06
HRB21_79	2.96e-05	2.73e-05	1.92e-05	5.37e-06	1.92e-05	2.76e-04	1.39e-05	8.82e-06	3.94e-06
HRB21_80	5.44e-05	4.18e-05	2.61e-05	6.18e-06	2.45e-05	1.73e-03	1.81e-05	9.47e-06	3.77e-06
HRB21_81	6.66e-05	5.13e-05	3.19e-05	6.40e-06	3.46e-05	2.54e-03	2.49e-05	1.28e-05	5.01e-06
HRB21_82	8.66e-05	7.81e-05	5.51e-05	1.27e-05	6.49e-05	9.46e-04	4.83e-05	2.39e-05	9.46e-06
HRB21_83	5.60e-05	4.92e-05	3.42e-05	5.63e-06	3.20e-05	5.99e-04	2.21e-05	1.19e-05	3.70e-06
HRB21_84	6.58e-05	5.60e-05	4.12e-05	7.29e-06	3.81e-05	6.31e-04	2.73e-05	1.53e-05	5.56e-06
HRB21_85	5.93e-05	5.28e-05	3.81e-05	6.97e-06	3.50e-05	6.96e-04	2.65e-05	1.37e-05	4.92e-06
HRB21_86	5.64e-05	5.20e-05	3.71e-05	7.58e-06	2.94e-05	5.74e-04	2.32e-05	1.34e-05	5.26e-06
cycle 4									

*Not analyzed.
**Sample taken through the holdup tank.

Appendix A-1

(CONTINUED)

Sample	^{85m}Kr	^{88}Kr	^{87}Kr	^{90}Kr	^{135}Xe	^{133}Xe	^{135m}Xe	^{138}Xe	^{137}Xe
HRB21_87	5.51e-06	5.36e-06	5.96e-06	1.18e-06	5.24e-06	6.96e-02	3.00e-06	5.07e-06	1.68e-06
HRB21_88	4.34e-06	5.17e-06	5.41e-06	1.08e-06	3.86e-06	6.01e-02	2.37e-06	4.60e-06	1.77e-06
HRB21_89	1.09e-05	1.05e-05	1.01e-05	1.44e-06	6.98e-06	4.59e-02	4.11e-06	6.93e-06	2.13e-06
HRB21_90	2.01e-05	1.84e-05	1.68e-05	2.58e-06	1.00e-05	3.67e-02	6.11e-06	9.90e-06	3.10e-06
HRB21_91	3.09e-05	3.03e-05	2.73e-05	4.04e-06	1.24e-05	3.45e-02	8.90e-06	1.35e-05	4.34e-06
HRB21_92	3.96e-05	4.21e-05	3.53e-05	5.83e-06	1.80e-05	1.81e-02	1.12e-05	1.64e-05	4.81e-06
HRB21_93	4.25e-05	4.37e-05	3.63e-05	6.77e-06	2.52e-05	4.98e-03	1.45e-05	1.58e-05	5.19e-06
HRB21_94	4.15e-05	4.26e-05	3.38e-05	5.73e-06	2.42e-05	2.14e-03	1.36e-05	1.41e-05	4.69e-06
HRB21_95	6.72e-05	6.28e-05	4.46e-05	7.53e-06	3.59e-05	7.04e-04	2.39e-05	1.81e-05	5.72e-06
HRB21_96	9.16e-05	8.31e-05	6.03e-05	1.35e-05	6.02e-05	5.35e-04	4.34e-05	2.58e-05	1.02e-05
HRB21_97	6.79e-05	6.23e-05	4.28e-05	7.16e-06	4.53e-05	3.80e-04	2.96e-05	1.71e-05	5.19e-06
HRB21_98	7.14e-05	6.55e-05	4.59e-05	8.05e-06	4.52e-05	4.68e-04	3.01e-05	1.84e-05	6.15e-06
HRB21_99	8.20e-05	7.54e-05	5.39e-05	1.05e-05	5.17e-05	5.35e-04	3.78e-05	2.30e-05	8.56e-06
HRB21_100	7.92e-05	7.35e-05	5.41e-05	1.25e-05	5.10e-05	4.55e-04	3.81e-05	2.47e-05	1.32e-05
HRB21_101	8.74e-05	8.09e-05	5.97e-05	1.17e-05	5.16e-05	5.10e-04	3.62e-05	2.38e-05	8.14e-06
HRB21_102	9.56e-05	9.00e-05	6.56e-05	1.75e-05	4.91e-05	6.98e-04	3.59e-05	2.53e-05	9.60e-06
HRB21_103	9.03e-05	8.45e-05	6.16e-05	1.64e-05	4.62e-05	6.60e-04	3.37e-05	2.37e-05	9.00e-06
HRB21_104	9.12e-05	8.62e-05	6.50e-05	1.48e-05	4.85e-05	4.62e-04	3.59e-05	2.45e-05	8.82e-06
HRB21_105	9.10e-05	8.49e-05	6.30e-05	1.37e-05	4.86e-05	5.48e-04	3.43e-05	2.31e-05	8.21e-06

*Not analyzed.
**Sample taken through the holdup tank.

Appendix A-1

(CONTINUED)

Sample	^{85m}Kr	^{88}Kr	^{87}Kr	^{89}Kr	^{135}Xe	^{133}Xe	^{135m}Xe	^{138}Xe	^{137}Xe
HRB21_106	9.99e-05	9.19e-05	6.61e-05	1.37e-05	5.19e-05	6.75e-04	3.67e-05	2.38e-05	8.82e-06
HRB21_107	9.29e-05	8.33e-05	6.00e-05	1.24e-05	4.49e-05	1.13e-03	3.18e-05	2.15e-05	8.46e-06
cycle 5									
HRB21-108	9.05e-06	8.42e-06	9.00e-06	3.04e-06	7.45e-06	2.18e-02	5.20e-06	8.56e-06	4.13e-06
HRB21-109	9.80e-06	1.08e-05	1.08e-05	2.57e-05	8.84e-06	8.21e-02	5.41e-06	1.05e-05	4.28e-06
HRB21-110	1.96e-05	1.97e-05	1.96e-05	5.27e-06	1.05e-05	5.67e-02	9.64e-06	1.66e-05	7.04e-06
HRB21-111	3.27e-05	3.24e-05	3.08e-05	6.09e-06	1.68e-05	3.05e-02	1.25e-05	2.05e-05	7.57e-06
HRB21-112	6.38e-05	6.16e-05	5.68e-05	1.05e-05	2.83e-05	4.44e-02	2.08e-05	3.27e-05	1.17e-05
HRB21-113	9.33e-05	9.92e-05	8.50e-05	1.95e-05	4.69e-05	4.21e-02	3.11e-05	4.38e-05	1.55e-05
HRB21-114	1.03e-04	1.07e-04	8.62e-05	2.06e-05	6.45e-05	8.31e-03	3.63e-05	3.91e-05	1.52e-05
HRB21-115	1.08e-04	1.09e-04	8.67e-05	1.88e-05	6.10e-05	4.12e-03	3.71e-05	3.64e-05	1.48e-05
HRB21-116	1.13e-04	1.07e-04	7.84e-05	1.85e-05	5.99e-05	5.22e-04	4.18e-05	3.21e-05	nd
HRB21-117	1.08e-04	1.01e-04	7.57e-05	1.51e-05	6.14e-05	3.96e-04	4.29e-05	2.97e-05	1.07e-05
HRB21-118	1.86e-04	1.75e-04	1.29e-04	2.54e-05	1.23e-04	1.05e-03	8.38e-05	4.65e-05	1.63e-05
HRB21-119	2.13e-04	1.99e-04	1.49e-04	3.09e-05	1.37e-04	1.17e-03	9.40e-05	5.36e-05	1.95e-05
HRB21-120	1.96e-04	1.85e-04	1.41e-04	2.82e-05	1.33e-04	9.95e-04	9.09e-05	5.22e-05	1.93e-05

*Not analyzed.
**Sample taken through the holdup tank.

Appendix A-1

(CONTINUED)

Sample	^{85m}Kr	^{85}Kr	^{87}Kr	^{88}Kr	^{135}Xe	^{133}Xe	^{135m}Xe	^{138}Xe	^{137}Xe
HRB21-121	1.84e-04	1.73e-04	1.33e-04	3.16e-05	1.09e-04	8.51e-04	7.89e-05	5.09e-05	1.97e-05
HRB21-122	8.73e-05	8.16e-05	6.09e-05	1.20e-05	4.77e-05	4.22e-04	3.27e-05	2.26e-05	6.92e-06
HRB21-123	1.88e-04	1.78e-04	1.37e-04	3.09e-05	1.02e-04	9.61e-04	7.48e-05	5.38e-05	2.24e-05
HRB21-124	2.05e-04	1.94e-04	1.50e-04	3.41e-05	1.10e-04	1.07e-03	8.17e-05	5.90e-05	2.28e-05
HRB21-125	2.01e-04	1.90e-04	1.45e-04	3.23e-05	1.04e-04	1.20e-03	7.35e-05	5.39e-05	1.96e-05
HRB21-126	2.20e-04	2.03e-04	1.52e-04	2.92e-05	1.20e-04	1.59e-03	8.41e-05	5.84e-05	2.12e-05
HRB21-127	2.08e-04	1.98e-04	1.50e-04	3.11e-05	1.25e-04	1.51e-03	8.43e-05	5.64e-05	nd
HRB21-127A	2.07e-04	1.89e-04	1.43e-04	nd	1.24e-04	1.51e-03	nd	nd	nd
HRB21-128	1.97e-04	1.66e-04	nd	nd	1.18e-04	1.14e-03	nd	nd	nd
HRB21-128A	1.94e-04	1.58e-04	nd	nd	1.16e-04	1.13e-03	nd	nd	nd
HRB21-128B	1.76e-04	nd	nd	nd	1.04e-04	1.03e-03	nd	nd	nd
finis									

*Not analyzed.
**Sample taken through the holdup tank.

APPENDIX A-2

CAPSULE CONDITIONS AT R/B SAMPLING TIME

Appendix A-2

CAPSULE CONDITIONS AT R/B SAMPLING TIMES

Sample I.D.	sample date	sample time	elapsed days	full power days	power (%)	exit flow (cc/min)	%He	zone 4	
								temp °C	fluence* x10^{25}
HRB21_1	6/20/91	16:59:59	-0.052	-0.052	10	94.2	100		0.00
HRB21_2	6/20/91	17:21:00	-0.037	-0.037	30	93.7	100		0.00
HRB21_3	6/20/91	17:43:00	-0.022	-0.022	50	93.7	100		0.00
HRB21_3B	6/20/91	17:43:00	-0.022	-0.022	50	93.7	100		0.00
HRB21_4	6/20/91	17:59:00	-0.011	-0.011	70	93.2	100		0.00
HRB21_5	6/20/91	18:15:00	0	0	90	93	100	777	0.00
HRB21_6	6/20/91	19:04:59	0.035	0.035	100	95.7	100	790	0.00
HRB21_7	6/20/91	22:07:59	0.162	0.162	100	90.7	100	834	0.01
HRB21_7B	6/20/91	22:07:59	0.162	0.162	100	90.7	100	834	0.01
HRB21_7C	6/20/91	22:07:59	0.162	0.162	100	90.7	100	834	0.01
HRB21_8	6/21/91	15:38:32	0.891	0.891	100	88.5	100	851	0.03
HRB21_9	6/21/91	16:45:32	0.938	0.938	100	62.8	100	887	0.03
HRB21_10	6/22/91	8:22:59	1.589	1.589	100	86.2	100	895	0.05
HRB21_11	6/22/91	8:59:00	1.614	1.614	100	83.7	100	895	0.05
HRB21_12	6/23/91	8:13:31	2.582	2.582	100	76.9	100	898	0.08

*HTGR: >29 fJ (0.18 MeV).
**Sample taken through the holdup tank.

Appendix A-2

(CONTINUED)

Sample I.D.	sample date	sample time	elapsed days	full power days	power (%)	exit flow (cc/min)	%He	zone 4	
								temp °C	fluence* $x10^{25}$
HRB21_13	6/23/91	8:38:59	2.6	2.6	100	74.4	100	897	0.08
HRB21_14	6/24/91	16:33:02	3.929	3.929	100	84.2	100	898	0.12
HRB21_15	6/24/91	17:07:01	3.953	3.953	100	83.2	100	898	0.12
HRB21_16	6/25/91	17:17:15	4.96	4.96	100	71.7	72.9	960	0.15
HRB21_16B	6/25/91	17:17:15	4.96	4.96	100	71.7	72.9	960	0.15
HRB21_16C	6/25/91	17:17:15	4.96	4.96	100	71.7	72.9	960	0.15
HRB21_17	6/25/91	17:51:59	4.984	4.984	100	70.1	72.7	960	0.15
HRB21_17B	6/25/91	17:51:59	4.984	4.984	100	70.1	72.7	960	0.15
HRB21_18	6/26/91	8:54:00	5.61	5.61	100	93.7	70.7	962	0.17
HRB21_18B	6/26/91	8:54:00	5.61	5.61	100	93.7	70.7	962	0.17
HRB21_18C	6/26/91	8:54:00	5.61	5.61	100	93.7	70.7	962	0.17
HRB21_19	6/26/91	13:45:00	5.813	5.813	100	90.3	70.7	963	0.18
HRB21_19B	6/26/91	13:45:00	5.813	5.813	100	90.3	70.7	963	0.18
HRB21_20**	6/27/91	16:08:59	6.912	6.912	100	76.7	72.5	957	0.21
HRB21_20B	6/27/91	16:08:59	6.912	6.912	100	76.7	72.5	957	0.21

*HTGR: >29 fJ (0.18 MeV).
**Sample taken through the holdup tank.

Appendix A-2

(CONTINUED)

Sample I.D.	sample date	sample time	elapsed days	full power days	power (%)	exit flow (cc/min)	%He	zone 4 temp °C	zone 4 fluence* x10^{25}
HRB21_21	6/28/91	8:37:59	7.599	7.599	100	74.5	72.4	954	0.24
HRB21_21B	6/28/91	8:37:59	7.599	7.599	100	74.5	72.4	954	0.24
HRB21_21C	6/28/91	8:37:59	7.599	7.599	100	74.5	72.4	954	0.24
HRB21_22	6/28/91	12:54:59	7.778	7.778	100	74.6	72.6	956	0.24
HRB21_22B	6/28/91	12:54:59	7.778	7.778	100	74.6	72.6	956	0.24
HRB21_22C	6/28/91	12:54:59	7.778	7.778	100	74.6	72.6	956	0.24
HRB21_22D	6/28/91	12:54:59	7.778	7.778	100	74.6	72.6	956	0.24
HRB21_23	7/1/91	8:50:00	10.608	10.608	100	60.9	62.1	971	0.33
HRB21_23B	7/1/91	8:50:00	10.608	10.608	100	60.9	62.1	971	0.33
HRB21_23C	7/1/91	8:50:00	10.608	10.608	100	60.9	62.1	971	0.33
HRB21_24	7/1/91	13:00:00	10.781	10.781	100	60.4	62.1	972	0.33
HRB21_24B	7/1/91	13:00:00	10.781	10.781	100	60.4	62.1	972	0.33
HRB21_24C	7/1/91	13:00:00	10.781	10.781	100	60.4	62.1	972	0.33
HRB21_25	7/3/91	8:37:00	12.599	12.599	100	70.8	60.1	977	0.39
HRB21_25B	7/3/91	8:37:00	12.599	12.599	100	70.8	60.1	977	0.39

*HTGR: >29 fJ (0.18 MeV).
**Sample taken through the holdup tank.

Appendix A-2

(CONTINUED)

Sample I.D.	sample date	sample time	elapsed days	full power days	power (%)	exit flow (cc/min)	%He	zone 4 temp °C	zone 4 fluence* x10^{25}
HRB21_25C	7/3/91	8:37:00	12.599	12.599	100	70.8	60.1	977	0.39
HRB21_26	7/3/91	14:47:00	12.856	12.856	100	70.1	60	977	0.40
HRB21_26B	7/3/91	14:47:00	12.856	12.856	100	70.1	60	977	0.40
HRB21_26C	7/3/91	14:47:00	12.856	12.856	100	70.1	60	977	0.40
HRB21_27	7/5/91	9:29:00	14.635	14.635	100	69.1	59.8	952	0.45
HRB21_27B	7/5/91	9:29:00	14.635	14.635	100	69.1	59.8	952	0.45
HRB21_27C	7/5/91	9:29:00	14.635	14.635	100	69.1	59.8	952	0.45
HRB21_28	7/5/91	10:29:00	14.676	14.676	100	74.4	100	882	0.45
HRB21_28B	7/5/91	10:29:00	14.676	14.676	100	74.4	100	882	0.45
HRB21_28C	7/5/91	10:29:00	14.676	14.676	100	74.4	100	882	0.45
HRB21_29	7/8/91	8:59:00	17.614	17.614	100	62.3	100	888	0.55
HRB21_29B	7/8/91	8:59:00	17.614	17.614	100	62.3	100	888	0.55
HRB21_29C	7/8/91	8:59:00	17.614	17.614	100	62.3	100	888	0.55
HRB21_30	7/8/91	13:23:27	17.798	17.798	100	58.8	100	889	0.55
HRB21_30B	7/8/91	13:23:27	17.798	17.798	100	58.8	100	889	0.55

*HTGR: >29 fJ (0.18 MeV).
**Sample taken through the holdup tank.

Appendix A-2

(CONTINUED)

Sample I.D.	sample date	sample time	elapsed days	full power days	power (%)	exit flow (cc/min)	%He	zone 4 temp °C	zone 4 fluence* x10^{25}
HRB21_30D	7/8/91	13:23:27	17.798	17.798	100	58.8	100	889	0.55
HRB21_31	7/10/91	8:24:00	19.59	19.59	100	82.2	100	891	0.61
HRB21_31B	7/10/91	8:24:00	19.59	19.59	100	82.2	100	891	0.61
HRB21_31C	7/10/91	8:24:00	19.59	19.59	100	82.2	100	891	0.61
HRB21_32	7/10/91	16:14:00	19.916	19.916	100	80.4	100	891	0.62
HRB21_32B	7/10/91	16:14:00	19.916	19.916	100	80.4	100	891	0.62
HRB21_32C	7/10/91	16:14:00	19.916	19.916	100	80.4	100	891	0.62
end cycle 1	7/11/91	6:53:00	20.526	20.526	0	0	0	877	0.64
start cycle 2	7/25/91	22:10:00	35.163	20.526	0	0	0	871	0.64
HRB21_33	7/25/91	20:59:03	35.114	20.526	10	77.2	100	231	0.64
HRB21_34	7/25/91	21:18:18	35.127	20.526	30	74.4	100	280	0.64
HRB21-35	7/25/91	21:38:00	35.141	20.526	50	74.6	100	330	0.64
HRB21_36	7/25/91	21:57:12	35.154	20.526	70	75.2	100	379	0.64
HRB21_37	7/25/91	22:11:00	35.164	20.526	90	74.5	100	871	0.64
HRB21_38	7/25/91	22:43:15	35.186	20.549	100	74.5	100	872	0.64

*HTGR: >29 fJ (0.18 MeV).
**Sample taken through the holdup tank.

Appendix A-2

(CONTINUED)

Sample I.D.	sample date	sample time	elapsed days	full power days	power (%)	exit flow (cc/min)	%He	zone 4 temp °C	zone 4 fluence* x10^{25}
HRB21_39	7/25/91	23:22:00	35.213	20.576	100	74.6	100	878	0.64
HRB21_40	7/26/91	11:02:04	35.699	21.063	100	70.7	61.3	993	0.65
HRB21_40B	7/26/91	11:02:04	35.699	21.063	100	70.7	61.3	993	0.65
HRB21_40D	7/26/91	11:02:04	35.699	21.063	100	70.7	61.3	993	0.65
HRB21_40E	7/26/91	11:02:04	35.699	21.063	100	70.7	61.3	993	0.65
HRB21_41	7/26/91	12:53:00	35.776	21.14	100	71.8	61	981	0.65
HRB21_41B	7/26/91	12:53:00	35.776	21.14	100	71.8	61	981	0.65
HRB21_42	7/26/91	14:38:00	35.849	21.213	100	77.1	100	928	0.66
HRB21_42B	7/26/91	14:38:00	35.849	21.213	100	77.1	100	928	0.66
HRB21_43	7/27/91	8:44:19	36.604	21.967	100	71.6	100	933	0.68
HRB21_43B	7/27/91	8:44:19	36.604	21.967	100	71.6	100	933	0.68
HRB21_44	7/28/91	8:21:46	37.588	22.951	100	76.9	100	933	0.71
HRB21_44B	7/28/91	8:21:46	37.588	22.951	100	76.9	100	933	0.71
HRB21_45	7/29/91	8:41:53	38.602	23.965	100	78.9	100	932	0.74
HRB21_45B	7/29/91	8:41:53	38.602	23.965	100	78.9	100	932	0.74

*HTGR: >29 fJ (0.18 MeV).
**Sample taken through the holdup tank.

Appendix A-2

(CONTINUED)

Sample I.D.	sample date	sample time	elapsed days	full power days	power (%)	exit flow (cc/min)	%He	zone 4	
								temp °C	fluence* x10^{25}
HRB21_46	7/30/91	11:57:06	39.738	25.101	100	76.2	100	932	0.78
HRB21_46B	7/30/91	11:57:06	39.738	25.101	100	76.2	100	932	0.78
HRB21_47	7/31/91	9:32:09	40.637	26	100	78.8	100	931	0.81
HRB21_47B	7/31/91	9:32:09	40.637	26	100	78.8	100	931	0.81
HRB21_48	7/31/91	12:31:57	40.762	26.125	100	77.5	100	931	0.81
HRB21_48A	7/31/91	12:31:57	40.762	26.125	100	77.5	100	931	0.81
HRB21_48B	7/31/91	12:31:57	40.762	26.125	100	77.5	100	931	0.81
HRB21_49	8/2/91	8:35:00	42.597	27.96	100	78.4	100	930	0.87
HRB21_50	8/2/91	10:37:44	42.682	28.046	100	76.4	100	931	0.87
HRB21_51	8/5/91	8:54:27	45.611	30.974	100	77.8	100	932	0.96
HRB21_52	8/5/91	15:01:09	45.865	31.229	100	71.9	66.8	1013	0.97
HRB21_52B	8/5/91	15:01:09	45.865	31.229	100	71.9	66.8	1013	0.97
HRB21_53	8/5/91	16:53:10	45.943	31.306	100	72.3	66.5	1016	0.97
HRB21_54	8/5/91	18:10:11	45.997	31.36	100	72.5	66.4	1017	0.97
HRB21_54G	8/5/91	18:10:11	45.997	31.36	100	72.5	66.4	1017	0.97

*HTGR: >29 fJ (0.18 MeV).
**Sample taken through the holdup tank.

Appendix A-2

(CONTINUED)

Sample I.D.	sample date	sample time	elapsed days	full power days	power (%)	exit flow (cc/min)	%He	zone 4 temp °C	zone 4 fluence* x10^{25}
HRB21_54I	8/5/91	18:10:11	45.997	31.36	100	72.5	66.4	1017	0.97
HRB21_55	8/6/91	15:20:01	46.878	32.242	100	73	66	1017	1.00
HRB21_55B	8/6/91	15:20:01	46.878	32.242	100	73	66	1017	1.00
HRB21_56	8/7/91	8:48:46	47.607	32.97	100	79.4	65.8	1019	1.02
HRB21_56B	8/7/91	8:48:46	47.607	32.97	100	79.4	65.8	1019	1.02
HRB21_57	8/7/91	12:41:04	47.768	33.131	100	78.8	65.8	1019	1.03
HRB21_57B	8/7/91	12:41:04	47.768	33.131	100	78.8	65.8	1019	1.03
HRB21_58*	8/7/91	sample not analyzed due to contaminated bottle							
HRB21_59**	8/7/91	15:13:04	47.874	33.237	100	78.7	65.8	1020	1.03
HRB21_59B	8/7/91	15:13:04	47.874	33.237	100	78.7	65.8	1020	1.03
HRB21_60**	8/8/91	11:10:48	48.705	34.069	100	78.5	65.8	1020	1.05
HRB21_60B	8/8/91	11:10:48	48.705	34.069	100	78.5	65.8	1020	1.05
HRB21_61**	8/9/91	9:01:38	49.616	34.979	100	57.2	100	957	1.08
HRB21_61B	8/9/91	9:01:38	49.616	34.979	100	57.2	100	957	1.08
HRB21_62**	8/9/91	11:44:38	49.729	35.092	100	78.4	67.6	1022	1.09

*HTGR: >29 fJ (0.18 MeV).
**Sample taken through the holdup tank.

Appendix A-2

(CONTINUED)

Sample I.D.	sample date	sample time	elapsed days	full power days	power (%)	exit flow (cc/min)	%He	zone 4 temp °C	zone 4 fluence* x10^25
HRB21_62B	8/9/91	11:44:38	49.729	35.092	100	78.4	67.6	1022	1.09
HRB21_63**	8/12/91	8:47:28	52.606	37.969	100	79.9	65.8	1033	1.18
HRB21_63B	8/12/91	8:47:28	52.606	37.969	100	79.9	65.8	1033	1.18
HRB21_64**	8/14/91	15:53:25	54.902	40.265	100	74	90.8	972	1.25
end cycle 2	8/15/91	8:55:00	55.611	40.974	0	0	0	951	1.27
start cycle 3	8/28/91	11:48:00	68.731	40.974	0	0	0	942	1.27
HRB21_65	8/28/91	10:20:41	68.671	40.974	10	72.4	100	162	1.27
HRB21_66	8/28/91	10:42:42	68.686	40.974	30	79.9	100	195	1.27
HRB21-67	8/28/91	11:02:42	68.7	40.974	50	80.9	100	270	1.27
HRB21_68	8/28/91	11:22:42	68.714	40.974	70	80.5	100	346	1.27
HRB21_69	8/28/91	11:39:42	68.725	40.974	90	80.5	100	410	1.27
HRB21_70	8/28/91	12:09:42	68.746	40.989	100	80.9	100	945	1.27
HRB21_71**	8/28/91	13:37:42	68.807	41.05	100	79.9	100	960	1.27
HRB21_72**	8/28/91	14:57:42	68.863	41.106	100	79.8	100	970	1.27
HRB21_73	8/29/91	9:19:00	69.628	41.871	100	83.1	100	1009	1.30

*HTGR: >29 fJ (0.18 MeV).
**Sample taken through the holdup tank.

Appendix A-2

(CONTINUED)

Sample I.D.	sample date	sample time	elapsed days	full power days	power (%)	exit flow (cc/min)	%He	zone 4 temp °C	zone 4 fluence* x10^{25}
HRB21_74	8/30/91	10:23:36	70.673	42.916	100	83.7	100	1007	1.33
HRB21_75	8/30/91	14:36:14	70.848	43.091	100	72.4	85.3	1039	1.33
HRB21_75A	8/30/91	14:36:14	70.848	43.091	100	72.4	85.3	1039	1.33
HRB21_76	8/31/91	7:18:05	71.544	43.787	100	75.2	84.4	1049	1.36
HRB21_77	9/1/91	8:55:16	72.611	44.854	100	73.7	84.5	1050	1.39
HRB21_77A	9/1/91	8:55:16	72.611	44.854	100	73.7	84.5	1050	1.39
HRB21_78	9/3/91	9:10:04	74.622	46.865	100	73.2	84.4	1050	1.45
HRB21_79	9/4/91	13:20:08	75.795	48.038	100	74.5	84.4	1054	1.49
HRB21_80	9/6/91	8:37:55	77.599	49.842	100	75.6	84.3	1055	1.54
HRB21_81	9/9/91	8:51:28	80.609	52.852	100	76.6	83.7	1064	1.64
HRB21_82	9/11/91	8:28:00	82.592	54.835	100	76.3	83.7	1067	1.70
HRB21_83	9/13/91	9:55:19	84.653	56.896	100	73.7	90	1054	1.76
HRB21_84	9/13/91	12:33:19	84.763	57.006	100	72.8	90.1	1051	1.77
HRB21_85	9/16/91	8:48:50	87.607	59.85	100	74.1	96.4	1038	1.85
HRB21_86	9/17/91	8:38:47	88.6	60.843	100	71.5	96.3	1037	1.88

*HTGR: >29 fJ (0.18 MeV).
**Sample taken through the holdup tank.

Appendix A-2

(CONTINUED)

Sample I.D.	sample date	sample time	elapsed days	full power days	power (%)	exit flow (cc/min)	%He	zone 4	
								temp °C	fluence* $x10^{25}$
end cycle 3	9/17/91	17:44:00	88.978	61.222	0	0	0	1026	1.90
start cycle 4	9/27/91	21:18:00	99.127	61.222	0	0	0	998	1.90
HRB21_87	9/27/91	19:10:17	99.038	61.222	10	77.4	100	172	1.90
HRB21_88	9/27/91	19:34:17	99.055	61.222	30	78.1	100	216	1.90
HRB21_89	9/27/91	20:30:58	99.094	61.222	50	77.4	100	320	1.90
HRB21_90	9/27/91	20:54:15	99.111	61.222	70	77.6	100	374	1.90
HRB21_91	9/27/91	21:15:42	99.125	61.222	90	77.5	100	451	1.90
HRB21_92	9/27/91	21:35:30	99.139	61.234	100	77.4	100	998	1.90
HRB21_93	9/27/91	22:52:08	99.192	61.287	100	77.8	100	1012	1.90
HRB21_94	9/28/91	0:06:11	99.244	61.338	100	77.4	100	1024	1.90
HRB21_95	9/28/91	9:56:33	99.654	61.748	100	70.6	100	1064	1.91
HRB21_96	9/29/91	8:28:59	100.593	62.688	100	71.9	100	1074	1.94
HRB21_97	9/30/91	8:48:05	101.606	63.701	100	72.5	100	1071	1.97
HRB21_98	10/1/91	8:03:49	102.576	64.67	100	71.5	100	1068	2.00
HRB21_99	10/2/91	8:31:15	103.595	65.689	100	72.9	100	1069	2.03

*HTGR: >29 fJ (0.18 MeV).
**Sample taken through the holdup tank.

Appendix A-2

(CONTINUED)

Sample I.D.	sample date	sample time	elapsed days	full power days	power (%)	exit flow (cc/min)	%He	zone 4 temp °C	zone 4 fluence* x10^{25}
HRB21_100	10/4/91	8:23:20	105.589	67.684	100	72.9	100	1070	2.10
HRB21_101	10/7/91	9:37:10	108.64	70.735	100	75.8	100	1072	2.19
HRB21_102	10/9/91	8:29:00	110.593	72.688	100	73.9	100	1071	2.25
HRB21_103	10/11/91	8:28:00	112.592	74.687	100	70.5	100	1078	2.31
HRB21_104	10/11/91	10:36:05	112.681	74.776	100	69.9	100	1075	2.32
HRB21_105	10/14/91	10:40:18	115.684	77.779	100	69.5	100	1080	2.41
HRB21_106	10/16/91	8:29:45	117.594	79.688	100	71.5	100	1088	2.47
HRB21_107	10/18/91	8:27:55	119.592	81.687	100	69.9	100	1085	2.53
end cycle 4	10/19/91	17:35:00	120.972	83.067	0	0	0	1080	2.57
start cycle 5	10/30/91	12:00:00	131.781	83.067	0	0	0	280	2.57
HRB21-108	10/30/91	10:24:56	131.715	83.067	10	72.2	100	78	2.57
HRB21-109	10/30/91	10:41:03	131.726	83.067	30	71.5	100	112	2.57
HRB21-110	10/30/91	11:06:50	131.744	83.067	50	72.1	100	167	2.57
HRB21-111	10/30/91	11:29:31	131.76	83.067	70	71.8	100	215	2.57
HRB21-112	10/30/91	11:54:26	131.777	83.067	90	71.8	100	268	2.57

*HTGR: >29 fJ (0.18 MeV).
**Sample taken through the holdup tank.

Appendix A-2

(CONTINUED)

Sample I.D.	sample date	sample time	elapsed days	full power days	power (%)	exit flow (cc/min)	%He	zone 4	
								temp °C	fluence* x10^{25}
HRB21-113	10/30/91	12:19:55	131.795	83.08	100	71.9	100	364	2.57
HRB21-114	10/30/91	13:55:07	131.861	83.147	100	71.4	100	1071	2.57
HRB21-115	10/30/91	15:37:20	131.932	83.218	100	71.2	100	1089	2.58
HRB21-116	10/31/91	8:42:33	132.644	83.93	100	72.5	100	1094	2.60
HRB21-117	11/1/91	9:08:46	133.662	84.948	100	73.1	100	1096	2.63
HRB21-118	11/2/91	8:13:07	134.624	85.909	100	74.6	100	1144	2.66
HRB21-119	11/3/91	9:08:04	135.662	86.947	100	75.9	100	1143	2.69
HRB21-120	11/4/91	9:20:02	136.67	87.956	100	73.6	100	1134	2.72
HRB21-121	11/6/91	9:22:03	138.672	89.957	100	73.4	100	1132	2.79
HRB21-122	11/8/91	11:31:59	140.762	92.047	100	71.6	100	1130	2.85
HRB21-123	11/11/91	11:41:56	143.769	95.054	100	71.4	100	1133	2.94
HRB21-124	11/13/91	11:35:21	145.764	97.05	100	71.4	100	1132	3.01
HRB21-125	11/15/91	10:13:03	147.707	98.992	100	71.8	100	1134	3.07
HRB21-126	11/18/91	10:14:19	150.708	101.993	100	70.2	100	1135	3.16
HRB21-127	11/20/91	11:00:15	152.74	104.025	100	71.1	100	1132	3.22

*HTGR: >29 fJ (0.18 MeV).
**Sample taken through the holdup tank.

Appendix A-2

(CONTINUED)

Sample I.D.	sample date	sample time	elapsed days	full power days	power (%)	exit flow (cc/min)	%He	zone 4	
								temp °C	fluence* $x10^{25}$
HRB21-127A	11/20/91	11:00:15	152.74	104.025	100	71.1	100	1132	3.22
HRB21-128	11/20/91	15:40:31	152.934	104.22	100	71.4	100	1133	3.23
HRB21-128A	11/20/91	15:40:31	152.934	104.22	100	71.4	100	1133	3.23
HRB21-128B	11/20/91	15:40:31	152.934	104.22	100	71.4	100	1133	3.23
finis	11/21/91	2:18:00	153.377	104.663	0	0	0	1132	3.24

*HTGR: >29 fJ (0.18 MeV).
**Sample taken through the holdup tank.

APPENDIX A-3

FISSION GAS CONCENTRATION IN SWEEP GAS

Appendix A-3

FISSION GAS CONCENTRATION IN SWEEP GAS

Sample I.D.	Concentration (uCi per cm³)								
	^{85m}Kr	^{88}Kr	^{87}Kr	^{89}Kr	^{135}Xe	^{133}Xe	^{135m}Xe	^{138}Xe	^{137}Xe
cycle 1									
HRB21_1	nd	nd	nd	nd	nd	nd	nd	1.64e-04	nd
HRB21_2	nd	nd	nd	nd	nd	nd	nd	3.11e-04	nd
HRB21_3	nd	nd	nd	nd	nd	nd	nd	9.08e-04	nd
HRB21_3B	nd	1.67e-04	nd	nd	nd	nd	nd	nd	nd
HRB21_4	nd	1.50e+00	nd	nd	nd	nd	nd	1.46e+00	nd
HRB21_5	3.89e-05	1.67e-04	3.65e-04	nd	nd	nd	nd	2.01e-03	nd
HRB21_6	0.00	nd	1.83e-05	nd	nd	nd	nd	0.00	nd
HRB21_7	6.83e-05	3.78e-04	5.45e-04	nd	1.74e-05	nd	nd	1.96e-03	nd
HRB21_7B	nd	4.61e+00	nd	nd	2.49e-05	nd	nd	nd	nd
HRB21_7C	7.00e-05	nd	nd	nd	1.71e-05	nd	nd	nd	nd
HRB21_8	1.89e-04	7.67e-04	7.78e-04	nd	nd	nd	3.29e-04	3.12e-03	nd
HRB21_9	1.73e-04	7.35e-04	9.26e-04	nd	1.05e-04	nd	4.27e-04	1.97e-03	nd
HRB21_10	1.48e-04	7.70e-04	7.85e-04	8.87e-03	8.51e-05	nd	5.95e-04	2.27e-03	nd
HRB21_11	1.64e-04	5.63e-04	8.76e-04	1.01e-02	7.06e-05	nd	3.18e-04	2.15e-03	nd
HRB21_12	1.81e-04	6.73e-04	9.71e-04	2.21e-02	8.37e-05	nd	1.69e-04	1.66e-03	nd

*Not analyzed.
**Sample taken through the holdup tank.

Appendix A-3

(CONTINUED)

Sample I.D.	Concentration (uCi per cm^3)								
	^{85m}Kr	^{85}Kr	^{87}Kr	^{88}Kr	^{135}Xe	^{133}Xe	^{135m}Xe	^{138}Xe	^{137}Xe
HRB21_13	1.84e-04	8.21e-04	9.20e-04	9.00e-03	8.41e-05	nd	2.93e-04	2.20e-03	nd
HRB21_14	1.85e-04	6.55e-04	8.57e-04	6.55e-03	1.22e-04	nd	2.29e-04	2.03e-03	nd
HRB21_15	1.74e-04	7.72e-04	8.23e-04	6.19e-03	6.07e-05	nd	3.76e-04	2.03e-03	nd
HRB21_16	6.06e-04	1.99e-03	1.96e-03	7.41e-03	9.63e-05	nd	nd	3.75e-03	nd
HRB21_16B	6.65e-04	1.62e-03	nd	nd	7.64e-05	6.40e-05	nd	nd	nd
HRB21_16C	nd	nd	nd	nd	nd	4.66e-05	nd	nd	nd
HRB21_17	5.45e-04	1.91e-03	1.91e-03	1.73e-02	7.07e-05	nd	5.93e-04	3.12e-03	nd
HRB21_17B	nd	nd	nd	nd	nd	5.62e-05	nd	nd	nd
HRB21_18	2.76e-04	1.26e-03	1.59e-03	1.65e-02	5.09e-05	nd	4.23e-04	2.04e-03	nd
HRB21_18B	3.26e-04	1.18e-03	1.33e-03	nd	9.41e-05	nd	nd	nd	nd
HRB21_18C	nd	nd	nd	nd	nd	1.75e-05	nd	nd	nd
HRB21_19	3.20e-04	1.21e-03	1.59e-03	9.22e-03	7.37e-05	nd	6.17e-04	2.79e-03	nd
HRB21_19B	nd	nd	nd	nd	nd	nd	nd	nd	nd
HRB21_20**	3.62e-04	1.30e-03	1.31e-03	nd	9.48e-05	nd	nd	nd	nd
HRB21_20B	nd	nd	nd	nd	nd	3.32e-05	nd	nd	nd
HRB21_21	4.07e-04	1.52e-03	1.62e-03	1.12e-02	nd	nd	nd	3.28e-03	nd

*Not analyzed.
**Sample taken through the holdup tank.

Appendix A-3

(CONTINUED)

Sample I.D.	Concentration (uCi per cm^3)								
	^{85m}Kr	^{88}Kr	^{87}Kr	^{89}Kr	^{135}Xe	^{133}Xe	^{135m}Xe	^{138}Xe	^{137}Xe
HRB21_21B	3.75e-04	1.38e-03	1.48e-03	9.71e-03	7.99e-05	nd	8.17e-04	3.18e-03	nd
HRB21_21C	nd	nd	nd	nd	nd	3.60e-05	nd	nd	nd
HRB21_22	2.08e-04	1.46e-03	1.41e-03	1.04e-02	nd	nd	4.66e-04	2.74e-03	nd
HRB21_22B	2.66e-04	1.02e-03	1.34e-03	5.77e-03	1.06e-04	nd	2.78e-04	1.92e-03	nd
HRB21_22C	nd	nd	nd	nd	nd	2.73e-05	nd	nd	nd
HRB21_22D	nd	nd	nd	nd	nd	2.66e-05	nd	nd	nd
HRB21_23	6.01e-04	2.07e-03	2.60e-03	7.97e-03	nd	nd	4.89e-04	3.00e-03	nd
HRB21_23B	5.37e-04	1.95e-03	2.19e-03	1.50e-02	1.19e-04	6.12e-05	9.28e-04	3.12e-03	nd
HRB21_23C	nd	nd	nd	nd	nd	4.71e-05	nd	nd	nd
HRB21_24	4.70e-04	2.37e-03	2.74e-03	nd	nd	nd	7.33e-04	4.58e-03	nd
HRB21_24B	5.97e-04	2.19e-03	2.55e-03	8.84e-03	1.16e-04	6.39e-05	7.54e-04	3.98e-03	nd
HRB21_24C	nd	nd	nd	nd		4.54e-05	nd	nd	nd
HRB21_25	6.32e-04	2.28e-03	2.24e-03	1.35e-02	2.25e-04	nd	nd	3.83e-03	nd
HRB21_25B	5.79e-04	2.25e-03	2.41e-03	1.53e-02	1.22e-04	8.01e-05	7.98e-04	2.89e-03	nd
HRB21_25C	nd	nd	nd	nd	nd	4.12e-05		nd	nd
HRB21_26	7.64e-04	2.18e-03	2.60e-03	1.62e-02	nd	nd	7.95e-04	3.33e-03	nd

*Not analyzed.
**Sample taken through the holdup tank.

Appendix A-3

(CONTINUED)

Sample I.D.	Concentration (uCi per cm^3)								
	^{85m}Kr	^{85}Kr	^{87}Kr	^{88}Kr	^{135}Xe	^{133}Xe	^{135m}Xe	^{138}Xe	^{137}Xe
HRB21_26B	6.16e-04	2.23e-03	2.47e-03	1.01e-02	1.28e-04	7.87e-05	4.89e-04	3.12e-03	nd
HRB21_26C	nd	nd	nd	nd	nd	5.83e-05	nd	nd	nd
HRB21_27	8.44e-04	2.80e-03	3.38e-03	1.20e-02	2.56e-04	nd	6.31e-04	4.55e-03	nd
HRB21_27B	7.10e-04	2.85e-03	3.23e-03	1.76e-02	1.65e-04	5.45e-05	7.03e-04	4.18e-03	nd
HRB21_27C	nd	nd	nd	nd	nd	7.39e-05	nd	nd	nd
HRB21_28	1.75e-04	7.01e-04	8.97e-04	9.84e-03	1.55e-04	nd	4.70e-04	2.01e-03	nd
HRB21_28B	1.86e-04	4.72e-04	8.56e-04	9.26e-03	1.25e-04	nd	7.70e-04	2.25e-03	nd
HRB21_28C	nd	nd	nd	nd	nd	1.81e-05	nd	nd	nd
HRB21_29	3.03e-04	1.42e-03	1.60e-03	5.28e-03	1.44e-04	nd	3.89e-04	2.71e-03	5.73e-03
HRB21_29B	3.37e-04	1.24e-03	1.39e-03	3.42e-03	1.15e-04	nd	5.62e-04	2.31e-03	nd
HRB21_29C	nd	nd	nd	nd		nd	nd	nd	nd
HRB21_30	3.29e-04	1.26e-03	1.46e-03	6.45e-03	1.43e-04	nd	6.43e-04	1.92e-03	nd
HRB21_30B	3.24e-04	1.10e-03	1.27e-03	9.32e-03	8.94e-05	4.65e-05	4.76e-04	2.17e-03	nd
HRB21_30D	nd	nd	nd	nd	nd	2.62e-05	nd	nd	nd
HRB21_31	3.37e-04	1.12e-03	1.34e-03	1.35e-02	1.03e-04	nd	4.74e-04	2.70e-03	nd
HRB21_31B	2.88e-04	1.07e-03	1.26e-03	9.04e-03	9.22e-05	nd	5.91e-04	1.96e-03	nd

*Not analyzed.
**Sample taken through the holdup tank.

Appendix A-3

(CONTINUED)

Sample I.D.	Concentration (uCi per cm³)								
	^{85m}Kr	^{85}Kr	^{87}Kr	^{88}Kr	^{135}Xe	^{133}Xe	^{135m}Xe	^{138}Xe	^{137}Xe
HRB21_31C	nd	nd	nd	nd	9.60e-05	2.33e-05	nd	nd	nd
HRB21_32	3.40e-04	1.35e-03	1.27e-03	9.50e-03	7.15e-05	nd	5.52e-04	2.43e-03	3.51e-03
HRB21_32B	2.88e-04	1.08e-03	1.25e-03	1.10e-02	9.26e-05	nd	4.62e-04	2.56e-03	nd
HRB21_32C	nd	nd	nd	nd	3.57e-05	2.40e-05	nd	nd	nd
cycle 2									
HRB21_33	nd	nd	nd	nd	nd	nd	nd	1.08e-04	nd
HRB21_34	nd	nd	2.75e-05	nd	nd	nd	nd	2.17e-04	nd
HRB21-35	nd	3.69e-05	5.66e-05	nd	nd	nd	nd	4.75e-04	nd
HRB21_36	nd	9.78e-05	7.58e-05	1.63e-03	nd	nd	4.47e-05	5.62e-04	nd
HRB21_37	4.01e-05	1.51e-04	2.77e-04	1.96e-03	nd	nd	1.40e-04	1.23e-03	nd
HRB21_38	7.24e-05	3.22e-04	4.06e-04	4.09e-03	nd	nd	nd	1.51e-03	nd
HRB21_39	8.56e-05	3.32e-04	5.02e-04	3.77e-03	2.03e-05	nd	1.51e-04	1.45e-03	nd
HRB21_40	4.33e-02	1.26e-01	8.47e-02	1.35e-01	1.38e-02	1.26e-01	6.57e-02	1.18e-01	nd
HRB21_40B	4.34e-02	1.25e-01	8.34e-02	1.17e-01	1.43e-02	1.24e-01	6.32e-02	1.16e-01	nd
HRB21_40D	nd	nd	nd	nd	1.82e-02	1.28e-01	nd	nd	nd

*Not analyzed.
**Sample taken through the holdup tank.

Appendix A-3

(CONTINUED)

Sample I.D.	Concentration (uCi per cm^3)								
	^{85m}Kr	^{88}Kr	^{87}Kr	^{89}Kr	^{135}Xe	^{133}Xe	^{135m}Xe	^{138}Xe	^{137}Xe
HRB21_40E	nd	nd	nd	nd	nd	1.29e-01	nd	nd	nd
HRB21_41	9.57e-03	3.15e-02	2.83e-02	1.64e-01	2.70e-02	8.75e-03	1.18e-01	3.46e-02	7.15e-02
HRB21_41B	9.79e-03	3.09e-02	2.76e-02	1.33e-01	2.82e-02	8.46e-03	1.15e-01	3.56e-02	nd
HRB21_42	2.36e-03	8.44e-03	9.81e-03	5.85e-02	3.04e-02	1.82e-03	1.28e-01	2.00e-02	nd
HRB21_42B	2.36e-03	8.44e-03	9.66e-03	6.43e-02	3.17e-02	1.98e-03	1.25e-01	1.86e-02	nd
HRB21_43	4.99e-03	1.85e-02	2.11e-02	1.05e-01	6.26e-03	1.32e-03	2.80e-02	3.36e-02	4.76e-02
HRB21_43B	4.87e-03	1.80e-02	2.03e-02	1.10e-01	6.73e-03	1.33e-03	2.83e-02	3.34e-02	5.44e-02
HRB21_44	4.59e-03	1.73e-02	1.87e-02	9.19e-02	3.01e-03	1.11e-03	1.37e-02	3.27e-02	3.67e-02
HRB21_44B	4.54e-03	1.66e-02	1.90e-02	1.16e-01	3.08e-03	1.04e-03	1.35e-02	3.23e-02	nd
HRB21_45	3.99e-03	1.41e-02	1.63e-02	8.67e-02	2.33e-03	8.87e-04	9.57e-03	2.87e-02	4.04e-02
HRB21_45B	3.96e-03	1.44e-02	1.61e-02	9.54e-02	2.31e-03	8.64e-04	1.05e-02	2.87e-02	6.56e-02
HRB21_46	3.90e-03	1.37e-02	1.64e-02	1.00e-01	2.32e-03	8.43e-04	1.07e-02	2.83e-02	3.84e-02
HRB21_46B	3.91e-03	1.43e-02	1.59e-02	7.75e-02	2.22e-03	8.64e-04	9.78e-03	2.77e-02	nd
HRB21_47	5.17e-03	2.02e-02	2.21e-02	1.46e-01	2.80e-03	1.38e-03	1.36e-02	4.16e-02	5.61e-02
HRB21_47B	5.28e-03	1.90e-02	2.17e-02	1.34e-01	3.01e-03	1.38e-03	1.34e-02	3.98e-02	nd
HRB21_48	5.35e-03	1.98e-02	2.19e-02	1.30e-01	2.84e-03	1.49e-03	1.31e-02	3.88e-02	5.64e-02

*Not analyzed.
**Sample taken through the holdup tank.

Appendix A-3

(CONTINUED)

Sample I.D.	Concentration (uCi per cm³)								
	^{85m}Kr	^{85}Kr	^{87}Kr	^{88}Kr	^{135}Xe	^{133}Xe	^{135m}Xe	^{138}Xe	^{137}Xe
HRB21_48A	5.01e-03	1.98e-02	2.22e-02	1.14e-01	2.97e-03	1.25e-03	1.36e-02	3.87e-02	7.95e-02
HRB21_48B	5.17e-03	1.88e-02	2.14e-02	1.22e-01	3.04e-03	1.32e-03	1.37e-02	3.73e-02	nd
HRB21_49	5.96e-03	2.15e-02	2.47e-02	1.41e-01	3.61e-03	1.66e-03	1.60e-02	4.35e-02	6.85e-02
HRB21_50	5.63e-03	2.00e-02	2.68e-02	1.14e-01	3.35e-03	2.02e-03	1.50e-02	4.16e-02	6.64e-02
HRB21_51	6.52e-03	2.35e-02	2.68e-02	1.91e-01	4.00e-03	2.50e-03	1.85e-02	4.84e-02	5.43e-02
HRB21_52	1.28e-01	3.52e-01	2.70e-01	8.32e-01	3.17e-02	9.49e-01	1.77e-01	3.97e-01	3.90e-01
HRB21_52B	1.32e-01	3.60e-01	2.67e-01	7.70e-01	3.45e-02	9.85e-01	1.68e-01	3.87e-01	nd
HRB21_53	1.39e-01	3.69e-01	2.73e-01	7.32e-01	1.61e-01	9.43e-01	7.46e-01	3.93e-01	2.99e-01
HRB21_54	1.66e-01	4.34e-01	3.03e-01	8.56e-01	2.17e-01	1.12e+00	9.99e-01	4.55e-01	3.66e-01
HRB21_54G	1.87e-01	4.66e-01	3.17e-01	8.22e-01	2.53e-01	1.15e+00	9.83e-01	4.23e-01	nd
HRB21_54I	2.08e-01	4.75e-01	3.92e-01	nd	2.84e-01	1.31e+00	nd	nd	nd
HRB21_55	9.01e-02	2.70e-01	2.90e-01	1.42e+00	3.65e-01	2.35e-01	1.80e+00	7.43e-01	9.99e-01
HRB21_55B	8.87e-02	2.77e-01	2.75e-01	1.65e+00	3.98e-01	2.43e-01	1.76e+00	7.42e-01	7.38e-01
HRB21_56	1.12e-01	3.81e-01	4.01e-01	2.71e+00	2.85e-01	2.11e-01	1.48e+00	1.58e+00	2.47e+00
HRB21_56B	1.17e-01	3.65e-01	3.76e-01	1.69e+00	3.11e-01	2.26e-01	1.42e+00	1.57e+00	2.46e+00
HRB21_57	8.45e-02	2.97e-01	3.55e-01	2.61e+00	2.65e-01	1.56e-01	1.40e+00	1.62e+00	2.58e+00

*Not analyzed.
**Sample taken through the holdup tank.

Appendix A-3

(CONTINUED)

Sample I.D.	Concentration (uCi per cm^3)								
	^{85m}Kr	^{88}Kr	^{87}Kr	^{89}Kr	^{135}Xe	^{133}Xe	^{135m}Xe	^{138}Xe	^{137}Xe
HRB21_57B	8.94e-02	3.03e-01	3.44e-01	1.72e+00	2.96e-01	1.56e-01	1.36e+00	1.64e+00	2.33e+00
HRB21_58	Sample not analyzed because bottle contaminated								
HRB21_59**	1.07e-01	3.40e-01	3.21e-01	nd	3.02e-01	2.57e-01	6.24e-01	7.47e-01	nd
HRB21_59B	1.08e-01	3.36e-01	3.15e-01	nd	3.08e-01	2.58e-01	6.15e-01	7.35e-01	nd
HRB21_60**	1.09e-01	3.46e-01	3.30e-01	nd	2.73e-01	2.57e-01	5.93e-01	7.85e-01	nd
HRB21_60B	1.09e-01	3.45e-01	3.25e-01	nd	2.81e-01	2.58e-01	5.87e-01	7.68e-01	nd
HRB21_61**	7.21e-02	2.48e-01	2.39e-01	nd	2.35e-01	1.29e-01	4.68e-01	6.75e-01	nd
HRB21_61B	7.15e-02	2.39e-01	2.36e-01	nd	2.36e-01	1.19e-01	4.69e-01	6.59e-01	nd
HRB21_62**	1.55e-01	4.76e-01	4.25e-01	nd	1.76e-01	5.98e-01	4.29e-01	9.29e-01	nd
HRB21_62B	1.57e-01	4.94e-01	4.21e-01	nd	1.81e-01	6.00e-01	4.00e-01	8.51e-01	nd
HRB21_63**	1.90e-01	6.60e-01	6.66e-01	nd	3.98e-01	4.86e-01	8.79e-01	2.06e+00	nd
HRB21_63B	2.00e-01	6.65e-01	6.60e-01	nd	4.15e-01	5.07e-01	nd	nd	nd
HRB21_64**	1.02e-01	3.74e-01	3.81e-01	nd	1.77e-01	9.54e-02	4.03e-01	1.17e+00	nd
cycle 3									
HRB21_65	1.24e-03	5.06e-03	7.72e-03	6.63e-02	4.46e-04	1.38e-02	3.53e-03	6.16e-02	8.68e-02

*Not analyzed.
**Sample taken through the holdup tank.

Appendix A-3

(CONTINUED)

Sample I.D.	Concentration (uCi per cm^3)								
	^{85m}Kr	^{88}Kr	^{87}Kr	^{89}Kr	^{135}Xe	^{133}Xe	^{135m}Xe	^{138}Xe	^{137}Xe
HRB21_66	3.32e-03	1.51e-02	2.38e-02	2.05e-01	1.06e-03	6.50e-02	9.06e-03	1.86e-01	2.74e-01
HRB21-67	1.16e-02	5.06e-02	7.88e-02	4.82e-01	3.10e-03	1.38e-01	2.74e-02	5.26e-01	7.33e-01
HRB21_68	2.27e-02	9.89e-02	1.51e-01	1.08e+00	5.11e-03	1.01e-01	5.21e-02	9.63e-01	1.29e+00
HRB21_69	4.62e-02	2.04e-01	3.00e-01	2.40e+00	9.66e-03	1.35e-01	1.05e-01	1.90e+00	2.40e+00
HRB21_70	6.00e-02	2.64e-01	3.74e-01	3.24e+00	1.53e-02	7.79e-01	1.42e-01	2.38e+00	nd
HRB21_71**	6.46e-02	2.78e-01	3.37e-01	nd	2.27e-02	3.82e-02	9.63e-02	1.21e+00	nd
HRB21_72**	7.36e-02	3.07e-01	3.49e-01	nd	3.32e-02	2.35e-02	1.09e-01	1.15e+00	nd
HRB21_73	1.22e-01	4.26e-01	4.80e-01	4.32e+00	1.84e-01	7.13e-02	9.18e-01	2.42e+00	5.01e+00
HRB21_74	1.48e-01	5.32e-01	6.31e-01	6.31e+00	2.94e-01	9.59e-02	1.59e+00	3.50e+00	6.26e+00
HRB21_75	6.15e-01	1.75e+00	1.62e+00	9.89e+00	5.27e-01	1.21e+00	2.84e+00	6.51e+00	1.04e+01
HRB21_75A	6.43e-01	1.67e+00	nd	nd	5.89e-01	1.26e+00	nd	nd	nd
HRB21_76	3.01e-01	1.07e+00	1.30e+00	1.08e+01	6.76e-01	2.24e-01	3.57e+00	7.34e+00	1.30e+01
HRB21_77	3.38e-01	1.21e+00	1.46e+00	1.31e+01	7.15e-01	3.08e-01	3.81e+00	8.50e+00	1.53e+01
HRB21_77A	3.61e-01	1.28e+00	1.43e+00	nd	8.02e-01	3.27e-01	nd	nd	nd
HRB21_78	2.41e-01	9.04e-01	1.11e+00	1.21e+01	3.76e-01	1.85e-01	2.11e+00	6.04e+00	1.18e+01
HRB21_79	2.70e-01	9.78e-01	1.17e+00	1.19e+01	3.73e-01	3.84e-01	1.99e+00	5.65e+00	1.01e+01

*Not analyzed.
**Sample taken through the holdup tank.

Appendix A-3

(CONTINUED)

Sample I.D.	Concentration (uCi per cm^3)								
	^{85m}Kr	^{86}Kr	^{87}Kr	^{89}Kr	^{135}Xe	^{133}Xe	^{135m}Xe	^{138}Xe	^{137}Xe
HRB21_80	4.84e-01	1.46e+00	1.54e+00	1.34e+01	4.65e-01	2.34e+00	2.54e+00	5.90e+00	9.46e+00
HRB21_81	5.86e-01	1.78e+00	1.87e+00	1.36e+01	6.45e-01	3.37e+00	3.46e+00	7.85e+00	1.24e+01
HRB21_82	7.81e-01	2.76e+00	3.30e+00	2.76e+01	1.24e+00	1.28e+00	6.87e+00	1.50e+01	2.40e+01
HRB21_83	5.41e-01	1.86e+00	2.20e+00	1.31e+01	6.54e-01	8.59e-01	3.37e+00	8.03e+00	1.01e+01
HRB21_84	6.45e-01	2.23e+00	2.68e+00	1.72e+01	7.88e-01	9.17e-01	4.23e+00	1.04e+01	1.54e+01
HRB21_85	6.08e-01	2.12e+00	2.59e+00	1.71e+01	7.58e-01	1.05e+00	4.28e+00	9.74e+00	1.42e+01
HRB21_86	6.10e-01	2.21e+00	2.66e+00	1.97e+01	6.72e-01	9.17e-01	3.96e+00	1.01e+01	1.60e+01
cycle 4									
HRB21_87	5.46e-03	2.28e-02	4.13e-02	3.48e-01	2.30e-03	3.28e-01	2.16e-02	3.23e-01	4.43e-01
HRB21_88	1.28e-02	6.53e-02	1.11e-01	9.53e-01	5.05e-03	8.42e-01	5.07e-02	8.71e-01	1.38e+00
HRB21_89	5.40e-02	2.24e-01	3.49e-01	2.13e+00	1.53e-02	1.08e+00	1.48e-01	2.21e+00	2.81e+00
HRB21_90	1.39e-01	5.45e-01	8.12e-01	5.31e+00	3.08e-02	1.21e+00	3.07e-01	4.40e+00	5.70e+00
HRB21_91	2.75e-01	1.16e+00	1.70e+00	1.07e+01	4.90e-02	1.46e+00	5.76e-01	7.73e+00	1.03e+01
HRB21_92	3.85e-01	1.59e+00	2.27e+00	1.32e+01	7.92e-02	8.55e-01	8.08e-01	1.04e+01	1.27e+01
HRB21_93	4.11e-01	1.64e+00	2.33e+00	1.53e+01	1.32e-01	3.56e-01	1.11e+00	1.00e+01	1.36e+01

*Not analyzed.
**Sample taken through the holdup tank.

Appendix A-3

(CONTINUED)

Sample I.D.	Concentration (uCi per cm³)								
	^{85m}Kr	^{85}Kr	^{87}Kr	^{88}Kr	^{135}Xe	^{133}Xe	^{135m}Xe	^{138}Xe	^{137}Xe
HRB21_94	4.04e-01	1.61e+00	2.18e+00	1.30e+01	1.71e-01	2.66e-01	1.17e+00	9.00e+00	1.24e+01
HRB21_95	7.16e-01	2.59e+00	3.14e+00	1.86e+01	6.01e-01	3.63e-01	3.37e+00	1.25e+01	1.64e+01
HRB21_96	9.50e-01	3.33e+00	4.13e+00	3.24e+01	1.24e+00	5.43e-01	6.94e+00	1.73e+01	2.83e+01
HRB21_97	6.92e-01	2.45e+00	2.87e+00	1.69e+01	9.31e-01	4.75e-01	4.70e+00	1.12e+01	1.42e+01
HRB21_98	7.31e-01	2.59e+00	3.10e+00	1.91e+01	9.33e-01	6.40e-01	4.79e+00	1.21e+01	1.68e+01
HRB21_99	8.15e-01	2.90e+00	3.53e+00	2.42e+01	1.04e+00	7.37e-01	5.84e+00	1.47e+01	2.27e+01
HRB21_100	7.79e-01	2.78e+00	3.50e+00	2.83e+01	1.01e+00	6.34e-01	5.81e+00	1.56e+01	3.45e+01
HRB21_101	8.11e-01	2.91e+00	3.68e+00	2.51e+01	9.65e-01	6.76e-01	5.25e+00	1.42e+01	2.02e+01
HRB21_102	9.19e-01	3.33e+00	4.15e+00	3.87e+01	9.41e-01	9.46e-01	5.36e+00	1.55e+01	2.45e+01
HRB21_103	9.19e-01	3.33e+00	4.15e+00	3.87e+01	9.41e-01	9.46e-01	5.36e+00	1.55e+01	2.45e+01
HRB21_104	9.42e-01	3.43e+00	4.42e+00	3.52e+01	1.00e+00	6.69e-01	5.76e+00	1.62e+01	2.42e+01
HRB21_105	9.95e-01	3.57e+00	4.52e+00	3.45e+01	1.06e+00	8.31e-01	5.84e+00	1.62e+01	2.40e+01
HRB21_106	1.10e+00	3.91e+00	4.79e+00	3.48e+01	1.15e+00	1.04e+00	6.29e+00	1.69e+01	2.61e+01
HRB21_107	1.09e+00	3.77e+00	4.64e+00	3.35e+01	1.06e+00	1.85e+00	5.84e+00	1.63e+01	2.67e+01
cycle 5									

*Not analyzed.
**Sample taken through the holdup tank.

Appendix A-3

(CONTINUED)

Sample I.D.	Concentration (uCi per cm^3)								
	^{85m}Kr	^{85}Kr	^{87}Kr	^{88}Kr	^{135}Xe	^{133}Xe	^{135m}Xe	^{138}Xe	^{137}Xe
HRB21-108	9.61e-03	3.83e-02	6.68e-02	9.63e-01	3.75e-03	1.11e-01	4.45e-02	5.77e-01	1.18e+00
HRB21-109	3.15e-02	1.50e-01	2.44e-01	2.46e+01	1.35e-02	1.26e+00	1.40e-01	2.14e+00	3.70e+00
HRB21-110	1.04e-01	4.49e-01	7.27e-01	8.36e+00	2.65e-02	1.44e+00	4.14e-01	5.59e+00	1.01e+01
HRB21-111	2.44e-01	1.04e+00	1.61e+00	1.36e+01	5.95e-02	1.09e+00	7.56e-01	9.70e+00	1.52e+01
HRB21-112	6.13e-01	2.54e+00	3.82e+00	3.01e+01	1.29e-01	2.04e+00	1.62e+00	1.99e+01	3.02e+01
HRB21-113	1.04e+00	4.23e+00	6.22e+00	4.87e+01	2.37e-01	2.15e+00	2.67e+00	2.96e+01	4.45e+01
HRB21-114	1.15e+00	4.59e+00	6.35e+00	5.17e+01	4.29e-01	7.88e-01	3.43e+00	2.66e+01	4.40e+01
HRB21-115	1.22e+00	4.69e+00	6.39e+00	4.74e+01	5.57e-01	7.09e-01	4.00e+00	2.49e+01	4.31e+01
HRB21-116	1.24e+00	4.49e+00	5.64e+00	4.55e+01	1.15e+00	3.82e-01	6.65e+00	2.13e+01	nd
HRB21-117	1.16e+00	4.17e+00	5.35e+00	3.63e+01	1.27e+00	4.46e-01	7.10e+00	1.93e+01	2.95e+01
HRB21-118	1.94e+00	6.98e+00	8.81e+00	5.92e+01	2.48e+00	1.33e+00	1.35e+01	2.92e+01	4.37e+01
HRB21-119	2.17e+00	7.71e+00	9.96e+00	7.02e+01	2.69e+00	1.54e+00	1.47e+01	3.28e+01	5.07e+01
HRB21-120	2.05e+00	7.33e+00	9.60e+00	6.56e+01	2.66e+00	1.37e+00	1.45e+01	3.27e+01	5.14e+01
HRB21-121	1.89e+00	6.81e+00	9.00e+00	7.28e+01	2.16e+00	1.18e+00	1.25e+01	3.15e+01	5.18e+01
HRB21-122	9.10e-01	3.26e+00	4.18e+00	2.80e+01	9.57e-01	5.97e-01	5.24e+00	1.42e+01	1.85e+01
HRB21-123	1.98e+00	7.17e+00	9.44e+00	7.27e+01	2.06e+00	1.36e+00	1.21e+01	3.40e+01	6.02e+01
HRB21-124	2.21e+00	7.94e+00	1.05e+01	8.16e+01	2.26e+00	1.53e+00	1.35e+01	3.81e+01	6.26e+01
HRB21-125	2.21e+00	7.97e+00	1.04e+01	7.91e+01	2.19e+00	1.75e+00	1.24e+01	3.58e+01	5.54e+01

*Not analyzed.
**Sample taken through the holdup tank.

Appendix A-3

(CONTINUED)

Sample I.D.	Concentration (uCi per cm^3)								
	^{85m}Kr	^{85}Kr	^{87}Kr	^{88}Kr	^{135}Xe	^{133}Xe	^{135m}Xe	^{138}Xe	^{137}Xe
HRB21-126	2.60e+00	9.19e+00	1.18e+01	7.74e+01	2.75e+00	2.51e+00	1.54e+01	4.22e+01	6.51e+01
HRB21-127	2.53e+00	9.19e+00	1.20e+01	8.48e+01	2.94e+00	2.45e+00	1.58e+01	4.21e+01	nd
HRB21-127A	2.52e+00	8.81e+00	1.14e+01	nd	2.92e+00	2.45e+00	nd	nd	nd
HRB21-128	2.40e+00	7.72e+00	nd	nd	2.79e+00	1.85e+00	nd	nd	nd
HRB21-128A	2.36e+00	7.36e+00	nd	nd	2.75e+00	1.84e+00	nd	nd	nd
HRB21-128B	2.15e+00	nd	nd	nd	2.46e+00	1.68e+00	nd	nd	nd
finis									

*Not analyzed.
**Sample taken through the holdup tank.

APPENDIX B

IONIZATION CHAMBER SPIKE DATA

APPENDIX B

IONIZATION CHAMBER SPIKE DATA

spike No.	DAY & TIME (dd/mm/yy h:m)	EFPD	HEIGHT (picoamps)	FWHM (min)	S*	COMMENTS
1	6/20/91 17:25	-0.035	0.2	2.1	0	50 % power
2	6/20/91 17:43	-0.022	0.1	2.6	0	70 % power
3	6/20/91 22:01	0.157	0.2	1.3	0	100 % power
4	6/25/91 16:47	4.94	0.1	1.5	1	
5	6/25/91 17:11	4.956	0.3	1.3	1	fission gas #16
6	6/25/91 17:13	4.957	0.2	0.9	1	fission gas #16
7	6/25/91 17:16	4.959	0.4	0.9	1	fission gas #16
8	6/25/91 17:47	4.981	0.2	1.2	1	fission gas #17
9	6/26/91 8:49	5.607	0.7	1	2	18 % Ne, fission gas #18
10	6/26/91 8:51	5.609	1.3	1	2	fission gas #18
11	6/26/91 13:40	5.809	0.7	0.8	2	fission gas #19
12	6/26/91 13:42	5.811	1.1	1.3	2	fission gas #19
13	6/26/91 18:26	6.008	1.3	6.5	2	
14	6/26/91 18:33	6.013	1.1	5.7	2	
15	6/27/91 16:04	6.909	0.7	0.8	2	fission gas #20
16	6/28/91 8:37	7.599	0.5	0.7	2	fission gas #21
17	6/28/91 8:41	7.601	0.7	1.3	2	fission gas #21
18	6/28/91 12:51	7.775	0.7	0.9	2	fission gas #22
19	6/28/91 12:54	7.777	0.5	0.8	2	fission gas #22
20	7/1/91 13:40	10.81	11.6	1.7	2	~38 % Ne, vent primary pressure
21	7/2/91 20:30	12.094	0.9	1	2	~40 % Ne fission gas #25
22	7/2/91 20:32	12.095	1.1	1	2	fission gas #25
23	7/3/91 14:42	12.852	0.9	1.1	2	fission gas #26
24	7/3/91 14:44	12.854	0.7	1.8	2	fission gas #26
25	7/3/91 18:36	13.015	0.5	0.8	2	fission gas #27
26	7/3/91 18:37	13.016	0.7	0.7	2	fission gas #27
27	7/5/91 9:40	14.643	0.9	1.4	0	switch 100% He
						end of cycle 1
28	7/26/91 10:18	21.032	3.9	6.6	1	

*Codes given at end of table.

APPENDIX B

(CONTINUED)

spike No.	DAY & TIME (dd/mm/yy h:m)	EFPD	HEIGHT (picoamps)	FWHM (min)	S*	COMMENTS
29	7/26/91 10:25	21.037	9.3	5.7	1	
30	7/26/91 10:34	21.044	1.8	2.5	1	
31	7/26/91 10:42	21.049	0.9	2.4	2	
32	7/26/91 10:46	21.052	1.1	2.4	2	
33	7/26/91 10:52	21.056	1.3	1.2	2	fission gas #40
34	7/26/91 10:55	21.058	1.8	0.8	2	fission gas #40
35	7/26/91 11:32	21.084	0.7	1.3	2	
36	7/26/91 11:48	21.095	4.7	3	2	
37	7/26/91 12:17	21.115	1.3	2.6	2	
38	7/26/91 12:21	21.118	2.2	2	2	
39	7/26/91 12:47	21.136	1.3	1.2	2	
40	7/26/91 12:48	21.137	1.3	0.6	2	
41	7/26/91 13:19	21.158	1.5	1.8	2	
42	7/26/91 14:05	21.19	1.6	2.4	0	swith 100% He
43	7/26/91 20:14	21.446	10.3	2.4	0	
44	7/31/91 4:56	25.809	9.1	1.9	0	
45	7/31/91 10:43	26.049	0.3	1.3	0	
46	8/2/91 21:55	28.517	0.2	1.4	0	
47	8/3/91 15:27	29.247	0.2	2.1	0	
48	8/3/91 18:23	29.369	0.4	2.1	0	
49	8/3/91 20:46	29.468	5.3	1.3	0	
50	8/4/91 20:17	30.448	8.2	1.8	0	
51	8/5/91 10:23	31.036	0.4	1.3	0	
52	8/5/91 13:45	31.176	4.7	1.4	1	
53	8/5/91 13:52	31.181	6.2	1.2	1	
54	8/5/91 13:58	31.185	1.3	1.4	1	fission gas #52
55	8/5/91 14:00	31.187	1.1	0.6	1	fission gas #52
56	8/5/91 14:05	31.19	9.1	1.2	1	
57	8/5/91 14:19	31.2	21.3	1.2	1	
58	8/5/91 14:21	31.201	18	1.2	2	~35 % Ne
59	8/5/91 14:57	31.226	10.7	0.8	2	

*Codes given at end of table.

APPENDIX B

(CONTINUED)

spike No.	DAY & TIME (dd/mm/yy h:m)	EFPD	HEIGHT (picoamps)	FWHM (min)	S*	COMMENTS
60	8/5/91 15:01	31.229	12.7	2.1	2	
61	8/5/91 15:04	31.231	9.3	2.1	2	
62	8/5/91 15:07	31.233	14.7	3.9	2	
63	8/5/91 15:14	31.238	3.3	1.3	2	
64	8/5/91 15:26	31.246	10	2	2	
65	8/5/91 15:28	31.248	5.3	1.2	2	
66	8/5/91 15:29	31.248	6.7	1.4	2	
67	8/5/91 15:32	31.25	21.8	1.7	2	
68	8/5/91 15:33	31.251	18.8	1.7	2	
69	8/5/91 15:36	31.253	10.9	3.2	2	
70	8/5/91 15:43	31.258	7.3	1.4	2	
71	8/5/91 15:51	31.264	11.5	1.7	2	
72	8/5/91 16:09	31.276	4.8	1.3	2	
73	8/5/91 16:18	31.282	6.1	1.3	2	
74	8/5/91 16:27	31.289	6.7	1.4	2	
75	8/5/91 16:46	31.302	4.7	1.8	2	fission gas #54
76	8/5/91 16:49	31.304	8	1.2	2	fission gas #54
77	8/5/91 16:51	31.305	6	0.9	2	
78	8/5/91 16:52	31.306	6.7	1.4	2	
79	8/5/91 16:55	31.308	14	1.9	2	
80	8/5/91 16:59	31.311	6.7	2.8	2	
81	8/5/91 17:03	31.314	6	1.9	2	
82	8/5/91 17:07	31.316	5.3	2.1	2	
83	8/5/91 17:09	31.318	17.3	1.9	2	
84	8/5/91 17:14	31.321	4.7	0.8	2	
85	8/5/91 17:16	31.323	5.3	1.8	2	
86	8/5/91 17:21	31.326	128	1.9	2	
87	8/5/91 17:30	31.332	37.3	4.4	2	
88	8/5/91 17:37	31.337	16.7	2	2	
89	8/5/91 17:57	31.351	5.3	2.1	2	
90	8/5/91 18:05	31.356	7.3	1.8	2	

*Codes given at end of table.

APPENDIX B

(CONTINUED)

spike No.	DAY & TIME (dd/mm/yy h:m)	EFPD	HEIGHT (picoamps)	FWHM (min)	S*	COMMENTS
91	8/5/91 18:07	31.358	4.7	2	2	
92	8/5/91 18:09	31.36	4	1.4	2	
93	8/5/91 18:14	31.363	8	2.1	2	
94	8/5/91 18:15	31.364	6.7	1.4	2	
95	8/5/91 18:31	31.374	7.3	1.2	2	
96	8/5/91 18:35	31.378	6	1.8	2	
97	8/5/91 18:38	31.379	6	1.4	2	
98	8/5/91 18:40	31.381	6	1.2	2	
99	8/5/91 18:44	31.383	14	2.4	2	
100	8/5/91 18:48	31.387	10.7	1.4	2	
101	8/5/91 18:54	31.391	8.7	1.2	2	
102	8/5/91 18:59	31.394	4	1.4	2	
103	8/5/91 19:02	31.396	3.3	1.8	2	
104	8/5/91 19:13	31.404	14.7	1.2	2	
105	8/5/91 19:38	31.421	22.7	2	2	
106	8/5/91 19:41	31.423	14.7	1.8	2	
107	8/5/91 19:44	31.425	8	2.4	2	
108	8/5/91 19:55	31.433	23.3	1.7	2	
109	8/5/91 20:02	31.438	5.3	1.2	2	
110	8/5/91 20:08	31.442	11.3	2.5	2	
111	8/5/91 20:11	31.444	11.3	2.4	2	
112	8/5/91 20:15	31.447	8	3	2	
113	8/5/91 20:21	31.451	8.7	2.4	2	
114	8/5/91 20:22	31.452	7.3	1.7	2	
115	8/5/91 20:23	31.453	3	1.7	2	
116	8/5/91 20:29	31.457	13.3	2	2	
117	8/5/91 20:54	31.474	12.1	1.3	2	
118	8/5/91 20:57	31.476	5.5	1.8	2	
119	8/5/91 20:58	31.477	3.6	1.2	2	
120	8/5/91 21:01	31.479	3	1.4	2	
121	8/5/91 21:11	31.486	3.6	2.4	2	

*Codes given at end of table.

APPENDIX B

(CONTINUED)

spike No.	DAY & TIME (dd/mm/yy h:m)	EFPD	HEIGHT (picoamps)	FWHM (min)	S*	COMMENTS
122	8/5/91 21:14	31.488	6.1	2.6	2	
123	8/5/91 21:19	31.491	15.2	3	2	
124	8/5/91 21:25	31.495	7.3	2	2	
125	8/5/91 21:30	31.499	37.6	2	2	
126	8/5/91 21:37	31.504	6.1	1.4	2	
127	8/5/91 21:40	31.506	12.1	1.2	2	
128	8/5/91 21:46	31.51	5.5	1.8	2	
129	8/5/91 21:53	31.515	7.3	2	2	
130	8/5/91 21:56	31.517	4.8	1.5	2	
131	8/5/91 21:59	31.519	15.2	1.9	2	
132	8/5/91 22:01	31.52	12.1	2	2	
133	8/5/91 22:08	31.525	12.7	3.6	2	
134	8/5/91 22:11	31.528	6.1	2	2	
135	8/5/91 22:17	31.532	4.8	1.2	2	
136	8/5/91 22:22	31.535	12.1	3	2	
137	8/5/91 22:31	31.542	13.9	1.2	2	
138	8/5/91 22:34	31.543	6.7	1.8	2	
139	8/5/91 22:37	31.546	4.2	2	2	
140	8/5/91 22:46	31.551	6.1	1.3	2	
141	8/5/91 22:50	31.555	6.7	1.1	2	
142	8/5/91 22:54	31.557	7.9	1.1	2	
143	8/5/91 23:03	31.564	6.7	1.1	2	
144	8/5/91 23:05	31.565	6.7	1.7	2	
145	8/5/91 23:08	31.567	12.1	1.2	2	
146	8/5/91 23:12	31.57	12.1	1.8	2	
147	8/5/91 23:15	31.572	6.1	1.7	2	
148	8/5/91 23:22	31.577	8.5	2.7	2	
149	8/5/91 23:28	31.581	6.1	1.2	2	
150	8/5/91 23:32	31.584	10.9	1.8	2	
151	8/5/91 23:34	31.585	4.8	1.1	2	
152	8/5/91 23:38	31.588	12.1	1.7	2	

*Codes given at end of table.

APPENDIX B

(CONTINUED)

spike No.	DAY & TIME (dd/mm/yy h:m)	EFPD	HEIGHT (picoamps)	FWHM (min)	S*	COMMENTS
153	8/5/91 23:41	31.59	4.8	1.8	2	
154	8/5/91 23:47	31.594	4.8	0.7	2	
155	8/5/91 23:52	31.598	6.7	1.2	2	
156	8/5/91 23:58	31.602	35.8	1.4	2	
157	8/6/91 0:00	31.603	13.3	1.5	2	
158	8/6/91 0:06	31.607	12.1	2.4	2	
159	8/6/91 0:18	31.616	3.6	1.1	2	
160	8/6/91 0:24	31.62	4.8	1.3	2	
161	8/6/91 0:26	31.621	6.7	2.1	2	
162	8/6/91 0:32	31.626	4.8	3.6	2	
163	8/6/91 0:36	31.628	8.5	1.4	2	
164	8/6/91 0:56	31.642	4.8	1.5	2	
165	8/6/91 1:01	31.645	4.8	2.7	2	
166	8/6/91 1:07	31.649	13.3	3	2	
167	8/6/91 1:10	31.652	15.8	2.7	2	
168	8/6/91 1:13	31.654	19.4	2.6	2	
169	8/6/91 1:17	31.657	4.8	1.8	2	
170	8/6/91 1:20	31.658	7.3	1.7	2	
171	8/6/91 1:22	31.66	3	2.8	2	
172	8/6/91 1:24	31.662	3	1.3	2	
173	8/6/91 1:35	31.669	3.6	1.3	2	
174	8/6/91 1:40	31.672	6.7	1.8	2	
175	8/6/91 1:46	31.677	4.2	1.5	2	
176	8/6/91 1:58	31.685	25.5	1.4	2	
177	8/6/91 2:04	31.689	4.2	1.4	2	
178	8/6/91 2:07	31.691	3	2.6	2	
179	8/6/91 2:13	31.696	10.9	2.4	2	
180	8/6/91 2:26	31.705	9.1	1.3	2	
181	8/6/91 2:28	31.706	4.2	1.5	2	
182	8/6/91 2:31	31.708	4.8	1.9	2	
183	8/6/91 2:33	31.71	3	1.3	2	

*Codes given at end of table.

APPENDIX B

(CONTINUED)

spike No.	DAY & TIME (dd/mm/yy h:m)	EFPD	HEIGHT (picoamps)	FWHM (min)	S*	COMMENTS
184	8/6/91 2:41	31.715	3.6	1.2	2	
185	8/6/91 2:51	31.722	4.2	2	2	
186	8/6/91 2:55	31.724	7.9	0.9	2	
187	8/6/91 3:04	31.731	25.5	2.4	2	
188	8/6/91 3:15	31.738	13.9	2.4	2	
189	8/6/91 3:27	31.747	10.3	1.2	2	
190	8/6/91 3:34	31.751	24.2	1.5	2	
191	8/6/91 3:47	31.761	13	2.7	2	
192	8/6/91 3:51	31.764	4.8	1.8	2	
193	8/6/91 3:57	31.768	4.8	1.5	2	
194	8/6/91 4:02	31.771	6.7	2.4	2	
195	8/6/91 4:04	31.773	4.2	1.8	2	
196	8/6/91 4:18	31.782	4.8	0.8	2	
197	8/6/91 4:26	31.788	3	2	2	
198	8/6/91 4:29	31.79	4.2	1.3	2	
199	8/6/91 4:45	31.801	6.7	1.8	2	
200	8/6/91 4:51	31.805	6.1	1.5	2	
201	8/6/91 4:52	31.806	4.2	1.7	2	
202	8/6/91 4:55	31.808	4.2	1.4	2	
203	8/6/91 4:58	31.81	19.4	1.7	2	
204	8/6/91 5:01	31.812	6.7	0.8	2	
205	8/6/91 5:03	31.813	6.1	1.1	2	
206	8/6/91 5:11	31.819	6.1	1.2	2	
207	8/6/91 5:22	31.826	10.9	1.4	2	
208	8/6/91 5:27	31.831	3	1.7	2	
209	8/6/91 5:35	31.835	9.7	1.3	2	
210	8/6/91 5:42	31.84	4.8	1.4	2	
211	8/6/91 6:15	31.863	3.6	1.4	2	
212	8/6/91 6:17	31.865	6.1	1.2	2	
213	8/6/91 6:40	31.881	12.1	2.4	2	
214	8/6/91 6:53	31.89	3.9	2	2	

*Codes given at end of table.

APPENDIX B

(CONTINUED)

spike No.	DAY & TIME (dd/mm/yy h:m)	EFPD	HEIGHT (picoamps)	FWHM (min)	S*	COMMENTS
215	8/6/91 7:03	31.897	8.5	3	2	
216	8/6/91 7:09	31.901	21.2	2	2	
217	8/6/91 7:17	31.906	9.1	1.4	2	
218	8/6/91 7:20	31.909	10.3	2.6	2	
219	8/6/91 7:24	31.911	6.7	2	2	
220	8/6/91 7:27	31.914	10.9	1.8	2	
221	8/6/91 7:32	31.917	3.6	0.9	2	
222	8/6/91 7:40	31.923	3	1.3	2	
223	8/6/91 7:47	31.928	20	3.9	2	
224	8/6/91 8:03	31.938	24.2	2.1	2	
225	8/6/91 8:09	31.943	4.2	2	2	
226	8/6/91 8:22	31.952	5.5	1.2	2	
227	8/6/91 8:24	31.953	4.8	1.2	2	
228	8/6/91 8:31	31.958	13.9	2.4	2	
229	8/6/91 8:32	31.959	13.3	1.7	2	
230	8/6/91 8:35	31.961	15.8	3.8	2	
231	8/6/91 8:38	31.963	12.1	1.5	2	
232	8/6/91 8:42	31.966	4.2	1.8	2	
233	8/6/91 8:47	31.969	7.3	3.8	2	
234	8/6/91 8:50	31.971	8.5	4.7	2	
235	8/6/91 9:01	31.979	7.3	8.7	2	
236	8/6/91 9:08	31.984	6.1	1.8	2	
237	8/6/91 9:17	31.99	3.6	1.3	2	
238	8/6/91 10:23	32.036	3	1.7	2	
239	8/6/91 10:42	32.049	7.3	1.2	2	
240	8/6/91 11:03	32.064	3	0.8	2	
241	8/6/91 11:09	32.068	3	1.2	2	
242	8/6/91 11:36	32.087	4.2	0.8	2	
243	8/6/91 11:41	32.09	9.7	1.3	2	
244	8/6/91 12:07	32.108	4.8	1.1	2	
245	8/6/91 12:24	32.12	3.6	1.4	2	

*Codes given at end of table.

APPENDIX B

(CONTINUED)

spike No.	DAY & TIME (dd/mm/yy h:m)	EFPD	HEIGHT (picoamps)	FWHM (min)	S*	COMMENTS
246	8/6/91 12:31	32.124	3.6	1.1	2	
247	8/6/91 13:29	32.165	11.5	0.9	2	
248	8/6/91 13:36	32.17	3	1.3	2	
249	8/6/91 13:49	32.179	6.7	1.3	2	
250	8/6/91 13:55	32.183	3.6	1.1	2	
251	8/6/91 14:01	32.187	3	1.9	2	
252	8/6/91 14:17	32.199	3.6	1.5	2	
253	8/6/91 14:57	32.226	12.7	1.2	2	
254	8/6/91 15:00	32.228	3	1.4	2	
255	8/6/91 15:38	32.255	3	0.9	2	
256	8/6/91 15:51	32.264	13.3	2.4	2	
257	8/6/91 16:04	32.273	3	1.4	2	
258	8/6/91 16:20	32.283	3.6	1.2	2	
259	8/6/91 16:21	32.284	8.5	0.8	2	
260	8/6/91 17:44	32.342	8.5	0.7	2	
261	8/6/91 17:48	32.345	3	1.4	2	
262	8/6/91 17:52	32.348	3	1.4	2	
263	8/6/91 18:00	32.353	3.6	0.8	2	
264	8/6/91 18:25	32.371	90.9	1.2	2	
265	8/6/91 18:37	32.379	51.5	1.7	2	
266	8/6/91 18:50	32.388	7.3	0.9	2	
267	8/6/91 19:00	32.394	3	1.2	2	
268	8/6/91 19:07	32.399	9.1	1.2	2	
269	8/6/91 19:14	32.404	6.1	1.5	2	
270	8/6/91 19:17	32.407	5.5	1.2	2	
271	8/6/91 19:29	32.415	3	0.8	2	
272	8/6/91 19:39	32.422	4.8	1.2	2	
273	8/6/91 19:49	32.429	3.6	0.8	2	
274	8/6/91 19:54	32.432	3	1.7	2	
275	8/6/91 20:23	32.452	3	1.3	2	
276	8/6/91 20:55	32.474	3.6	1.3	2	

*Codes given at end of table.

APPENDIX B

(CONTINUED)

spike No.	DAY & TIME (dd/mm/yy h:m)	EFPD	HEIGHT (picoamps)	FWHM (min)	S*	COMMENTS
277	8/6/91 21:00	32.478	3.6	1.3	2	
278	8/6/91 21:36	32.503	3.6	0.8	2	
279	8/6/91 22:03	32.522	3.6	0.9	2	
280	8/6/91 20:38	32.463	3	0.8	2	
281	8/6/91 22:45	32.551	12.7	1.4	2	
282	8/6/91 22:50	32.554	4.8	1.1	2	
283	8/6/91 22:52	32.556	10.9	1.8	2	
284	8/6/91 23:09	32.567	17.6	0.8	2	
285	8/6/91 23:17	32.573	11.5	2.4	2	
286	8/6/91 23:20	32.576	6.7	1.2	2	
287	8/6/91 23:54	32.599	6.7	1.4	2	
288	8/6/91 23:56	32.6	3.6	2	2	
289	8/7/91 0:02	32.604	3	1.2	2	
290	8/7/91 0:08	32.609	3	1.3	2	
291	8/7/91 0:37	32.629	4.8	1.8	2	
292	8/7/91 0:40	32.631	4.8	1.4	2	
293	8/7/91 1:14	32.655	4.8	1.1	2	
294	8/7/91 1:43	32.674	9.7	1.2	2	
295	8/7/91 1:54	32.683	4.2	1.2	2	
296	8/7/91 1:58	32.685	9.1	1.4	2	
297	8/7/91 2:53	32.723	4.8	0.6	2	
298	8/7/91 2:54	32.724	6.7	0.8	2	
299	8/7/91 2:57	32.726	11.5	1.1	2	
300	8/7/91 3:59	32.769	7.3	1.5	2	
301	8/7/91 4:16	32.781	3	0.8	2	
302	8/7/91 4:38	32.796	3.3	1.2	2	
303	8/7/91 5:33	32.834	3	1.3	2	
304	8/7/91 5:56	32.851	3	1.4	2	
305	8/7/91 6:09	32.86	5.5	1.2	2	
306	8/7/91 6:24	32.87	3	1.8	2	
307	8/7/91 6:58	32.893	3	1.4	2	

*Codes given at end of table.

APPENDIX B

(CONTINUED)

spike No.	DAY & TIME (dd/mm/yy h:m)	EFPD	HEIGHT (picoamps)	FWHM (min)	S*	COMMENTS
308	8/7/91 7:00	32.895	3	1.4	2	
309	8/7/91 7:16	32.906	3.6	1.2	2	
310	8/7/91 7:18	32.907	3	1.7	2	
311	8/7/91 7:22	32.91	6.1	1.8	2	
312	8/7/91 7:58	32.935	3	1.2	2	
313	8/7/91 8:01	32.937	3.6	1.7	2	
314	8/7/91 8:02	32.938	3	1.8	2	
315	8/7/91 8:42	32.966	3.6	1.4	2	
316	8/7/91 8:46	32.968	3	0.6	2	
317	8/7/91 8:47	32.969	3.6	0.7	2	
318	8/7/91 9:01	32.979	3	1.3	2	
319	8/7/91 9:55	33.016	10.9	0.5	2	
320	8/7/91 10:24	33.037	8.2	1.8	2	
321	8/7/91 13:33	33.168	20	2.6	2	
322	8/8/91 1:24	33.662	12.7	1.2	2	
323	8/8/91 1:31	33.666	16.4	1.2	2	
324	8/8/91 1:47	33.677	49.1	1.8	2	
325	8/8/91 2:51	33.722	10.9	1.2	2	
326	8/8/91 5:47	33.844	7.3	3.6	2	
327	8/8/91 6:33	33.876	7.3	1.4	2	
328	8/8/91 8:17	33.948	14.5	1.2	2	
329	8/8/91 16:55	34.308	7.3	1.4	2	
330	8/8/91 19:33	34.418	10.9	2.4	2	
331	8/9/91 9:38	35.005	3	0.1	0	
332	8/9/91 10:04	35.023	3	2.6	1	
333	8/9/91 10:16	35.031	90.9	1.5	1	
334	8/9/91 10:22	35.035	66.1	3.8	1	
335	8/9/91 10:25	35.037	57.6	1.3	1	
336	8/9/91 17:43	35.341	9.1	1.2	2	~35% Ne
337	8/9/91 21:30	35.499	14.5	1.2	2	
338	8/10/91 4:49	35.804	20	0.9	2	

*Codes given at end of table.

APPENDIX B

(CONTINUED)

spike No.	DAY & TIME (dd/mm/yy h:m)	EFPD	HEIGHT (picoamps)	FWHM (min)	S*	COMMENTS
339	8/10/91 5:56	35.851	32.7	0.9	2	
340	8/10/91 7:12	35.903	19.1	0.8	2	
341	8/10/91 7:20	35.909	9.1	0.8	2	
342	8/10/91 11:22	36.077	10.9	0.9	2	
343	8/10/91 13:37	36.17	21.8	1.1	2	
344	8/10/91 22:37	36.546	14.5	1.5	2	
345	8/11/91 0:30	36.624	23.6	2.1	2	
346	8/11/91 2:00	36.687	20.9	1.5	2	
347	8/11/91 2:15	36.697	88.2	1.1	2	
348	8/11/91 9:33	37.001	58.2	1.2	2	
349	8/11/91 10:22	37.035	9.1	0.8	2	
350	8/11/91 12:36	37.128	36.4	1.2	2	
351	8/11/91 15:42	37.258	9.1	1.3	2	
352	8/12/91 3:06	37.732	7.3	1.2	2	
353	8/12/91 7:03	37.897	105.5	1.2	2	
354	8/12/91 8:26	37.954	17.3	1.1	2	
355	8/12/91 17:25	38.329	10.9	1.5	2	~20 % Ne
356	8/12/91 17:29	38.332	18.2	1.6	2	
357	8/13/91 4:33	38.793	9.1	1.6	2	
358	8/13/91 10:01	39.021	16.4	1.2	2	
359	8/15/91 1:15	40.655	54.5	1.4	0	
360	8/15/91 9:02	40.979	107.3	3.1	3	
361	8/15/91 9:30	40.999	5.5	4.7	3	
						end of cycle 2
362	8/28/91 11:14	40.951	1.9	3.7	0	70 % Power
363	8/28/91 11:24	40.958	1.6	1.9	0	90 % power
364	8/28/91 11:42	40.971	4.2	3.6	0	100 % Power
365	8/28/91 16:52	41.186	23.6	1.2	0	
366	8/28/91 17:42	41.22	15.8	1.2	0	
367	8/28/91 20:00	41.316	7.3	1.5	0	
368	8/28/91 20:28	41.336	23.6	1.2	0	

*Codes given at end of table.

APPENDIX B

(CONTINUED)

spike No.	DAY & TIME (dd/mm/yy h:m)	EFPD	HEIGHT (picoamps)	FWHM (min)	S*	COMMENTS
369	8/28/91 23:19	41.455	29.1	1.3	0	
370	8/29/91 1:18	41.537	10.9	1.2	0	
371	8/29/91 2:53	41.603	9.1	1.3	0	
372	8/29/91 3:00	41.608	9.1	1.4	0	
373	8/29/91 12:12	41.991	10.9	1.2	0	
374	8/29/91 12:44	42.013	12.7	1.2	0	
375	8/29/91 12:52	42.019	7.3	2.1	0	
376	8/29/91 14:30	42.087	16.4	1.2	0	
377	8/29/91 14:36	42.091	27.3	1.4	0	
378	8/29/91 18:06	42.237	21.8	1.2	0	
379	8/30/91 0:13	42.492	9.1	1.3	0	
380	8/30/91 2:38	42.593	10.9	1.2	0	
381	8/30/91 7:57	42.814	10.9	1.2	0	
382	8/30/91 11:14	42.951	20	1.8	0	
383	8/30/91 13:15	43.035	5.5	1.7	0	
384	8/30/91 13:31	43.046	10.9	1.2	0	
385	8/30/91 13:53	43.062	10.9	1.2	0	
386	8/30/91 13:54	43.062	14.5	2.7	0	
387	8/30/91 14:07	43.071	27.3	3.1	1	
388	8/30/91 14:12	43.075	14.5	5	1	
389	8/30/91 14:29	43.086	12.7	2.1	2	~15 % Ne
390	8/30/91 15:17	43.12	7.3	1.8	2	
391	8/30/91 15:22	43.123	10.9	1.7	2	
392	8/30/91 15:28	43.127	12.7	1.4	2	
393	8/30/91 19:17	43.286	7.3	2.8	2	
394	8/30/91 20:25	43.334	7.3	1.2	2	
395	8/31/91 2:00	43.566	7.3	1.9	2	
396	8/31/91 12:08	43.988	7.3	0.8	2	
397	8/31/91 14:16	44.077	7.3	1.2	2	
398	8/31/91 14:53	44.103	10	2	2	
399	8/31/91 15:06	44.112	12.7	1.8	2	

*Codes given at end of table.

APPENDIX B

(CONTINUED)

spike No.	DAY & TIME (dd/mm/yy h:m)	EFPD	HEIGHT (picoamps)	FWHM (min)	S*	COMMENTS
400	8/31/91 17:36	44.216	7.3	0.9	2	
401	8/31/91 20:48	44.35	30.9	1.8	2	
402	8/31/91 22:14	44.409	9.1	2	2	
403	8/31/91 22:52	44.435	29.1	1.1	2	
404	9/1/91 10:16	44.91	27.3	1.2	2	
405	9/1/91 12:54	45.021	10.9	1.8	2	
406	9/1/91 18:51	45.268	9.1	2	2	
407	9/1/91 20:27	45.335	7.3	1.2	2	
408	9/2/91 0:47	45.516	14.5	1.2	2	
409	9/2/91 6:00	45.733	14.5	1.1	2	
410	9/2/91 9:13	45.867	7.3	1.3	2	
411	9/2/91 18:04	46.235	7.3	1.2	2	
412	9/2/91 23:36	46.467	7.3	1.4	2	
413	9/2/91 23:40	46.469	10.9	1.2	2	
414	9/3/91 6:14	46.743	7.3	1.1	2	
415	9/3/91 13:59	47.066	7.3	1.4	2	
416	9/3/91 19:59	47.315	7.3	0.8	2	
417	9/3/91 21:55	47.396	10.9	1.2	2	
418	9/4/91 5:28	47.711	23.6	2.4	2	
419	9/4/91 9:22	47.873	10.9	1.2	2	
420	9/4/91 16:22	48.165	9.1	1.2	2	
421	9/4/91 21:46	48.39	9.1	1.4	2	
422	9/4/91 23:09	48.447	10.9	1.1	2	
423	9/5/91 1:55	48.563	7.3	1.2	2	
424	9/5/91 3:07	48.613	7.3	1.4	2	
425	9/5/91 3:27	48.627	10.9	0.9	2	
426	9/5/91 4:30	48.671	9.1	0.9	2	
427	9/5/91 4:34	48.673	10.9	1.2	2	
428	9/5/91 6:01	48.734	12.7	1.4	2	
429	9/5/91 6:16	48.744	12.7	0.9	2	
430	9/5/91 6:30	48.754	10.9	1.2	2	

*Codes given at end of table.

APPENDIX B

(CONTINUED)

spike No.	DAY & TIME (dd/mm/yy h:m)	EFPD	HEIGHT (picoamps)	FWHM (min)	S*	COMMENTS
431	9/5/91 7:27	48.793	9.1	0.8	2	
432	9/5/91 9:10	48.865	9.1	1.8	2	
433	9/5/91 9:11	48.866	9.1	0.9	2	
434	9/5/91 9:18	48.871	10.9	2.8	2	
435	9/5/91 11:47	48.974	12.7	3.6	2	
436	9/5/91 12:56	49.022	90.9	1.2	2	
437	9/5/91 13:25	49.042	12.7	0.9	2	
438	9/5/91 13:51	49.06	14.5	1.4	2	
439	9/5/91 14:16	49.077	12.7	1.1	2	
440	9/5/91 18:55	49.271	9.1	1.3	2	
441	9/5/91 21:54	49.396	7.3	0.9	2	
442	9/5/91 21:59	49.399	6.4	1.2	2	
443	9/6/91 0:56	49.522	9.1	1.2	2	
444	9/6/91 3:16	49.619	18.2	0.9	2	
445	9/6/91 6:41	49.761	21.8	1.1	2	
446	9/6/91 6:44	49.764	7.3	1.3	2	
447	9/6/91 8:46	49.848	9.1	3.8	2	
448	9/6/91 10:27	49.918	9.1	1.2	2	
449	9/6/91 10:28	49.919	7.3	0.9	2	
450	9/6/91 13:46	50.056	8.2	1.2	2	
451	9/6/91 13:59	50.066	10.9	1.8	2	
452	9/6/91 14:00	50.066	7.3	1.4	2	
453	9/6/91 14:13	50.075	9.1	1.2	2	
454	9/6/91 19:39	50.302	143.6	0.8	2	
455	9/7/91 2:32	50.589	87.3	1.2	2	
456	9/7/91 2:37	50.592	16.4	3	2	
457	9/7/91 2:38	50.593	11.8	1.2	2	
458	9/7/91 2:40	50.594	10.9	2.7	2	
459	9/7/91 2:44	50.597	12.7	3.1	2	
460	9/7/91 2:46	50.598	12.7	3.6	2	
461	9/7/91 2:50	50.601	10.9	3.3	2	

*Codes given at end of table.

APPENDIX B

(CONTINUED)

spike No.	DAY & TIME (dd/mm/yy h:m)	EFPD	HEIGHT (picoamps)	FWHM (min)	S*	COMMENTS
462	9/7/91 2:53	50.603	10	3	2	
463	9/7/91 3:10	50.615	12.7	1.9	2	
464	9/7/91 3:44	50.639	7.3	1.3	2	
465	9/7/91 3:48	50.641	10.9	1.4	2	
466	9/7/91 6:43	50.763	18.2	1.7	2	
467	9/7/91 15:52	51.144	9.1	2	2	
468	9/7/91 17:02	51.193	70.9	1.2	2	
469	9/7/91 20:35	51.341	10.9	1.5	2	
470	9/8/91 1:36	51.55	9.1	1.2	2	
471	9/8/91 3:37	51.634	10.9	1.8	2	
472	9/8/91 14:16	52.078	9.1	1.2	2	
473	9/8/91 14:40	52.094	16.4	3.4	2	
474	9/8/91 18:32	52.255	18.2	1.2	2	
475	9/8/91 18:52	52.269	7.3	1.2	2	
476	9/8/91 19:22	52.29	25.5	2.7	2	
477	9/8/91 19:41	52.303	14.5	1.4	2	
478	9/8/91 22:09	52.406	18.2	1.5	2	
479	9/9/91 1:52	52.56	9.1	1.5	2	
480	9/9/91 2:45	52.597	7.3	1.4	2	
481	9/9/91 5:08	52.697	10	1.4	2	
482	9/9/91 7:25	52.792	7.3	5.4	2	
483	9/9/91 7:31	52.796	11.8	8.6	2	
484	9/9/91 8:25	52.834	21.8	1.2	2	
485	9/9/91 8:39	52.843	10.9	1.7	2	
486	9/9/91 8:43	52.846	23.6	3.8	2	
487	9/9/91 8:46	52.848	12.7	3	2	
488	9/9/91 8:51	52.852	12.7	0.8	2	
489	9/9/91 8:54	52.854	7.3	1.5	2	
490	9/9/91 11:22	52.956	8.2	1.3	2	
491	9/9/91 22:14	53.409	7.3	2.7	2	
492	9/10/91 0:40	53.511	7.3	0.8	2	

*Codes given at end of table.

APPENDIX B

(CONTINUED)

spike No.	DAY & TIME (dd/mm/yy h:m)	EFPD	HEIGHT (picoamps)	FWHM (min)	S*	COMMENTS
493	9/10/91 1:15	53.535	65.5	1.2	2	
494	9/10/91 1:30	53.546	49.1	3	2	
495	9/10/91 2:43	53.596	7.3	1	2	
496	9/10/91 2:56	53.605	18.2	1	2	
497	9/10/91 4:13	53.659	7.3	1.4	2	
498	9/10/91 7:03	53.777	9.1	1	2	
499	9/10/91 7:08	53.78	18.2	1.5	2	
500	9/10/91 7:13	53.784	10.9	1.5	2	
501	9/10/91 13:25	54.042	16.4	3.8	2	
502	9/10/91 14:06	54.07	101.8	1.4	2	
503	9/10/91 14:11	54.074	12.7	4.8	2	
504	9/10/91 14:15	54.077	10.9	3	2	
505	9/10/91 16:34	54.173	7.3	1.8	2	
506	9/10/91 19:12	54.283	7.3	2.1	2	
507	9/10/91 19:18	54.287	9.1	1.3	2	
508	9/10/91 20:05	54.32	9.1	0.9	2	
509	9/10/91 22:06	54.404	10.9	1.3	2	
510	9/10/91 22:36	54.424	9.1	0.9	2	
511	9/11/91 1:42	54.554	69.1	1.1	2	
512	9/11/91 2:31	54.588	7.3	0.9	2	
513	9/11/91 7:36	54.8	49.1	1.2	2	
514	9/11/91 8:54	54.854	67.3	1.2	2	
515	9/11/91 8:58	54.856	14.5	1.8	2	
516	9/11/91 18:31	55.254	21.8	1.2	2	~10 % Ne
517	9/12/91 12:27	56.002	34.5	1.1	2	
518	9/12/91 14:56	56.105	7.3	1.4	2	
519	9/12/91 14:58	56.107	9.1	1.2	2	
520	9/12/91 16:31	56.171	10.9	1.3	2	
521	9/12/91 16:32	56.172	14.5	1.8	2	
522	9/12/91 18:22	56.248	7.3	1.3	2	
523	9/12/91 18:53	56.27	7.3	1.1	2	

*Codes given at end of table.

APPENDIX B

(CONTINUED)

spike No.	DAY & TIME (dd/mm/yy h:m)	EFPD	HEIGHT (picoamps)	FWHM (min)	S*	COMMENTS
524	9/12/91 22:46	56.431	10.9	1.7	2	
525	9/12/91 23:59	56.482	7.3	1.1	2	
526	9/13/91 5:14	56.701	7.3	1.8	2	
527	9/13/91 6:35	56.758	109.1	1.5	2	
528	9/14/91 0:07	57.488	69.1	1.2	2	~ 4 % Ne
529	9/14/91 0:34	57.507	109.1	1.3	2	
530	9/14/91 0:52	57.519	36.4	3	2	
531	9/14/91 12:11	57.991	67.3	1.2	2	
532	9/14/91 14:24	58.083	7.3	0.8	2	
533	9/15/91 2:59	58.608	10.9	1.2	2	
534	9/15/91 7:21	58.789	34.5	1.5	2	
535	9/15/91 9:52	58.894	14.5	1.2	2	
536	9/15/91 13:40	59.053	7.3	1.1	2	
537	9/15/91 14:33	59.089	9.1	1.1	2	
538	9/15/91 16:05	59.153	12.7	1.1	2	
539	9/15/91 17:52	59.227	14.5	1.1	2	
540	9/15/91 19:39	59.302	9.1	1.4	2	
541	9/15/91 21:11	59.365	9.1	1.4	2	
542	9/15/91 22:48	59.433	103.6	2	2	
543	9/15/91 23:19	59.454	10.9	1.8	2	
544	9/16/91 0:00	59.483	52.7	1.2	2	
545	9/16/91 1:53	59.561	7.3	1.2	2	
546	9/16/91 2:08	59.572	7.3	0.9	2	
547	9/16/91 4:37	59.676	7.3	1.7	2	
548	9/16/91 7:14	59.784	16.4	1.9	2	
549	9/16/91 9:42	59.887	12.7	1.8	2	
550	9/16/91 10:49	59.934	18.2	1.2	2	
551	9/16/91 16:02	60.151	16.4	2.4	2	
552	9/16/91 16:46	60.182	21.8	1.3	2	
553	9/16/91 17:02	60.193	12.7	2.4	2	
554	9/16/91 17:15	60.202	14.5	1.3	2	

*Codes given at end of table.

APPENDIX B

(CONTINUED)

spike No.	DAY & TIME (dd/mm/yy h:m)	EFPD	HEIGHT (picoamps)	FWHM (min)	S*	COMMENTS
555	9/16/91 18:29	60.253	36.4	2.4	2	
556	9/16/91 20:08	60.322	9.1	2	2	
557	9/16/91 23:13	60.451	70.9	1.2	2	
558	9/17/91 6:47	60.766	9.1	0.8	2	
559	9/17/91 12:38	61.009	25.5	1.1	0	
560	9/17/91 13:00	61.025	7.3	0.9	0	
561	9/17/91 16:12	61.158	10.9	0.9	0	
562	9/17/91 17:52	61.227	114.5	3.6	3	
						end of cycle 3
563	9/27/91 18:48	61.227	1.4	4.1	0	
564	9/27/91 18:56	61.227	1.2	4.7	0	
565	9/27/91 20:22	61.227	1.8	2.6	0	50 % power
566	9/27/91 20:42	61.227	4.2	1.2	0	70% power
567	9/27/91 20:46	61.227	1.5	1.8	0	
568	9/27/91 21:05	61.227	8.2	1.5	0	90% power
569	9/27/91 21:08	61.227	3.3	1.5	0	
570	9/27/91 21:23	61.227	3	1.8	0	100% power
571	9/27/91 21:29	61.23	4.2	1.5	0	
572	9/28/91 0:47	61.367	22.4	1.5	0	
573	9/28/91 2:33	61.44	19.4	1.4	0	
574	9/28/91 9:07	61.714	22.4	1.5	0	
575	9/28/91 10:28	61.771	10.9	1.4	0	
576	9/28/91 11:28	61.812	9.1	2.4	0	
577	9/28/91 19:58	62.166	15.2	1.2	0	
578	9/29/91 0:48	62.368	10.9	1.2	0	
579	9/29/91 4:39	62.528	24.2	1.4	0	
580	9/29/91 7:08	62.632	15.2	1.5	0	
581	9/29/91 11:17	62.804	9.1	1.5	0	
582	9/29/91 14:46	62.95	10.9	1.2	0	
583	9/29/91 17:07	63.048	18.2	1.2	0	
584	9/29/91 20:30	63.189	48.5	1.4	0	

*Codes given at end of table.

APPENDIX B

(CONTINUED)

spike No.	DAY & TIME (dd/mm/yy h:m)	EFPD	HEIGHT (picoamps)	FWHM (min)	S*	COMMENTS
585	9/29/91 22:08	63.257	12.1	1.4	0	
586	9/30/91 7:04	63.629	10.9	1.4	0	
587	9/30/91 7:52	63.662	12.1	1.8	0	
588	9/30/91 9:18	63.722	10.9	1.4	0	
589	9/30/91 12:27	63.853	15.2	1.5	0	
590	9/30/91 12:44	63.865	9.1	1.4	0	
591	9/30/91 17:52	64.079	48.5	1.4	0	
592	9/30/91 18:24	64.101	12.1	3.5	0	
593	10/1/91 2:44	64.448	9.1	4.1	0	
594	10/1/91 6:48	64.618	6.1	1.8	0	
595	10/1/91 7:18	64.638	6.1	1.8	0	
596	10/1/91 12:18	64.847	7.3	1.4	0	
597	10/1/91 13:54	64.914	27.3	1.7	0	
598	10/2/91 2:41	65.446	6.1	1.8	0	
599	10/3/91 10:18	66.764	6.1	1.7	0	
600	10/3/91 15:13	66.968	10.3	1.2	0	
601	10/3/91 21:44	67.24	6.7	1.8	0	
602	10/4/91 3:21	67.474	30.3	1.3	0	
603	10/4/91 11:21	67.807	12.1	1.2	0	
604	10/4/91 14:50	67.952	24.2	1.4	0	
605	10/5/91 4:15	68.512	12.1	1.4	0	
606	10/5/91 17:15	69.053	10.9	1.2	0	
607	10/5/91 20:11	69.175	7.9	2.1	0	
608	10/6/91 9:21	69.724	18.2	1.5	0	
609	10/8/91 6:29	71.604	9.1	2.4	0	
610	10/8/91 8:14	71.678	57.6	1.2	0	
611	10/10/91 0:58	73.375	121.2	1.5	0	
612	10/10/91 3:59	73.501	12.1	2.4	0	
613	10/10/91 9:21	73.724	6.1	1.8	0	
614	10/10/91 9:46	73.741	9.1	1.8	0	
615	10/10/91 10:53	73.788	6.1	1.2	0	

*Codes given at end of table.

APPENDIX B

(CONTINUED)

spike No.	DAY & TIME (dd/mm/yy h:m)	EFPD	HEIGHT (picoamps)	FWHM (min)	S*	COMMENTS
616	10/10/91 12:13	73.843	6.1	1.2	0	
617	10/10/91 14:00	73.918	9.1	1.2	0	
618	10/10/91 16:42	74.03	6.1	2.4	0	
619	10/10/91 21:53	74.246	24.2	1.5	0	
620	10/10/91 22:03	74.253	7.3	3.5	0	
621	10/10/91 22:22	74.266	21.2	3	0	
622	10/13/91 6:40	76.612	18.2	0.9	0	
623	10/13/91 0:37	76.36	36.4	1.8	0	
624	10/13/91 2:22	76.433	30.3	1.1	0	
625	10/13/91 9:34	76.733	24.2	0.8	0	
626	10/13/91 15:48	76.993	24.2	0.7	0	
627	10/13/91 20:10	77.174	48.5	1.2	0	
628	10/14/91 18:42	78.114	21.2	2.2	0	
629	10/14/91 20:42	78.197	18.2	1.3	0	
630	10/15/91 3:00	78.46	30.3	1.4	0	
631	10/15/91 8:07	78.672	48.5	1.5	0	
632	10/15/91 17:42	79.072	18.2	1.2	0	
633	10/15/91 20:07	79.173	18.2	0.9	0	
634	10/15/91 22:53	79.288	18.2	0.8	0	
635	10/16/91 1:54	79.414	24.2	0.9	0	
636	10/16/91 3:41	79.488	66.7	1.1	0	
637	10/16/91 11:40	79.821	72.7	1.2	0	
638	10/16/91 17:48	80.076	42.4	1.2	0	
639	10/16/91 22:38	80.277	30.3	0.8	0	
640	10/17/91 5:24	80.56	66.7	1.2	0	
641	10/17/91 5:34	80.566	30.3	1.2	0	
642	10/17/91 8:56	80.706	84.8	1.2	0	
643	10/17/91 9:15	80.72	18.2	0.7	0	
644	10/17/91 20:46	81.2	18.2	0.8	0	
645	10/18/91 17:13	82.051	18.2	0.8	0	
646	10/19/91 1:42	82.406	60.6	1.2	0	

*Codes given at end of table.

APPENDIX B

(CONTINUED)

spike No.	DAY & TIME (dd/mm/yy h:m)	EFPD	HEIGHT (picoamps)	FWHM (min)	S*	COMMENTS
647	10/19/91 6:34	82.608	84.8	1.2	0	
648	10/19/91 9:18	82.722	24.2	0.9	0	
649	10/19/91 9:59	82.751	24.2	0.8	0	
650	10/19/91 11:53	82.83	48.5	0.9	0	
651	10/19/91 17:44	83.073	1515.2	4.7	3	
						end of cycle 4
652	10/30/91 10:32	83.006	9.1	2.6	0	30 % Power
653	10/30/91 10:39	83.011	3.6	5.3	0	
654	10/30/91 10:49	83.018	1.8	1.2	0	50 % Power
655	10/30/91 10:55	83.022	1.8	5.3	0	
656	10/30/91 11:15	83.036	30.3	7.1	0	70 % Power
657	10/30/91 11:36	83.051	24.2	1.2	0	90 % Power
658	10/30/91 11:41	83.054	30.3	1.8	0	
659	10/30/91 12:03	83.069	18.2	1.2	0	100 % Power
660	10/30/91 12:05	83.07	42.4	1.8	0	
661	10/30/91 12:51	83.103	36.4	1.2	0	
662	10/31/91 14:42	84.179	18.2	1.1	0	
663	10/31/91 17:11	84.283	21.2	1.3	0	
664	10/31/91 17:34	84.299	18.2	1.1	0	
665	10/31/91 19:16	84.37	21.2	0.8	0	
666	10/31/91 23:06	84.53	18.2	1.2	0	
667	11/1/91 7:39	84.885	18.2	0.8	0	
668	11/1/91 10:16	84.995	24.2	1.8	0	
669	11/1/91 16:50	85.268	24.2	0.9	0	
670	11/1/91 17:04	85.278	1090.9	2.1	0	
671	11/1/91 23:27	85.544	63.6	1.2	0	
672	11/1/91 19:11	85.366	27.3	1.8	0	
673	11/3/91 2:42	86.68	18.2	1.8	0	
674	11/4/91 2:00	87.65	14.5	1.2	0	
675	11/4/91 5:52	87.811	27.3	1.2	0	
676	11/5/91 11:37	89.051	18.2	1.2	0	

*Codes given at end of table.

APPENDIX B

(CONTINUED)

spike No.	DAY & TIME (dd/mm/yy h:m)	EFPD	HEIGHT (picoamps)	FWHM (min)	S*	COMMENTS
677	11/5/91 21:41	89.47	25.5	1.2	0	
678	11/6/91 5:05	89.779	18.2	1.2	0	
679	11/6/91 11:46	90.057	54.5	1.2	0	
680	11/7/91 5:01	90.776	72.7	0.9	0	
681	11/7/91 8:30	90.921	90.9	1.1	0	
682	11/8/91 9:05	91.946	72.7	0.9	0	
683	11/8/91 22:38	92.51	32.7	0.9	0	
684	11/8/91 23:59	92.566	54.5	0.8	0	
685	11/9/91 3:08	92.698	23.6	1.3	0	
686	11/9/91 12:41	93.096	54.5	1.3	0	
687	11/9/91 13:50	93.143	54.5	0.8	0	
688	11/9/91 19:38	93.385	72.7	0.8	0	
689	11/10/91 2:38	93.677	54.5	0.8	0	
690	11/10/91 10:28	94.003	27.3	1.2	0	
691	11/11/91 1:08	94.615	27.3	1.2	0	
692	11/11/91 1:38	94.635	23.6	1.8	0	
693	11/11/91 3:04	94.695	27.3	1.2	0	
694	11/11/91 11:03	95.028	36.4	1.2	0	
695	11/11/91 20:15	95.411	54.5	0.6	0	
696	11/11/91 20:21	95.415	54.5	0.9	0	
697	11/12/91 15:23	96.208	90.9	0.9	0	
698	11/12/91 15:31	96.214	54.5	0.9	0	
699	11/12/91 15:47	96.225	14.5	2.4	0	
700	11/12/91 16:02	96.235	14.5	1.2	0	
701	11/12/91 23:31	96.547	27.3	1.2	0	
702	11/13/91 0:45	96.599	27.3	1.2	0	
703	11/13/91 13:42	97.138	54.5	0.7	0	
704	11/13/91 18:28	97.337	90.9	0.9	0	
705	11/13/91 19:59	97.4	18.2	2.4	0	
706	11/14/91 4:58	97.774	14.5	1.2	0	
707	11/14/91 10:35	98.008	14.5	1.2	0	

*Codes given at end of table.

APPENDIX B

(CONTINUED)

spike No.	DAY & TIME (dd/mm/yy h:m)	EFPD	HEIGHT (picoamps)	FWHM (min)	S*	COMMENTS
708	11/14/91 17:33	98.298	23.6	1.2	0	
709	11/14/91 17:49	98.31	14.5	1.2	0	
710	11/14/91 19:42	98.388	54.5	0.8	0	
711	11/14/91 21:51	98.477	36.4	1.2	0	
712	11/15/91 2:26	98.669	90.9	1.1	0	
713	11/15/91 2:30	98.671	54.5	1.3	0	
714	11/15/91 13:25	99.126	30.9	1.2	0	
715	11/16/91 20:41	100.429	90.9	0.8	0	
716	11/16/91 21:52	100.478	23.6	1.2	0	
717	11/16/91 22:01	100.484	23.6	1.2	0	
718	11/17/91 0:42	100.596	27.3	1.2	0	
719	11/17/91 7:11	100.866	90.9	0.9	0	
720	11/17/91 9:57	100.982	72.7	0.8	0	
721	11/17/91 11:38	101.051	23.6	1.8	0	
722	11/17/91 14:20	101.164	54.5	0.9	0	
723	11/17/91 15:01	101.193	27.3	1.8	0	
724	11/17/91 16:37	101.259	14.5	1.2	0	
725	11/17/91 18:01	101.318	54.5	0.8	0	
726	11/17/91 19:19	101.372	27.3	1.8	0	
727	11/17/91 21:38	101.468	27.3	1.8	0	
728	11/17/91 21:46	101.474	90.9	1.4	0	
729	11/17/91 21:53	101.479	27.3	1.2	0	
730	11/17/91 22:41	101.512	36.4	2.1	0	
731	11/18/91 1:26	101.627	54.5	1.2	0	
732	11/18/91 4:48	101.767	54.5	0.7	0	
733	11/18/91 14:40	102.178	54.5	1.1	0	
734	11/18/91 17:18	102.288	90.9	1.1	0	
735	11/19/91 11:13	103.035	54.5	0.8	0	
736	11/19/91 12:17	103.079	72.7	0.8	0	
737	11/19/91 22:12	103.492	72.7	0.8	0	
738	11/19/91 22:40	103.512	54.5	0.8	0	

*Codes given at end of table.

APPENDIX B

(CONTINUED)

spike No.	DAY & TIME (dd/mm/yy h:m)	EFPD	HEIGHT (picoamps)	FWHM (min)	S*	COMMENTS
739	11/20/91 1:40	103.637	127.3	0.9	0	
740	11/20/91 1:46	103.64	90.9	1.6	0	
741	11/20/91 2:48	103.684	54.5	1.4	0	
742	11/20/91 6:08	103.823	54.5	1.4	0	
743	11/20/91 12:27	104.086	72.7	1.2	0	
744	11/20/91 17:38	104.302	127.3	1.2	0	
745	11/20/91 17:38	104.302	200	1.2	0	
746	11/20/91 17:41	104.304	145.5	1.1	0	
747	11/20/91 17:43	104.305	254.5	1.4	0	
748	11/20/91 17:51	104.311	72.7	0.8	0	
749	11/20/91 21:01	104.442	72.7	0.8	0	
750	11/20/91 22:49	104.518	72.7	1.1	0	
751	11/21/91 2:25	104.667	1927.3	2.7	3	

S codes:
- 0 100% He sweep gas
- 1 Neon being added
- 2 Constant sweep gas mixture of He and Ne
- 3 Reactor shut down

APPENDIX C

TRIGA STEADY-STATE R/B RESULTS FOR HRB-21 COMPACTS

Appendix C

TRIGA STEADY-STATE R/B RESULTS FOR HRB-21 COMPACTS[a]

Compact No.	Temp.(°C)	Release Rate /Birth Rate (R/B)				
		^{85m}Kr	^{87}Kr	^{88}Kr	^{89}Kr	^{138}Xe
5A	1100	5.0E-4	5.1E-4	5.1E-4	5.3E-4	4.9E-4
5B	1100	3.3E-4	3.5E-4	3.5E-4	3.8E-4	3.7E-4
5C	1100	3.8E-4	3.9E-4	3.7E-4	4.1E-4	4.0E-4
5C	900	1.9E-4	2.0E-4	1.8E-4	2.4E-4	2.4E-4
5C	900	2.4E-4	2.4E-4	2.4E-4	2.8E-4	2.8E-4
Holder 5 Average		4.1E-4	4.2E-4	4.1E-4	4.4E-4	4.2E-4
6A	1100	3.3E-4	3.5E-4	3.2E-4	3.9E-4	3.9E-4
6B	1100	2.1E-4	2.1E-4	2.1E-4	2.2E-4	2.2E-4
6C	1100	2.0E-4	2.2E-4	2.2E-4	2.6E-4	2.8E-4
6C[a]	900	1.5E-4	1.5E-4	1.4E-4	2.1E-4	2.2E-4
6C	900	1.8E-4	1.7E-4	1.6E-4	2.3E-4	2.3E-4
Holder 6 Average	1100	2.5E-4	2.6E-4	2.5E-4	2.9E-4	3.0E-4
7A	1100	7.2E-5	8.2E-5	8.4E-5	9.8E-5	6.8E-5
7B	1100	7.7E-5	9.1E-5	8.6E-5	1.1E-4	9.1E-5
7C	1100	9.5E-5	1.1E-4	1.1E-4	1.3E-4	1.0E-4
7C	900	9.4E-5	9.7E-5	8.8E-5	1.4E-4	1.2E-4
7C	900	9.9E-5	1.0E-4	1.0E-4	1.4E-4	1.2E-4
Holder 7 Average	1100	8.1E-5	9.4E-5	9.3E-5	1.1E-4	8.6E-5
8A	1100	1.8E-7	1.5E-7	6.6E-8	nd[C]	nm[D]
8B[a]	1100	2.9E-6	2.8E-6	2.8E-6	3.4E-6	6.2E-7
8C	1100	1.0E-6	1.1E-6	1.1E-6	1.1E-6	3.0E-7
8C	900	4.1E-7	4.3E-7	4.3E-7	4.8E-7	1.9E-7
8C	900	5.1E-7	4.9E-7	4.7E-7	4.8E-7	2.0E-7
Holder 8 Average	1100	1.4E-6	1.4E-6	1.3E-6	1.5E-6	3.1E-7

[a]J. J. Saurwein, "Addendum: Fission Gas Release Testing of Fuel Compacts from Irradiation capsule HRB-21," attachment to GA/ORNL 021-93, General Atomics, San Diego, July 1993.

[b]Irradiation time was less than 30 min due to an unplanned reactor scram. The fission gas birth terms were corrected to be consistent with the actual irradiation time.

[c]Nd = Not detected.

[d]nm = Not measured.

APPENDIX D-1

COMPILATION OF CERAMOGRAPHIC DATA ON HRB-21 COMPACT PARTICLES

Appendix D-1

COMPILATION OF CERAMOGRAPHIC DATA ON HRB-21 COMPACT PARTICLES

Type	ID 1	ID 2	ID 3	ID 4	PPyC Damage	OPyC Damage	SiC Damage	IPyC Damage	Comments
fertile	1C	seg 1	sec 3	MET6068	X		XC		Circumferential crack 70 deg
fertile	1C	seg 1	sec 3	MET6068	X				
fertile	1C	seg 1	sec 3	MET6068					
fertile	1C	seg 1	sec 3	MET6068					
fertile	1C	seg 1	sec 3	MET6068			XC		Circumferential crack 230 deg
fertile	1C	seg 1	sec 3	MET6068					
fertile	1C	seg 1	sec 3	MET6068					
fertile	1C	seg 1	sec 3	MET6068			XC		Circumferential crack 70 deg
fertile	1C	seg 1	sec 3	MET6068					
fertile	1C	seg 1	sec 3	MET6068			XC		Circumferential crack 90 deg
fertile	1C	seg 1	sec 3	MET6068	X				
fertile	1C	seg 1	sec 3	MET6068	X				
fertile	1C	seg 1	sec 3	MET6068	X		XC		Circumferential crack 90 deg
fertile	1C	seg 1	sec 3	MET6068	X				
fertile	1C	seg 1	sec 3	MET6068	X		XC		Circumferential crack 150 deg
fertile	1C	seg 1	sec 3	MET6068					
fertile	1C	seg 1	sec 3	MET6068	X				

X = Damage/crack XC = Circumferential crack

Appendix D-1

(CONTINUED)

Type	ID 1	ID 2	ID 3	ID 4	PPyC Damage	OPyC Damage	SiC Damage	IPyC Damage	Comments
fertile	1C	seg 1	sec 3	MET6068	X				
fissile	1C	seg 1	sec 3	MET6068	X				
fertile	1C	seg 1	sec 3	MET6068			XC		Circumferential crack 90 deg
fertile	1C	seg 1	sec 3	MET6068	X				
fertile	1C	seg 1	sec 3	MET6068	X		XC		Circumferential crack 45 deg
fertile	1C	seg 1	sec 3	MET6068	X				
fertile	1C	seg 1	sec 3	MET6068	X				
fertile	1C	seg 1	sec 3	MET6068	X				
fertile	1C	seg 1	sec 3	MET6068					
fertile	1C	seg 1	sec 3	MET6068	X				
fertile	1C	seg 1	sec 3	MET6068					
fertile	1C	seg 1	sec 3	MET6068	X				
fertile	1C	seg 1	sec 3	MET6068	X				
fertile	1C	seg 1	sec 3	MET6068	X				
fertile	1C	seg 1	sec 3	MET6068	X				
fertile	1C	seg 1	sec 3	MET6068	X				
fertile	1C	seg 1	sec 3	MET6068	X				

X = Damage/crack XC = Circumferential crack

Appendix D-1

(CONTINUED)

Type	ID 1	ID 2	ID 3	ID 4	PPyC Damage	OPyC Damage	SiC Damage	IPyC Damage	Comments
fertile	1C	seg 1	sec 3	MET6068	X				
fertile	1C	seg 1	sec 3	MET6068			XC		Circumferential crack 90 deg
fertile	1C	seg 1	sec 3	MET6068					
fertile	1C	seg 1	sec 3	MET6068					
fertile	1C	seg 1	sec 3	MET6068					
fertile	1C	seg 1	sec 3	MET6068					
fertile	1C	seg 1	sec 3	MET6068					
fertile	1C	seg 1	sec 3	MET6068					
fertile	1C	seg 1	sec 3	MET6068	X				
fertile	1C	seg 1	sec 3	MET6068			XC		Circumferential crack 45 deg
fissile	1C	seg 1	sec 3	MET6068					
fertile	1C	seg 1	sec 4	MET6068	X	X			
fertile	1C	seg 1	sec 4	MET6068	X	X			
fertile	1C	seg 1	sec 4	MET6068			XC		Circumferential crack 45 deg
fertile	1C	seg 1	sec 4	MET6068	X	X			
fertile	1C	seg 1	sec 4	MET6068					
fissile	1C	seg 1	sec 4	MET6068	X	X			

X = Damage/crack XC = Circumferential crack

Appendix D-1

(CONTINUED)

Type	ID 1	ID 2	ID 3	ID 4	PPyC Damage	OPyC Damage	SiC Damage	IPyC Damage	Comments
fertile	1C	seg 1	sec 4	MET6068	X	X			
fissile	1C	seg 1	sec 4	MET6068	X	X			
fertile	1C	seg 1	sec 4	MET6068	X	X		X	
fissile	1C	seg 1	sec 4	MET6068	X	X			
fissile	1C	seg 1	sec 4	MET6068	X	X			
fissile	1C	seg 1	sec 4	MET6068	X	X			
fertile	1C	seg 1	sec 4	MET6068	X	X			
fissile	1C	seg 1	sec 4	MET6068	X	X			
fertile	1C	seg 1	sec 4	MET6068	X	X			
fertile	1C	seg 1	sec 4	MET6068	X	X			
fertile	1C	seg 1	sec 4	MET6068	X	X	XC		Circumferential crack 30 deg
fissile	1C	seg 1	sec 4	MET6068	X	X			
fertile	1C	seg 1	sec 4	MET6068	X	X			
fissile	1C	seg 1	sec 4	MET6068	X	X			
fertile	1C	seg 1	sec 4	MET6068	X	X			
fissile	1C	seg 1	sec 4	MET6068	X	X			
fertile	1C	seg 1	sec 4	MET6068	X	X	XC		Circumferentall crack 20 deg

X = Damage/crack XC = Circumferential crack

Appendix D-1

(CONTINUED)

Type	ID 1	ID 2	ID 3	ID 4	PPyC Damage	OPyC Damage	SiC Damage	IPyC Damage	Comments
fertile	1C	seg 1	sec 4	MET6068	X	X	XC		Circumferentail crack 60 deg
fertile	1C	seg 1	sec 4	MET6068	X	X	XC		Circumferential cracks (2) totaling 50 deg
fissile	1C	seg 1	sec 4	MET6068	X	X			
fissile	1C	seg 1	sec 4	MET6068	X	X			
fertile	1C	seg 1	sec 4	MET6068	X	X			
fertile	1C	seg 1	sec 4	MET6068	X	X			
fertile	1C	seg 1	sec 4	MET6068	X	X			
fissile	1C	seg 1	sec 4	MET6068	X	X			
fissile	1C	seg 1	sec 4	MET6068	X	X			
fertile	1C	seg 1	sec 4	MET6068	X	X	XC		Circumferential crack 45 deg
fertile	1C	seg 1	sec 4	MET6068	X	X			
fissile	1C	seg 1	sec 4	MET6068	X	X			
fertile	1C	seg 1	sec 4	MET6068	X	X			
fertile	1C	seg 1	sec 5	MET6068	X				
fissile	1C	seg 1	sec 5	MET6068	X				
fertile	1C	seg 1	sec 5	MET6068					
fertile	1C	seg 1	sec 5	MET6068	X		XC		Circumferential crack 5 deg

X = Damage/crack XC = Circumferential crack

Appendix D-1

(CONTINUED)

Type	ID 1	ID 2	ID 3	ID 4	PPyC Damage	OPyC Damage	SiC Damage	IPyC Damage	Comments
fertile	1C	seg 1	sec 5	MET6068	X				
fertile	1C	seg 1	sec 5	MET6068	X				
fissile	1C	seg 1	sec 5	MET6068	X				
fertile	1C	seg 1	sec 5	MET6068					
fertile	1C	seg 1	sec 5	MET6068	X		XC		Circumferential crack 5 deg
fertile	1C	seg 1	sec 5	MET6068	X		XC		Circumferential crack 10 deg
fertile	1C	seg 1	sec 5	MET6068					
fertile	1C	seg 1	sec 5	MET6068	X		XC		Circumferential crack 10 deg
fissile	1C	seg 1	sec 5	MET6068					
fertile	1C	seg 1	sec 5	MET6068					
fissile	1C	seg 1	sec 5	MET6068					
fertile	1C	seg 1	sec 5	MET6068			XC		Circumferential crack 45 deg
fertile	1C	seg 1	sec 5	MET6068					
fertile	1C	seg 1	sec 5	MET6068	X		XC		Circumferential cracks 70 deg and 90 deg
fertile	1C	seg 1	sec 5	MET6068	X				
fertile	1C	seg 1	sec 5	MET6068	X		XC		Circumferential cracks (2) 10 deg
fertile	1C	seg 1	sec 5	MET6068	X				

X = Damage/crack XC = Circumferential crack

Appendix D-1

(CONTINUED)

Type	ID 1	ID 2	ID 3	ID 4	PPyC Damage	OPyC Damage	SiC Damage	IPyC Damage	Comments
fertile	1C	seg 1	sec 5	MET6068					
fertile	1C	seg 1	sec 5	MET6068					
fissile	1C	seg 1	sec 5	MET6068					
fissile	1C	seg 1	sec 5	MET6068					
fertile	1C	seg 1	sec 5	MET6068	X				
fertile	1C	seg 1	sec 5	MET6068	X	X	XC		Circumferential cracks 100 deg
fissile	1C	seg 1	sec 5	MET6068	X				
fertile	1C	seg 1	sec 5	MET6068	X				
fissile	1C	seg 1	sec 5	MET6068					
fertile	1C	seg 1	sec 5	MET6068	X				
fertile	1C	seg 1	sec 5	MET6068	X				
fertile	1C	seg 1	sec 5	MET6068	X				
fissile	1C	seg 1	sec 5	MET6068					
fertile	1C	seg 1	sec 5	MET6068			XC		Circumferential crack at SiC interface that breaks to surface one
fertile	1C	seg 1	sec 5	MET6068	X				
fertile	1C	seg 1	sec 5	MET6068	X				
fissile	1C	seg 1	sec 5	MET6068	X				

X = Damage/crack XC = Circumferential crack

Appendix D-1

(CONTINUED)

Type	ID 1	ID 2	ID 3	ID 4	PPyC Damage	OPyC Damage	SiC Damage	IPyC Damage	Comments
fertile	1C	seg 1	sec 5	MET6068	X				
fertile	1C	seg 1	sec 5	MET6068	X				
fertile	1C	seg 1	sec 5	MET6068	X				
fertile	1C	seg 1	sec 5	MET6068	X		XC		Circumferential cracks 1-220 deg 1-45 deg
fertile	1C	seg 1	sec 5	MET6068	X				
fissile	1C	seg 1	sec 5	MET6068	X				
fertile	1C	seg 1	sec 5	MET6068					
fissile	1C	seg 1	sec 5	MET6068	X				
fertile	1C	seg 1	sec 5	MET6068					
fertile	1C	seg 1	sec 5	MET6068					
fissile	1C	seg 1	sec 5	MET6068	X				
fissile	1C	seg 1	sec 5	MET6068					
fertile	1C	seg 1	sec 5	MET6068			XC		Circumferential crack 150 deg goes to surface at both ends
fertile	1C	seg 1	sec 5	MET6068					
fertile	1C	seg 1	sec 6	MET6068					
fissile	1C	seg 1	sec 6	MET6068					
fissile	1C	seg 1	sec 6	MET6068	X				

X = Damage/crack XC = Circumferential crack

Appendix D-1

(CONTINUED)

Type	ID 1	ID 2	ID 3	ID 4	PPyC Damage	OPyC Damage	SiC Damage	IPyC Damage	Comments
fertile	1C	seg 1	sec 6	MET6068	X				
fertile	1C	seg 1	sec 6	MET6068					
fertile	1C	seg 1	sec 6	MET6068	X				
fertile	1C	seg 1	sec 6	MET6068	X				
fertile	1C	seg 1	sec 6	MET6068	X				
fissile	1C	seg 1	sec 6	MET6068	X				
fertile	1C	seg 1	sec 6	MET6068			XC		Circumferential crack 20 deg
fissile	1C	seg 1	sec 6	MET6068	X				
fertile	1C	seg 1	sec 6	MET6068	X				
fertile	1C	seg 1	sec 6	MET6068	X				
fertile	1C	seg 1	sec 6	MET6068	X				
fertile	1C	seg 1	sec 6	MET6068	X		XC		Circumferential cracks 10 deg & 20 deg goes to inside
fertile	1C	seg 1	sec 6	MET6068					
fertile	1C	seg 1	sec 6	MET6068	X				
fissile	1C	seg 1	sec 6	MET6068	X				
fertile	1C	seg 1	sec 6	MET6068	X		X		

X = Damage/crack XC = Circumferential crack

Appendix D-1

(CONTINUED)

Type	ID 1	ID 2	ID 3	ID 4	PPyC Damage	OPyC Damage	SiC Damage	IPyC Damage	Comments
fertile	1C	seg 1	sec 6	MET6068			XC		Circumferential crack 180 deg goes to inner SiC both ends
fertile	1C	seg 1	sec 6	MET6068	X				
fertile	1C	seg 1	sec 6	MET6068					
fertile	1C	seg 1	sec 6	MET6068	X				
fertile	1C	seg 1	sec 6	MET6068					
fertile	1C	seg 1	sec 6	MET6068					
fertile	1C	seg 1	sec 6	MET6068	X				
fertile	1C	seg 1	sec 6	MET6068	X				
fissile	1C	seg 1	sec 6	MET6068	X				
fissile	1C	seg 1	sec 6	MET6068	X				
fertile	1C	seg 1	sec 6	MET6068	X				
fertile	1C	seg 1	sec 6	MET6068	X	X			
fertile	1C	seg 1	sec 6	MET6068	X		X		One piece broke off and adhere to IPyC
fissile	1C	seg 1	sec 6	MET6068	X				
fertile	1C	seg 1	sec 6	MET6068					
fertile	1C	seg 1	sec 6	MET6068	X				
fertile	1C	seg 2	sec 2	MET6070	X	X			

X = Damage/crack XC = Circumferential crack

Appendix D-1

(CONTINUED)

Type	ID 1	ID 2	ID 3	ID 4	PPyC Damage	OPyC Damage	SiC Damage	IPyC Damage	Comments
fertile	1C	seg 2	sec 2	MET6070	X	X			
fertile	1C	seg 2	sec 2	MET6070	X	X	XC		Circumferential crack 90 deg
fissile	1C	seg 2	sec 2	MET6070					
fissile	1C	seg 2	sec 2	MET6070	X	X			
fissile	1C	seg 2	sec 2	MET6070	X	X			
fertile	1C	seg 2	sec 2	MET6070	X	X			
fertile	1C	seg 2	sec 2	MET6070	X	X			
fissile	1C	seg 2	sec 2	MET6070	X	X			
fissile	1C	seg 2	sec 2	MET6070	X	X			
fissile	1C	seg 2	sec 2	MET6070	X	X			
fertile	1C	seg 2	sec 2	MET6070	X	X			
fissile	1C	seg 2	sec 2	MET6070	X	X			
fertile	1C	seg 2	sec 2	MET6070	X	X			
fissile	1C	seg 2	sec 2	MET6070	X	X			
fertile	1C	seg 2	sec 2	MET6070	X	X			
fertile	1C	seg 2	sec 2	MET6070	X	X			
fertile	1C	seg 2	sec 2	MET6070	X	X			

X = Damage/crack XC = Circumferential crack

Appendix D-1

(CONTINUED)

Type	ID 1	ID 2	ID 3	ID 4	PPyC Damage	OPyC Damage	SiC Damage	IPyC Damage	Comments
fertile	1C	seg 2	sec 2	MET6070	X	X	XC		Circumferential crack 100 deg
fertile	1C	seg 2	sec 2	MET6070	X	X	XC		
fertile	1C	seg 2	sec 2	MET6070	X	X	XC		Circumferential crack 90 deg
fertile	1C	seg 2	sec 2	MET6070	X	X	XC		Circumferential cracks (2) totaling 270 deg
fissile	1C	seg 2	sec 2	MET6070	X	X			
fissile	1C	seg 2	sec 2	MET6070	X	X			
fissile	1C	seg 2	sec 2	MET6070	X	X			
fissile	1C	seg 2	sec 2	MET6070	X	X			
fissile	1C	seg 2	sec 2	MET6070	X	X			
fertile	1C	seg 2	sec 2	MET6070	X	X			
fissile	1C	seg 2	sec 2	MET6070	X	X			
fissile	1C	seg 2	sec 2	MET6070	X	X			
fertile	1C	seg 2	sec 2	MET6070	X	X			
fissile	1C	seg 2	sec 2	MET6070	X	X			
fertile	1C	seg 2	sec 2	MET6070	X	X			
fissile	1C	seg 2	sec 2	MET6070	X	X			
fertile	1C	seg 2	sec 3	MET6070	X				

X = Damage/crack XC = Circumferential crack

Appendix D-1

(CONTINUED)

Type	ID 1	ID 2	ID 3	ID 4	PPyC Damage	OPyC Damage	SiC Damage	IPyC Damage	Comments
fertile	1C	seg 2	sec 3	MET6070	X				
fertile	1C	seg 2	sec 3	MET6070	X				
fissile	1C	seg 2	sec 3	MET6070	X				
fissile	1C	seg 2	sec 3	MET6070	X				
fissile	1C	seg 2	sec 3	MET6070	X				
fertile	1C	seg 2	sec 3	MET6070	X				
fissile	1C	seg 2	sec 3	MET6070	X				
fertile	1C	seg 2	sec 3	MET6070	X				
fissile	1C	seg 2	sec 3	MET6070					
fissile	1C	seg 2	sec 3	MET6070	X				
fertile	1C	seg 2	sec 3	MET6070	X				
fertile	1C	seg 2	sec 3	MET6070	X				
fertile	1C	seg 2	sec 3	MET6070	X				
fertile	1C	seg 2	sec 3	MET6070	X				
fertile	1C	seg 2	sec 3	MET6070	X		XC		Circumferential crack 45 deg
fertile	1C	seg 2	sec 3	MET6070					
fertile	1C	seg 2	sec 3	MET6070	X				

X = Damage/crack XC = Circumferential crack

Appendix D-1

(CONTINUED)

Type	ID 1	ID 2	ID 3	ID 4	PPyC Damage	OPyC Damage	SiC Damage	IPyC Damage	Comments
fertile	1C	seg 2	sec 3	MET6070	X		XC		Circumferential cracks (3) totaling 220 deg
fertile	1C	seg 2	sec 3	MET6070	X		XC		Circumferential crack 60 deg
fissile	1C	seg 2	sec 3	MET6070	X				
fissile	1C	seg 2	sec 3	MET6070	X				
fissile	1C	seg 2	sec 3	MET6070	X				
fertile	1C	seg 2	sec 3	MET6070	X		XC		Circumferential cracks totaling 45 deg
fissile	1C	seg 2	sec 3	MET6070	X				
fissile	1C	seg 2	sec 3	MET6070	X				
fertile	1C	seg 2	sec 3	MET6070	X				
fissile	1C	seg 2	sec 3	MET6070	X				
fertile	1C	seg 2	sec 3	MET6070	X		XC		Circumferential crack 120 deg
fertile	1C	seg 2	sec 3	MET6070	X		XC		Circumferential crack 90 deg
fissile	1C	seg 2	sec 3	MET6070	X				
fissile	1C	seg 2	sec 3	MET6070	X				
fertile	1C	seg 2	sec 3	MET6070	X				
fissile	1C	seg 2	sec 3	MET6070	X	X			
fissile	1C	seg 2	sec 3	MET6070					

X = Damage/crack XC = Circumferential crack

Appendix D-1

(CONTINUED)

Type	ID 1	ID 2	ID 3	ID 4	PPyC Damage	OPyC Damage	SiC Damage	IPyC Damage	Comments
fissile	1C	seg 2	sec 3	MET6070	X				
fissile	1C	seg 2	sec 3	MET6070	X				
fissile	1C	seg 2	sec 3	MET6070	X				
fertile	1C	seg 2	sec 3	MET6070	X				
fissile	1C	seg 2	sec 3	MET6070	X				
fissile	1C	seg 2	sec 3	MET6070	X				
fertile	1C	seg 2	sec 3	MET6070	X				
fissile	1C	seg 2	sec 3	MET6070	X				
fissile	1C	seg 2	sec 3	MET6070					
fertile	1C	seg 2	sec 3	MET6070					
fissile	1C	seg 2	sec 3	MET6070	X				
fissile	1C	seg 2	sec 3	MET6070					
fissile	1C	seg 2	sec 4	MET6070					Stain(?) on SiC Photo B
fertile	1C	seg 2	sec 4	MET6070	X	?			Gouge penetrating into outer pyrocarbon
fissile	1C	seg 2	sec 4	MET6070					
fissile	1C	seg 2	sec 4	MET6070	X				
fissile	1C	seg 2	sec 4	MET6070					

X = Damage/crack XC = Circumferential crack

Appendix D-1

(CONTINUED)

Type	ID 1	ID 2	ID 3	ID 4	PPyC Damage	OPyC Damage	SiC Damage	IPyC Damage	Comments
fissile	1C	seg 2	sec 4	MET6070	X				
fertile	1C	seg 2	sec 4	MET6070	X				
fissile	1C	seg 2	sec 4	MET6070	X				
fertile	1C	seg 2	sec 4	MET6070					
fertile	1C	seg 2	sec 4	MET6070	X				
fissile	1C	seg 2	sec 4	MET6070	X				
fertile	1C	seg 2	sec 4	MET6070	X				
fissile	1C	seg 2	sec 4	MET6070					
fertile	1C	seg 2	sec 4	MET6070	X				
fertile	1C	seg 2	sec 4	MET6070	X				
fissile	1C	seg 2	sec 4	MET6070	X				
fertile	1C	seg 2	sec 4	MET6070	X				
fertile	1C	seg 2	sec 4	MET6070	X				
fertile	1C	seg 2	sec 4	MET6070	X				
fissile	1C	seg 2	sec 4	MET6070	X	X			
fertile	1C	seg 2	sec 4	MET6070	X				
fertile	1C	seg 2	sec 4	MET6070	X				

X = Damage/crack XC = Circumferential crack

Appendix D-1

(CONTINUED)

Type	ID 1	ID 2	ID 3	ID 4	PPyC Damage	OPyC Damage	SiC Damage	IPyC Damage	Comments
fertile	1C	seg 2	sec 4	MET6070	X				
fissile	1C	seg 2	sec 4	MET6070					
fissile	1C	seg 2	sec 4	MET6070	X				
fertile	1C	seg 2	sec 4	MET6070	X				
fertile	1C	seg 2	sec 4	MET6070	X		XC		Circumferential crack 30 deg at outer edge of compact
fissile	1C	seg 2	sec 4	MET6070	X				
fertile	1C	seg 2	sec 4	MET6070	X				
fertile	1C	seg 2	sec 4	MET6070	X				
fertile	1C	seg 2	sec 4	MET6070	X				
fissile	1C	seg 2	sec 4	MET6070					
fissile	1C	seg 2	sec 4	MET6070	X				
fertile	1C	seg 2	sec 4	MET6070	X				
fissile	1C	seg 2	sec 4	MET6070					
fissile	1C	seg 2	sec 4	MET6070	X				
fissile	1C	seg 2	sec 4	MET6070	X				
fertile	1C	seg 2	sec 4	MET6070	X				
fertile	1C	seg 2	sec 4	MET6070	X		XC		Circumferential crack 60 deg

X = Damage/crack XC = Circumferential crack

Appendix D-1

(CONTINUED)

Type	ID 1	ID 2	ID 3	ID 4	PPyC Damage	OPyC Damage	SiC Damage	IPyC Damage	Comments
fertile	1C	seg 2	sec 4	MET6070			XC		Circumferential crack 30 near edge of compact
fissile	1C	seg 2	sec 4	MET6070	X				
fertile	1C	seg 2	sec 4	MET6070	X				
fertile	1C	seg 2	sec 4	MET6070	X				
fertile	1C	seg 2	sec 4	MET6070	X				
fertile	1C	seg 2	sec 4	MET6070	X				
fertile	1C	seg 2	sec 4	MET6070	X				
fertile	1C	seg 2	sec 4	MET6070					
fissile	2A	top	long	MET6111	X	X			
fissile	2A	top	long	MET6111	X	X			
fertile	2A	top	long	MET6111	X	X			
fertile	2A	top	long	MET6111	X	X			
fertile	2A	top	long	MET6111	X	X			
fissile	2A	top	long	MET6111					
fertile	2A	top	long	MET6111	X	X			
fertile	2A	top	long	MET6111	X	X			
fertile	2A	top	long	MET6111	X	X			

X = Damage/crack XC = Circumferential crack

Appendix D-1

(CONTINUED)

Type	ID 1	ID 2	ID 3	ID 4	PPyC Damage	OPyC Damage	SiC Damage	IPyC Damage	Comments
fissile	2A	top	long	MET6111	X	X			
fertile	2A	top	long	MET6111	X	X			
fertile	2A	top	long	MET6111	X	X			
fertile	2A	top	long	MET6111	X				
fissile	2A	top	long	MET6111	X	X			
fertile	2A	top	long	MET6111	X	X	XC		circumferential crack 60 deg inner to inner
fissile	2A	top	long	MET6111	X	X			
fertile	2A	top	long	MET6111	X	X			
fissile	2A	top	long	MET6111	X				
fertile	2A	top	long	MET6111	X	X			
fissile	2A	top	long	MET6111	X	X			
fertile	2A	top	long	MET6111	X	X			
fertile	2A	top	long	MET6111	X				
fissile	2A	top	long	MET6111	X	X			
fertile	2A	top	long	MET6111	X	X			
fissile	2A	top	long	MET6111	X	X			
fissile	2A	top	long	MET6111	X				

X = Damage/crack XC = Circumferential crack

Appendix D-1

(CONTINUED)

Type	ID 1	ID 2	ID 3	ID 4	PPyC Damage	OPyC Damage	SiC Damage	IPyC Damage	Comments
fertile	2A	top	long	MET6111					
fertile	2A	top	long	MET6111	X	X			
fertile	2A	top	long	MET6111	X	X			
fissile	2A	top	long	MET6111	X	X			
fissile	2A	top	long	MET6111	X	X			
fissile	2A	top	long	MET6111	X	X		X	
fertile	2A	top	long	MET6111	X	X			
fissile	2A	top	long	MET6111	X	X			
fertile	2A	top	long	MET6111	X	X			
fertile	2A	top	long	MET6111	X	X			
fissile	2A	top	long	MET6111	X	X			
fertile	2A	top	long	MET6111	X	X			
fertile	2A	top	long	MET6111	X	X			
fertile	2A	top	long	MET6111	X				
fertile	2A	top	long	MET6111	X				
fissile	2A	top	long	MET6111	X	X			
fertile	2A	top	long	MET6111	X	X			

X = Damage/crack XC = Circumferential crack

Appendix D-1

(CONTINUED)

Type	ID 1	ID 2	ID 3	ID 4	PPyC Damage	OPyC Damage	SiC Damage	IPyC Damage	Comments
fertile	2A	top	long	MET6111	X				
fertile	2A	top	long	MET6111	X	X			
fertile	2A	top	long	MET6111	X				
fertile	2A	top	long	MET6111	X	X			
fissile	2A	top	long	MET6111	X	X			
fissile	2A	top	long	MET6111	X				
fertile	2A	top	long	MET6111	X				
fertile	2A	top	long	MET6111	X				
fertile	2A	top	long	MET6111					
fertile	2A	top	long	MET6111	X				
fertile	2A	top	long	MET6111	X				
fertile	2A	top	long	MET6111	X	X			
fertile	2A	top	long	MET6111	X				
fertile	2A	top	long	MET6111	X				
fissile	2A	top	long	MET6111					
fertile	2A	top	long	MET6111	X				
fissile	2A	top	long	MET6111	X				

X = Damage/crack XC = Circumferential crack

Appendix D-1

(CONTINUED)

Type	ID 1	ID 2	ID 3	ID 4	PPyC Damage	OPyC Damage	SiC Damage	IPyC Damage	Comments
fertile	2A	top	long	MET6111					
fissile	2A	top	long	MET6111	X				
fertile	2A	top	long	MET6111	X				
fertile	2A	top	long	MET6111	X				
fertile	2A	top	long	MET6111	X				
fissile	2A	top	long	MET6111					
fissile	2A	top	long	MET6111	X				
fissile	2A	top	long	MET6111	X				
fertile	2A	top	long	MET6111					
fissile	2A	top	long	MET6111					
fertile	2A	center	long	MET6112	X				
fertile	2A	center	long	MET6112	X	X			
fertile	2A	center	long	MET6112	X	X			
fertile	2A	center	long	MET6112	X	X			
fertile	2A	center	long	MET6112	X	X		X	Failed buffer
fertile	2A	center	long	MET6112	X	X			
fertile	2A	center	long	MET6112	X	X		X	

X = Damage/crack XC = Circumferential crack

Appendix D-1

(CONTINUED)

Type	ID 1	ID 2	ID 3	ID 4	PPyC Damage	OPyC Damage	SiC Damage	IPyC Damage	Comments
fertile	2A	center	long	MET6112	X				
fertile	2A	center	long	MET6112	X				
fertile	2A	center	long	MET6112	X	X		X	
fissile	2A	center	long	MET6112	X	X			
fissile	2A	center	long	MET6112	X	X		X	
fertile	2A	center	long	MET6112	X	X			
fertile	2A	center	long	MET6112	X	X			Failed buffer
fertile	2A	center	long	MET6112	X	X			
fissile	2A	center	long	MET6112	X	X			
fissile	2A	center	long	MET6112	X	X		X	
fertile	2A	center	long	MET6112	X	X			
fertile	2A	center	long	MET6112	X	X			Failed buffer
fertile	2A	center	long	MET6112	X	X			
fissile	2A	center	long	MET6112	X	X			
fertile	2A	center	long	MET6112	X	X			
fertile	2A	center	long	MET6112	X	X			
fissile	2A	center	long	MET6112	X	X			

X = Damage/crack XC = Circumferential crack

Appendix D-1

(CONTINUED)

Type	ID 1	ID 2	ID 3	ID 4	PPyC Damage	OPyC Damage	SiC Damage	IPyC Damage	Comments
fertile	2A	center	long	MET6112	X	X			
fissile	2A	center	long	MET6112	X				
fissile	2A	center	long	MET6112	X	X			
fertile	2A	center	long	MET6112	X	X			
fertile	2A	center	long	MET6112	X	X			
fissile	2A	center	long	MET6112	X	X			
fertile	2A	center	long	MET6112	X	X			Failed buffer
fertile	2A	center	long	MET6112	X	X			
fertile	2A	center	long	MET6112	X	X			
fertile	2A	center	long	MET6112	X	X		X	
fissile	2A	center	long	MET6112	X	X			
fissile	2A	center	long	MET6112	X	X			
fissile	2A	center	long	MET6112	X	X		X	
fissile	2A	center	long	MET6112	X	X			
fertile	2A	center	long	MET6112	X	X			
fertile	2A	center	long	MET6112	X	X			
fertile	2A	center	long	MET6112	X	X			

X = Damage/crack XC = Circumferential crack

Appendix D-1

(CONTINUED)

Type	ID 1	ID 2	ID 3	ID 4	PPyC Damage	OPyC Damage	SiC Damage	IPyC Damage	Comments
fertile	2A	center	long	MET6112	X	X			
fertile	2A	center	long	MET6112	X				
fertile	2A	center	long	MET6112	X	X			
fertile	2A	center	long	MET6112	X	X			Failed buffer
fertile	2A	center	long	MET6112	X	X			
fertile	2A	center	long	MET6112	X	X		X	
fissile	2A	center	long	MET6112	X	X			
fertile	2A	center	long	MET6112	X	X			
fissile	2A	center	long	MET6112	X				
fertile	2A	center	long	MET6112	X	X			
fertile	2A	center	long	MET6112	X	X			
fissile	2A	bottom	long	MET6113	X				
fertile	2A	bottom	long	MET6113	X	X			
fissile	2A	bottom	long	MET6113	X	X			
fertile	2A	bottom	long	MET6113	X	X			
fissile	2A	bottom	long	MET6113	X	X			Failed buffer
fertile	2A	bottom	long	MET6113	X	X			

X = Damage/crack XC = Circumferential crack

Appendix D-1

(CONTINUED)

Type	ID 1	ID 2	ID 3	ID 4	PPyC Damage	OPyC Damage	SiC Damage	IPyC Damage	Comments
fertile	2A	center	long	MET6112	X	X			Failed buffer
fissile	2A	center	long	MET6112	X	X			
fissile	2A	center	long	MET6112	X	X			
fertile	2A	center	long	MET6112	X	X			
fertile	2A	center	long	MET6112	X	X			
fissile	2A	center	long	MET6112	X	X			
fertile	2A	center	long	MET6112	X	X			
fertile	2A	center	long	MET6112	X	X			
fertile	2A	center	long	MET6112	X	X			
fertile	2A	center	long	MET6112	X	X			Failed buffer
fertile	2A	center	long	MET6112	X	X			
fertile	2A	center	long	MET6112	X	X			
fertile	2A	center	long	MET6112	X	X			
fertile	2A	center	long	MET6112	X	X			
fissile	2A	center	long	MET6112	X	X			
fertile	2A	center	long	MET6112	X	X		X	
fertile	2A	center	long	MET6112	X	X			

X = Damage/crack XC = Circumferential crack

Appendix D-1

(CONTINUED)

Type	ID 1	ID 2	ID 3	ID 4	PPyC Damage	OPyC Damage	SiC Damage	IPyC Damage	Comments
fissile	2A	bottom	long	MET6113					
fissile	2A	bottom	long	MET6113	X	X		X	
fertile	2A	bottom	long	MET6113	X	X			
fissile	2A	bottom	long	MET6113	X	X			
fertile	2A	bottom	long	MET6113	X	X			
fertile	2A	bottom	long	MET6113	X	X			
fertile	2A	bottom	long	MET6113	X	X			
fertile	2A	bottom	long	MET6113	X	X		X	Failed buffer
fertile	2A	bottom	long	MET6113	X	X			
fertile	2A	bottom	long	MET6113	X	X			
fertile	2A	bottom	long	MET6113	X	X			
fertile	2A	bottom	long	MET6113	X				
fissile	2A	bottom	long	MET6113	X				
fertile	2A	bottom	long	MET6113	X				
fertile	2A	bottom	long	MET6113	X	X			
fertile	2A	bottom	long	MET6113	X	X			Failed buffer
fertile	2A	bottom	long	MET6113	X	X			

X = Damage/crack XC = Circumferential crack

Appendix D-1

(CONTINUED)

Type	ID 1	ID 2	ID 3	ID 4	PPyC Damage	OPyC Damage	SiC Damage	IPyC Damage	Comments
fertile	2A	bottom	long	MET6113	X	X			
fertile	2A	bottom	long	MET6113	X	X			
fertile	2A	bottom	long	MET6113	X	X		X	
fissile	2A	bottom	long	MET6113	X	X			
fertile	2A	bottom	long	MET6113	X	X			
fertile	2A	bottom	long	MET6113	X				
fertile	2A	bottom	long	MET6113	X				
fertile	2A	bottom	long	MET6113	X	X		X	
fertile	2A	bottom	long	MET6113	X	X		X	Failed buffer
fertile	2A	bottom	long	MET6113	X	X			
fissile	2A	bottom	long	MET6113	X	X			
fertile	2A	bottom	long	MET6113	X	X			
fissile	2A	bottom	long	MET6113	X	X			
fertile	2A	bottom	long	MET6113	X	X			
fertile	2A	bottom	long	MET6113	X	X			Failed buffer
fertile	2A	bottom	long	MET6113	X	X		X	
fertile	2A	bottom	long	MET6113	X	X			

X = Damage/crack XC = Circumferential crack

Appendix D-1

(CONTINUED)

Type	ID 1	ID 2	ID 3	ID 4	PPyC Damage	OPyC Damage	SiC Damage	IPyC Damage	Comments
fissile	2A	bottom	long	MET6113	X	X			
fissile	2A	bottom	long	MET6113	X	X			
fertile	2A	bottom	long	MET6113	X	X			
fertile	2A	bottom	long	MET6113	X	X		X	
fertile	2A	bottom	long	MET6113	X	X			
fissile	2A	bottom	long	MET6113	X	X			
fertile	2A	bottom	long	MET6113	X	X			
fertile	2A	bottom	long	MET6113	X	X			
fissile	2A	bottom	long	MET6113	X	X			
fertile	2A	bottom	long	MET6113	X	X			
fertile	2A	bottom	long	MET6113	X	X			
fertile	2A	bottom	long	MET6113	X				
fertile	2A	bottom	long	MET6113	X	X			
fertile	2A	bottom	long	MET6113	X	X			
fissile	2A	bottom	long	MET6113	X	X			
fissile	2A	bottom	long	MET6113	X	X			
fissile	2A	bottom	long	MET6113	X	X		X	Failed buffer

X = Damage/crack XC = Circumferential crack

Appendix D-1

(CONTINUED)

Type	ID 1	ID 2	ID 3	ID 4	PPyC Damage	OPyC Damage	SiC Damage	IPyC Damage	Comments
fertile	2A	bottom	long	MET6113	X	X		X	
fertile	2A	bottom	long	MET6113	X	X		X	
fertile	2A	bottom	long	MET6113	X	X		X	
fissile	2A	bottom	long	MET6113	X	X			
fertile	2A	bottom	long	MET6113	X	X		X	
fissile	2A	bottom	long	MET6113	X	X			
fertile	2A	bottom	long	MET6113	X	X			
fertile	2A	bottom	long	MET6113	X	X			Failed buffer
fertile	2A	bottom	long	MET6113	X	X			
fissile	2A	bottom	long	MET6113	X	X			
fissile	2A	bottom	long	MET6113	X	X			
fissile	2A	bottom	long	MET6113	X	X			
fissile	2B	seg 1	sec 2	MET6067	X	X			
fertile	2B	seg 1	sec 2	MET6067	X	X			
fertile	2B	seg 1	sec 2	MET6067	X	X			
fertile	2B	seg 1	sec 2	MET6067	X	X			
fertile	2B	seg 1	sec 2	MET6067	X	X			

X = Damage/crack XC = Circumferential crack

Appendix D-1

(CONTINUED)

Type	ID 1	ID 2	ID 3	ID 4	PPyC Damage	OPyC Damage	SiC Damage	IPyC Damage	Comments
fissile	2B	seg 1	sec 2	MET6067	X	X			
fertile	2B	seg 1	sec 2	MET6067	X	X			
fissile	2B	seg 1	sec 2	MET6067	X	X			
fertile	2B	seg 1	sec 2	MET6067	X	X			
fissile	2B	seg 1	sec 2	MET6067	X	X			
fertile	2B	seg 1	sec 2	MET6067	X	X			
fissile	2B	seg 1	sec 2	MET6067	X	X			
fertile	2B	seg 1	sec 2	MET6067	X	X			
fertile	2B	seg 1	sec 2	MET6067	X	X			
fertile	2B	seg 1	sec 2	MET6067	X	X		X	
fertile	2B	seg 1	sec 2	MET6067	X	X			
fissile	2B	seg 1	sec 2	MET6067	X	X			
fertile	2B	seg 1	sec 2	MET6067	X	X			
fertile	2B	seg 1	sec 2	MET6067	X	X			
fissile	2B	seg 1	sec 2	MET6067	X	X			
fertile	2B	seg 1	sec 2	MET6067	X	X			
fertile	2B	seg 1	sec 2	MET6067	X	X			

X = Damage/crack XC = Circumferential crack

Appendix D-1

(CONTINUED)

Type	ID 1	ID 2	ID 3	ID 4	PPyC Damage	OPyC Damage	SiC Damage	IPyC Damage	Comments
fissile	2B	seg 1	sec 2	MET6067	X	X			
fissile	2B	seg 1	sec 2	MET6067	X	X			
fertile	2B	seg 1	sec 2	MET6067	X	X			
fertile	2B	seg 1	sec 2	MET6067	X	X			
fissile	2B	seg 1	sec 2	MET6067	X	X			
fertile	2B	seg 1	sec 2	MET6067	X	X			
fissile	2B	seg 1	sec 2	MET6067	X	X			
fissile	2B	seg 1	sec 2	MET6067	X	X			
fertile	2B	seg 1	sec 2	MET6067	X	X		X	
fissile	2B	seg 1	sec 2	MET6067	X	X			
fertile	2B	seg 1	sec 2	MET6067	X	X			
fissile	2B	seg 1	sec 2	MET6067	X	X			
fertile	2B	seg 1	sec 2	MET6067	X	X			
fertile	2B	seg 1	sec 2	MET6067	X	X			
fertile	2B	seg 1	sec 2	MET6067	X	X			
fertile	2B	seg 1	sec 2	MET6067	X	X			
fertile	2B	seg 1	sec 2	MET6067	X	X			

X = Damage/crack XC = Circumferential crack

Appendix D-1

(CONTINUED)

Type	ID 1	ID 2	ID 3	ID 4	PPyC Damage	OPyC Damage	SiC Damage	IPyC Damage	Comments
fissile	2B	seg 1	sec 2	MET6067	X	X		X	
fissile	2B	seg 1	sec 2	MET6067	X	X			
fertile	2B	seg 1	sec 2	MET6067	X	X			
fertile	2B	seg 1	sec 2	MET6067	X	X			
fissile	2B	seg 1	sec 2	MET6067	X	X			
fertile	2B	seg 1	sec 2	MET6067	X	X		X	
fissile	2B	seg 1	sec 2	MET6067	X	X			
fissile	2B	seg 1	sec 2	MET6067	X	X			
fertile	2B	seg 1	sec 2	MET6067	X	X			
fertile	2B	seg 1	sec 2	MET6067	X	X			
fertile	2B	seg 2	sec 1	MET6067	X				Small inclusion in SiC photo 3
fertile	2B	seg 2	sec 1	MET6067					
fertile	2B	seg 2	sec 1	MET6067	X				
fertile	2B	seg 2	sec 1	MET6067	X		X		15 deg cresent shaped crack starting and ending at SiC/IPyC interface
fertile	2B	seg 2	sec 1	MET6067	X				
fertile	2B	seg 2	sec 1	MET6067	X		XC		Circumferential crack 15 deg
fertile	2B	seg 2	sec 1	MET6067	X		XC		Circumferential crack 20 deg photo 5

X = Damage/crack XC = Circumferential crack

Appendix D-1

(CONTINUED)

Type	ID 1	ID 2	ID 3	ID 4	PPyC Damage	OPyC Damage	SiC Damage	IPyC Damage	Comments
fissile	2B	seg 2	sec 1	MET6067					
fertile	2B	seg 2	sec 1	MET6067					
fissile	2B	seg 2	sec 1	MET6067	X				
fertile	2B	seg 2	sec 1	MET6067	X				
fertile	2B	seg 2	sec 1	MET6067					
fertile	2B	seg 2	sec 1	MET6067	X				
fertile	2B	seg 2	sec 1	MET6067	X				
fertile	2B	seg 2	sec 1	MET6067	X				
fertile	2B	seg 2	sec 1	MET6067	X				Blocky inclusive area in SiC photo 6
fertile	2B	seg 2	sec 1	MET6067	X				
fissile	2B	seg 2	sec 1	MET6067	X				Corrosion/reaction on edge inside SiC. photo 1
fertile	2B	seg 2	sec 1	MET6067	X		X		2 SiC cracks starting inside leading to center
fertile	2B	seg 2	sec 1	MET6067					
fertile	2B	seg 2	sec 1	MET6067	X				
fertile	2B	seg 2	sec 1	MET6067					
fertile	2B	seg 2	sec 1	MET6067					
fissile	2B	seg 2	sec 1	MET6067					

X = Damage/crack XC = Circumferential crack

Appendix D-1

(CONTINUED)

Type	ID 1	ID 2	ID 3	ID 4	PPyC Damage	OPyC Damage	SiC Damage	IPyC Damage	Comments
fissile	2B	seg 2	sec 1	MET6067	X				
fissile	2B	seg 2	sec 1	MET6067	X				
fissile	2B	seg 2	sec 1	MET6067					
fertile	2B	seg 2	sec 1	MET6067	X				
fissile	2B	seg 2	sec 1	MET6067					
fertile	2B	seg 2	sec 1	MET6067					
fissile	2B	seg 2	sec 1	MET6067					
fertile	2B	seg 2	sec 1	MET6067	X				
fissile	2B	seg 2	sec 1	MET6067					
fissile	2B	seg 2	sec 1	MET6067					
fertile	2B	seg 2	sec 1	MET6067					
fissile	2B	seg 2	sec 1	MET6067					
fertile	2B	seg 2	sec 1	MET6067	X				
fissile	2B	seg 2	sec 1	MET6067					
fertile	2B	seg 2	sec 2	MET6067	X				
fertile	2B	seg 2	sec 2	MET6067	X				
fertile	2B	seg 2	sec 2	MET6067	X				

X = Damage/crack XC = Circumferential crack

Appendix D-1

(CONTINUED)

Type	ID 1	ID 2	ID 3	ID 4	PPyC Damage	OPyC Damage	SiC Damage	IPyC Damage	Comments
fertile	2B	seg 2	sec 2	MET6067	X				
fertile	2B	seg 2	sec 2	MET6067	X				
fertile	2B	seg 2	sec 2	MET6067	X				
fertile	2B	seg 2	sec 2	MET6067	X				
fertile	2B	seg 2	sec 2	MET6067	X				
fissile	2B	seg 2	sec 2	MET6067	X				
fissile	2B	seg 2	sec 2	MET6067					Reaction/Corrosion in SiC near compact edge photo 1
fertile	2B	seg 2	sec 2	MET6067					
fissile	2B	seg 2	sec 2	MET6067	X				
fertile	2B	seg 2	sec 2	MET6067	X				
fertile	2B	seg 2	sec 2	MET6067	X				
fissile	2B	seg 2	sec 2	MET6067	X				
fertile	2B	seg 2	sec 2	MET6067	X				
fertile	2B	seg 2	sec 2	MET6067					
fertile	2B	seg 2	sec 2	MET6067	X				
fertile	2B	seg 2	sec 2	MET6067	X		X		Small crescent shaped crack on OD of SiC
fertile	2B	seg 2	sec 2	MET6067	X				

X = Damage/crack XC = Circumferential crack

Appendix D-1

(CONTINUED)

Type	ID 1	ID 2	ID 3	ID 4	PPyC Damage	OPyC Damage	SiC Damage	IPyC Damage	Comments
fertile	2B	seg 2	sec 2	MET6067	X				
fissile	2B	seg 2	sec 2	MET6067					
fertile	2B	seg 2	sec 2	MET6067	X				
fertile	2B	seg 2	sec 2	MET6067	X				
fissile	2B	seg 2	sec 2	MET6067	X				
fissile	2B	seg 2	sec 2	MET6067	X				
fertile	2B	seg 2	sec 2	MET6067					
fertile	2B	seg 2	sec 2	MET6067					
fissile	2B	seg 2	sec 2	MET6067					
fertile	2B	seg 2	sec 2	MET6067	X				4 very small crack/flaw near ID of SiC photo 3
fertile	2B	seg 2	sec 2	MET6067	X				
fissile	2B	seg 2	sec 2	MET6067	X				
fissile	2B	seg 2	sec 2	MET6067					
fissile	2B	seg 2	sec 2	MET6067					
fertile	2B	seg 2	sec 2	MET6067	X				
fertile	2B	seg 2	sec 2	MET6067					
fissile	2B	seg 2	sec 3	MET6067					

X = Damage/crack XC = Circumferential crack

Appendix D-1

(CONTINUED)

Type	ID 1	ID 2	ID 3	ID 4	PPyC Damage	OPyC Damage	SiC Damage	IPyC Damage	Comments
fertile	2B	seg 2	sec 3	MET6067					
fertile	2B	seg 2	sec 3	MET6067					
fertile	2B	seg 2	sec 3	MET6067					
fissile	2B	seg 2	sec 3	MET6067					
fertile	2B	seg 2	sec 3	MET6067					
fissile	2B	seg 2	sec 3	MET6067					
fertile	2B	seg 2	sec 3	MET6067					
fissile	2B	seg 2	sec 3	MET6067					
fertile	2B	seg 2	sec 3	MET6067					
fertile	2B	seg 2	sec 3	MET6067	X				
fissile	2B	seg 2	sec 3	MET6067					
fissile	2B	seg 2	sec 3	MET6067					
fertile	2B	seg 2	sec 3	MET6067					
fertile	2B	seg 2	sec 3	MET6067	X				
fissile	2B	seg 2	sec 3	MET6067					
fertile	2B	seg 2	sec 3	MET6067	X				
fertile	2B	seg 2	sec 3	MET6067					Gold Spot

X = Damage/crack XC = Circumferential crack

Appendix D-1

(CONTINUED)

Type	ID 1	ID 2	ID 3	ID 4	PPyC Damage	OPyC Damage	SiC Damage	IPyC Damage	Comments
fertile	2B	seg 2	sec 3	MET6067					
fertile	2B	seg 2	sec 3	MET6067	X				
fissile	2B	seg 2	sec 3	MET6067	X				
fertile	2B	seg 2	sec 3	MET6067					
fertile	2B	seg 2	sec 3	MET6067					
fissile	2B	seg 2	sec 3	MET6067					
fertile	2B	seg 2	sec 3	MET6067					
fertile	2B	seg 2	sec 3	MET6067					
fertile	2B	seg 2	sec 3	MET6067					
fissile	2B	seg 2	sec 3	MET6067					
fissile	2B	seg 2	sec 3	MET6067	X				
fertile	2B	seg 2	sec 3	MET6067					
fertile	2B	seg 2	sec 3	MET6067					
fertile	2B	seg 2	sec 3	MET6067					
fertile	2B	seg 2	sec 3	MET6067					
fertile	2B	seg 2	sec 3	MET6067	X				
fissile	2B	seg 2	sec 3	MET6067	X				

X = Damage/crack XC = Circumferential crack

Appendix D-1

(CONTINUED)

Type	ID 1	ID 2	ID 3	ID 4	PPyC Damage	OPyC Damage	SiC Damage	IPyC Damage	Comments
fertile	2B	seg 2	sec 3	MET6067					
fissile	2B	seg 2	sec 3	MET6067					
fertile	2B	seg 2	sec 3	MET6067	X				
fertile	2B	seg 2	sec 3	MET6067					
fissile	2B	seg 2	sec 3	MET6067	X	X			
fissile	2B	seg 2	sec 3	MET6067					
fertile	2B	seg 2	sec 3	MET6067					
fertile	2B	seg 2	sec 3	MET6067	X				
fertile	2B	seg 2	sec 3	MET6067					
fertile	2B	seg 2	sec 3	MET6067					
fertile	2B	seg 2	sec 3	MET6067	X				
fissile	2B	seg 2	sec 3	MET6067					
fertile	2B	seg 2	sec 3	MET6067					
fertile	2B	seg 2	sec 3	MET6067	X				
fertile	2B	seg 2	sec 3	MET6067	X				
fertile	2B	seg 2	sec 3	MET6067	X				
fertile	2B	seg 2	sec 3	MET6067	X				

X = Damage/crack XC = Circumferential crack

Appendix D-1

(CONTINUED)

Type	ID 1	ID 2	ID 3	ID 4	PPyC Damage	OPyC Damage	SiC Damage	IPyC Damage	Comments
fertile	2B	seg 2	sec 3	MET6067	X				
fissile	2B	seg 2	sec 3	MET6067	X				
fertile	2B	seg 2	sec 3	MET6067	X				
fertile	2B	seg 2	sec 3	MET6067	X				
fertile	2B	seg 3	sec 1	MET6073	X	X			
fertile	2B	seg 3	sec 1	MET6073	X	X			
fertile	2B	seg 3	sec 1	MET6073	X				
fissile	2B	seg 3	sec 1	MET6073	X	X			
fertile	2B	seg 3	sec 1	MET6073	X				
fissile	2B	seg 3	sec 1	MET6073	X	X			
fissile	2B	seg 3	sec 1	MET6073	X	X			
fertile	2B	seg 3	sec 1	MET6073	X			X	
fertile	2B	seg 3	sec 1	MET6073	X	X			
fertile	2B	seg 3	sec 1	MET6073	X	X	X		Partile 1 photo
fertile	2B	seg 3	sec 1	MET6073	X				
fertile	2B	seg 3	sec 1	MET6073	X	X			
fertile	2B	seg 3	sec 1	MET6073	X	X			

X = Damage/crack XC = Circumferential crack

Appendix D-1

(CONTINUED)

Type	ID 1	ID 2	ID 3	ID 4	PPyC Damage	OPyC Damage	SiC Damage	IPyC Damage	Comments
fissile	2B	seg 3	sec 1	MET6073	X	X			
fertile	2B	seg 3	sec 1	MET6073	X	X		X	
fissile	2B	seg 3	sec 1	MET6073	X	X			
fissile	2B	seg 3	sec 1	MET6073	X	X			
fertile	2B	seg 3	sec 1	MET6073	X	X			
fertile	2B	seg 3	sec 1	MET6073	X				
fertile	2B	seg 3	sec 1	MET6073	X				
fertile	2B	seg 3	sec 1	MET6073	X				
fertile	4A	seg 1	sec 3	MET6069	X	X		X	
fissile	4A	seg 1	sec 3	MET6069	X	X			
fertile	4A	seg 1	sec 3	MET6069	X	X			
fissile	4A	seg 1	sec 3	MET6069	X	X			
fertile	4A	seg 1	sec 3	MET6069	X	X		X	
fertile	4A	seg 1	sec 3	MET6069	X	X		X	
fertile	4A	seg 1	sec 3	MET6069	X	X			
fissile	4A	seg 1	sec 3	MET6069	X	X			
fissile	4A	seg 1	sec 3	MET6069	X	X			

X = Damage/crack XC = Circumferential crack

Appendix D-1

(CONTINUED)

Type	ID 1	ID 2	ID 3	ID 4	PPyC Damage	OPyC Damage	SiC Damage	IPyC Damage	Comments
fertile	4A	seg 1	sec 3	MET6069	X	X		X	
fertile	4A	seg 1	sec 3	MET6069	X	X		X	
fissile	4A	seg 1	sec 3	MET6069	X	X			
fertile	4A	seg 1	sec 3	MET6069	X	X			
fertile	4A	seg 1	sec 3	MET6069	X	X		X	
fertile	4A	seg 1	sec 3	MET6069	X	X			
fissile	4A	seg 1	sec 3	MET6069	X	X			
fertile	4A	seg 1	sec 3	MET6069	X	X		X	
fissile	4A	seg 1	sec 3	MET6069	X	X			
fissile	4A	seg 1	sec 3	MET6069	X	X		X	
fertile	4A	seg 1	sec 3	MET6069	X	X		X	
fissile	4A	seg 1	sec 3	MET6069	X	X			
fertile	4A	seg 1	sec 3	MET6069	X				
fertile	4A	seg 1	sec 3	MET6069	X	X			
fertile	4A	seg 1	sec 3	MET6069	X	X			
fissile	4A	seg 1	sec 3	MET6069	X	X		X	
fissile	4A	seg 1	sec 3	MET6069	X	X		X	

X = Damage/crack XC = Circumferential crack

Appendix D-1

(CONTINUED)

Type	ID 1	ID 2	ID 3	ID 4	PPyC Damage	OPyC Damage	SiC Damage	IPyC Damage	Comments
fertile	4A	seg 1	sec 3	MET6069	X	X			
fertile	4A	seg 1	sec 3	MET6069	X	X		X	
fertile	4A	seg 1	sec 3	MET6069	X	X			
fertile	4A	seg 1	sec 3	MET6069	X	X	XC		Heavy circumferential inclusion
fertile	4A	seg 1	sec 3	MET6069	X	X			
fertile	4A	seg 1	sec 3	MET6069	X	X		X	
fertile	4A	seg 1	sec 3	MET6069	X	X			
fertile	4A	seg 1	sec 3	MET6069	X	X		X	
fertile	4A	seg 1	sec 3	MET6069	X	X			
fertile	4A	seg 1	sec 3	MET6069	X	X		X	
fertile	4A	seg 1	sec 3	MET6069	X	X			
fertile	4A	seg 1	sec 3	MET6069	X	X			
fertile	4A	seg 1	sec 3	MET6069	X	X			
fertile	4A	seg 1	sec 3	MET6069	X	X		X	
fertile	4A	seg 1	sec 3	MET6069	X	X		X	
fissile	4A	seg 1	sec 3	MET6069	X	X			
fertile	4A	seg 1	sec 4	MET6069	X	X			

X = Damage/crack XC = Circumferential crack

Appendix D-1

(CONTINUED)

Type	ID 1	ID 2	ID 3	ID 4	PPyC Damage	OPyC Damage	SiC Damage	IPyC Damage	Comments
fissile	4A	seg 1	sec 4	MET6069	X	X			Plastic deformation in kernel
fissile	4A	seg 1	sec 4	MET6069	X	X			Plastic deformation in kernel
fertile	4A	seg 1	sec 4	MET6069	X	X		X	
fertile	4A	seg 1	sec 4	MET6069	X	X		X	
fertile	4A	seg 1	sec 4	MET6069	X	X			
fertile	4A	seg 1	sec 4	MET6069	X	X		X	
fertile	4A	seg 1	sec 4	MET6069	X	X			
fertile	4A	seg 1	sec 4	MET6069	X	X		X	
fertile	4A	seg 1	sec 4	MET6069	X	X		X	
fertile	4A	seg 1	sec 4	MET6069	X	X			
fissile	4A	seg 1	sec 4	MET6069	X	X			
fertile	4A	seg 1	sec 4	MET6069	X	X			Unusal buffer
fertile	4A	seg 1	sec 4	MET6069	X	X			
fertile	4A	seg 1	sec 4	MET6069	X	X			
fertile	4A	seg 1	sec 4	MET6069	X	X			
fertile	4A	seg 1	sec 4	MET6069	X	X			
fertile	4A	seg 1	sec 4	MET6069	X	X			

X = Damage/crack XC = Circumferential crack

Appendix D-1

(CONTINUED)

Type	ID 1	ID 2	ID 3	ID 4	PPyC Damage	OPyC Damage	SIC Damage	IPyC Damage	Comments
fissile	4A	seg 1	sec 4	MET6069	X	X	X	X	3 cracks, Deformed kernel
fertile	4A	seg 1	sec 4	MET6069	X	X			
fertile	4A	seg 1	sec 4	MET6069	X	X		X	
fissile	4A	seg 1	sec 4	MET6069	X	X			Deformed kernel
fissile	4A	seg 1	sec 4	MET6069	X	X			
fissile	4A	seg 1	sec 4	MET6069	X	X			
fertile	4A	seg 1	sec 4	MET6069	X	X			
fissile	4A	seg 1	sec 4	MET6069	X	X			
fertile	4A	seg 1	sec 4	MET6069	X	X			
fertile	4A	seg 1	sec 4	MET6069	X	X			
fertile	4A	seg 1	sec 4	MET6069	X	X		X	
fissile	4A	seg 1	sec 4	MET6069	X	X		X	Deformed kernel
fertile	4A	seg 1	sec 4	MET6069	X	X		X	
fertile	4A	seg 1	sec 4	MET6069	X	X		X	
fertile	4A	seg 1	sec 4	MET6069	X	X		X	
fertile	4A	seg 1	sec 4	MET6069	X	X		X	
fertile	4A	seg 1	sec 4	MET6069	X	X			

X = Damage/crack XC = Circumferential crack

Appendix D-1

(CONTINUED)

Type	ID 1	ID 2	ID 3	ID 4	PPyC Damage	OPyC Damage	SiC Damage	IPyC Damage	Comments
fertile	4A	seg 1	sec 4	MET6069	X	X			
fertile	4A	seg 1	sec 4	MET6069	X	X	X	X	A Y shape thru SiC & short circumferential
fertile	4A	seg 1	sec 4	MET6069	X	X		X	
fertile	4A	seg 1	sec 4	MET6069	X	X			
fertile	4A	seg 1	sec 4	MET6069	X	X			
fertile	4A	seg 1	sec 4	MET6069	X	X			
fissile	4A	seg 1	sec 4	MET6069	X	X			Deformed kernel
fertile	4A	seg 1	sec 4	MET6069	X	X			
fertile	4A	seg 1	sec 4	MET6069	X	X	XC		Circumferential crack 70 deg breaks to inside of SiC
fertile	4A	seg 1	sec 4	MET6069	X				
fertile	4A	seg 1	sec 4	MET6069	X	X			
fertile	4A	seg 1	sec 4	MET6069	X	X			
fertile	4A	seg 1	sec 4	MET6069	X	X		X	
fertile	4A	seg 1	sec 4	MET6069	X	X			
fertile	4A	seg 1	sec 4	MET6069	X	X			
fissile	4A	seg 1	sec 5	MET6069	X	X	X	X	Outer surface SiC radial cracks photo 4
fertile	4A	seg 1	sec 5	MET6069	X	X			

X = Damage/crack XC = Circumferential crack

Appendix D-1

(CONTINUED)

Type	ID 1	ID 2	ID 3	ID 4	PPyC Damage	OPyC Damage	SiC Damage	IPyC Damage	Comments
fertile	4A	seg 1	sec 5	MET6069	X	X		X	
fertile	4A	seg 1	sec 5	MET6069	X	X		X	
fertile	4A	seg 1	sec 5	MET6069	X	X			
fissile	4A	seg 1	sec 5	MET6069	X	X		X	UCO shows plastic deformation photo 5
fertile	4A	seg 1	sec 5	MET6069	X	X			
fertile	4A	seg 1	sec 5	MET6069	X	X	X	X	4 cracks in SiC SiC separation photo 1
fissile	4A	seg 1	sec 5	MET6069	X	X		X	plastic deformation of kernel corrosion photo series 3
fertile	4A	seg 1	sec 5	MET6069	X	X			
fissile	4A	seg 1	sec 5	MET6069	X	X			Plastic deformation in UCO
fertile	4A	seg 1	sec 5	MET6069	X	X		X	
fertile	4A	seg 1	sec 5	MET6069	X	X		X	
fertile	4A	seg 1	sec 5	MET6069	X	X	X	X	
fertile	4A	seg 1	sec 5	MET6069	X	X	X	X	Cresent shaped crack in SiC inner surface photo 6
fissile	4A	seg 1	sec 5	MET6069	X	X		X	
fertile	4A	seg 1	sec 5	MET6069	X	X		X	
fertile	4A	seg 1	sec 5	MET6069	X	X			

X = Damage/crack XC = Circumferential crack

Appendix D-1

(CONTINUED)

Type	ID 1	ID 2	ID 3	ID 4	PPyC Damage	OPyC Damage	SiC Damage	IPyC Damage	Comments
fertile	4A	seg 1	sec 5	MET6069	X	X		X	
fertile	4A	seg 1	sec 5	MET6069	X	X		X	
fertile	4A	seg 1	sec 5	MET6069	X	X			
fertile	4A	seg 1	sec 5	MET6069	X	X			
fissile	4A	seg 1	sec 5	MET6069	X	X			
fertile	4A	seg 1	sec 5	MET6069	X	X		X	
fertile	4A	seg 1	sec 5	MET6069	X	X		X	
fertile	4A	seg 1	sec 5	MET6069	X	X		X	
fertile	4A	seg 1	sec 5	MET6069	X	X			
fissile	4A	seg 1	sec 5	MET6069	X	X			
fertile	4A	seg 1	sec 5	MET6069	X	X		X	
fissile	4A	seg 1	sec 5	MET6069	X	X			Slight plastic deformation
fertile	4A	seg 1	sec 5	MET6069	X	X			
fertile	4A	seg 1	sec 5	MET6069	X	X			
fissile	4A	seg 1	sec 5	MET6069	X	X			
fertile	4A	seg 1	sec 5	MET6069	X	X		X	
fertile	4A	seg 1	sec 5	MET6069	X	X			

X = Damage/crack XC = Circumferential crack

Appendix D-1

(CONTINUED)

Type	ID 1	ID 2	ID 3	ID 4	PPyC Damage	OPyC Damage	SiC Damage	IPyC Damage	Comments
fertile	4A	seg 1	sec 5	MET6069	X	X		X	
fertile	4A	seg 1	sec 5	MET6069	X	X			
fertile	4A	seg 1	sec 5	MET6069	X	X			
fertile	4A	seg 1	sec 5	MET6069	X	X			
fertile	4A	seg 1	sec 5	MET6069	X	X			
fertile	4A	seg 1	sec 5	MET6069	X	X		X	
fertile	4A	seg 1	sec 5	MET6069	X	X			
fertile	4A	seg 1	sec 5	MET6069	X	X			
fertile	4A	seg 1	sec 5	MET6069	X	X			
fertile	4A	seg 1	sec 5	MET6069	X	X			
fertile	4A	seg 1	sec 5	MET6069	X	X	X	X	Cresent shaped cracks starting at inner surface photo 2

X = Damage/crack XC = Circumferential crack

APPENDIX D-2

PARTICLES WITH SiC DAMAGE

Appendix D-2

PARTICLES WITH SiC DAMAGE

Type	ID 1	ID 2	ID 3	ID 4	PPyC Damage	OPyC Damage	SiC Damage	IPyC Damage	Comments
fertile	1C	seg 1	sec 6	MET6068	X		X		
fertile	1C	seg 1	sec 6	MET6068	X		X		One piece broke off and adhere to IPyC
fertile	2B	seg 2	sec 1	MET6067	X		X		15 deg cresent shaped crack starting and ending at SiC/IPyC interface
fertile	2B	seg 2	sec 1	MET6067	X		X		2 SiC cracks starting inside leading to center
fertile	2B	seg 2	sec 2	MET6067	X		X		Small crescent shaped crack on OD of SiC
fertile	2B	seg 3	sec 1	MET6073	X	X	X		Partile 1 photo
fissile	4A	seg 1	sec 4	MET6069	X	X	X	X	3 cracks Deformed kernel
fertile	4A	seg 1	sec 4	MET6069	X	X	X	X	A Y shape thru SiC & short circumferential
fissile	4A	seg 1	sec 5	MET6069	X	X	X	X	Outer surface SiC radial cracks photo 4
fertile	4A	seg 1	sec 5	MET6069	X	X	X	X	4 cracks in SiC SiC separation photo 1
fertile	4A	seg 1	sec 5	MET6069	X	X	X	X	
fertile	4A	seg 1	sec 5	MET6069	X	X	X	X	Cresent shaped crack in SIC inner surface photo 6
fertile	4A	seg 1	sec 5	MET6069	X	X	X	X	Cresent shaped cracks starting at inner surface photo 2

X = Damage/crack XC = Circumferential crack

APPENDIX D-3

PARTICLES WITH IPyC DAMAGE

Appendix D-3

PARTICLES WITH IPyC DAMAGE

Type	ID 1	ID 2	ID 3	ID 4	PPyC Damage	OPyC Damage	SiC Damage	IPyC Damage	Comments
fertile	1C	seg 1	sec 4	MET6068	X	X		X	
fissile	2A	top	long	MET6111	X	X		X	
fertile	2A	center	long	MET6112	X	X		X	Failed buffer
fertile	2A	center	long	MET6112	X	X		X	
fertile	2A	center	long	MET6112	X	X		X	
fissile	2A	center	long	MET6112	X	X		X	
fissile	2A	center	long	MET6112	X	X		X	
fertile	2A	center	long	MET6112	X	X		X	
fissile	2A	center	long	MET6112	X	X		X	
fertile	2A	center	long	MET6112	X	X		X	
fertile	2A	center	long	MET6112	X	X		X	
fissile	2A	bottom	long	MET6113	X	X		X	
fertile	2A	bottom	long	MET6113	X	X		X	Failed buffer
fertile	2A	bottom	long	MET6113	X	X		X	
fertile	2A	bottom	long	MET6113	X	X		X	
fertile	2A	bottom	long	MET6113	X	X		X	Failed buffer
fertile	2A	bottom	long	MET6113	X	X		X	

X = Damage/crack XC = Circumferential crack

Appendix D-3

(CONTINUED)

Type	ID 1	ID 2	ID 3	ID 4	PPyC Damage	OPyC Damage	SiC Damage	IPyC Damage	Comments
fertile	2A	bottom	long	MET6113	X	X		X	
fissile	2A	bottom	long	MET6113	X	X		X	Failed buffer
fertile	2A	bottom	long	MET6113	X	X		X	
fertile	2A	bottom	long	MET6113	X	X		X	
fertile	2A	bottom	long	MET6113	X	X		X	
fertile	2A	bottom	long	MET6113	X	X		X	
fertile	2B	seg 1	sec 2	MET6067	X	X		X	
fertile	2B	seg 1	sec 2	MET6067	X	X		X	
fissile	2B	seg 1	sec 2	MET6067	X	X		X	
fertile	2B	seg 1	sec 2	MET6067	X	X		X	
fertile	2B	seg 3	sec 1	MET6073	X			X	
fertile	2B	seg 3	sec 1	MET6073	X	X		X	
fertile	4A	seg 1	sec 3	MET6069	X	X		X	
fertile	4A	seg 1	sec 3	MET6069	X	X		X	
fertile	4A	seg 1	sec 3	MET6069	X	X		X	
fertile	4A	seg 1	sec 3	MET6069	X	X		X	
fertile	4A	seg 1	sec 3	MET6069	X	X		X	

X = Damage/crack XC = Circumferential crack

Appendix D-3

(CONTINUED)

Type	ID 1	ID 2	ID 3	ID 4	PPyC Damage	OPyC Damage	SiC Damage	IPyC Damage	Comments
fertile	4A	seg 1	sec 3	MET6069	X	X		X	
fertile	4A	seg 1	sec 3	MET6069	X	X		X	
fissile	4A	seg 1	sec 3	MET6069	X	X		X	
fertile	4A	seg 1	sec 3	MET6069	X	X		X	
fissile	4A	seg 1	sec 3	MET6069	X	X		X	
fissile	4A	seg 1	sec 3	MET6069	X	X		X	
fertile	4A	seg 1	sec 3	MET6069	X	X		X	
fertile	4A	seg 1	sec 3	MET6069	X	X		X	
fertile	4A	seg 1	sec 3	MET6069	X	X		X	
fertile	4A	seg 1	sec 3	MET6069	X	X		X	
fertile	4A	seg 1	sec 3	MET6069	X	X		X	
fertile	4A	seg 1	sec 3	MET6069	X	X		X	
fertile	4A	seg 1	sec 4	MET6069	X	X		X	
fertile	4A	seg 1	sec 4	MET6069	X	X		X	
fertile	4A	seg 1	sec 4	MET6069	X	X		X	
fertile	4A	seg 1	sec 4	MET6069	X	X		X	
fertile	4A	seg 1	sec 4	MET6069	X	X		X	

X = Damage/crack XC = Circumferential crack

Appendix D-3

PARTICLES WITH IPyC DAMAGE

Type	ID 1	ID 2	ID 3	ID 4	PPyC Damage	OPyC Damage	SiC Damage	IPyC Damage	Comments
fissile	4A	seg 1	sec 4	MET6069	X	X	X	X	3 cracks Deformed kernel
fertile	4A	seg 1	sec 4	MET6069	X	X		X	
fertile	4A	seg 1	sec 4	MET6069	X	X		X	
fissile	4A	seg 1	sec 4	MET6069	X	X		X	Deformed kernel
fertile	4A	seg 1	sec 4	MET6069	X	X		X	
fertile	4A	seg 1	sec 4	MET6069	X	X		X	
fertile	4A	seg 1	sec 4	MET6069	X	X		X	
fertile	4A	seg 1	sec 4	MET6069	X	X		X	
fertile	4A	seg 1	sec 4	MET6069	X	X	X	X	A Y shape thru SiC & short circumferential
fertile	4A	seg 1	sec 4	MET6069	X	X		X	
fertile	4A	seg 1	sec 4	MET6069	X	X		X	
fissile	4A	seg 1	sec 5	MET6069	X	X	X	X	Outer surface SiC radial cracks photo 4
fertile	4A	seg 1	sec 5	MET6069	X	X		X	
fertile	4A	seg 1	sec 5	MET6069	X	X		X	
fissile	4A	seg 1	sec 5	MET6069	X	X		X	UCO shows plastic deformation photo 5
fertile	4A	seg 1	sec 5	MET6069	X	X	X	X	4 cracks in SiC SiC separation photo 1
fissile	4A	seg 1	sec 5	MET6069	X	X		X	plastic deformation of kernel corrosion photo series 3

X = Damage/crack XC = Circumferential crack

Appendix D-3

(CONTINUED)

Type	ID 1	ID 2	ID 3	ID 4	PPyC Damage	OPyC Damage	SiC Damage	IPyC Damage	Comments
fertile	4A	seg 1	sec 5	MET6069	X	X		X	
fertile	4A	seg 1	sec 5	MET6069	X	X		X	
fertile	4A	seg 1	sec 5	MET6069	X	X	X	X	
fertile	4A	seg 1	sec 5	MET6069	X	X	X	X	Cresent shaped crack in SiC inner surface photo 6
fissile	4A	seg 1	sec 5	MET6069	X	X		X	
fertile	4A	seg 1	sec 5	MET6069	X	X		X	
fertile	4A	seg 1	sec 5	MET6069	X	X		X	
fertile	4A	seg 1	sec 5	MET6069	X	X		X	
fertile	4A	seg 1	sec 5	MET6069	X	X		X	
fertile	4A	seg 1	sec 5	MET6069	X	X		X	
fertile	4A	seg 1	sec 5	MET6069	X	X		X	
fertile	4A	seg 1	sec 5	MET6069	X	X		X	
fertile	4A	seg 1	sec 5	MET6069	X	X		X	
fertile	4A	seg 1	sec 5	MET6069	X	X		X	
fertile	4A	seg 1	sec 5	MET6069	X	X	X	X	Cresent shaped cracks starting at inner surface photo 2

X = Damage/crack XC = Circumferential crack

APPENDIX D-4

HRB-21 PARTICLE FAILURE SUMMARY

Appendix D-4

HRB-21 PARTICLE FAILURE SUMMARY

Compact 1C					
Particle Type	Number Examined	Number of Failures (percent failures)			
		IPyC	SiC	OPyC	PPyC
fissile	99	0	0	32	78
		0.00%	0.00%	32.32%	78.79%
fertile	197	1	2	39	147
		0.51%	1.02%	19.80%	74.62%
total	296	1	2	71	225
		0.34%	0.68%	23.99%	76.01%

Compact 2A					
Particle Type	Number Examined	Number of Failures (percent failures)			
		IPyC	SiC	OPyC	PPyC
fissile	67	6	0	51	62
		8.96%	0.00%	76.12%	92.54%
fertile	141	16	0	112	137
		11.35%	0.00%	79.43%	97.16%
total	208	22	0	163	199
		10.58%	0.00%	78.37%	95.67%

Appendix D-4

(CONTINUED)

Compact 2B					
Particle Type	Number Examined	Number of Failures (percent failures)			
		IPyC	SiC	OPyC	PPyC
fissile	66	1	0	26	40
		1.52%	0.00%	39.39%	60.61%
fertile	134	5	4	38	97
		3.73%	2.99%	28.36%	72.39%
total	200	6	4	64	137
		3.00%	2.00%	32.00%	68.50%

Compact 4A					
Particle Type	Number Examined	Number of Failures (percent failures)			
		IPyC	SiC	OPyC	PPyC
fissile	31	9	2	31	31
		29.03%	6.45%	100.00%	fertile 100.00%
fertile	107	46	5	105	107
		42.99%	4.67%	98.13%	100.00%
total	138	55	7	136	138
		39.86%	5.07%	98.55%	100.00%

INTERNAL DISTRIBUTION

1-2. Central Research Library
3. Document Reference Section
4-5. Laboratory Records Department
6. Laboratory Records, ORNL RC
7. ORNL Patent Section
8-10. M&C Records Office
11-15. C. A. Baldwin
16. G. L. Bell
17. C. R. Brinkman
18. L. C. Emerson
19. W. A. Gabbard
20-24. M. L. Grossbeck
25. O. F. Kimball
26. G. E. Michaels
27-31. F. C. Montgomery
32-36. R. N. Morris
37. B. F. Myers
38-42. N. H. Packan
43. J. T. Parks
44. P. L. Rittenhouse
45. O. M. Stansfield

EXTERNAL DISTRIBUTION

46. ABB/CENP, M/S 9354-0422, 1000 Prospect Hill Road, Windsor, CT 06095-0500

    S. A. Caspersson

47. BECHTEL NATIONAL, P.O. Box 193965, 15D7, San Francisco, CA 94119

    S. K. Ghose

48. GAS-COOLED REACTOR ASSOCIATES, 10240 Sorrento Valley Road, Suite 300, San Diego, CA 92121-1605

    L. D. Mears

49-57. GENERAL ATOMICS, P.O. Box 85608, San Diego, CA 92186-9784

    R. Acharya (5)
    G. L. Lee
    D. W. McEachern
    W. J. Scheffel
    C. B. Scott

58. KNOLLS ATOMIC POWER LABORATORY, P.O. Box 1072, Bldg. G2, Room 152, Schenectady, NY 12301-1072

    M. J. Kania

59. PLANT DESIGN CONTROL OFFICE-EAST, 3206 Tower Oaks Blvd., Suite 300, Rockville, MD 20852

R. R. Mills

60-61. PLANT DESIGN CONTROL OFFICE-WEST, P.O. Box 85608, San Diego, CA 92186-9784

J. Kendall
Dave Pettycord

62. STONE & WEBSTER, P.O. Box 2325, Boston, MA 02107

W. J. Parker

63. WESTINGHOUSE ELECTRIC CORPORATION, P.O. Box 79, Bettis Atomic Power Lab, West Mifflin, PA 15122-0079

J. L. Hollenbeck

64-66. U.S. DEPARTMENT OF ENERGY, Office of Nuclear Energy, Actinide Recycle Division, NE-42, Washington, DC 20585

Warren P. Chernock, Acting Director
F. J. Goldner
J. W. Herczeg

67. U.S. DEPARTMENT OF ENERGY, Oakland Operations Office, 1301 Clay Street, Oakland, CA 94612-5208

S. El-Safwany

68-69. U.S. DEPARTMENT OF ENERGY, Oak Ridge Operations, ER-111, Building 4500N, MS 6269, Oak Ridge, TN 37831-6269

H. E. Clark
S. R. Martin

70-72. DOE, OFFICE OF SCIENTIFIC AND TECHNICAL INFORMATION, Office of Information Services, P.O. Box 62, Oak Ridge, TN 37831

For distribution by microfiche as shown in TIC-4500, Distribution Category UC-522T (Gas-Cooled Reactor Technology)